

UNIVERSIDAD DE GRANADA



**SÍNTESIS DE NUEVOS MATERIALES
MULTIFUNCIONALES BASADOS EN
LIGANDOS NITROGENADOS CON GRUPOS
CARBOXILATO**

Tesis Doctoral

DEPARTAMENTO DE QUÍMICA INORGÁNICA

PROGRAMA DEL DOCTORADO EN QUÍMICA

ANTONIO ANDRÉS GARCÍA VALDIVIA

JULIO 2020

**SÍNTESIS DE NUEVOS MATERIALES MULTIFUNCIONALES
BASADOS EN LIGANDOS NITROGENADOS CON GRUPOS
CARBOXILATO**

Memoria de Tesis Doctoral presentada por Antonio Andrés García
Valdivia para aspirar al Grado de Doctor por la Universidad de
Granada

Fdo. Antonio Andrés García Valdivia

DIRECTORES DE TESIS

Dr. Antonio Rodríguez Diéguez

Dra. Belén Fernández López

Editor: Universidad de Granada. Tesis Doctorales
Autor: Antonio Andrés García Valdivia
ISBN: 978-84-1306-637-0
URI: <http://hdl.handle.net/10481/63917>

Agradecimientos

Sin duda alguna los agradecimientos han sido la parte más difícil de escribir, no solo por el intento de no dejar a nadie atrás si no por la gran carga emocional reflejada en estas palabras hacia las personas que me han apoyado durante esta etapa de mi vida.

En primer lugar, quiero agradecer a mis directores de Tesis, el Prof. Antonio Rodríguez Diéguez y a la Dra. Belén Fernández López, sin ellos no hubiese podido llevar a buen puerto este trabajo. En especial a Antonio por su dedicación y total entrega para que todo saliese lo mejor posible, llegando a ser más que un director, un amigo. No sé que más decir para agradecer todo lo que has hecho, tanto en el ámbito académico, como personal.

A los doctores José Manuel Seco Botana, Javier Cepeda, José Ángel García, Itziar Oyarzabal, Eider San Sebastián, Sonia Pérez Yañez y a los doctorandos Estitxu Echenique Errandonea y Andoni Zabala Lekuona de la Universidad del País Vasco por su ayuda en la realización e interpretación de las medidas de magnetismo y luminiscencia presentes en la mayoría de los artículos de esta Tesis.

Al doctor Santiago Gómez Ruiz de la Universidad Rey Juan Carlos, a los doctores Elisa Abas y Mariano Laguna de la Universidad de Zaragoza, a los doctores Marta Medina Odonnell, José Antonio Lupiáñez y Fernando Reyes Zurita y la doctoranda Fatin Jannu de la Universidad de Granada, por la realización de los diferentes ensayos biológicos antitumorales y anticancerígenos incluidos en esta Tesis.

A los doctores José Manuel Delgado López y Gloria Belén Ramírez Rodríguez de la Universidad de Granada por su ayuda con los ensayos citotóxicos de muchos de los materiales presentes en esta Tesis.

Al doctor Ginés Miguel Esteban Parra de la Universidad de Granada y al doctor José Manuel Méndez Arriaga de la Universidad Rey Juan Carlos por su ayuda con todo lo relacionado con las medidas biológicas antiparasitarias.

Al doctor Manuel Pérez Mendoza de la Universidad de Granada y a los doctores Guillermo Mínguez Espallargas y Manuel Souto del Instituto de Ciencia Molecular (ICMol) de Valencia por las medidas de adsorción realizadas a algunos de los compuestos contenidas en esta Tesis.

Al doctor Ignacio Fernández de la Nieves de la Universidad de Almería por la ayuda a la hora de llevar a cabo la síntesis de algunos de los ligandos utilizados durante la realización de esta Tesis.

Al doctor Duane Choquesillo Lazarte del Laboratorio de Estudios Cristalográficos de Granada por su ayuda en la resolución estructural de aquellos compuestos que debido a su complejidad se escapaban de mi conocimiento.

Al Centro de Instrumentación Científica, y en especial a Pepe Romero por toda su ayuda a la hora de realizar las medidas de Difracción de Rayos X así como hacer que los días de medidas fueran más amenos.

A mi "Petifu" por todo el apoyo y cariño que me ha brindado desde que la conocí hasta estos mismos instantes. Agradezco el día que te conocí, en el cual no sabía aún lo importante que serías y eres para mí. Me faltan palabras para agradecer a la persona más perfecta del mundo por cruzarse en mi vida. Gracias.

A mi familia y en especial a mis abuelos, padres y hermano por apoyarme en todo lo que he hecho y permitirme realizar todos mis estudios sin preocupaciones ajenas a los mismos, por levantarme en mis caídas y por alegrarse de mis triunfos. Gracias a ellos estoy aquí.

A mis amigos Medel, Lucía, Gloria y Tomás por su amistad a lo largo de la carrera, así como después de ésta. A mis amigos y compañeros de hobbies Lopey, Jesús, Ennachachi, Juanmi y Juanlu por su amistad durante todos los años desde que los conocí.

A mis compañeros de Laboratorio Amalia, Cristi, Arturo, Maria, Mayte, Ainhoa, Ana Delia, Carmen y Javi por hacer el día a día en el trabajo más entretenido y llevadero.

Por último agradecer al Grupo FQM394 y a la Junta de Andalucía por los proyectos (FQM-1484 y FQM-394) así como al Ministerio de Economía y competitividad por los proyectos (PGC2018-102052-B-C21 y PGC2018-102052-A-C22) sin los cuales el desarrollo de esta Tesis hubiese resultado imposible.

Finalmente quiero agradecer a todas las personas que han ido apareciendo a lo largo de mi vida y que, por azares del destino, no les he podido agradecer directamente en estas palabras, pues les debo el haber llegado a donde estoy y como soy.

Resumen

En las últimas décadas, los compuestos de coordinación han sido unos de los materiales más ampliamente estudiados por la comunidad científica. El interés por estos compuestos radica en el gran abanico de propiedades que pueden llegar a exhibir. Esta diversidad de posibles propiedades los convierte en materiales con un gran potencial de aplicación en casi cualquier campo como, por ejemplo, en magnetismo, luminiscencia, catálisis, almacenamiento y separación de gases, biomedicina, etcétera.

El conocimiento de la estructura molecular de estos sistemas va a ser la base para diseñarlos, sintetizarlos y poder modular sus propiedades con el fin de mejorar las propiedades físicas exhibidas.

Sin embargo, lo más interesante de estos materiales no consiste en que sean capaces de presentar distintos tipos de propiedades, sino en que logren presentar varias de estas características simultáneamente obteniéndose así, compuestos de coordinación multifuncionales. Esta multifuncionalidad permite a estos materiales adentrarse en otros campos aun más específicos como son los sensores o los sistemas magnético-ópticos. Por todo lo mencionado anteriormente, el desarrollo y optimización de compuestos de coordinación multifuncionales es, hoy en día, uno de los retos de la Química de la Coordinación.

Partiendo de esta premisa, el trabajo y desarrollo de esta Tesis doctoral trata sobre la síntesis, la caracterización estructural y el estudio de las propiedades físico-químicas y biológicas de compuestos de coordinación basados en ligandos nitrogenados con grupos carboxilato sintetizados mediante métodos solvotermiales.

Todos los materiales que se presentan en esta Tesis Doctoral han sido sintetizados en nuestro laboratorio y se han caracterizado mediante difracción de rayos X de monocristal (DRX) complementada por otras técnicas instrumentales tales como espectroscopía Infrarroja (IR), análisis elemental (AE) y/o difracción de rayos X en polvo (DRXP).

La agrupación de las distintas familias de materiales sintetizados viene dividida en Capítulos (para aquellos artículos publicados o aceptados) y anexos (aquellos artículos que están en fase de ser enviados próximamente a revistas científicas).

En primera instancia se utilizó un ligando heterocíclico nitrogenado con un grupo carboxilato (ácido 1-metil-1H-imidazol-5-carboxílico (mimc)) y metales de la primera serie de transición, obteniéndose tres compuestos bidimensionales y un compuesto mononuclear, recogidos en el Capítulo 1. Los materiales más interesantes recogidos en esta familia son, por una parte, el $[\text{Co}(\mu\text{-mimc})_2]_n$ pues presenta a nivel magnético relajación lenta de la magnetización con una barrera térmica de 26K, situándose entre los compuestos de Cobalto con mayor temperatura de bloqueo (14K). Por otra parte, el compuesto $[\text{Cd}(\mu\text{-mimc})_2(\text{H}_2\text{O})]_n$ presenta una fosforescencia de aproximadamente un segundo a baja temperatura, corroborada por cálculos TD-DFT estimando que dicha fosforescencia está regida por un mecanismo LCCT (singlete-singlete y triplete-singlete).

Con la intención de aumentar el ángulo del ciclo aromático y a su vez mantener la distancia entre los grupos funcionales coordinantes en las estructuras, se optó por utilizar el ácido 5-bromonicotínico (5-BrNic), obteniéndose cuatro compuestos de coordinación con diferentes estructuras y dimensionalidades basados en iones lantánidos, recogidos en el Capítulo 2. La gran diferencia encontrada entre las estructuras cristalinas se debe a la gran variedad de modos de coordinación que presenta este ligando. Los estudios citotóxicos unidos a las destacables propiedades luminiscentes de esta familia de compuestos, los convierten en materiales con potencial para aplicaciones biomédicas, siendo el material $[\text{Tb}(5\text{-BrNic})_2(\text{H}_2\text{O})_4] \cdot [\text{Tb}(5\text{-BrNic})_4(\text{H}_2\text{O})_2] \cdot (5\text{-HBrNic})_2$ el más destacable al mostrar tiempos de vida de fosforescencia más largos (aproximadamente 1ms).

Seguidamente, al comprobar la gran versatilidad que estos ligandos podían llegar a mostrar, se decidió intentar alejar los grupos funcionales presentes en el ligando para separar con mayor eficiencia los centros metálicos en las redes cristalinas. Con esta idea en mente nos centramos en dos tipos de ligandos: el ácido 5-aminopiridin-2-carboxílico y el 2-aminopiridin-4-carboxilato de metilo.

Con el primero de ellos, el 5-aminopiridin-2-carboxílico (ampy), se sintetizaron tres compuestos 1D de iones lantánidos isoestructurales y dos basados en metales de la primera serie de transición reunidos en el Capítulo 3. De esta familia cabe destacar el compuesto $[\text{YbNa}(\text{ampy})_4]_n$ que muestra relajación lenta de la magnetización en la que intervienen diferentes procesos de relajación, y el compuesto

$[\text{ErNa}(\text{ampy})_4]_n$ que presenta señales ligeramente dependientes de la frecuencia fuera de fase, compuestos que podrían ser efectivos para estudios citotóxicos activados mediante un campo magnético aplicado.

La segunda familia, basada en el 2-aminopiridin-4-carboxilato de metilo (2ain) y recogida en el Capítulo 4 de esta Tesis, contiene tres compuestos isoestructurales basados en metales de la primera serie de transición. Dichos compuestos presentan una estructura 3D tipo diamante abierto que permite la cristalización de una red interpenetrada y, a su vez, conservar una gran porosidad. Además, los compuestos $\{[\text{Co}(\mu\text{-}2\text{ain})_2]\cdot\text{DMF}\}_n$ y $\{[\text{Zn}(\mu\text{-}2\text{ain})_2]\cdot\text{DMF}\}_n$ muestran un gran potencial como sensores. Mientras que el compuesto de Co ve alteradas sus propiedades magnéticas cuando las moléculas de la red cristalina son reemplazadas por MeOH o DMSO, el compuesto de Zn ve modificadas sus propiedades luminiscentes en disolución en presencia de diferentes iones metálicos.

Tras ver los interesantes resultados obtenidos y con la idea de conferir mayor rigidez estructural, se utilizaron como ligandos una familia de ácidos carboxílicos derivados de indazoles variando la posición del grupo ácido dentro del esqueleto orgánico.

Partiendo de esta premisa, el primer indazol probado fue el ácido 1H-Indazol-5-carboxílico (5-inca), del cual se obtuvieron 2 compuestos isoestructurales bidimensionales recogidos en el Capítulo 9. Por otra parte, en el Anexo 1 se presenta un compuesto 3D de Zn junto a otros dos bi- y tridimensionales que se han obtenido tras un ordenamiento estructural influenciado por el tiempo. Este compuesto 3D, aun siendo inestable en condiciones normales, presenta un gran interés a nivel estructural debido a su gran similitud con el famoso material MOF-5.

Con la idea de mejorar la estabilidad de la estructura tridimensional del compuesto de zinc recogido en el Anexo 1 y a su vez modificar el tamaño de los canales se agregó al seno de la reacción dos ligandos nitrogenados (4,4'-Bipiridina (4,4-bipy) y 3,6-Di(4-piridinil)-1,2,4,5-tetrazina(pbptz)) para que actuaran como espaciadores, obteniéndose así 2 compuestos tridimensionales isorreticulares recogidos en el Capítulo 10. Ambos materiales han mostrado propiedades luminiscentes fascinantes que han sido corroboradas mediante cálculos teóricos. El

compuesto $\{[\text{Zn}(5\text{-inca})(\text{pbptz})_{0.5}] \cdot (\text{DMF})\}_n$ exhibe un destacable termocromismo apreciado en la tonalidad de emisión en el color azul mientras que el $\{[\text{Zn}(5\text{-inca})(4,4\text{-bipy})_{0.5}] \cdot (\text{DMF})\}_n$ presenta fosforescencia con un tiempo de vida de 950 ms perceptible por el ojo humano.

Otra estrategia utilizada para mejorar la estabilidad de estos sistemas fue la utilización de ácido benzotriazol-5-carboxílico cuya diferencia con el ácido 1H-Indazol-5-carboxílico radica en la presencia de un nitrógeno más en la estructura aromática. Con este ligando se obtuvo un compuesto tridimensional con excelentes propiedades catalíticas. Dicho compuesto no se ha presentado en esta Tesis Doctoral.

Con el objetivo de comprobar si el resto de indazoles de esta familia pudiesen mostrar estructuras y propiedades de interés similares a las anteriores, se probaron los siguientes ligandos: ácido 1H-Indazol-4-carboxílico, ácido 1H-Indazol-6-carboxílico y ácido indazol-3-carboxílico.

Con el primero de estos indazoles se consiguieron sintetizar cinco nuevos compuestos bidimensionales agrupados en el Capítulo 5, donde se puede apreciar para los compuestos de $[\text{Co}(\text{L})_2(\text{H}_2\text{O})_2]_n$ y $[\text{Cu}(\text{L})_2(\text{H}_2\text{O})]_n$, un magnetismo fuertemente influenciado por la corta distancia entre los centros metálicos. Esta corta distancia es debida a las torsiones estructurales presentes y al empaquetamiento cristalino. Estos rasgos estructurales también se ven reflejados en las propiedades luminiscentes de los compuestos $[\text{Zn}(\text{L})_2]_n$ y $[\text{Cd}(\text{L})_2]_n$, causando un efecto hipsocrómico en la señal emitida.

Para el segundo indazol se sintetizaron dos compuestos de diferente dimensionalidad con unas excelentes emisiones fotoluminiscentes centradas en el ligando de tipo $\pi\text{-}\pi^*$. Los análisis *in vitro* de la citotoxicidad revelaron, para el compuesto Cd, una disminución de la viabilidad celular en HEK-293 y B16-F10 para concentraciones superiores a 20 $\mu\text{g/ml}$. Todos estos datos se han recogido en el Capítulo 6.

Por último, con el tercer indazol mencionado anteriormente se han sintetizado cinco compuestos de coordinación mononucleares basados en metales de la primera serie de transición, muy prometedores debido a su potencial como agentes anticancerígenos, todos ellos recogidos en el Capítulo 8 de esta tesis.

Con la idea de aunar las propiedades de los ligandos piridina e indazol se optó por probar ligandos tipo pirimidina, puesto que presentan a nivel estructural, el mismo número de nitrógenos en los anillos aromáticos, pero con distinta disposición. Se utilizó el ligando 4-hidroxiimidina-5-carbonitrilo debido a que sus tres átomos coordinantes, colocados de forma asimétrica, propagarían la estructura en tres direcciones coplanares y, tal y como esperábamos, se logró sintetizar un compuesto de Cu bidimensional plano, que se muestra en el Capítulo 11. En este caso, gracias al entorno de coordinación trigonal del átomo de cobre, y a la disposición de los nitrógenos en el ligando, se pudo obtener una estructura laminar muy interesante haciendo de este material un excelente candidato para estudiar su conductividad, debido a su similitud con el grafeno, y estudiar la modificación de sus propiedades al aplicarle presión.

Por último, se decidió utilizar un ligando no nitrogenado, como por ejemplo el ácido 2,5-dihidroxitereftálico, para sopesar el uso de ligandos de esta naturaleza en futuros estudios. Se obtuvo así, un material de disprosio interesante debido a sus propiedades magnéticas y recogido en el Capítulo 7. Estas propiedades fueron ensalzadas gracias al efecto de dilución magnética empleando ytrio en lugar de disprosio y sintetizando el correspondiente compuesto isoestructural.

En resumen, en esta Tesis doctoral se recoge la síntesis, caracterización y estudio de las diferentes propiedades que presentan nuevos compuestos de coordinación multidimensionales, a partir del uso de ligandos nitrogenados con grupos carboxilato. Con todo lo anterior se ha demostrado la versatilidad y multifuncionalidad que estos materiales pueden llegar a presentar, sirviendo a su vez de base para que la comunidad científica siga desarrollando y mejorando esta familia de materiales basados en la Química de la Coordinación.

INDICE

INTRODUCCIÓN	29
1. QUÍMICA DE LA COORDINACIÓN	31
2. COMPUESTOS DE COORDINACIÓN.....	31
2.1. <i>Compuestos Mononucleares</i>	34
2.2. <i>Entidades discretas</i>	35
2.3. <i>Polímeros de Coordinación</i>	36
3. PROPIEDADES FÍSICO-QUÍMICAS	39
3.1. <i>Magnetismo</i>	40
3.2. <i>Luminiscencia</i>	50
3.3. <i>Adsorción</i>	56
4. PROPIEDADES BIOLÓGICAS	61
4.1. <i>Propiedades Antitumorales</i>	61
4.2. <i>Otras Propiedades Biológicas</i>	63
5. HIPÓTESIS.....	65
6. OBJETIVOS	66
7. REFERENCIAS.....	69
CAPÍTULO 1.....	81
DESIGNING SINGLE-ION MAGNETS AND PHOSPHORESCENT MATERIALS WITH 1-METHYLIMIDAZOLE-5-CARBOXYLATE AND TRANSITION-METAL IONS	81
ABSTRACT.....	83
1. INTRODUCTION	84
2. EXPERIMENTAL PROCEDURES.....	86
2.1. <i>Chemicals</i>	86
2.2. <i>Synthesis</i>	86
2.3. <i>Physical Measurements</i>	87
2.4. <i>X-ray Diffraction</i>	88
2.5. <i>Computational details</i>	89
3. RESULTS AND DISCUSSION.....	90
3.1. <i>Structural Description</i>	90
3.2. <i>Magnetic Properties</i>	101
3.3. <i>Photoluminescence Properties</i>	109
4. CONCLUSIONS	116
5. REFERENCES	118
CAPÍTULO 2.....	133
MULTIFUNCTIONAL COORDINATION COMPOUNDS BASED ON LANTHANIDE IONS AND 5-BROMONICOTINIC ACID. MAGNETIC, LUMINESCENCE AND ANTI-CANCER PROPERTIES	133
ABSTRACT.....	135
1. INTRODUCTION	135
2. EXPERIMENTAL	137
2.1. <i>Materials and physical measurements</i>	137
2.2. <i>Preparation of complexes</i>	138
2.3. <i>Crystallographic refinement and structure solution</i>	139
2.4. <i>Growth Inhibition Assay</i>	140

3. RESULTS AND DISCUSSION.....	141
3.1. Description of the structures.....	141
3.2. Magnetic Measurements.....	146
3.3. Photoluminescence Studies.....	151
3.4. Cytotoxicity of the lanthanide complexes.....	159
4. CONCLUSIONS.....	161
5. REFERENCES.....	162
CAPITULO 3.....	167
5-AMINOPYRIDINE-2-CARBOXYLIC ACID AS APPROPRIATE LIGAND FOR CONSTRUCTING COORDINATION POLYMERS WITH LUMINESCENCE, SLOW MAGNETIC RELAXATION AND ANTI-CANCER PROPERTIES	167
ABSTRACT.....	169
1. INTRODUCTION.....	170
2. EXPERIMENTAL SECTION.....	173
2.1. General Procedures.....	173
2.2. Preparation of complexes.....	173
2.3. Physical measurements.....	174
2.4. Single-Crystal Structure Determination.....	174
2.5. Luminescence measurements.....	176
2.6. Magnetic measurements.....	176
2.7. Antiproliferative Activity.....	176
3. RESULTS AND DISCUSSION.....	177
3.1. Description of the structures.....	177
3.2. Luminescence Properties.....	183
3.3. Magnetic Measurements.....	186
3.4. Potential Antiproliferative Activities.....	189
4. CONCLUSIONS.....	192
5. REFERENCES.....	193
CAPÍTULO 4.....	197
MAGNETIC AND PHOTOLUMINESCENT SENSORS BASED ON METAL-ORGANIC FRAMEWORKS BUILT UP FROM 2-AMINOISONICOTINATE.....	197
ABSTRACT.....	199
1. INTRODUCTION.....	200
2. RESULTS AND DISCUSSION.....	202
2.1. Structural description of $\{[M(\mu\text{-}2\text{ain})_2]\cdot\text{DMF}\}_n$ [$M^{\text{II}} = \text{Co (1), Ni (2), Zn (3)}$].....	202
2.2. Static magnetic properties.....	208
2.3. Dynamic magnetic properties.....	212
2.4. Solvent-dependent magnetic behaviour of compound 1.....	214
2.5. Photoluminescence properties of compound 3.....	218
2.6. PL Sensing Properties.....	223
3. CONCLUSIONS.....	230
4. EXPERIMENTAL SECTION.....	231
4.1. Chemicals.....	231
4.2. Physical measurements.....	232
4.3. X-ray Diffraction Data Collection and Structure Determination.....	233
4.4. Computational details.....	236
5. REFERENCES.....	236

CAPÍTULO 5.....	247
2D-COORDINATION POLYMERS BASED ON 1H-INDAZOLE-4-CARBOXYLIC ACID AND TRANSITION METAL IONS: MAGNETIC, LUMINESCENT AND BIOLOGICAL PROPERTIES.....	247
ABSTRACT.....	249
1. INTRODUCTION	250
2. RESULTS AND DISCUSSION	251
2.1. <i>Description of the structures</i>	251
2.2. <i>Magnetic Properties</i>	257
2.3. <i>Photoluminescence studies</i>	265
2.4. <i>Cytotoxicity of the coordination polymers</i>	266
3. CONCLUSION	267
4. EXPERIMENTAL	268
4.1. <i>Preparation of complexes</i>	268
4.2. <i>Physical measurements</i>	270
4.3. <i>Cell viability assay</i>	271
4.4. <i>Single-crystal structure determination</i>	272
5. NOTES AND REFERENCES	275
CAPÍTULO 6.....	279
PHOTOLUMINESCENCE AND <i>IN VITRO</i> CYTOTOXICITY IN COORDINATION POLYMERS BASED ON D¹⁰ TRANSITION METALS AND 1H-INDAZOLE-6-CARBOXYLIC ACID	279
ABSTRACT.....	281
1. INTRODUCTION	282
2. RESULTS AND DISCUSSION	284
2.1. <i>Description of the structures</i>	285
2.2. <i>FT-IR spectrum</i>	288
2.3. <i>Luminescence properties</i>	289
2.4. <i>In vitro cytotoxicity</i>	291
3. CONCLUSIONS	292
4. EXPERIMENTAL SECTION	293
4.1. <i>Materials and physical measurements</i>	293
4.2. <i>Crystallographic refinement and structure solution</i>	294
4.3. <i>Photophysical measurements</i>	296
4.4. <i>In vitro cell viability assays</i>	296
5. REFERENCES	297
CAPÍTULO 7.....	301
DILUTION EFFECT ON THE SLOW RELAXATION OF A LUMINESCENT DYSPROSIUM METAL-ORGANIC FRAMEWORK BASED ON 2,5-DIHYDROXYTEREPHTHALIC ACID	301
ABSTRACT.....	303
1. INTRODUCTION	304
2. EXPERIMENTAL	306
2.1. <i>General</i>	306
2.2. <i>Preparation of the complexes</i>	306
2.3. <i>Physical measurements</i>	307
2.4. <i>Single-crystal structure determination</i>	307
3. RESULTS AND DISCUSSION	309
3.1. <i>Crystal structure of Compound 1</i>	309

3.2. <i>Magnetic properties</i>	312
3.3. <i>Luminescence properties</i>	318
4. CONCLUSIONS.....	321
5. REFERENCES	322
CAPÍTULO 8.....	327
ANTICANCER AND ANTI-INFLAMMATORY ACTIVITIES A NEW FAMILY OF COORDINATION COMPOUNDS BASED ON DIVALENT TRANSITION METAL IONS AND INDAZOLE-3-CARBOXYLIC ACID	327
ABSTRACT.....	329
1. INTRODUCTION	330
2. EXPERIMENTAL PROCEDURES	332
2.1. <i>Chemicals</i>	332
2.2. <i>Synthesis</i>	333
2.3. <i>Crystallographic refinement and structure solution</i>	333
2.4. <i>Cell culture</i>	334
2.5. <i>Cell viability assay</i>	335
2.6. <i>Determination of nitrite concentration</i>	336
3. STRUCTURAL DESCRIPTION.....	336
4. BIOLOGICAL PROPERTIES.....	340
4.1. <i>Cytotoxicity cancer cells</i>	340
4.2. <i>Raw 264.7 cell viability</i>	341
4.3. <i>Nitro Oxide Production</i>	342
5. CONCLUSIONS.....	344
6. REFERENCES	345
CAPÍTULO 9.....	349
ANTIPARASITIC, ANTI-INFLAMMATORY AND CYTOTOXIC ACTIVITIES OF 2D COORDINATION POLYMERS BASED ON 1H-INDAZOLE-5-CARBOXYLIC ACID	349
ABSTRACT.....	351
1. INTRODUCTION	351
2. EXPERIMENTAL.....	354
2.1. <i>Materials and physical measurements</i>	354
2.2. <i>Synthesis of complexes</i>	355
2.3. <i>Crystallographic refinement and structure solution</i>	355
2.4. <i>Parasite culture and in vitro activity</i>	356
2.5. <i>Cell culture and cytotoxicity test</i>	357
2.6. <i>Determination of nitrite concentration</i>	358
2.7. <i>Photocatalytic performance measurements</i>	358
3. RESULTS AND DISCUSSION.....	359
3.1. <i>Structural descriptions</i>	359
3.2. <i>Magnetic Properties</i>	363
3.3. <i>Photocatalytic degradation of vanillic acid</i>	366
3.4. <i>In vitro antiparasitic activity</i>	367
3.5. <i>Cytotoxicity on Raw 264.7 cell line</i>	369
3.6. <i>Nitro Oxide Production</i>	370
4. CONCLUSION	373
5. REFERENCES	374
CAPÍTULO 10.....	379

INTERPENETRATED LUMINESCENT METAL-ORGANIC FRAMEWORKS BASED ON 1H-INDAZOLE-5-CARBOXYLIC ACID	379
ABSTRACT.....	381
1. INTRODUCTION	381
2. EXPERIMENTAL PROCEDURES.....	385
3. RESULTS AND DISCUSSION.....	388
3.1. Structural description of $\{[Zn(5-inca)(pbptz)_{0.5}](DMF)_n\}_n$ (1).	389
3.2. Structural description of $\{[Zn(5-inca)(4,4-bipy)_{0.5}](DMF)_n\}_n$ (2).	394
3.3. Photoluminescence Properties.....	396
4. CONCLUSIONS	409
5. REFERENCES	410
CAPÍTULO 11	419
RATIONAL DESIGN OF AN UNUSUAL 2D-MOF BASED ON CU(I) AND 4-HYDROXYPYRIMIDINE-5-CARBONITRILE AS LINKER WITH CONDUCTIVE CAPABILITIES. A THEORETICAL APPROACH BASED ON HIGH-PRESSURE XRD.....	419
ABSTRACT.....	421
1. INTRODUCTION	422
2. RESULTS	423
3. CONCLUSIONS	432
4. EXPERIMENTAL PROCEDURES.....	433
5. HIGH-PRESSURE X-RAY DIFFRACTION.....	434
6. NOTES AND REFERENCES	435
ANEXOS	439
ANEXO 1	441
TIME-INDUCED SINGLE CRYSTAL TO SINGLE CRYSTAL TRANSFORMATION AND LUMINESCENCE OF A DYNAMIC 3D METAL-ORGANIC FRAMEWORK BASED ON ZN(II) AND 1H-INDAZOLE-5-CARBOXYLIC ACID	441
ABSTRACT.....	443
1. INTRODUCTION	443
2. CRYSTAL STRUCTURES	444
3. REFERENCES	449
CONCLUSIONES GENERALES.....	451
ARTÍCULOS RELACIONADOS CON LA TESIS	461
ARTÍCULOS PUBLICADOS.....	467

Abreviaturas

Abreviaturas

Ac: corriente alterna.

AF: Antiferromagnético.

CCs: Clusters de Coordinación.

D: Anisotropía Magnética

Dc: corriente continua.

DMF: N,N-Dimetilformamida

DSC: Calorimetría diferencial de Barrido

F: Ferromagnético.

IUPAC: International Union of Pure and Applied Chemistry.

J: constante de acoplamiento

J_{af}: Constante de acoplamiento antiferromagnético

J_f: Constante de acoplamiento ferromagnético

LMCT: Transferencia de Carga Ligando-Metal.

M: Magnetización.

MLCT: Transferencia de Carga Metal-Ligando.

MOFs: Metal-Organic Frameworks.

MTT: Bromuro de 3(4,5 dimetil-2-tiazolil)-2,5- difeniltetrazólico.

OCs: Oligómeros de Coordinación.

OMS: Organización Mundial de la Salud.

PCP: Polímero de Coordinación Poroso.

PCs: Polímeros de Coordinación.

PCs-1D (2D) o (3D): Polímeros de Coordinación Monodimensionales (bidimensionales) o (Tridimensionales).

QTM: efecto de túnel cuántico.

S: Valor de espín del estado fundamental.

SCM: Single-chain magnets.

SIM: Single ion-magnet.

SMM: Single molecule magnet.

T_b: Temperatura de Bloqueo.

T_c: Temperatura Crítica.

T_c: Temperatura de Curie.

TG: Termogravimetría.

T_N: Temperatura de Néel.

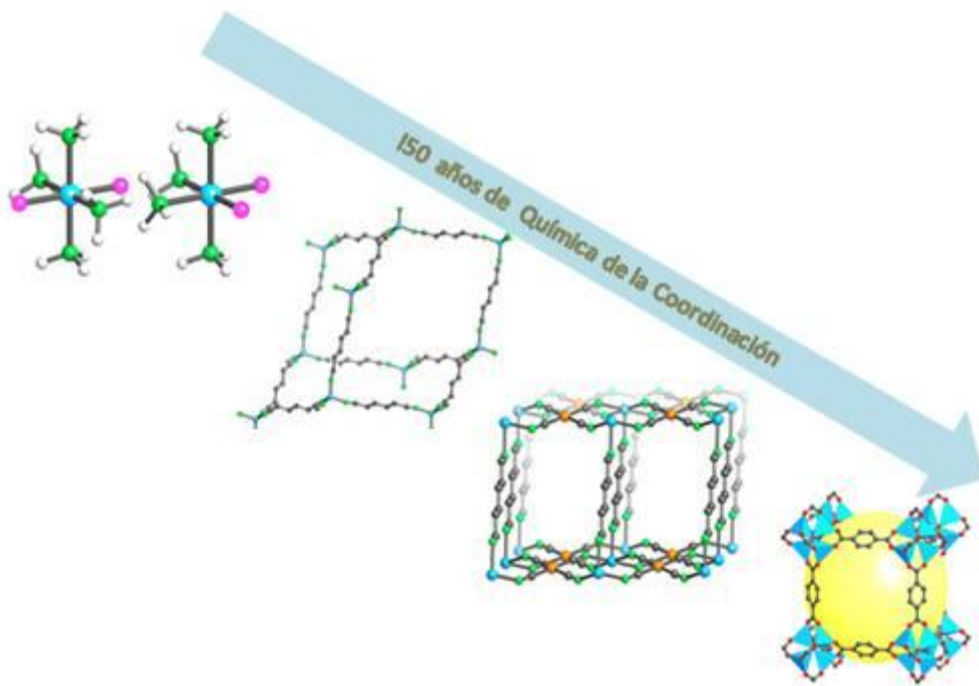
ZFS: zero-field splitting.

χ : Susceptibilidad magnética.

χ' : susceptibilidad magnética fuera de fase.

χ'' : susceptibilidad magnética en fase.

Introducción



1. Química de la Coordinación

En las últimas décadas la Química de la Coordinación ha pasado a ser uno de los campos más importantes de la Química Inorgánica. Este área tiene como objetivo estudiar los compuestos de coordinación (también denominados complejos) que son moléculas neutras o iones, en los que un grupo de moléculas, átomos o iones denominados ligandos forman uniones con un ión o átomo central (normalmente un metal). Esta definición abarca un gran número de sustancias que no habían sido consideradas complejos. Si alguien se preguntase en qué año nació la Química de la Coordinación habría que remontarse a 1893 donde Alfred Werner publicó un trabajo sobre la disposición espacial de ligandos alrededor de un centro metálico.¹

La Química de la Coordinación ha ido desarrollándose, tanto a nivel teórico, como en los métodos de síntesis y búsqueda de aplicaciones de estos materiales.

2. Compuestos de Coordinación

Con el paso de los años se han desarrollado una gran variedad de materiales que pueden ser incluidos en el término “Compuesto de Coordinación”. Para entender su significado hay que remontarse a 1916 cuando Yuji Shibata empleó por primera vez el término polímero de coordinación para describir dímeros y trímeros de cobalto(II)², desde entonces empiezan a descubrirse un gran variedad de compuestos que entran en esta definición³ sintetizándose en 1959 (Figura 1) la primera red de coordinación⁴, llegando a publicarse la primera revisión bibliográfica en 1964.⁵ Pocos años más tarde, se vio que la forma, el tamaño y la selectividad de las cavidades de las redes de coordinación, denominadas clatratos de Hofmaan, podían modificarse mediante el empleo de ligandos diferentes.⁶

A pesar de la longevidad del concepto, no es hasta los años noventa cuando surgen con fuerza, debido al interés en distintas aplicaciones de estos nuevos materiales, dos términos que continúan usándose en la actualidad: Polímeros de Coordinación (PCs) y redes Metalorgánicas (más conocidas por su nombre en inglés *Metal-Organic Frameworks*, MOFs), siendo en 1995 (Figura 1), O. M. Yaghi el primer investigador en utilizar el nombre de MOF al sintetizar diversos compuestos

bidimensionales.⁷ Pocos años después, en 1999, (Figura 1) fue él quien sintetizó el primer MOF tridimensional cuya superficie específica constituyó el valor más alto conocido hasta ese momento.⁸

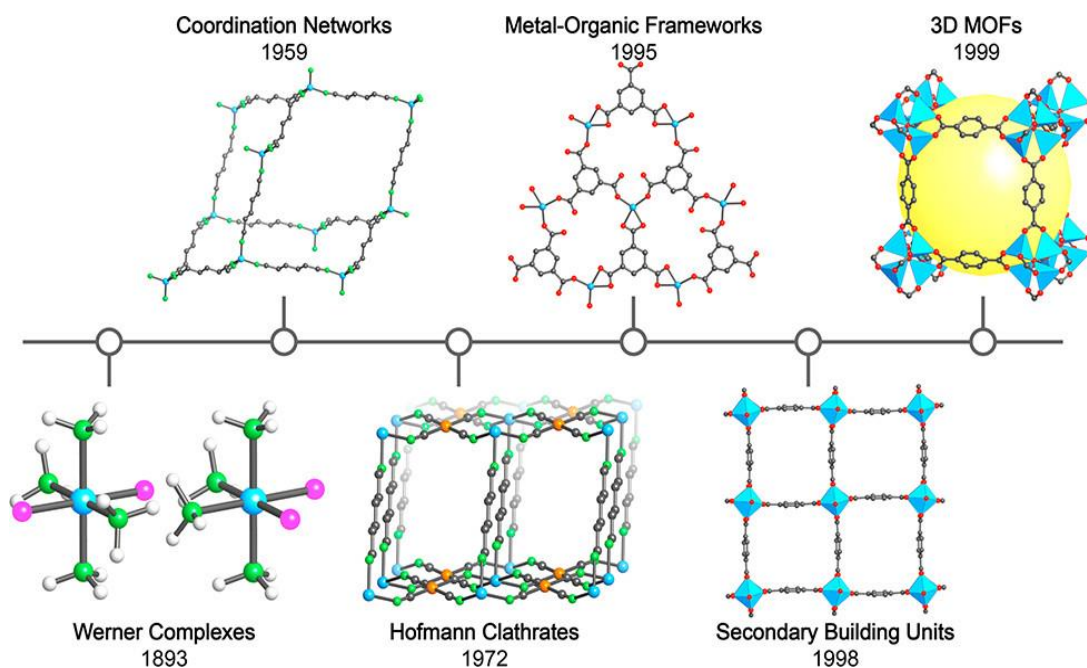
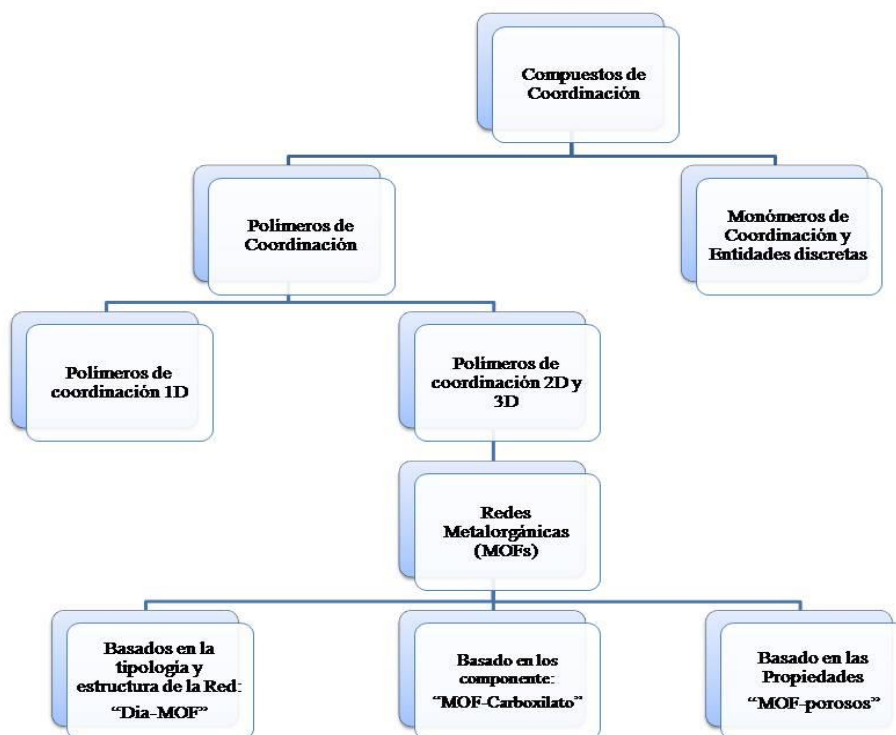


Figura 1. Evolución de la *Química de la Coordinación* desde Warner hasta la actualidad por Yaghi.⁹

La existencia de ambas terminologías (PCs y MOFs) ha causado bastantes enfrentamientos entre la comunidad científica debido a que algunos autores defendían su similitud mientras que otros defendían sus diferencias. A causa de esto, en 2009 la IUPAC encargó un proyecto titulado *Coordination Polymers and Metal Organic Frameworks: Terminology and nomenclature Guidelines*, que en 2013 dio como resultado una publicación donde se recogía una recomendación provisional.¹⁰ En este artículo se definen los polímeros de coordinación como compuestos de coordinación que se extienden en 1, 2 o 3 dimensiones a través del espacio. Mientras que MOFs se define como aquellos polímeros de coordinación que presentan una estructura abierta que contiene, potencialmente, poros. También se pueden utilizar otros términos para resaltar alguna característica concreta del material. Por ejemplo, “MOF-carboxilato” (destaca el grupo funcional), “dia-MOF” (indica la topología de la red, diamante en este caso) ó “PCP” (para polímeros de coordinación porosos). En

el Esquema 1, surgido de este proyecto, se puede ver la clasificación y el tipo de nomenclatura.



Esquema 1. Clasificación y nomenclatura de los Compuestos de Coordinación establecidos por la IUPAC. Siguiendo la terminología del artículo de O'Keeffe et al.¹¹

La importancia de estos compuestos radica en su capacidad de presentar un gran abanico de propiedades (almacenamiento, adsorción, separación y purificación de gases¹², catálisis heterogénea¹³, biomedicina¹⁴, magnetismo¹⁵, luminiscencia¹⁶ y/o electrónicas¹⁷, entre otras), las cuales, en la mayoría de los casos, coexisten complementándose, obteniendo un gran potencial a la hora de buscar aplicaciones a estos materiales multifuncionales.

A continuación, se explicará con más detalle los diferentes tipos de compuestos de coordinación, destacando algunas de las propiedades más relevantes de cada familia.

2.1. Compuestos Mononucleares

Los compuestos mononucleares pueden considerarse los compuestos más básicos de la ingeniería cristalina, siendo el inicio de la revolución de esta rama de la Química. Suelen presentar estructuras simples y discretas que difieren unas de otras en su número de coordinación y/o geometría¹⁸ donde el centro metálico está coordinado a una o más moléculas de ligando que puede ser de naturaleza orgánica, como por ejemplo carboxilatos o aminas, y/o de naturaleza inorgánica como por ejemplo moléculas de agua o halogenuros (Figura 2).

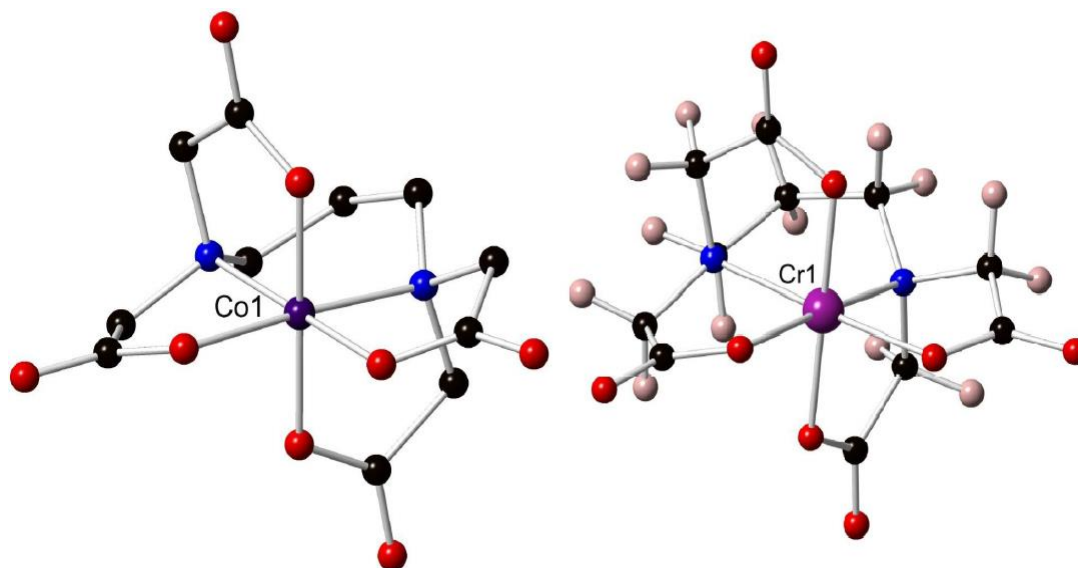


Figura 2. Ejemplos de estructuras monoméricas: Izquierda: Primera estructura cristalina reportada de un complejo de 1,3-propylenediaminetetraacetate $K[Co^{III}(1,3\text{-pdta})]2H_2O$ sin determinar los Hidrógenos. Derecha, estructura aniónica de $Na[Cr^{III}(1,3\text{-pdta})]3H_2O$.¹⁹

A pesar de que este grupo de materiales presenta menor relevancia en la actualidad frente a familias de mayor dimensionalidad²⁰, dentro de esta agrupación existen monómeros con gran diversidad de propiedades²¹, destacando aquellas relacionadas con los campos de la medicina²² o la catálisis²³ donde se ha podido explotar su potencial.

Aunque los compuestos mononucleares se encuentran englobados en el siguiente apartado “Entidades Discretas”, la importancia de ellos en el nacimiento de este campo de la Química, los ha hecho merecedores de un punto propio.

2.2. Entidades discretas

En el siguiente escalafón de complejidad estructural se encontraría el resto de sustancias del grupo denominado entidades discretas. En este grupo se engloban aquellos compuestos de coordinación cuya estructura es adimensional y pueden presentar uno (compuestos mononucleares) o más núcleos metálicos (homometálicos²⁴ o heterometálicos²⁵). Así pues, se pueden agrupar de cierto modo en oligómeros de coordinación (OCs)²⁶ y en clusters de coordinación (CCs).²⁷

Los OCs (Figura 3) son materiales en cuya estructura, además de tener más de un núcleo metálico, los núcleos están unidos mediante un ligando o molécula puente. De igual forma que los compuestos de coordinación mononucleares, los OCs presentan una gran variedad de propiedades, entre las que cabría destacarlas propiedades magnéticas²⁸ y catalíticas.²⁹

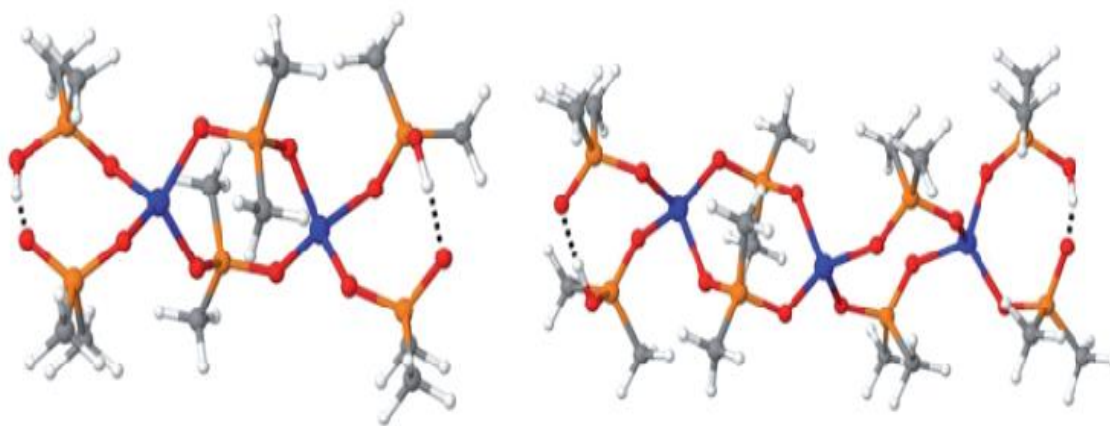


Figura 3. Ejemplos de estructuras oligoméricas: Izquierda, dímero de Co(II) con fórmula $Co_2(C_2H_6PO_2)_4(C_2H_6POOH)_2$. Derecha, trímero de Co(II) con fórmula $Co_3(C_2H_6PO_2)_6(C_2H_6POOH)_2$.³⁰

Los CCs (Figura 4) son materiales con una estructura caracterizada por presentar dos o más núcleos metálicos formando mayoritariamente enlaces entre sí directamente o mediante un tercer átomo no metálico. El interés en los clusters, aparte de en sus características magnéticas³¹ y luminiscentes³², se basa en su posible utilidad como bloque de construcción, en química supramolecular, para el diseño de polímeros de coordinación.³³

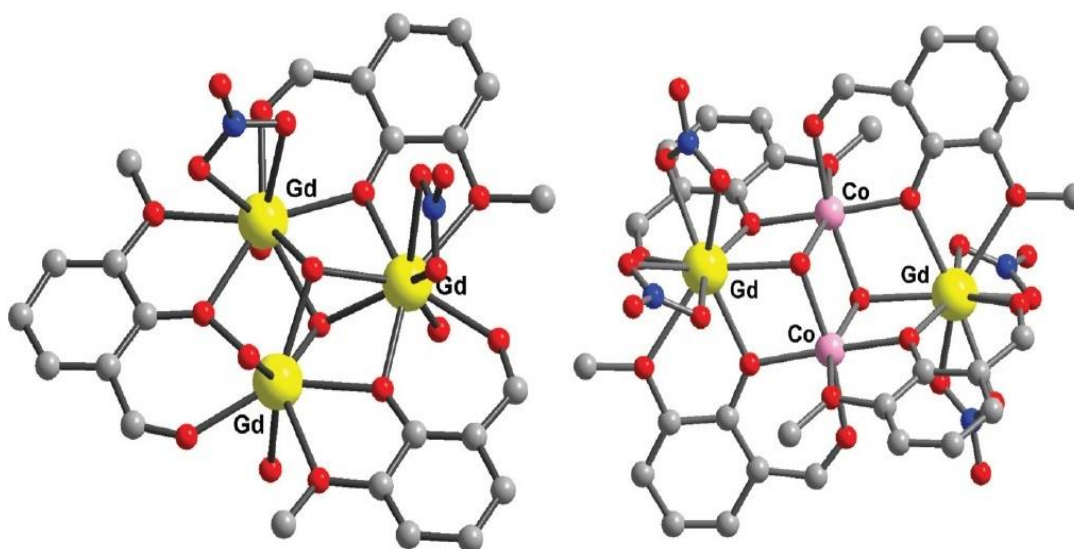


Figura 4. Ejemplos de Clusters de Coordinación: Izquierda, cluster homometálico de gadolinio $[Gd_3(\mu_3-OH)_2(o-van)_3(O_2NO)_2(OH_2)_4]^{2+}$. Derecha, cluster heterometálico de gadolinio y cobalto $[(NO_3)_2Gd(o-van)_2(\mu_3-HO)Co_2(\mu_3-OH)-(o-van)_2Gd(NO_3)_2]$.³⁴

2.3. Polímeros de Coordinación

Los PCs abarcan el resto compuestos de coordinación y son uno de los campos más relevantes en la Química de la Coordinación. Debido a su potencial multifuncional han despertado gran interés en todas las áreas de la ciencia.³⁵ Se dividen en 3 grandes grupos: Monodimensionales, Bidimensionales y Tridimensionales.

2.3.1. Polímeros de Coordinación Monodimensionales

Los Polímeros de coordinación Monodimensionales (PCs-1D) (Figura 5) son aquellos cuya estructura se propaga a través de enlaces químicos en una de las direcciones del espacio, formando cadenas poliméricas que interaccionan entre sí mediante fuerzas intermoleculares.

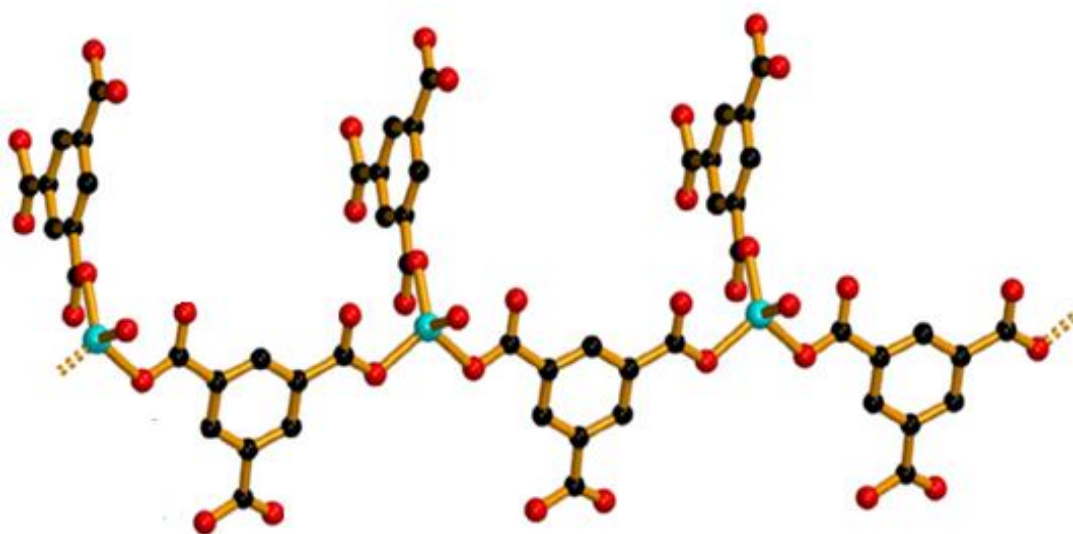


Figura 5. Ejemplo de PCs-1D con fórmula $[Zn(H_2O)(1,3,5\text{-benzenetricarboxylic acid})(\mu\text{-}1,3,5\text{-benzenetricarboxylic acid})]_n^{-2}$.³⁶

Entre las propiedades que puede presentar esta familia de polímeros cabría destacar sus propiedades magnéticas (*Single-chain magnets* (SCMs))³⁷, luminiscentes³⁸ y biológicas.³⁹

2.3.2. Polímeros de Coordinación Bidimensionales

Los Polímeros de coordinación Bidimensionales (PCs-2D) (Figura 6) son aquellos cuya estructura se propaga mediante enlaces químicos en dos de las direcciones del espacio, formando redes poliméricas 2D interconectadas mediante fuerzas intermoleculares.

Esta familia de compuestos, al igual que los PCs-1D, tiene gran importancia en el ámbito científico por su gran abanico de propiedades. Además de la capacidad de presentar buenas propiedades magnéticas⁴⁰ y luminiscentes⁴¹, hay que resaltar la capacidad de presentar conductividad eléctrica (estructuras laminares totalmente planas similares al Grafeno)⁴². Es por esto que este grupo de materiales es utilizado en la industria y en nanotecnología como sensores.⁴³

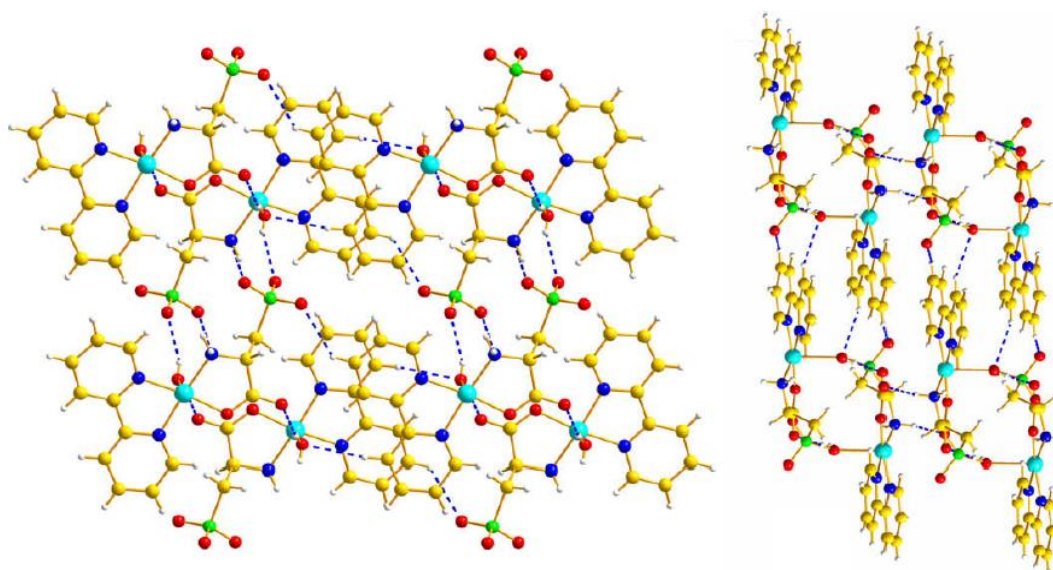


Figura 6. Ejemplo de PCs-2D con fórmula $[Cu(L-cysteate)(2,2'-bipyridyl)(H_2O)]_n^{-2}$ mostrando las interacciones por enlaces de hidrógeno entre las distintas láminas.⁴⁴

2.3.3. Polímeros de Coordinación Tridimensionales

Para concluir, en el último nivel de complejidad estructural se encuentran los Polímeros de coordinación Tridimensionales (PCs-3D) (Figura 7) cuya estructura se propaga mediante enlaces químicos en las tres direcciones del espacio, formando redes tridimensionales. El gran interés de la comunidad científica en estos materiales radica principalmente en los MOFs debido a su capacidad para adsorber gases.

Aunque existen materiales tridimensionales muy interesantes (magnéticos, luminiscentes, etc)⁴⁵ sin esta peculiaridad, la capacidad de presentar porosidad y todo lo derivado de ella (adsorción, separación, almacenamiento de gases⁴⁶ y transporte y

liberación controlada de fármacos)⁴⁷ sería la propiedad más destacable, actualmente, de esta familia.

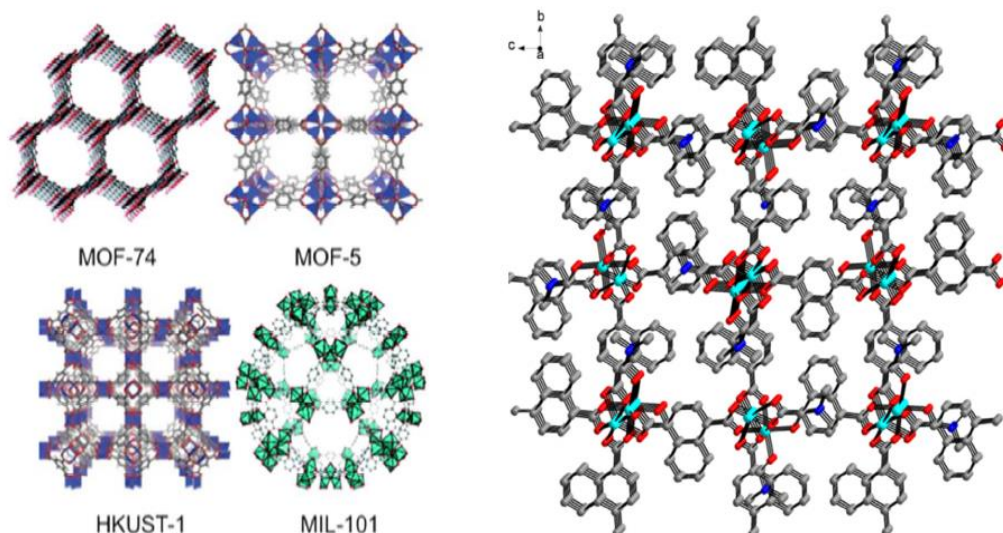


Figura 7. Ejemplos de Estructuras Tridimensionales: Izquierda, 4 estructuras cristalinas de 4 MOFs publicados en la base de datos CCDC. Derecha, estructura de un polímero de coordinación tridimensional con fórmula $[Co_2(\text{naphthalenedicarboxylate})_2(\text{DMF})_2]_n$.⁴⁸

3. Propiedades Físico-Químicas

Los compuestos de coordinación y más concretamente aquellos de mayor dimensionalidad destacan, como ya hemos comentado con anterioridad, por sus múltiples propiedades y potenciales aplicaciones. A continuación, se detallarán con mayor profundidad aquellas propiedades que han sido analizadas en los diferentes materiales sintetizados en esta Tesis Doctoral, así como algunos ejemplos de compuestos de coordinación destacados en estos campos.

3.1. Magnetismo

El magnetismo, en Química de la Coordinación, se encarga del estudio de las propiedades magnéticas presentes en los compuestos de coordinación. Para que un material tenga propiedades magnéticas es necesario que presente electrones desapareados. Estos materiales magnéticos son de gran interés en campos como la informática, la resonancia magnética, electrónica, etc.⁴⁹

La utilidad del magnetismo, en la Química de la Coordinación, se remonta a hace décadas cuando el estudio de las propiedades magnéticas se utilizaba, básicamente, como diagnóstico estructural a partir del número de electrones presentes en un compuesto de coordinación.

A partir de entonces, el interés del magnetismo fue desarrollándose hacia el estudio de las propiedades magnéticas en sí, sobre todo cuando empezó a observarse que algunos compuestos de coordinación que presentaban varios centros metálicos unidos por ligandos puente presentaban acoplamiento antiferromagnético (AF) (los espines de los núcleos vecinos están colocados antiparalelamente) o ferromagnético (F) (donde los espines están colocados paralelamente). Uno de los primeros casos observados fue el acoplamiento AF de los iones de Cu (II), por medio de los ligandos puente acetato, en el compuesto $[\text{Cu}_2(\text{Ac})_4 \cdot 2\text{H}_2\text{O}]$.⁵⁰ Desde ese momento la información derivada del estudio de las propiedades magnéticas de estos materiales, permitió establecer una relación entre las estructuras y las propiedades magnéticas (correlación magnetoestructural) y su desarrollo teórico para el estudio de los mecanismos de interacción magnética.

Aunque se han determinado un gran número de correlaciones magnetoestructurales para diferentes compuestos de coordinación, los compuestos dinucleares son los más ampliamente estudiados debido a su simplicidad y la facilidad para establecer correlaciones y extrapolarlas a estructuras de mayor complejidad.⁵¹ Desde el principio, en compuestos de Cobre, se atribuyó una relación importante entre las propiedades magnéticas y el ángulo (θ) (Figura 8a) que formaban los iones metálicos con el átomo puente oxo (M-O-M), llegando a producirse un cambio en el acoplamiento (J) antiferromagnético-ferromagnético para un valor de θ de $97,5^\circ$.⁵² Más adelante, en 1977, se vio que la desviación del plano de

los grupos unidos al oxígeno favorecen el cambio AF-F a ángulos θ más pequeños.⁵³ A estos 2 parámetros hay que agregarle un tercero que sería el ángulo (γ) (Figura 8b) formado entre los átomos metálicos y la línea que uniría a ambos átomos de oxígeno, donde al aumentar su valor disminuye la interacción AF.⁵⁴

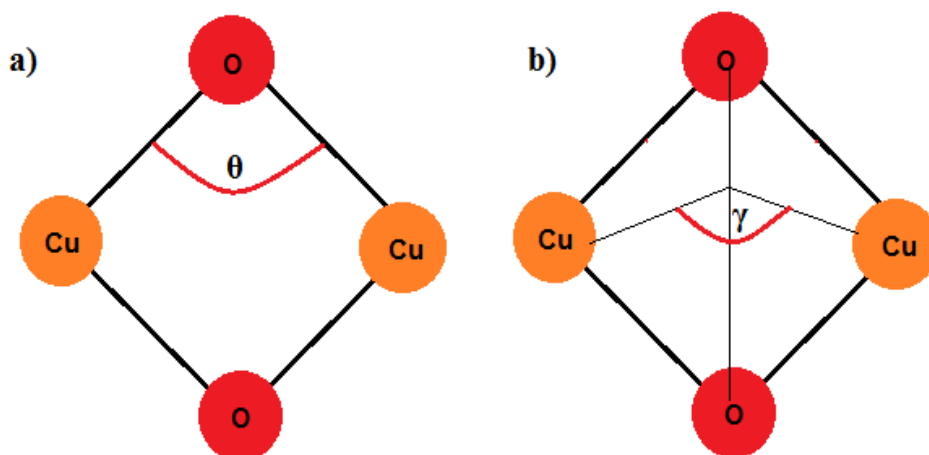


Figura 8. a) Figura representativa del ángulo θ . b) Figura representativa del ángulo γ .

Otro grupo funcional importante por su participación en el magnetismo es el grupo carboxilato. Aunque este grupo dispone de muchas posibilidades de interacción a la hora de participar como puente entre 2 núcleos metálicos, existen 3 interacciones más frecuentes (*syn-anti*, *syn-syn*, *anti-anti*) (Figura 9).

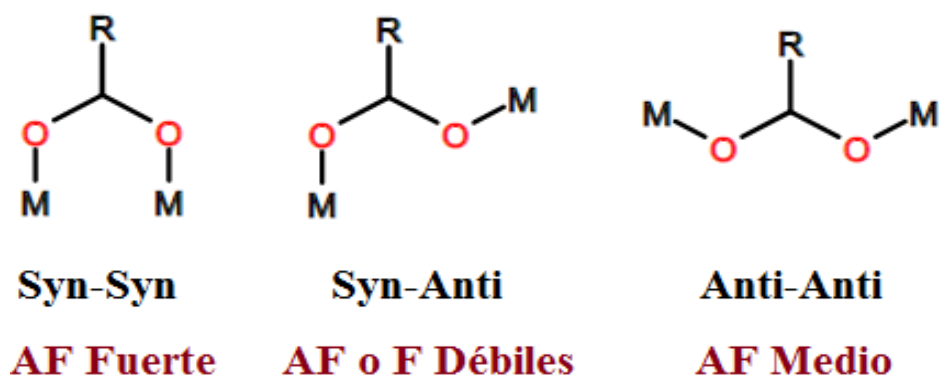


Figura 9. Conformaciones más frecuentes del grupo carboxilato puente en los compuestos de coordinación y su tipo de acoplamiento (AF: antiferromagnético y F: ferromagnético).

Las disposiciones *syn-syn* y *anti-anti*, desembocan en una interacción AF, debido a que la constante de acoplamiento (J) en este caso, es resultado de la contribución del acoplamiento antiferromagnético (J_{af}) y de la relación de J_{af} con el solapamiento de orbitales (S).⁵⁵ En el caso de la disposición *syn-anti* la contribución de los orbitales p a los orbitales s es menor debido a su orientación y no favorecen el solapamiento, disminuyendo así el valor de J_{af} , llegando a observarse interacciones de tipo F.⁵⁶

Actualmente, además de dilucidar nuevas correlaciones magnetoestructurales, el magnetismo molecular también busca nuevos materiales que puedan poseer interés aplicado. Estos materiales se pueden clasificar en: Materiales magnéticos con transición de Espín, materiales con interacciones moleculares de largo alcance e imanes monomoleculares (SMM, *Single-Molecule Magnet*).

Conceptualmente, los materiales magnéticos con transición de espín son aquellos que poseen centros metálicos electrónicamente activos que tienen la capacidad de cambiar entre los estados de bajo y alto espín y, por tanto, pueden presentar magnetismo o no según las variaciones de presión, temperatura, radiación o inclusión de moléculas huésped.⁵⁷

Esta Tesis recoge compuestos que se engloban en las categorías: interacciones moleculares de largo alcance e imanes monomoleculares (SMM, *Single-Molecule Magnet*), por lo que estas familias serán detalladas con más profundidad.

3.1.1. Interacciones moleculares de largo alcance

A pesar de que es un fenómeno en esencia tridimensional, un sistema bidimensional puede presentar orden magnético de largo alcance si todos los momentos magnéticos siguen una misma dirección de anisotropía uniaxial. Como es de esperar en la mayoría de los compuestos de coordinación con un estado fundamental magnético, estos materiales presentan un orden tridimensional magnético por debajo de una temperatura crítica, T_c . Si la interacción entre los centros vecinos es ferromagnética, todos los momentos magnéticos se orientan de forma paralela y el compuesto presenta magnetización espontánea por debajo de T_c

(Temperatura de Curie) y por tanto, si sufre una relajación lenta de la magnetización podría tener un comportamiento imán. Estos complejos son denominados Ferromagnéticos (Figura 10).

Si en cambio, la interacción entre los núcleos vecinos es antiferromagnética, los momentos magnéticos se colocan de forma antiparalela y los espines locales son equivalentes, se obtiene un estado fundamental no magnético por debajo de la temperatura crítica, T_N (Temperatura de Néel). Estos materiales son denominados Anti-ferromagnéticos (Figura 10). Si los espines no son equivalentes y la interacción AF no compensa los momentos magnéticos, el compuesto presenta magnetización espontánea por debajo de T_c . En este caso se denomina Ferrimagnético (Figura 10).

En algunos casos más particulares sucede que, aún teniendo una interacción AF y espines equivalentes, los momentos magnéticos no se orientan exactamente de forma antiparalela, sino que se encuentran ladeados (*spin-canting*) a causa de la baja simetría estructural. Debido a esto su magnetización es pequeña y son denominados Ferromagnéticos débiles.

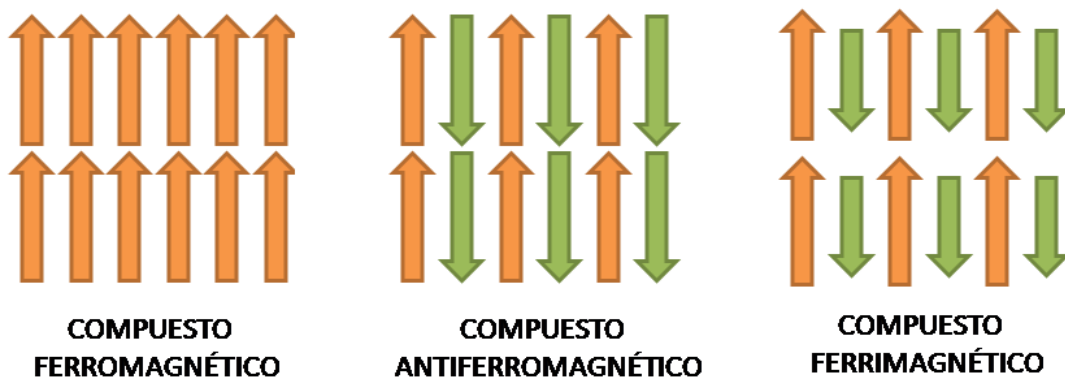


Figura 10. Ordenamiento tridimensional de los espines que dan lugar a los diferentes tipos de materiales magnéticos.

3.1.2. Imanes monomoleculares (SMMs)

Los imanes presentan ciclo de histéresis (Figura 11) caracterizado por los siguientes valores: *Magnetización remanente* (M_r) que es la magnetización cuando se elimina el campo magnético ($H=0$) y el *Campo coercitivo* (H_c), es decir, el campo necesario aplicar para que la magnetización sea 0. Para observar la magnetización es necesario un pequeño campo magnético para que los momentos magnéticos se coloquen paralelamente. Quedando el compuesto magnetizado tras retirar el campo.

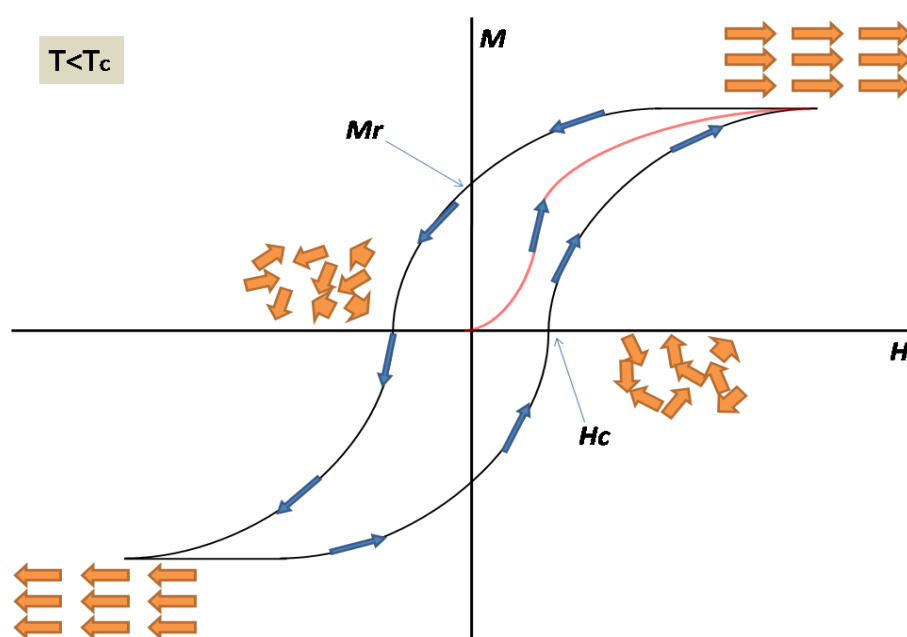


Figura 11. Ciclo de Histéresis en compuestos con propiedades magnéticas.

Aunque la mayoría de familias de imanes moleculares presentan una anisotropía uniaxial⁵⁸, recientemente se han llegado a sintetizar materiales que presentan una anisotropía *easy-plane* (parámetro de anisotropía axial positivo) y octaedro distorsionado con interesantes propiedades magnéticas,⁵⁹ como el compuesto de Cobalto que se recoge en el Capítulo 1 de esta Tesis.

Un buen ejemplo de este tipo de complejos con anisotropía positiva ($D > 0$) es el compuesto de Cobalto (Figura 12), $[\text{Co}(1,1,1\text{-tris-[2N-(1,1,3,3\text{-tetrametilguanidino)metil]etano)}_3\text{Cl}]^+$. Este complejo pseudotetraédrico presenta un

parámetro $D=12,7 \text{ cm}^{-1}$, tal como se ve en el diagrama simulado de Zeeman, y muestra a su vez, una relajación lenta de la magnetización bajo un campo aplicado.

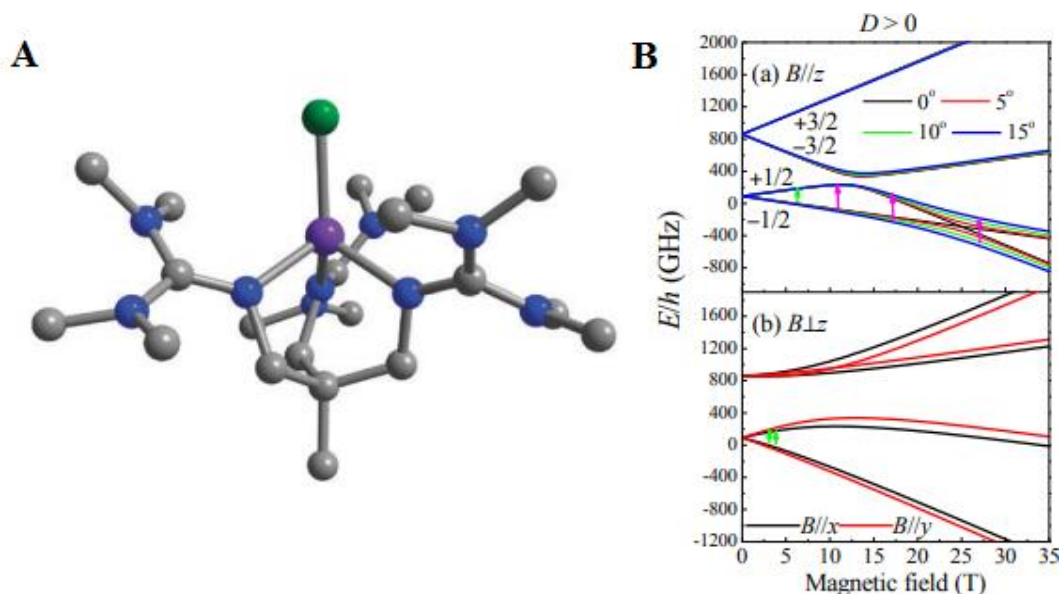


Figura 12. (A) *Compuesto de Cobalto con anisotropía easy-plane.* (B) *Simulación del campo paralelo y perpendicular para el compuesto de Co con una anisotropía positiva.*^{58a}

Los imanes monomoleculares (SMMs) suelen ser compuestos mononucleares o clusters metálicos que presentan una relajación muy lenta de la magnetización por debajo de una temperatura, denominada Temperatura de Bloqueo (T_b), y como consecuencia histéresis magnética. En algunos casos los SMMs suelen presentar efectos cuánticos a temperaturas cercanas a cero.⁶⁰

El primer compuesto donde se observó este comportamiento de imán monomolecular, fue en el cluster de manganeso $(\text{Mn}_{12}\text{O}_{12}(\text{O}_2\text{CCH}_3)_{16}(\text{H}_2\text{O})_4)$, cuya estructura consiste en un cubano de $\text{Mn}(\text{IV})_4\text{O}_4$ rodeado por otros 8 $\text{Mn}(\text{III})$ unidos entre sí con puentes oxo y acetato. La histéresis de este material no viene dada por el ordenamiento 3D de largo alcance, propio de los ferro- y ferri-compuestos, si no de las interacciones magnéticas intramoleculares. Los núcleos de $\text{Mn}(\text{III})$ del $(\text{Mn}_{12}\text{O}_{12}(\text{O}_2\text{CCH}_3)_{16}(\text{H}_2\text{O})_4)$ presentan una distorsión Jahn-Teller (distorsión causada por la existencia de niveles no igualmente ocupados) por elongación provocando una destacable anisotropía local. Además, esta molécula es lo

suficientemente pequeña para presentar efectos cuánticos, coexistiendo así 2 modos de relajación, el efecto clásico de activación térmica y el efecto de túnel cuántico (QTM) (Figura 13).⁶¹

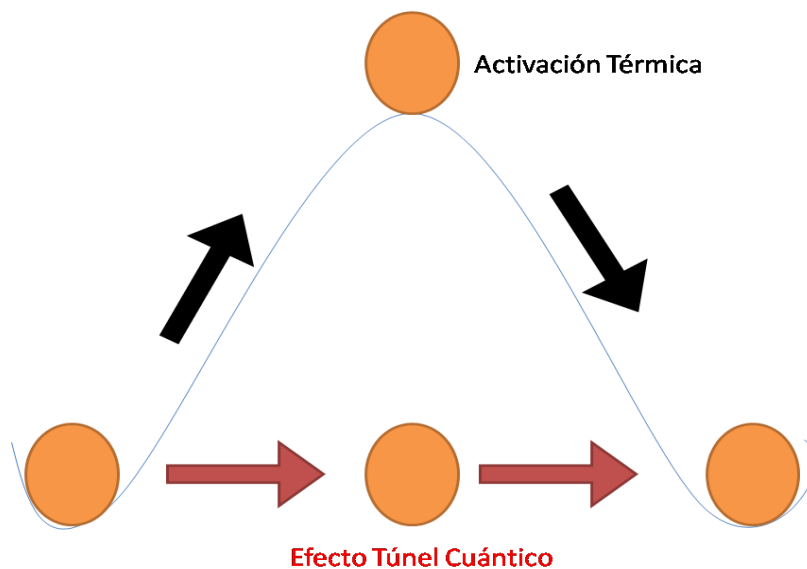


Figura 13. Activación térmica y Efecto del túnel cuántico en SMMs.

En SMMs la barrera de activación térmica depende del valor de espín del estado fundamental (S) y de la anisotropía negativa, relacionado con el acoplamiento espín-orbita junto a la distorsión del poliedro del metal. Esta anisotropía negativa hace que a un determinado valor de S los valores de $2S+1$ asociados no se encuentre degenerados a campo cero (*zero-field splitting*, ZFS).

El valor de la barrera térmica (U) se ve afectada por el valor de espín y del parámetro de ZFS, tal como se puede ver en las siguientes ecuaciones.

$$U = S^2 |D| (S \text{ entero}) ; \quad U = (S^2 - \frac{1}{4}) |D| (S \text{ semientero})$$

El tiempo de relajación por tanto depende del valor de la barrera y de la temperatura, según refleja la ecuación de Arrhenius.

$$\tau = \tau_0 \exp\left(\frac{U}{k_b T}\right)$$

Sí esta molécula se ve expuesta a un campo externo lo suficientemente fuerte, los momentos magnéticos se orientan en la dirección del mismo y la magnetización (M) se satura. Tras eliminar la influencia del campo aplicado, la molécula tiende a relajarse hasta alcanzar el estado de equilibrio (M=0) si la temperatura es suficiente para superar la barrera energética. En el caso de que la temperatura sea inferior a T_b , la magnetización queda bloqueada y su relajación hacia el equilibrio es muy lenta (Figura 14). Este efecto causa histéresis magnética en esta familia de materiales concediendo a estos compuestos una biestabilidad de gran interés en el campo del almacenamiento de información.⁶²

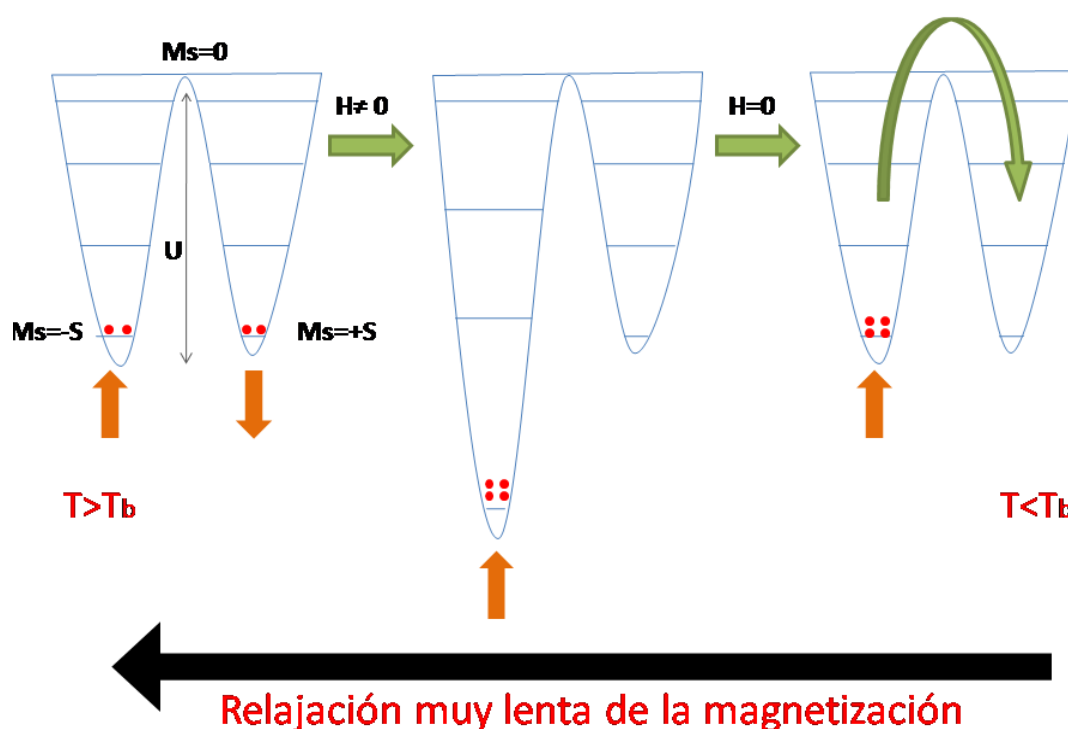


Figura 14. Proceso activado térmicamente para la relajación de la magnetización en SMMs.

A pesar de que una de las condiciones para que exista este efecto es presentar anisotropía negativa, recientemente se han publicado algunos complejos de Co(II) y Yb(II) que presentan comportamiento de SMMs con anisotropía positiva.⁶³

Por otro lado, la capacidad cuántica de estos compuestos posibilita la inversión del momento magnético, como ya se ha visto con anterioridad, por efecto túnel. Para sistemas con $D < 0$ y $S = \text{entero}$, la anisotropía transversal permite la mezcla de estados degenerados permitiendo el túnel cuántico. Sin embargo, si S es semientero (sistema Kramers) la mezcla de estados degenerados a campo cero está prohibida, debido a que el teorema de Kramers predice que el número mínimo de estados degenerados es dos. Sin embargo, el efecto túnel puede ser inducido tanto por interacciones dipolares, entre los momentos magnéticos, como por interacciones hiperfinas, entre el espín electrónico y el espín nuclear.

Otro efecto curioso que sucede en este tipo de materiales es el denominado túnel cuántico térmicamente activado. Consiste en que el efecto de túnel cuántico puede ocurrir entre pares de estados excitados degenerados, existiendo en este caso una barrera de activación térmica efectiva, U_{eff} (de menor energía que la energía de activación térmica esperada, U).⁶⁴

De todo esto se llega a la conclusión de que, para que un complejo polinuclear de iones metálicos se comporte como un imán molecular, tiene que cumplir los siguientes requisitos:

1. El espín del estado fundamental (S) debe ser tan alto como sea posible.
2. Las interacciones de canje deben ser grandes para que el nivel fundamental se encuentre separado de los niveles excitados.
3. Poseer anisotropía uniaxial lo más elevada posible, para lo que las moléculas deben estar colocadas en el cristal de forma que los ejes tengan la misma dirección.
4. Las interacciones intermoleculares deben ser insignificantes para evitar el ordenamiento 3D.

Aunque a lo largo de las últimas décadas se han preparado cientos de clusters de metales de transición que muestran comportamientos de molécula imán, la barrera energética observada en ellos suelen ser en su mayoría muy pequeñas.⁶⁵ A continuación se describirán brevemente algunos compuestos con alguna propiedad fuera de lo convencional dentro de estos materiales. En este gran abanico, el

compuesto que posee mayor barrera de activación es un compuesto hexanuclear de $[\text{Mn(III)}]_6$ con un valor de $U_{\text{eff}}=62 \text{ cm}^{-1}$ (los iones Mn^{III} presentan acoplamiento espín-órbita y desdoblamiento a campo cero).⁶⁶

Los primeros intentos de aumentar la barrera y la T_b en SMMs se basaban en aumentar el número de centros metálicos para conseguir un estado fundamental de espín más elevado, hasta llegar al compuesto de Mn (Figura 15) siendo el primero que alcanza un $S=83/2$. Sin embargo, al aumentar el número de núcleos, la anisotropía se hacía insignificante, eliminando el comportamiento de SMMs.⁶⁷

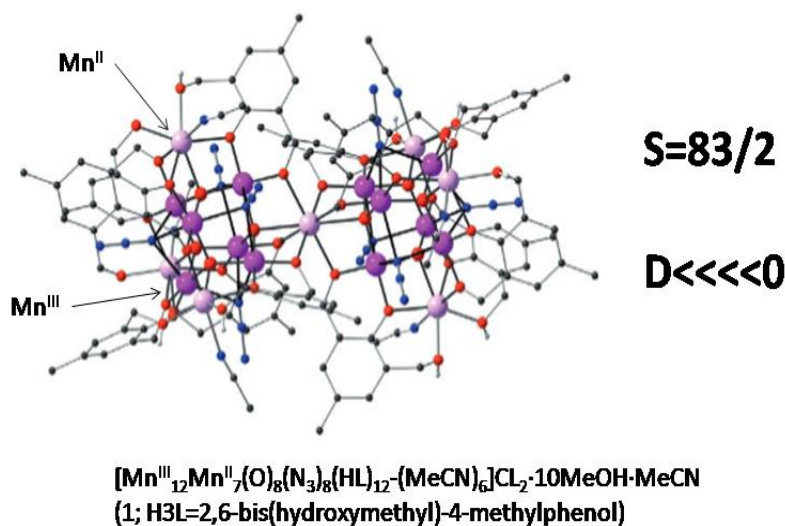


Figura 15. Estructura del compuesto con mayor spin fundamental.

Por ello, actualmente se está trabajando en sintetizar SMMs mononucleares con iones metálicos que presentan una gran anisotropía magnética (contribución espín-órbita de primer orden) como el Co(II) , Fe(II) ó el Fe(I) . Siendo este último, un compuesto mononuclear de Fe(I) , el primero en mostrar una barrera de activación térmica de $U_{\text{eff}}=226 \text{ cm}^{-1}$.⁶⁸

Otro camino a seguir en la formación de moléculas con propiedades de SMMs es la utilización de iones de tierras raras, ya que poseen una elevada anisotropía a consecuencia de la combinación de momentos magnéticos elevados en el estado fundamental y de los efectos de acoplamiento espín-órbita. Pero las

estrategias más destacables han sido el uso de complejos combinando metales de transición y tierras raras (3d-4f), así como el uso de complejos mononucleares de actínidos y lantánidos. Aunque estos materiales basados en tierras raras han llegado a barreras de activación (U) en torno a los 650 cm^{-1} la gran facilidad de presentar efecto túnel cuántico, ha complicado su uso en aplicaciones relacionadas con el almacenamiento de información.⁶⁹

3.2. Luminiscencia

Cuando una sustancia es excitada mediante una fuente de energía, esta tiende a liberar dicha energía mediante diferentes procesos (Figura 16). Uno de esos procesos es el conocido como luminiscencia. Este proceso consiste, básicamente, en que en una molécula tiene lugar una absorción de energía y, posteriormente, un proceso de emisión de radiación electromagnética en el que intervienen, básicamente, los estados electrónicos moleculares excitados y fundamentales. Dicha emisión luminiscente puede ser de 2 tipos: fluorescente o fosforescente. Que la emisión sea de un tipo u otro es debido a la multiplicidad de spin de los estados de energía durante el proceso de relajación. La fluorescencia se da cuando los estados presentan la misma multiplicidad de spin, con un tiempo de vida no superior a varios nanosegundos, mientras que la fosforescencia se da entre estados de diferente multiplicidad de spin (tiene que darse un cruce entre sistemas), cuya duración se encuentra entre microsegundos y segundos, lo que implica una emisión más prolongada que la fluorescencia.

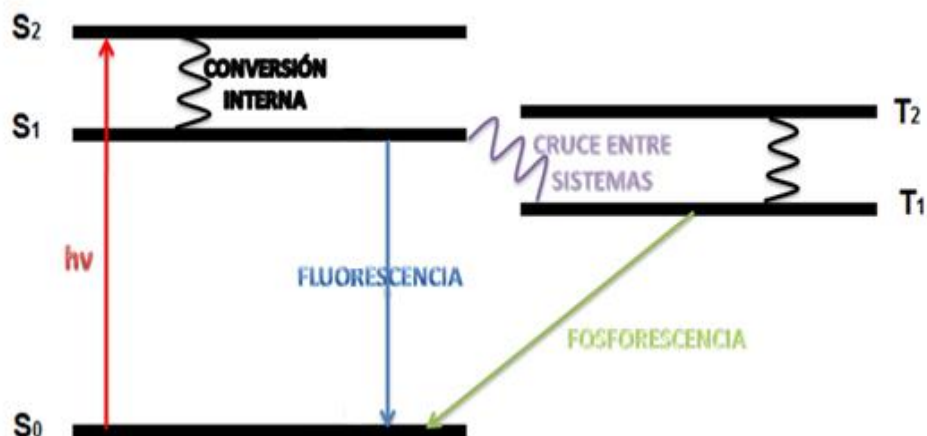


Figura 16. Diagrama de Jablonski que muestra los diferentes modos de relajación que participan en los procesos de luminiscencia.

La luminiscencia de estos compuestos puede deberse a diversos factores: el ligando orgánico (altamente conjugado), el centro metálico (especialmente en lantánidos, mediante efecto antena), transferencia de carga desde el ligando al metal (*ligand-to-metal charge transfer*, LMTC) o desde el metal al ligando (*metal-to-ligand charge transfer*, MLTC) y, por último, puede ser debida a las moléculas huésped alojadas en el interior del polímero de coordinación.⁷⁰

Los materiales que poseen esta propiedad suele presentar potencial en el campo de los sensores.⁷¹

3.2.1. Luminiscencia basada en el Ligando

A la hora de diseñar un compuesto de coordinación se suelen utilizar una gran variedad de tipos de ligandos orgánicos, siendo los más comunes aquellos que son π -conjugados debido a su esqueleto rígido y funcionalizado con varios grupos coordinantes (carboxilatos, aminas, heterociclos, etc). La emisión del ligando orgánico normalmente corresponde a la transición desde el estado excitado singlete de menor energía al estado fundamental singlete. Sin embargo, en los compuestos de coordinación es algo diferente a la que presenta como molécula libre debido a que el ligando se estabiliza en la estructura, permitiendo variar la intensidad y su tiempo de vida medio.

Uno de los últimos materiales de este tipo de luminiscencia son los complejos $[\text{ZnX}_2(4-([2,2':6',2''\text{-terpiridin}]-4'\text{-yl})-N,N\text{-difenil}anilina)]$ (para $X = \text{Cl}$ (complex 1), Br (complex 2), I (complex 3)).⁷² Se observa para este caso un desplazamiento en los máximos de emisión (desde los 510 nm a la zona de los 550-580 nm) debido al aumento de la estabilidad del ligando al coordinarse al metal y al interactuar con los halógenos presentes en la estructura (Figura 17b). Por otra parte, la presencia de estos halógenos aumenta la intensidad de emisión, aunque al aumentar el peso atómico del halógeno el aumento de intensidad decrece (Figura 17a).

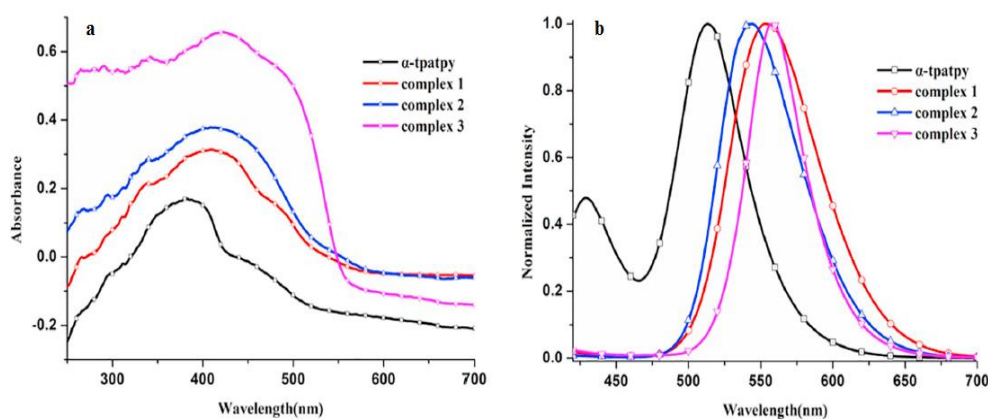


Figura 17. a) Espectro de emisión del ligando y los 3 compuestos. b) Espectro de emisión normalizado para el ligando y los compuestos.

3.2.2. Luminiscencia basada en el Metal

Normalmente este tipo de luminiscencia se produce en compuestos de coordinación donde el centro metálico es un lantánido. Esto se debe a que estos iones metálicos presentan una gran variedad de niveles energéticos electrónicos gracias a la intervención de los orbitales f .⁷³

Sin embargo, los lantánidos poseen una absorción de luz muy débil debido a las transiciones $f-f$ prohibidas, por lo que se necesita de otras especies que presenten una absorción destacable y puedan participar en los procesos de transferencia de energía, dando lugar a lo que se conoce como efecto antena.⁷⁴ En este proceso, la luz es absorbida por el ligando, situado en el entorno de coordinación del centro metálico, se transfiere y es emitida por el núcleo lantánido (Figura 18). La emisión

del ligando es sustituida por la del metal, aunque en algunos casos la poca eficiencia de este proceso provoca la emisión de ambos.

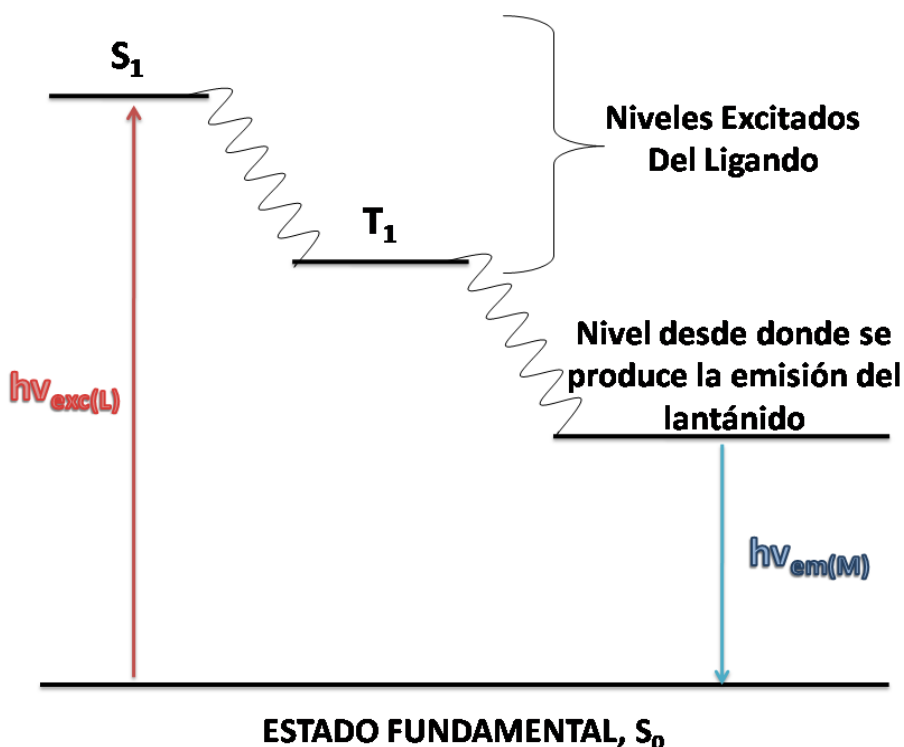


Figura 18. Esquema representativo del efecto antena.

Este efecto, a parte del ligando perteneciente a la estructura, también pueden provocarlo las diferentes moléculas huésped situadas en el interior de la estructura.

Un ejemplo reciente de compuestos que presentan luminiscencia basada en este efecto son los complejos $[\text{EuL}_2(\text{H}_2\text{O})_4]_4 \cdot n\text{NO}_3$ y $[\text{TbL}_2(\text{H}_2\text{O})_4]_4 \cdot n\text{NO}_3$ ($L=1$ - $(4$ -carboxilfenil)- 3 - $($ prazin- 2 -yl)- 1 H- $1,2,4$ -triazol). En este trabajo se observa que los complejos emiten en las longitudes de onda propias de los centros metálicos. Cuando es excitado a 338 nm el espectro de emisión del complejo de Eu muestra claramente las bandas de emisión del metal correspondientes a las transiciones ${}^5\text{D}_0 \rightarrow {}^7\text{F}_1$ y ${}^5\text{D}_0 \rightarrow {}^7\text{F}_2$. Del mismo modo, al excitar a 340 nm, el espectro del compuesto de Tb muestra 4 picos característicos pertenecientes a las transiciones ${}^5\text{D}_4 \rightarrow {}^7\text{F}_6$, ${}^5\text{D}_4 \rightarrow {}^7\text{F}_5$, ${}^5\text{D}_4 \rightarrow {}^7\text{F}_4$ y ${}^5\text{D}_4 \rightarrow {}^7\text{F}_3$ (Figura 19).⁷⁵

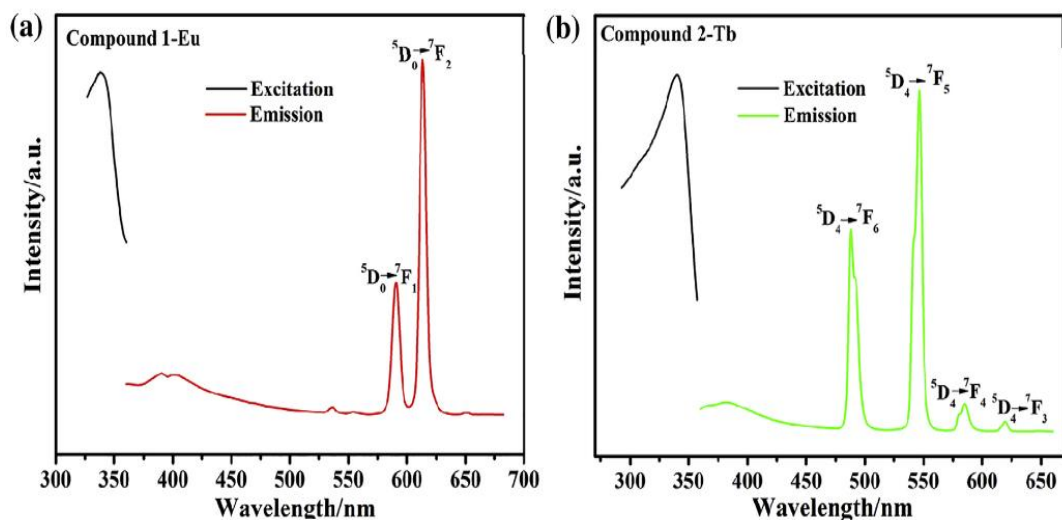


Figura 19. Espectros de emisión para los compuestos de Eu y Tb.

3.2.3. Luminiscencia basada en transferencia de carga

Este tipo de luminiscencia se genera gracias a las transiciones permitidas desde un estado excitado a su estado fundamental dividiéndose en 2 subtipos: Transferencia de carga Metal-Ligando (MLCT) y Transferencia de carga Ligando-Metal (LMCT). En el Proceso MLCT se producen transiciones electrónicas desde un orbital del metal hacia un orbital del ligando, mientras que en el caso de la LMCT sucede el proceso inverso, la transferencia electrónica sucede desde un orbital del ligando a uno del metal.

Un ejemplo de este tipo de luminiscencia es, el proceso MLCT que sucede en los complejos Fe(bi-terperidina) y Ru(bi-terperidina). En sus espectros de absorción se pueden ver la banda perteneciente al proceso MLCT situada a 580 nm para el complejo de hierro y a 505 nm para el de rutenio (Figura 20).⁷⁶

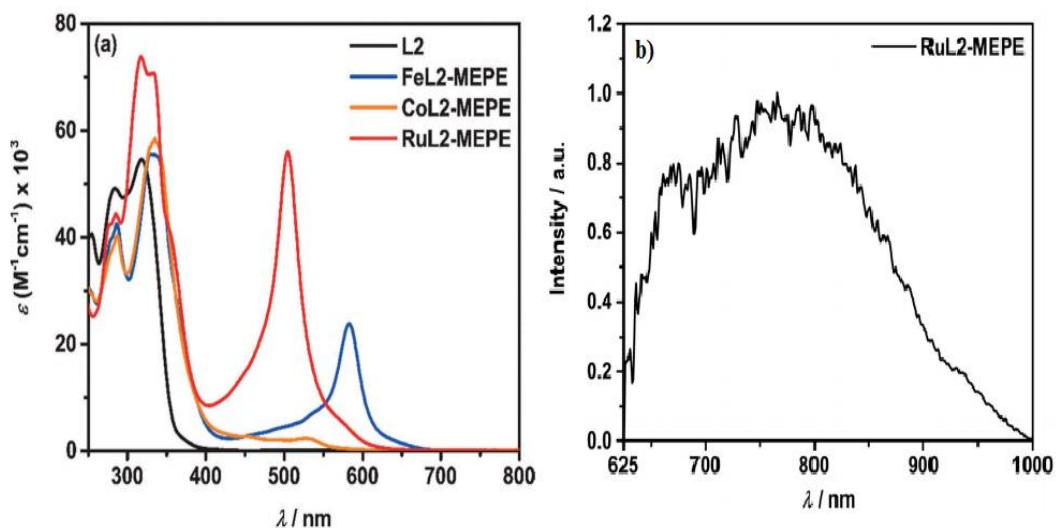


Figura 20. (a) Espectros de absorción de el ligando y los complejos $M(\text{bi-terperidina})$. (b) Espectro de emisión del complejo de Ru excitado a 505 nm (transición MLTC).

3.2.4. Luminiscencia basada en una molécula huésped

Este tipo de luminiscencia, como se puede intuir, queda reservada a polímeros de coordinación que presentan porosidad. Se produce al encapsular dentro de la estructura cristalina especies que presenten una fosforescencia o fluorescencia destacable.

Como se puede ver en el compuesto $[\text{Cd}_2(\text{tpt})_2(\text{CBA})_2(\text{H}_2\text{O})_2]$ (tpt: 2,4,6-tri(piridin-4-il)-1,3,5-triazina) y CBA: 4-carboximetil benzoato), según la molécula orgánica aromática residente en la estructura emite en un color diferente (Figura 21). Naranja-amarillo para el coroneno, rojo para el perileno y verde para el trifenileno.⁷⁷

Este tipo de fluorescencia es muy versátil ya que se puede modificar, dentro de los huecos del material, la molécula huésped. Esto permite una gran adaptación, presentando potencial, en campos tan relevantes como la medicina.⁷⁸

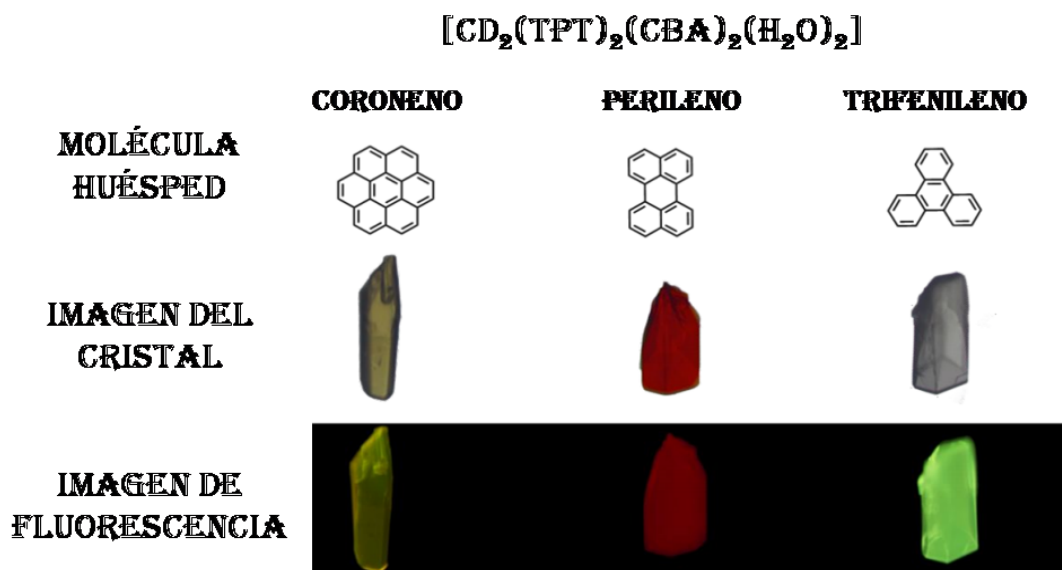


Figura 21. Luminiscencia del material de Cd según el tipo de molécula huésped alojada en su interior.

3.3. Adsorción

La adsorción es el proceso mediante el que un material retiene una sustancia, principalmente gas, en su superficie (Figura 22). La adsorción puede denominarse con 2 nombres distintos dependiendo si la molécula retenida sufre una rotura de enlace: *fisisorción*, sólo intervienen fuerzas y *quimisorción*, se produce una rotura y formación de enlace.

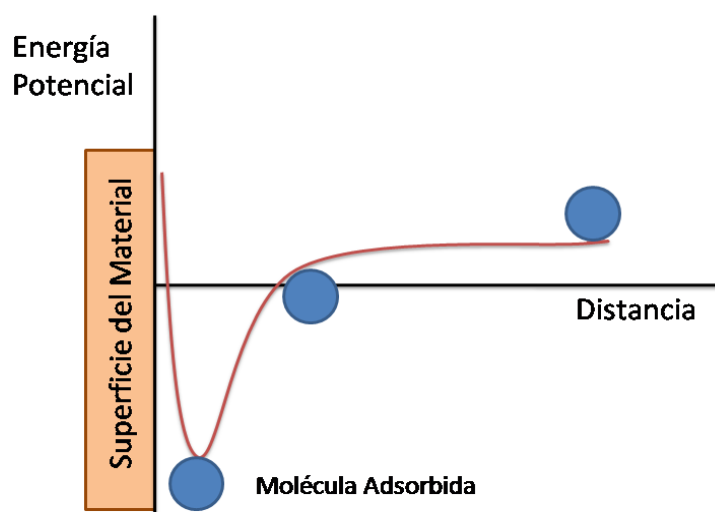


Figura 22. Proceso de acercamiento de una molécula de gas a una superficie.

Para que se pueda considerar que un compuesto presenta adsorción es necesario que presente poros. La porosidad, por tanto, se define como la fracción de volumen de la masa del material que está ocupada por poros o espacio vacío.

Esta propiedad es muy interesante debido a su gran potencial para poner solución a muchos de los problemas presentes en la actualidad: sustitución y reducción de combustibles fósiles (almacenamiento de CH_4 y H_2), reducción de gases contaminantes (adsorción de CO_2), separación de gases, etc.

3.3.1. Almacenamiento de Gases

Por estas razones, muchos investigadores han intentado mejorar la capacidad de almacenamiento de gases en MOFs modulando la interacción de gas con la red polimérica, mediante posiciones de coordinación insaturadas y/o mediante uso de ligandos con los grupos funcionales adecuados.⁷⁹

El estudio de la capacidad de los MOFs en el almacenamiento de gases se centra, fundamentalmente, en CH_4 , H_2 y CO_2 . El interés radica en los siguientes motivos:

- **CH_4 :** Es el combustible cuya relación hidrógeno/carbono es mayor.
- **H_2 :** Es uno de los combustibles más prometedores ya que presenta una alta capacidad energética (123 MJ/kg) y su producto de oxidación es H_2O . Además, el agotamiento de reservas de combustibles fósiles, aumenta el interés en este gas, como sustituto energético. Actualmente el mayor problema de su uso es el almacenamiento y transporte del mismo.
- **CO_2 :** El aumento de las emisiones de este gas debido a las acciones humanas ha crecido de forma exponencial paralelamente al desarrollo de la industria, contribuyendo el calentamiento global y al aumento de la acidez de los mares. Por tanto la reducción de su emisión, así como su captura, es actualmente un reto de la sociedad.

Para el *almacenamiento de H₂* el mayor obstáculo se encuentra en la falta de sistemas eficientes, seguros y capaces de liberar la cantidad de hidrógeno necesaria en condiciones ambientales. Entre los materiales que son capaces de responder correctamente a esta necesidad, se encuentran los que están constituidos por ligandos con grupos carboxílicos. Dentro de estos grupos son los ligandos di- y tricarboxílicos los más utilizados al presentar una mayor variedad de modos de coordinación.

Si hubiese que poner una familia estandarte en este campo, los materiales más interesantes son los MOFs desarrollados por O. M. Yaghi basados en cluster Zn₄O y ligandos carboxílicos (MOF-5, IRMOF-1, IRMOF-8, IRMOF-11, IRMOF-18, MOF-177).⁸⁰ De esta familia hay que destacar el MOF-177 (Figura 23), con una de las mejores capacidades de adsorción conocidas: 7.5wt% a 77K y 70 bares.

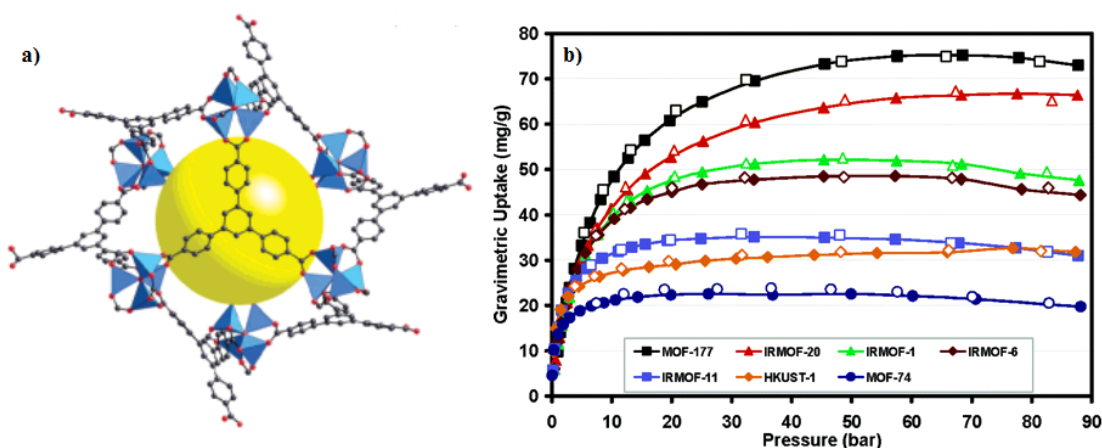


Figura 23. a) Estructura del MOF-177. b) Isotermas de H₂ a alta presión y 77K de diferentes materiales MOFs.

Otro de los retos energéticos es el *almacenamiento de CH₄*. Este gas natural es abundante y sólo cuesta la mitad que la gasolina necesaria para suministrar la misma energía. El problema es que su baja densidad energética obliga a que deba ser bombeado desde tanques de alta presión, caros y con volúmenes considerablemente grandes para su uso móvil. El reto para los investigadores, por tanto, consiste en encontrar materiales lo suficientemente buenos para hacer más económico y viable su uso.⁸¹

Uno de los materiales más prometedores en este campo es $[\{\text{CuSiF}_6(4,4'\text{-bipy})_2 \cdot 8 \text{H}_2\text{O}\}_n]$ debido a que su adsorción de metano (0,21 g/mL a 36 atm a 298K) supera ampliamente a zeolitas tradicionales como la Zeolita A5 (Figura 24).⁸²

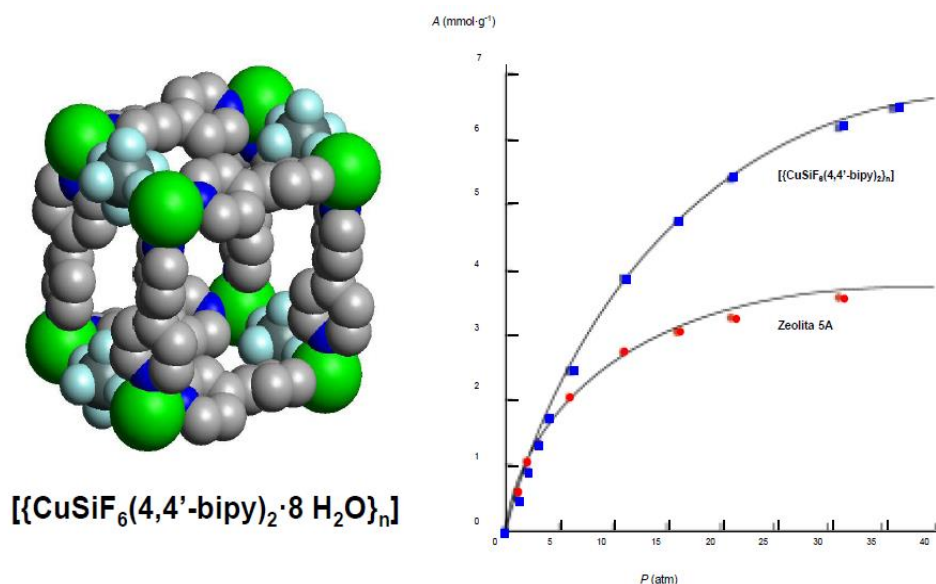


Figura 24. a) Estructura del $[\{\text{CuSiF}_6(4,4'\text{-bipy})_2 \cdot 8 \text{H}_2\text{O}\}_n]$. b) Isotermas de CH_4 a diferentes presiones y 298K del compuesto comparándolo con la Zeolita 5A.

Por último, el reto contra la contaminación es la búsqueda de materiales con buena *adsorción de CO_2* . Consiste en encontrar un adsorbente con buena capacidad de almacenamiento y capaz de regenerarse satisfactoriamente, problemas que se dan en materiales normalmente usados en este ámbito (Carbones y Zeolitas).⁸³

Por esta razón los MOFs son una de las áreas más activas en este campo de investigación. Para aumentar la selectividad de estos compuestos frente al CO_2 , se suelen modificar el tamaño de poro y la afinidad del ligando hacia el CO_2 empleando ligandos con extensiones considerables.

Partiendo de estas premisas, uno de los materiales más relevantes es el MOF-210.⁸⁴ Este material con una superficie BET de 6240 m²/g y una capacidad de adsorción de 54,5 mol/kg a una temperatura de 298K y 50 bares de presión, es uno de los materiales con la mayor capacidad de adsorción de CO_2 (Figura 25).

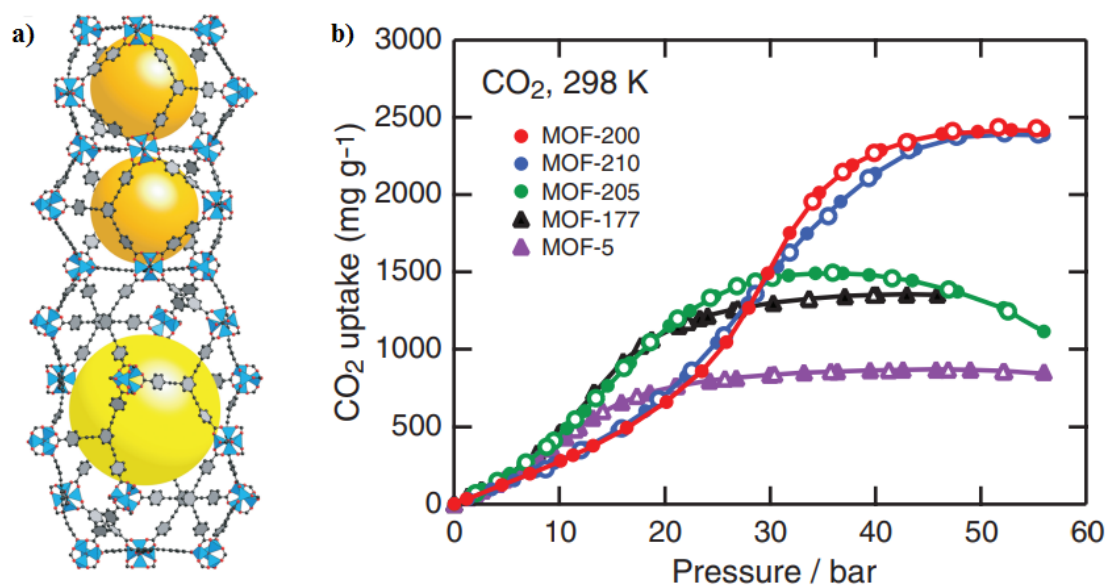


Figura 25. a) Estructura del MOF-210. b) Isotermas de CO₂ a alta presión y 298K de diferentes MOFs.

3.3.2. Separación de Gases

Los procesos de purificación y separación de gases tienen gran peso en la industria. Desde hace unas décadas se han utilizado diferentes materiales inorgánicos para este cometido, desde gel de sílice o carbón activado hasta tamices moleculares y zeolitas. Debido a este último grupo, se ha impulsado el desarrollo de MOFs destinados a esta función.

La separación se puede dar por diferentes factores estéricos, cinéticos y/o de naturaleza química. Los primeros, como su nombre indica, hacen referencia a las diferencias de tamaño entre las moléculas a separar (adsorbato) y el tamaño de poro del material. Los segundos, vienen definidos por la diferencia entre los procesos de adsorción y desorción. Y, por último, los terceros se basan en interacciones adsorbato-adsorbente, por lo que es importante conocer las propiedades fisicoquímicas del adsorbato.

A parte de la búsqueda de materiales que sean selectivos a los tres gases expuestos en el apartado anterior, se buscan materiales que también sean capaces de retirar otros contaminantes (NH₃, SO₂ y Cl₂). Por este motivo, diversos MOFs conocidos (MOF-199, MOF-5, MOF-74, etc.) fueron puestos a prueba para estos

gases. El resultado mostró que el MOF-74, MOF-199 y IRMOF-3 presentan buena adsorción para el SO_2 y NH_3 (Figura 26),⁸⁵ a consecuencia de los grupos oxo de la estructura y a la presencia de un centro metálico activo.

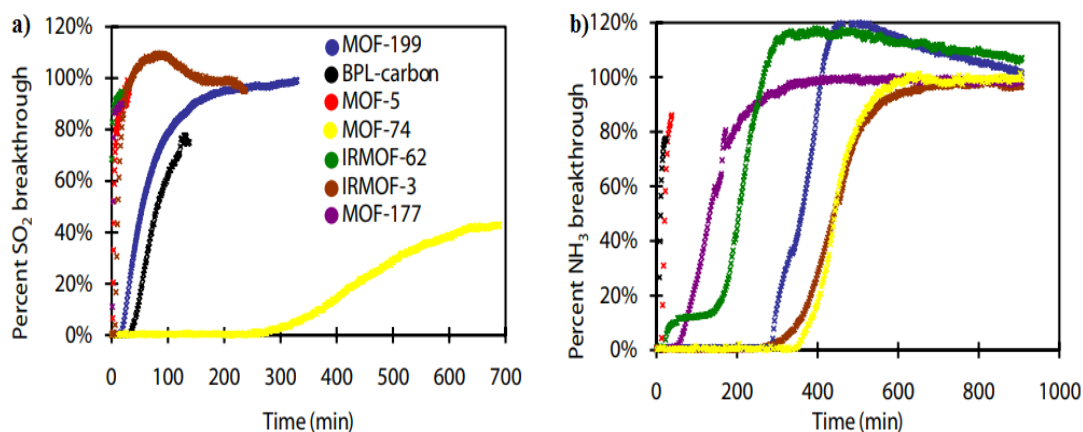


Figura 26. Curva de ruptura para contaminantes gaseosos para diferentes MOFs (a) SO_2 y (b) NH_3

4. Propiedades Biológicas

En las últimas décadas, en la Química de la coordinación ha surgido un gran interés en el desarrollo de compuestos que presenten actividad biológica contra enfermedades de este siglo (Cáncer, Parkinson, Alzheimer, Diabetes, etc.) haciendo que estos compuestos actúen como fármacos en sí o usándolos para el encapsulamiento de fármacos conocidos para su transporte y mejora de su eficacia.⁸⁶ En esta Tesis se recogen algunos materiales a los que se les ha medido la actividad biológica antitumoral, antiinflamatoria y antiparasitaria.

4.1. Propiedades Antitumorales

El cáncer es una de las predominantes causas de muerte en el mundo. En países desarrollados se considera la principal causa de mortalidad y amenaza con alcanzar este número en el resto de países. Las principales causas están asociadas al estilo de vida adoptado en esos países (tabaco, sedentarismo y dietas).⁸⁷

Hasta la fecha, el tratamiento más efectivo es la cirugía seguido por tratamientos de radioterapia y/o quimioterapia. Sin embargo, la cirugía sólo es eficaz contra tumores primarios, mientras que para otros casos el uso de las terapias, no es lo suficientemente eficaz contra cánceres más desarrollados.⁸⁸

Es por tanto que estos últimos años se ha hecho hincapié en el desarrollo de nuevos fármacos basados en compuestos de coordinación debido a su capacidad de presentar propiedades físico-químicas poco comunes en comparación con los fármacos orgánicos. Además, la versatilidad metal-ligando permite interacciones con moléculas biológicas diana.⁸⁹

Durante los años sesenta Rosenberg y su grupo de investigación, mientras estudiaban la interacción de campos magnéticos sobre la división celular, se percataron de que el platino presente en las bobinas del imán era el causante de que la división celular no se produjese correctamente.⁹⁰ Tras esto en 1969 publicaron el primer artículo que atribuía a un compuesto de coordinación (*cis-platino*, $[\text{PtCl}_2(\text{NH}_3)_2]$) propiedades antitumorales, sentando así las bases para la síntesis de agentes quimioterapéuticos.⁹¹ A pesar de ser uno de los medicamentos más efectivos, sus graves efectos secundarios (daño renal, náuseas, vómitos severos y destrucción de médula ósea) limitan su uso clínico. Buscando el equilibrio entre las ventajas e inconvenientes que presentaba el *cis-platino*, diferentes derivados (Figura 27), denominados carboplatinos y oxaliplatinos, han sido investigados y han logrado su aprobación y uso mundial.⁹²

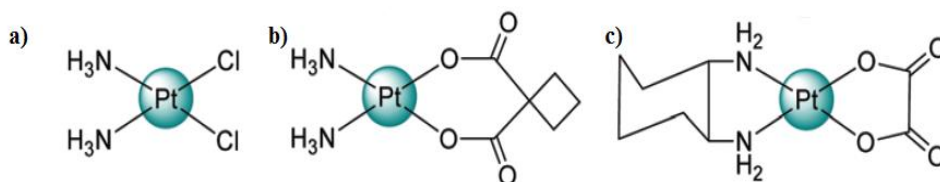


Figura 27. Estructuras de diferentes compuestos de platino con propiedades antitumorales. a) *cis-platino*, b) *carboplatino* y c) *oxaliplatino*.

Tras el potencial mostrado por los materiales de platino, la comunidad científica empezó a buscar agentes terapéuticos en complejos metálicos con

diferentes núcleos, siendo los de rutenio los que presentan mayor ventaja frente a otros metales. Presentan diferentes estados de oxidación en condiciones biológicas y han mostrado menores efectos tóxicos en células sanas al presentar mayor selectividad frente a células cancerosas.⁹³ Entre los compuestos de esta familia cabe destacar NAMI-A y NKP-1339 (Figura 28), que se encuentran ya en ensayos clínicos.⁹⁴

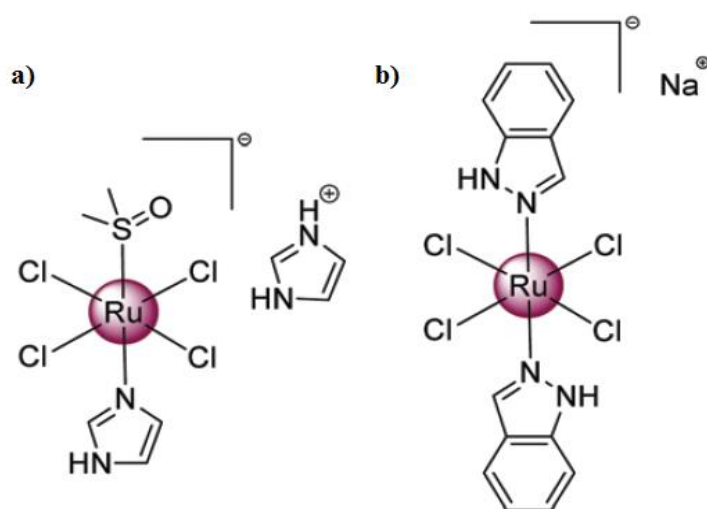


Figura 28. Estructuras de diferentes compuestos de rutenio con propiedades antitumorales. a) NAMI-A y b)) NKP-1339.

Aunque estas dos familias de fármacos son las más prometedoras en la lucha contra el cáncer, actualmente se están desarrollando una gran variedad de compuestos de coordinación basados en diferentes metales (Cu, Zn, Ni, V...) que también posean el potencial necesario para combatir esta enfermedad.⁹⁵

4.2. Otras Propiedades Biológicas

Aunque las otras dos propiedades (antiinflamatoria y antiparasitaria) presentes entre los compuestos recogidos en esta Tesis, son a priori de menor importancia en comparación al cáncer, bien es cierto que son área de interés en Química de la Coordinación.

La Leishmaniasis es una de las enfermedades parasitarias que más preocupa en los últimos años. Según la OMS (Organización Mundial de la Salud), dicha enfermedad causada por protozoos del género *Leishmania*, es endémica en más de 98 países y se estima que cada año se producen de 900.000 a 1,3 millones de nuevos casos y entre 26.000 y 65.000 muertes, convirtiéndola en la novena enfermedad infecciosa a nivel mundial.⁹⁶ En la actualidad no existe un tratamiento eficaz contra la enfermedad, siendo los antimoniales pentavalentes, como el Pentosam ® o el Glucantime ® (Figura 29), los que constituyen la primera línea de fármacos para el tratamiento de la leishmaniasis. Sin embargo, presentan severos efectos secundarios y pueden dar lugar a la resistencia entre los patógenos.

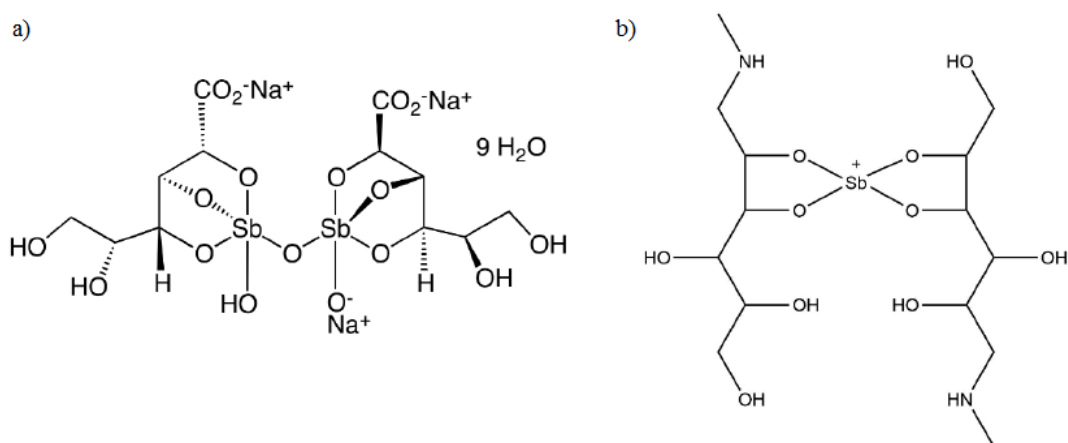


Figura 29. Estructura de (a) Pentosam ® y (b) Glucantime ®.

Es por ello, que la comunidad científica está centrada en la búsqueda de nuevos materiales que sean capaces de solventar estos inconvenientes. Entre estos nuevos compuestos de coordinación desarrollados cabría destacar el uso de derivados de las 1,2,4-triazolopirimidinas por su gran selectividad hacia los parásitos en comparación a las células huésped.⁹⁷

Por último, otro gran reto de la comunidad científica se ha centrado en la búsqueda de nuevos fármacos antiinflamatorios, que no presenten los efectos secundarios (principalmente relacionados con el tracto digestivo) que suelen

presentar los medicamentos antiinflamatorios no esteroideos, como por ejemplo el ibuprofeno o el ácido acetilsalicílico (Figura 30).⁹⁸

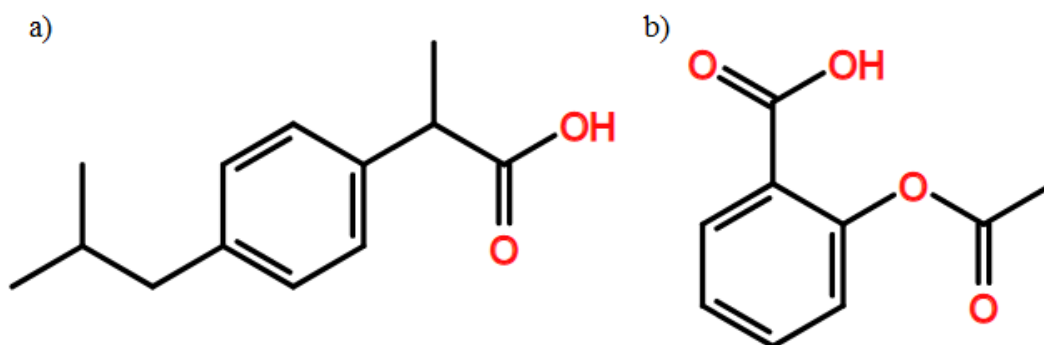


Figura 30. Estructura de (a) ibuprofeno y (b) ácido acetilsalicílico.

El proceso de inflamación está relacionado de forma directa con la liberación de óxido nítrico (NO). Por tanto la búsqueda de nuevos compuestos antiinflamatorios se encuentra centrada en la reducción de este radical mediante su eliminación o interfiriendo en la actividad enzimática responsable de su liberación. Recientemente una gran variedad de compuestos de coordinación basados en metales de la primera serie de transición o lantánidos están mostrando una excelente respuesta antiinflamatoria.⁹⁹

5. Hipótesis

Los ligandos nitrogenados con grupos carboxilato son unos estupendos bloques de construcción a la hora de desarrollar nuevos polímeros de coordinación multifuncionales debido a los múltiples modos de coordinación que exhiben, lo que les generan un gran potencial para sintetizar materiales que puedan poseer un gran abanico de propiedades. En este sentido, en esta Tesis Doctoral, nos planteamos sintetizar una gran variedad de compuestos de coordinación multidimensionales basados en ligandos de este tipo que fuesen nuevos o que hubiesen sido muy poco utilizados. La adecuada elección de los centros metálicos y los distintos ligandos

orgánicos, nos llevaría a ser capaces de obtener distintos tipos de materiales que podrían exhibir interesantes propiedades de interés en campos tan distintos como magnetismo, luminiscencia, cáncer, adsorción, catálisis, electrónica y sensores. Con todo lo anterior, deberíamos ser capaces de obtener cristales de estos nuevos materiales para estudiar sus propiedades estructurales y tuneirlas, con el objetivo fundamental de llegar a obtener nuevos sistemas de diversa dimensionalidad diseñados adrede para conseguir transformar una idea plasmada en un papel en una realidad con interesantes aplicaciones.

6. Objetivos

Basándonos en todo lo explicado anteriormente, queda claro que la búsqueda de nuevos compuestos de coordinación multifuncionales es uno de los retos actuales de la Química de la Coordinación. Esta Tesis Doctoral se encuentra situada dentro de este reto y tiene como objetivo fundamental la búsqueda de nuevos compuestos de coordinación así como su caracterización estructural y estudio de las posibles propiedades que puedan mostrar. La utilización de ligandos con una gran diversidad de formas de coordinación parece ser la herramienta perfecta para desarrollar nuevos materiales. Por lo tanto, la utilización de ligandos nitrogenados que contengan grupos carboxilato es un buen recurso para llevar a cabo este objetivo principal.

Los objetivos derivados que se persiguen son:

- 1- Obtener una familia de compuestos de coordinación, utilizando un ligando con una estructura sencilla derivado del imidazol (Figura 31) que será nuestro punto de partida para desarrollar materiales con diferente dimensionalidad. Se estudiarán las propiedades de los materiales sintetizados y se analizará al comportamiento de los grupos funcionales de este ligando en presencia de iones metálicos.

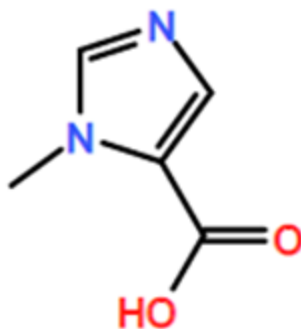


Figura 31. *Ligando imidazol que se usará: Ácido 1-metilimidazol-5-carboxílico.*

- 2- Intentar sintetizar compuestos más complejos estructuralmente, mediante el aumento el ángulo del ciclo aromático manteniendo relativamente las distancias entre los grupos funcionales del ligando para separar adecuadamente los centros metálicos en la estructura. Para ello se utilizarán ligandos carboxílicos derivados de la piridina (Figura 32).

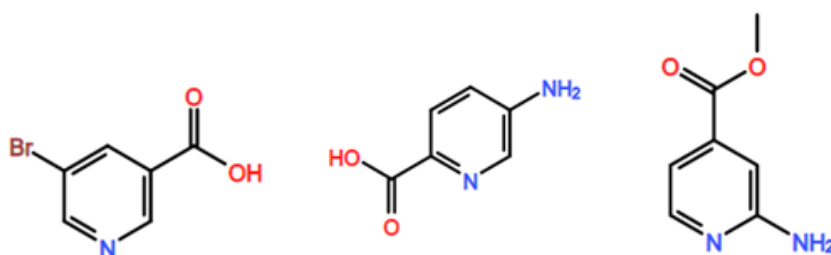


Figura 32. *Ligandos derivados de piridina que se quieren estudiar durante el desarrollo de esta Tesis. De izquierda a derecha: ácido 5-bromonicotínico, ácido 5-amino-2-carboxílico y Metil-2-aminoisonicotinato.*

- 3- Sintetizar compuestos multifuncionales con mayor rigidez estructural, mediante la utilización de ligandos carboxílicos derivados del indazol y a su vez estudiar la relevancia del posicionamiento relativo de los grupos funcionales mediante la variación de la posición del ácido carboxílico en la estructura (Figura 33).

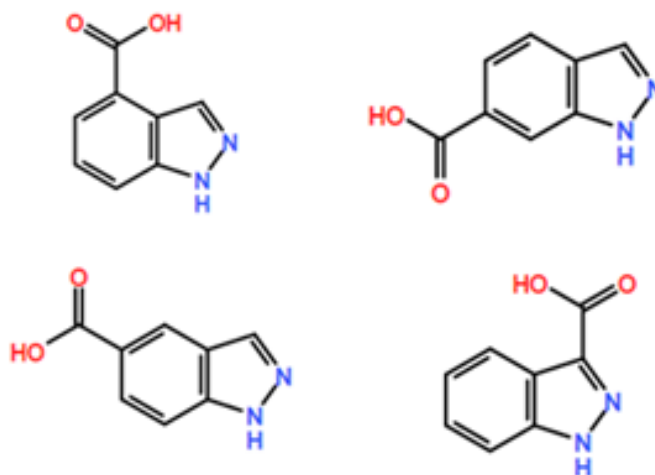


Figura 33. Ligandos derivados de indazol que se estudiarán en esta Tesis. De izquierda a derecha y de arriba a abajo: ácido 1H-Indazol-4-carboxílico, ácido 1H-Indazol-6-carboxílico, ácido 1H-Indazol-5-carboxílico y ácido Indazol-3-carboxílico.

- 4- Por último, se analizará la ausencia de alguno de los grupos funcionales anteriores y/o la utilización de otros grupos funcionales tales como alcoholes o carbonitrilos, sintetizando compuestos de coordinación mediante el uso de ligandos que cumplan los requisitos estructurales deseados (Figura 34).



Figura 34. Ligandos que presentan variación de los grupos funcionales que serán estudiados en esta Tesis. De izquierda a derecha: 4-hidroxipirimidina-5-carbonitrilo y ácido 2,5-dihidroxitereftálico.

7. Referencias

1. Werner, A., *Z. Anorg. Allg. Chem.*, **1893**, 3, 267-330.
2. (a) Shibata, Y. *Journal of the College of Science, Imperial University of Tokyo*, **1916**, 37(8),1-17. (b) Shibata, Y. *Journal of the College of Science, Imperial University of Tokyo*, **1916**, 37(8), 19-31.
3. (a) Wyart, J. *Bull. Soc. Fr.Mineral*, **1926**, 49, 148. (b) Pfab, W. Fisher, E. Z. *Anorg. Allg. Chem.*, **1953**, 274, 316-322.
4. Kinoshita, Y.; Matsubara, I.; Saito, Y. *Bull. Chem. Soc. Jpn.*, **1959**, 32, 741-747.
5. Bailar, J.C.Jr. *Preparative Inorg. Reactions*, **1964**, 1, 1-27.
6. (a) Iwamoto, T.; Miyoshi, T.; Sasaki, Y.; Fujiwara, S. *Bull. Chem. Soc. Jpn.*, **1967**, 40, 1174-1178. (b) Nishikiori S. I. Iwamoto, T. *Chem. Lett.*, **1984**, 13, 319-322.
7. (a) Yaghi O. M.; Li, H. *J. Am. Chem. Soc.*, **1995**, 117, 10401-10402. (b) Yaghi, O. M.; Li, G.; Li, H. *Nature*, **1995**, 378, 703-706.
8. Li, H.; Eddaoudi, M.; O'Keeffe, M.; Yaghi, O. M. *Nature*, **1999**, 402,276-279.
9. Diercks, C. S.; Kalmutzki, M. J.; Diercks N. J.; Yaghi O. M. *ACS Cent. Sci.*, **2018**, 4, 1457-1464.
10. (a) Coordination Polymers and Metal Organic Frameworks: Terminology and nomenclature Guidelines, https://iupac.org/projects/project-details/?project_nr=2009-012-2-200. (b) Batten, S. R.; Champness, N.R.; Chen X.M.; García-Martinez, J.; Kitawaga S.; Öhrström, L.; O'Keeffe, M.; Suh, M. P.; Reedijk, J. *Pure Appl. Chem.*, **2013**, 85(8), 1715-1724.
11. O'Keeffe, M.; Peskov, M. A.; Ramsden S. J.; Yaghi O. M. *Acc. Chem. Res.*, **2008**, 41(12), 1782-1789.
12. (a) Calahorro, A. J.; López-Viseras M.; Salinas-Castillo, A.; Fairen-Jimenez, D.; Colacio, E.; Cano, J.; Rodríguez-Diéguez A. *CrystEngComm*, **2012**, 14, 6390-

6393.(b) Zhao, Y.; Wang, L.; Fan, N.; Han, M.; Yang, G. *Cryst. Growth Des.*, **2018**, 18, 7114-7121. (c) Zheng, J.; Cui, X.; Yang, Q.; Ren, Q.; Yang, Y.; Xing, H. *Chem. Eng. J.*, **2018**, 354, 1075-1082.

13. Parmar, B.; Patel, P.; Kureshy, R.I.; Khan, N. H. *Chem. Eur. J.*, **2018**, 24, 15831-15839.

14. (a) Oliveri V, Puglisi A, Vecchio G. *Dalton Trans.*, **2011**, 40(12), 2913-2919. (b) Ibrahim, M.; Sabouni, R.; Hussein, G. A. *J. Nanosci. Nanotechnol.*, **2018**, 18(8), 5266-5273.

15. (a) Calahorra, A. J.; Salinas-Castillo, A.; Seco, J. M.; Zuñiga, J.; Colacio, E. Rodríguez-Diéguez, A. *CrystEngComm.*, **2013**, 15, 7636-7639. (b) Rodríguez-Diéguez, A.; Pérez-Yáñez, S.; Ruiz-Rubio, L.; Seco, J. M.; Cepeda, J. *CrystEngComm.*, **2017**, 19, 2229-2242.

16. (a) Cepeda, J.; Pérez-Yáñez, S.; Beobide, G.; Castillo, O.; García, J. A.; Lanchas, M.; Luque, A. *Dalton Trans.*, **2015**, 44, 6972–6986. (b) Lin, R.-B.; Liu, S. Y.; Ye, J. W.; Li, X. Y.; Zhang, J. P. *Adv. Sci.*, **2016**, 3, 1500434–1500454.

17. Pedersen, K. S.; Perlepe, P.; Aubrey, M. L.; Woodruff, D. N.; Reyes-Lillo, S. E.; Reinholdt, A.; Voigt, L.; Li, Z.; Borup, K.; Rouziers, M.; Samohvalov, D.; Wilhelm, F.; Rogalev, A.; Neaton, J. B.; Long, J. R.; Clerac, Rodolphe. *Nat. Chem.*, **2018**, 10, 1056-1061.

18. Chen, M.L.; Zhou, Z.H. *Inorg. Chim. Acta*, **2017**, 458, 199-217.

19. (a) Nagao, R.; Marumo, F.; Saito, Y. *Acta Cryst.*, **1972**, B28, 1852. (b) Herak, R.; Srdanov G.; Djuran, M. I.; Radanovic, D. J.; Bruvo, M. *Inorg. Chim. Acta*, **1984**, 83, 55-64.

20. Archer, R. D. *Coord. Chem. Rev.*, **1993**, 128, 48-69.

21. (a) Mossin, S.; Tran, B. L.; Adhikari, D.; Pink, M.; Heinemann, F. W.; Sutter, S.; Meyer, K.; Mindiola D. J. *J. Am. Chem. Soc.*, **2012**, 134, 13651-13661. (b) Gautam, R.; Petritis, S.J.; Astashkin A.V.; Tomat, E. *Inorg. Chem.*, **2018**, 57, 15240-15246.

22. (a) Thompson, K. H.; Liboiron, B.D.; Sun, Y.; Bellman, K.D.D.; Setyawati, I.A.; Patrick, B.O.; Karunaratne, V.; Rawji, G.; Wheeler, J.; Sutton, K.; Bhanot, S.; Cassidy, C.; McNeill, J. H.; Yuen, V. G.; Orvig, C. *J. Biol. Inorg. Chem.*, **2003**, 8, 66-74. (b) Kumar, D.; Kumar, A.; Sharma, J. *J. Chem-Ny.*, **2012**, 2013, 1-7.
23. (a) Meník, M.; Mikus, P. *J. Organomet. Chem.*, **2017**, 830, 62-66. (b) Li, H.; Wang, L.; Dai, Y.; Pu, Z.; Lao, Z.; Chen, Y.; Wang, M.; Zheng, X.; Zhu, J.; Zhang, W.; Si, R.; Ma, C.; Zeng, J. *Nat. Nanotechnol.*, **2018**, 13, 411-417. (c) Meník, M.; Mikus, P. *Transit. Metal Chem.*, **2018**, 43, 367-376.
24. (a) Trost, B. M.; Jaratjarinphong, J.; Reutrakul, V. *J. Am. Chem. Soc.*, **2006**, 128, 2778-2779. (b) Xu, J. H.; Guo, L. Y.; Su, H. F.; Gao, X.; Wu, X. F.; Wang, W. G.; Tung C. H.; Sun, D. *Inorg. Chem.*, **2017**, 56, 1591-1598.
25. (a) Nesterov, D. S.; Chygorin, E. N.; Kokozay, V. N.; Bon, V. V.; Boča, R.; Kozlov, Y. N.; Shul'pina, L. S.; Jezierska, J.; Ozarowski, A.; Pombeiro A. J. L.; Shul'pin, G. B. *Inorg. Chem.*, **2012**, 51, 9110-9122. (b) Tsukamoto, T.; Kambe, T.; Nakao, A.; Imaoka, T.; Yamamoto K. *Nat. Commun.*, **2018**, 9, 3873-3880.
26. (a) Solomon, E. I.; Sundaram, U. M.; Machonkin, T. E. *Chem. Rev.*, **1996**, 96, 2563-2606. (b) Gómez-Ruiz, S.; Wolf, R.; Bauer, S.; Bitting, H.; Schisler, A.; Lönnecke, P.; Hey-Hawkins, E. *Chem. Eur. J.*, **2008**, 14, 4511-4520. (c) Yang, L.; Powell, R.; Houser, R. P. *Polyhedron*, **2010**, 29, 1946-1955.
27. (a) Kostakis, G. E.; Ako, A. M.; Powell, A. K. *Chem. Soc. Rev.*, **2010**, 39, 2238-2271. (b) Sampani, S. I.; Aubert S.; Cattoen, M.; Griffiths, K.; Abdul-Sada, A.; Akien, G. R.; Tizzard, G. J.; Coles, S. J.; Arseniyadis, S.; Kostakis, G. E. *Dalton Trans.*, **2018**, 47, 4486-4493. (c) Chai, J.; Tian, R.; Wu, D.; Wei, D.; Xu, Q.; Mathey, F. *Dalton Trans.*, **2018**, 47, 13342-13344.
28. (a) Barra, A. L.; Caneschi, A.; Cornia, A.; De Biani, F. F.; Gatteschi, D.; Sangregorio, C.; Sessoli, R.; Sorace, L. *J. Am. Chem. Soc.*, **1999**, 121, 5302-5310. (b) Wang, S. Y.; Wemple, S. Y.; Yoo, J.; Folting, K.; Huffman, J. C.; Hagen, K. S.; Hendrickson, D. N.; Christou, G. *Inorg. Chem.*, **2000**, 39, 1501-1513. (c)

Bhattacharjee, A.; Miyazaki, Y.; Nakano, M.; Yoo, J.; Christou, G.; Hendrickson, D. N.; Sorai, M. *Polyhedron*, **2001**, 20, 1607-1613.

29. (a) Kirillov, A.M.; Kopylovich, M.N.; Kirillova, M.V.; Haukka, M.; da Silva, M.; Pombeiro, A.J.L. *Angew. Chem., Int. Ed. Engl.*, **2005**, 44, 4345-4449. (b) Gagnon, K.; Aly, S. M.; Brisach-Wittmeyer, A.; Bellows, D.; Bérubé J. F.; Caron, L.; Abd-El-Aziz, A. S.; Fortin, D.; Harvey P. D. *Organometallics*, **2008**, 27, 2201-2214.

30. Carson, I.; Tasker, P. A.; Love, J. B. Moser, M.; Fischmann, A. J.; Jakovjevic, B.; Soderstrom, M. D.; Morrison C. A. *Eur. J. Inorg. Chem.*, **2018**, 13, 1511-1521.

31. (a) Papatriantafyllopoulou, C.; Moushi, E. E.; Christou, G.; Tasiopoulos, A. J. *Chem. Soc. Rev.*, **2016**, 45, 1597-1628. (b)Abbasi, P.; Quinn, K.; Alexandropoulos, D. I.; Damjanović, M.; Wernsdorfer, W.; Escuer, A.; Mayans, J.; Pilkington, M.; Stamatatos, T. C. *J. Am. Chem. Soc.*, **2017**, 139, 15644–15647. (c) Wu, J; Li, X. L.; Gou, M.; Zhao, L.; Zhang Y. Q.; Tang, J. *Chem. Commun.*, **2018**, 54, 1065–1068.

32. (a) Hagen, S.; Pantenburg, I.; Weigand, F.; Wickleder, C.; Wesemann, L. *Angew. Chem. Int. Ed.*, **2003**, 42, 1501-1505.(b)Cossairt, B. M.; Juhas, P.; Billinge, S. J. L.; Owen J. S. *J. Phys. Chem. Lett.*, **2011**, 2, 3075-3080.(c)Ostrowska, M.; Fritsky, I. O.; Gumienna-Kontecka E.; Pavlishchuk, A. V. *Coord. Chem. Rev.*, **2016**, 327–328, 304–332.

33. (a) Saalfrank, R. W.; Scheurer, A. *Top. Curr. Chem.*, **2012**, 319, 125-170.(b) Heindl, C.; Peresyphkina, E. V.; Virovets, A. V.; Komarov, V. Y.; Scheer, M. *Dalton Trans.*, **2015**, 44, 10245-10252. (c) Lynes, A. D.; Hawes, C. S.; Byrne, K.; Schmitt, W.; Guanlaugsson, T. *Dalton Trans.*, **2018**, 47, 5259-5268.

34. (a) Costes, J. P.; Dahan F.; Nicodème, F. *Inorg. Chem.*, **2001**, 40, 5285-5287. (b) Costes, J. P.; Vendier, L.; Wernsdorfer, W. *Dalton Trans.*, **2011**, 40, 1700-1706.

35. (a)Batten, S. R.; Murray, K. S. *Coord. Chem. Rev.* **2003**, 246, 103–130. (b) Li, M.; Li, D.; O’Keeffe, M.; Yaghi, O. M. *Chem. Rev.* **2014**, 114, 1343–1370. (c) Allendorf, M. D.; Stavila, V. *CrystEngComm.*, **2015**, 17, 229–246.

36. Gu, J. H.; Li, W. X.; Li, H. X.; Li, H. Y.; Lang J. P. *Polyhedron*, **2018**, 154, 47-53.
37. (a) Bogani, L.; Sangregorio, C.; Sessoli, R.; Gatteschi, D. *Angew. Chem. Int. Ed.*, **2005**, 44, 5817-5821. (b) Long, Q. Q.; Hu, Z. B.; Wang, H. S.; Yin, C. L.; Chen, Y.; Song, Y.; Zhang, Z. C.; Xia, B. T.; Pan, Z. Q. *Inorg.Chem.Commun.*, **2018**, 98, 127-131.(c) Roy, M.; Adhikary, A.; Mondal, A. K.; Mondal, R. *ACS Omega*, **2018**, 3, 15315-15324.
38. (a) Li, J. J.; Wang, C. C.; Guo, J.; Cui, J. R., Wang, P. *Polyhedron*, **2017**, 126, 17-22. (b) Xu, H.; Feng, L.; Wang, Q.; Huang, W.; Zhou, H. *Polyhedron*, **2019**, 157, 49-53. (c) Li, S.; Lu, L.; Feng, S.; Zhu, M. *J. Solid State Chem.*, **2019**, 269, 56-54.
39. (a) Yang, Y.; Zhu, W.; Chao, Y.; Xu, L.; Chen, M.; Liu, Z. *Adv. Mater.*, **2017**, 29, 1703588-1703600. (b) Razaei, M.; Abbasi, A.; Dinarvand, R.; Jeddi-Tehrani, M.; Janczak, J. *ACS Appl. Mater. Interfaces*, **2018**, 10, 17594-17604.
40. (a) Mondal, P.; Dey, B.; Roy, S.; Bera, S. P.; Nasani, R.; Santra, A.; Konar, S. K. *Cryst. Growth Des.*, **2018**, 18, 6211-6220. (b) Wang, X. K.; Tian, J. W., Huang, D. D. Wu, Y. P.; Pan, L. Q.; Li, D. S. *J. Solid State Chem.*, **2019**, 269, 348-353.
41. (a) Salinas-Castillo, A.; Calahorra, A. J.; Choquesillo-Lazarte, D.; Seco, J. M. Rodríguez-Diéguez, A. *Polyhedron*, **2010**, 30, 1290-1298. (b) Wang, C. X.; Xia, Y. P.; Yao, Z. Q.; Xu, J.; Chang, Z.; Bu, X. H. *Dalton Trans.*, **2019**, 48, 387-394.
42. (a) Pedersen, K. S.; Perlepe, P.; Aubrey, M. L.; Woodruff, D. N.; Reyes-Lillo, S. E.; Reinholdt, A.; Voigt, L.; Li, Z.; Borup, K.; Rouzières, M.; Samohvalov, D.; Wilhelm, F.; Rogalev, A.; Neaton, J. F.; Long, J. R.; Clérac, R. *Nat. Chem.*, **2018**, 10, 1056-1061. (b) Choi, B.; Lee, K.; Voevodin, A.; Wang, J.; Steigerwald, M. L.; Batail, P.; Zhu, X.; Roy, X. *J. Am. Chem. Soc.*, **2018**, 140, 9369-9373.
43. Wang, Q. H.; Kalantar-Zadeh, K.; Kis, A, Coleman, J. N.; Strano, M. S. *Nat. Nanotechnol.*, **2012**, 7, 699-712.

44. Kathalikkattil, A. C.; Bisht, K. K.; Subramanian, P. S.; Suresh, E. *Polyhedron*, **2010**, 29, 1801-1809.
45. (a) Pettinari, C.; Marchetti, F.; Mosca, N. Tosi, G.; Drozdov, A. *Polym. Int.*, **2017**, 66, 731-744. (b) Gu, J. J.; Cai, Y.; Qian, Z. Y.; Wen, M.; Shi, Z. F.; Lv, D. Y.; Kirillov, A. M. *Dalton Trans.*, **2018**, 47, 7431-7444. (c) Wei, X. J.; Liu, D.; Li, Y. H.; Cui, G. H. *Polyhedron*, **2019**, 158, 357-364.
46. (a) De Voorde, B. V.; Bueken, B.; Denayer, J.; Vos, D. D. *Chem. Soc. Rev.*, **2014**, 43, 5766-5788. (b) Lyu, H.; Zhang, Q.; Wang, Y.; Duan, J. *Dalton Trans.*, **2018**, 47, 4424-4227.
47. (a) Vinogradov A. V.; Zaaker-Hertling, H.; Drozdov, A. S.; Lönnecke, P.; Seisenbaeva, G. A.; Kessler, V. G.; Vinogradov, A. V.; Hey-Hawkins, E. *Chem. Commun.*, **2015**, 51, 17764-17767. (b) Pander, M.; Zelichowska, A.; Bury, W. *Polyhedron*, **2018**, 156, 131-137.
48. Choi, I. H.; Kim, Y.; Lee, D. N.; Huh, S. *Polyhedron*, **2016**, 105, 96-103.
49. (a) Botta, M. *Eur. J. Inorg. Chem.*, **2000**, 399-408. (b) Gou, F.S.; Leng, J.D.; Lin, J.L.; Tong, M.L. *Inorg. Chem.*, **2012**, 51, 405-413. (c) Ganzhorn, M.; Klyatskaya, S.; Ruben, M.; Wernsdorfer, W. *Nature Nanotech.*, **2013**, 8, 165-169. (d) Thiele, S.; Balestro, F.; Ballou, R.; Klyatskaya, S.; Ruben, M.; Wernsdorfer, W. *Science*, **2014**, 344, 1135-1138.
50. Blaney, B.; Bowers, K.D. *Proc. Roy. Soc. London Ser. (A)*, **1952**, 214, 451.
51. Ruiz, E.; Álvarez, S.; Rodríguez-Fortea, A.; Alemany, P.; Pouillon, Y.; Massobrio, C. *Magnetism: Molecules to Materials II, Chapter 7*, J. S. Miller, M. Drillon (Editors), **2003**, 227-279, Wiley-VCH, Weinheim, Germany.
52. (a) Lewis, D.L.; Hatfield, W.E.; Hodgson, D.J. *Inorg. Chem.*, **1972**, 2216-2221. (b) Crawford, H.; Richardson, H.; Hodgson, D.J.; Hatfield, W.E. *Inorg. Chem.*, **1976**, 15, 2107-2110.

- 53.** (a) Ruiz, E.; Alemany, P.; Alvarez, S.; Cano, J. *J. Am. Chem. Soc.*, **1997**, 119, 1297-1303. (b) Ruiz, E.; Alemany, P.; Alvarez, S.; Cano, J. *Inorg. Chem.*, **1997**, 36, 3683-3688.
- 54.** (a) Martínez-Pérez, M. J.; Cardona-Serra, S.; Schlegel, C.; Moro, F.; Alonso, P. J.; Prima-García, H.; Clemente-Juan, J. M.; Evangelisti, M.; Gaita-Ariño, A.; Sesé, J.; Van Slageren, J.; Coronado, E.; Luis, F. *Phys. Rev. Lett.*, **2012**, 108, 247213-247217. (b) P. Seppälä, P.; Colacio, E.; Mota, A. J.; Sillanpää, R. *Inorg. Chem.*, **2013**, 52, 11096-11109.
- 55.** (a) Kato, M.; Muto, Y. *Coord. Chem. Rev.*, **1988**, 92, 45.83. (b) Colacio, E.; Domínguez-Vera, J.M.; Ghazi, M.; Kivekäs, R.; Klinga, M.; Moreno, J.M. *Eur. J. Inorg. Chem.*, **1999**, 441-445.
- 56.** Colacio, E.; Ghazi, M.; Kivekas, R.; Moreno, J.M. *Inorg. Chem.*, **2000**, 39, 2882-2890.
- 57.** (a) Vallée, A.; Train, C.; Roux, C. *J. Chem. Educ.*, **2013**, 90, 1071-1076. (b) Clements, J. E.; Airey, P. R.; Ragon, F.; Shang, V.; Kepert, C. J.; Neville, S. M. *Inorg. Chem.*, **2018**, 57, 14930-14938. (c) Srinivasan, A.; Wang, X.; Clerac, R.; Rouzieres, M.; Falvello, L. R.; McGrady, J. E.; Hillard, E. A. *Dalton Trans.*, **2018**, 47, 16798-16806.
- 58.** (a) Coronado, E.; Galán-Mascarós, J.R.; Gómez-García C. J.; Martínez-Agudo, J.M. *Inorg. Chem.*, **2001**, 40, 113-120. (b) Clemente-León, M.; Coronado, E.; Gómez-García, C. J.; Soriano-Portillo, A. *Inorg. Chem.*, **2006**, 45, 5653-5660.
- 59.** (a) Zadrozny, J. M.; Liu, J.; Piro, N. A.; Chang, C. J.; Hill, S.; Long, J. R. *Chem. Commun.*, **2012**, 48, 3927-3929. (b) Huang, W.; Liu, T.; Wu, D.; Cheng, J.; Ouyang, Z. W.; Duan, C. *Dalton Trans.*, **2013**, 42, 15326-15331. (c) Ziegenbalg, S.; Hornig, D.; Görls, H.; Plass, W. *Inorg. Chem.*, **2016**, 55, 4047-4058.
- 60.** (a) Gatteschi, D.; Sessoli, R. *Angew. Chem. Int. Ed.*, **2003**, 42, 268-297. Das, A.; Gieb, K.; Krupskaya, Y.; Demeshko, S.; Dechert, S.; Klingeler, R.; Kataev, V.;

Buchner, B.; Muller, P.; Meyer, F.J. *Am. Chem. Soc.*, **2011**, 133, 3433-3443. (c) Chakarawet, K.; Bunting, P. C.; Long, J.R. *J. Am. Chem. Soc.*, **2018**, 140, 2058-2061.

61. (a) Sessoli, R.; Tsai, H. L.; Schake, A. R.; Wang, S.; Vincent, J. B.; Folting, K.; Gatteschi, D.; Christou, G.; Hendrickson, D. N. *J. Am. Chem. Soc.*, **1993**, 115, 1804-1816. (b) Sessoli, R.; Gatteschi, D.; Caneschi, A.; Novak, M. A. *Nature*, **1993**, 365, 141-143.

62. Brougham, D. F.; Caciuffo, R.; Horsewill, A. J. *Nature*, **1999**, 397, 241-243.

63. (a) Ruiz, J.; Lorusso, G.; Evangelisti, M.; Brechin, E.K.; Pope, S.J.; Colacio, E. *Inorg Chem.*, **2014**, 7, 3586-3594. (b) Zhou, J.; Song, J.; Yuan, A.; Wang, Z.; Chen, L.; Ouyang, Z. W. *Inorg. Chim. Acta*, **2018**, 479, 113-119.

64. (a) Leuenberger, M. N.; Loss, D.; *Phys. Rev. B*, **2000**, 61, 1286-1302. (b) Pohjola, T.; Schoeller, H. *Phys. Rev. B*, **2000**, 62, 15026-15041.

65. (a) Craig, G.A.; Murrie, M. *Chem. Soc. Rev.*, **2015**, 44, 2135-2147. (b) Cook, A. W.; Hayton, T. W. *Acc. Chem. Res.*, **2019**, 51, 2456-2464.

66. Milios, C.J.; Vinslava, A.; Wernsdorfer, W.; Moggach, S.; Parsons, S.; Perlepes, S.P.; Christou, G.; Brechin, E.K. *J. Am. Chem. Soc.*, **2007**, 129, 2754-2755.

67. Ako, A. M.; Hewitt, I. J.; Mereacre, V.; Clérac, R.; Wernsdorfer, W.; Anson, C.E.; Powell, A.K. *Angew. Chem. Int. Ed.*, **2006**, 45, 4926-4929.

68. Zadrozny, J.M.; Xiao, D.J.; Atanasov, M.; Long, G.J.; Grandjean, F.; Neese, F.; Long, J.R. *Nat. Chem.*, **2013**, 5, 577-581.

69. (a) Sessoli, R.; Powell, A. K. *Coord. Chem. Rev.*, **2009**, 253, 2328-2341. (b) Ganivet, C.R.; Ballesteros, B.; de la Torre, G.; Clemente-Juan, J.M.; Coronado, E.; Torres, T. *Chem. Eur. J.*, **2013**, 19, 1457-1465. (c) Chakraborty, A.; Goura, J.; Kalita, P.; Swain, A.; Rajaraman, G.; Chandrasekhar, V. *Dalton Trans.*, **2018**, 47, 8841-8864.

70. Allendorf, M. D.; Bauer, C. A.; Bhakta, R.K.; Houk, R. J. T. *Chem. Soc. Rev.*, **2009**, 38, 1330-1352.
71. (a) Wang, C. Y.; Yu, B.; Fu, H.; Wang, P.; Wang, C. C. *Polyhedron*, **2018**, 159, 298-307. (b) Zhang, X. J.; Su, F. Z.; Chen, D.; Yu, P.; Guo, W. Y.; Liu, C.; Du, M. *Dalton Trans.*, **2018**, 47, 1-7.
72. Hu, Z.; Zhang, Q.; Zhang, M.; Du, W.; Wang, T.; Zhang, J.; Wu, J.; Tian, Y.; Fang, M. *Inorg. Chem. Commun.*, **2018**, 97, 149-156.
73. (a) Richardson, F. S. *Chem. Rev.* **1982**, 82, 541-552. (b) Moore, E. G.; Samuel, A. P. S.; Raymond, K. N. *Accounts Chem. Res.*, **2009**, 42, 542-552.
74. (a) Ji, G.; Liu, J.; Gao, X.; Sun, W.; Wang, J. Z.; Zhao, S.; Liu, Z. *J. Mater. Chem. A*, **2017**, 5, 10200-10205. (b) Du, Q.; Wu, P.; Dramou, P.; Chen, R.; He, H. *New J. Chem.*, **2019**, 43, 1291-1298.
75. Zheng L. N.; Wei, F. H.; Hu, H. M.; Bai, C.; Yang, X. L.; Wang, X.; Xue, G. *Polyhedron*, **2019**, 161, 47-55.
76. Pai, S.; Schott, M.; Niklaus, L.; Kurth, D. G. *J. Mater. Chem. C*, **2018**, 6, 3310-3321.
77. Liu, X. T.; Zhao, B.; Zhang, Y. H.; Chen, S. S.; Zhu, J., Chang, Z.; Bu, X. H. *Cryst. Growth Des.*, **2019**, 19, 1391-1398.
78. (a) Zhao S. S.; Zhang, H.; Wang, L.; Chen, L.; Xie, Z. *J. Mater. Chem. C.*, **2018**, 6, 11701-11706. (b) Bohrman, J. A.; Carreon, M. A. *Chem. Commun.*, **2012**, 48, 5130-5132.
79. (a) Dinca, M.; Long, J. R. *Angew. Chem. Int. Ed.*, **2008**, 47, 6766-6779. (b) Montoro, C.; García E.; Calero, S.; Pérez-Fernández, M. A.; López, A. L.; Barea, E.; Navarro, J. A. R. *J. Mater. Chem.*, **2012**, 22, 10155-10158.
80. (a) Roswell, J. L. C.; Millward, A. R.; Park, K. S.; Yaghi, O. M. *J. Am. Chem. Soc.*, **2004**, 126, 5666-5667. (b) Chen, B.; Ockwig, N.W.; Millward A. R.; Contreras,

D. S.; Yaghi O. M. *Angew. Chem. Int. Ed.*, **2005**, 44, 4745-4749. (c) Wong-Foy, A. G.; Matzger, A. J.; Yaghi, O. M. *J. Am. Chem. Soc.*, **2006**, 128, 3494-3495.

81. Service, R. F. *Science*, **2014**, 346, 538-541.

82. Noro, S. I.; Kitagawa, S.; Kondo, M.; Seki, K. *Angew.Chem.Int.Ed.*, **2000**, 39, 2081-2084.

83. (a) Bae, J. Y. *J. Nanosci. Nanotechno.*, **2018**, 18, 6101-6105. (b) Henrique, A.; Karimi, M.; Silva, J. A. C. Rodrigues, A. E. *Chem. Eng. Technol.*, **2019**, 42, 327-342.

84. Furakawa, H.; Ko, N.; Go, Y. B.; Aratani, N.; Choi, S. B.; Choi, E.; Yazaydin, A. Ö.; Snurr, R. Q.; O’Keeffe, M.; Kim, J.; Yaghi, O. M. *Science*, **2010**, 329, 424-428.

85. Britt, D.; Tranchemontagne, D.; Yaghi, O. M. *p. Natl. Acad. Sci. USA.*, **2008**, 105, 11623-11627.

86. (a)Thompson, K. H.; Orvig, C. *Coordin. Chem. Rev.*, **2001**, 219-221, 1033-1053. (b) Gill, M. R.; Vallis, K. A. *Chem. Soc. Rev.*, **2019**, 48, 540-557 (c) Zhang, W.; Christofferson, A. J.; Besford, Q. A.; Richardson, J. J.; Guo, J.; Ju, Y.; Kempe, K.; Yarovsky, I.; Caruso, F. *Nanoscale*, **2019**, 11, 1921-1928.

87. Torre, L. A.; Siegel, R. L.; Ward, E. M.; Jemal, A. *Cancer Epidemiol. Biomarkers Prev.*, **2015**, 25, 16-27.

88. Urruticoechea, A.; Alemany, R.; Balart, J.; Villanueva, A.; Viñals, F.; Capellá G. *Curr. Pharm. Des.*, **2010**, 16, 3–10.

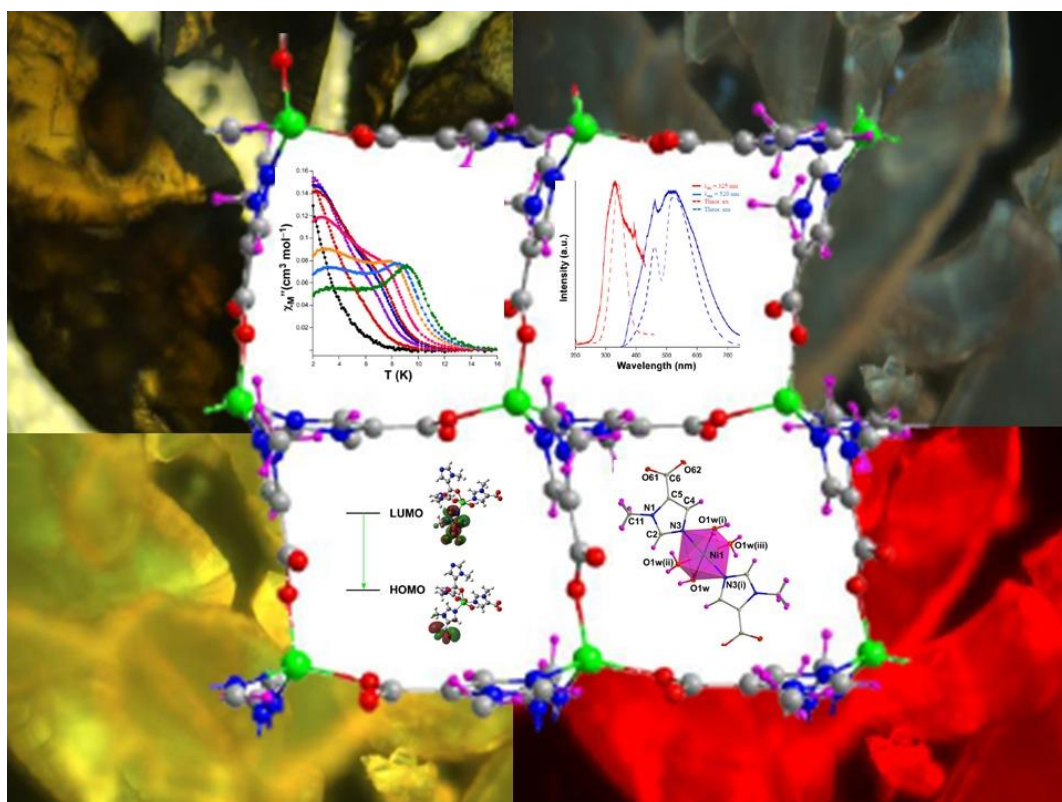
89. (a) Fricker, S. P. *Dalton Trans.*, **2007**, 0, 4903–4917. (b) Singh, V.; Azad, G. K.; Reddy, M. A. ;Baranwal S. ; Tomar, R. S. *Eur. J. Pharmacol.*, **2014**, 736, 77–85.

90. (a) Rosenberg, B.; van Camp L.; Krigas, T. *Nature*, **1965**, 205, 698–699. (b) Rosenberg, B.; van Camp, L.; Grimley E. B.; Thomson, A. J. *J. Biol. Chem.*, **1967**, 242, 1347–1352.

91. Rosenberg, B.; van Camp, L.; Trosko, J. E.; Mansour, V. H. *Nature*, **1969**, 222, 385-386.
92. Wong, E.; Giandomenico, C. M. *Chem. Rev.*, **1999**, 99, 2451–2466.
93. Antonarakis E. S.; Emadi, A. *Cancer Chemother. Pharmacol.*, **2010**, 66, 1–9.
94. Trondl, R.; Heffeter, P.; Kowol, C. R.; Jakupec, M.; Berger W.; Keppler, B. K. *Chem. Sci.*, **2014**, 5, 2925–2932.
95. (a) Jabeen, M.; Ali, S.; Shahzadi, S.; Shahid, M.; Sharma, S. K.; Qanungo, K. *Russ. J. Gen. Chem.* **2017**, 87, 530-538. (b) Hanif, M.; Hartinger, C. G. *Future Med. Chem.* **2018**, 10, 6115-617. (c) Xianchao, S.; Fang, H.; Guo, Y.; Yuan, H.; Gou, Z.; Wang, W. *J. Inorg. Biochem.* **2019**, 190, 38-44. (d) Tesarova, B.; Charousova, M.; Dostalova, S.; Bienko, A.; Kopel, P.; Kruszynski, R.; Hynek, D.; Michalek, P.; Eckschlager, T.; Stiborova, M.; Adam, V.; Heger, Z. *Int. J. Biol. Macromol.* **2019**, 126, 1099-1111.
96. *Control de las leishmaniasis: Informe de una reunión del Comité de Expertos de la OMS sobre el Control de las Leishmaniasis, Ginebra, 22 a 26 de marzo de 2010*; World Health Organization, Ed.; Serie de Informes Técnicos; Organización Mundial de la Salud: Ginebra, 2012.
97. (a) Caballero, A. B.; Rodríguez-Diéguez, A.; Quirós, M.; Salas, J. M.; Huertas, Ó.; Ramírez-Macías, I.; Olmo, F.; Marín, C.; Chaves-Lemaur, G.; Gutierrez-Sánchez, R.; Sánchez-Moreno, M. *Eur. J. Med. Chem.* **2014**, 85, 526–534. (b) Salas, J. M.; Caballero, A. B.; Esteban-Parra, G. M.; Mendez-Arriaga, J. M. *Curr. Med. Chem.* **2017**, 24, 2796–2806.
98. (a) Psomas, G.; Kessissoglou, D. P. *Dalton Trans.*, **2013**, 42, 6252-6276. (b) Banti, N.; Hadjikakou, S. K. *Eur. J. Inorg. Chem.*, **2016**, 19, 3048–3071.
99. (a) Sun, L.; Sha, L-Y.; Jiang, J. *Biomed. Res.-India.*, **2017**, 28, 2152-2155. (b) Zeng, Y.; Xu, T. *Lat Am J Pharm.*, **2016**, 35, 1228-1233.

Capítulo 1

Designing Single-Ion Magnets and Phosphorescent Materials with 1-Methylimidazole-5-carboxylate and Transition-Metal Ions



Designing Single-Ion Magnets and Phosphorescent Materials with 1-Methylimidazole-5-carboxylate and Transition-Metal Ions

Inorganic Chemistry

Cite This: *Inorg. Chem.* 2017, 56, 13897-13912

Article

pubs.acs.org/IC

Designing Single-Ion Magnets and Phosphorescent Materials with 1-Methylimidazole-5-carboxylate and Transition-Metal Ions

Antonio A. García-Valdivia,[†] Jose M. Seco,[‡] Javier Cepeda,^{*,‡,§} and Antonio Rodríguez-Diéguez^{*,†,§}

[†]Departamento de Química Inorgánica, Universidad de Granada, 18071 Granada, Spain

[‡]Departamento de Química Aplicada, Facultad de Química, Universidad del País Vasco/Euskal Herriko Unibertsitatea, UPV/EHU, 20018 San Sebastián, Spain

Abstract

Detailed structural, magnetic and photoluminescence (PL) characterization of four new compounds based on 1-methylimidazole-5-carboxylate (mimc) ligand and transition metal ions, namely [Ni(mimc)₂(H₂O)₄] (**1**), [Co(μ-mimc)₂]_n (**2**), {[Cu₂(μ-mimc)₄(H₂O)]·2H₂O}_n (**3**) and [Cd(μ-mimc)₂(H₂O)]_n (**4**) is reported. The structural diversity found in the family of compounds derives from the coordination versatility of the ligand, which coordinates as terminal ligand to give a supramolecular network of monomeric entities in **1** or acts as bridging linker to build isorecticular 2D coordination polymers (CPs) in **2**, **3** and **4**. Magnetic direct-current (*dc*) susceptibility data have been measured for compounds **1**, **2** and **3** to analyze the exchange interactions among paramagnetic centers, which have been indeed supported by calculations based on broken symmetry (BS) and density functional theory (DFT) methodology. Temperature dependence of susceptibility and magnetization data of **2** are indicative of easy-plane anisotropy ($D = +40 \text{ cm}^{-1}$, $E = +6.6 \text{ cm}^{-1}$) that involves bi-stable $M_s = \pm 1/2$ ground state. Alternating-current (*ac*) susceptibility curves exhibit field-induced single-ion magnet (SIM) behavior that occurs below 14 K when applying an external *dc* field, which is characterized by two thermally activated Arrhenius spin relaxation processes ($U_{\text{eff}} = 5.9$ and 17.8 K) governed by transverse anisotropy. Exhaustive PL analysis of compound **4** in solid state confirms low temperature phosphorescent green emission consisting of radiative components with lifetimes in the range of 0.25-0.43 s, which explains afterglow lasting for about one

second after the removal of the UV source. Time-dependent DFT along with computational calculations to estimate phosphorescent vertical transitions have been also employed to provide accurate description of the PL performance of this long-lasting phosphor.

1. Introduction

The construction of coordination polymers (CPs) is a hot topic in crystal engineering that is receiving an increasing interest from many different areas of science owing to the continuous advances shown by these multifunctional materials.¹ The success of CPs is mainly due to their intriguing architectures and topologies resulting from the self-assembly of bridging organic ligands with appropriate metal ions or clusters, which offers endless possibilities given the large list of both components and their combinations obeying the principles of reticular chemistry.² In this regard, an important aspect to exert control towards the desired crystalline frameworks lies on controlling synthetic conditions (temperature, solvent, stoichiometry, pH, and so on),³ the selection of adequate metal ions and organic ligands, indeed, is not of less importance in tuning the structures. Although the particular subclass of metal-organic frameworks (MOFs), enclosing impressive surface areas and versatile pores, occupies an important part of this research area,⁴ a wide variety of equally fascinating properties arise from non-porous CPs, among which optical storage, drug delivery, catalysis, magnetism or luminescence may be highlighted.⁵ It is at this point, in fact, where the intrinsic characteristics of the structural components (ions and ligands) make the difference to endorse these metal-organic materials with outstanding functionalities. On the one hand, ligands containing carboxylate groups are widely employed owing to their high coordination capacity as well as flexibility that permits them adopting different binding modes to fit into most of first row transition metal environments and crystal packing requirements.⁶ Moreover, the chemical nature of the spacer is not a less important concern, since, for example, aromatic spacers afford greater rigidity than aliphatic ones owing to their limited geometric characteristics that may restrict the structural variability, a fact of major importance when only one ligand is employed. On the

other hand, first row transition metal ions are undoubtedly a great choice in seeking for materials with best-in-class magnetic and photoluminescent (PL) properties.⁷

Particularly for molecular magnetism, actual scientific efforts are focused on understanding the physics governing the slow magnetic relaxation behavior of molecular systems with only one spin carrier, large magnetic anisotropy and no intermetallic exchange interactions of thence called single ion magnets (SIMs).⁸ In this regard, as already corroborated by many works since Chang and Long et. al. first proved in 2010,⁹ slow magnetic relaxation is achieved for mononuclear transition metal based compounds provided that they afford ground states with high spin (S) and magnetic anisotropy consisting of zero-field splitting D and E parameters (stand for axial and transverse anisotropy).¹⁰ More recently, it could be demonstrated that SIM behavior was not exclusively manifested in mononuclear species so it has rapidly been extended over polymeric species and first SIM-CPs have been reported.¹¹ At first sight, Co(II) is clearly the most acknowledged ion among first-row transition metals to build SIM-CPs given that its non-integer spin ground state, according to Kramers theorem, reduces the probability of fast quantum tunneling of the magnetization process that bypasses the desired slow relaxation.¹² Although different coordination geometries and donor environments are available for Co(II) based SIMs, the vast majority contain tetrahedral or pseudotetrahedral geometries.¹³ The main reason lies on the fact that low coordination number is beneficial for designing SIMs given that first-order orbital angular momentum is largely quenched by the ligand field so that spin-orbit coupling may be compensated.¹⁴ In this sense, a low coordination number is able to afford a weak ligand field, thus preventing the quenching up to a point.

Regarding the photoluminescent performance, recent research works have shifted the attention towards CPs containing d^{10} metal ions¹⁵ owing to their capacity to stabilize long-lasting phosphorescence (LLP) or afterglow phenomena in the resulting materials so that they could bring a significant step in the field of enhanced organic light-emitting diodes (OLEDs).¹⁶ This fact is derived from the intrinsic characteristics of these metal ions (namely the absence of potential quenching processes owing to their closed-shell configuration) which, combined with the appropriate fluorescent organic ligands, promotes the reorganization of the energy

levels in the compounds that leads to stronger and brighter emission [via ligand centered (LCCT) or ligand-to-metal charge transfers (LMCT)] compared to that of free organic molecule.¹⁷

All in all, we have made use of the latter considerations to design new CPs showing SIMs and LLP behaviors, for which adequate transition metal ions have been reacted with 1-methylimidazole-5-carboxylate (mimc). The selection of this ligand, yet not employed in the construction of CPs so far, is due to its ability to play two essential roles while it sequentially bridges metal ions: separate spin carriers spatially in the network by favoring metal ions to adopt low coordination numbers, all which promotes slow relaxation phenomenon; and act as an effective fluorescent molecule that allows for intense photoluminescent transitions.

2. Experimental Procedures

2.1. Chemicals

All the chemicals were of reagent grade and were used as commercially obtained.

2.2. Synthesis

Synthesis of [Ni(mimc)₂(H₂O)₄] (1). 0.08 mmol (10.00 mg) of Hmimc were dissolved in 0.5 mL of DMF and mixed with a distilled water solution containing 0.04 mmol of Ni(NO₃)₂·6H₂O (11.63 mg). Then, 1 mL of DMF is added to the mixture and stirred until homogeneity. The resulting solution was placed in a closed glass vessel and introduced in an oven at 95°C for 24h. Light green single crystals were grown during the heating procedure under autogenous pressure, which were filtered off and collected at open atmosphere and washed with water and methanol. Yield: 30% based on metal. Anal. calc. for C₁₀H₁₈N₄NiO₈ (%): C, 31.53; H, 4.76; N, 14.71. Found: C, 31.65; H, 4.58; N, 14.52.

Synthesis of $[\text{Co}(\mu\text{-mimc})_2]_n$ (2**).** Well shaped purple single crystals of **2** were obtained after carrying out the same general procedure described for **1** but replacing $\text{Ni}(\text{NO}_3)_2 \cdot 6\text{H}_2\text{O}$ by $\text{Co}(\text{NO}_3)_2 \cdot 6\text{H}_2\text{O}$ (11.65 mg). Yield: 43% based on metal. Anal. calc. for $\text{C}_{10}\text{H}_{10}\text{CoN}_4\text{O}_4$ (%): C, 38.85; H, 3.26; N, 18.12. Found: C, 38.71; H, 3.18; N, 18.15.

Synthesis of $\{[\text{Cu}_2(\mu\text{-mimc})_4(\text{H}_2\text{O})] \cdot 2\text{H}_2\text{O}\}_n$ (3**).** The general procedure described for **1** was followed using $\text{Cu}(\text{NO}_3)_2 \cdot \text{H}_2\text{O}$ (9.66 mg) as metal source, which led to single crystals of **3**. Yield: 25% based on metal. Anal. calc. for $\text{C}_{20}\text{H}_{26}\text{Cu}_2\text{N}_8\text{O}_{11}$ (%): C, 35.24; H, 3.84; N, 16.44. Found: C, 35.42; H, 3.64; N, 16.53.

Synthesis of $[\text{Cd}(\mu\text{-mimc})_2(\text{H}_2\text{O})]_n$ (4**).** The general procedure described for **1** was followed using $\text{Cd}(\text{NO}_3)_2 \cdot 4\text{H}_2\text{O}$ (15.88 mg) as metal source, which led to well shaped single crystals of **4**. Yield: 23% based on metal. Anal. calc. for $\text{C}_{10}\text{H}_{12}\text{CdN}_4\text{O}_5$ (%): C, 31.55; H, 3.18; N, 14.72. Found: C, 31.37; H, 3.10; N, 14.62.

2.3. Physical Measurements

Elemental analyses (C, H, N) were performed on an Euro EA Elemental Analyzer. FTIR spectra (KBr pellets) were recorded on a Nicolet IR 6700 spectrometer in the $4000\text{--}400\text{ cm}^{-1}$ spectral region. Magnetic susceptibility measurements were performed on polycrystalline samples of the complexes with a Quantum Design SQUID MPMS-7T or MPMS-XL5 (only for compound **3**) susceptometers at an applied magnetic field of 1000 G. The susceptibility data were corrected for the diamagnetism estimated from Pascal's Tables,¹⁸ the temperature-independent paramagnetism and the magnetization of the sample holder. Magnetization and alternating-current (*ac*) susceptibility measurements were carried out on a PPMS (Physical Property Measurement System)-Quantum Design Model 6000 magnetometer under a 3.5 Oe *ac* field and frequencies ranging from 60 to 10,000 Hz. Thermal analyses (TG/DTA) were performed on a TA Instruments SDT 2960 thermal analyzer in a synthetic air atmosphere (79% N_2 / 21% O_2) with a heating rate of $5^\circ\text{C} \cdot \text{min}^{-1}$. A closed cycle helium cryostat enclosed in an Edinburgh

Instruments FLS920 spectrometer was employed for recording photoluminescence (PL) measurements of polycrystalline samples of **4** in the 10–250 K range. For steady state measurements an IK3552R-G HeCd continuous laser (325 nm) and a Müller-Elektronik- Optik SVX1450 Xe lamp were used as excitation source. Photographs of irradiated single-crystal and polycrystalline samples were taken at room temperature in a micro-PL system included in an Olympus optical microscope illuminated with a HeCd laser or a Hg lamp. Lifetime measurements were performed under excitation at the maximum (325 nm) for selected emission wavelengths in the 350–650 nm range. Decay curves were recorded with microsecond pulse lamps as excitation source employing exposure times as to achieve 10^4 counts in the pulse of reference, and they were analyzed tail fitting.

2.4. X-ray Diffraction

X-ray data collection of suitable single crystals of all compounds were done at 100(2) K on a Bruker VENTURE area detector equipped with graphite monochromated Mo-K α radiation ($\lambda = 0.71073$ Å) by applying the ω -scan method. The data reduction was performed with the APEX2¹⁹ software and corrected for absorption using SADABS.²⁰ Crystal structures were solved by direct methods using the SIR97 program²¹ and refined by full-matrix least-squares on F^2 including all reflections using anisotropic displacement parameters by means of the WINGX crystallographic package.²² All hydrogen atoms were located in difference Fourier maps and included as fixed contributions riding on attached atoms with isotropic thermal displacement parameters 1.2 times or 1.5 times those of their parent atoms for the organic ligands and the water molecules, respectively. Details of the structure determination and refinement of compounds **1–4** are summarized in Table 1. Crystallographic data (excluding structure factors) for the structures reported in this paper have been deposited with the Cambridge Crystallographic Data Center as supplementary publication nos. CCDC 1566132-1566135. Copies of the data can be obtained free of charge on application to the Director, CCDC, 12 Union Road, Cambridge, CB2 1EZ, U.K. (Fax: +44-1223-335033; e-mail: deposit@ccdc.cam.ac.uk or <http://www.ccdc.cam.ac.uk>).

Table 1. Crystallographic data and structure refinement details of all compounds.

Compound	1	2	3	4
Chem. form.	C ₁₀ H ₁₈ N ₄ NiO ₈	C ₁₀ H ₁₀ CoN ₄ O ₄	C ₂₀ H ₂₆ Cu ₂ N ₈ O ₁₁	C ₁₀ H ₁₂ CdN ₄ O ₅
Form. weight	380.97	309.15	681.56	380.64
Cryst. system	Monoclinic	Monoclinic	Monoclinic	Monoclinic
Space group	C2/m	P2 ₁ /c	P2/c	P2 ₁ /n
<i>a</i> (Å)	14.7901(8)	12.494(2)	12.885(1)	8.0827(4)
<i>b</i> (Å)	6.9602(3)	13.420(2)	5.604(1)	12.2183(6)
<i>c</i> (Å)	7.6649(4)	7.392(1)	18.544(1)	12.9795(6)
α (°)	90	90	90	90
β (°)	113.977(2)	100.05(1)	93.17(4)	95.100(2)
γ (°)	90	90	90	90
V (Å ³)	720.95(6)	1220.4(3)	1337.0(2)	1266.9(1)
Z	2	4	2	4
GOF ^a	1.142	0.939	1.142	1.047
Rint	0.0340	0.0827	0.0459	0.0577
R ₁ ^b / wR ₂ ^c [I > 2σ(I)]	0.0198 / 0.0199	0.1029 / 0.2511	0.0820 / 0.2182	0.0241 / 0.0274
R ₁ ^b / wR ₂ ^c (all data)	0.0500 / 0.0500	0.1138 / 0.2551	0.0870 / 0.2233	0.0626 / 0.0608

[a] $S = [\sum w(F_o^2 - F_c^2)^2 / (N_{obs} - N_{param})]^{1/2}$ [b] $R_1 = \sum ||F_o| - |F_c|| / \sum |F_o|$ [c] $wR_2 = [\sum w(F_o^2 - F_c^2)^2 / \sum wF_o^2]^{1/2}$; $w = 1/[\sigma^2(F_o^2) + (aP)^2 + bP]$ where $P = (\max(F_o^2, 0) + 2F_c^2)/3$ with $a = 0.0163$ (1), 0.0174 (2), 0.1392 (3), 0.0298 (4); and $b = 0.9304$ (1), 46.3883 (2), 18.5744 (3), 0.9904 (4).

Powder X-ray diffraction (PXRD) patterns were collected on a Phillips X'PERT powder diffractometer with Cu-K α radiation ($\lambda = 1.5418$ Å) over the range $5 < 2\theta < 50^\circ$ and using a fixed slit, a step size of 0.026° and an acquisition time of 2.5 s per step at 25°C. Pattern-matching analyses of the diffractograms were done by means of the FULLPROF program (pattern-matching analysis)²³ on the basis of the space group and the cell parameters found for single crystal X-ray diffraction.

2.5. Computational details

TD-DFT theoretical calculations were performed at 10K using the Gaussian 09 package,²⁴ using the Becke three parameter hybrid functional with the non-local correlation functional of Lee-Yang-Parr (B3LYP)²⁵ along with 6-311G(d)²⁶ basis set was adopted for all atoms but for the central cadmium cation, where the LANL2DZ²⁷ basis set along with the corresponding effective core potential (ECP) was used,

whereas. The latter strategy has proven successful in describing luminescence performance of cadmium-based coordination compounds.²⁸ The 40 lowest excitation and emission energies were calculated on model 4 by the TD-DFT method. Results were analyzed with GaussSum program package²⁹ and molecular orbitals plotted using GaussView 5.³⁰ A detailed description of the computational strategy adopted in this work to compute the magnetic coupling constant (J_{calc}) value of **2** and **3** consists of Nodlemann's Broken Symmetry Approach.³¹ One calculation was performed to determine the high-spin state and another to determine the low-spin broken symmetry state, employing the dispersion corrected B97D functional³² and Gaussian implemented 6-311G++(d,p) basis set³³ for all non-metallic atoms or LANL2DZ pseudo-potential for the cobalt(II) atoms. The correctness of this method is supported by the work of Kumar Singh and Rajaraman,³⁴ whereas the nature of both spin states was confirmed by means of its spin density distribution.

3. Results and Discussion

3.1. Structural Description

Structural description of [Ni(mimc)₂(H₂O)₄] (1). Compound **1** crystallizes in the *C2/m* and consists of a supramolecular crystal building in which neutral monomers of the title formula are linked together by means of hydrogen bonding and π - π interactions. In the centrosymmetric complex, four water molecules occupy the basal plane that crosses Ni1 atom while two mimc- $\kappa N3$ terminal ligands are coordinated at the apical positions, thus rendering a slightly compressed octahedron as confirmed by continuous shape measures ($S_{\text{OC}} = 0.04$) calculated by the SHAPE program (Figure 1, Table 2).³⁵

Table 2. Selected bond lengths (Å) for compound **1**.^a

Ni1–N3	2.064(2)	Ni1–O1w(i)	2.102(2)
Ni1–N3(i)	2.064(2)	Ni1–O1w(ii)	2.102(2)
Ni1–O1w	2.102(2)	Ni1–O1w(iii)	2.102(2)

^aSymmetry operations: (i) = $-x-1, -y, -z$; (ii) = $x, -y, z$; (iii) = $-x-1, y, -z$.

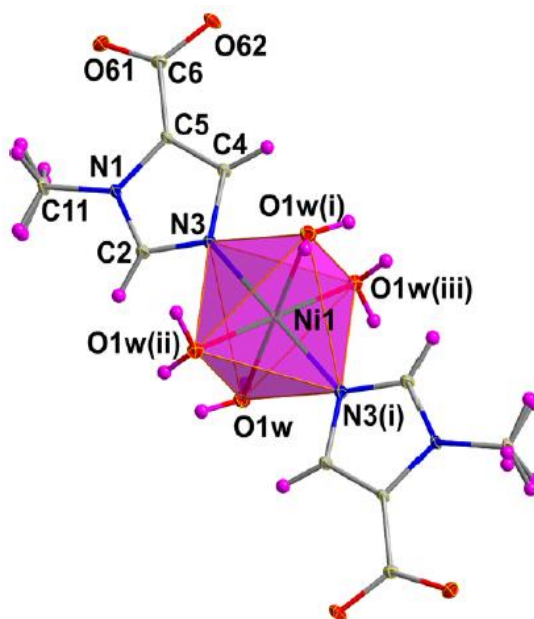


Figure 1. View of complex **1** (ellipsoids 50% of probability) showing the coordination polyhedron and numbering scheme used.

The monomeric entity resembles that contained in the recently reported compound $[\text{Cd}(\text{HMPCA})_2(\text{H}_2\text{O})_4]$ (where HMPCA = 3-methyl-1H-pyrazole-4-carboxylate), in which apical mimc ligands are replaced by HMPCA ligands.³⁶ Within the molecule, carboxylate groups of mimc ligands remain completely planar and are exposed outwards so as to act as receptors of $\text{Ow}-\text{Hw}\cdots\text{Ocarb}$ hydrogen bonding interactions starting at coordination water molecules of adjacent monomers. First, a sort of supramolecular array is established along the crystallographic c axis by successive double hydrogen bonds formed between two coordination water arranged in *cis* and O62 atom, where mimc ligands are forced to remain coplanar by means of weak $\text{C}-\text{H}\cdots\text{O}$ interactions. Hereafter, additional $\text{Ow}-\text{Hw}\cdots\text{Ocarb}$ bonds are set to join the monomers along the remaining directions (Figure 2), such that the resulting 3D building is completed and sustained by relatively strong face-to-face π -

π stacking interactions among the aromatic rings of mimic ligands (Tables 3 and 4). As a matter of fact, considering that all supramolecular interactions make each complex molecule be surrounded by six ones, it is concluded that they are organized in a **pcu** topological framework as confirmed by TOPOS program.³⁷

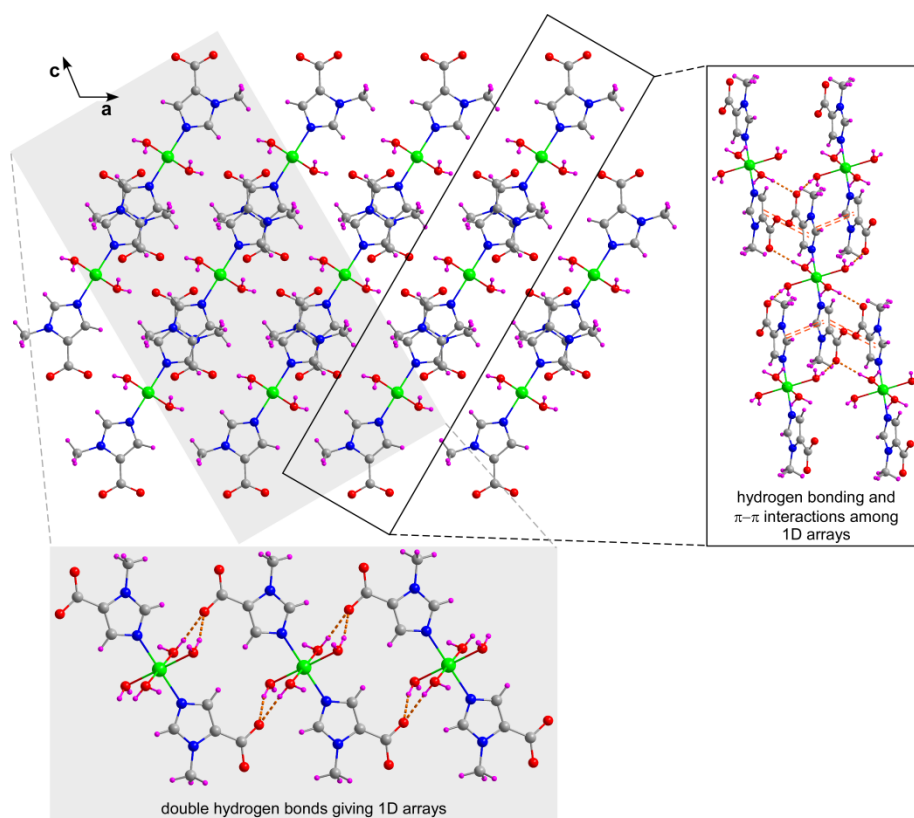


Figure 2. Views of the packing of compound **1** showing the supramolecular interactions taking place among monomeric molecules.

Table 3. Structural parameters (\AA , $^\circ$) of hydrogen bonds in compound **1**.^a

$D-H\cdots A^b$	$D-H$	$H\cdots A$	$D\cdots A$	$D-H\cdots A$
O1w-H11w \cdots O61(iv)	0.86	1.86	2.719(1)	175.5
O1w-H12w \cdots O62(v)	0.82	1.95	2.745(1)	163.5

^aSymmetrycodes: (iv) = $-x-3/2, y-1/2, -z-1$; (v) = $x, y, z+1$. ^bD: donor. A: acceptor.

Table 4. Structural parameters (\AA , $^\circ$) of π - π interactions of compound **1**.^a

Ring...Ring ^b	α	DC	β	DZ	DXY	Dist.
1A-1A(iv)	0.02	3.883(1)	26.34	3.480	1.723	3.49-3.54
1A-1A(vi)	0.02	3.883(1)	26.34	3.480	1.723	3.49-3.54
1A-1A(vii)	0.02	3.883(1)	26.34	3.480	1.723	3.49-3.54
1A-1A(viii)	0.02	3.883(1)	26.34	3.480	1.723	3.49-3.54

^a Symmetry: (iv) = $-x-3/2, y-1/2, -z-1$; (vi) = $-x-3/2, y+1/2, -z-1$; (vii) = $-x-3/2, -y-1/2, -z-1$; (viii) = $-x-3/2, -y+1/2, -z-1$. α : dihedral angle between mean planes of the rings ($^\circ$). DC: distance between ring centroids (\AA). β : angle between DC vector and normal to plane(I) ($^\circ$). DZ: perpendicular distance of the centroids of ring(I) on plane of ring(II) (\AA). DXY: slippage (\AA). Dist.: shorter distances between non-hydrogen atoms of rings (I) and (II). ^bRings: **1A**: N1, C2, N3, C4, C5.

Structural description of $[\text{Co}(\mu\text{-mimc})_2]_n$ (2**).** Crystal structure of compound **2** grows from the piling of neutral 2D layers held together by π - π stacking interactions. In the asymmetric unit, Co1 is coordinated to four mimc ligands through two imidazole nitrogen and two carboxylate oxygen atoms since O62B atom (at distance of ca. 2.85\AA) cannot be considered to be coordinated (Table 5) which gives coordination polyhedron that resembles a distorted tetrahedron ($S_T = 0.73$, Figure 3). It is worth noticing that the two crystallographically independent mimc ligands remain essentially planar (carboxylate groups rotate *ca.* 1.5 and 4.6° with regard to the imidazole ring respectively for A and B ligands) to bridge Co1 atoms one another by acquiring the $\mu\text{-}\kappa\text{N1}:\kappa\text{O61}$ mode, which imposes Co...Co distances of *ca.* 7.8\AA and 11.5\AA for the edge and square diagonal, respectively. Taking into account that each metal centre is surrounded by four ligands and that they acquire parallel dispositions in pairs (A and B ligands on their part), the resulting $\text{Co}(\text{N})_2(\text{CO}_2)_2$ building unit may be considered as a pseudo-square planar node from the topological point of view. The parallel arrangement between symmetry related A ligands seems to come from an intramolecular C2A-H2A...O62A hydrogen bond between the aromatic ring and nonbonding carboxylate oxygen atom, which, in turn, prevents the latter atom from coordinating to Co1 atom. Accordingly, the linkage of these units one another gives rise to somewhat corrugated open 2D layers showing square windows and thus, of the **sql** topological class and $(4^4 \cdot 6^2)$ point symbol.

Table 5. Bond lengths for coordination environment of compound **2**.^a

Co1–O61A	1.933(9)	Co1–N3A(ii)	2.002(10)
Co1–O61B(i)	1.953(9)	Co1–N3B	2.032(11)

^a Symmetries: (i) = $-x, y - 1/2, -z + 1/2$; (ii) = $x, y, z + 1$.

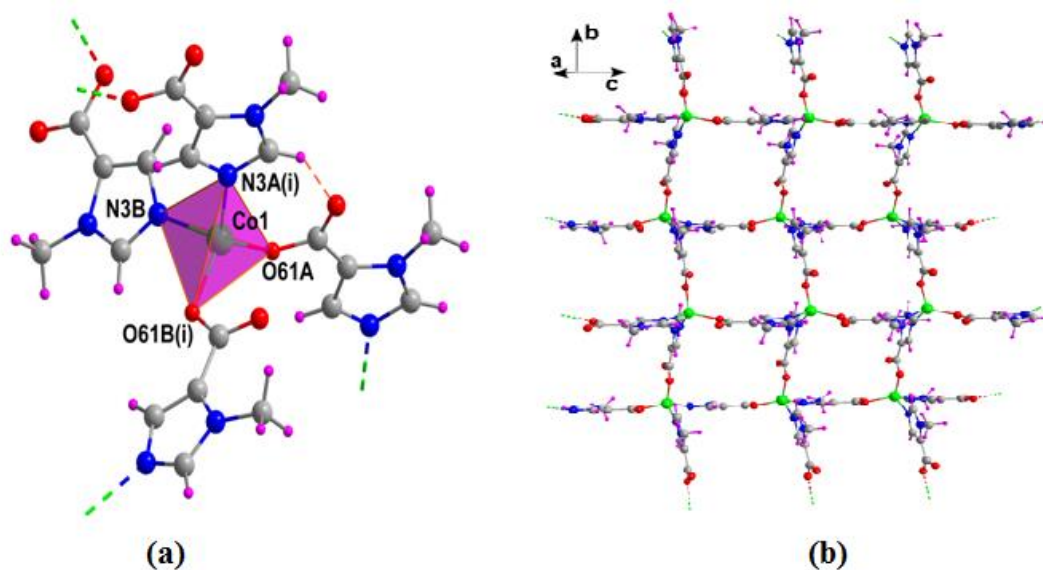


Figure 3. (a) Building unit of compound **2** with atom labels of coordination sphere. Note that A and B labels stand for A and B ligands and that orange dashed line represent the intramolecular hydrogen bond. (b) 2D layer showing the square grid.

These kinds of layers are frequently found for CPs resulting of the combination of tetrahedral nodes with ligands capable of acting as $\mu\text{-}\kappa N:\kappa O$ linkers since four-membered M–O–C–O–M chelating rings are prevented, as it is the case of $\{[\text{Co}(\mu\text{-}6\text{ani})_2]\cdot\text{H}_2\text{O}\}_n$ compound based on 6-aminonicotinato ligand.^{11e} Probably as a consequence of the large section of the square windows within the layers, mimic ligands are allowed to cross through the windows, which brings a 2-fold interpenetration in the overall crystal building. Within the entangled layers, the second subnet is placed closed to the first one in order to favour strong face-to-face $\pi\text{-}\pi$ interactions (Figure 4) between the aromatic rings of mimic B ligands when crossing the rings of the first subnet in addition to comparatively weak stacking interactions among A ligands (Table 6). These entangled layers are packed one another along *a* axis in the absence of any remarkable interaction unless very weak

contacts involving the methyl groups and aromatic rings of mimic ligands that belong to different subnets. Moreover, the entangled layers show no offset along the packing directions, such that the overall building contains no voids (Figure 4).

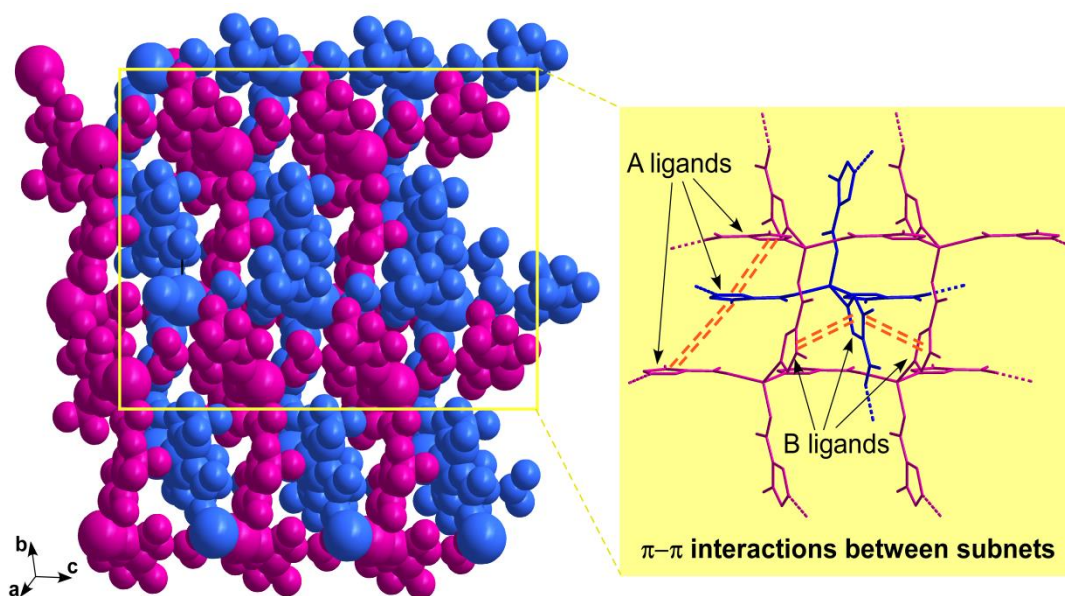


Figure 4. View of the 2-fold interpenetrated building of compound **2** (red and blue layers represent independent subnets) showing π - π interactions among mimic ligands.

Table 6. Structural parameters (\AA , $^\circ$) of π - π interactions of compound **2**.^a

Ring...Ring ^b	α	DC	β	DZ	DXY	Dist.
1A-1A(iii)	12.92	5.240(8)	42.41	3.512	–	4.69–4.70
1A-1A(iv)	12.92	5.240(8)	42.41	3.512	–	4.03–4.65
1B-1B(iii)	20.15	4.019(7)	13.48	3.356	–	3.72–4.41
1B-1B(iv)	20.15	4.019(7)	33.38	3.908	–	3.72–4.41

^a Symmetry: (iii) = $x, -y - 1/2, z - 1/2$; (iv) = $x, -y + 1/2, z + 1/2$; (v) = $-x, -y, -z$. α : dihedral angle between mean planes of the rings ($^\circ$). DC: distance between ring centroids (\AA). β : angle between DC vector and normal to plane(I) ($^\circ$). DZ: perpendicular distance of the centroids of ring(I) on plane of ring(II) (\AA). DXY: slippage (\AA). Dist.: shorter distances between non-hydrogen atoms of rings (I) and (II). ^bRings: **1A**: N1A, C2A, N3A, C4A, C5A; **1B**: N1B, C2B, N3B, C4B, C5B.

Structural description of $\{[\text{Cu}(\mu\text{-mimc})_2(\text{H}_2\text{O})]\cdot 2\text{H}_2\text{O}\}_n$ (3). Crystal structure of compound **3** crystallizes in $P2/c$ group and consists of a compact framework built up from similar 2D layers to those described for **2** that are held together by means of hydrogen bonding interactions. The asymmetric unit contains two crystallographically independent copper (II) atoms (both of which are sited on a binary axis), a coordination water molecule, two mimc bridging ligands, and a lattice water molecule (Figure 5).

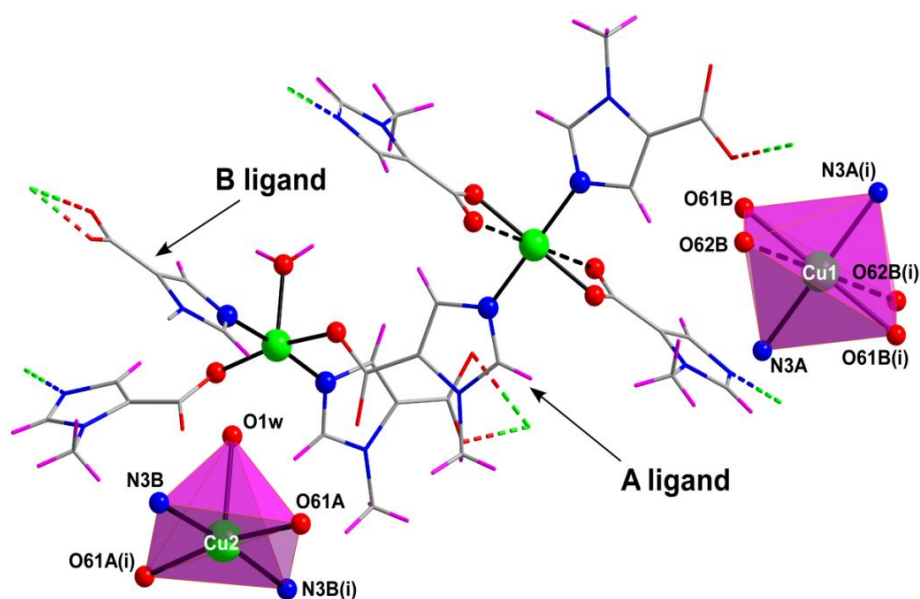


Figure 5. Excerpt of crystal structure of compound **3** showing the coordination polyhedra of Cu1 and Cu2 atoms and the numbering scheme of donor atoms.

Cu1 lies on an inversion center and describes a severely distorted 4 + 2 octahedron ($S_{\text{OC}} = 9.74$) in which the basal plane is formed by two O61B carboxylate oxygen atoms and two N3A imidazole atoms, whereas the elongated axis is occupied by O62B atoms pertaining to the chelating carboxylate group. Cu2 displays an almost ideal square pyramidal (SPY) environment ($S_{\text{SPY}} = 0.43$) established by two monodentate carboxylate oxygen atoms and two N3B atoms of mimc ligands, whereas an apically elongated water molecule completes the coordination shell (Table 7).

Table 7. Bond lengths (Å) for coordination environment of compound **3**.^a

Cu1–N3A	1.966(10)	Cu2–N3B(ii)	1.961(10)
Cu1–N3A(i)	1.966(10)	Cu2–N3B(iii)	1.961(10)
Cu1–O61B	1.948(8)	Cu2–O61A	2.000(8)
Cu1–O61B(i)	1.948(8)	Cu2–O61A(iv)	2.000(8)
Cu1–O62B	2.762(8)	Cu2–O1w	2.153(17)
Cu1–O62B(i)	2.762(8)		

^a Symmetries: (i) = $-x+1, -y+2, -z+1$; (ii) = $-x, -y+2, -z+1$; (iii) = $x, -y+2, z-1/2$; (iv) = $-x, y, -z+1/2$.

Hence, copper(II) atoms are sequentially joined by two types of mimc ligands describing slightly different coordination modes, i.e. μ -mimc- κ N3A: κ O61A (A ligand) and μ -mimc- κ N3B: κ^2 O61B,O62B (B ligand), imposing Cu1...Cu2 distances of *ca.* 7.79 Å and 8.21 Å. The non-equality of those bridges promotes substantial distortion on the square grid of the 2D layers that spread along the crystallographic *ac* plane. Moreover, mimc ligands are forced to be folded required by the coordination shells, thus arranged in a non perpendicular disposition (angle of 55.2 and 52.5° for A and B ligands, respectively, with respect to the mean plane of 2D layer), although the 2D network preserves the **sql** topology (Figure 6). This structural feature closes to a large extent the accessibility of the square rings thereby preventing any possible π - π stacking interaction among mimc ligands belonging to adjacent layers. Instead, layers are packed in a parallel fashion along *b* axis in such a way that layers get mutually eclipsed, which is achieved by means of hydrogen bonding interactions provided by coordination O1w water molecule (Table 8). As a consequence, very narrow pores, filled with crystallization water molecules, are left within the framework.

Table 8. Structural parameters (Å, °) of hydrogen bonds in compound **3**.^a

$D-H\cdots A^b$	$D-H$	$H\cdots A$	$D\cdots A$	$D-H\cdots A$
O1w–H11w...O62(v)	0.86	1.77	2.618(13)	169.1

^a Symmetry codes: (v) = $-x, y + 1, -z + 1/2$; (vi) = $x, y + 1, z$. ^bD: donor. A: acceptor

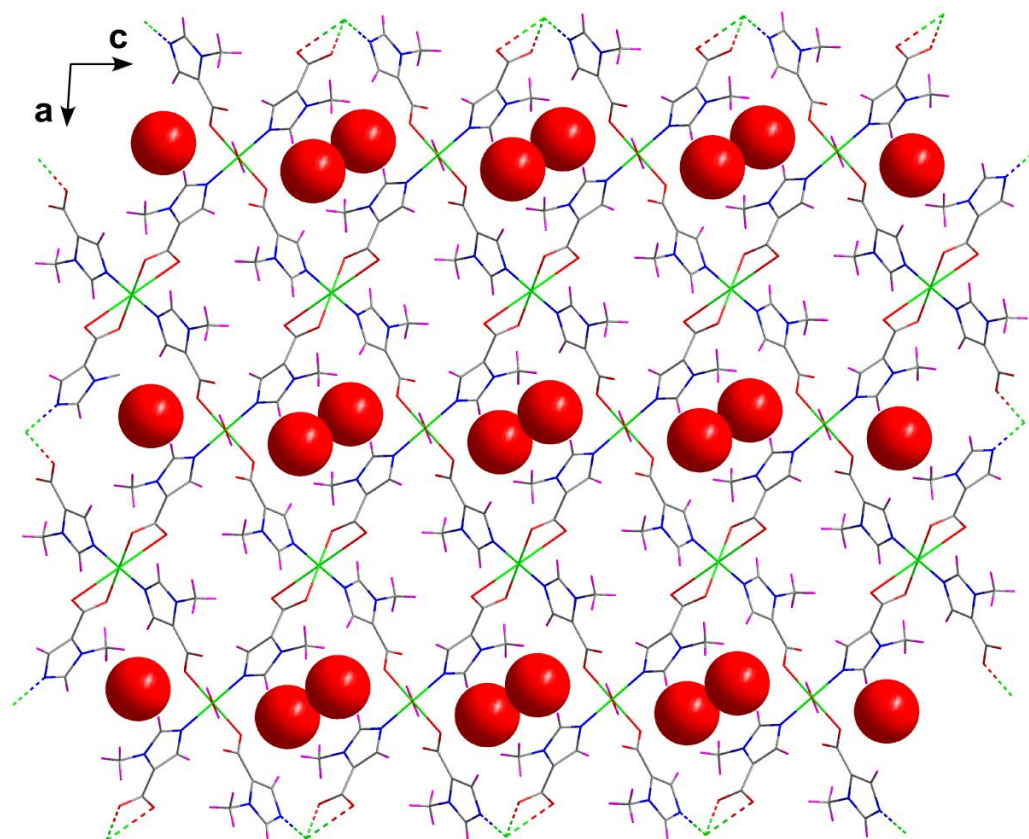


Figure 6. Packing of compound **3** along *b* axis showing the lattice water molecules occupying the voids of the structure.

Structural description of $[\text{Cd}(\mu\text{-mimc})_2(\text{H}_2\text{O})]_n$ (4**).** Compound **4** presents a 2D-layered framework that can be considered as another variant of square-grid networks shown by compounds **2** and **3**. Cd1 atom is placed in the centre of a severely distorted octahedron ($S_{\text{OC}} = 3.02$) established by two nitrogen atoms of two independent mimc ligands, two oxygen atoms from a chelating carboxylate group, a monodentate carboxylate oxygen atom and water molecule (Figure 7, Table 9).

Table 9. Selected bond lengths (Å) for compound **4**.^a

Cd1–N3A	2.258(2)	Cd1–O61B(ii)	2.437(2)
Cd1–N3B	2.243(2)	Cd1–O62B(ii)	2.345(2)
Cd1–O62A(i)	2.282(2)	Cd1–O1w	2.355(3)

^aSymmetries: (i) = $-x + 1/2, y - 1/2, -z + 3/2$; (ii) = $x + 1/2, -y + 1/2, z + 1/2$.

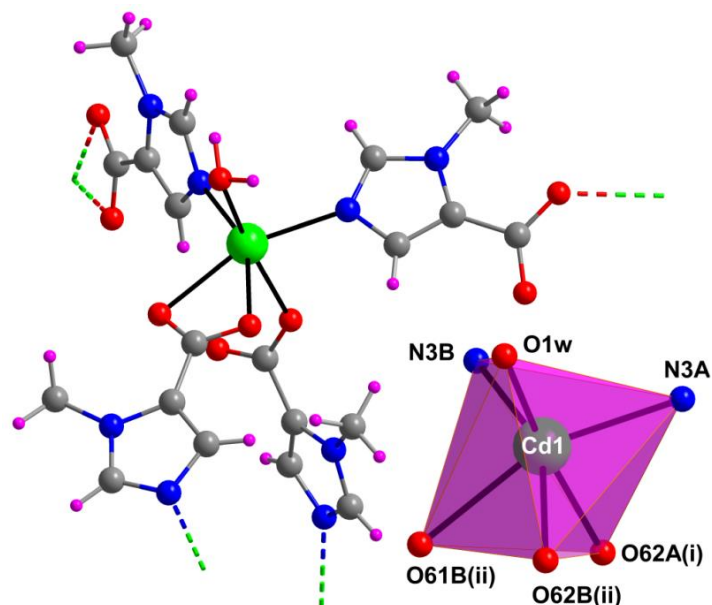


Figure 7. *Relative disposition of square rings within the layer, hydrogen bonding interactions between layers and their mutual packing in compound 4.*

The disposition of the four mimc ligands (two showing the $\mu\text{-}\kappa\text{N}:\kappa\text{O}$ (A ligands) and two the $\mu\text{-}\kappa\text{N}:\kappa^2\text{O},\text{O}'$ (B ligands) coordinated to Cd1 atoms is such that the junction of the $[\text{Cd}(\text{N}_{\text{mimc}})_2(\text{CO}_2)_2]$ 4-connected nodes by the linear linkers gives rise to highly corrugated square-grid. In fact, considering the mean plane formed by metal centers, adjacent 4-member rings are largely folded to acquire a relative almost perpendicular disposition (80.6°). An important structural feature concerns the relative disposition of mimc ligands within the 4-member rings, since it allows $\pi\text{-}\pi$ stacking interactions in the overall building of **4** among consecutive layers in spite of their lack of planarity (Figure 8).

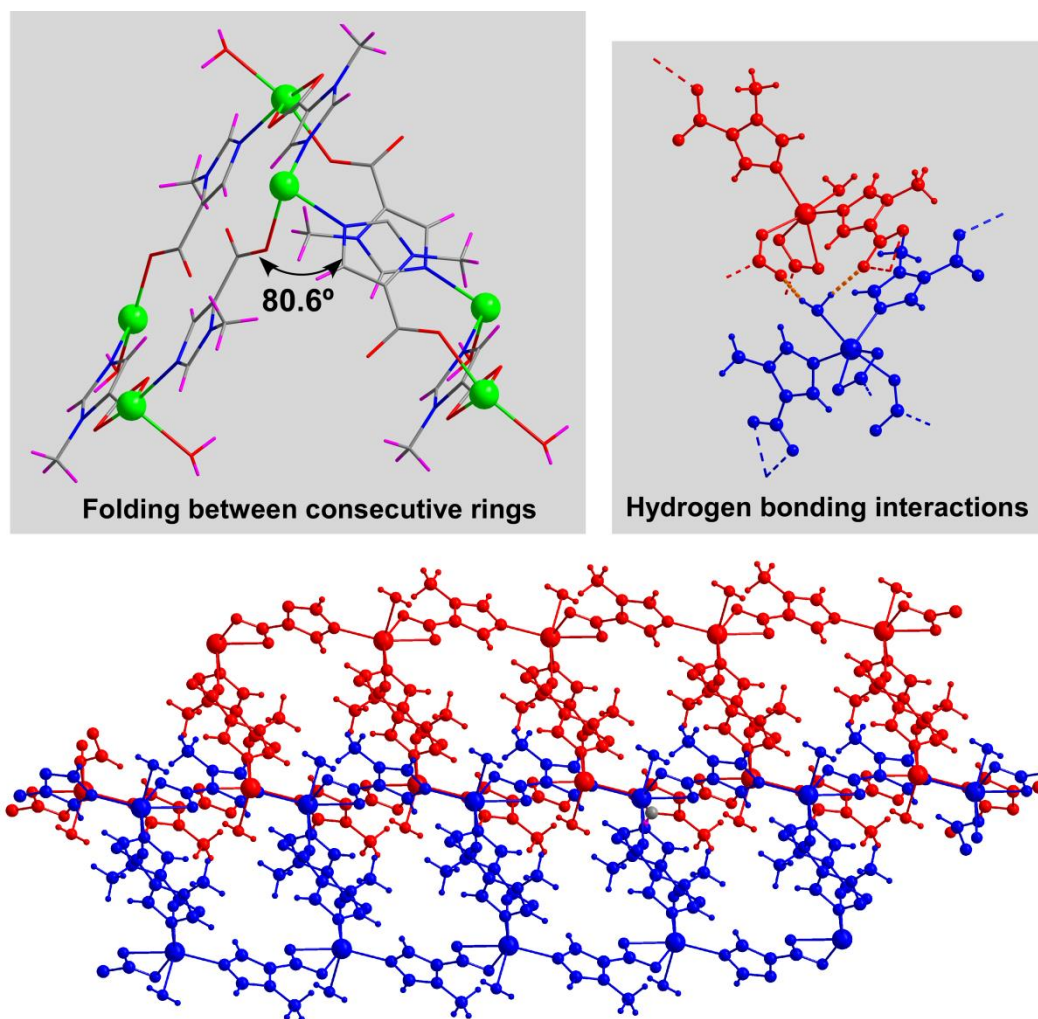


Figure 8. Relative disposition of square rings within the layer, hydrogen bonding interactions between layers and their mutual packing in compound **4**.

Furthermore, strong hydrogen bonds are established between the layers through O1w...Ocarboxylate interactions, which reinforce the cohesiveness and lead to a dense 3D packing that leaves no voids (Table 10).

Table 10. Structural parameters (Å, °) of hydrogen bonds in compound **4**.^a

$D-H\cdots A^b$	$D-H$	$H\cdots A$	$D\cdots A$	$D-H\cdots A$
O1w-H11w...O61A(iii)	0.89	1.87	2.730(2)	163.7
O1w-H12w...O62B(iv)	0.86	1.89	2.746(2)	170.1

^a Symmetry codes: (iii) = $x - 1, y, z$; (iv) = $-x - 1/2, y + 1/2, -z + 3/2$. ^b D: donor. A: acceptor.

3.2. Magnetic Properties

Static Magnetic Measurements. The temperature dependent magnetic susceptibility data were measured on polycrystalline samples of compounds **1–3** under an applied magnetic field of 1000 Oe in the 5–300 K range (Table 11). The magnetic behavior of compound **1** in the form of $\chi_M T$ vs T (where χ_M stands for the magnetic susceptibility per nickel(II) ion) exhibits a $\chi_M T$ value at room temperature that is close to that expected for an isolated spin doublet ($1.00 \text{ cm}^3 \text{ mol}^{-1} \text{ K}$ with $g = 2.01$, see Figure 9).

Table 11. Best least-squares fits of the experimental curves and theoretically or computationally calculated magnetic data.

Compound	$\chi_M T$ (300 K) ^[a]		J (cm ⁻¹) ^[b]		g ^[b]	$R \times 10^6$ ^[b]
	Exp.	Calcd.	Exp.	DFT		
2	2.67	1.87	–	–0.15	–	
3	0.389	0.375	–6.4(1)	–5.8	2.13	1.75

[a] $R = \sum_i [(\chi_M T)_{\text{obsd.}(i)} - (\chi_M T)_{\text{calcd.}(i)}]^2 / \sum_i [(\chi_M T)_{\text{obsd.}(i)}]^2$. [b] Experimental and calculated room temperature $\chi_M T$ values expressed in $\text{cm}^3 \text{ K mol}^{-1}$. [c] Coupling constants from best-fitting of experimental curves and BS-DFT calculations.

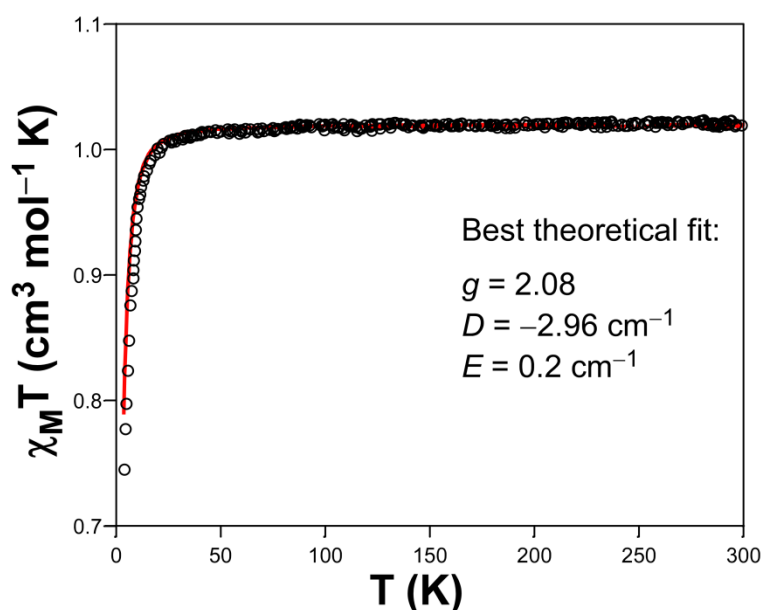


Figure 9. Fitting (red line) of $\chi_M T$ vs T (\circ) curve of compound **1**.

Upon cooling, $\chi_M T$ product remains almost constant up to 40 K, where it decreases abruptly and reaches a value of $0.74 \text{ cm}^3 \text{ mol}^{-1} \text{ K}$ probably as a consequence of the occurrence of zero-field splitting (ZFS) considering the large Ni...Ni distances mediating through hydrogen bonding (*ca.* 7.7 Å) and face-to-face π - π (*ca.* 8.9 Å) interactions among monomeric complexes in the crystal structure of compound **1**. In fact, computational calculations have shown the occurrence of negligible antiferromagnetic couplings through similar face-to-face π - π stackings in a recent work.³⁸ The *dc* magnetic susceptibility data and magnetization curves were simultaneously analyzed using the PHI program³⁹ with the following effective spin Hamiltonian (eq 1):

$$\hat{H} = D(\hat{S}_z^2 - \hat{S}^2/3) + E(\hat{S}_x^2 + \hat{S}_y^2) + \mu_B \bar{B} \cdot g \cdot \hat{S} \quad (\text{eq 1})$$

Where first and second terms stand for axial and rhombic anisotropic ZFS interactions parameterized by D and E , respectively; \hat{S} is the spin operator with x , y or z components and the last term accounts for the Zeeman interaction with the local magnetic field (\bar{B}), parameterized through the Landé g tensor. Best fitting of the experimental curve was achieved with the following set of parameters: $g = 2.08$, $D = +2.41 \text{ cm}^{-1}$ and $E < +0.1 \text{ cm}^{-1}$ with $R = 9.3 \times 10^{-4}$. The weak rhombicity signified by the E parameter and the value of D is consistent with the magnetostructural correlation of this parameter based on Ni(II) complexes containing a {NiN₂O₄} chromophore with a compressed tetragonal bipyramid geometry.⁴⁰ Although it is true that most of the latter compounds present an experimental negative sign of D parameter, the present case fits well the predicted positive sign of D by CASSCF calculations.⁴¹

The $\chi_M T$ vs T plot for **2** (Figure 10) shows that the room temperature $\chi_M T$ product ($2.67 \text{ cm}^3 \text{ mol}^{-1} \text{ K}$) is within the range expected for one high-spin d⁷Co^{II} ion ($S = 3/2$) with some orbital angular momentum contribution.⁴²

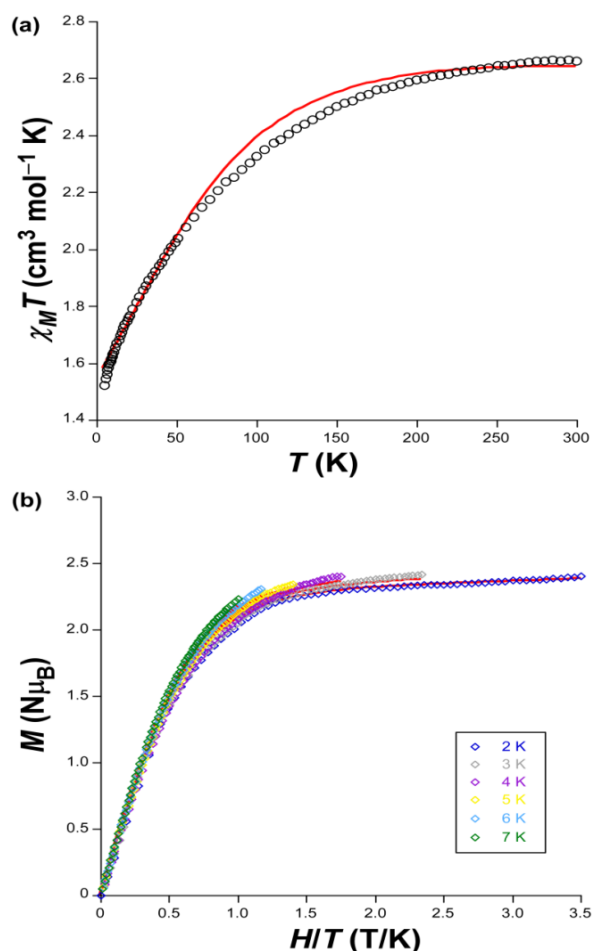


Figure 10. (a) $\chi_M T$ vs T (\circ) plot and (b) M vs H/T curves showing best fittings for compound **2**.

$\chi_M T$ exhibits a continuous decrease cooling down the sample, which is indicative of significant spin-orbit coupling (SOC) that makes the fitting of these data somewhat tricky. In particular, the drop is more abrupt below 50 K (where it reaches a value of $1.51 \text{ cm}^3 \text{ mol}^{-1} \text{ K}$) probably owing to intrinsic magnetic anisotropy of the Co^{II} ions taking into account the large $\text{Co}\cdots\text{Co}$ distance along μ -mimc bridges (*ca.* 7.8 \AA) in the structure. Fitting of the χ_M^{-1} vs T curve to the Curie-Weiss law in the 50–300 K range gives values of $C = 2.88 \text{ cm}^3 \text{ K mol}^{-1}$ and $\theta = -22.6 \text{ K}$. Despite the apparent antiferromagnetic nature of compound **2**, an estimation of the exchange interactions with the phenomenological equation proposed by Rueff et al.⁴³ (equation 2) that gives $A + B = 2.93 \text{ cm}^3 \text{ K mol}^{-1}$ (very close to the Curie parameter), $E_1/\kappa = +49(1) \text{ K}$ (so called within the range for similar cobalt(II) compounds),⁴⁴ and $-E_2/\kappa = -0.56(3) \text{ K}$, suggests the presence of almost negligible antiferromagnetic interactions (Figure 11).

$$\chi_M T = A \exp(-E_1/\kappa T) + B \exp(-E_2/\kappa T) \quad (\text{eq. 2})$$

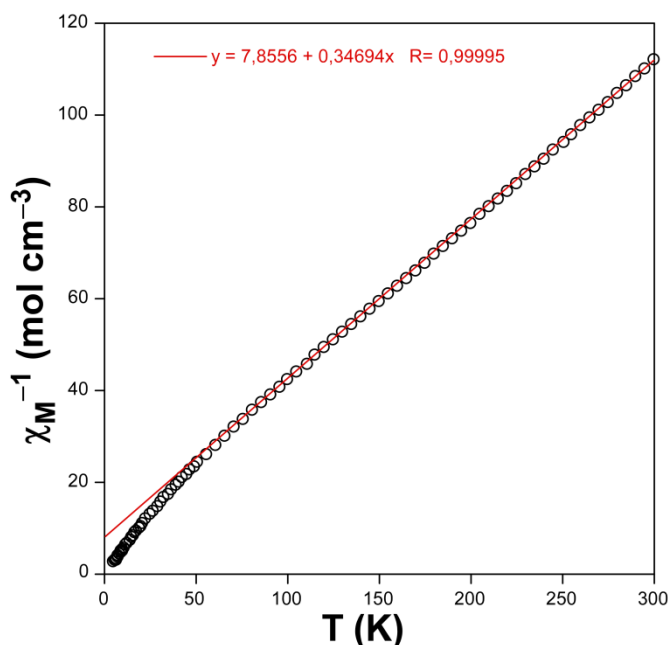


Figure 11. Curie-Weiss fitting (red line) of χ_M^{-1} vs T (\circ) curve.

BS-DFT calculations performed on a suitable dimeric model of **2** confirm the occurrence of very weak antiferromagnetic exchange in **2**, allowing us to consider it as 2D network of isolated Co^{II} ions. Magnetization data were collected at several temperatures (2–7 K) under an applied field ranging from 0 to 3.5 T. At first glance, the value of M at 2K ($2.23 N\mu_{\text{B}}$) does not reach the theoretical saturation for $S = 3/2$ ($M_{\text{sat}} = 3.3$, with $g = 2.2$). Moreover, isothermal curves do not collapse in a single master curve, which supports the presence of significant magnetic anisotropy. The simultaneous fitting of both data with the spin Hamiltonian that includes the ZFS term and electron Zeeman interaction (equation 1) by means of PHI program allowed us estimating the value and sign of the magnetic anisotropy: $D = +12.9 \text{ cm}^{-1}$, $E = +0.5 \text{ cm}^{-1}$ with $R = 8.6 \times 10^{-3}$. Note that the fit required a slight anisotropy in the gyromagnetic tensor: $g_x = g_y = 2.17$ $g_z = 2.36$. In spite of the fact that these parameters should be taken with care given the limitations of the Hamiltonian employed,⁴⁵ a deep analysis of the residual obtained along the fitting according to the

magnitude and sign of D and E (through the survey mode of PHI) clearly suggests a positive sign for the axial magnetic anisotropy parameter (so called easy-plane anisotropy). Although the existence of positive D limits to few recent works,^{14a, 46} high-spin d^7 configuration, especially with pseudo-tetrahedral environment, appears to be very promising in giving moderate D values and, in turn, promising SIM behavior.⁴⁷ Possible reasons explaining such a moderate value of D point out to both the low distortion of the metal environment on compound **2** ($S_T = 0.73$) and its inherent positive sign. While it is true that the larger distortion (less symmetry) the larger magnetic anisotropy, positive D parameters tend to be smaller than those of negative sign.^{47a}

The $\chi_M T$ value at room temperature for **3** is close to that expected for a magnetically isolated copper(II) ion (Table 11). The $\chi_M T$ curve shows a very slight decrease upon cooling up to 60 K, below which it describes a sharper drop to reach an almost null value (Figure 12). On its part, the thermal evolution of the magnetic susceptibility exhibits a maximum around 5 K. This behavior is indicative of dominant weak antiferromagnetic interactions among Cu(II) atoms. In spite of the fact that the square-grid of the 2D layer contains two crystallographically independent copper(II) atoms joined through two almost equivalent types of μ -mimc bridges (A and B ligands with μ - $\kappa N:\kappa O$ and μ - $\kappa N:\kappa^2 O, O'$ modes), the magnetic network adequately described as a regular quadratic layer. Accordingly, fitting of the curve by means of a magnetic model based on $H = -JS_1 \cdot S_2$ spin-only Hamiltonian, in which a high-temperature series expansion above a possible Néel temperature is considered, gave a reliable estimate of the exchange coupling.⁴⁴ The goodness of the result is indeed corroborated by the DFT computed coupling constant. This type of antiferromagnetic interaction results from a poor magnetic exchange between neighbouring copper(II) atoms through long superexchange pathways (*ca.* 7.8–8.2 Å), which has been previously observed for systems containing similar μ - $\kappa N:\kappa O$ bridges.^{11e,46a,46b}

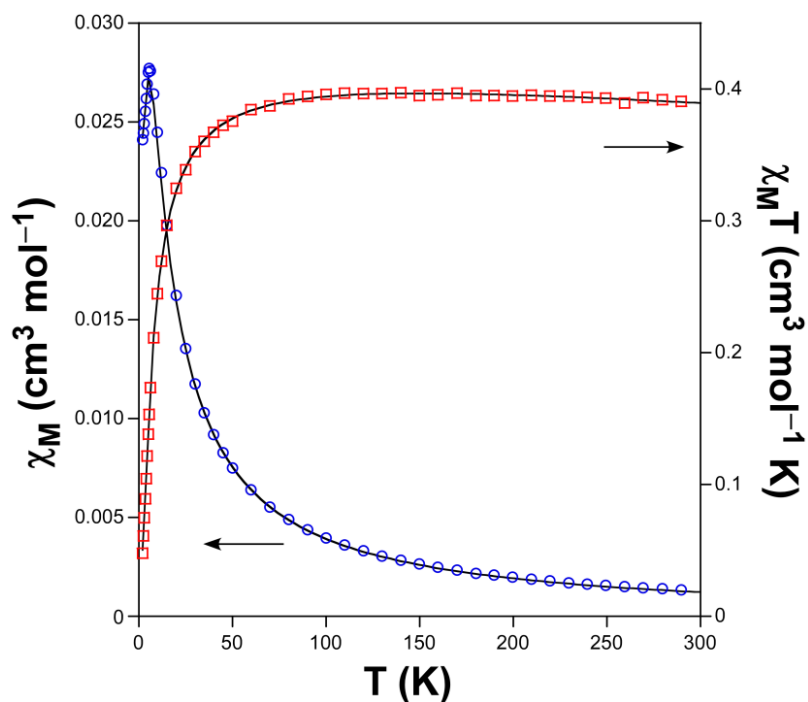


Figure 12. Magnetic susceptibility χ_M vs T (\circ) and $\chi_M T$ vs T (\square) curves of compound **3** with best fitting (—).

Dynamic Magnetic Properties. Spin dynamics were evaluated for cobalt based compound (**2**) by means of alternating-current (*ac*) susceptibility measurements. No frequency dependent signals could be observed in the lack of an external *dc* field, which is not surprising for a compound with easy-plane anisotropy.^{14a,46c,48} According to Kramers theorem,^{12a} spin-lattice relaxation in easy-plane ($D > 0$) half-integer systems is allowed to occur directly between the ground $M_S = \pm 1/2$ levels in the absence of transverse, hyperfine, and dipolar interactions, in such a way that fast relaxation is expected even under an applied field. Nonetheless, if the existing spin-phonon coupling is weak or if there are very few phonons of the appropriate frequency, the relaxation could be slowed down, an effect known as phonon bottleneck, in such a way that direct relaxation is somewhat hindered as to enable an Orbach relaxation through the higher energy $M_S = \pm 3/2$ levels.^{14a} At any rate, this fact does not necessarily discard the existence of additional relaxation mechanisms involved in the spin reversal. When an external *dc* field of 1000 Oe is applied, compound **2** exhibits SIM behavior below 14 K with two out-of-phase maxima peaking at 2.3 K (2000 Hz) – 3.2 K (10000 Hz) and 7.3 K (2000 Hz) – 9.1 K (10000 Hz) ranges, which can be attributed to the occurrence of slow (SR) and fast

relaxation (FR) processes, respectively (Figure 13). The presence of two maxima is a quite uncommon phenomenon^{5j,48,49} that could not be anticipated considering the fact that the crystal structure contains a unique independent Co(II) ion. In any case, fast tunneling at low temperatures is not to be fully discarded, given the divergence in the out-of-phase signal below the blocking temperature.

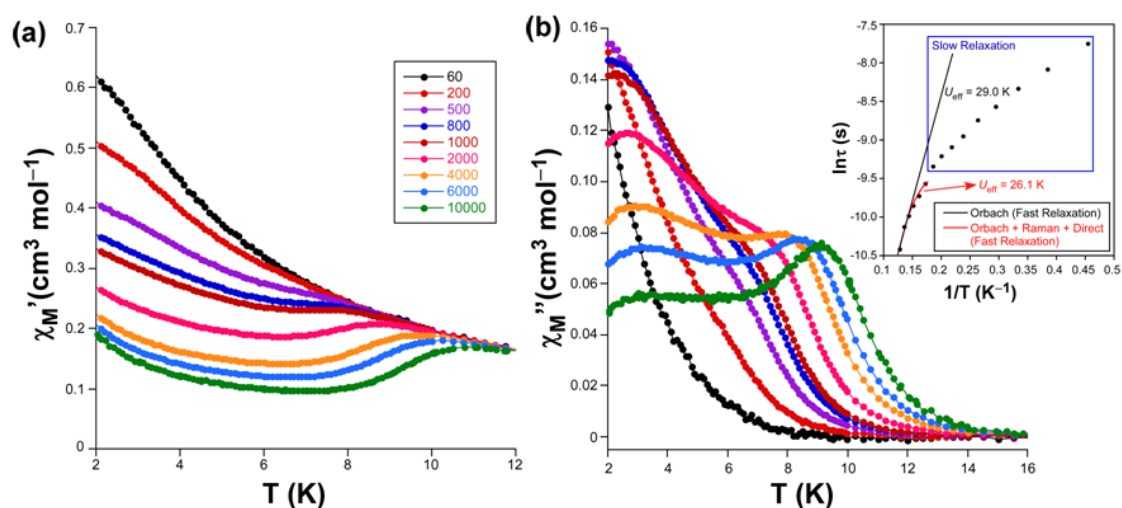


Figure 13. Temperature dependence of (a) in-phase and (b) out-of-phase ac magnetic susceptibilities under an applied field of 1000 Oe for compound 2. Inset: Arrhenius plot of relaxation times with best fittings

Cole-Cole plots were generated each 0.4 K in the 2–9 K range to cover the whole frequency dependent region (below the high frequency maximum, Figure 14).

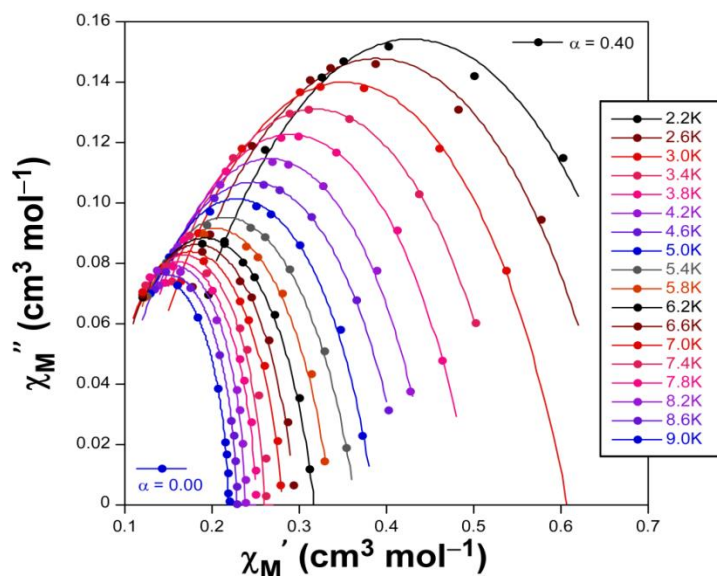


Figure 14. Cole-Cole plot for compound 2 under an applied dc field of 1 KOe.

The semicircular distributions seem to confirm the thermal evolution and coexistence of SR and FR processes. The semicircle at 2.2 K, attributed to the SR, suffers a progressive widening with increasing temperature in such a way that a broad semicircle is observed at 3.0 K, suggesting that the mixture of both processes could be taking place (superposition of two semicircles). On its part, the comparatively narrower semicircles shown above 3.8 K may be related with the FR process, in good agreement with the progressive decrease of α value estimated from fitting with the generalized Debye model.⁵⁰ Accordingly, the Arrhenius-like diagram (in the form of $\ln(\tau)$ vs $1/T$) possesses two branches that were individually analyzed.^{49,51} The faster relaxation was processed with equation 3 which accounts for spin reversal through Orbach but also direct and Raman mechanisms.

$$\tau = \tau_0 \exp(-U_{\text{eff}}/k_B T) + A_{\text{direct}} T + B_{\text{Raman}} T^n \quad (\text{eq. 3})$$

Where $A_{\text{direct}} = 257 \text{ s}^{-1}\text{K}^{-1}$, $B_{\text{Raman}} = 4.2 \text{ s}^{-1}$, $n = 7.1$, $\tau_0 = 9.98 \times 10^{-7} \text{ s}$ and $U_{\text{eff}} = 26.1 \text{ K}$ are estimated. It is remarkable that parameters associated with direct and Raman processes are comparable to other in bibliography, while τ_0 falls within the typical range found for cobalt(II) based SIMs (between 1.0×10^{-6} and 1.0×10^{-11}).^{46f} When the three highest-temperature points the obtained U_{eff} (29.0 K that equals to 20.2 cm^{-1} , with $\tau_0 = 3.36 \times 10^{-7} \text{ s}$) is in good agreement with the gap between $M_s =$

$\pm 1/2$ and $M_s = \pm 3/2$ (equivalent to $2D$). The occurrence of the second much slower relaxation could be due to weak exchange interactions among spin carriers both through the 2D network itself and/or strong π - π stackings between mimic ligands belonging to adjacent metal-organic layers (with C \cdots C as short as 3.59 Å).⁵² Within this assumption, the SR process could originate in the formation of a polymeric array whereas the FR corresponds to the relaxation of single ions, both of which may coexist in a certain temperature.

3.3. Photoluminescence Properties

CPs built from closed-shell d^{10} metal centers and aromatic ligands are known to exhibit PL in solid state, covering interesting behaviors such as dual fluorescent/phosphorescent emissions and/or tunable emission colors according to the temperature.^{7c,53} Therefore, PL measurements were carried out on polycrystalline sample of compound **4** varying the temperature in the 10–250 K range. At 10 K, **4** shows a broad and intense band that extends over the whole visible spectrum (400–700 nm) under excitation at monochromatic 325 nm light, which corresponds to the excitation maximum (Figure 15). Within the emission band, the maximum is centered at 520 nm though an additional and sharper peak at 460 nm is also distinguished, which is the responsible for the pale green emission of **4** under continuous excitation. The band progressively loses intensity as the temperature is increased whereas it keeps a similar shape, in such a way that at room temperature, the emission of the material is comparatively weak (Figure 15).

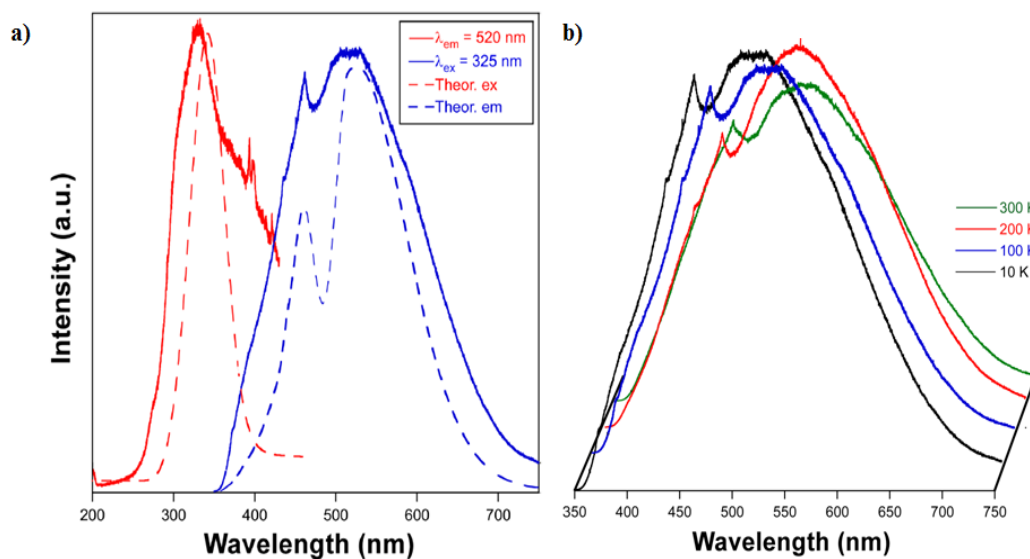


Figure 15. (a) Experimental (solid line) and calculated (dotted line) excitation and emission spectra of compound **4**. (b) Variable-temperature emission spectra of compound **4**.

This fact is in good agreement with the micro-PL photographs taken at room temperature on crystals of **4** (Figure 16). As observed, a negligible emission is shown when using $\lambda_{\text{exc}} = 365$ nm, whereas bright greenish yellow emission can be clearly inferred from the micrograph taken with 435 nm excitation line. Moreover, crystals exhibit red emission when they are exposed to the green (546 nm) excitation line, which confirms the multicolored emission of this material.

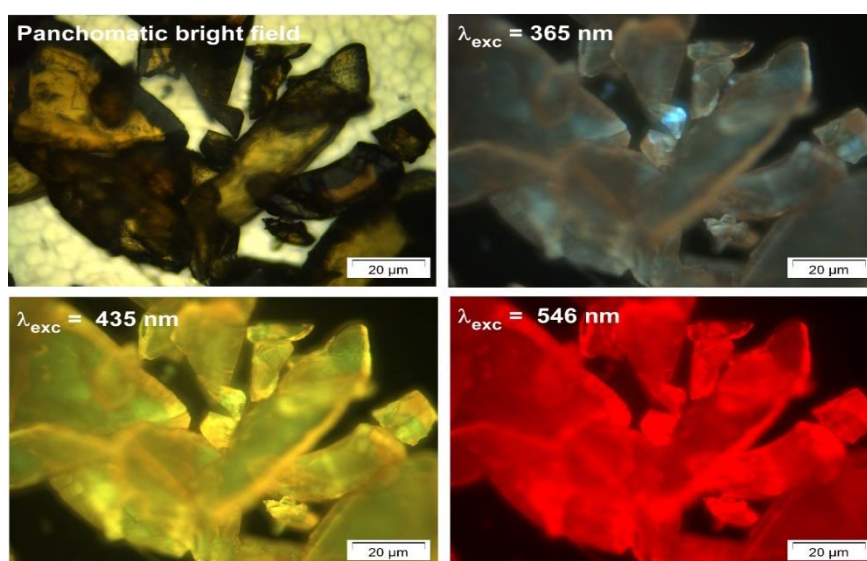


Figure 16. Room-temperature micro-PL images taken at different excitation lines.

Compared to the emission of the free Hmimc ligand, compound **4** shows a large bathochromic shift (of *ca.* 110 nm) that seems to be related to its coordination to cadmium atoms (Figure 17).⁵⁴

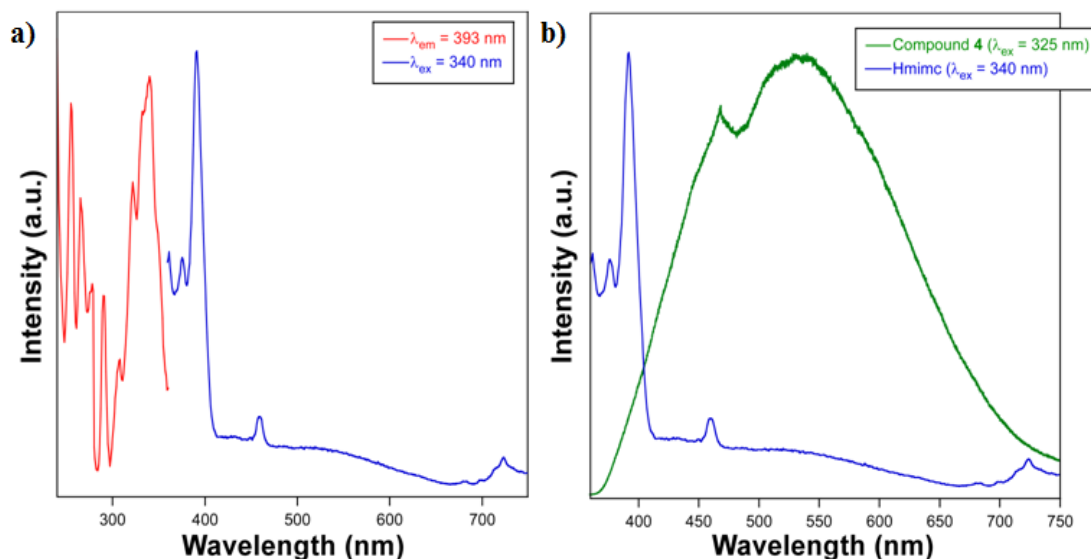


Figure 17. (a) Excitation and emission spectra of Hmimc ligand. (b) Comparison of emission profiles between Hmimc and compound **4**.

TD-DFT calculations were carried out on a suitable model of **4** to provide further insights into the PL performance of this compound. As inferred from Figure 15, the calculated spectra reproduce fairly well the experimental ones, finding very small shifts between their maxima. The two main $S_0 \rightarrow S_1$ excitations (at 328 and 335 nm) that conform the band stand for $\text{HOMO}-4 \rightarrow \text{LUMO}+2$ and $\text{HOMO}-3 \rightarrow \text{LUMO}+2$ transitions, meaning that the compound is excited via $\sigma \rightarrow \pi^*$ and $\pi \rightarrow \pi^*$ transitions between different ligands (LLCT). After these singlet excitations, the emission proceeds through similar processes for both bands. The first one (centered at 460 nm) contains three transitions: $\text{HOMO}-2 \rightarrow \text{LUMO}$, $\text{HOMO}-1 \rightarrow \text{LUMO}+3$, and $\text{HOMO}-2 \rightarrow \text{LUMO}+3$; whereas the main band with (maximum at 520 nm) results from several $\text{HOMO}-1 \rightarrow \text{LUMO}$ transitions involving different vibrational states of the latter levels (Table 12). As observed in Figure 18, $\text{HOMO}-n$ levels show a predominant σ character and lie mainly on the carboxylate groups of the ligands, so taking into account the π nature of $\text{LUMO}+n$ molecular orbitals, it

can be concluded that the singlet emission of this compound is again of the LLCT type.

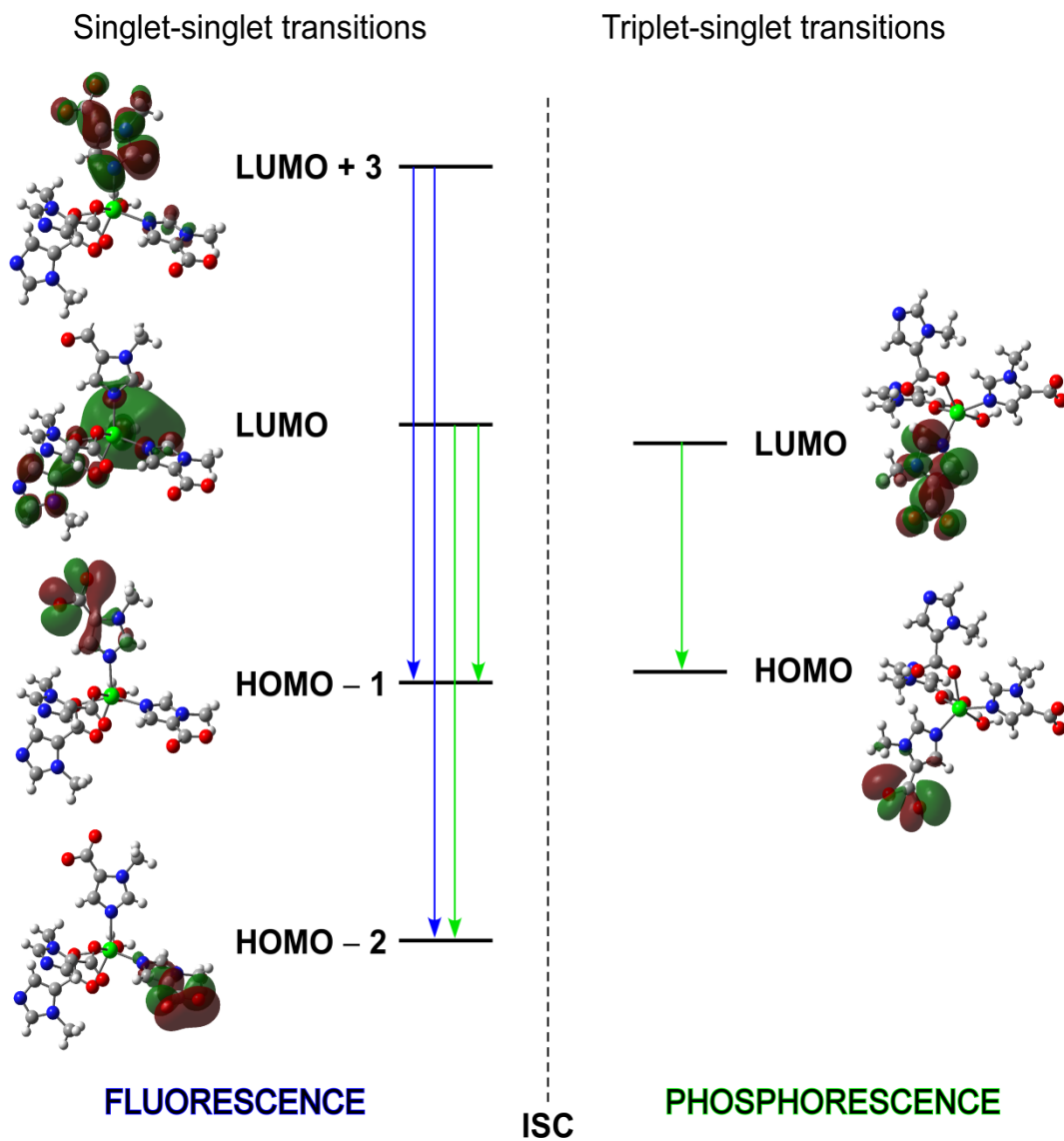


Figure 18. Energy diagram of the orbitals onto model 4 involved in the electronic transitions of 4 resulting in fluorescent and phosphorescent blue and green emissions. ISC: Intersystem crossing.

Table 12. TD-DFT calculated main excitation and emission energies (nm) and electronic transitions of all ligands.

Main excitations			
Calcd. λ	Calcd. band λ	Exp. λ	Involved orbitals / osc. st.^[a]
328	332	380	HOMO – 4 \rightarrow LUMO + 2 (87%) / 0.095
335			HOMO – 3 \rightarrow LUMO + 2 (8%) / 0.072
Main emissions			
Calcd. λ	Calcd. band λ	Exp. λ	Involved orbitals / osc. st.^[a]
407	455	460	HOMO – 1 \rightarrow LUMO + 3 (56%) / 0.079
408			HOMO – 2 \rightarrow LUMO + 3 (38%) / 0.062
450			HOMO – 1 \rightarrow LUMO + 3 (68%) / 0.078
462			HOMO – 2 \rightarrow LUMO + 3 (35%) / 0.062
498	525	520	HOMO – 2 \rightarrow LUMO (79%) / 0.0912
510	525	520	HOMO – 1 \rightarrow LUMO (99%) / 0.0763
533			HOMO – 1 \rightarrow LUMO (100%) / 0.0832

[a] Oscillator strengths.

During the PL characterization of this compound at low temperature, it was observed that the solid sample preserves a significant pale green afterglow when the excitation beam is turned off, indicating that it exhibits LLP. This fact prompted us to further investigate the phosphorescent emission of the material, for which decay curves were recorded for some representative wavelengths (each 20 nm) over the emission spectrum. At first sight, two opposite regions were distinguished according to the profile of the curves, indicative of rapid or slow deactivation processes (Table 13).

Table 13. Best fit results of decay curves measured at 10 K for compound **4** ($\lambda_{\text{ex}} = 325$ nm; $\lambda_{\text{em}} = 400\text{--}340$ nm). Note that accompanying lifetime values, percentages for each component are also given.

Wavelength (nm)	τ_1 (ms)	τ_2 (ms)	τ_3 (ms)	Chi Sq.
400	51(6) / 100%	–	–	1.544
420	6(2) / 4%	46(7) / 27%	245(18) / 69%	1.538
440	39(1) / 30%	227(5) / 70%	–	1.517
460	9(1) / 4%	67(3) / 37%	318(8) / 59%	1.435
480	14(1) / 7%	78(4) / 38%	369(13) / 55%	1.522
500	16(2) / 9%	76(6) / 34%	320(14) / 57%	1.389
520	19(1) / 9%	97(3) / 36%	427(9) / 56%	1.431
540	15(2) / 9%	75(7) / 35%	321(17) / 56%	1.476
560	34(2) / 32%	195(6) / 68%	–	1.255
580	26(1) / 27%	179(14) / 73%	–	1.515
600	28(2) / 30%	171(5) / 70%	–	1.769
620	22(1) / 30%	148(5) / 70%	–	1.658
640	68(5) / 100%	–	–	1.613

On the one hand, curves measured for λ_{em} included within 350–400 and 640–750 nm ranges reveal very short emission processes (in the order of few *ns*). On the other hand, slow and gradual decays derived from the occurrence of successive long-lived processes are described for the curves corresponding to the central and most representative region of the emission band (420–620 nm). The analysis of these curves with a multi-exponential [$I_t = A_0 + A_1 \exp(-t/\tau_1) + A_2 \exp(-t/\tau_2) + A_3 \exp(-t/\tau_3)$] expression revealed the presence of three kinds of components: persistent emissions of 0.25–0.43 s, intermediate lifetimes of 0.05–0.23 s and very short processes attributed to the lamp pulse (6–39 *ms*). Despite the fact that some Cd^{II} based compounds showing green phosphorescence have been recently reported,¹⁵ all of them display mixed blue-to-green emission as the fluorescent signal under UV excitation turns into green phosphorescent afterglow, which differs from the bright green-to-pale green transition described by compound **4**. Among those few reported materials, the structure of **4** resembles the recently characterized LLP with $[\text{Cd}(\mu\text{-6aminonicotinato})_2]_n$ formula, that presents the longest emission lifetimes (of above 0.8 s).^{15f} Taking into account the close similarity between both ligands (N/O donor ligands), the more modest lifetimes achieved for this compound may be tentatively

attributed to the presence of coordination water molecules, whose O–H bonds act as efficient quenchers on radiative processes through a vibronic coupling mechanism.⁵⁵ In any case, the occurrence of such behavior seems to indicate that, according to the well established Kasha's rule,⁵⁶ the phosphorescent emission should proceed via a spin forbidden $T_1 \rightarrow S_0$ transition. This involves, in turn, that the triplet state of the complex is accessible through intersystem crossing phenomenon facilitated by the spin-orbit coupling of the d^{10} metal atom, in addition to the absence of efficient quenchers that could be coupled to the $T_1 \rightarrow S_0$ emission. In order to the latter hypothesis, the lowest-lying T_1 state was geometrically optimized, from which the vertical emission energy ($\lambda_{\text{vert-phosp}}$ as described by Adamo et al.⁵⁷) was estimated to be of 478 nm. This value is quite close to 520 nm, the wavelength of the emission maximum that corresponds to the longest lifetime recorded, which confirms that phosphorescent emission proceeds through $T_1 \rightarrow S_0$ transition. Nonetheless, it cannot be discarded that the emitted signal is indeed also composed from fluorescent emission, as revealed by singlet-singlet transitions studied by TD-DFT. On another level, the long lasting emission remains stable up to 100 K (Table 14 and Figure 19), whereas it is practically prevented at higher temperatures owing to the increase of molecular vibrations that bring a significant non-radiative quenching, such that only the fluorescent emission takes place.

Table 14. Best fit results of decay curves performed at variable temperatures monitoring the emission wavelength with longest lifetime (520 nm).

Temperature (K)	τ_1 (ms)	τ_2 (ms)	τ_3 (ms)	Chi Sq.
10	19(1) / 9%	97(3) / 36%	427(9) / 56%	1.431
50	16(2) / 12%	76(6) / 39%	370(8) / 49%	1.387
100	18(1) / 25%	188(8) / 75%	–	1.428
200	65(15) / 100%	–	–	1.443

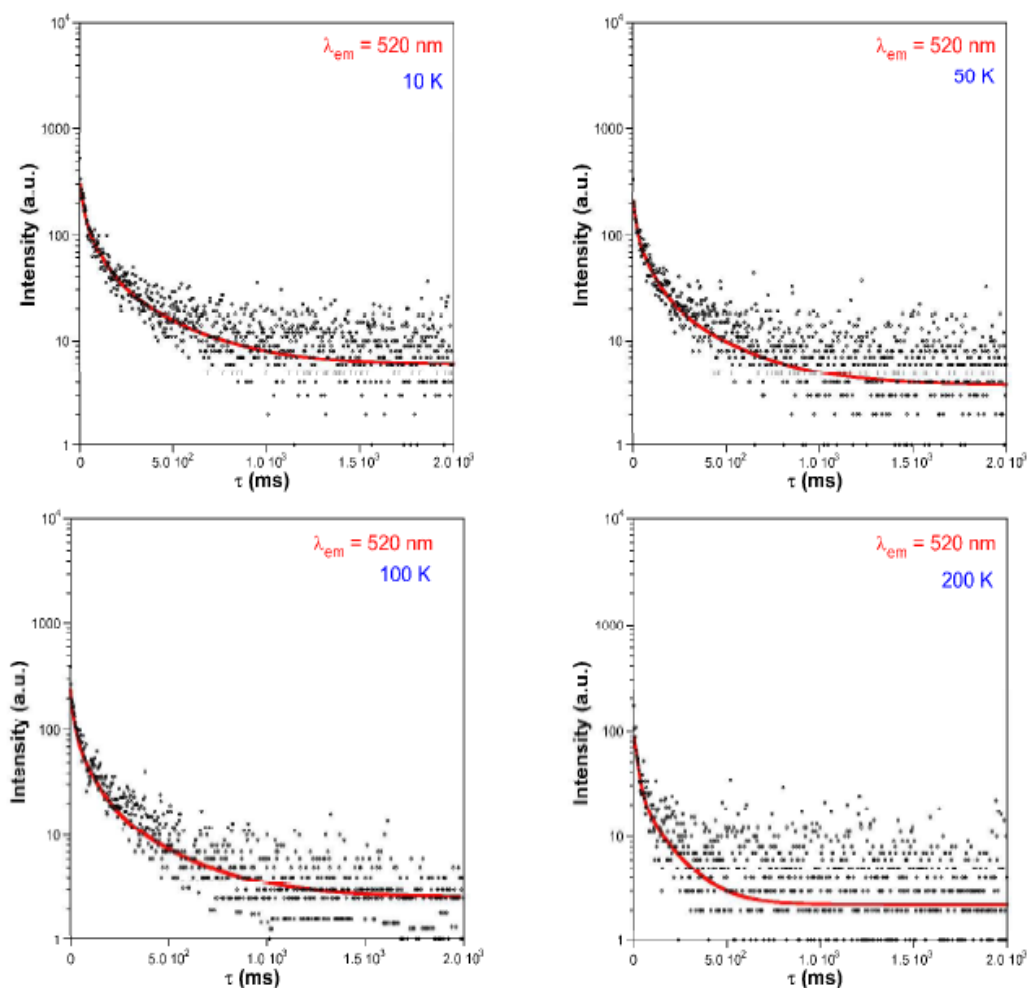


Figure 19. Variable-temperature decay curves at $\lambda_{ex} = 325$ nm and $\lambda_{em} = 520$ nm showing the best fitting.

4. Conclusions

A family of four new compounds grown from the coordination of 1-methylimidazole-5-carboxylate (mimc) ligand to first row transition metal(II) ions has been synthesized under solvothermal conditions. Single crystal X-ray analysis reveals the largest possible structural diversity in the family despite the limited coordination versatility of the ligand. In fact, it coordinates as terminal ligand to nickel(II) atoms and forms monomeric entities in **1**, whereas it acts as bridging linker among metal ions to give 2D CPs of **sql** topology in **2**, **3**, and **4**. The structural dissimilarities of the latter (small distortions of the topological network) may be attributed to subtle changes occurring in the coordination shells owing to the features imposed by cobalt(II), copper(II) and cadmium(II) ions (ion radii and preferred

geometries) when coordinating to the carboxylate moiety of the ligand, forcing it to adopt different modes that maintain the metal-to-ligand connectivity. Measurements of the magnetic susceptibility in static conditions indicate that mimc ligands show almost negligible exchange interactions among metal centers, also confirmed by DFT computed values of the coupling parameter, which allow considering these systems as networks of magnetically isolated spins. This fact results particularly interesting for the Co(II) based CP (**2**) because it shows field-induced slow magnetic relaxation arising from a moderate magnetic anisotropy of positive sign ($D = +12.9 \text{ cm}^{-1}$, $E = +0.5 \text{ cm}^{-1}$) estimated from simultaneous fitting of $\chi_M T(T)$ and $M(H)$ curves, which may in turn be attributed to the pseudo-tetrahedral environment. The analysis of the spin dynamics of **2** through *ac* measurements show the occurrence of fast quantum tunneling of the magnetization that can be partially suppressed by applying a *dc* field, allowing two relaxation processes to be identified. The faster process refers to the relaxation of single ions in the structure which proceeds through multiple mechanisms (i.e. Orbach, direct and Raman) given the combination of positive axial and low transverse magnetic anisotropy, from which a thermally activated barrier of *ca.* 26 K is estimated. Contrarily, the slower relaxation is assigned to weak exchange interactions through the 2D network or π - π stackings among mimc ligands belonging to adjacent metal-organic layers. In any case, the blocking temperature (of *ca.* 14 K) deserves to be highlighted since it lies on the high edge found for cobalt(II) based SIMs.

On another level, the cadmium(II) based CP presents an interesting bright green emission which characterizes for a long-persistent phosphorescence that is responsible for the low temperature afterglow observed for at least one second after the removal of the UV source. In fact, measurements of the decay curves reveal the occurrence of fluorescent/phosphorescent emissions, consisting of several lifetimes that account for persistent (0.25-0.43 s), intermediate (0.05-0.23 s) as well as short (6–39 *ms*) components. TD-DFT calculations combined with a computational strategy to estimate the vertical transitions related to the phosphorescent emission not only allow surmising the LCCT mechanism governing both singlet-singlet and triplet-singlet transitions but also give an accurate description of the photoluminescent performance of the compound.

5. References

1. (a) Li, M.; Li, D.; O’Keeffe, M.; Yaghi, O. M. Topological Analysis of Metal–Organic Frameworks with Polytopic Linkers and/or Multiple Building Units and the Minimal Transitivity Principle. *Chem. Rev.* **2014**, 114, 1343-1370. (b) Batten, S. R.; Murray, K. S. Structure and magnetism of coordination polymers containing dicyanamide and tricyanomethanide. *Coord. Chem. Rev.* **2003**, 246, 103-130. (c) Hoskins, B. F.; Robson, R. Infinite polymeric frameworks consisting of three dimensionally linked rod-like segments. *J. Am. Chem. Soc.* **1989**, 111, 5962-5964. (d) Allendorf, M. D.; Stavila, V. Crystal engineering, structure–function relationships, and the future of metal–organic frameworks. *CrystEngComm* **2015**, 17, 229-246.
2. (a) Chen, C. T.; Suslick, S. One-dimensional coordination polymers: Applications to material science. *Coord. Chem. Rev.* **1993**, 128, 293-322. (b) Kawata, S.; Kitagawa, S.; Kondo, M.; Furuchi, L.; Munakata, M. Two-Dimensional Sheets of Tetragonal Copper(II) Lattices: X-Ray Crystal Structure and Magnetic Properties of [Cu(C₆O₄Cl₂)(C₄H₄N₂)]_n. *Angew. Chem., Int. Ed.* **1994**, 33, 1759-1761. (c) Furukawa, S. Reboul, J.; Diring, S.; Sumida, K.; Kitagawa, S. Structuring of metal-organic frameworks at the mesoscopic/macroscopic scale. *Chem. Soc. Rev.* **2014**, 43, 5700-5734. (d) Colacio, E; Rodríguez-Diéguez, A. Possibilities with 2-pyrimidinecarbonitrile to design MOFs. *Polyhedron* **2014**, 80, 173–179.
3. (a) Ma, S.; Sun, D.; Ambrogio, M.; Fillinger, J. A.; Parkin, S.; Zhou, H.-C. Framework-catenation isomerism in metal–organic frameworks and its impact on hydrogen uptake. *J. Am. Chem. Soc.* **2007**, 129, 1858-1859. (b) Zhang, J.; Wotjas, L.; Larsen, R. W.; Eddaoudi, M.; Zaworotko, M. J. Temperature and concentration control over interpenetration in a metal–organic material. *J. Am. Chem. Soc.* **2009**, 131, 17040-17041. (c) Wang, J. H.; Li, M.; Li, D. A dynamic, luminescent and entangled MOF as a qualitative sensor for volatile organic solvents and a quantitative monitor for acetonitrile vapour. *Chem. Sci.* **2013**, 4, 1793-1801. (d) Cepeda, J.; Pérez-Yáñez, S.; Beobide, G.; Castillo, O.; García, J. A.; Luque, A. Photoluminescence modulation in lanthanide(III)/pyrazine-2,5-dicarboxylato/nitrato

frameworks. *Eur. J. Inorg. Chem.* **2015**, 2015, 4318-4328. (e) Takashima, Y.; Martinez, V. M.; Furukawa, S.; Kondo, M.; Shimomura, S.; Uehara, H.; Nakahama, M.; Sugimoto, K.; Kitagawa, S. Molecular decoding using luminescence from an entangled porous framework. *Nat. Commun.* **2011**, 2, 168. (f) Stock, N.; Biswas, S. Synthesis of metal-organic frameworks (MOFs): routes to various MOF topologies, morphologies, and composites. *Chem. Rev.* **2012**, 112, 933-969.

4. (a) Loiseau, T.; Serre, C.; Huguenard, C.; Fink, G.; Taulelle, F.; Henry, M.; Bataille, T.; Férey, G. A Rationale for the Large Breathing of the Porous Aluminum Terephthalate (MIL-53) Upon Hydration. *Chem.- Eur. J.* **2004**, 10, 1373 – 1382 (b) Murray, L. J.; Dinca, M.; Long, J. R. Hydrogen storage in metal-organic frameworks. *Chem. Soc. Rev.* **2009**, 38, 1294–1314. (c) Millward, A. R.; Yaghi, O. M. Metal-Organic Frameworks with Exceptionally High Capacity for Storage of Carbon Dioxide at Room Temperature. *J. Am. Chem. Soc.* **2005**, 127, 17998–17999. (d) Llewellyn, P. L.; Bourrelly, S.; Serre, C.; Vimont, A.; Daturi, M.; Hamon, L.; De Weireld, G.; Chang, J. S.; Hong, D. Y.; Hwang, Y. K.; Jung, S. H.; Férey, G. High Uptakes of CO₂ and CH₄ in Mesoporous Metal—Organic Frameworks MIL-100 and MIL-101. *Langmuir* **2008**, 24, 7245–7250. (e) Farha, O. K.; Yazaydin, A. Ö.; Eryazici, I.; Malliakas, C. D.; Hauser, B. G.; Kanatzidis, M. G.; Nguyen, S. T.; Snurr, R. Q.; Hupp, J.T. De novo synthesis of a metal-organic framework material featuring ultrahigh surface area and gas storage capacities. *Nat. Chem.* **2010**, 2, 944–948. (f) Pérez-Yáñez, S.; Beobide, G.; Castillo, O.; Cepeda, J.; Fröba, M.; Hoffmann, F.; Luque, A.; Román, P. Improving the performance of a poorly adsorbing porous material: template mediated addition of microporosity to a crystalline submicroporous MOF. *Chem. Commun.* **2012**, 48, 907–909. (g) Jiang, H.-L.; Makal, T. A.; Zhou, H.-C. Interpenetration control in metal-organic frameworks for functional applications. *Coord. Chem. Rev.* **2013**, 257, 2232–2249. (h) Seco, J.M.; Fairén-Jimenez, D.; Calahorra, A.J.; Méndez-Liñán, L.; Pérez-Mendoza, M.; Casati, N.; Colacio, E.; Rodríguez-Diéguez, A. Modular structure of a robust microporous MOF based on Cu₂ paddle-wheels with high CO₂ selectivity. *Chem. Commun.* **2013**, 49, 11329-11331. (i) Spanopoulos, I.; Bratsos, I.; Tampaxis, C.; Kourtellaris, A.; Tasiopoulos, A.; Charalambopoulou, G.; Steriotis, T. A.; Trikalitis, P. N. Enhanced

gas-sorption properties of a high surface area, ultramicroporous magnesium formate. *CrystEngComm* **2015**, *17*, 532–539.

5. (a) Russell, S.E.; Gosset, C.; Agache, X.; Volkringer, C.; Henry, N.; Decadt, R.; Van D.R.; Visseaux, M.; Loiseau, T. A new series of trivalent lanthanide (Ce, Pr, Nd, Sm, Eu, Gd, Tb, Dy) coordination polymers with a 1,2-cyclohexanedicarboxylate ligand: synthesis, crystal structure, luminescence and catalytic properties. *CrystEngComm* **2016**, *18*, 3594-3605. (b) Quah, H. S.; Chen, W.; Schreyer, M. K.; Yang, H.; Wong, M. W.; Ji, W.; Vittal, J. J. Multiphoton harvesting metal–organic frameworks. *Nat. Comm.* **2015**, *6*, 7954-7961. (c) Li, H.-Y.; Wei, Y.-L.; Dong, X.-Y.; Zang, S.-Q.; Mak, T. C. W. Novel Tb-MOF Embedded with Viologen Species for Multi-Photofunctionality: Photochromism, Photomodulated Fluorescence, and Luminescent pH Sensing. *Chem. Mater.* **2015**, *27*, 1327-1331. (d) Baldoví, J. J.; Coronado, E.; Gaita-Ariño, A.; Gamer, C.; Giménez-Marqués, M.; Mínguez-Espallargas, G. A SIM-MOF: Three-Dimensional Organisation of Single-Ion Magnets with Anion-Exchange Capabilities. *Chem. – Eur. J.* **2014**, *20*, 10695-10702. (e) Shi, P.-F.; Zhao, B.; Xiong, G.; Hou, Y.-L.; Cheng, P. Fast capture and separation of, and luminescent probe for, pollutant chromate using a multi-functional cationic heterometal-organic framework. *Chem. Commun.* **2012**, *48*, 8231-8233. (f) Wu, M.-X. Yang, Y.-W. *Adv. Mater.* **2017**, *29*, 160134. (g) Cepeda, J.; Pérez-Yáñez, S.; Beobide, G.; Castillo, O.; García, J. A.; Lanchas, M.; Luque, A. Enhancing luminescence properties of lanthanide(III)/pyrimidine-4,6-dicarboxylato system by solvent-free approach. *Dalton Trans.* **2015**, *44*, 6972-6986. (h) Rocha, J.; Brites, C. D. S.; Carlos, L. D. Lanthanide Organic Framework Luminescent Thermometers. *Chem. – Eur. J.* **2016**, *22*, 14782-14795. (i) Lin, R.-B.; Liu, S.-Y.; Ye, J.-W.; Li, X.-Y.; Zhang, J.-P. Photoluminescent Metal–Organic Frameworks for Gas Sensing. *Adv. Sci.* **2016**, *3*, 1500434-1500454. (j) Calahorra, A.J.; Oyarzabal, I.; Fernández, B.; Seco, J.M.; Tian, T.; Fairen-Jimenez, D.; Colacio, E.; Rodríguez-Diéguez, A. Rare earth anthracenedicarboxylate metal–organic frameworks: slow relaxation of magnetization of Nd³⁺, Gd³⁺, Dy³⁺, Er³⁺ and Yb³⁺ based materials, *Dalton Trans.* **2016**, *45*, 591–598.

6. (a) Ma, L. F.; Wang, L. Y.; Du, M.; Batten, S. R. Unprecedented 4- and 6-connected 2D coordination networks based on 44-subnet tectons, showing unusual

supramolecular motifs of rotaxane and helix. *Inorg. Chem.* **2010**, 49, 365-367. (b) Chen, S. P.; Ren, Y. X.; Wang, W. T.; Gao, S. L. Nanoporous lanthanide-carboxylate frameworks based on 5-nitroisophthalic acid. *Dalton Trans.* **2010**, 39, 1552-1557

7. (a) Almeida Paz, F. A.; Klinowski, J.; Vilela, S. M. F.; Tomé, J. P. C.; Cavaleiro, J. A. S.; Rocha, J. Ligand design for functional metal–organic frameworks. *Chem. Soc. Rev.* **2012**, 41, 1088–1110. (b) Heine, J.; Müller-Buschbaum, K. Engineering metal-based luminescence in coordination polymers and metal–organic frameworks. *Chem. Soc. Rev.* **2013**, 42, 9232–9242; (c) Cepeda, J.; Rodríguez-Diéguez, A. Tuning the luminescence performance of metal–organic frameworks based on d10 metal ions: from an inherent versatile behaviour to their response to external stimuli. *CrystEngComm* **2016**, 18, 8556–8573. (d) Wiers, B. M.; Foo, M.-L.; Balsara, N. P.; Long, J. R. A Solid Lithium Electrolyte via Addition of Lithium Isopropoxide to a Metal–Organic Framework with Open Metal Sites. *J. Am. Chem. Soc.* **2011**, 133, 14522–14525. (e) Férey, G.; Millange, F.; Morcrette, M.; Serre, C.; Doublet, M. L.; Grenèche, J.-M.; Tarascon, J.-M. Mixed-valence li/fe-based metal-organic frameworks with both reversible redox and sorption properties. *Angew. Chem., Int. Ed.* **2007**, 46, 3259–3263. (f) Kurmoo, M. Magnetic metal–organic frameworks. *Chem. Soc. Rev.* **2009**, 38, 1353–1379.

8. (a) Meng, Y.-S.; Jiang, S.-D.; Wang, B.-W.; Gao, S. Understanding the Magnetic Anisotropy toward Single-Ion Magnets. *Acc. Chem. Res.* **2016**, 49, 2381–2389. (b) Fernández, B.; Oyarzabal, I.; Fischer-Fodor, E.; Macavei, S.; Sánchez, I.; Seco, J.M.; Gómez-Ruiz, S.; Rodríguez-Diéguez, A. Multifunctional applications of a dysprosium based metal–organic chain with single-ion magnet behavior. *CrystEngComm* **2016**, 18, 8718–8721.

9. (a) Freedman, D. E.; Harman, W. H.; Harris, T. D.; Long, G. J.; Chang, C. J.; Long, J. R. Slow Magnetic Relaxation in a High-Spin Iron(II) Complex. *J. Am. Chem. Soc.* **2010**, 132, 1224. (b) Harman, W. h.; Harris, T. D.; Fong, H.; Chang, A.; Rinehart, J. D.; Ozarowski, A.; Sougrati, M. T.; Grandjean, F.; Long, G. J.; Long, J. R.; Chang, C. J. Slow Magnetic Relaxation in a Family of Trigonal Pyramidal Iron(II) Pyrrolide Complexes. *J. Am. Chem. Soc.* **2010**, 132, 18115-18126.

10. Huang, X.-C.; Zhou, C.; Shao, D.; Wang, X.-Y. Field-Induced Slow Magnetic Relaxation in Cobalt(II) Compounds with Pentagonal Bipyramid Geometry. *Inorg. Chem.* **2014**, *53*, 12671–12673.

11. (a) Frost, J. M.; Harriman, K. L. M.; Murugesu, M. The rise of 3-d single-ion magnets in molecular magnetism: towards materials from molecules? *Chem. Sci.* **2016**, *7*, 2470-2491. (b) Craig, G. A.; Murrie, M. 3d single-ion magnets. *Chem. Soc. Rev.* **2015**, *44*, 2135–2147. (c) Ion, A. E.; Nica, S.; Madalan, A. M.; Shova, S.; Vallejo, J.; Julve, M.; Lloret, F.; Andruh, M. Two-Dimensional Coordination Polymers Constructed Using, Simultaneously, Linear and Angular Spacers and Cobalt(II) Nodes. New Examples of Networks of Single-Ion Magnets. *Inorg. Chem.* **2015**, *54*, 16-18. (d) Mondal, A. K.; Khatua, S.; Tomar, K.; Konar, S. Field-Induced Single-Ion-Magnetic Behavior of Octahedral CoII in a Two-Dimensional Coordination Polymer. *Eur. J. Inorg. Chem.* **2016**, 2016, 3545-3552. (e) Rodríguez-Diéguez, A.; Pérez-Yáñez, S.; Ruiz-Rubio, L.; Seco, J. M.; Cepeda, J. From isolated to 2D coordination polymers based on 6-aminonicotinate and 3d-metal ions: towards field-induced single-ion-magnets. *CrystEngComm* **2017**, *19*, 2229-2242. (f) Palion-Gazda, J.; Klemens, T.; Machura, B.; Vallejo, J.; Lloret, F.; Julve, M. Single ion magnet behaviour in a two-dimensional network of dicyanamide-bridged cobalt(II) ions. *Dalton Trans.* **2015**, *44*, 2989–2992.

12. (a) Kramers, H. A.; *Proc. R. Acad. Sci. Amsterdam*, **1930**, *33*, 959. (b) Atherton, N. M.; *Principles of Electron Spin Resonance*, Ellis Horwood Limited, Chichester, 1993. (c) Ishikawa, N.; Sugita, M.; Wernsdorfer, W. Quantum tunneling of magnetization in lanthanide single-molecule magnets: bis(phthalocyaninato)terbium and bis(phthalocyaninato)dysprosium anions. *Angew. Chem. Int. Ed.*, **2005**, *44*, 2931-2935.

13. (a) Zadrozny, J. M.; Long, J. R. Slow Magnetic Relaxation at Zero Field in the Tetrahedral Complex [Co(SPh)₄]₂⁻. *J. Am. Chem. Soc.* **2011**, *133*, 20732-20734. (b) Cucos, P.; Tuna, F.; Sorace, L.; Matei, I.; Maxim, C.; Shova, S.; Gheorghe, R.; Caneschi, A.; Hillebrand, M.; Andruh, M. *Inorg. Chem.* **2014**, *53*, 7738-7747. (c) Cao, D.-K.; Feng, J.-Q.; Ren, M.; Gu, Y.-W.; Song, Y.; Ward, M. D. *Chem. Commun.* **2013**, *49*, 8863-8865. (d) Rechkemmer, Y.; Breitgoff, F. D.; van der Meer,

M.; Atanasov, M.; Hakl, M.; Orlita, M.; Neugebauer, P.; Neese, F.; Sarkar, B.; van Slageren, J. *Nat. Commun.* **2016**, 7, 10467. (e) Carl, E.; Demeshko, S.; Meyer, F.; Stalke, D. *Chem.-Eur. J.* **2015**, 21, 10109-10115.

14. (a) Zadrozny, J. M.; Liu, J.; Piro, N. A.; Chang, C. J.; Hill, S.; Long, J. R. Slow magnetic relaxation in a pseudotetraahedralcobalt(II) complex with easy-plane anisotropy. *Chem. Commun.* **2012**, 48, 3927-3929. (b) A. F. Orchard, *Magnetochemistry*, Oxford University Press, Oxford, 2003.

15. (a) Calahorro, A. J.; Salinas-Castillo, A.; Fairen-Jimenez, D.; Seco, J. M.; Mendicute-Fierro, C.; Gómez-Ruiz, S.; López-Viseras, M.; Rodríguez-Diéguez, A. Long lifetime photoluminescence emission of 3D cadmium metal-organic frameworks based on the 5-(4-pyridyl)tetrazole ligand. *Inorg. Chim. Acta* **2015**, 427, 131-137. (b) Yuan, S.; Deng, Y.-K.; Sun, D. Unprecedented Second-Timescale Blue/Green Emissions and Iodine-Uptake-Induced Single-Crystal-to-Single-Crystal Transformation in ZnII/CdII Metal-Organic Frameworks. *Chem.-Eur. J.* **2014**, 20, 10093-10098. (c) Cepeda, J.; San Sebastian, E.; Padro, D.; Rodríguez-Diéguez, A.; García, J. A.; Ugalde, J.; Seco, J. M. A Zn based coordination polymer exhibiting long-lasting phosphorescence. *Chem. Commun.* **2016**, 52, 8671-8674. (d) Yang, X.; Yan, D. Strongly Enhanced Long-Lived Persistent Room Temperature Phosphorescence Based on the Formation of Metal-Organic Hybrids. *Adv. Opt. Mater.* **2016**, 4, 897-905. (e) Yang, Y.; Wang, K.-Z.; Yan D. Ultralong Persistent Room Temperature Phosphorescence of Metal Coordination Polymers Exhibiting Reversible pH-Responsive Emission. *ACS Appl. Mater. Interfaces* **2016**, 8, 15489-15496. (f) Seco, J. M.; Rodríguez-Diéguez, A.; Padro, D.; García, J. A.; Ugalde, J. M.; San Sebastian, E.; Cepeda, J. Experimental and Theoretical Study of a Cadmium Coordination Polymer Based on Aminonicotinate with Second-Timescale Blue/Green Photoluminescent Emission. *Inorg. Chem.* **2017**, 56, 3149-3152.

16. (a) Murawski, C.; Leo, K.; Gather, M. C. Efficiency roll-off in organic light-emitting diodes. *Adv. Mater.* **2013**, 25, 6801-6827. (b) Hong, K.; Lee, J.-L. Review paper: Recent developments in light extraction technologies of organic light emitting diodes. *Electron. Mater. Lett.* **2011**, 7, 77-91.

17. (a) McClenagan, N. D.; Leydet, Y.; Maubert, B.; Indelli, M. T.; Campagna, S. Excited-State Equilibration: A Process Leading to Long-Lived Metal-to-Ligand Charge Transfer Luminescence in Supramolecular Systems. *Coord. Chem. Rev.* **2005**, 249, 1336–1350. (b) Indelli, M. T.; CGhirotti, M.; Prodi, A.; Chiorboli, C.; Scandola, F.; MacClenaghan, N. D.; Puntoriero, F.; Campagna, S. Solvent Switching of Intramolecular Energy Transfer in Bichromophoric Systems. Photophysics of (2,2'-Bipyridine)tetracyanoruthenate(II)/Pyrenyl Complexes. *Inorg. Chem.* **2003**, 42, 5489–5497.
18. Earnshaw, A. *Introduction to Magnetochemistry*; Academic Press: London, **1968**.
19. Bruker Apex2, Bruker AXS Inc., Madison, Wisconsin, USA, **2004**.
20. Sheldrick, G.M. *SADABS, Program for Empirical Adsorption Correction*, Institute for Inorganic Chemistry, University of Gottingen: Germany, **1996**.
21. Altomare, A.; Burla, M. C.; Camilla, M.; Cascarano, G. L.; Giacovazzo, C.; Guagliardi, A.; Moliterni, A. G. G.; Polidori, G.; Spagna, R. SIR97: a new tool for crystal structure determination and refinement. *J. Appl. Crystallogr.* **1999**, 32, 115–119.
22. (a) Sheldrick, G. M. *SHELX-2014, Program for Crystal Structure Refinement*; University of Göttingen, Göttingen, Germany, 2014. (b) Farrugia, L. J. WinGX suite for small-molecule single-crystal crystallography. *J. Appl. Cryst.* **1999**, 32, 837–838.
23. (a) Rodríguez-Carvajal, J. FULLPROF, Program Rietveld for Pattern Matching Analysis of Powder Patterns; Abstracts of the Satellite Meeting on Powder Diffraction of the XV Congress of the IUCr: Toulouse, France, **1990**, 127. (b) Rodríguez-Carvajal, J. FULLPROF 2000, version 2.5d; Laboratoire Léon Brillouin (CEA-CNRS), Centre d'Études de Saclay, Gif sur Yvette Cedex: France, **2003**.
24. Frisch, M. J.; Trucks, G. W.; Schlegel, H. B.; Scuseria, G. E.; Robb, M. A.; Cheeseman, J. R.; Scalmani, G.; Barone, V.; Mennucci, B.; Petersson, G. A.; Nakatsuji, H.; Caricato, M.; Li, X.; Hratchian, H. P.; Izmaylov, A. F.; Bloino, J.; Zheng, G.; Sonnenberg, J. L.; Hada, M.; Ehara, M.; Toyota, K.; Fukuda, R.; Hasegawa, J.; Ishida, M.; Nakajima, T.; Honda, Y.; Kitao, O.; Nakai, H.; Vreven, T.;

Montgomery Jr., J. A.; Peralta, J. E.; Ogliaro, F.; Bearpark, M.; Heyd, J. J.; Brothers, E.; Kudin, K. N.; Staroverov, V. N.; Kobayashi, R.; Normand, J.; Raghavachari, K.; Rendell, A.; Burant, J. C.; Iyengar, S. S.; Tomasi, J.; Cossi, M.; Rega, N.; Millam, J. M.; Klene, M.; Knox, J. E.; Cross, J. B.; Bakken, V.; Adamo, C.; Jaramillo, J.; Gomperts, R.; Stratmann, R. E.; Yazyev, O.; Austin, A. J.; Cammi, R.; Pomelli, C.; Ochterski, J. W.; Martin, R. L.; Morokuma, K.; Zakrzewski, V. G.; Voth, G. A.; Salvador, P.; Dannenberg, J. J.; Dapprich, S.; Daniels, A. D.; Farkas, O.; Foresman, J. B.; Ortiz, J. V.; Cioslowski, J. Fox, D. J. Gaussian 09, revision A.02, Gaussian, Inc., Wallingford, CT, **2009**.

25. (a) Becke, A. D. Density-functional thermochemistry. III. The role of exact exchange. *J. Chem. Phys.* **1993**, 98, 5648-5652. (b) Miehlich, B.; Savin, A.; Stoll, H.; Preuss, H. Results obtained with the correlation energy density functionals of Becke and Lee, Yang and Parr. *Chem. Phys. Lett.* **1989**, 157, 200-206. (c) Development of the Colic-Salvetti correlation-energy formula into a functional of the electron density. Lee, C.; Yang, W.; Parr, R. G. *Phys. Rev. B* **1988**, 37, 785-789.

26. (a) Rassolov, V. A.; Ratner, M. A.; Pople, J. A.; Redfern, P. C.; Curtiss, L. A. 6-31G* basis set for third-row atoms. *J. Comput. Chem.* **2001**, 22, 976-984. (b) Francel, M. M.; Pietro, W. J.; Hehre, W. J.; Binkley, J. S.; DeFrees, D. J.; Pople, J. A.; Gordon, M. S. Self-consistent molecular orbital methods. XXIII. A polarization-type basis set for second-row elements. *J. Chem. Phys.* **1982**, 77, 3654-3665. (c) Hariharan, P. C.; Pople, J. A. Accuracy of AHn equilibrium geometries by single determinant molecular orbital theory. *Mol. Phys.* **1974**, 27, 209-214.

27. (a) Hay, P. J.; Wadt, W. R. Ab initio effective core potentials for molecular calculations. Potentials for the transition metal atoms Sc to Hg. *J. Chem. Phys.* **1985**, 82, 270-283. (b) Wadt, W. R.; Hay, P. J. Ab initio effective core potentials for molecular calculations. Potentials for main group elements sodium to bismuth. *J. Chem. Phys.* **1985**, 82, 284-298. (c) Hay, P. J.; Wadt, W. R. Ab initio effective core potentials for molecular calculations. Potentials for potassium to gold including the outermost core orbitals. *J. Chem. Phys.* **1985**, 82, 299-310.

28. (a) Shuhong, X.; Chunlei, W.; Zhuyuan, W.; Yiping, C. *J. Mol. Model.* **2014**, 20, 2184. (b) Kangcheng, Z.; Xuwen, L.; Hong, D.; Hui, C.; Fengcun, Y.; Liangnian, J.

Theoretical and experimental studies on electron transfer among complexes [M(phen)₃]²⁺ [M=Os(II), Ru(II), Co(III) and Zn(II)] binding to DNA. *J. Mol. Struct.: THEOCHEM* **2003**, 626, 295-304.

29. O'Boyle, N. M.; Tenderholt, A. L.; Langner, K. M. cclib: A library for package-independent computational chemistry algorithms. *J. Comput. Chem.* **2008**, 29, 839-845.

30. *GaussView, Version 5*, Dennington, R.; Keith, T.; Millam, J. Semichem Inc., Shawnee Mission: KS, **2009**.

31. (a) Ruiz, E.; Cano, J.; Álvarez, S.; Alemany, P. Broken symmetry approach to calculation of exchange coupling constants for homobinuclear and heterobinuclear transition metal complexes. *J. Comput. Chem.* **1999**, 20, 1391-1400. (b) Ruiz, E.; Rodríguez-Forteza, A.; Cano, J.; Álvarez, S.; Alemany, P. About the calculation of exchange coupling constants in polynuclear transition metal complexes. *J. Comput. Chem.* **2003**, 24, 982-989.

32. Grimme, S. *J. Comput. Chem.* **2006**, 27, 1787-1799.

33. Noodleman, L.; Case, D. A.; Aizman, A. Broken symmetry analysis of spin coupling in iron-sulfur clusters. *J. Am. Chem. Soc.* **1988**, 110, 1001-1005.

34. Kumar Singh, M.; Rajaraman, G. Can CH \cdots p Interactions Be Used To Design Single-Chain Magnets? *Chem.-Eur. J.* **2015**, 21, 980-983.

35. (a) Llunel, M.; Casanova, D.; Cirera, J.; Bofill, J. M.; Alemany, P.; Alvarez, S.; Pinsky, M.; Avnir, D. SHAPE (1.7), University of Barcelona, Barcelona, **2010**; (b) Alvarez, S.; Alemany, P.; Casanova, D.; Cirera, J.; Llunell, M.; Avnir, D. Shape Maps and Polyhedral Interconversion Paths in Transition Metal Chemistry. *Coord. Chem. Rev.* **2005**, 249, 1693-1708. (c) Alvarez, S.; Llunell, M. Continuous symmetry measures of penta-coordinate molecules: Berry and non-Berry distortions of the trigonal bipyramid. *J. Chem. Soc., Dalton Trans.* **2000**, 3288-3303. (d) Alvarez, S.; Avnir, D.; Llunell, M.; Pinsky, M. Continuous symmetry maps and shape classification. The case of six-coordinated metal compounds. *New J. Chem.* **2002**, 26, 996-1009.

36. Liu, J.; Cheng, M.-L.; Yu, L.-L.; Chen, S.-C.; Shao, Y.-L.; Liu, Q.; Zhai, C.-W.; Yin, F.-X. Three metal complexes derived from 3- methyl-1H-pyrazole-4-carboxylic acid: synthesis, crystal structures, luminescence and electrocatalytic properties. *RSC Adv.* **2016**, 6, 52040–52047.
37. (a) TOPOS Main Page. <http://www.topos.ssu.samara.ru> (accessed September 6, 2016). (b) Blatov, V. A. Multipurpose crystallochemical analysis with the program package TOPOS. *IUCR CompComm Newsletter* **2006**, 7, 4-38. (c) Blatov, V. A.; O’Keeffe, M.; Proserpio, D. M. Vertex-, face-, point-, Schläfli-, and Delaney-symbols in nets, polyhedra and tilings: recommended terminology. *CrystEngComm* **2010**, 12, 44-48. (d) Alexandrov, E. V.; Blatov, V. A.; Kochetkov, A. V.; Proserpio, D. M. Underlying nets in three-periodic coordination polymers: topology, taxonomy and prediction from a computer-aided analysis of the Cambridge Structural Database. *CrystEngComm* **2011**, 13, 3947-3958.
38. Singh, M. K.; Rajaraman, C.G. CH \cdots π Interactions Be Used To Design Single-Chain Magnets. *Chem. – Eur. J.* **2015**, 21, 980-983.
39. Chilton, N. F.; Anderson, R. P.; Turner, L. D.; Soncini, A.; Murray, K. S. PHI: A powerful new program for the analysis of anisotropic monomeric and exchange-coupled polynuclear d- and f-block complexes. *J. Comput. Chem.* **2013**, 4, 1164-1175.
40. (a) Boča, R. Zero-field splitting in metal complexes. *Coord. Chem. Rev.* **2004**, 248, 757-815; (b) Titiš, J.; Boča, R. Magnetostructural D Correlation in Nickel(II) Complexes: Reinvestigation of the Zero-Field Splitting. *Inorg. Chem.* **2010**, 49, 3971-3973.
41. Singh, S. K.; Gupta, T.; Badkur, P.; Rajaraman, G. Magnetic Anisotropy of Mononuclear NiII Complexes: On the Importance of Structural Diversity and the Structural Distortions. *Chem.-Eur. J.* **2014**, 20, 10305-10313.
42. (a) Lloret, F.; Julve, M.; Cano, J.; Ruiz-Garcia, R.; Pardo, E. Magnetic properties of six-coordinated high-spin cobalt(II) complexes: Theoretical background and its application. *Inorg. Chim. Acta* **2008**, 361, 3432–3445. (b) Sakiyama, H.; Ito, R.;

Kumagai, H.; Inoue, K.; Sakamoto, M.; Nishida, Y.; Yamadsaki, M. Dinuclear cobalt(II) complexes of an acyclic phenol-based dinucleating ligand with four methoxyethyl chelating arms - first magnetic analyses in an axially distorted octahedral field. *Eur. J. Inorg. Chem.* **2001**, 2001, 2027–2032.

43. (a) Rueff, J.-M.; Masciocchi, N.; Rabu, P.; Sironi, A.; Skoulios, A. Structure and Magnetism of a Polycrystalline Transition Metal Soap – CoII[OOC(CH₂)₁₀COO](H₂O)₂. *Eur. J. Inorg. Chem.* **2001**, 2001, 2843-2848. (b) Rabu, P.; Rueff, J.-M.; Huang, Z. L.; Angelov, S.; Souletie, J.; Drillon, M. Copper(II) and cobalt(II) dicarboxylate-based layered magnets: influence of π electron ligands on the long range magnetic ordering. *Polyhedron* **2001**, 20, 1677-1685.

44. (a) Cui, L.; Yang, P. Y.; Wu, W.-P.; Miao, H.-H.; Shi, Q.-Z.; Wang, Y.-Y. Solvents and auxiliary ligands co-regulate three antiferromagnetic Co(II) MOFs based on a semi-rigid carboxylate ligand. *Dalton Trans.* **2014**, 43, 5823-5830. (b) García-Couceiro, U.; Castillo, O.; Luque, A.; García-Terán, J. P.; Beobide, G.; Román, P. Rational Design of 2D Magnetic Metal- Organic Coordination Polymers Assembled from Oxalato and Dipyridyl Spacers. *Cryst. Growth Des.* **2006**, 6, 1839-1847. (c) Si, C.-D.; Hu, D.-C.; Fan, Y.; Dong, X.-Y.; Yao, X.-Q.; Yang, Y.-X.; Liu, J.-C. Three-Dimensional Supramolecular Architectures with CoII Ions Assembled from Hydrogen Bonding and $\pi \cdots \pi$ Stacking Interactions: Crystal Structures and Antiferromagnetic Properties. *Cryst. Growth Des.* **2015**, 15, 5781-5793.

45. Pali, A. V.; Clemente-Juan, J. M.; Coronado, E.; Klokishner, S. I.; Ostrovsky, S. M.; Reu, O. S. Role of Orbital Degeneracy in the Single Molecule Magnet Behavior of a Mononuclear High-Spin Fe(II) Complex. *Inorg. Chem.* **2010**, 49, 8073-8077.

46. (a) Šebová, M.; Jorík, V.; Moncol, J.; Kožíšek, J.; Boča, R. Structure and magnetism of Co(II) complexes with bidentate heterocyclic ligand Hsalbim derived from benzimidazole. *Polyhedron* **2011**, 30, 1163-1170. (b) Petit, S.; Pilet, G.; Luneau, D.; Chibotaru, L. F.; Ungur, L. A dinuclear cobalt(II) complex of calix[8]arenes exhibiting strong magnetic anisotropy. *Dalton Trans.* **2007**, 4582-4588. (c) Vaidya, S.; Tewary, S.; Kumar Singh, S.; Langley, S. K.; Murray, K. S.; Lan, Y.; Wernsdorfer, W.; Rajaraman, G.; Shanmugam, M. What Controls the Sign and Magnitude of Magnetic Anisotropy in Tetrahedral Cobalt(II) Single-Ion Magnets?

Inorg. Chem. **2016**, 55, 9564-9578. (d) Ziegenbalg, S.; Hornig, D.; Görls, H.; Plass, W. Cobalt(II)-Based Single-Ion Magnets with Distorted Pseudotetrahedral [N₂O₂] Coordination: Experimental and Theoretical Investigations. *Inorg. Chem.* **2016**, 55, 4047-4058.

47. (a) Gomez-Coca, S.; Cremades, E.; Alaga-Alcalde, N.; Ruiz, E. Mononuclear Single-Molecule Magnets: Tailoring the Magnetic Anisotropy of First-Row Transition-Metal Complexes. *J. Am. Chem. Soc.* **2013**, 135, 7010-7018. (b) Boča, R. Zero-field splitting in metal complexes. *Coord. Chem. Rev.* **2004**, 248, 757-815.

48. (a) Huang, W.; Liu, T.; Wu, D.; Cheng, J.; Ouyang, Z. W.; Duan, C. Field-induced slow relaxation of magnetization in a tetrahedral Co(II) complex with easy plane anisotropy. *Dalton Trans.* **2013**, 42, 15326-15331. (b) Gomez-Coca, S.; Urtizberea, A.; Cremades, E.; Alonso, P. J.; Camon, A.; Ruiz, E.; Luis, F. Origin of slow magnetic relaxation in Kramers ions with non-uniaxial anisotropy. *Nat. Commun.* **2014**, 5, 4300.

49. (a) Ruiz, J.; Mota, A. J.; Rodríguez-Diéguez, A.; Titos, S.; Herrera, J. M.; Ruiz, E.; Cremades, E.; Costes, J. P.; Colacio, E. Field and dilution effects on the slow relaxation of a luminescent DyO₉ low symmetry single-ion magnet. *Chem. Commun.* **2012**, 48, 7916-7918. (b) Habib, F.; Korobkov, I.; Murugesu, M. Exposing the intermolecular nature of the second relaxation pathway in a mononuclear cobalt(II) single-molecule magnet with positive anisotropy. *Dalton Trans.* **2015**, 44, 6368-6373.

50. Cole, K. S.; Cole, R. H. Dispersion and Absorption in Dielectrics I. Alternating Current Characteristics. *J. Chem. Phys.* **1941**, 9, 341-351.

51. (a) Cuccinota, G.; Perfetti, M.; Luzon, J.; Etienne, M.; Car, P.-E.; Caneschi, A.; Calvez, G.; Bernot, K.; Sessoli, R. Magnetic Anisotropy in a Dysprosium/DOTA Single-Molecule Magnet: Beyond Simple Magneto-Structural Correlations. *Angew. Chem., Int. Ed.* **2012**, 51, 1606-1610. (b) Jiang, S. D.; Liu, S.-S.; Zhou, L.-N.; Wang, B. W.; Wang, Z. M.; Gao, S. Series of Lanthanide Organometallic Single-Ion Magnets. *Inorg. Chem.* **2012**, 51, 3079-3087. (c) Meihaus, K. R.; Rinehart, J. R.; Long, J. R. Dilution-Induced Slow Magnetic Relaxation and Anomalous Hysteresis

in Trigonal Prismatic Dysprosium(III) and Uranium(III) Complexes. *Inorg. Chem.* **2011**, *50*, 8484-8489. (d) Wang, Y.-L.; Chen, L.; Liu, C.-M.; Du, Z.-Y.; Chen, L.-L.; Liu, Q.-Y. *Dalton Trans.* **2016**, *45*, 7768-7775

52. Miklovič, J.; Valigura, D.; Boča, R.; Titiš, J. A mononuclear Ni(II) complex: a field induced single-molecule magnet showing two slow relaxation processes. *Dalton Trans.* **2015**, *44*, 12484-12487.

53. Beck, J. B.; Rowan, S. J. Multistimuli, MultiresponsiveMetallo-Supramolecular Polymers. *J. Am. Chem. Soc.* **2003**, *125*, 13922-13923. (c) Uchiyama, S., Prasanna de Silva, A.; Iwai, K. Luminescent Molecular Thermometers. *J. Chem. Educ.* **2006**, *83*, 720-727.

54. (a) Zheng, Q.; Yang, F.; Deng, M.; Ling, Y. Liu, X.; Chen Z.; Wang, Y.; Weng, L.; Zhou, Y. A porous metal-organic framework constructed from carboxylate-pyrazolate shared heptanuclear zinc clusters: synthesis, gas adsorption, and guest-dependent luminescent properties. *Inorg. Chem.* **2013**, *52*, 10368-10374. (b) Ren, H.-Y.; Han, C.-Y.; Qu, M.; Zhang, X.-M. Luminescent group 12 metal tetracarboxylate networks as probe for metal ions. *RSC Adv.* **2014**, *4*, 49090-49097.

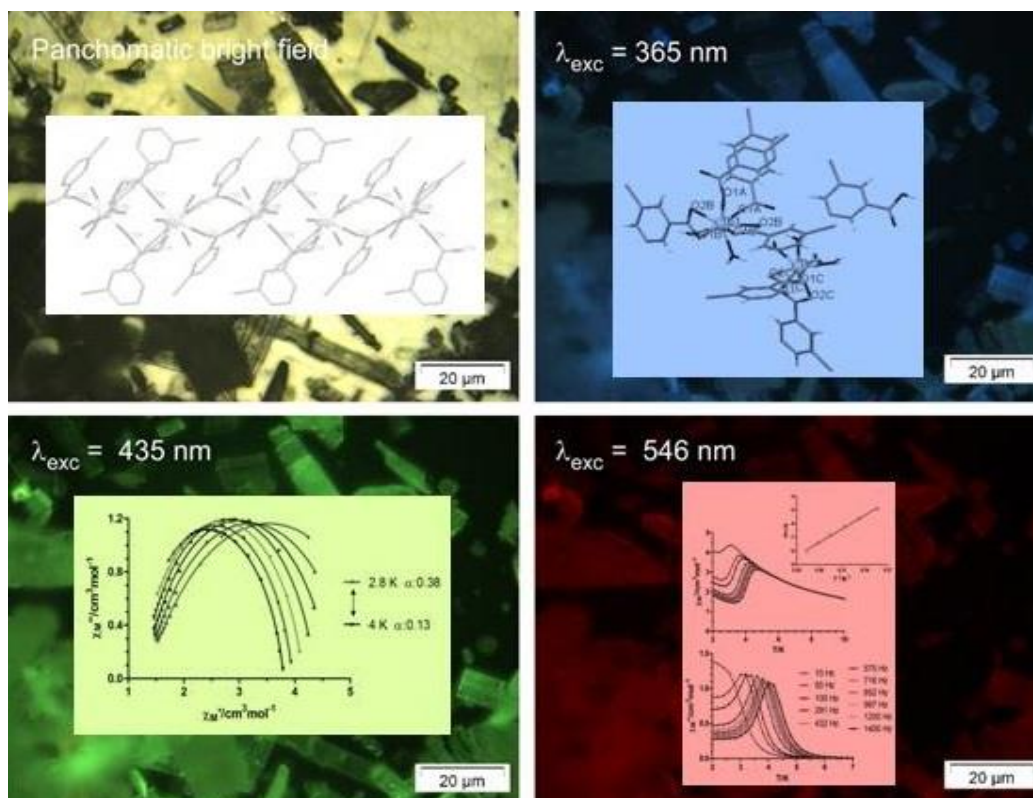
55. (a) Eliseeva, S. V.; Pleshkov, D. N.; Lyssenko, K. A.; Lepnev, L. S.; Bünzli, J. C.; Kuzmina, N. P. Highly luminescent and triboluminescent coordination polymers assembled from lanthanide β -diketonates and aromatic bidentate O-donor ligands. *Inorg. Chem.* **2010**, *49*, 9300-9311. (b) de Bettencourt-Dias, A.; Barber, P. S.; Viswanathan, S.; de Lill, D. T.; Rollett, A.; Ling, G.; Altun, S. Paraderivatizedpybox ligands as sensitizers in highly luminescent Ln(III) complexes. *Inorg. Chem.* **2010**, *49*, 8848-8861. (c) Beeby, A.; Clarkson, I. M.; Dickins, R. S.; Faulkner, S.; Parker, D.; Royle, L.; de Sousa, A. S.; Gareth Williams, J. A.; Woods, M. Non-radiative deactivation of the excited states of europium, terbium and ytterbium complexes by proximate energy-matched OH, NH and CH oscillators: an improved luminescence method for establishing solution hydration states. *J. Chem. Soc., Perkin Trans* **1999**, *2*, 493-503.

56. Kasha, M. Characterization of electronic transitions in complex molecules. *Discuss. Faraday Soc.* **1950**, *9*, 14-19.

57. Adamo, C.; Jacquemin, D. The calculations of excited-state properties with Time-Dependent Density Functional Theory. *Chem. Soc. Rev.* **2013**, 42, 845-856.

Capítulo 2

Multifunctional Coordination Compounds Based on Lanthanide Ions and 5-Bromonicotinic Acid. Magnetic, Luminescence and Anti-Cancer Properties

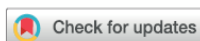


Multifunctional Coordination Compounds Based on Lanthanide Ions and 5-Bromonicotinic Acid. Magnetic, Luminescence and Anti-Cancer Properties

CrystEngComm



PAPER

View Article Online
View Journal | View IssueCite this: *CrystEngComm*, 2019, 21, 3881

Multifunctional coordination compounds based on lanthanide ions and 5-bromonicotinic acid: magnetic, luminescence and anti-cancer properties†

Cristina Ruiz,^a Antonio A. García-Valdivia,^{ID}^a Belén Fernández,^b Javier Cepeda,^{ID}^c Itziar Oyarzabal,^{ID}^{c,g} Elisa Abas,^d Mariano Laguna,^d Jose Angel García,^e Ignacio Fernández,^{ID}^f Eider San Sebastian ^{ID}^{*c} and Antonio Rodríguez-Diéguez ^{ID}^{**a}

Abstract

We report the formation of four novel multifunctional coordination compounds based on 5-bromonicotinic acid and different lanthanide(III) ions (Dy, Tb, Yb and Nd), synthesized by simple hydrothermal routes. These materials possess different structures and dimensionalities and show interesting magnetic and luminescent properties, as well as a complete absence of cytotoxicity both in cancer and non-cancer Caco-2 cells, transforming these new compounds in excellent candidates to be further investigated in the field of luminescence materials with biomedical applications.

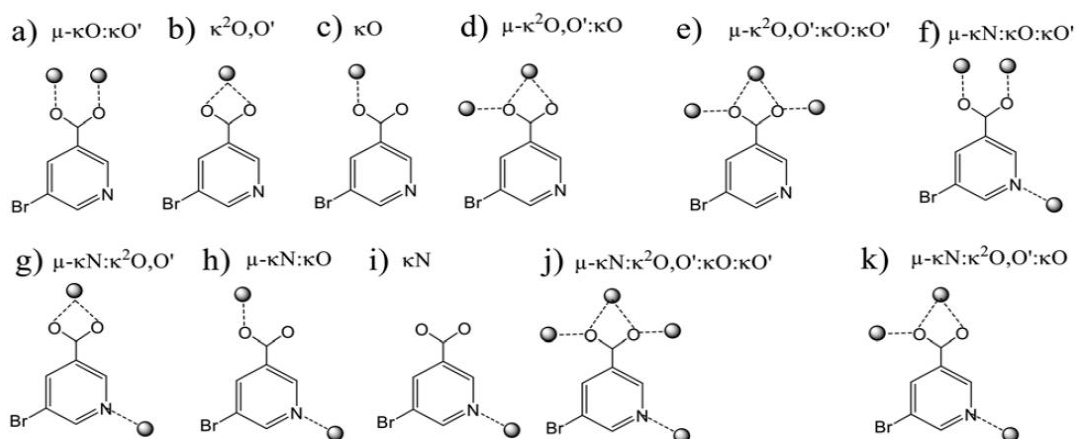
1. Introduction

The interest in coordination polymers (CPs), also known as metal-organic frameworks (MOFs), has undergone an exponential growth,¹ derived from their multiple types of verified industrial applications, such as gas storage and purification,

catalysis, luminescence and magnetism,² as well as their ease of synthesis. Of particular interest is the fact that their metal–organic hybrid nature offers potentially limitless arrangement types and topological architectures,³ reinforcing their versatility of use. The latter is particularly true for Ln(III)-based CPs, where, large coordination numbers (8-12) are usually observed for the central cation, yielding fanciful structures that, conversely, are hardly anticipated via a rational design process. Still, the adequacy of the election of Ln(III) ions for the generation of multifunctional CPs in the field of new magnetic and/or luminescent materials is well supported by their intrinsic features such as a large intrinsic magnetic anisotropy and large magnetic moment in the ground state (key to generate molecular magnets). On the other hand, due to the open-shield character of the trivalent lanthanide ions as well as the efficient shielding of their valence f-orbitals, all lanthanide ions (but La³⁺ and Lu³⁺) emit highly pure-colored light, with long-lived emissions and large quantum yield values,⁴ from the ultraviolet (UV) to the visible region (Eu³⁺, Tb³⁺, Sm³⁺ and Tm³⁺) as well as in the near infra-red (NIR) region (Yb³⁺, Nd³⁺ and Er³⁺).⁵ Unfortunately, the forbidden character of the f–f transitions in lanthanide ions prevents the latter from being able to efficiently absorb light. The solution to the latter issue lays on the use of organic linkers that promote the well-known antenna effect,⁶ where light absorbed by the ligand is efficiently transferred to the outermost orbitals in the metal, increasing the efficiency of the light emitted by the latter.

The attention in the present study was focused on the synthesis, structural and functional characterization of Ln(III) based coordination complexes and CPs using the 5-bromonicotinic acid (5-HBrNic) as linker ligand. With one carboxyl group and one N atom as potential metal coordination groups, 5-HBrNic possesses, in addition, a Br atom capable of potentially establishing N···Br or O···Br halogen bonds, as well as additional Br··· π and Br···Br interactions. Few examples have been reported where 5-HBrNic coordinates to a Ln(III) ion to generate coordination complexes or CPs. Still, this ligand has shown its potential to form metalorganic compounds of different dimensionality with luminescent, magnetic and absorptive properties.⁷ In addition, 5-bromonicotinate (5-BrNic) possesses a wide variety of coordination modes to metal cations (Scheme 1), yielding multiple types of molecular architectures. We hereby report the synthesis as well as structural and functional characterization of four novel Ln(III)- and 5-BrNic-based coordination compounds of different dimensionalities,

with dual magnetic and luminescent properties. Additionally, the antitumor activity of this family of compounds has been tested with the aim of characterizing their cytotoxic behavior in potential biomedical applications.



Scheme 1. Plausible coordination modes of 5-BrNic.

2. Experimental

2.1. Materials and physical measurements

All reagents were obtained from commercial sources and used as received. Elemental (C, H, and N) analyses were performed on a Leco CHNS-932 microanalyzer. IR spectra of powdered samples were recorded in the 400–4000 cm^{-1} region on a Nicolet 6700 FTIR spectrophotometer using KBr pellets. Alternating current magnetic measurements were performed under zero and 1000 Oe applied static fields on a Quantum Design SQUID MPMS XL-5 device by using an oscillating *ac* field of 3.5 G and *ac* frequencies ranging from 10 to 1400 Hz. A Varian Cary-Eclipse Fluorescence spectrofluorimeter was used to obtain the fluorescence spectra at room temperature. The spectrofluorimeter is equipped with a xenon discharge lamp (peak power equivalent to 75 kW), Czerny-Turner monochromators, R-928 photomultiplier tube which is red sensitive (even 900 nm) with manual or automatic voltage. The photomultiplier detector voltage was 600 V

and the instrument excitation and emission slits were set at 5 nm. A closed cycle helium cryostat enclosed in an Edinburgh Instruments FLS920 spectrometer was employed for steady state photoluminescence (PL) and lifetime measurements carried out at 10 K. All samples were set under high vacuum (of *ca.* 10^{-7} mbar) to avoid the presence of oxygen or water in the sample holder. Steady-state spectra were measured with a IK3552R-G He-Cd continuous laser (325 nm) as excitation source, whereas a microsecond pulsed lamp was employed for recording the lifetime measurements. Photographs of irradiated single-crystal and polycrystalline samples were taken at room temperature in a micro-PL system included in an Olympus optical microscope illuminated with a Hg lamp.

2.2. Preparation of complexes

Synthesis of [Dy(5-BrNic)₃(H₂O)₄] (1). Compound **1** was obtained by hydrothermal routes through the following procedure: a mixture of DyCl₃·6H₂O (0.24 mmol), 5-HBrNic (0.24 mmol) and 10 mL of distilled water was sealed in a Teflon reactor and heated at 95°C under autogenous pressure for 48h. The reaction vessel was then slowly cooled down to room temperature during a period of about 3h, yielding yellow crystals of **1**. Yield: 47%, based on Dy. Anal. Calcd. for C₁₈H₁₇Br₃DyN₃O₁₀: C 25.81, H 2.04, N 5.01. Found: C 25.63, H 2.19, N 4.83.

Synthesis of [Tb(5-BrNic)₂(H₂O)₄][Tb(5-BrNic)₄(H₂O)₂](5-HBrNic)₂ (2). Yellow crystals of compound **2** were obtained following a procedure similar to that used in the synthesis of **1**, with the following modifications: The reactor was left in the oven for 96h and crystals only appeared 24h after of cooling down the sample slowly. Yield: 51%, based on Tb. Anal. Calcd. for C₂₄H₁₉Br₄N₄O₁₁Tb: C 28.32, H 1.88, N 5.50. Found: C 29.01, H 1.92, N 5.66.

Synthesis of [Yb(5-BrNic)₂(H₂O)₄][Yb(5-BrNic)₄(H₂O)₂](5-HBrNic)₂ (3). Colorless crystals of **3** were obtained following the same procedure as the one used

for the synthesis of **2**. Yield: 57%, based on Yb. Anal. Calcd. for $C_{24}H_{19}Br_4N_4O_{11}Yb$: C 27.93, H 1.86, N 5.43. Found: C 28.75, H 1.85, N 5.99.

*Synthesis of $\{[Nd(5-BrNic)_3(H_2O)_3] \cdot H_2O\}_n$ (**4**).* Pink crystals of **4** were obtained following the same procedure as the one used for the synthesis of **2**. Yield: 47%, based on Nd. Anal. Calcd. for: $C_{18}H_{17}Br_3NdN_3O_{10}$: C 26.39, H 2.09, N 5.13. Found: C 28.01, H 2.12, N 5.61.

2.3. Crystallographic refinement and structure solution

X-ray data collection of suitable single crystals of compounds were done at 100(2) K on a Bruker VENTURE area detector equipped with graphite monochromated Mo-K α radiation ($\lambda = 0.71073 \text{ \AA}$) by applying the ω -scan method. The data reduction were performed with the APEX2 software⁸ and corrected for absorption using SADABS.⁹ Crystal structures were solved by direct methods using the SIR97 program¹⁰ and refined by full-matrix least-squares on F^2 including all reflections using anisotropic displacement parameters by means of the WINGX crystallographic package.¹¹ Compound **4** contains one lattice water molecule which presents a significantly prolate shaped ellipsoid so it has been disordered into two equivalent positions (each with a 50% of occupancy). All hydrogen atoms were included as fixed contributions riding on attached atoms with isotropic thermal displacement parameters 1.2 times or 1.5 times those of their parent atoms for the organic ligands. Details of the structure determination and refinement of compounds are summarized in Table 1.

Table 1. Crystallographic data and refinement details of compounds **1-4**.

Compound	1	2	3	4
Chem. form.	C ₁₈ H ₁₇ Br ₃ DyN ₃ O ₁₀	C ₂₄ H ₁₉ Br ₄ N ₄ O ₁₁ Tb	C ₂₄ H ₁₉ Br ₄ N ₄ O ₁₁ Yb	C ₁₈ H ₁₇ Br ₃ N ₃ NdO ₁₀
CCDC	1882984	1882985	1882986	1882987
Form. weight	837.57	1017.99	1032.11	819.31
Cryst. system	Triclinic	Monoclinic	Monoclinic	Triclinic
Space group	<i>P</i> -1	<i>P</i> 2/ <i>c</i>	<i>P</i> 2/ <i>c</i>	<i>P</i> -1
<i>a</i> (Å)	7.4580(4)	11.686(5)	11.686(5)	10.1630(5)
<i>b</i> (Å)	10.6630(6)	15.970(5)	15.970(5)	11.5260(6)
<i>c</i> (Å)	15.6770(7)	16.742(5)	16.742(4)	11.6110(6)
α (°)	82.162(2)	90.000(5)	90.000(5)	88.319(2)
β (°)	87.933(2)	90.246(5)	90.246(5)	85.525(2)
γ (°)	72.310(2)	90.000(5)	90.000(5)	69.254(2)
<i>V</i> (Å ³)	1176.64(11)	3124.45(19)	3132.45(21)	1268.03(11)
<i>Z</i>	2	4	4	2
GoF ^a	1.024	1.030	1.023	1.017
R _{int}	0.0787	0.1106	0.1487	0.0721
R ₁ ^b / wR ₂ ^c [I > 2σ(I)]	0.0275	0.0355	0.0558	0.0278
R ₁ ^b / wR ₂ ^c (all data)	0.0446	0.0613	0.1166	0.0431

$$[a] S = [\sum w(F_0^2 - F_c^2)^2 / (N_{\text{obs}} - N_{\text{param}})]^{1/2}$$

$$[b] R_1 = \sum ||F_0| - |F_c|| / \sum |F_0| \quad [c] wR_2 = [\sum w(F_0^2 - F_c^2)^2 / \sum wF_0^2]^{1/2}$$

$$w = 1/[\sigma^2(F_0^2) + (aP)^2 + bP] \quad \text{where } P = (\max(F_0^2, 0) + 2F_c^2)/3$$

2.4. Growth Inhibition Assay

Human Caco-2 cell line (TC7 clon) were kindly provided by Dr. Edith Brot-Laroche (Université Pierre et Marie Curie-Paris 6, UMR S 872, Les Cordeliers, France). Caco-2 cells were maintained in a humidified atmosphere of 5% CO₂ and 95% of air at 37°C. Cells (passages 32–42) were grown in Dulbecco's modified Eagle's medium (DMEM; Gibco Invitrogen, Paisley, U.K.) with high glucose concentration (4.5 g/L) supplemented with 20% fetal bovine serum (FBS) previously decomplexed (30 min at 56°C), 1% non-essential aminoacids, 1% penicillin (1000 U·mL⁻¹), 1% streptomycin (1000 µg·mL⁻¹), and 2% L-glutamine (200 mM). Stock solutions of the complexes in DMSO were diluted in a medium without FBS to the required concentration. DMSO was also tested at the same concentrations and no effects on the cytotoxicity were shown. Cells were seeded in 96-well plates at a

density of 20×10^3 cells well⁻¹. Experiments were performed 48h postseeding and the culture medium was replaced with the fresh medium (without FBS) containing the complexes at concentrations varying from 0 to 20 μM , with an exposure time of 72h.

For cell viability studies of differentiated (enterocyte-like) cells, Caco-2/TC7 cells were seeded in 96-well plates at a density of 4×10^3 cells well⁻¹ and incubated for 12 days, with the culture medium changed every 3 days, up to confluence, the cells were treated with the complexes and at the same concentrations explained before. Thereafter, cell survival was measured using the 3-(4,5-dimethyl-2-thiazoyl)-2,5-diphenyltetrazolium bromide (MTT, Merck) test as previously described. The assay is dependent on the cellular reduction of MTT by the mitochondrial dehydrogenase of viable cells to a blue formazan product, which can be measured spectrophotometrically. Following appropriate incubation of the cells, with or without metallic complexes, MTT was added to each well in an amount equal to 10% of the culture volume, and incubation was continued at 37°C for 2.5h. Afterwards, the medium and MTT were removed, and DMSO was added to each well. At the end, the results were obtained by measuring the absorbance with a scanning multiwell spectrophotometer (BIOTEX SINERGY HT SIAFRTD) at a wavelength of 575 nm and compared to the values of control cells incubated in the absence of complexes. Experiments were conducted in quadruplicate wells and repeated for three times.

3. Results and Discussion

3.1. Description of the structures

Compound **1**, of general formula $[\text{Dy}(\text{5-BrNic})_3(\text{H}_2\text{O})_4]$, crystallizes in the *P*-1 space group. As observed in Figure 1, the lanthanide ion coordinates to three 5-BrNic ligands, one of which establishes a chelating ring (O1C/O2C, coordination mode b in Scheme 1) whereas the remaining two bind in a monodentate mode (O1A and O1B, coordination mode c in Scheme 1). Besides, four water molecules complete the octacoordinated (DyO_8) sphere of the Dy ion, which displays a triangular

dodecahedral shape. Dy-O distances in the mononuclear compound fall within the range of 2.280(2)-2.515(2) Å.

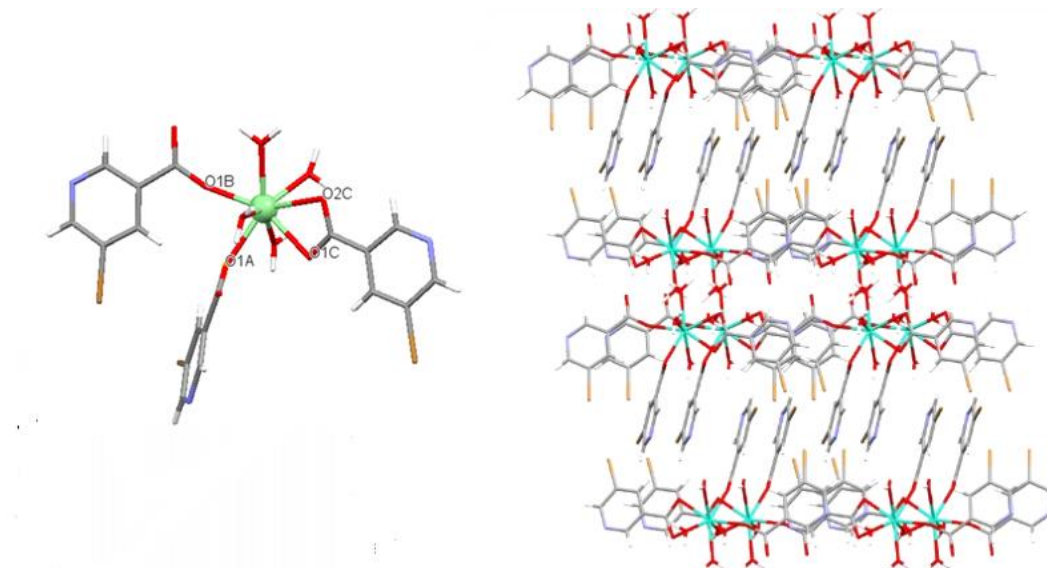


Figure 1. *Left: Structure of the monomeric entity of compound 1. Right: Perspective view of the packing of compound 1 along a^* axis. Color code: Dysprosium, green; oxygen, red; nitrogen, blue; carbon, grey; bromine, brown; hydrogen, white.*

Coordination water molecules are involved in a complex hydrogen-bond network in which non-bonding carboxylate oxygen and pyridine nitrogen atoms act as acceptors to sequentially bring the monomers along the a axis. In the same line, π - π stacking interactions established between the aromatic pyridine rings of adjacent monomers along the b axis, further stabilize the packing of **1** (Figure 1).

Compounds **2** and **3**, of general formula $[\text{Ln}(5\text{-BrNic})_2(\text{H}_2\text{O})_4] \cdot [\text{Ln}(5\text{-BrNic})_4(\text{H}_2\text{O})_2] \cdot (5\text{-HBrNic})_2$, where Ln stands for Tb or Yb in **2** and **3**, respectively, are isostructural and crystallize in the monoclinic $P2_1/c$ space group (Table 1). The description of compound **2** found in the lines below will therefore be equivalent to that of **3** (omitted).

The unit cell of **2** contains four distinct entities (Figure 2), consisting of a monomeric complex with a Tb(III) cation (Tb1) coordinated to four 5-BrNic ligand units and two water molecules, a second monomeric complex with a Tb(III) cation (Tb2) coordinated to two 5-BrNic ligand units and four water molecules and, lastly,

two protonated crystallization 5-HBrNic ligand molecules. Both Tb1 and Tb2 units show a TbO₈ distorted polyhedra resembling less habitual Snub diphenooid and square antiprism, respectively, derived from the coordination of i) two perpendicular 5-BrNic ligands bound to Tb1 in a bidentate fashion, two copies of a monodentated ligand parallel to each other along the *b* axis, and two water molecules in the case of the Tb1 unit, and ii) four water molecules and two bidentated copies of the ligand in the Tb2 unit.

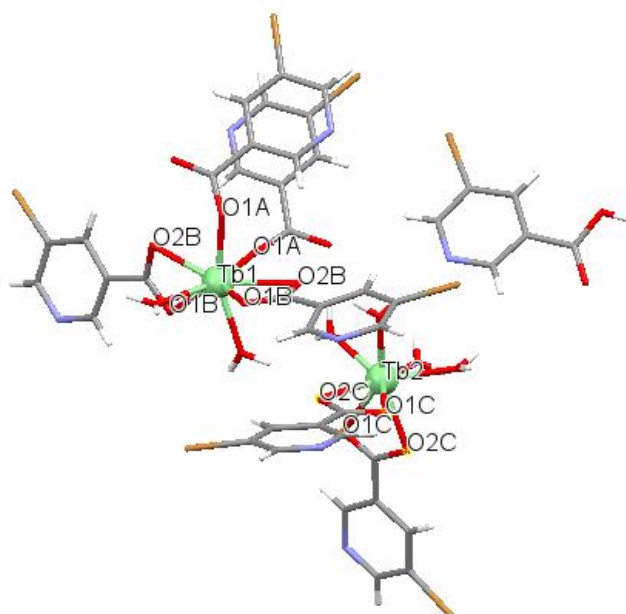


Figure 2. Asymmetric unit of compound **2**. Color code: Terbium, green; oxygen, red; nitrogen, blue; carbon, grey; bromine, brown; hydrogen, white.

The remaining two units consist of protonated 5-HBrNic crystallization ligands. It is worth noticing that the two monodentate 5-BrNic establish quite strong π - π stacking interactions, a fact that sets their orientation outwards the monomeric entity. The packing of the structure reveals a unit cell containing two [Tb(5-BrNic)₄(H₂O)₂]⁻ (**Tb1**) units, two [Tb(5-BrNic)₂(H₂O)₄]⁺ (**Tb2**) units and four copies of a 5-HBrNic crystallization ligand. Notwithstanding the fact that monomeric complexes are hydrogen bonded with each other along the packing, the crystallization 5-HBrNic molecule serves as an effective supramolecular glue by acting as both hydrogen-bonding donor and acceptor as well as an intermediate to extend π - π stacking all along the crystal. The same type of description applies to compound **3**, except that Ln(III)-O distances in **2** are larger than in **3** (Table 2), which

is consistent with the larger nuclear charge of the former. Additional details on the packing of compounds **2** and **3** can be found on Figure 3.

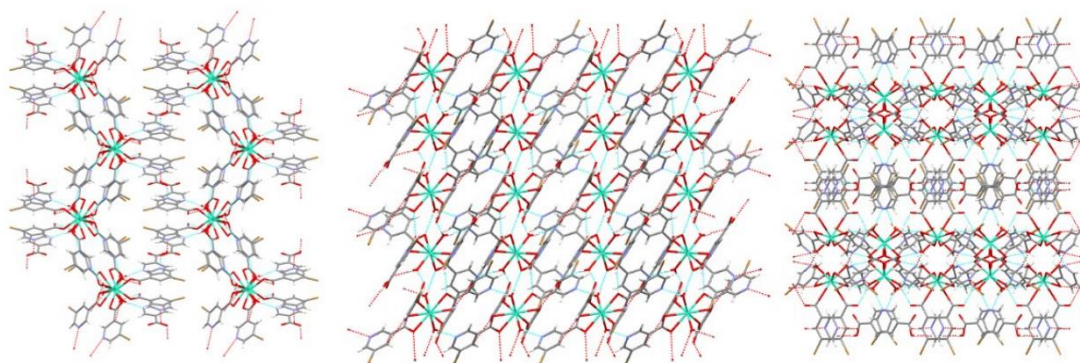


Figure 3. Perspective views of compound **2** and **3** along *a* (left), *b* (centre) and *c* (right) axes.

Table 2. Selected bond distances (Å) in compounds **1-4**.

	1	2	3	4			
Dy(1)-O(1)	2.280 (2)	Tb(1)-O(1)	2.517(3)	Yb(1)-O(1)	2.494(4)	Nd(1)-O(1)	2.386(2)
Dy(1)-O(2)	2.334 (2)	Tb(1)-O(2)	2.456(3)	Yb(1)-O(2)	2.411(4)	Nd(1)-O(4)	2.507(3)
Dy(1)-O(3)	2.515 (2)	Tb(1)-O(3)	2.456(3)	Yb(1)-O(3)	2.411(4)	Nd(1)-O(6)	2.407(2)
Dy(1)-O(4)	2.373 (2)	Tb(1)-O(4)	2.517(3)	Yb(1)-O(4)	2.494(4)	Nd(1)-O(7)	2.445(2)
Dy(1)-O(5)	2.328 (2)	Tb(1)-O(5)	2.274(3)	Yb(1)-O(5)	2.222(4)	Nd(1)-O(8)	2.476(3)
Dy(1)-O(6)	2.381 (3)	Tb(1)-O(6)	2.274(3)	Yb(1)-O(6)	2.222(4)	Nd(1)-O(9)	2.518(2)
Dy(1)-O(7)	2.364 (3)	Tb(1)-O(7)	2.317(3)	Yb(1)-O(7)	2.267(5)		
Dy(1)-O(8)	2.401 (3)	Tb(1)-O(8)	2.317(3)	Yb(1)-O(8)	2.267(5)		
		Tb(2)-O(9)	2.382(3)	Yb(2)-O(9)	2.340(5)		
		Tb(2)-O10	2.518(3)	Yb(2)-O10	2.463(5)		
		Tb(2)-O11	2.518(3)	Yb(2)-O11	2.463(5)		
		Tb(2)-O12	2.382(3)	Yb(2)-O12	2.340(5)		
		Tb(2)-O13	2.334(3)	Yb(2)-O13	2.290(5)		
		Tb(2)-O14	2.288(3)	Yb(2)-O14	2.245(4)		
		Tb(2)-O15	2.288(3)	Yb(2)-O15	2.290(5)		
		Tb(2)-O16	2.334(3)	Yb(2)-O16	2.245(4)		

Compound **4** is nearly isostructural to the Tb compound reported by Song et al.^{7a} Our compound, of general formula $\{[\text{Nd}(\mu\text{-5-BrNic})_2(5\text{-BrNic})(\text{H}_2\text{O})_3]\cdot\text{H}_2\text{O}\}_n$, crystallizes in the $P\bar{1}$ space group (Table 1), and consists of a racemic mixture of linear chains of Nd(III) atoms bridged by means of two 5-BrNic ligands along the crystallographic a axis. Lanthanide ions show a NdO_8 environment where an almost ideal triangular dodecahedron is generated (Figure 4) when five 5-BrNic ligands bind to the lanthanide through a deprotonated carboxylic oxygen each (O1A, O2A, O2B, O1C and O2C). The metal ion completes its coordination sphere with three water molecules (O1W, O2W and O3W), the last of which plays a key role in the generation of the H-bond network in the crystal, and particularly with a crystallization water molecule found in the structure (which is disordered into two equivalent dispositions). All Nd-O distances are in the 2.386(2)-2.518(2) Å range (Table 2).

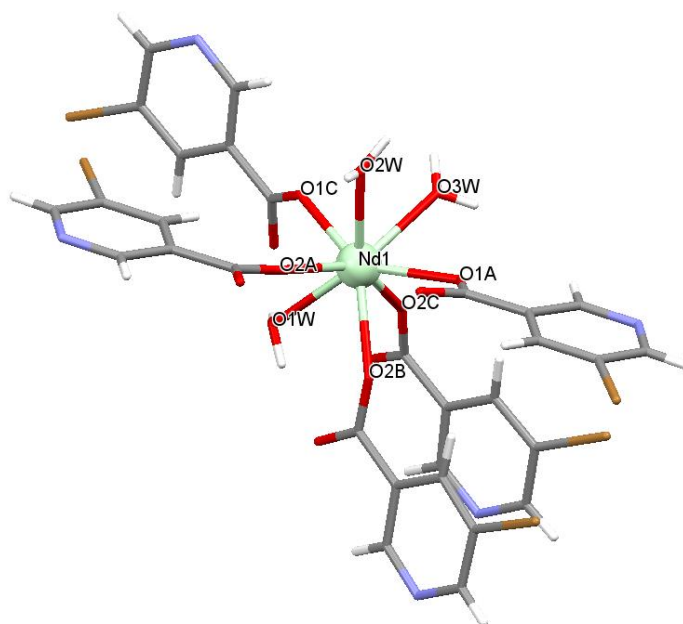


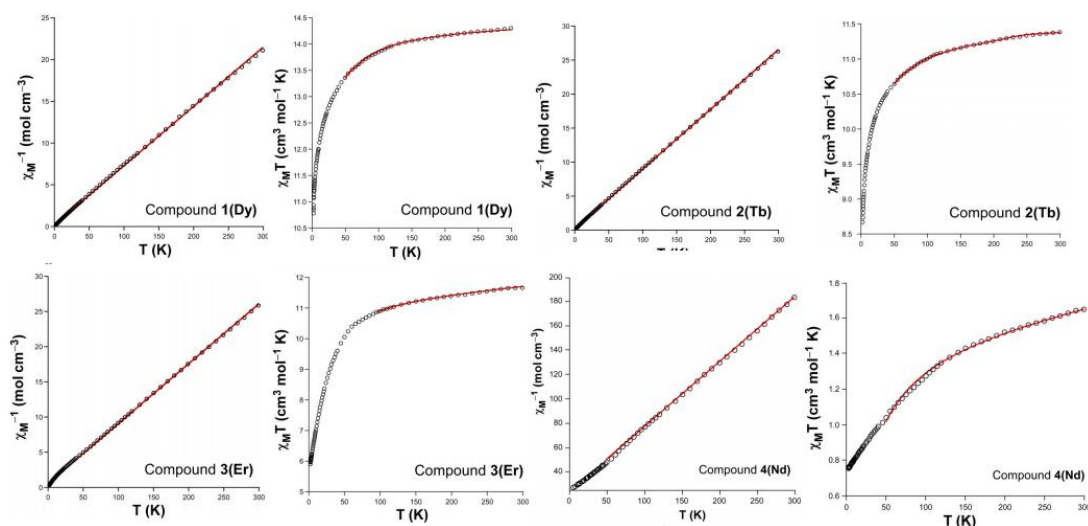
Figure 4. Fragment of **4** showing complete ligands around the coordination sphere of Nd1 atom. Color code: Neodymium, green; oxygen, red; nitrogen, blue; carbon, grey; bromine, brown; hydrogen, white.

1D chains of **4** are generated along a axis via the sequential coordination of A and C copies of 5-BrNic ligands to Nd1 atoms (Figure 5), where carboxylate oxygen atoms link nearby neodymium(III) cations one another adopting one of the

Table 3. Comparison between best least-squares fitting results of experimental curves and theoretically calculates magnetic data.

Comp.	g_J (exp./theor.) ^[a]	$\chi_M T$ (exp./theor.) ^[b]	Δ (cm ⁻¹)
1(Dy)	1.32(1) / 1.33	14.32 / 14.17	0.34
2(Tb)	1.49(1) / 1.5	11.38 / 11.76	0.10
3(Er)	1.22(1) / 1.2	11.57 / 11.53	0.48
4(Nd)	0.70(1) / 0.73	1.61 / 1.67	2.31

Cooling down the temperature causes a progressive drop in the $\chi_M T$, as expected for the selective depopulation of the excited Stark sublevels (Figure 6).

**Figure 6.** χ_M^{-1} vs T and $\chi_M T$ vs T plots of compounds 1-4 showing best theoretical fitting (red line).

However, this magnetic response could also involve a significant contribution from antiferromagnetic exchange interactions between lanthanide ions, especially for compounds in which there are short ligand mediated pathways,¹³ as it is the case of carboxylate bridges in **4**. The χ_M^{-1} vs. T curves for these compounds follow the Curie–Weiss law almost in the whole temperature range, finding only small deviations for **3** below 30 K (Figure 6). As far as we are aware, there is no available expression to determine the magnetic susceptibilities of 3D systems with large anisotropy, so $\chi_M T$ vs. T curves were fitted in the high temperature range (50–300 K)

with expressions (Equations 1–4) that assume only a splitting of the m_j energy levels ($H = \Delta Jz^2$) in an axial crystal field.¹⁴

$$\chi_{Dy} = \frac{Ng^2\beta^2}{kT} \left(\frac{0.5e^{-0.25\Delta/kT} + 4.5e^{-2.25\Delta/kT} + 12.5e^{-6.25\Delta/kT} + 24.5e^{-12.25\Delta/kT}}{1 + 2e^{-\Delta/kT} + 2e^{-2\Delta/kT} + 2e^{-9\Delta/kT} + 2e^{-16\Delta/kT} + 2e^{-25\Delta/kT} + 2e^{-36\Delta/kT}} + \frac{40.5e^{-20.25\Delta/kT} + 60.5e^{-30.25\Delta/kT} + 84.5e^{-42.25\Delta/kT} + 112.5e^{-56.25\Delta/kT}}{1 + 2e^{-\Delta/kT} + 2e^{-2\Delta/kT} + 2e^{-9\Delta/kT} + 2e^{-16\Delta/kT} + 2e^{-25\Delta/kT} + 2e^{-36\Delta/kT}} \right)$$

(Eq. 1)

$$\chi_{Tb} = \frac{Ng^2\beta^2}{kT} \frac{2e^{-\Delta/kT} + 4e^{-2\Delta/kT} + 18e^{-9\Delta/kT} + 32e^{-16\Delta/kT} + 50e^{-25\Delta/kT} + 72e^{-36\Delta/kT}}{1 + 2e^{-\Delta/kT} + 2e^{-2\Delta/kT} + 2e^{-9\Delta/kT} + 2e^{-16\Delta/kT} + 2e^{-25\Delta/kT} + 2e^{-36\Delta/kT}}$$

(Eq. 2)

$$\chi_{Er} = \frac{Ng^2\beta^2}{kT} \left(\frac{0.5e^{-0.25\Delta/kT} + 4.5e^{-2.25\Delta/kT} + 12.5e^{-6.25\Delta/kT} + 24.5e^{-12.25\Delta/kT}}{1 + 2e^{-\Delta/kT} + 2e^{-2\Delta/kT} + 2e^{-9\Delta/kT} + 2e^{-16\Delta/kT} + 2e^{-25\Delta/kT} + 2e^{-36\Delta/kT}} + \frac{40.5e^{-20.25\Delta/kT} + 60.5e^{-30.25\Delta/kT} + 84.5e^{-42.25\Delta/kT} + 112.5e^{-56.25\Delta/kT}}{1 + 2e^{-\Delta/kT} + 2e^{-2\Delta/kT} + 2e^{-9\Delta/kT} + 2e^{-16\Delta/kT} + 2e^{-25\Delta/kT} + 2e^{-36\Delta/kT}} \right)$$

(Eq. 3)

$$\chi_{Nd} = \frac{Ng^2\beta^2}{4kT} \frac{81e^{-81\Delta/4kT} + 49e^{-49\Delta/4kT} + 25e^{-25\Delta/4kT} + 9e^{-9\Delta/4kT} + e^{-9\Delta/4kT}}{e^{-81\Delta/4kT} + e^{-49\Delta/4kT} + e^{-25\Delta/4kT} + e^{-9\Delta/4kT} + e^{-9\Delta/4kT}}$$

(Eq. 4)

In these expressions, Δ is the zero-field splitting and the Zeeman splitting was treated isotropically for the sake of simplicity. Additionally, a zJ' parameter based on the molecular field approximation to account for the magnetic interaction between Ln(III) ions did not improve the fitting and brought almost negligible values (*ca.* -0.01 cm^{-1}), meaning that lanthanide(III) ions may be considered as magnetically isolated centers in all cases.

With the aim of getting insights on the magnetic properties of these Ln(III) complexes, dynamic alternating current magnetic measurements were carried out on **1** (Figure 7), which revealed that **1** does not show any significant frequency

dependency of the out-of-phase signals (χ_M''). This could be a consequence of either a lack of a slow relaxation of the magnetization or to the presence of quantum tunneling of the magnetization (QTM). With the aim of suppressing the possible QTM effect, measurements were repeated in the presence of an external field of 1000 Oe and, as derived from Figure 7, compound **1** showed frequency dependent signals; still since χ_M' and χ_M'' stayed above zero at low temperatures, was therefore concluded that QTM was not completely removed.

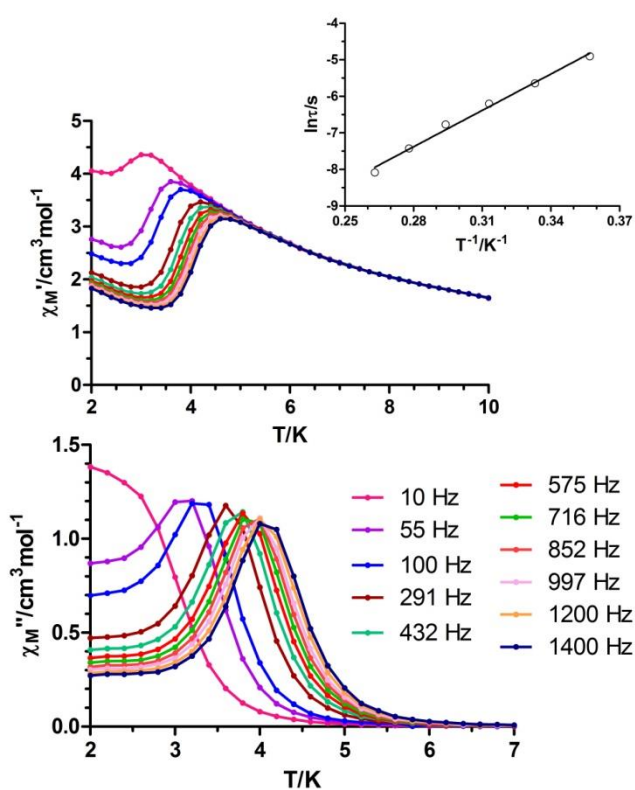


Figure 7. Temperature dependence of in-phase (top) and out-of-phase (bottom) components of the ac susceptibility of compound **1** measured under 1000 Oe dc field. Inset: Arrhenius plots for the relaxation times. The black line corresponds to the best fits to the Orbach process.

The latter is consistent with the α values derived from the Cole–Cole plots (in the range of 0.38 (2.8 K) – 0.13 (4 K)), compatible with the existence of more than one relaxation processes (Figure 8).

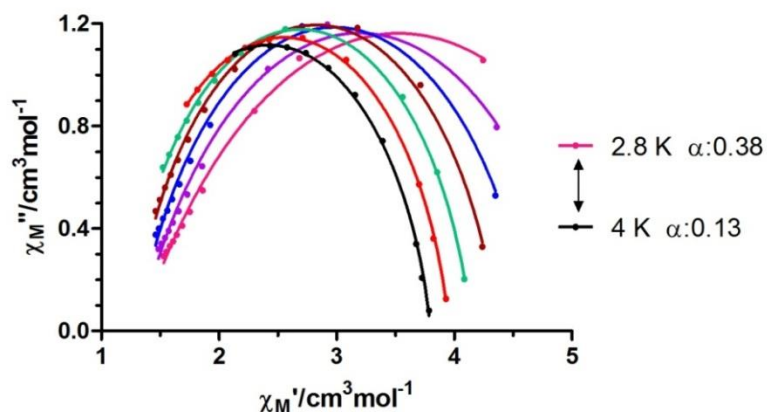


Figure 8. Cole–Cole plots for **1** under 1000 Oe dc field.

The linear portion of the relaxation times was fitted to the Arrhenius equation, obtaining an effective energy barrier of 33.1 K with $\tau_0 = 5.90 \times 10^{-8}$ s (Figure 7, inset). In general, Dy(III) ions with the highest symmetric coordination environments ($C_{\infty v}$, $D_{\infty h}$, S_8 (I_4), D_{5h} , and D_{4d} symmetries) show better Single Molecule Magnet (SMM) properties than the ones with lower symmetry, due to the reduction of QTM.¹⁵ Thus, the triangular dodecahedron coordination environment of the Dy(III) ions (D_{2d} symmetry),¹⁶ together with the hydrogen bonding interactions (known to suppress the SMM behavior), explain the modest energy barrier observed for this compound. Despite the fact that other electronic effects are known to strongly modulate the SMM behavior,¹⁷ a trend of the symmetry of the coordination environment may be inferred by analyzing the results for those selected reported complexes shown in Table 4.

Table 4. Comparison between best least-squares fitting results of experimental curves and theoretically calculates magnetic data.

Dy-SMM	Pseudo local symmetry	Ueff (K)	Ref.
[Dy(DOTA)(H ₂ O)]	C _{4v}	59	18
1	D _{2d}	38	thiswork
[Dy(FTA) ₃ (BBO)]	D _{2d}	53	19
[Dy(acac) ₃ (1,10-phen)]	D _{4d}	62	20
[DyPc ₂] ⁻	D _{4d}	40	21
[Dy(acac) ₃ (H ₂ O) ₂]	σ _h	66	22
[Dy(OPCy ₃) ₂ (H ₂ O) ₅] ³⁺	C _{5h} /D _{5h}	543	23
[Dy(BIPMTMS) ₂] ⁻	S ₄ /D _{2d}	721	24
[Dy(Cp ^{III}) ₂] ⁺	C _∞	1837	25

3.3. Photoluminescence Studies

Solid state photoluminescence measurements were performed on polycrystalline samples of compounds **1–4**, both at room temperature and 50 K, with the aim of getting a more representative characterization of the emissive performance of the materials for potential applications as light-emitting diodes and chemical sensors. In this sense, the excitation spectra of compound **1** (Figure 9) monitored around the metal's more intense emission lines ($\lambda_{em} = 484$ nm and 575 nm, respectively) revealed, among others, a wide and relatively intense maximum around 300 nm and multiple narrower signals centered around 370 nm, which can be attributed to typical $\pi \leftarrow \pi^*$ transitions inside the ligand.

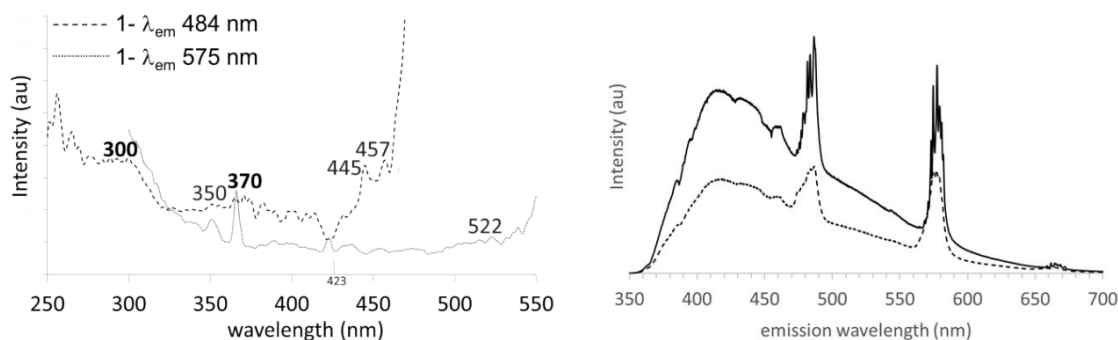


Figure 9. Left: room temperature solid state excitation spectra of **1**, monitored at $\lambda_{em} = 484$ nm (dashed line) and $\lambda_{em} = 575$ nm (solid line). The excitation spectra revealed, among others, a wide maximum around 300 nm and a narrow maximum around 370 nm, signals assigned to $\pi \leftarrow \pi^*$ transitions inside the ligand. Right: low temperature (50 K, dashed line) and room temperature (solid line) solid state emission spectra of **1** upon sample excitation at $\lambda_{ex} = 325$ nm.

The emission spectrum of **1** was then recorded at room temperature (Figure 10) using two distinct excitation wavelengths ($\lambda_{ex} = 300$ nm and 370 nm, respectively) centered at the ligand. In addition to the wide emission bands in the 360-400 nm (with a peak at 393 nm) and in the 420-460 nm regions (attributed to ligand-to-ligand electronic relaxation processes), the intense emission peaks observed at 486 and 577 nm, respectively, are clearly ascribed to $^4F_{9/2} \rightarrow ^6H_J$ transitions in the metal, confirming the existence of a significant antenna effect.²⁶

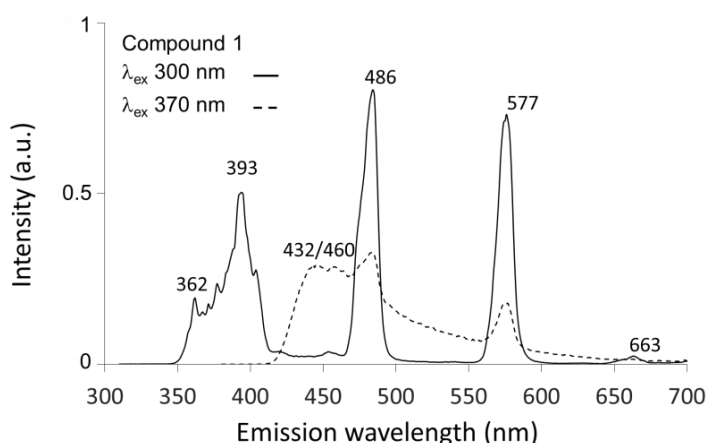


Figure 10. Room temperature solid state emission spectra of **1** upon sample excitation at $\lambda_{ex} = 300$ nm (solid line) and $\lambda_{ex} = 370$ nm (dashed line).

The emission spectra of a solid sample of **1** was also excited with a monochromatic beam of 325 nm, both at low (50 K) and room temperatures (Figure 9), showing in both cases an equivalent behavior to that observed in Figure 10. To gain further insight into the main luminescence processes described so far, the decay curves (50 K) of the mentioned main transitions were monitored at the most intense line of the main transitions, i.e., at 432 nm, 460 nm, 486 nm and 577 nm, respectively (Figure 11).

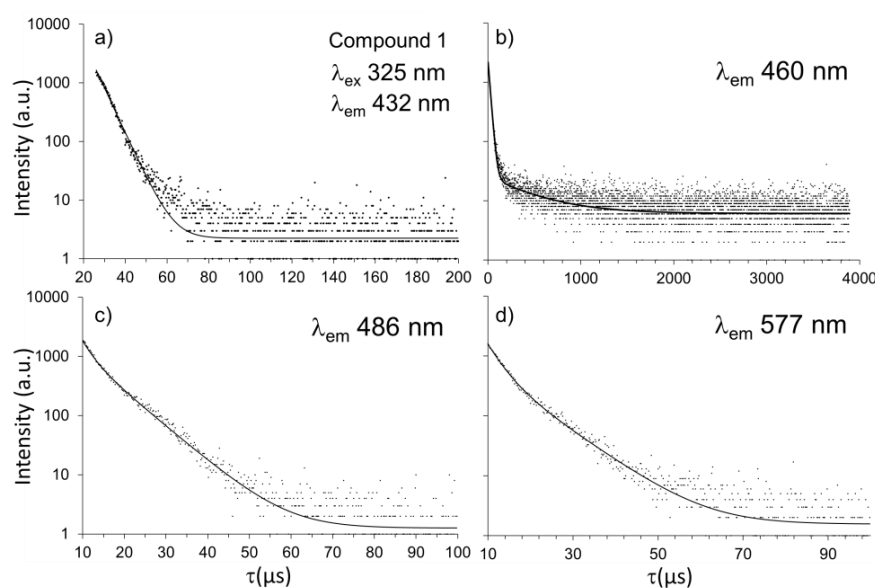


Figure 11. Luminescence decay curves for main transitions in **1** (50 K, $\lambda_{ex}=325$ nm).

The emission decay curve for the process with a maximum at $\lambda_{em}=432$ nm was well fitted by a single-exponential function [$I_t = A_0 + A_1 \cdot \exp(-t/\tau)$], τ being the luminescence lifetime, A_0 the background and A_1 the weighting parameter. As summarized in Table 5, the lifetime of the mentioned transition was in the range of a few microseconds, which indicates that the process is fluorescent in nature. On the contrary, other signals in the emission spectrum displayed a decay curve with two components and where therefore fitted to equations of the form [$I_t = A_0 + A_1 \exp(-t/\tau) + A_2 \exp(-t/\tau)$], where A_n are the two weighting parameters. Observed lifetimes (few microseconds) were equally indicative of the existence of associated fluorescent processes.

Table 5. Comparison between best least-squares fitting results of experimental curves and theoretically calculates magnetic data.

Comp	$\lambda_{\text{ex}}/\lambda_{\text{em}}$	Assign.	$\tau \text{ exp}(\mu\text{s})$
1	325/432	L-L	5.62(2)
	325/460	L-L	5.42(3)/115(4)
	325/486	$^4F_{9/2} \rightarrow ^6H_{15/2}$	2.29(3)/7.32(7)
	325/577	$^4F_{9/2} \rightarrow ^6H_{15/2}$	2.97(4)/8.7(1)
2	292/558	$^5D_4 \rightarrow ^7F_5$	938(3)

The photoluminescence properties of **2** were studied following the same procedure as in **1**. Room temperature excitation spectra of **2** were monitored around the metal's (Tb^{3+}) most intense emission lines (Figure 12, left), which revealed multiple signals in the 300–410 nm range arising from electronic transitions inside the ligand. Two emission spectra of **2** (Figure 12, right) were then recorded at room temperature and 50 K, respectively, upon exciting the ligand with $\lambda_{\text{ex}}=325$ nm. Whereas at room temperature the signals derived from electronic transitions inside the ligand (centered around 400 nm) were significantly more intense than those ascribed to metal-metal electronic transition (weak wide band centered around 550 nm), at low temperature relative intensities were inverted, which permitted a clear visualization of narrow multiplet signals derived from the well know transitions of Tb(III) (Table 5).

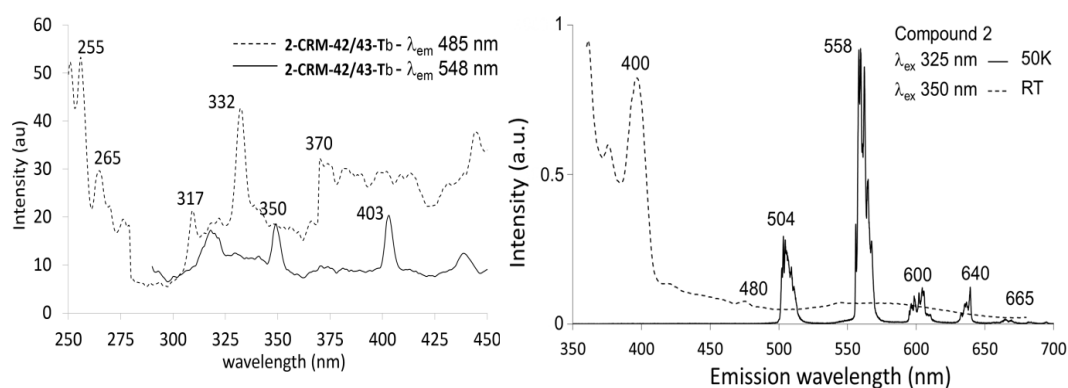


Figure 12. Left: room temperature solid state excitation spectra of **2**, monitored around the metal's (Tb^{3+}) more intense emission lines, $\lambda_{\text{em}}=485$ nm (dashed line) and $\lambda_{\text{em}}=548$ nm (solid line), assigned to $^5D_4 \rightarrow ^7F_J$ transitions. Right: room temperature (dashed line) and 50 K (solid line) solid state emission spectra of **2** upon sample excitation with a laser beam of $\lambda_{\text{ex}}=350$ nm and $\lambda_{\text{ex}}=325$ nm, respectively.

The latter results are consistent with the existence of a significant antenna effect. The most intense signal among the latter, centered around 558 nm and attributed to $^5D_4 \rightarrow ^7F_5$ transitions was characterized by the acquisition of corresponding decay curves. As observed in Figure 13 and summarized in Table 5, emission decay curve for the luminescence process characterized by a $\lambda_{em}=558$ nm was well fitted to a single-exponential function, which yielded an emission lifetime of $938(3)$ μ s.

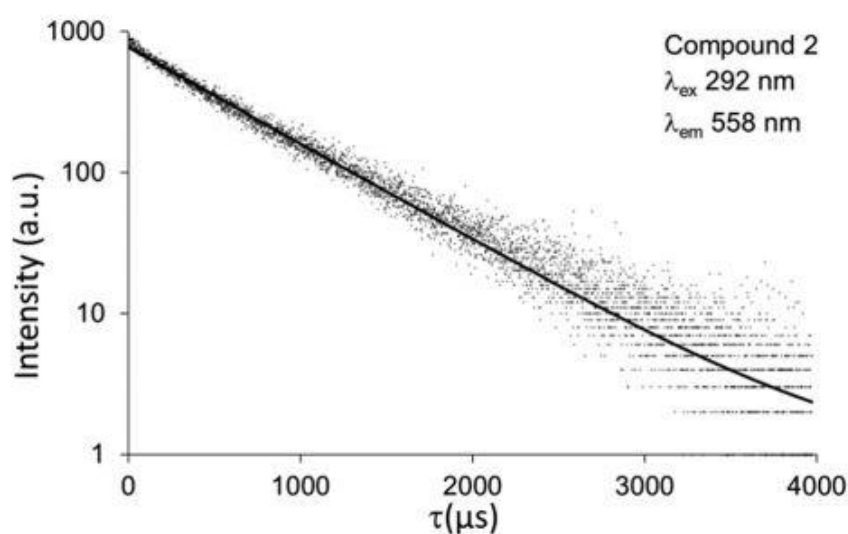


Figure 13. Luminescence decay curve for the emission of **2** centered at 558 nm, measured at 50 K ($\lambda_{ex}=292$ nm).

The latter value, in the border between classical lifetime for fluorescent and phosphorescent processes, suggests that there is an efficient phosphorescent charge transfer from the ligand-based triplet state to the 5D_4 level of the Tb^{3+} ion as a consequence of the antenna effect, which provides such a long-lived intraionic emission in **2**.

The solid-state photoluminescence spectra on a polycrystalline sample of **3** at room temperature revealed, upon sample (ligand) excitation with $\lambda_{ex}=339$ nm (dashed line in Figure 14), two intense emission bands centered around 391 and 495 nm, respectively, and multiple weaker signals (461, 534, 605 nm, for instance). Whereas the signal at 391 nm might be ascribed to electronic processes involving the

ligand only, additional signals in the spectrum might be derived from electronic relaxation processes involving the central Yb(III) metal cation. Equivalent maxima were revealed when **3** was excited with a $\lambda_{\text{ex}}=444$ nm.

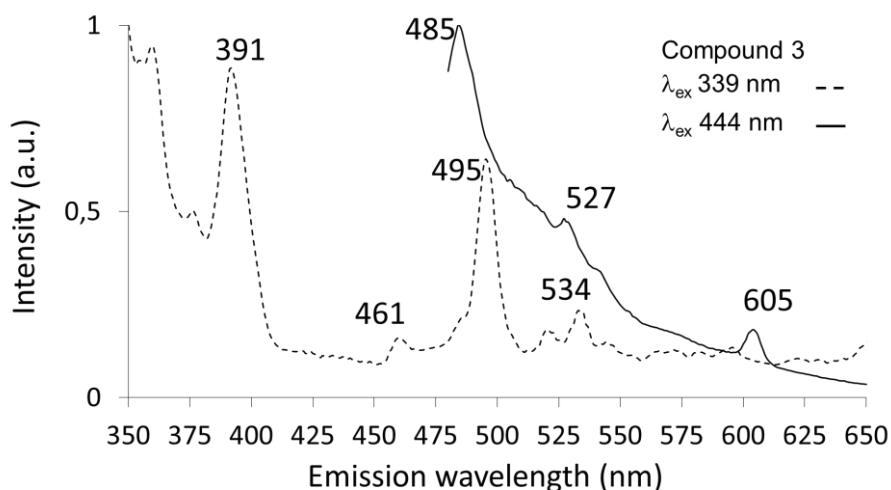


Figure 14. Room temperature solid state emission spectra of **3** upon sample excitation with a laser of $\lambda_{\text{ex}}=339$ nm (dashed line) or of $\lambda_{\text{ex}}=444$ nm (solid line).

The behavior of **4** upon excitation of a polycrystalline sample with a 325 nm laser beam at 50 K was equivalent to the one at room temperature (Figure 15), and was characterized by a wide band centered around 540 nm, attributed to $\pi\leftarrow\pi^*$ transitions inside the 5-BrNic ligands, similar to those shown by compounds **1** and **2**. Unfortunately, compounds **3** and **4** did not display emissive properties in the NIR region (data not shown).

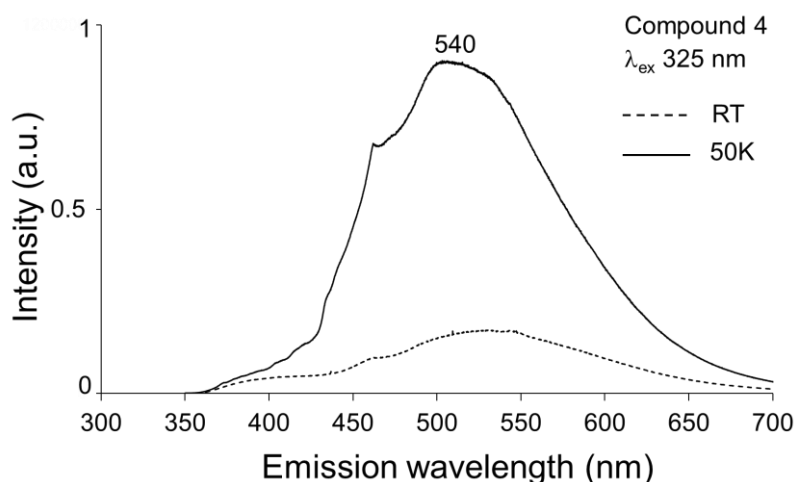


Figure 15. RT (dashed line) and 50 K (solid line) emission spectra of **4** ($\lambda_{ex}=325\text{nm}$).

The room temperature photoluminescence behavior of **1** and **2** was also studied in solution (water), which revealed that metal derived emission processes are quenched significantly by the solvent (Figure 16), as opposed to the ligand related emission bands, which were observed to be equivalent to the ones described before for the solid state emission spectra.

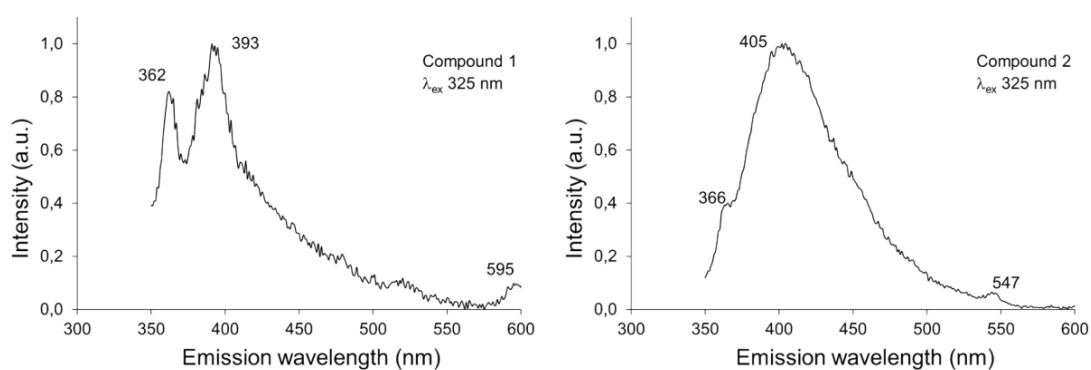


Figure 16. Room temperature emission spectra of water solutions of **1** (left) and **2** (right) ($\lambda_{ex}=325\text{ nm}$). The emission spectra revealed that luminescent processes in **1** or **2**, involving the central metal cations, are largely quenched in solution; in this respect, a weak band is observed centered at ca. 595 nm in **1** and ca. 547 nm in **2**, which are negligible compared to the ligand derived emission bands observed at shorter wavelengths.

With the aim of getting a more representative characterization of the emissive performance of the materials for potential applications as light-emitting diodes and chemical sensors, photographs were taken on single crystals of **1** (Figure 17) and a polycrystalline sample of **2** (Figure 18) in an optical microscope.

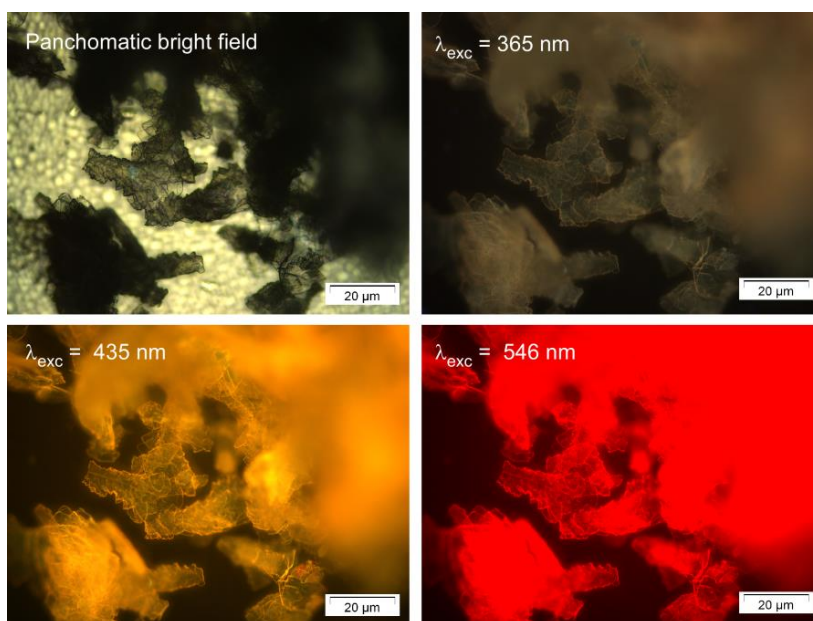


Figure 17. Micro-PL images taken on single crystals of **1**.

Excitation of **1** crystals with UV light of 365 nm (ligand), revealed a blue emission ascribed to $\pi \leftarrow \pi^*$ electronic transitions of the aromatic ring of the ligand, implying that Dy(III) ion is not yet effectively sensitized at that excitation line (as shown in Figure 10). Still, the relatively strong ${}^4F_{9/2} \rightarrow {}^6H_{13/2}$ transition provokes the emission of an intense green light when crystals are irradiated with blue light (435 nm), whereas excitation with green light (546 nm) reveals a red color arising from the metal. In this sense, it must be specified that the observed bright red emission should be taken with care and cannot be directly compared to previous emissions because the latter is a much more powerful excitation source.

Optical microscope images of **2** (Figure 18) revealed a weak emission when excited with UV light of 365nm at RT, whereas excitation at 435nm (centered on a region where the lanthanide ion possess various intraionic transitions), revealed the yellow/orange emission derived from the mixture of blue (ligands fluorescence) and

green (Tb(III) fluorescence). In the same line, if sample is irradiated with wavelengths larger than intraionic emissions (546 nm), a red light is emitted, which arises from the emission of the compound in the 550-700nm range (see also Figure 12b).

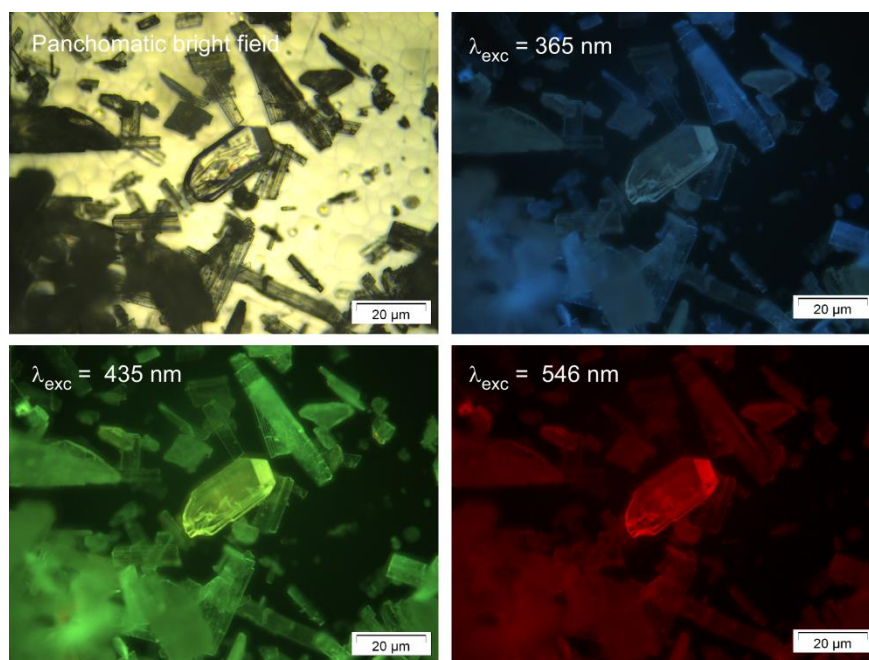


Figure 18. Micro-PL images taken on single crystals of **2**.

3.4. Cytotoxicity of the lanthanide complexes

With the aim of getting insight into potential applications of compounds **1–4** in biological/cellular environments, cell viability studies (3-(4,5-dimethyl-2-thiazoyl)-2,5-diphenyltetrazolium bromide, MTT assay, were carried out on human colon cancer cell line Caco-2 as well as human healthy (differentiated) Caco-2/TC7 cells, both in the presence and absence of increasing concentrations (0–20 μM) of each of the compounds. Figure 19 collects viability results for Caco-2 cancer cells; as observed, incubation with compound **1** provoked a very modest inhibition of cell growth at 1.5 μM concentration, decreasing cell viability in a 30% with respect to control experiment. Still, growth inhibition did not show a clear relationship with compound **1** concentration. On the other hand, Caco-2 cell incubation with either

compounds **2–4** provoked no clear inhibition of cell growth.

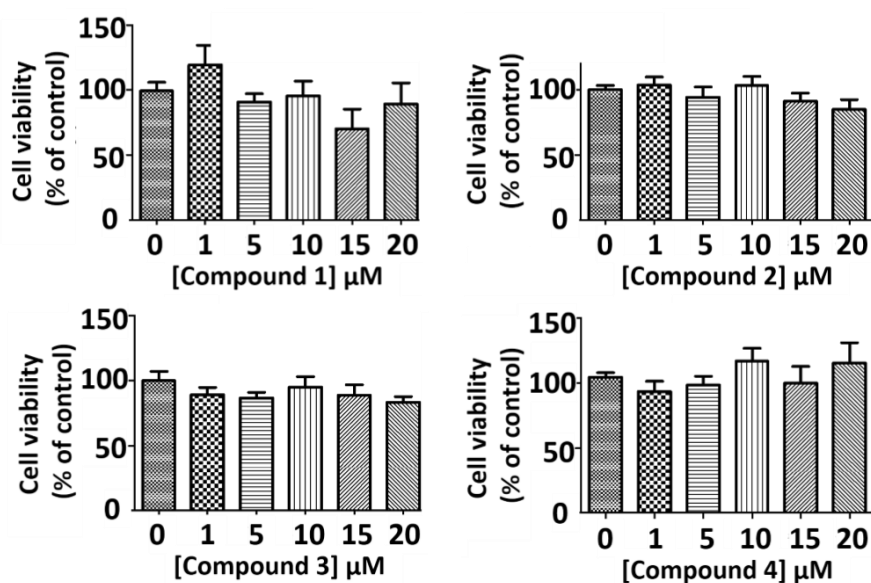


Figure 19. Cell viability study on Caco-2 cells upon incubation with increasing concentrations of compounds **1-4**.

Similarly, the effect of compounds **1-4** on non-neoplastic cells was studied by the analysis of their effect on the viability of Caco-2/TC7 cells, which consist of a monolayer of polarized and confluent Caco-2 cells that mimic a healthy human small-intestinal tissue both in terms of architecture and molecular environment. As derived from results plotted in Figure 20, incubation of healthy cells with increasing concentrations of compounds **1-4** resulted in no significant change on cell viability.

The absence of any significant toxicity effect of our compounds over either cancer or non-cancerous cells, strengthens the chances of success of this type of Ln(III) complexes when used either in biosensing or bioimaging applications.

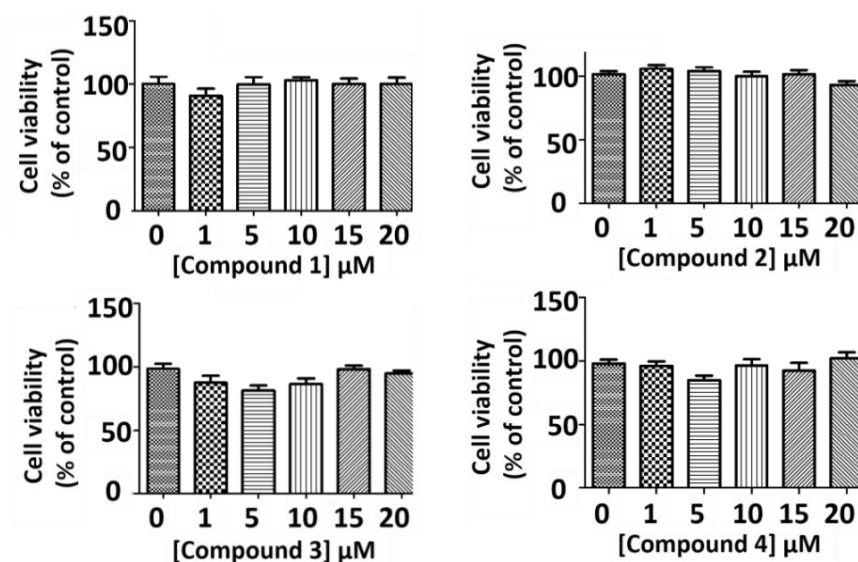


Figure 20. Cell viability study on Caco-2/TC7 (under confluence) cells upon incubation with increasing concentrations of compounds **1-4**.

4. Conclusions

In summary, four novel lanthanide coordination compounds, with three types of crystal structures, have been crystallized: $[\text{Dy}(\text{5-BrNic})_3(\text{H}_2\text{O})_4]$ (**1**), $[\text{Tb}(\text{5-BrNic})_2(\text{H}_2\text{O})_4] \cdot [\text{Tb}(\text{5-BrNic})_4(\text{H}_2\text{O})_2] \cdot (\text{5-HBrNic})_2$ (**2**), $[\text{Yb}(\text{5-BrNic})_2(\text{H}_2\text{O})_4][\text{Yb}(\text{5-BrNic})_4(\text{H}_2\text{O})_2] \cdot (\text{5-HBrNic})_2$ (**3**) and $\{[\text{Nd}(\text{5-BrNic})_3(\text{H}_2\text{O})_3] \cdot \text{H}_2\text{O}\}_n$ (**4**). Magnetic measurements confirm the presence of isolated lanthanide centers given the negligible antiferromagnetic interactions existing even in the case of 1D Nd-carboxylate chains of **4**. On its part, alternating current magnetic susceptibility measurements carried out on **1** have been accomplished by means of, revealing a U_{eff} of 33 K. Solid state photoluminescence spectra of compounds **1-4** showed the relevance of the antenna effect exerted by the 5-BrNic ligand. Decay lifetime measurements indicate short-lived excitation states in **1**, whereas the yellow/orange colored emission of **2** showed larger lifetimes (1 ms aprox). Cell viability studies on both cancer and non-cancer Caco-2 cells revealed a complete absence of cell growth inhibition exerted by either compound **1-4**. In conclusion, four new non-toxic luminescent Ln(III) compounds have been generated with the 5-BrNic ligand with interesting magnetic and luminescent properties, accompanied by a complete absence of toxicity in cellular assays.

5. References

- 1.- E. San Sebastian, A. Rodríguez-Diéguez, J. M. Seco and J. Cepeda, *Eur. J. Inorg. Chem.*, 2018, 2155-2174.
- 2.-(a) A. Dhakshinamoorthy and H. Garcia, *Chem. Soc. Rev.*, 2014, **43**, 5750-5765. (b) L. Ma, C. Abney and W. Lin, *Chem. Soc. Rev.*, 2009, **38**, 1248–1256. (c) P. Horcajada, R. Gref, T. Baati, P. K. Allan, G. Maurin, P. Couvreur, G. Ferey, R. E. Morris and C. Serre. *Chem. Rev.*, 2012, **112**, 1232–1268. (d) P. Ramaswamy, N. E. Wong and G. K. H. Shimizu, *Chem. Soc. Rev.*, 2014, **43**, 5913–5932. (e) K. Fujie, R. Ikeda, K. Otsubo, T. Yamada and S. Kitagawa, *Chem. Mater.*, 2015, **27**, 7355–7361. (f) S. Lee, E. A. Kapustin and O. M. Yaghi, *Science*, 2016, **353**, 808–811. (g) Y. Inokuma, S. Yoshioka, J. Ariyoshi, T. Arai, Y. Hitora, K. Takada, S. Matsunaga, K. Rissanen and M. Fujita, *Nature*, 2013, **495**, 461–466. (h) V. Stavila, A. A. Talin and D. Allendorf, *Chem. Soc. Rev.*, 2014, **43**, 5994-6010. (i) J. M. Frost, K. L. M. Harriman and M. Murugesu, *Chem. Sci.*, 2016, **7**, 2470–2491. (j) G. A. Craig and M. Murrie, *Chem. Soc. Rev.*, 2015, **44**, 2135–2147. (k) H. S. Quah, W. Chen, M. K. Schreyer, H. Yang, M. W. Wong, W. Ji and J. J. Vital, *Nat. Commun.*, 2015, **6**, 7954–7961.
- 3.-(a) V. Guillerm, D. Kim, J. F. Eubank, R. Luebke, X. Liu, K. Adil, M. S. Lah and M. Eddaoudi, *Chem. Soc. Rev.*, 2014, **43**, 6141–6172. (b) M. Eddaoudi, D. F. Sava, J. F. Eubank, K. Adil and V. Guillerm, *Chem. Soc. Rev.*, 2015, **44**, 228–249.
- 4.-(a) Y. Cui, B. Chen and G. Qian, *Coord. Chem. Rev.*, 2012, **112**, 1126–1162. (b) J. Rocha, L.D. Carlos, F.A.A. Paz and D. Ananias, *Chem. Soc. Rev.*, 2011, **40**, 926–940. (c) B. Li, H.-M. Wen, Y. Cui, G. Qian and B. Chen, *Prog. Polym. Sci.*, 2015, **48**, 40–84. (d) B. Chen, L. Wang, Y. Xiao, F.R. Fronczek, M. Xue, Y. Cui and G. Qian, *Angew. Chem., Int. Ed.*, 2009, **48**, 500–503.
- 5.-(a) S.V. Eliseeva and J.-C.G. Bünzli, *Chem. Soc. Rev.*, 2010, **39**, 189–227. (b) L.D. Carlos, R.A.S. Ferreira, V. de Zea Bermudez, B. Julián-López and P. Escribano, *Chem. Soc. Rev.*, 2011, **40**, 536–549. (c) J.-C.G. Bünzli and C. Piguet, *Chem. Rev.*, 2002, **102**, 1897–1928. (d) J.-C.G. Bünzli, *Chem. Rev.*, 2010, **110**, 2729–2755. (e) K. Binnemans, *Chem. Rev.*, 2009, **109**, 4283–4374. (f) E.G. Moore, A.P.S. Samuel and

K.N. Raymond, *Acc. Chem. Res.*, 2009, **42**, 542–552. (g) Y. Cui, J. Zhang, B. Chen and G. Qian, Lanthanide Metal-Organic Frameworks for Luminescent Applications. Handbook on the Physics and Chemistry of Rare Earths, 243–268.

6.- E.G. Moore, A.P.S. Samuel and K.N. Raymond, *Acc. Chem. Res.*, 2009, **42**, 542–552.

7.- (a) Y-S. Song, B. Yan and Z-X. Chen, *J. Solid State Chem.*, 2004, **177**, 3805–3814. (b) J-Z. Gu, J. Wu, A. M. Kirillov, D-Y. Lv, Y. Tang and J-C. Wu, *J. Solid State Chem.*, 2014, **213**, 256–267. (c) A. J. Calahorra, M. E. López-Viseras, A. Salinas-Castillo, D. Fairen-Jimenez, E. Colacio, J. Cano and A. Rodríguez-Diéguez, *CrystEngComm*, 2012, **14**, 6390–6393.

8.- Bruker Apex2, Bruker AXS Inc., Madison, Wisconsin, USA, 2004.

9.- G.M. Sheldrick, SADABS, Program for Empirical Adsorption Correction, Institute for Inorganic Chemistry, University of Gottingen, Germany, 1996.

10.- (a) G. M. Sheldrick, SHELX-2014, Program for Crystal Structure Refinement, University of Göttingen, Göttingen, Germany, 2014. (b) L. J. Farrugia, *J. Appl. Cryst.*, 1999, **32**, 837–838.

11.- A. Altomare, M. C. Burla, M. Camilla, G. L. Casciarano, C. Giacovazzo, A. Guagliardi, A. G. G. Moliterni, G. Polidori and R. Spagna, *J. Appl. Crystallogr.*, 1999, **32**, 115–119.

12.- (a) R. Sessoli and A. K. Powell, *Coord. Chem. Rev.*, 2009, **253**, 2328–2341. (b) P. Díaz-Gallifa, O. Fabelo, J. Pasán, L. Cañadillas-Delgado, F. Lloret, M. Julve and C. Ruiz-Pérez, *Inorg. Chem.*, 2014, **53**, 6299–6308.

13.- (a) D. Aguilà, L. A. Barrios, V. Velasco, L. Arnedo, N. Aliaga-Alcalde, M. Menelaou, S. J. Teat, O. Roubeau, F. Luis and G. Aromí, *Chem.–Eur. J.*, 2013, **19**, 5881–5891. (b) N. W. Waggoner, B. Saccoccia, I. A. Ibarra, V. M. Lynch, P. T. Wood and S. M. Humphrey, *Inorg. Chem.*, 2014, **53**, 12674–12676.

14.- (a) I. A. Kahwa, J. Selbin, C. J. O'Connor, J. W. Foise and G. L. McPherson, *Inorg. Chim. Acta*, 1988, **148**, 265–272. (b) H. Ke, L. Zhao, G.-F. Xu, Y.-N. Guo, J.

Tang, X.-Y. Zhang and H.-J. Zhang, *Dalton Trans.*, 2009, **47**, 10609–10613. (c) J. Cepeda, R. Balda, G. Beobide, O. Castillo, J. Fernández, A. Luque, S. Pérez-Yáñez, P. Román and D. Vallejo-Sánchez, *Inorg. Chem.*, 2011, **50**, 8437–8451. (d) C. J. O'Connor, *Prog. Inorg. Chem.*, 1982, **29**, 203.

15.- B. Yao, B. Gu, M. Su, G. Li, Y. Ma, L. Li, Q. Wang, P. Cheng and X. Zhang, *RSC Adv.*, 2017, **7**, 2766–2772.

16.- (a) Q.-W. Xie, S.-Q. Wu, W.-B Shi, C.-M. Liu, A.-L. Cui and H.-Z. Kou, *Dalton Trans.*, 2014, **43**, 11309–11316. (b) Y. Li, C. Zhang, J.-W. Yu, E.-C. Yang and X.-J. Zhao, *Inorg. Chim. Acta*, 2016, **445**, 110–116. (c) J. P. Costes, S. Titos-Padilla, I. Oyarzabal, T. Gupta, C. Duhayon, G. Rajaraman and E. Colacio, *Inorg. Chem.*, 2016, **55**, 4428–4440. (d) P.-Y. Shan, H.-F. Li, P. Chen, Y.-M. Tian, W.-B. Sun and P.-F. Yan, *Z. Anorg. Allg. Chem.*, 2015, **641**, 1119–1124.

17.- (a) J.-L. Liu, Y.-C. Chen and M.-L. Tong, *Chem. Soc. Rev.*, 2018, **47**, 2431–2453. (b) D. N. Woodruff, R. E. P. Winpenny and R. A. Layfield, *Chem. Rev.*, 2013, **113**, 5110–5148.

18.- P. E. Car, M. Perfetti, M. Mannini, A. Favre, A. Caneschi and R. Sessoli, *Chem. Commun.*, 2011, **47**, 3751–3753.

19.- D. Li, T. Wang, C. Li, D. Liu, Y. Li and X. You, *Chem. Commun.*, 2010, **46**, 2929–2931.

20.- G. Chen, C. Gao, J. Tian, J. Tang, W. Gu, X. Liu, S. Yan, D. Liao and P. Cheng, *Dalton Trans.*, 2011, **40**, 5579–5583.

21.- N. Ishikawa, M. Sugita, T. Ishikawa, S.-Y. Koshihara and Y. Kaizu, *J. Am. Chem. Soc.*, 2003, **125**, 8694–8695.

22.- S. Jiang, B. Wang, G. Su, Z. Wang and S. Gao, *Angew. Chem., Int. Ed.*, 2010, **49**, 7448–7451.

23.- Y.-C. Chen, J.-L. Liu, L. Ungur, J. Liu, Q.-W. Li, L.-F. Wang, Z.-P. Ni, L. F. Chibotaru, X.-M. Chen and M.-L. Tong, *J. Am. Chem. Soc.*, 2016, **138**, 2829–2837.

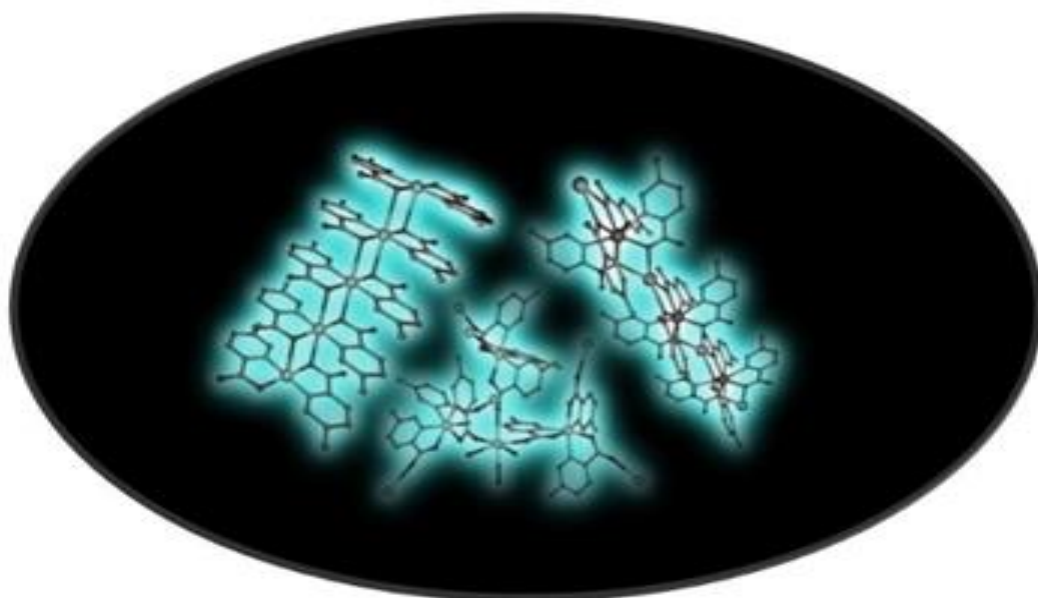
24.- M. Gregson, N. F. Chilton, A.-M. Ariciu, F. Tuna, I. F. Crowe, W. Lewis, A. J. Blake, D. Collison, E. J. L. McInnes, R. E. P. Winpenney and S. T. Liddle, *Chem. Sci.*, 2016, **7**, 155–165.

25.- (a) C. A. P. Goodwin, F. Ortu, D. Reta, N. F. Chilton and D. P. Mills, *Nature*, 2017, **548**, 439–442. (b) F.-S. Guo, B. M. Day, Y.-C. Chen, M.-L. Tong, A. Mansikkamaki and R. A. Layfield, *Angew. Chem., Int. Ed.*, 2017, **56**, 11445–11449.

26.- (a) M. D. Allendorf, C. A. Bauer, R. K. Bhakta and R. J. T. Houk, *Chem. Soc. Rev.*, 2009, **38**, 1330–1352. (b) J. Cepeda, S. Pérez-Yáñez, G. Beobide, O. Castillo, J. A. García, M. Lanchas and A. Luque, *Dalton Trans.*, 2015, **44**, 6792–6786. (c) K. Müller-Buschbaum, S. G. Torres, P. Larsen and C. Wickleder, *Chem. Mater.*, 2007, **19**, 655–659.

Capitulo 3

5-Aminopyridine-2-Carboxylic Acid as Appropriate Ligand for Constructing Coordination Polymers with Luminescence, Slow Magnetic Relaxation and Anti-Cancer Properties



5-aminopyridine-2-carboxylic acid as Appropriate Ligand for Constructing Coordination Polymers with Luminescence, Slow Magnetic Relaxation and Anti-Cancer Properties

Journal of Inorganic Biochemistry 207 (2020) 111051



Contents lists available at ScienceDirect

Journal of Inorganic Biochemistry

journal homepage: www.elsevier.com/locate/jinorgbio



5-Aminopyridine-2-carboxylic acid as appropriate ligand for constructing coordination polymers with luminescence, slow magnetic relaxation and anti-cancer properties^{†*}



Antonio A. García-Valdivia^a, Javier Cepeda^b, Belén Fernández^{c,*}, Marta Medina-O'donnell^d, Itziar Oyarzabal^b, Jerónimo Parra^a, Fatin Jannus^e, Duane Choquesillo-Lazarte^g, José A. García^h, José Antonio Lupiáñez^c, Santiago Gómez-Ruiz^f, Fernando Reyes-Zurita^{e,*}, Antonio Rodríguez-Diéguez^{a,*}

^a Department of Inorganic Chemistry, University of Granada, 18071 Granada, Spain

^b Department of Applied Chemistry, Faculty of Chemistry, University of The Basque Country UPV/EHU, Paseo Manuel Lardizabal 3, 20018 Donostia-San Sebastián, Spain

^c Institute of Parasitology and Biomedicine "López-Neyra", CSIC, Av. Conocimiento s/n, 18600 Granada, Spain

^d Department of Organic Chemistry, University of Granada, 18071 Granada, Spain

^e Dept. of Biochemistry and Molecular Biology I, Severo Ochoa s/n, University of Granada, 18071 Granada, Spain

^f Department of Biology and Geology, Physics and Inorganic Chemistry, E.S.C.E.T., Rey Juan Carlos University, c/ Tulipán s/n, 28933 Móstoles, Spain

^g Laboratorio de Estudios Cristalográficos, IACT (CSIC-UGR), Avda. de las Palmeras 4, 18100 Armilla, Granada, Spain

^h Departamento de Física Aplicada II, Facultad de Ciencia y Tecnología, Universidad del País Vasco (UPV/EHU), 48940 Leioa, Spain

[†] *In memoriam of Professor Juan Manuel Salas Peregrín and his contribution to the research on bioinorganic chemistry in Spain*

Keywords: Coordination polymers; CPs; Lanthanides; Transition metals; Slow relaxation of magnetization; SMM; Luminescence Properties; Anticancer activity.

Abstract

Five new coordination polymers (CPs) constructed of aminopyridine-2-carboxylate (ampy) ligand have been synthesized and fully characterized. Three of them correspond to metal-organic chains built from the coordination of ampy to sodium and lanthanides with formulae $[MNa(ampy)_4]_n$ ($M =$ terbium (**1**), erbium (**2**), and ytterbium (**3**)) resembling a previously reported dysprosium material which shows anticancer activity. On another level, the reaction of Hampy with cobalt and

copper ions ($\{[\text{CoK}(\text{ampy})_3(\text{H}_2\text{O})_3](\text{H}_2\text{O})_3\}_n$ (**4**) and $[\text{Cu}(\text{ampy})_2]_n$ (**5**)) lead to CPs with variable dimensionalities, which gives the opportunity of analyzing the structural properties of this new family. Lanthanide materials display solid state intense photoluminescent emissions in both the visible and near-infrared region and exhibit slow relaxation of magnetization with frequency dependence of the out-of-phase susceptibility. More interestingly, in our search on multifunctional materials, we have carried out antitumor measurements of these compounds. These multidisciplinary studies of metal complexes opens up the possibility of further exploring the applications in the fields of metal-based drugs.

1. Introduction

In the last years, Single-Ion Magnets (SIMs) have been intensively studied due to their potential applications in quantum-computing devices¹ and molecular spintronics². In the same time, coordination polymers (CPs) have received great interest due to their structural diversity as well as the properties that arise from their topological features³. In particular, the study of lanthanide-based CPs has evolved enormously in areas such as luminescence⁴, gas adsorption⁵, optical storage⁶, magnetism⁷ and biology as drug-delivery systems⁸ or cytotoxic agents⁹. Coordination polymers are obtained by the self-assembly of metal ions with appropriate bridging organic ligands generating multidimensional materials with different properties. During the recent years, we have also focused on designing novel organic ligands to construct SIMs¹⁰ and Ln-PCs based on carboxylic linkers¹¹ that behave as magnets. It is worth noting that there are not many examples of mixed 3s-4f systems so the synthesis and study of these systems could provide materials with interesting properties, reason why we decided to focus on this type of SIMs. In this line, our research group has recently obtained and characterized an interesting metal-organic chain (MOC) based on dysprosium which, to the best of our knowledge, can be regarded as the first example of a SIM material showing magnetic field dependent cytotoxicity and modulation of the multidrug resistance¹². In this work, the cytotoxicity of both the ligand and complex was quantified by the IC_{50} values, showing that complex and its ligand exert a mild cytotoxic activity against HT-29 and DLD-1 colon carcinoma cells, while complex has a very weak cytotoxicity

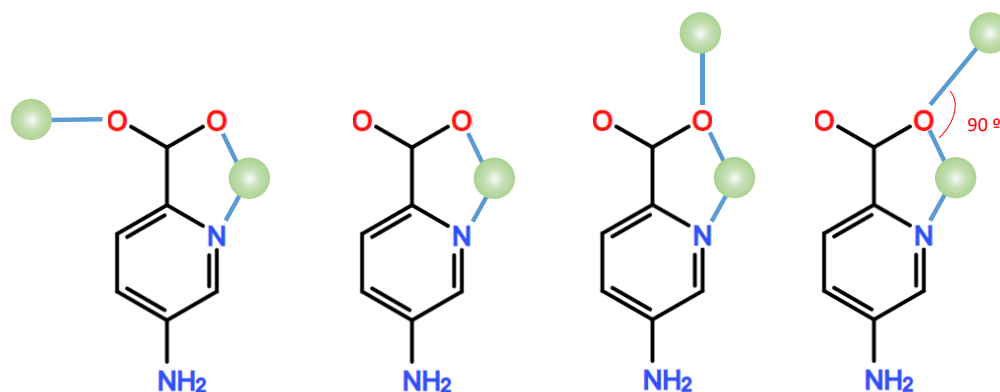
against Caco-2 cells as none of the concentrations, not even 20 mM, inhibited 100% of the living cells.

In the development of biological applications, this type of metal-organic compounds could be used for variable purposes with different points of view. These systems can be used as bioluminescent markers¹³ when present a low cytotoxicity or, alternatively, they can be used as cytotoxic compounds with a cytotoxicity modulated by an external magnetic field or by the structural properties.¹⁴ These properties feature a wide range of potential uses such as allow determining the organism distribution of the compound, and once reached the target tumor area, its toxicity could be activated in response to a magnetic field and minimize nonspecific interactions as it happens with other anticancer agents such as aripterpenic acids derivatives.¹⁵

Due to the potential application of these materials, we have synthesized similar coordination polymers based on terbium, erbium and ytterbium ions that show slow relaxation of magnetization with the aim of studying their cytotoxic properties with different cancer cell lines. In these studies, we have observed that the cytotoxic activity varies depending on the lanthanide ion used, which opens up the possibility of switching the biological activity of the compound while its multifunctional character is adapted. Moreover, we have synthesized two new multidimensional coordination polymers based on cobalt and copper with the same ligand to study the modification of the anti-cancer properties by the use of transition metal ions. On this occasion, we have used ligand 5-aminopyridine-2-carboxylic acid (Hampy), due to there was only one coordination compound in the literature¹⁶. In this case, the ligand showed a different coordination mode than the one shown in the previous work and in this manuscript.

Herein, we report the synthesis and structure of five novel coordination polymers based on 5-aminopyridine-2-carboxylic acid as linker, three MOCs with formulae $[\text{TbNa}(\text{ampy})_4]_n$ (**1**), $[\text{ErNa}(\text{ampy})_4]_n$ (**2**), $[\text{YbNa}(\text{ampy})_4]_n$ (**3**), and two multidimensional CPs $\{[\text{CoK}(\text{ampy})_3(\text{H}_2\text{O})_3] \cdot (\text{H}_2\text{O})_3\}_n$ (**4**) and $[\text{Cu}(\text{ampy})_2]_n$ (**5**) that present interesting magnetic, luminescence and biological properties. Thanks to its aromaticity, Hampy is a good candidate for enhanced emissive properties, which are tunable by coordination to metal with different coordination modes (Scheme 1).

These materials corroborate the potential of this pyridine derivative linker to construct new coordination polymers with interesting physical and biological properties. Moreover, in this work we assayed the cytotoxicity effects of five metal complexes, in three cellular lines: B16-F10 murine melanoma cells, Hep-G2 human hepatocarcinome cells, and HT29 human colon cancer cells. Our results showed that the compounds were especially cytotoxic in the carcinoma cells HT29 or Hep-G2, whereas no results were found in B16-F10 melanoma cells. Compound **4** seemed to be the more cytotoxic complex (including B16-F10 mealnome cells), whereas compound **1** did not have effects on any of the cancer cell lines assayed. One of our main objectives in this study is to search for new anticancer-drugs with new biochemical properties rather than improving actual anti-cancer drugs. In this sense the synthesis of new families of coordination compounds could be a new strategy with new applications, which may represent a useful mechanistic approach to both chemoprevention and chemotherapy in different types of cancer.



Scheme 1. *Different known coordination modes of Hampy ligand.*

2. Experimental Section

2.1. General Procedures

Unless stated otherwise, all reactions were conducted under solvothermal conditions, with the reagents purchased commercially and used without further purification.

2.2. Preparation of complexes

[TbNa(ampy)₄]_n (1): This reaction is achieved via the soft solvothermal reaction of terbium nitrate (1 mmol), NaOH (0.1 mmol) and 5-aminopyridine-2-carboxylic acid (4 mmol) in dimethylformamide (10 ml) at 95°C for 24h to give prismatic crystals of compound **1**. Yield: ca. 45% based on terbium. Anal. Calcd C₂₄H₂₀N₈NaO₈Tb: C 39.47, H 2.76, N 15.34. Found: C 39.43, H 2.67, N 15.41.

[ErNa(ampy)₄]_n (2) and **[YbNa(ampy)₄]_n (3):** They were carried out the same reaction as in the above compound but using erbium nitrate and ytterbium nitrate for **2** and **3**, respectively. Yield: ca. 38% and 43% based on metal ions for **2** and **3**, respectively. Anal. Calcd C₂₄H₂₀N₈NaO₈Er: C 39.02, H 2.73, N 15.17. Found: C 38.94, H 2.65, N 15.21. Anal. Calcd C₂₄H₂₀N₈NaO₈Yb: C 38.72, H 2.71, N 15.05. Found: C 38.64, H 2.63, N 15.11.

{[CoK(ampy)₃(H₂O)₃](H₂O)₃]_n (4): This reaction is achieved via the soft solvothermal reaction of cobalt nitrate (1 mmol), KOH (0.1 mmol) and 5-aminopyridine-2-carboxylic acid (3 mmol) in dimethylformamide (10 ml) at 95°C for 24h to give prismatic crystals of compound **4**. Yield: ca. 15% based on cobalt. Anal. Calcd C₁₈H₃₃CoKN₆O₁₅: C 32.19, H 4.95, N 12.51. Found: C 32.06, H 4.83, N 12.67.

[Cu(ampy)₂]_n (5): This reaction is achieved via the soft solvothermal reaction of copper nitrate (1 mmol) and 5-aminopyridine-2-carboxylic acid (2 mmol) in dimethylformamide (10 ml) at 95°C for 24h to give prismatic crystals of compound

5. Yield: ca. 41% based on copper. Anal. Calcd C₁₂H₁₀CuN₄O₄: C 42.67, H 2.98, N 16.59. Found: C 42.49, H 2.82, N 16.74.

2.3. Physical measurements

Elemental analyses were carried out at the Centro de Instrumentación Científica (University of Granada) on a Fisons-Carlo Erba analyser model EA 1108. FTIR spectra were recorded on a Nicolet IR 6700 spectrometer in the 4000–400 cm⁻¹ spectral region. The spectra of compounds show bands around 1710 cm⁻¹ (C=O, carboxylate) and 3350 cm⁻¹ and 1550 cm⁻¹ (N-H, amine group) with little displacement compared to 5-aminopyridine-2-carboxylic acid spectra's bands.

2.4. Single-Crystal Structure Determination

The crystal structure of compounds **1-5** were determined by single crystal X-ray crystallography. Suitable crystals of these materials were mounted on a glass fibre and used for data collection on a Bruker D8 Venture diffractometer using MoK α radiation ($\lambda = 0.71073\text{\AA}$). Absorption correction was applied using SADABS¹⁷. The structure was solved by direct methods and refined with full-matrix least-squares calculations on F^2 using the program SHELXL¹⁸ and Olex2 as the graphical interface¹⁹. Anisotropic temperature factors were assigned to all atoms except for hydrogen atoms, which are riding their parent atoms with an isotropic temperature factor chosen as 1.2 times or 1.5 times those of their parent atoms. Attempts to solve disorder problems with crystallization water molecules failed in compound **4**. During the structure refinement, regions of electron density were identified as highly disordered water molecules. Attempts to model these electron densities as water were not successful due to the extent of the disorder. In the final structure model, the contribution of the electron density from three water molecules per formula unit has been removed from the intensity data using the solvent mask tool in Olex2. The structure exhibits disorder of the coordinated ampy ligand, which was successfully refined using a two-site model with a 0.54:0.46 occupancy ratio. Compound **5** was refined as a pseudo-merohedral twin. From the original HKLF file,

a modified file was prepared by means of the TWINROTMAT option (twin matrix -1 0 0 0 -1 0 0 0 1) in PLATON²⁰ in such a way that final refinement gave twin fractions of 0.22 and 0.78. Details of the structure determination and refinement of the studied compounds are summarized in Table 1. Crystallographic data (excluding structure factors) for the structure reported in this paper have been deposited with the Cambridge Crystallographic Data Centre as supplementary publication nos. CCDC 1519675, 1519676 and 1944059-1944061. Copies of the data can be obtained free of charge on application to the Director, CCDC, 12 Union Road, Cambridge, CB2 1EZ, U.K. (Fax: +44-1223-335033; e-mail: deposit@ccdc.cam.ac.uk or <http://www.ccdc.cam.ac.uk>).

Table 1. Crystallographic Data and Structural Refinement Details

Compound	1	2	3	4	5
Chem. formula	C ₂₄ H ₂₀ N ₈ NaO ₈ Tb	C ₂₄ H ₂₀ ErN ₈ NaO ₈	C ₂₄ H ₂₀ N ₈ NaO ₈ Yb	C ₁₈ H ₃₃ CoKN ₆ O ₁₅	C ₁₂ H ₁₀ CuN ₄ O ₄
M/g·mol⁻¹	730.39	738.73	744.51	671.53	337.78
T(K)	100(2)	100(2)	298(2)	100(2)	100(2)
$\lambda/\text{Å}$	0.71073	0.71073	0.71073	0.71073	0.71073
Crystalsystem	Tetragonal	Tetragonal	Tetragonal	Cubic	Monoclinic
Spacegroup	I4 ₁ /a	I4 ₁ /a	I4 ₁ /a	P2 ₁ 3	P2 ₁ /c
a/Å	17.8670(17)	17.825(5)	18.007(4)	15.0415(11)	3.6280(3)
b/Å	17.8670(17)	17.825(5)	18.007(4)	15.0415(11)	13.6719(8)
c/Å	8.5065(8)	8.543(5)	8.5600(19)	15.0415(11)	11.5098(7)
$\alpha/^\circ$	90	90	90	90	90
$\beta/^\circ$	90	90	90	90	90.023(4)
$\gamma/^\circ$	90	90	90	90	90
V/Å³	2715.5(6)	2714(2)	2775.6(14)	3403.1(7)	570.91(7)
Z	4	4	4	4	2
$\rho_{\text{calcd}}(\text{g}\cdot\text{cm}^{-3})$	1.787	1.808	1.782	1.311	1.965
$\mu(\text{mm}^{-1})$	2.684	3.171	3.447	0.693	1.938
R(int)	0.0818	0.0437	0.0262	0.0612	0.0508
GOF on F²	1.064	1.073	1.069	1.057	1.095
R₁ [I > 2σ(I)]	0.0534	0.0248	0.0208	0.0417	0.0324
wR₂ [I > 2σ(I)]	0.1077	0.0616	0.0529	0.1047	0.0626

$$R_1 = \frac{\sum ||F_o| - |F_c||}{\sum |F_o|}; \quad wR^2 = \frac{[\sum w(F_o^2 - F_c^2)^2]}{\sum wF_o^2}^{1/2}$$

2.5. Luminescence measurements

Lifetime and steady-state photoluminescence (PL) measurements were carried out on crystalline samples at 10 K using a close cycle helium cryostat enclosed in an Edinburgh Instruments FLS920 spectrometer. All samples are first placed under high vacuum (of ca. 10^{-9} mbar) to avoid the presence of oxygen or water in the sample holder. For recording steady-state emission spectra an IK3552R-G HeCd continuous laser (325 nm) was used as excitation source. A Hamamatsu NIR-PMT PicoQuant FluoTime 200 detector was employed for collecting the spectra in the NIR region.

2.6. Magnetic measurements

Magnetization and variable-temperature (1.9–300 K) magnetic susceptibility measurements on polycrystalline samples were carried out with a Quantum Design SQUID MPMS XL-5 device operating at different magnetic fields. The experimental susceptibilities were corrected for the diamagnetism of the constituent atoms by using Pascal's tables. *Ac* susceptibility measurements under different applied static fields were performed by using an oscillating *ac* field of 3.5 Oe on a PPMS 6000 magnetometer.

Alternating current magnetic measurements were performed under zero and 1000 Oe applied static fields on a PPMS - Quantum Design Model 6000 magnetometer by using an oscillating *ac* field of 3.5 G and *ac* frequencies ranging from 60 to 10 000 Hz.

2.7. Antiproliferative Activity

The effect of treatment with the three 1D-coordination polymers (compound **1**, **2** and **3**) and two coordination polymer materials (compounds **4** and **5**) on cancer cell proliferation were assayed by MTT (3-(4,5-dimethylthiazol-2-yl)-2,5-diphenyltetrazolium bromide) assay, on HT29 colon cancer cells, Hep-G2 hepatome cells and B16-F10 melanome cells. The three cancer cell lines were treated with

increasing concentration of the compounds (range from 0 to 100 $\mu\text{g/mL}$). MTT is transformed by viability cells to formazan, therefore its concentration is proportional to the number of life cells. The percentage of viability cells were expressed with respect to untreated control cells. In all cells lines we determined the concentration of compounds required for 20%, 50%, and 80% of inhibition cell growth, IC_{20} , IC_{50} and IC_{80} , concentrations respectively.

3. Results and Discussion

The solvothermal reactions of the appropriate metallic salts at 95°C for 24h produced prismatic crystals of these coordination polymers. The crystal structures of terbium, erbium, ytterbium, cobalt and copper compounds were determined using single crystal X-ray crystallography.

3.1. Description of the structures

3.1.1. Structural descriptions of Tb-MOC (1), Er-MOC (2) and Yb-MOC (3).

The preparation of $[\text{TbNa}(\text{ampy})_4]_n$ is very simple and is achieved via the soft hydrothermal reaction of the terbium nitrate (1 mmol), NaOH (0.1 mmol) and 5-aminopyridine-2-carboxylic acid (4 mmol) in dimethylformamide (10 ml) at 95°C for 24h to give prismatic crystals of this Tb-MOC (**1**). Compounds **1** (M = Tb), **2** (M = Er) and **3** (M = Yb) are isostructural materials, and therefore we will only describe the latter. These compounds crystallize in the tetragonal space group $I4_1/a$. The 1D structure of **3** (Figure 1) is described by ytterbium and sodium ions bridged by four different (*ampy*)⁻ linkers. The (*ampy*)⁻ ligand shows a chelating coordination mode that involves the coordination of the oxygen atom pertaining to the carboxylate group and the nitrogen atom from the pyridine ring.

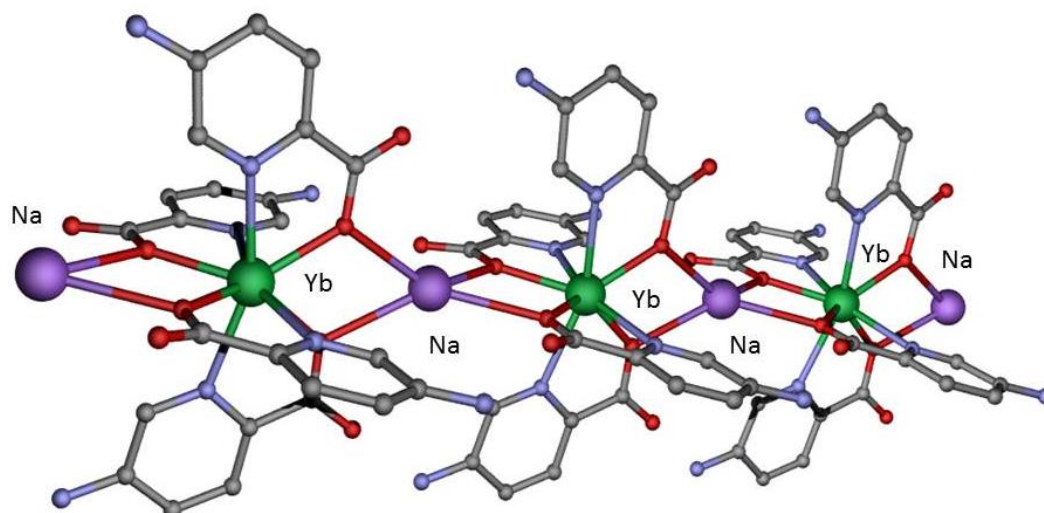


Figure 1. Perspective view of the ytterbium-sodium chain. Hydrogen atoms have been omitted for clarity. Colour code: Ytterbium, green; sodium, purple; oxygen, red; nitrogen, blue; carbon, grey.

The Yb^{III} atom exhibits a YbN₄O₄ coordination environment which is made of four oxygen atoms pertaining to four different (*ampy*)⁻ ligands and four nitrogen atoms belonging to four pyridine rings. The Yb–O_{carb} bond distance has a value of 2.282(2) Å whereas the Yb–N_{pyr} distance is 2.518(3) Å (Table 2). Within the one-dimensional coordination polymer, the intrachain Yb⋯Yb distance is of 8.560(10) Å, while the shortest interchain Yb⋯Yb distance is of 9.254(10) Å. These chains can be described by [Yb(*ampy*)₄]⁻ units bridged by Na⁺ ions, in which chains are packed thanks to an interesting hydrogen bond network (Figure 2) that involves the oxygen pertaining to carboxylate group and the amino group of the ligand with a distance of 2.972(6) Å.

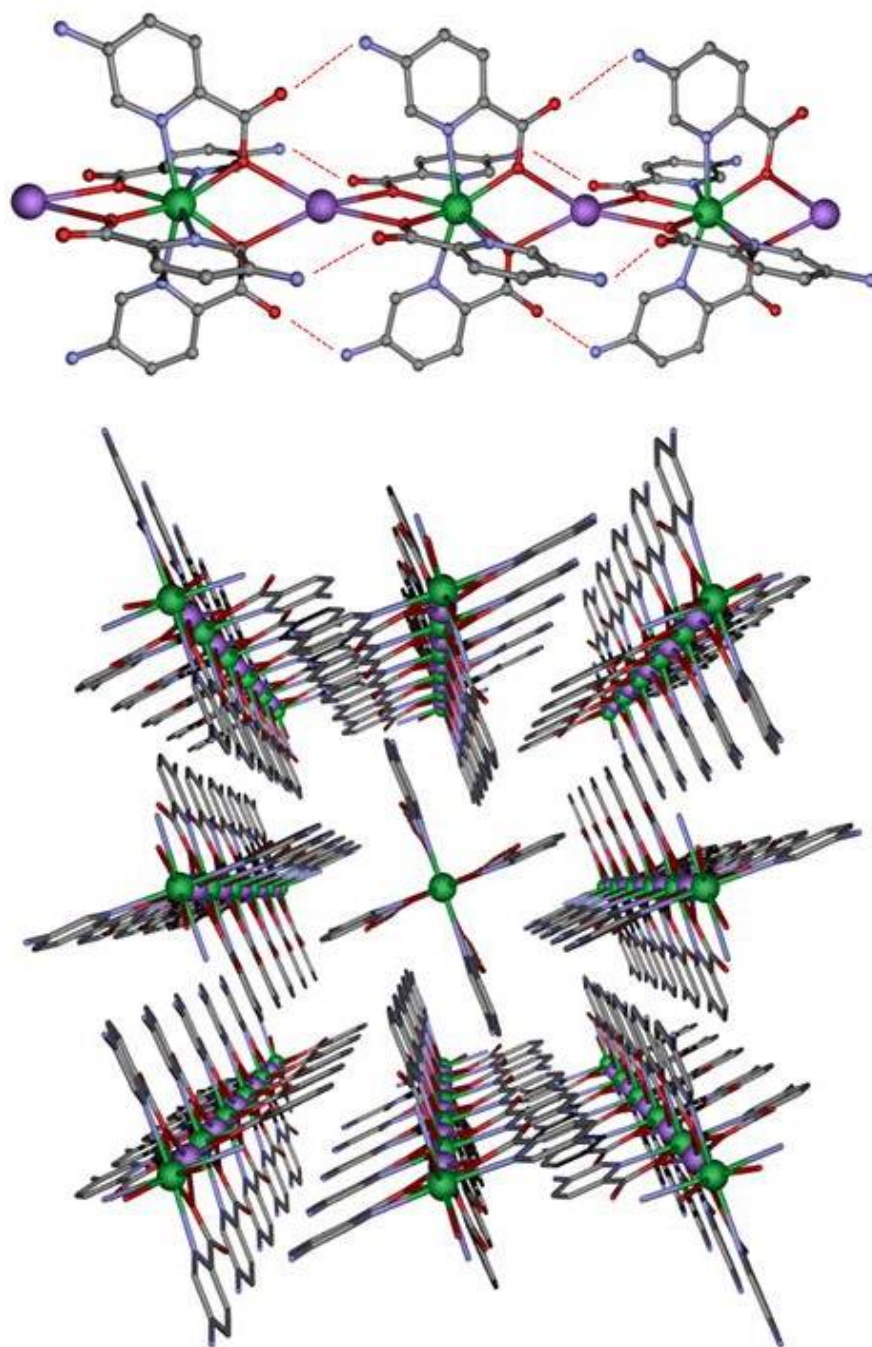


Figure 2. Top: Hydrogen bonds present in the chains pertaining to Yb-MOC. Bottom: Perspective view of packing in **3** along *c* axis in which can be observed π - π interactions among pyridine rings pertaining to the ligand.

In these three structures, Na^+ ions shows a very distorted tetrahedral coordination geometry of type NaO_4 , in which the bond distances Na-O are 2.736, 2.753 and 2.762 Å for **1**, **2** and **3**, respectively.

Table 2. Selected bond lengths and angles for compounds 1 - 3.

Tb1-O1	2.318(4)	Er1-O1	2.308(3)	Yb1-O1	2.282(2)
Tb1-N1	2.556(4)	Er1-N1	2.529(4)	Yb1-N1	2.518(3)
Tb1-Na1	4.253(8)	Er1-Na1	4.272(7)	Yb1-Na1	4.280(9)
Tb1-Tb1	8.507(9)	Er1-Er1	8.543(7)	Yb1-Yb1	8.560(10)

3.1.2. Structural description of Co-CP (4).

Compound **4** crystallizes in the cubic $P2_13$ space group. The cobalt(II) ion resides in a 3-fold axis, adopting an octahedral coordination polyhedron and is tris chelated by three ampy ligands which supply six donor atoms in a CoN_3O_3 coordination environment in *fac* disposition (Figure 3). The overall assembly consists of a three-dimensional coordination polymer that can be described as $[\text{Co}(\text{ampy})_3]^-$ units connected by K^+ ions.

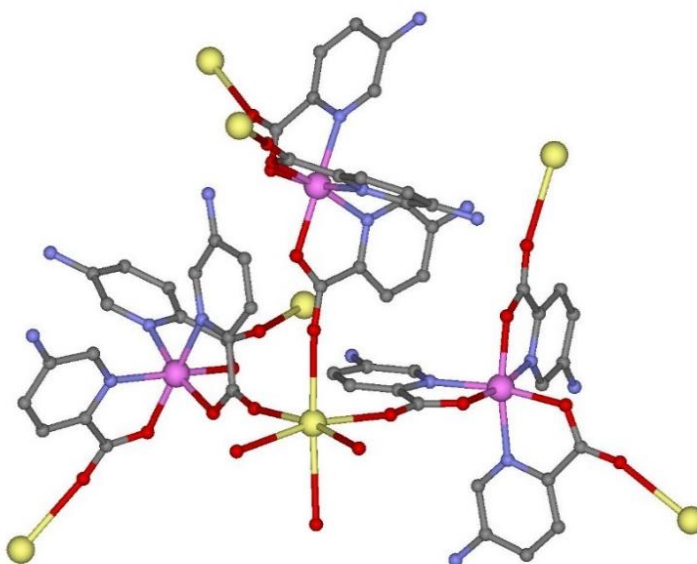


Figure 3. Perspective of one chain pertaining to Co-CP in which $[\text{Co}(\text{ampy})_3]^-$ units are connected by K^+ ions. Hydrogen atoms have been omitted for clarity. Colour code: Cobalt, pink; potassium, yellow; oxygen, red; nitrogen, blue; carbon, grey.

The potassium centers exhibit six-coordinate environments consisting of three bridging carboxylate O atoms and three terminal water molecules. It is observed that the K–O_{ampy} distances (2.686(4) Å) are shorter than that of the K–O_{water} (2.844(8) Å), indicating that the former bridges may play a more important role in stabilizing the network (Figure 4). Hydrogen bonding interactions involving –NH₂ groups reinforce the supramolecular architecture. Terminal water ligands also participate in a hydrogen network pointing towards the interior of cavities (26.9% of unit cell volume). These cavities are occupied by highly disordered water molecules that were masked by the Olex2 mask tool (see experimental section).

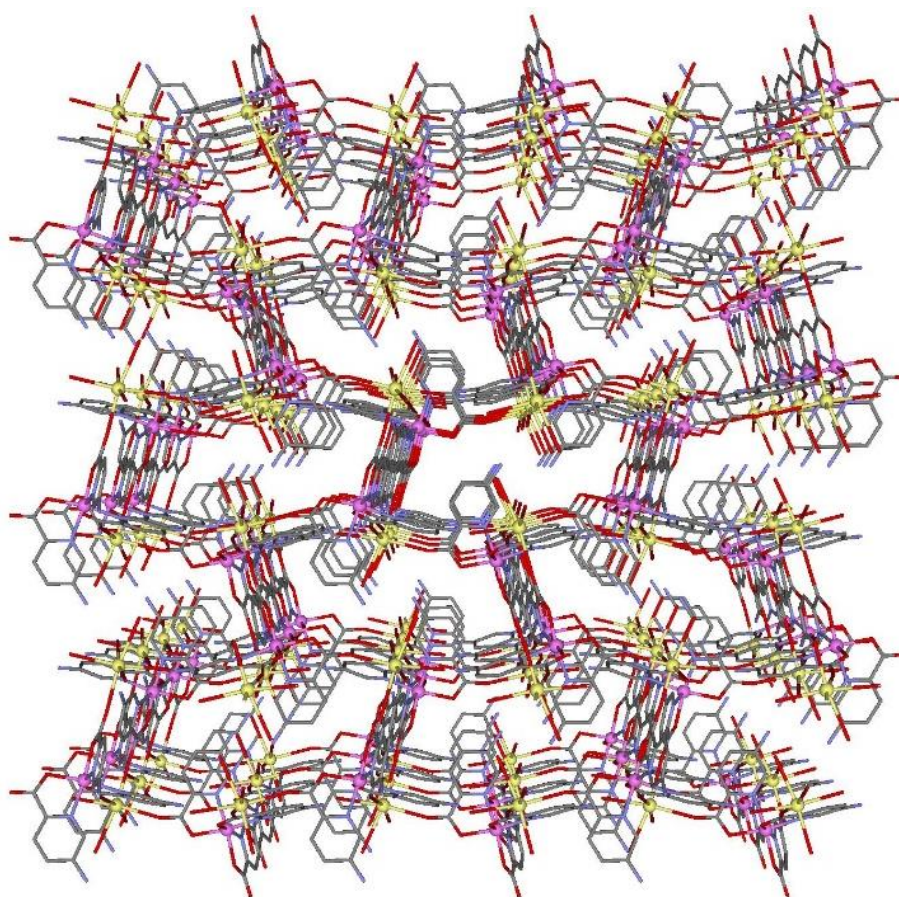


Figure 4. Perspective of the three-dimensional structure in Co-CP. Hydrogen atoms have been omitted for clarity. Colour code: Cobalt, pink; potassium, yellow; oxygen, red; nitrogen, blue; carbon, grey.

3.1.3. Structural description of Cu-CP (5).

The structure of **5** is made of planar $[\text{Cu}(\text{ampy})_2]$ units connected by weak Cu-O axial interactions to afford linear chains parallel to the a axis (Figure 5). This compound crystallizes in the $P21/c$ monoclinic space group in which Cu(II) ions exhibit a CuN_2O_4 coordination polyhedron with tetragonally distorted octahedral geometry. The equatorial positions are occupied by two nitrogen atoms and two oxygen atoms from two different *ampy* bridging ligands, which adopt a trans-planar configuration. Two carboxylate oxygen atoms, O1, are situated in axial positions at a longer distance of 2.961(3) Å. Neighbouring $[\text{Cu}(\text{ampy})_2]$ units are held together by a pair of complementary weak Cu-O1 interactions, which lead to the chain structure with syn-anti carboxylate bridges. The Cu...Cu distance along the chain is 3.628(4) Å, whereas the shortest interchain Cu...Cu distance is 8.936(4) Å.

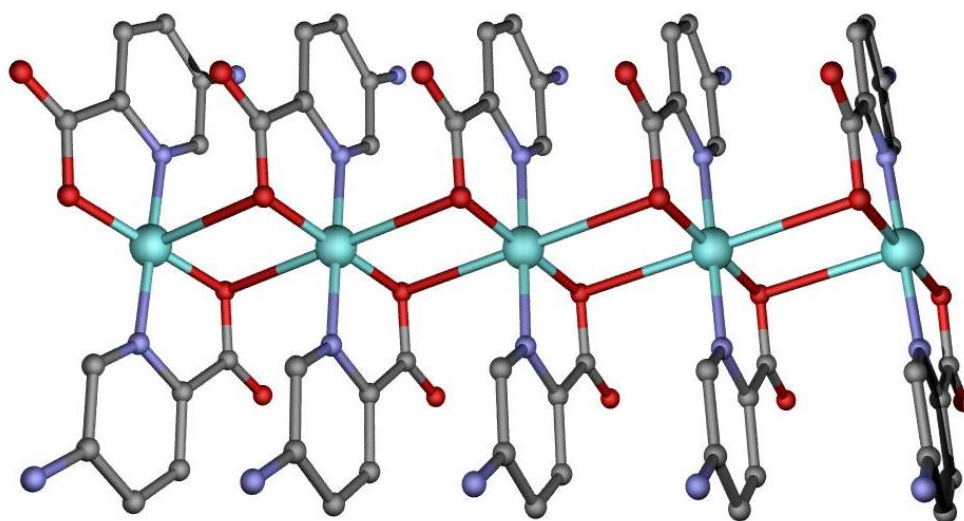


Figure 5. Perspective of one chain pertaining to **Cu-CP** parallel to a axis. Hydrogen atoms have been omitted for clarity. Colour code: Copper, cyan; oxygen, red; nitrogen, blue; carbon, grey.

These chains generate a three-dimensional network by means of strong hydrogen bonds (2.911 Å) involving the O2 atoms from the carboxylate groups and the N2 atoms from the amino groups pertaining to the *ampy* ligand (Figure 6).

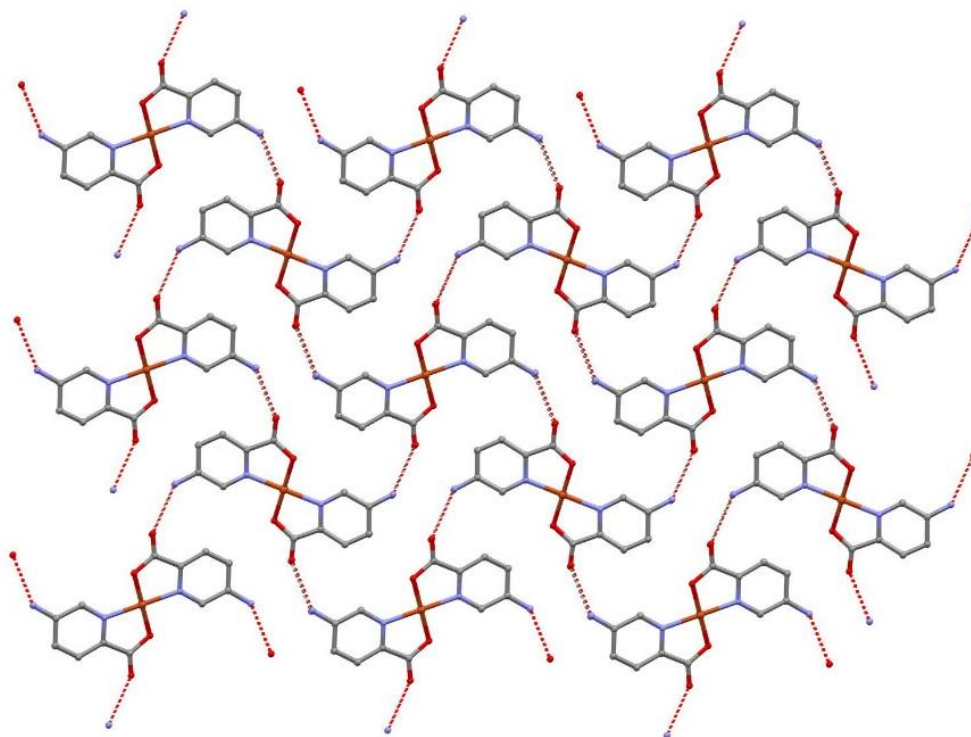


Figure 6. Perspective of the three-dimensional network generating by hydrogen bonds in compound 5.

3.2. Luminescence Properties

Among lanthanide ions, Tb(III) is one of the most strongly emitting members and accordingly, it has been widely employed for the characterization of the active metal environments in many macromolecules of biological interest²¹. Lanthanide luminophores present sharp emission bands and their luminescent lifetimes are often long, which allows easily discriminating their emission from background fluorescence, identifying it through time-resolved measurements and performing a selected detection when they are mixed with other emitting lanthanide cations^{10b}. On the other hand, a major drawback for lanthanide(III) ions is derived from their low absorption coefficients, since being based on Laporte forbidden *f-f* transitions, hinders their direct excitation. This inconvenient may be bypassed by the so-called “antenna effect”, in which ligands consisting of aromatic chromophores and

possessing a reasonably large molar absorption cross section mediate in the process, thus generating more efficient emissions originated at the lanthanides. The polycrystalline sample of compound **1** shows a brilliant green emission upon laser excitation at 325 nm. The emission spectrum shows seven multiplets assigned to the $^5D_4 \rightarrow ^7F_J$ ($J = 6, 5, 4, 3, 2, 1,$ and 0) transitions (Figure 7), among which the $^5D_4 \rightarrow ^7F_5$ (called hypersensitive transition) is the strongest one owing to its large probability being both electric-dipole and magnetic-dipole induced transition. Moreover, as observed in the spectrum, no remarkable emission is observed in the 350-450 nm region (characteristic of ligand fluorescence), so it may be assumed that the ligand acts as an effective antenna for the terbium(III) centre.

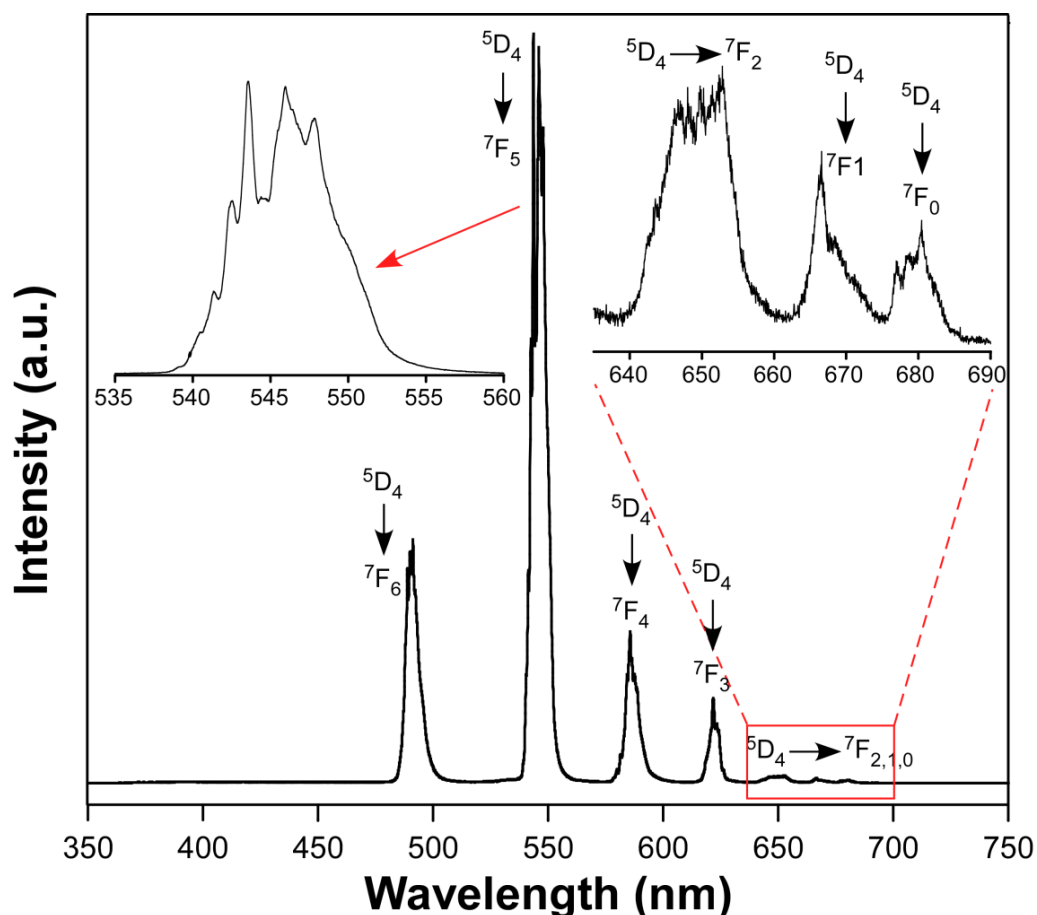


Figure 7. 10 K emission spectrum of compound **1** collected under excitation at 325 nm showing the characteristic transitions of the corresponding lanthanide (III) ion.

In the case of NIR emitters, the sensitization via ligands antenna effect is often more difficult to be achieved given the large energy difference between the excited levels of the ligands and the emissive levels of the lanthanide, which favours the occurrence of non-radiative processes to govern the deactivation process. Accordingly, the examples of NIR emitters based on CPs are somewhat scarce. As previously observed for other compounds based on amino substituted pyridinecarboxylate, these ligands have proven an effective UV light absorption capacity, so they could behave as sensitizers for lanthanide emission. In fact, as depicted in Figure 8, compounds **2** and **3** exhibit intense characteristic emission when the polycrystalline samples are excited at monochromatic 325 nm laser irradiation. In the emission spectrum of compound **2**, the very narrow band centred at 1542 nm shows a quite symmetric profile in which a fine-structure may be distinguished. These emission maxima are attributed to the $^4I_{13/2} \rightarrow ^4I_{15/2}$ transition of the intraionic levels of the Er^{III} ion, which are of particular interest in the field of amplification since 1540 nm is an appropriate wavelength in the third telecommunication window. When ampy ligand is introduced to sensitize Yb^{III} ion, the emission spectrum of **3** exhibits the characteristic emission bands sited around 980 nm assigned to the $^2F_{5/2} \rightarrow ^2F_{7/2}$ transition. It is worth mentioning that this emission is not a single sharp line but, in addition to the most intense one at 983 nm, it consists of an envelope of bands peaking at 975, 1004 and 1032 nm. The occurrence of those bands seems to correspond to the crystal-field splitting at the emitting and/or fundamental states as a consequence of the growth of the crystalline complex.

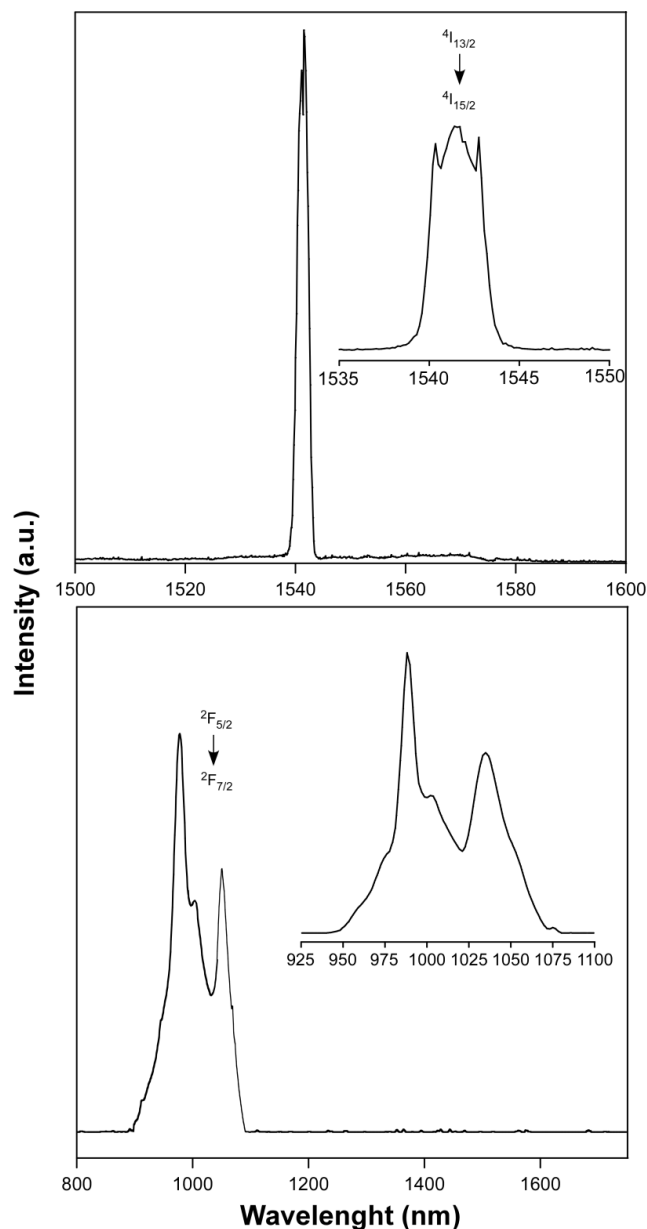


Figure 8. 10 K emission spectra of compounds **2** and **3** collected under excitation at 325 nm showing the characteristic transitions of the corresponding lanthanide(III) ion.

3.3. Magnetic Measurements

Dynamic alternating current (*ac*) magnetic measurements showed that in the absence of an external field none of these complexes exhibit frequency dependence of the out-of-phase susceptibility signals, which could be due to the lack of slow relaxation of magnetization or to the presence of quantum tunnelling of magnetization (QTM). When a small external *dc* field of 1000 Oe was applied to suppress QTM, the Er (**2**) counterpart showed slight frequency dependent signals

(Figure 9a), whereas the Yb compound (**3**) showed characteristic signals of SMM behaviour with maxima below 6 K (Figure 9b). The fact that the terbium based compound does not show slow magnetic relaxation in contrast to isostructural Er and Yb counterparts is not surprising, but it could be attributed to the different shape of the electron density of the employed lanthanide(III) ions. In particular, Tb(III) presents an oblate density whereas Er(III) and Yb(III) ions show a prolate distribution, which fits better the coordination environment described in **1-3**.²²

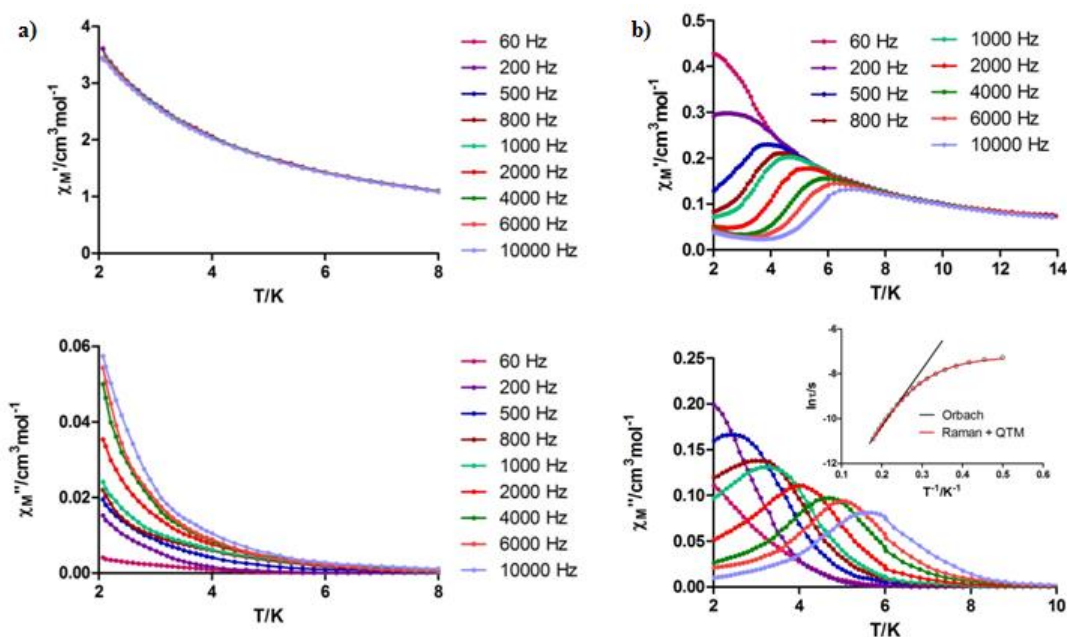


Figure 9. a) Temperature dependence of in-phase (top) and out-of-phase (bottom) components of the ac susceptibility measured under 1000 Oe applied dc field for **2**. b) Temperature dependence of in-phase (top) and out-of-phase (bottom) components of the ac susceptibility measured under 1000 Oe applied dc field for **3**. Inset: Arrhenius plots for the relaxation times. The black and red lines correspond to the best fits to Orbach and Raman + QTM processes, respectively.

However, the applied *dc* field of 1000 Oe is not enough to completely suppress the QTM for the Yb compound, as both χ_M' and χ_M'' components of the *ac* signals of the highest frequencies do not go to zero below the maxima at low temperature. The Cole-Cole plots (Figure 10), with α values in the 0.10(2 K)-0.03(5.4 K) range, also suggest the existence of multiple relaxation processes at least at the lowest temperatures.

The Arrhenius plot of the relaxation times affords U_{eff} and τ_0 values of 25 K and 2.2×10^{-7} s, respectively, for the Orbach process (Figure 9, inset). The obtained energy barrier is much lower than the energy gap between the ground and first excited states extracted from the photoluminescence spectra (Figure 8), which is of 120 K. This value is obtained from the position of the first two bands in the spectra (975 and 983 nm), as these bands are related to the emissions from the $^2F_{5/2}$ multiplet to the ground and first excited states of the $^2F_{7/2}$ multiplet. The differences between U_{eff} and the energy gap, together with the deviation of the relaxation times from linearity, clearly suggest the presence of additional relaxation mechanisms in this compound.

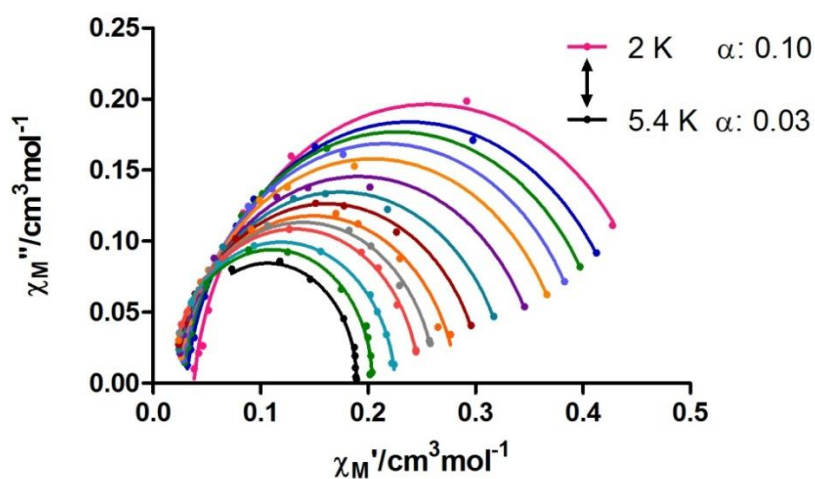


Figure 10. Cole-Cole plots for Yb Compound.

As for the most part of the Yb complexes Raman relaxation processes have been proposed²³, the relaxation times were fitted to $\tau^{-1} = \tau_{QTM}^{-1} + bT^n$, which includes contributions from Raman and QTM mechanisms (Figure 9, inset). The best fitting parameters were $b = 3.7$, $n = 5.5$ and $\tau_{QTM} = 7.4 \times 10^{-4}$ s. Although $n = 9$ is expected for Kramer's ions, depending on the structure of the levels n values between 1 and 6 can be considered as reasonable.²⁴ The excellent fit of the relaxation times to a combination of Raman and QTM processes suggests that the spin-lattice relaxation takes place through an optical-acoustic Raman-like process, instead of through a

thermally activated Orbach-like process. These results are in good agreement with the behavior observed in other Yb compounds reported by our group.²⁵

3.4. Potential Antiproliferative Activities

The results showed that compound **1** does not display cytotoxicity at any assayed conditions, in any cells lines. Compounds **2** and **3** showed relatively cytotoxicity in HT29 and Hep-G2 cells (not in B16-F10 cells) with IC₅₀ data range between 110 to 228 µg/mL, IC₂₀ data between 37 to 108 µg/mL, and IC₈₀ data between 123 to 353 µg/mL (Figure 11). Only Cu-complex was cytotoxic in all three cell lines assayed with IC₅₀ data between 38 to 62 µg/mL, IC₂₀ data between 18 to 51 µg/mL, and IC₈₀ between 65 to 81 µg/mL (Figure 11).

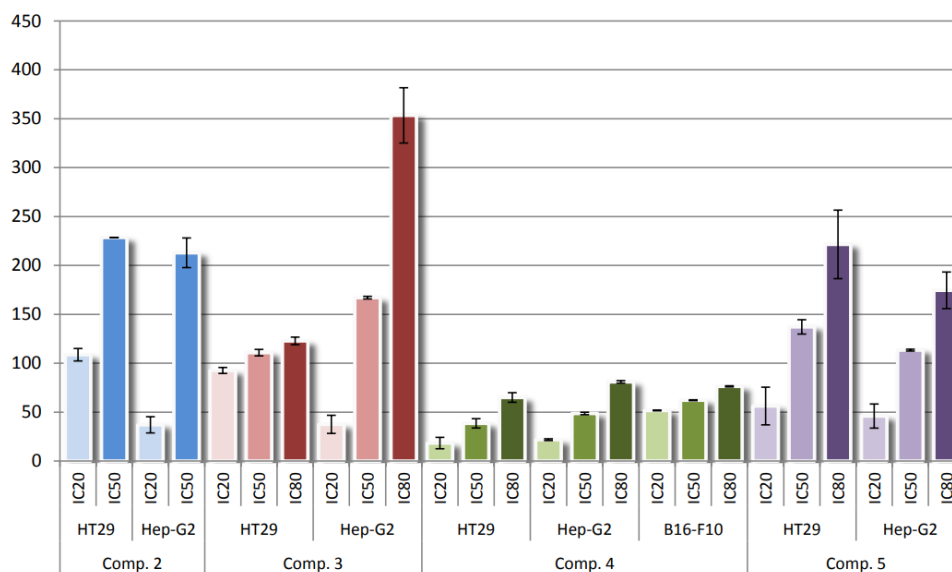


Figure 11. Growth-inhibitory effects (IC₂₀, IC₅₀, and IC₈₀, µg/mL) of compounds **2**, **3**, **4**, and **5** on the three cancer cell lines.

The effectiveness showed for these coordination complexes in the three cell lines assayed was similar in HT29 and Hep-G2 cell lines with cytotoxic effects for all compounds except for compound **1**. On the other hand, in B16-F10 melanoma cells any compounds assayed showed cytotoxicity but for compound **4** (Figure 12).

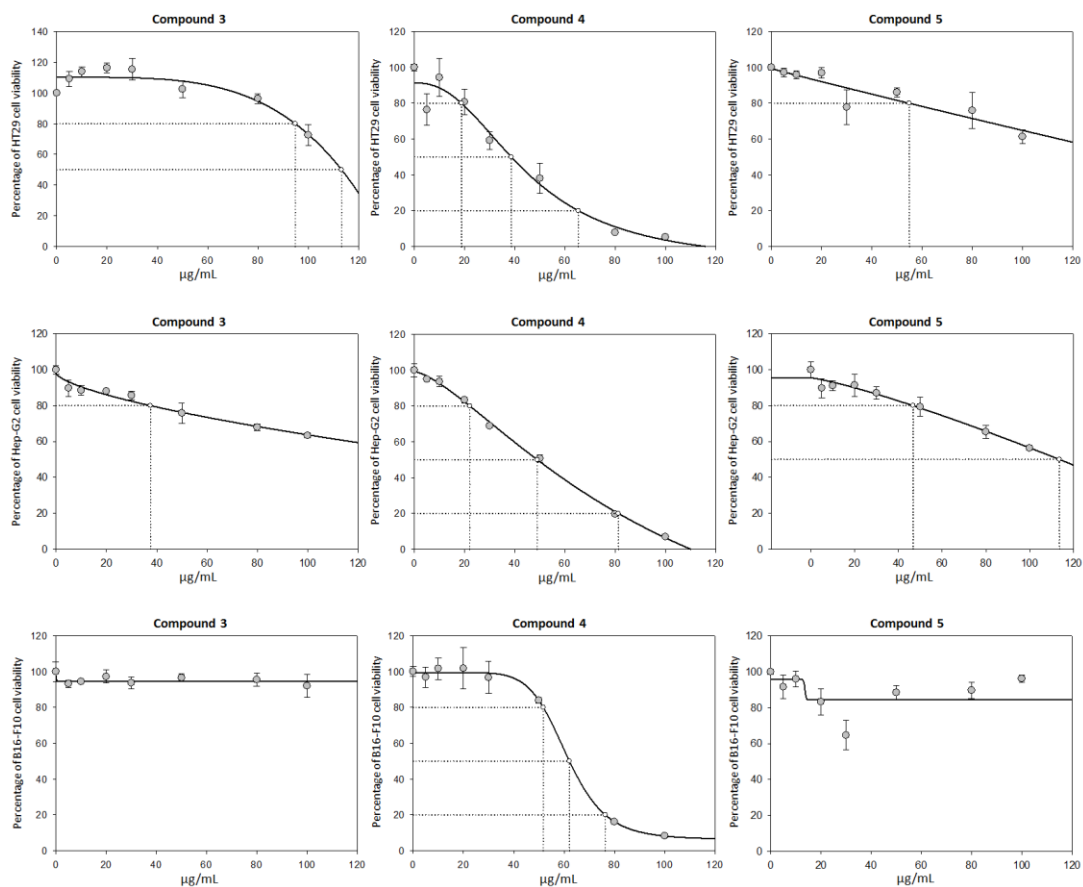


Figure 12. Effects of compounds **3**, **4** and **5**, on the viability of B16-F10, HT29, and Hep-G2 cancer cells, after treatment with the compounds for 72h in a range of 0 to 100 µg/mL, each point represents the mean value \pm SD of at least two independent experiments performed in triplicate.

The best results were obtained for compound **4** with the lowest IC₅₀ values, especially in HT29, with IC₅₀ values between 2.3 to 5.9 fold lower than the compounds **2**, **3**, and **5**, in both HT29 and Hep-G2 cells. In HT29 cell line, compound **4** displays cytotoxicity at lower concentrations than compounds **2**, **3** and **5**, whereas in Hep-G2 cells the onset of the cytotoxic effect were similar for all compounds (except **1**), with concentrations closed 35µg/mL (see IC₂₀ values, Table 3). The highest cytotoxic effect was reached before for the compound **4**, in both HT29 and Hep-G2 cells, with a concentration around 70 µg/mL, being between 1.9 to 4.3 fold lower than the rest of compounds (see IC₈₀ values, Table 3).

Table 3. Growth-inhibitory effects of compounds **1-5** on the three cancer cell lines.

Cell line	Comp. #	IC ₂₀	IC ₅₀	IC ₈₀
HT29	1	N/A	N/A	N/A
	2	108,75 ± 6,37	228,64 ± 0,00	N/A
	3	92,66 ± 3,06	110,86 ± 3,33	122,88 ± 3,90
	4	18,44 ± 5,84	38,57 ± 4,77	65,03 ± 4,90
	5	56,30 ± 19,27	137,21 ± 7,33	221,56 ± 35,03
Hep-G2	1	N/A	N/A	N/A
	2	37,08 ± 8,29	212,97 ± 15,14	N/A
	3	37,55 ± 9,25	167,10 ± 1,34	353,44 ± 28,27
	4	21,89 ± 0,88	48,68 ± 1,26	80,96 ± 1,28
	5	46,03 ± 12,34	113,44 ± 0,96	174,61 ± 18,69
B16-F10	1	N/A	N/A	N/A
	2	N/A	N/A	N/A
	3	N/A	N/A	N/A
	4	51,72 ± 0,31	62,22 ± 0,45	76,40 ± 0,58
	5	N/A	N/A	N/A

In general terms, we found that the complexes with lower IC₅₀ were the materials **4** and **5** with respect to MOC complexes, with Co²⁺ and Cu²⁺ ions. MOC complexes showed a moderate cytotoxicity, with similar results for complexes with Yb³⁺ and Er³⁺ metals, in both HT29 and Hep-G2 cells. Nevertheless, no cytotoxicity results were found for the Tb³⁺-MOC complex. With respect to cell lines only Cobalt compound produced cytotoxicity in B16-F10 murine melanoma cell line, the rest of compounds did not produce any effects on this cell line.

The fact of the relatively low cytotoxicity of several of these compounds is not a handicap, because these compounds could be used as *in vivo* biological probes, with the option to activate or increase its cytotoxicity in response to external magnetic field¹³. Future studies will be necessary to confirm this point. To determine the organism distribution of the compounds thinking of them as biological probes, the incident radiation must be able to penetrate the tissues to reach the chromophore, which rules UV light and part of visible spectrum²⁶. Therefore it is desirable to

design NIR-luminescent lanthanide complexes that produce luminescence after absorption of light at longer wavelengths. As consequence of the biological compartment of this type of compounds, which show clearly cytotoxicity in two of the three cancer cell lines assayed, that can be modulated externally with a magnetic field, and have intrinsic luminescent properties. These compounds could afford important and effective new tools for potential treatment from cancer, although more depth studies will be necessary to characterize completely its possible use as anti-cancer compounds.

4. Conclusions

We have succeeded in the design, synthesis, and characterization of the physical properties of a new family of coordination polymers based on terbium, erbium, ytterbium, cobalt and copper with the interesting 5-aminopyridine-2-carboxylic acid ligand. These lanthanide coordination polymers show isostructural 1D-structures and display intense photoluminescence properties in the solid state that have been fully characterized. The erbium material displays slightly frequency-dependent out-of-phase signals, whereas the ytterbium compound presents slow magnetic relaxation that proceeds through various relaxation mechanisms. The absence of magnet behaviour in the terbium-based compound seems to be related with its oblate shape, in contrast to the prolate shape of other lanthanides. The luminescence signal and potential magnetic properties of the compounds instigate their utility as multifunctional materials. On the other hand, the anti-cancer properties of these materials have been measured by MTT which show, in general, lanthanide compounds are not very active, while cobalt material **4** shows the lowest IC₅₀ values, especially in HT29, with IC₅₀ values between 2.3 to 5.9 fold all of them lower that values showed by compounds **2**, **3**, and **5**, in both HT29 and Hep-G2 cells, whereas in Hep-G2 cells the onset of the cytotoxic effect were similar for all compounds. In conclusion, this new family of compounds could suppose important and effective new tools for potential treatment from cancer, although more depth studies will be necessary to improve its possible use as anti-cancer drugs.

5. References

- 1 M.N. Leuenberger, D. Loss, *Nature* 410 (2001) 789-793.
- 2 S. Sanvito, *Chem. Soc. Rev.* 40 (2011) 3336-3355.
- 3 O.K. Farha, A.O. Yazaydin, I. Eryazici, C.D. Malliakas, B.D. Hauser, M.G. Kanatzidis, S.T. Nguyen, R.Q. Snurr, J.T. Hupp, *Nat. Chem.* 2 (2010) 944-948.
- 4 H.-Y. Li, Y.-L. Wei, X.-Y. Dong, S.-Q. Zang, T.C.W. Mak, *Chem. Mater.* 27 (2015) 1327-1334.
- 5 S. Biswas, H.S. Jena, S. Goswami, S. Sanda, S. Konar, *Cryst. Growth Des.* 14 (2014) 1287-1295.
- 6 P.-F. Shi, B. Zhao, G. Xiong, Y.-L. Hou, P. Cheng, *Chem. Commun.* 48 (2012) 8231-8232.
- 7 J.J. Baldov, E. Coronado, A. Gaita-Ariño, C. Gamer, M. Giménez-Marqués, G. Mínguez-Espallargas, *Chem. Eur. J.* 20 (2014) 10695-10702.
- 8 a) S. Rojas, A. Arenas-Vivo, P. Horcajada, *Coord. Chem. Rev.* 388 (2019) 202-226. b) M. Gimenez-Marques, T. Hidalgo, C. Serre, P. Horcajada, *Coord. Chem. Rev.* 307 (2016) 342-360.
- 9 K.J. Haxton, H.M. Burt, *J. Pharm. Sci.* 98 (2009) 2299-2316.
- 10 J. Ruiz, A.J. Mota, A. Rodríguez-Diéguez, S. Titos, J.M. Herrera, E. Ruiz, E. Cremades, J. Pierre Costes, E. Colacio, *Chem. Commun.* 48 (2012) 7916-7918.
- 11 a) A.J. Calahorro, I. Oyarzabal, B. Fernández, J.M. Seco, T. Tian, D. Fairen-Jimenez, E. Colacio, A. Rodríguez-Diéguez, *Dalton Trans.* 45 (2016) 591-598. b) I. Oyarzabal, B. Fernández, J. Cepeda, S. Gómez-Ruiz, A.J. Calahorro, J.M. Seco, A. Rodríguez-Diéguez, *CrystEngComm.* 18 (2016) 3055-3063. c) A.A. García-Valdivia, J.M. Seco, J. Cepeda, A. Rodríguez-Diéguez, *Inorg. Chem.* 56 (2017) 13897-13912.

12 B. Fernandez, I. Oyarzabal, E. Fischer-Fodor, S. Macavei, I. Sanchez, J.M. Seco, S. Gomez-Ruiz, A. Rodriguez-Dieguez, *CrystEngComm*. 18 (2016) 8718-8721.

13 A. Mayer, S. Neuenhofer, *Angew. Chem. Int. Edit.* 33 (1994) 1044-1072.

14 B. Fernández, I. Fernández, J. Cepeda, M. Medina-O'Donnell, E.E. Rufino-Palomares, A. Raya-Barón, S. Gómez-Ruiz, A. Pérez-Jiménez, J. Antonio Lupiáñez, F.J. Reyes-Zurita, A. Rodríguez-Diéguez, *Cryst. Growth Des.* 18 (2018) 969–978.

15 a) E.E. Rufino-Palomares, A. Perez-Jimenez, F.J. Reyes-Zurita, L. Garcia-Salguero, K. Mokhtari, A. Herrera-Merchan, P.P. Medina, J. Peragon, J.A. Lupianez, *Curr. Org. Chem.* 19 (2015) 919-947. b) M. Medina-O'Donnell, F. Rivas, F.J. Reyes-Zurita, A. Martinez, S. Martin-Fonseca, A. Garcia-Granados, R.M. Ferrer-Martin, J.A. Lupianez, A. Parra, *Eur. J. Med. Chem.* 118 (2016) 64-78.

16 B. Fernández, A. Gómez-Vílchez, C. Sánchez-González, J. Bayón, E. San Sebastián, S. Gómez-Ruiz, C. López-Chaves, P. Aranda, J. Llopis, A. Rodríguez-Diéguez, *New J. Chem.* 40 (2016) 5387-5393.

17 L. Krause, R. Herbst-Irmer, G.M. Sheldrick, D. Stalke, *J. Appl. Cryst.* 48 (2015) 3-10.

18 G.M. Sheldrick, *Acta Cryst. A* 64 (2008) 112–122.

19 O.V. Dolomanov, L.J. Bourhis, R.J. Gildea, J.A.K. Howard, H. Puschmann, *J. Appl. Cryst.* 42 (2009) 339–341.

20 A.L. Spek, *Acta Cryst. D* 65 (2009) 148-155.

21 D. Josse, W.H. Xie, P. Masson, L.M. Schopfer, O. Lockridge, *Chem.-Biol. Interact.* 119 (1999) 79-84.

22 a) A. Gorzynski, D. Marcinkowski, M. Kubicki, M. Loffler, M. Korabik, M. Karbowski, P. Wisniewski, C. Rudowicz, V. Patroniak, *Inorg. Chem. Front.* 5 (2018) 605-618. b) K.R. Vignesh, S.K. Langley, A. Swain, B. Moubaraki, M. Damjanovic, W. Wernsdorfer, G. Rajaraman, K.S. Murray, *Angew. Chem. Int. Ed.* 57 (2018) 779-784.

23 J. Ruiz, G. Lorusso, M. Evangelisti, E.K. Brechin, S.J. Pope, E. Colacio, *Inorg. Chem.* 53 (2014) 3586-3594.

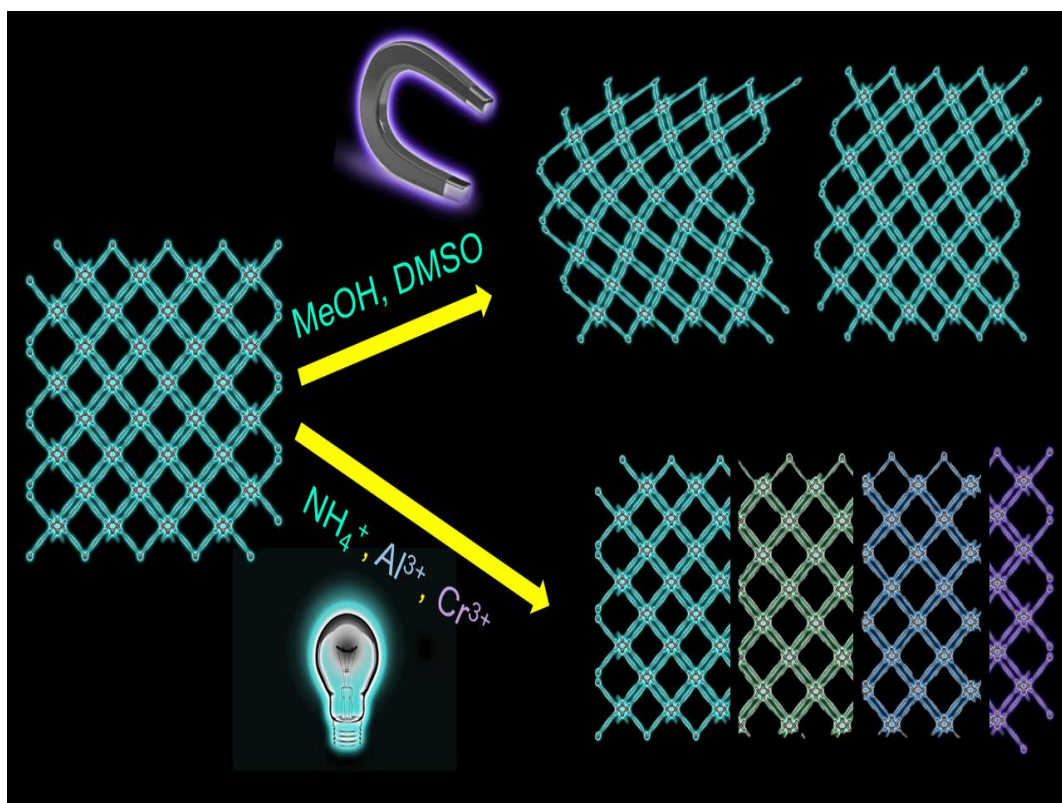
24 K.N. Shirivastava, *Phys. Status Solidi B* 117 (1983) 437-441.

25 a) I. Oyarzabal, B. Artetxe, A. Rodríguez-Diéguez, J.A. García, J.M. Seco, E. Colacio, *Dalton Trans.* 45 (2016) 9712-9726. b) A. Zabala, J. Cepeda, I. Oyarzabal, A. Rodriguez-Dieguez, J.A. Garcia, J.M. Seco, E. Colacio, *CrystEngComm.* 19 (2017) 256-264.

26 N.M. Shavaleev, G. Accorsi, D. Virgili, Z.R. Bell, T. Lazarides, G. Calogero, N. Armaroli, M.D. Ward, *Inorg. Chem.* 44 (2005) 61-72.

Capítulo 4

Magnetic and Photoluminescent Sensors Based on Metal-Organic Frameworks Built up from 2- aminoisonicotinate



Magnetic and Photoluminescent Sensors Based on Metal-Organic Frameworks Built up from 2-aminoisonicotinate

SCIENTIFIC
REPORTS
nature research



OPEN

Magnetic and Photoluminescent Sensors Based on Metal-Organic Frameworks Built up from 2-aminoisonicotinate

Antonio A. García-Valdivia¹, Sonia Pérez-Yáñez², Jose A. García³, Belén Fernández⁴, Javier Cepeda⁵ & Antonio Rodríguez-Diéguez¹

Abstract

In this work, three isostructural metal-organic frameworks based on first row transition metal ions and 2-aminoisonicotinate (2ain) ligands, namely, $\{[M(\mu\text{-}2\text{ain})_2]\cdot\text{DMF}\}_n$ [$M^{\text{II}} = \text{Co}$ (**1**), Ni (**2**), Zn (**3**)], are evaluated for their sensing capacity of various solvents and metal ions by monitoring the modulation of their magnetic and photoluminescence properties. The crystal structure consists of an open diamond-like topological 3D framework that leaves huge voids, which allows crystallizing two-fold interpenetrated architecture that still retains large porosity. Magnetic measurements performed on **1** reveal the occurrence of field-induced spin-glass behaviour characterized by a frequency-independent relaxation. Solvent-exchange experiments lead successfully to the replacement of lattice molecules by DMSO and MeOH, which, on its part, show dominating SIM behaviour with low blocking temperatures but substantially high energy barrier for the reversal of magnetization. Photoluminescence studies at variable temperature on compound **3** show its capacity to provide bright blue emission under UV excitation, which proceeds through a ligand-centred charge transfer mechanism as confirmed by time-

dependent DFT calculations. Turn off and/or shift of the emission is observed for suspensions of 3 in different solvents and aqueous solutions containing metal ions.

1. Introduction

The multifunctionalization of metal-organic frameworks (MOFs) has recently become one of the main research strategies of inorganic and materials chemistry to guide the construction of materials with sensing capacities.^{1,2,3} This is a consequence of the capacity of these materials to allow for multiple physical properties which may coexist or even cooperate in a synergistic way.^{4,5} As it is well known, MOFs are a class of potentially porous materials comprised of single metal ions or metal ion clusters linked one another by organic ligands to give an extended crystalline architecture.^{6,7,8} The variety of metal ions and organic ligands opens up an infinite number of possible combinations which allow designing MOFs almost a will in such a way that their structure responds as best as possible to a particular commitment.^{9,10,11,12,13,14,15} In particular, the rapid detection of toxic species in environmental and ecological systems is gaining increasing interest because of the large overlap between residential and surrounding industrial areas, which already causes many diseases in human being and tends to be expanded in near future.¹⁶ For instance, various salts containing Fe^{3+} and Cu^{2+} ions, usually employed in industry and, in spite of the control measures, large amounts of such metals are unfortunately still found damaging the ecosystems of rivers and streams.¹⁷ The same applies for some common solvents referred to as volatile organic compounds (VOCs) that are substantially toxic air and water pollutants and cause severe environmental problems.¹⁸ In this regard, MOFs are good candidates to drive the detection of all above mentioned molecules in liquid media owing to their specific functions bearing on the surface of the pores, since they are known to show strong interactions able to provide a reversible load/unload on the material and, hence, a significant change in a property.^{19,20}

Focusing on the sensor activity of the MOFs, the transduction mechanism by which the material manifests a change in a property when the target analyte is uploaded is undoubtedly a key point. Most of the systems studied so far are based on

luminescence detection because, making use of the changes (increase/decrease on the intensity or shift of the emission signal) in the photoluminescence (PL) of a probe MOF provoked by the presence of the analyte, is very desired for its relative ease of use, technical simplicity and broad adaptability.²¹ Moreover, PL in MOFs can have multiple origins which proceed through a complex electronic excitation/emission scenario in which different parts of the hybrid structure are involved: ligand centred (LC) and metal centred (MC) luminescence, charge transfers (CT) processes with different electron pathways, such as ligand-to-ligand (LLCT), ligand-to-metal (LMCT), metal-to-ligand (MLCT), or even guest molecules centred (GC) charge transfers.²² To that end, a promising strategy argues for the use of organic ligands with strong absorption (usually aromatic molecules with functionalities containing heteroatoms with lone-pairs) combined with metal ions with closed-shell electronic configuration, which avoid non-radiative quenching.^{23,24} Although comparatively less explored than PL sensing, a magnetic response dependent on different guest molecules, that is the change of the magnetic molecular properties of the MOF as a consequence of the analyte loaded in the voids, is an already plausible alternative despite the more complex technical requirements implied.²⁵ MOFs behaving as single-molecule magnets (SMMs) below a blocking temperature (T_B) consist of isolated spin carriers with large magnetic anisotropy which present no (or negligible) magnetic ordering by means of weak intermetallic exchange interactions.^{26,27,28} For transition metals, spin-reversal barrier that promotes slow magnetic relaxation is $U = |D| (S^2 - 1/4)$, where D and S stand for the ground state half-integer spin and axial parameter of the zero-field splitting (zfs). That is the reason why cobalt(II) systems, with not only high and non-integer ground state ($S = 3/2$) which reduces the probability of the quantum tunnelling of magnetization (QTM) but also large magnetic anisotropy, have been most widely studied during the last years.^{29,30,31}

In our continuous quest for metal-organic materials showing enhanced PL and magnetic properties, such as those recently reported based on aminonicotinic ligands,^{32,33,34} we are now giving a step forward and combining one of the latter properties with the porosity afforded by the family of isostructural MOFs of $\{[M(\mu\text{-}2\text{ain})_2]\cdot\text{DMF}\}_n$ (where $M^{\text{II}} = \text{Co}, \text{Ni}$ and Zn and $2\text{ain} = 2\text{-aminoisonicotinate}$) formulae. In particular, given that the porous nature of these materials was already confirmed by gas adsorption capacity and the fact that in those previous reports these

MOFs crystallized with different solvents occupying the voids,³⁵ magnetic behavior of the cobalt(II) counterpart and PL performance of the zinc(II) counterpart have been deeply analysed, focusing on their modulation by solvent-exchange experiments and/or capture of metal ions.

2. Results and Discussion

2.1. Structural description of $\{[M(\mu\text{-}2\text{ain})_2]\cdot\text{DMF}\}_n$ [$M^{\text{II}} = \text{Co (1), Ni (2), Zn (3)}$]

Title compounds are isostructural and crystallize in the orthorhombic *Fddd* space group so their structure will be described using compound **2** as a reference. The crystal structure consists of an entangled 3D open framework. Ni1 exhibits a N_2O_4 donor set exerted by its coordination to four symmetry related 2ain ligands by means of two pyridine nitrogen and four carboxylate oxygen atoms (Table 1 and Figure 1).

Table 1. Selected bond lengths for compound **2**.

Compound 1					
Co1–N1A	2.073(1)	Co1–O71A(v)	2.314(1)	Co1–O72A(v)	2.060(1)
Co1–N1A(iv)	2.073(1)	Co1–O71A(vi)	2.314(1)	Co1–O72A(vi)	2.060(1)
Compound 2					
Ni1–N1A	2.060(1)	Ni1–O71A(ii)	2.075(1)	Ni1–O72A(ii)	2.178(1)
Ni1–N1A(i)	2.060(1)	Ni1–O71A(iii)	2.075(1)	Ni1–O72A(iii)	2.178(1)
Compound 3					
Zn1–N1A	2.063(1)	Zn1–O71A(v)	2.034(1)	Zn1–O72A(v)	2.472(1)
Zn1–N1A(iv)	2.063(1)	Zn1–O71A(vi)	2.034(1)	Zn1–O72A(vi)	2.472(1)

Symmetries: (i) = $-x - 1/4, y, -z + 3/4$; (ii) = $x + 1/4, y + 1/4, -z + 1$; (iii) = $-x - 1/2, y + 7/4, z - 1/4$; (iv) = $-x + 5/4, y, -z + 1/4$; (v) = $x + 7/4, y + 7/4, -z$; (vi) = $-x, y + 7/4, z + 7/4$.

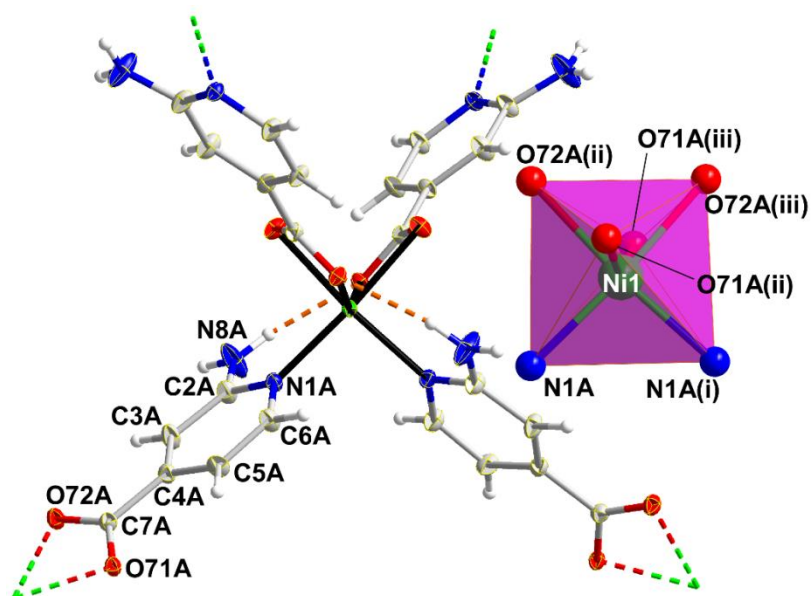


Figure 1. Fragment of crystal structure of compound **2** showing labelling mode and the distorted octahedral coordination environment. Connectivity of the structure is inferred by dashed double-colour lines whereas dashed orange lines stand for hydrogen bonds.

Given that the latter establish two four-member chelating rings with the metal centre, the resulting coordination polyhedron is severely distorted with regard to a perfect octahedron ($S_{OC} = 3.43$). It must be highlighted that bond distances are clearly more irregular in the coordination shell of compounds **1** and **3**, which translates into more distorted octahedra ($S_{OC} = 4.41$ and 4.96 for **1** and **3**, respectively; Figure 2).

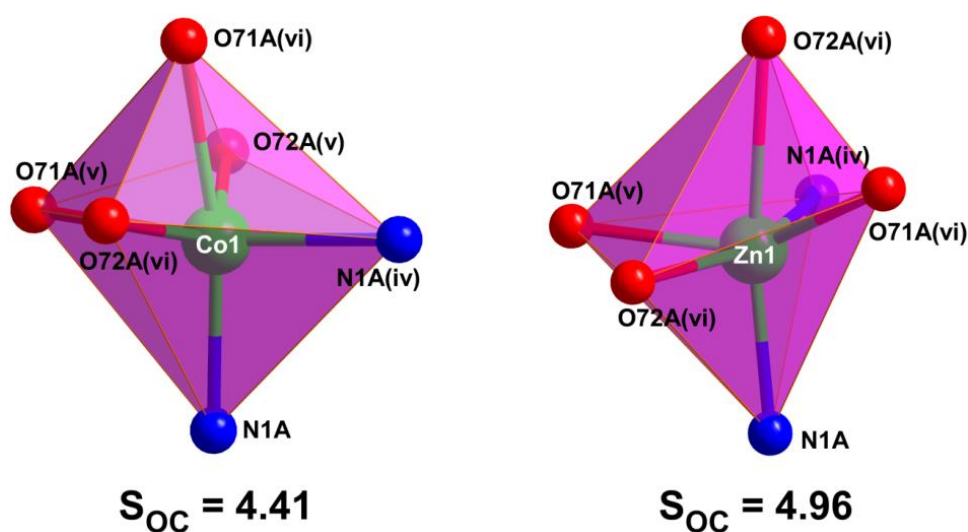


Figure 2. Coordination polyhedra of compounds **1** and **3**.

2ain anions acquire the $\mu\text{-}\kappa\text{N1A}:\kappa^2\text{O71A}, \text{O72A}$ bridging mode in such a way that the central Ni1 atom is connected to four neighbouring ones at a distance of *ca.* 8.77 Å. This coordination mode makes the ligands be somewhat twisted by breaking the planarity of the carboxylate group with respect to the aromatic ring (significantly rotated with an angle of *ca.* 15.9°), which, in turn, gives rise to a tetrahedral building unit from the topological point of view. This arrangement is supported by strong N–H···O hydrogen bonds established among amino and carboxylate groups of 2ain ligands. The junction of building units leads to an open 3D framework of **dia** topological class and (6⁶) point symbol^{36,37} which contains very large cavities where a sphere of 8 Å fits in within (Figure 3a). Nonetheless, the occurrence of such a large free volume allows the crystallization of an identical subnet, which drops the porosity of the eventual doubly-interpenetrated framework to a 36.1% of the unit cell volume (Figure 3b).

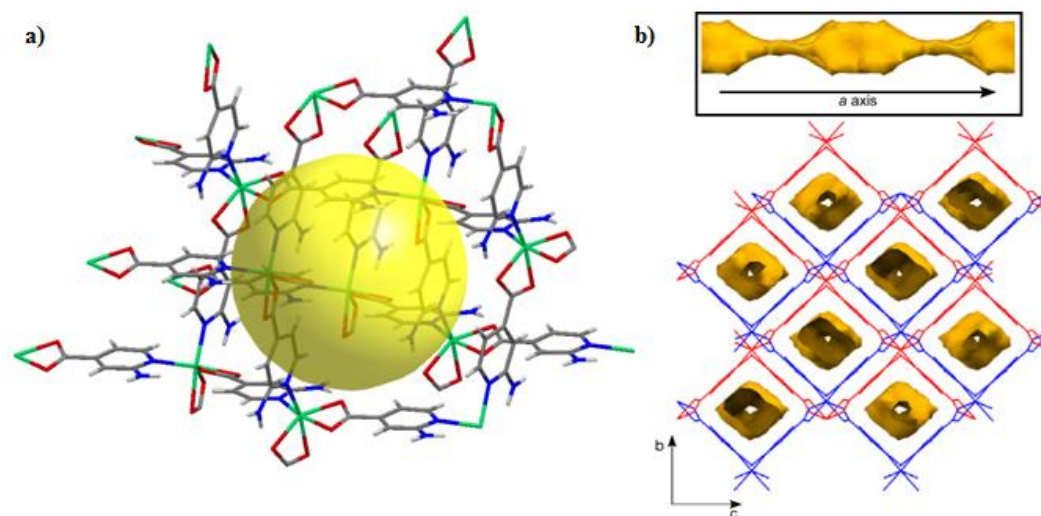


Figure 3. a) Fragment of the structure of compound **2** showing the potential void (sphere of *ca.* 8 Å diameter) left by the crystallization of one subnet. b) Crystal packing of compound **2** showing the two-fold interpenetrated structure and the microchannels.

Both subnets are mutually sustained by means of hydrogen bonding interactions among the exocyclic amino and carboxylate groups belonging to different subnets (Table 2 and Figure 4).

Table 2. Structural parameters (Å, °) of hydrogen bonds in compounds 1–3.^a

D–H···A ^b	D–H	H···A	D···A	D–H···A
Compound 1				
N8A–H81A···O72A(vii)	0.86	2.13	2.963(2)	162.2
N8A–H81A···O71A(viii)	0.86	2.19	2.948(2)	146.9
Compound 2				
N8A–H81A···O71A(ix)	0.86	2.08	2.908(2)	161.2
N8A–H81A···O72A(x)	0.86	2.20	2.973(2)	148.9
Compound 3				
N8A–H81A···O72A(xi)	0.86	2.18	2.961(2)	151.6
N8A–H81A···O72A(xii)	0.86	2.20	3.026(2)	161.6

^aSymmetrycodes: (vii) = $-x, y + 1/4, z + 1/4$; (viii) = $-x - 1/2, -y + 1/2, -z$; (ix) = $-x - 1/2, y + 1/4, z - 1/4$; (x) = $-x + 1/2, -y + 1/2, -z$; (xi) = $-x + 1, y + 1/4, z + 1/4$. ^bD: donor. A: acceptor.

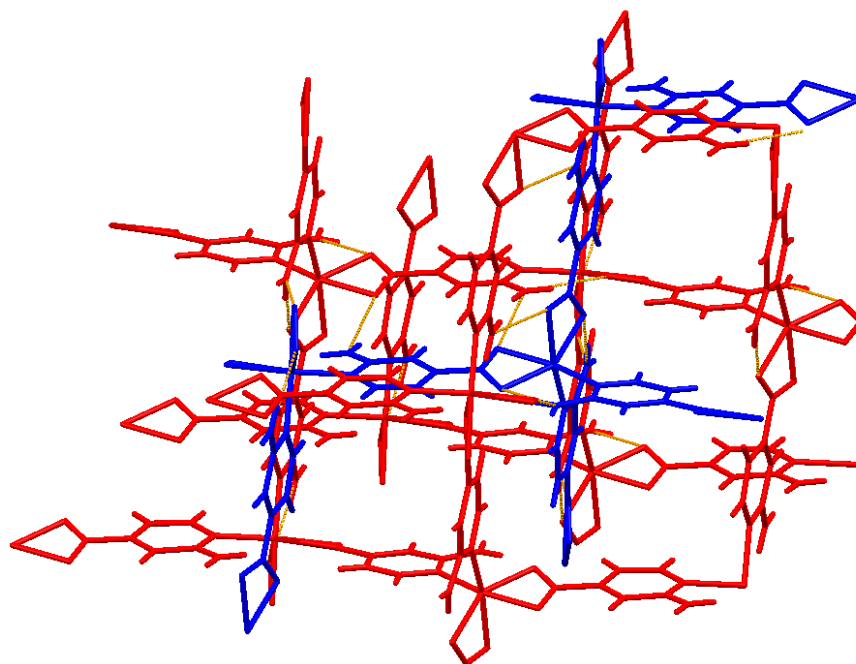


Figure 4. Interpenetration found in compound 2 showing the hydrogen bonding interactions (dashed orange lines) sustaining the overall framework.

These supramolecular interactions allows for the occurrence of a stable porous system which consists of narrow microchannels running along the crystallographic *a* axis. Despite the large disorder affecting the lattice solvent molecules occupying the voids, TGA/DTA and SQUEEZE routine results confirm that the content of the voids may be determined as one DMF molecule per formula

unit. These MOFs contains lattice solvent molecules that crystallize in a highly disordered arrangement, which prevents one determining the exact content during structure refinement stage. Accordingly, final refinement was performed with SQUEEZE routine and used to calculate the void space and the electron count. According to these results, and the fact that DMF was used as solvent without distillation, it was estimated that unit cell contain of the MOF contain voids of ca. 2500 Å³ (2460, 2431 and 2551 Å³ for compounds **1**, **2** and **3**) and ca. 550 electrons (542, 523 and 576 Å³ for compounds **1**, **2** and **3**). These data correspond to 16 DMF molecules (one DMF molecule per formula unit), which corresponds to 152–159 Å³ and 33–36 electrons per DMF, in good agreement with one DMF molecule (supposed to occupy around 150 Å³ and count on 40 electrons). Therefore, the formula for these MOFs may be estimated as $\{[M(\mu\text{-}2\text{ain})_2]\cdot\text{DMF}\}_n$.

TGA/DTA for Compounds **1–3** show a very similar thermal response owing to their isostructural nature. The MOFs adsorb some amount of water (around one water molecule per formula unit) as confirmed by both thermogravimetric and elemental analysis results. In this regard, the fact that water is lost at so low temperature (below 60 °C), is a clear evidence on the nature of water. This fact explains well the slight disagreement found when compared these results with the theoretical (crystallographic) formulae of the MOFs. TG curve of compound **1** (as a representative sample of the three MOFs) reveals that the loss of solvent (ca. one H₂O due to hydration of the MOFs and the lattice DMF molecule) takes place from room temperature up to 210 °C, released in two separate stages. The high temperature required to liberate the lattice DMF molecule seems to indicate that it is somewhat occluded in the pores of the MOF. Almost immediately to the loss of solvent, the framework starts to decompose following two strong exothermic processes to lead to Co₃O₄ as final residue at ca. 390 °C (Figure 5 and Table 3)

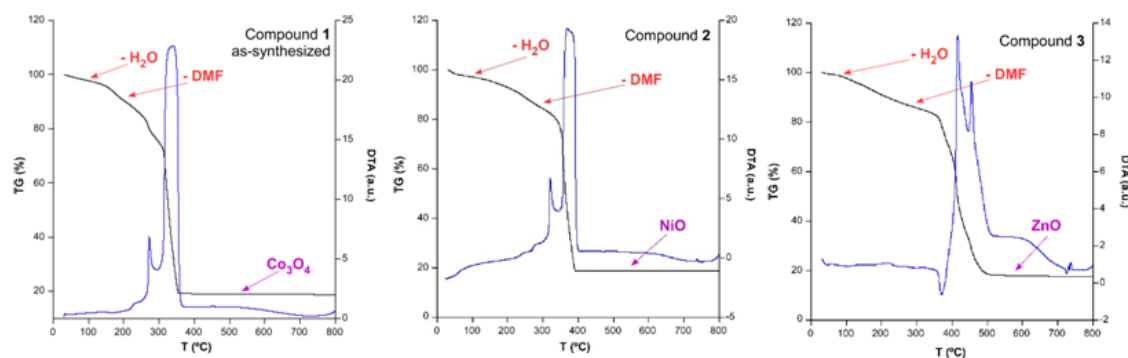


Figure 5. TG/DTA plot for compounds 1-3.

Table 3. TG/DTA and elemental analysis data for compounds 1–3.

C₁₅H₁₇CoN₅O₅ (compound 1) – hydrated		
Ti–Tf	ΣΔm(%)	ΣΔm(%)_{teor}
30–65	3.0	3.0 (–0.7 x H ₂ O)
60–280	20.9	21.3 (–1 x DMF)
280–370	81.4	81.1 (–2 x 2ain)
370–800		Remaining residue (1/3 Co ₃ O ₄)
C₁₅H₁₇N₅NiO₅ (compound 2) – hydrated		
Ti–Tf	ΣΔm(%)	ΣΔm(%)_{teor}
30–65	3.0	3.0 (–0.7 x H ₂ O)
60–315	18.9	20.0 (–1 x DMF)
315–390	81.9	82.3 (–2 x 2ain)
390–800		Remaining residue (NiO)
C₁₅H₁₇N₅O₅Zn (compound 3) – hydrated		
Ti–Tf	ΣΔm(%)	ΣΔm(%)_{teor}
30–70	2.3	2.3 (–0.6 x H ₂ O)
70–350	18.7	19.2 (–1 x DMF)
350–530	80.9	81.1 (–2 x 2ain)
530–800		Remaining residue (ZnO)

A further analysis of the compound by means of thermogravimetry shows that the release of solvent molecules does not bring any relevant structural change, as confirmed by the similar shape of the diffractograms recorded according to the increasing temperature.

2.2. Static magnetic properties

Variable temperature dependence of the magnetic susceptibility data were analysed in the 5–300 K range on polycrystalline samples of compounds **1** and **2**. Room temperature $\chi_M T$ product of **1** is $3.22 \text{ cm}^3 \text{ K mol}^{-1}$, which is significantly higher than that expected for a magnetically isolated spin triplet ($g = 2.01$) in octahedral coordination geometry ($1.87 \text{ cm}^3 \text{ K mol}^{-1}$). Upon cooling, $\chi_M T$ value experiments a slight and progressive decrease up to 50 K, below which it subtly drops off to reach $1.85 \text{ cm}^3 \text{ K mol}^{-1}$ at low temperature. This behaviour may be mainly attributed to the zero-field splitting (zfs) that may cause a high intrinsic magnetic anisotropy arising from the first order spin-orbit coupling (SOC) usually present in Co(II) atoms derived from its $^4T_{1g}$ ground state in high-spin octahedral geometry,^{38,39} though the occurrence of weak antiferromagnetic interactions cannot be discarded. Taking into account the absence of an appropriate mathematical expression to estimate the nature of the magnetic interactions for 3D networks containing cobalt(II) ions, the data were analysed with the Curie-Weiss law. Given the fact that compound **1** follows Curie–Weiss law in the whole temperature range, χ_M^{-1} vs T was fitted giving the results shown in Table 4. Moreover, the data were also fitted to the phenomenological equation proposed by Rueff and co-workers⁴⁰ (eq 1) in view of the SOC present, from which the antiferromagnetic exchange interactions were estimated:

$$\chi_M T = A \exp(-E_1/\kappa T) + B \exp(-E_2/\kappa T) \quad (\text{eq 1})$$

The fact that the sum of A and B parameters equals the Curie constant and the “activation energies” of SOC (E_1) and (E_2) exchange interactions (Table 3), which fall in the range of related Co(II) compounds,⁴¹ confirm the weak antiferromagnetic interactions may be claimed to occur among Co(II) ions in the 3D network.

Table 4. Best fitting results for compound **1**.

Compound 1							
Curie-Weiss law fitting ^[a]							
C	3.27		θ	-7.52 K			
Rueff phenomenological fitting (eq 1)							
A	0.93(4)	B	2.34(5)	E_1/κ	23(2)	$-E_2/\kappa$	-0.80(9)
Hamiltonian SOC (eq2) ^[b]							
λ	-110	σ	-1.12	Δ	188	g	2.10
Hamiltonian zfs (eq3) ^[c]							
g_x/g_y	2.36		g_z	3.26		D	-11.9

[a] Units: C constant and θ are given in $\text{cm}^3 \text{K mol}^{-1}$ and K, respectively. [b] λ and Δ parameters are expressed in cm^{-1} . [c] D parameter is given in cm^{-1} .

DFT calculations performed on a suitable model of compound **1** (Figure 6) give a value of the coupling constant (J) of -0.07 cm^{-1} , which concurs well with the mentioned negligible magnetic interactions.

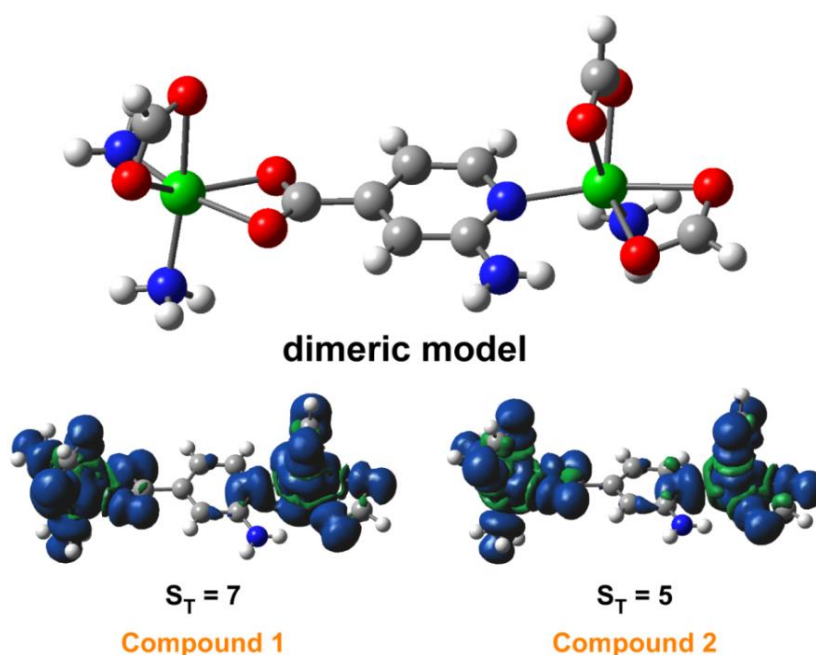


Figure 6. Model employed for calculation of J parameter and DFT high spin density distributions for models 1 and 2.

Calculations of the coupling constants through the broken symmetry strategy have been performed for compound **1** and **2** upon a suitable model based on a dimeric entity grown from crystallographic coordinates of X-ray crystal structure. Bridging and terminal ligands have been simplified replacing them by ammonia or formic acid.

Accordingly, cobalt(II) spin carriers may be considered to be isolated by the regular bridging ligands, bearing in mind that the shortest distance among them is of about 8.8 Å, thus allowing us to analyse the SOC effects by means of fitting of the magnetic susceptibility with the Hamiltonian given in equation 2:⁴²

$$\hat{H} = \sigma\lambda(L_{Co}S_{Co}) + \Delta[L_{z,Co}^2 - L_{Co}(L_{Co}+1)]/3 + \mu_B H \cdot (-\sigma L_{Co} + gS_{Co}) \quad (\text{eq 2})$$

Where all parameter have their usual meaning. The calculated curve using the PHI program⁴³ reproduces quite well the experimental one, though a slight deviation is found mainly for the high temperature data (Table 4 and Figure 7a).

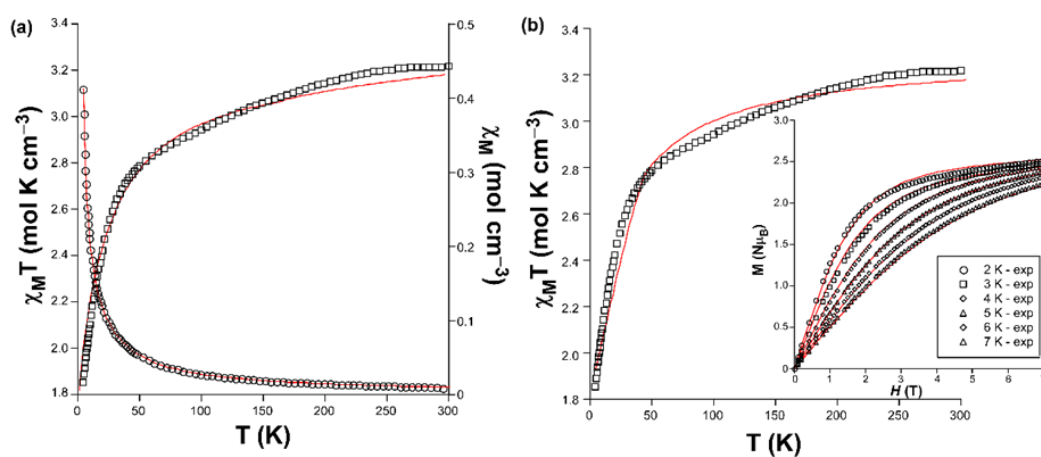


Figure 7. (a) χ_M and $\chi_M T$ vs T plots of **1** with best fit according to eq 2. (b) Simultaneous fitting of the $\chi_M T$ vs T and M vs H plots using eq 3.

Among the estimated parameters, it deserves to be mentioned the large and positive value of Δ , which suggests that only the two lowest Kramers doublets of the 4A_2 ground term are thermally populated, in turn meaning that the axial zfs within the quartet state matches well with the energy gap existing between them. Therefore, the

magnetic properties may be interpreted by means of the spin Hamiltonian of equation 3 (Figure 6b):

$$\hat{H} = D(\hat{S}_z^2 - \hat{S}^2/3) + E(\hat{S}_x^2 + \hat{S}_y^2) + \mu_B \bar{B} \cdot g \cdot \hat{S} \quad (\text{eq 3})$$

In which S is the spin of the ground state ($S = 3/2$), D and E are the axial and rhombic magnetic anisotropies, and H is the applied magnetic field. On its part, magnetization curves collected at several temperatures (2–7 K) under an applied field ranging from 0 to 7 T do not reach the theoretical saturation for $S = 3/2$ ($M_{\text{sat}} = 3.3$, with $g = 2.2$), but they show a value of ca. 2.45 $N\mu_B$ at 2 K. This behaviour together with the fact that isothermal curves do not collapse in a single master curve are indicative of magnetic anisotropy. A simultaneous fitting of susceptibility and magnetization data with PHI using eq 3 gives $D = -16.1 \text{ cm}^{-1}$, $E = -0.1 \text{ cm}^{-1}$, and $g = 2.29$, whereas the fitting was substantially improved by allowing a slightly anisotropic gyromagnetic tensor, such that the values found in Table 3 were achieved with an $R = 8.5 \times 10^{-4}$. Assuming an axial anisotropy, being $E \approx 0$, the energy separation between $\pm 1/2$ and $\pm 3/2$ doublets equals $2D$ due to the second-order SOC present in the distorted octahedral Co(II) ion.

$\chi_M T$ vs T plot of compound **2** shows a room temperature $\chi_M T$ value ($1.11 \text{ cm}^3 \text{ mol}^{-1} \text{ K}$) close to that expected for an isolated ion ($1.00 \text{ cm}^3 \text{ mol}^{-1} \text{ K}$ with $g = 2.01$; Figure 7). This curve shows a plateau down to very slight decrease from room temperature up to 25 K, where it experiments an abrupt drop up to $0.85 \text{ cm}^3 \text{ K mol}^{-1}$ at 5 K, probably due to the occurrence of zfs and weak antiferromagnetic interactions, which may be assumed given that the shortest 2ain mediated Ni···Ni distance along the network is of the same order of the cobalt(II) counterpart (larger than 8.7 Å) and the absence of significant π - π stacking interactions between the subnets (where Ni···Ni separations of ca. 8 Å are found). In this sense, the computed broken symmetry procedure upon model 2 supports the weak antiferromagnetic nature of the intramolecular exchange interaction ($J = -0.55$). Accordingly, the experimental $\chi_M T$ vs T data were fitted with the Hamiltonian shown in eq 3 with PHI, from which the following set of parameters were achieved: $g_{\text{iso}} = 2.11$ and $D = -4.4 \text{ cm}^{-1}$ (with a negligible value of $E < 0.1 \text{ cm}^{-1}$) with $R = 4.6 \times 10^{-5}$. It is worth noticing that the value of D lies within the range found for similar octahedral Ni^{II} complexes.⁴⁴

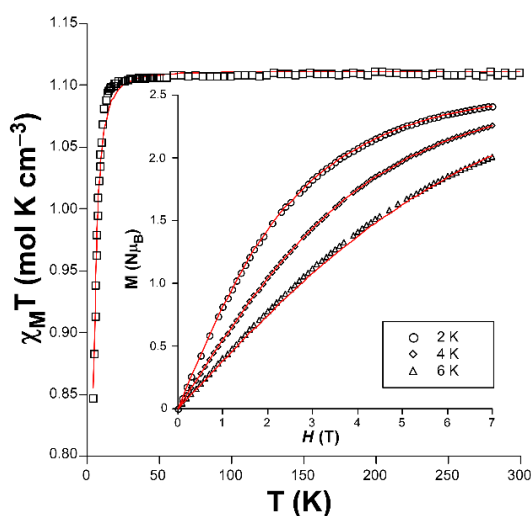


Figure 8. Simultaneous fitting of the $\chi_M T$ vs T and M vs H plots using eq 3 for compound 2.

2.3. Dynamic magnetic properties

The magnetic anisotropy found for compounds **1** and **2** prompted us to study their spin dynamics by means of *ac* magnetic susceptibility measurements (using an alternating field of 3.5 Oe). Compound **1** exhibited a slight frequency-dependent signal although the maxima remained below 2 K when applying a zero *dc* field, which did not allow further fitting of the data (Figure 9).

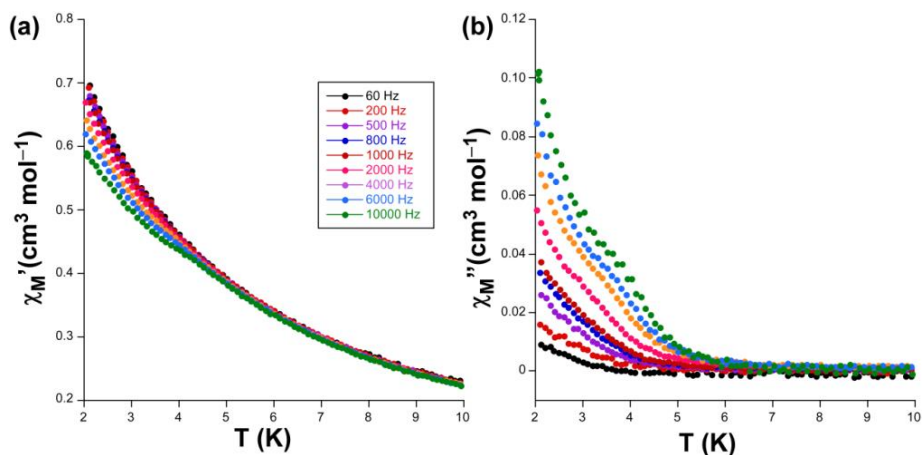


Figure 9. Temperature dependence of the (a) χ_M' and (b) χ_M'' signals for compound **1** with no applied *dc* field.

This behaviour seems to indicate that magnetic relaxation proceeds through a fast quantum tunnelling (QTM) derived from intramolecular and/or strong hyperfine interactions occurring with the $I = 7/2$ nuclear spin of the Co(II) atom.^{29d, 45} Interestingly, when a *dc* field of 1 kOe is applied, compound **1** shows temperature-dependent in-phase (χ_M') and out-of-phase (χ_M'') signals (Figure 10), whereas QTM could not be suppressed for compound **2** so no frequency dependence was observed. A first inspection of the ac data of **1** reveals that χ_M'' signals peaking at ca. 10 K present a remarkable width, mainly for the low frequency regime (60–1000 Hz), which makes one suspect about the occurrence of two consecutive and overlapped maxima. In any case, the most remarkable feature of the *ac* signals is clearly the fact both peaks (χ_M' and χ_M'') are weakly dependent of the frequency. In fact, the frequency shift calculated as $\phi = \Delta T_p / [T_p \Delta(\log f)]$ (where T_p corresponds to the peak of $\chi_M''(T)$ curve and f to the frequency) gives a low value of 0.03, which is a common value for spin glasses ($\phi < 0.1$).^{46,47} Accordingly, relaxation times (τ) were estimated from the $\tau = 1/(2 \pi f_{\max})$ expression based on $\chi_M''(T)$ peak give thermally activated relaxations with $\tau_0 = 9.4 \times 10^{-33}$ s, $U = 660$ K, values that agree well with those recorded for other reported spin-glass materials with slow dynamics^{48,49} At this point, it must be highlighted that this sort of glass-like magnetic behaviour is usually related to a field-dependence behaviour (derived from canted antiferromagnetism or long-ranged magnetic ordering) which, yet not observed in *dc* measurements, could be the present case in view of the chiral structure being comprised of two 3D sublattices. However, the fact that a weak SIM behaviour could be overlapped by the dominating glassy-state, in view of the width of the signal, is not to be fully discarded.

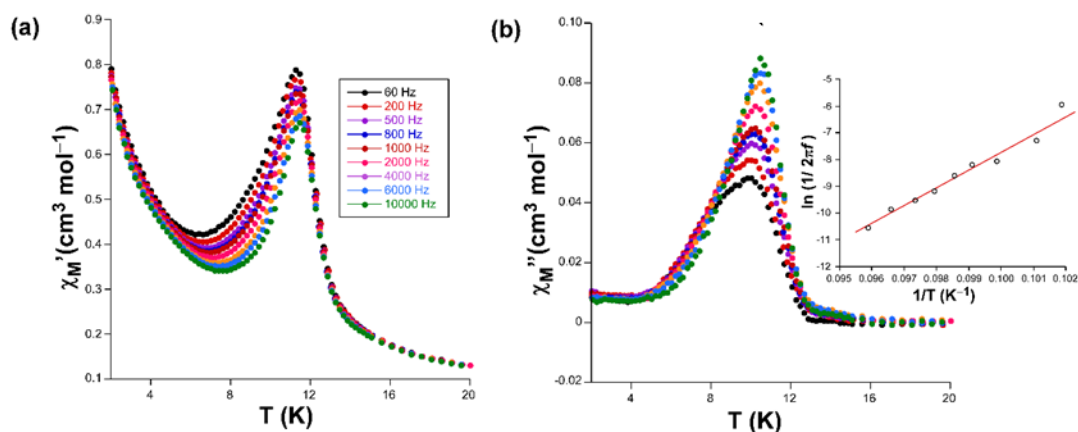


Figure 10. Temperature dependence of the (a) χ_M' and (b) χ_M'' signals for compound **1** under an applied field of 1000 Oe. Inset shows the Arrhenius plot with linear fitting to estimate the thermal barrier for the reversal of the magnetization.

2.4. Solvent-dependent magnetic behaviour of compound **1**

Solvent-exchange experiments were accomplished upon polycrystalline sample of compound **1** in view of its intriguing magnetic behaviour and potentially porous nature, which could a priori endow the material with a guest (solvent)-dependent magnetism. Two different solvents, such as DMSO and MeOH, were selected not only for their common use in the synthesis of MOFs but also for their hazardous nature. The exchange of lattice solvent molecules was successfully achieved by immersing fresh sample of **1** into 10 mL of the solvent and letting it to stand for two days under a soft stirring, which led to the isomorphous compounds $[\text{Co}(\mu\text{-}2\text{ain})_2]\cdot 2\text{MeOH}$ (**1-MeOH**) and $[\text{Co}(\mu\text{-}2\text{ain})_2]\cdot 1.5\text{DMSO}$ (**1-DMSO**). Note that the proposed formula was confirmed by elemental analyses, metal absorption, ICP/AES, and TG/DTA experiments (Figure 11).

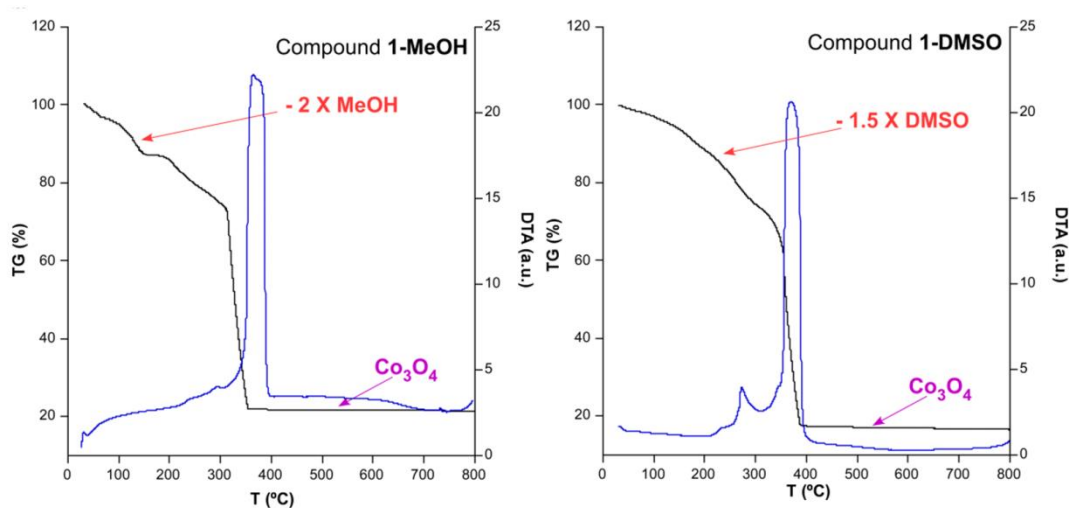


Figure 11. TG/DTA analysis for solvent exchanged compounds **1-MeOH** and **1-DMSO**.

Though both compounds retain the crystalline framework to a large extent, they experience some slight changes due to the replacement of the pore molecules. A careful evaluation of the cell parameters shows a common trend: a and b axes are shrunk whereas c is stretched. This behaviour seems to indicate that pore channels are somewhat crushed when replacing the DMF molecules by DMSO and MeOH, respectively for **1-DMSO** and **1-MeOH**, a fact that points to a relative displacement of the subnetworks. The analysis of the dc properties of the exchanged MOFs reveals a similar magnetic behaviour with progressive decrease of the $\chi_M T$ product as the temperature drops. Nonetheless, a larger magnetic anisotropy may be inferred from the steepest decrease of $\chi_M T$ in **1-DMSO** compared to **1-MeOH** together with the larger separation between magnetization curves. In fact, mathematical fitting of the data with above mentioned eq. 2 and 3 come to the same conclusion supporting a small increase of the axial parameter ($D = -20$ for **1-DMSO** and -16 cm^{-1} for **1-MeOH**, compared to -11.9 cm^{-1} for **1**). Even more exciting is the fact that such an increase in the anisotropy is accompanied by a deep change of the magnetic nature of the materials, since they can be now referred to as SIMs⁵⁰ under an external dc of 1000 Oe (no signal is observed with zero field) given their strong frequency-dependent χ_M'' signal. Moreover, it must be also noticed that these maxima become narrower than those shown by the neat compound (Figure 12).

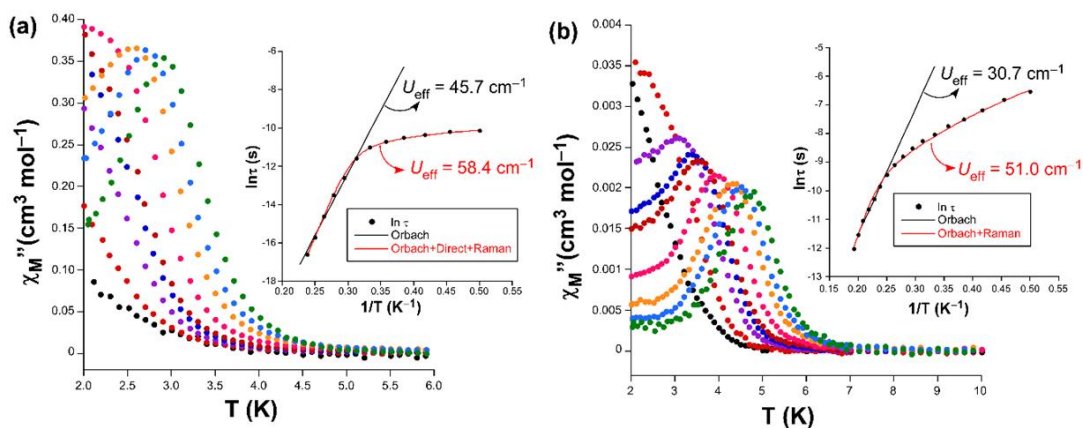


Figure 12. Temperature dependence of the χ_M'' signals and best fitting results for the relaxation times for compounds (a) **1-DMSO** and (b) **1-MeOH**.

At first sight, the blocking temperature (below which the compounds behaves as a SIM) drops down in both cases, among which **1-DMSO** presents well-defined maxima only those curves with an oscillating frequency above 1000 Hz. Instead, the maxima are much closer to each other for **1-DMSO** rather than **1-MeOH**, from which it is deduced that a faster magnetic relaxation occurs in the former. The Cole-Cole plots below 3.4 K for **1-DMSO** and 4.2 K for **1-MeOH** can be well fitted by a generalized Debye function, which it is an important difference with respect to double semicircles shown by pristine compound **1**, where α values ranging in 0.17–0.29 and 0.10–0.26 are found, respectively for **1-DMSO** and **1-MeOH** (Figure 13).

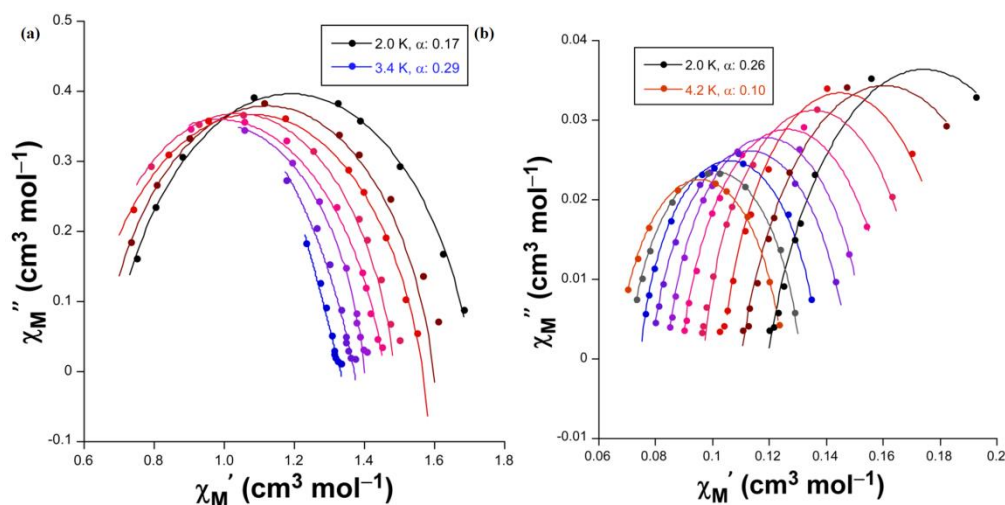


Figure 13. Cole-Cole plot for compounds (a) **1-DMSO** and (b) **1-MeOH** showing best fitting with debye model.

These values, implying a wide distribution of the relaxation times, are indicative of the occurrence of various mechanisms in the relaxation of the magnetization. In fact, Arrhenius plots in the form of $\ln(\tau)$ vs T^{-1} deviate from linearity at low temperature in both cases. Fitting of the high temperature data by means of Orbach process gives values of the effective barrier and pre-exponential factors of $U_{eff} = 65.3$ K (45.7 cm^{-1}) and $\tau_0 = 1.36 \times 10^{-12}$ s for **1-DMSO** and 43.9 K (30.7 cm^{-1}) and $\tau_0 = 1.54 \times 10^{-9}$ s for **1-MeOH**, which are somewhat higher than those reported for most of polymeric metal-organic compounds behaving as SIMs.²⁶ Note also that these energy barriers agree with the expected energy separation between Kramers doublet ($2D = 32 \approx 30.7$ cm^{-1} for **1-MeOH** and $2D = 40 \approx 45.7$ cm^{-1} for **1-DMSO**). However, it must be highlighted that the rise of the energy barrier is linked to the relaxation rate, among which the τ_0 of 1.36×10^{-12} s estimated for **1-DMSO** clearly exceeds the usual range (between $10^{-6} - 1 \times 10^{-11}$ s) attributed to Co(II)-based SIMs. This fact that comes to conclude that the exchange of DMSO in the pores modifies the disposition of the subnetworks such that spin carriers can probably interact through intermolecular interactions, explaining the more abrupt drop in the $\chi_M T$ vs T curve (Figure 14).

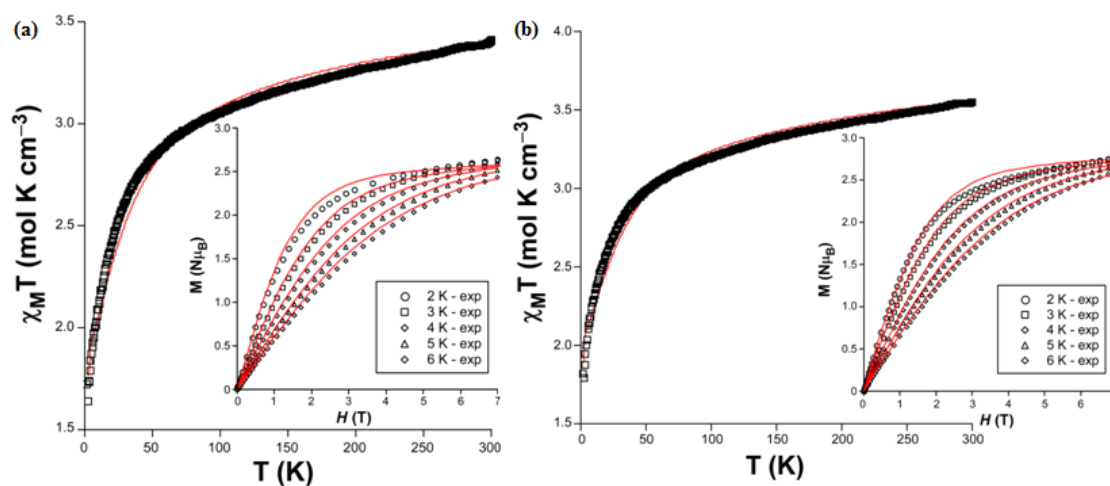


Figure 14. Variable temperature $\chi_M T$ vs T and M vs H plots with best fitting for (a) **1-DMSO** and (b) **1-MeOH** under an applied field of 1000 Oe.

On another level, very reliable fittings were achieved by combining the Orbach with Raman and/or direct relaxation processes (eq. 4 and/or 5), which have previously been employed successfully in the analysis of Co(II)-based compounds with related coordination environment.^{32 d,51}

$$\tau^{-1} = A_{\text{direct}}T + B_{\text{Raman}}T^n + \tau_0^{-1} \exp(-U_{\text{eff}}/\kappa_B T) \quad (\text{eq 4})$$

$$\tau^{-1} = B_{\text{Raman}}T^n + \tau_0^{-1} \exp(-U_{\text{eff}}/\kappa_B T) \quad (\text{eq 5})$$

Best fitting with the multiple relaxation processes gives $U_{\text{eff}} = 83.4$ K (58.4 cm^{-1}), $\tau_0 = 1.45 \times 10^{-14}$ s, $A_{\text{direct}} = 1190(30) \text{ s}^{-1} \text{ K}^{-1}$, $B_{\text{Raman}} = 4.1(2) \text{ s}^{-1}$, $n = 7.8(1)$ for **1-DMSO** and $U_{\text{eff}} = 72.8$ K (51.0 cm^{-1}), $\tau_0 = 6.12 \times 10^{-10}$ s, $B_{\text{Raman}} = 8.7(2) \text{ s}^{-1}$, $n = 4.1(2)$ for **1-MeOH**.

2.5. Photoluminescence properties of compound 3

Excitation and emission spectra were measured on polycrystalline sample of compound **3** since, being comprised of carboxylic pyridine ligands such as 2ain and metal ions with closed-shell electronic configuration, i.e. Zn(II), it is capable of unveiling interesting photoluminescence in solid state. The emission spectrum under UV light (at the shoulder $\lambda_{\text{ex}} = 305$ nm) at room temperature (295 K) shows a somewhat narrow band, composed of the maxima ($\lambda_{\text{em}} = 390$ nm) and a shoulder ($\lambda_{\text{em}} = 405$ nm), in addition to a wide and weaker band peaking around 550 nm (Figure 15a).

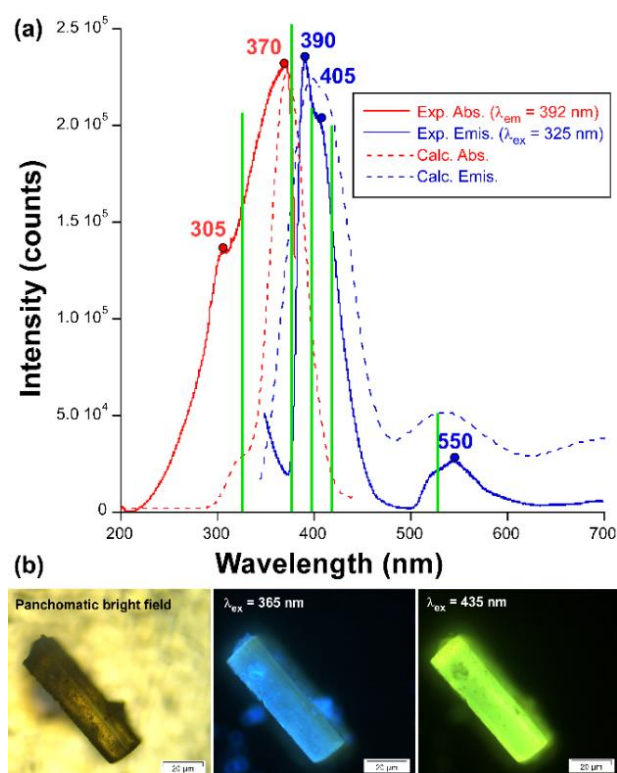


Figure 15. (a) Room temperature excitation (red) and emission (blue) spectra of compound **3** showing the most relevant experimental maxima (circles) and calculated (TD-DFT) main vertical excitations (green lines). (b) Micro-PL photographs of a single crystal of **3** illuminated with different lights.

The excitation spectra recorded at the main emission wavelength contains, in addition to the previous shoulder at 305 nm, another main contribution peaking at $\lambda_{\text{ex}} = 370$ nm, which shows the same PL mechanism in view of the identical emission spectrum achieved at the latter excitation wavelength (Figure 16a). To further investigate the origin of the less energetic band at $\lambda_{\text{em}} = 550$ nm, an excitation spectrum has been also measured, confirming that it arises from the same excitation path (Figure 16b).

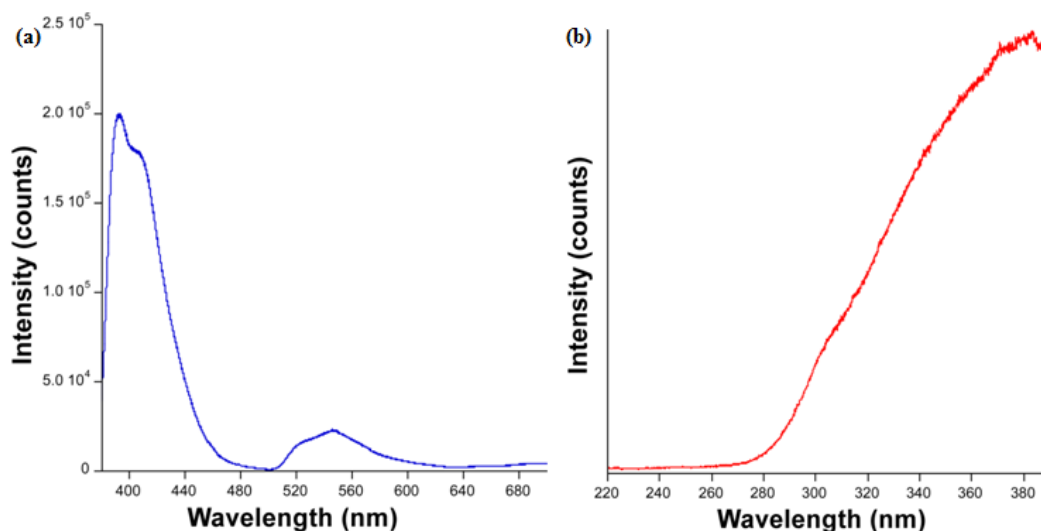


Figure 16. (a) Emission spectrum of compound **3** under excitation at 370 nm. (b) Excitation spectrum of compound **3** monitored under $\lambda_{em} = 550$ nm.

These two bands provide this material, as observed in the images taken on the microscope, with a variable emission consisting of a brilliant blue greenish light under excitation with UV radiation ($\lambda_{ex} = 365$ nm) or a lime green emission with a less energetic radiation ($\lambda_{ex} = 435$ nm), in such a way that those wavelengths corresponding to the maximum of the emission band are avoided (Figure 15b). The emission quantum yield measured in absolute terms with an integrated sphere is low (1.75%). The calculated PL spectra conducted on a suitable model of **3** reproduce very well both excitation and emission processes, finding only substantial differences for the relative intensities of the minor bands.

Starting from the molecular excitation of the compound, absorption of light at the two main contributions seems to proceed through slightly different electronic transitions (Table 5, note that these are the most intense transitions gathered as a representative sample of the band). On the one hand, the shoulder at 305 nm corresponds to a $\pi \rightarrow \pi^*$ transition in which the involved MOs are centred on the aromatic ring of 2ain ligands (Figure 17), while the band maximum at 370 nm may be better described as a $n \rightarrow \pi^*$ transition given that HOMO – 2/3 lie over the carboxylate group on the other. On its part, the PL emission takes also place through LCCT mechanism since electrons drop from excited LUMO – n orbitals, of π^* nature with lobes extended over the whole molecule or solely the aromatic ring (Figure 16),

to HOMOs consisting of n or π orbitals based on the carboxylate group for the main ($\lambda_{\text{em}} = 390$ and 405 nm) or the minor ($\lambda_{\text{em}} = 550$ nm) bands, respectively.

Table 5. Calculated main excitation and emission energies (nm), singlet electronic transitions and associated oscillator strengths of model 3.

Exp. λ	Calcd. λ	Electronic transisitons	Osc. strength (a.u.)
Excitation energies			
305	318	HOMO - 6 \rightarrow LUMO + 1 (51%) HOMO - 7 \rightarrow LUMO (49%)	0.083
370	372	HOMO - 3 \rightarrow LUMO + 2 (51%) HOMO - 2 \rightarrow LUMO + 3 (42%)	0.112
Emission energies			
390	388	HOMO - 2 \leftarrow LUMO + 4 (52%) HOMO - 2 \leftarrow LUMO + 2 (40%)	0.084
405	408	HOMO - 2 \leftarrow LUMO + 2 (89%)	0.081
550	539	HOMO \leftarrow LUMO (97%)	0.038

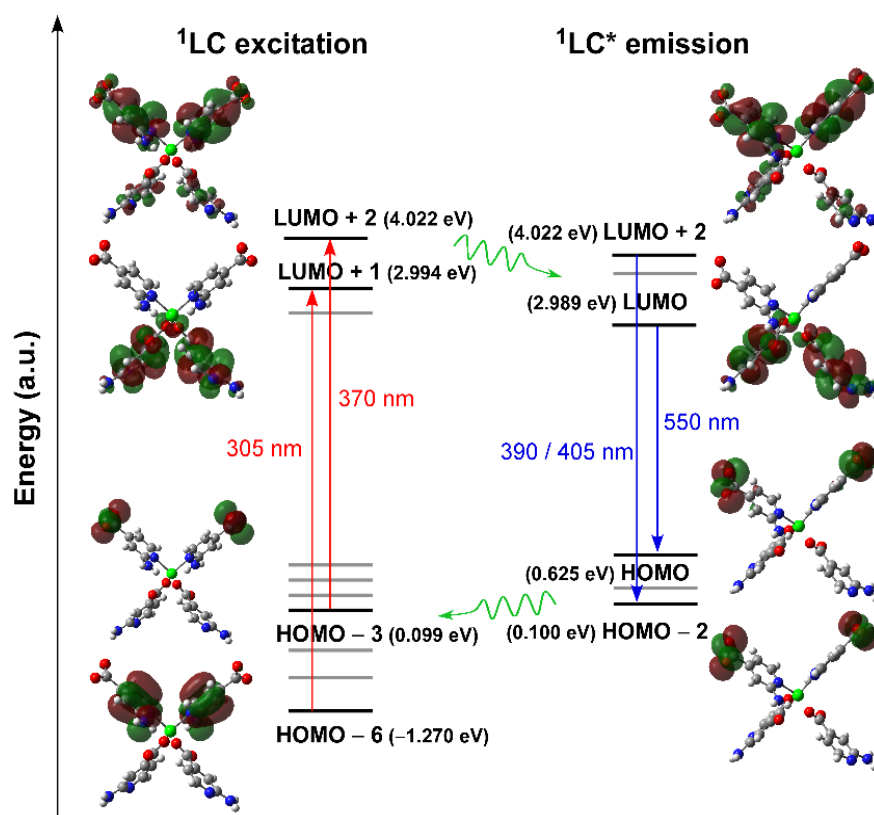


Figure 17. Schematic representation of the most intense excitation (red) and emission (blue) lines of compound 3 with their corresponding MOs. Values given between bracket represent the energies in eV.

For comparative purposes, emission spectra of **3** were recorded at different temperatures under the same experimental conditions in order to check how the suppression of the vibrational quenching, i.e. the molecular vibrations/motions occurring in the ligand that may be overlapped with the radiative emission and hence draw emission capacity to the system,⁵² as the temperature is dropped affects the PL response of the material. Upon cooling the system from RT down to 10 K, the band maximum does not show any remarkable shift although it progressively gains intensity, mainly in the temperature range of 200–150 K where the intensity shows a quantitative leap. To summarize, the emission intensity at $\lambda_{\text{max}} \approx 400$ nm is much greater for 10 K data compared to RT (about 55 times larger in terms of emitted integrated intensity, Figure 18).

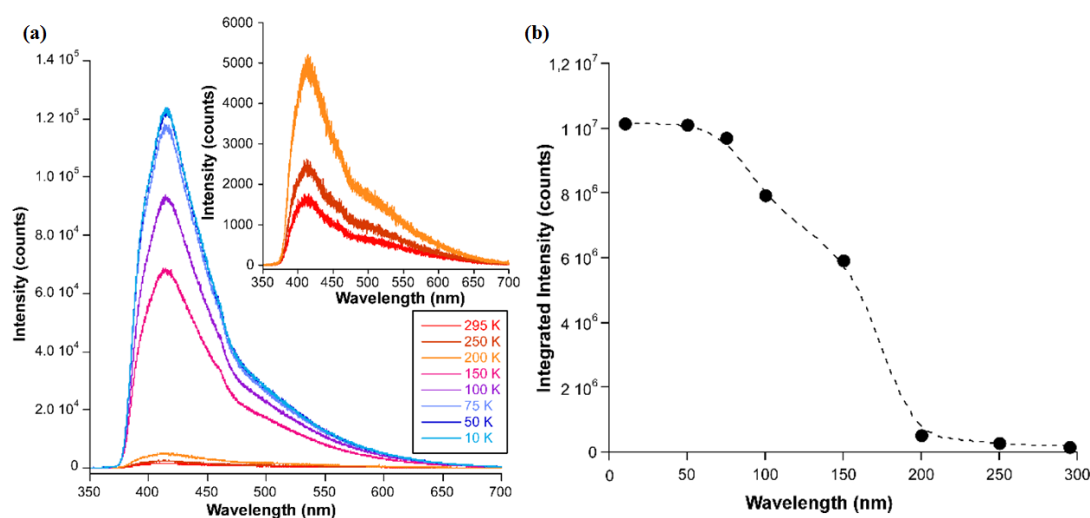


Figure 18. (a) Variable temperature emission spectra of **3** under excitation at 305 nm. (b) Evolution of the integrated intensity of the emission according to temperature.

With the aim of enlarging the temperature-dependent characterization, emission decay curves were also measured at three representative temperatures (295, 150 and 10 K), revealing very similar lifetimes in the range of hundreds of microseconds. In any case, it is worth highlighting that the observed lifetime remains constant along the whole emission spectrum and shows the expected trend with the temperature although the change is somewhat slight (τ being 239(2), 169(4) and 121(3) μs for the above mentioned temperatures, see Table 6), which indicates that a

unique PL mechanism is preserved irrespective of the temperature of the system. These short lifetimes contrast when compared to those measured for other systems consisting of Zn(II) and positional isomers of the 2ain ligand, as it is the case of $[\text{Zn}(\text{6ani})_2]_n$ and $[\text{Zn}(\text{2ani})_2]_n$,³² which displayed long-lasting phosphorescence (LLP) emissions that could be traced by human eye. As concluded from the analysis of molecular based phosphorescent reported so far,⁵³ a major reason for the occurrence of LLP in metal-organic compounds with closed-shell ions is attributed to the intermolecular forces established by ligands in the framework, in such a way that strong interactions are able to freeze the molecules and make lowest-lying triplet states (T_1) more accessible and shielded against quenching. As a matter of fact, the molecular N–H vibrations of the amino group, known to be a main oscillator which enables the non-radiative quenching,⁵⁴ seem to be less suppressed in compound **3** compared to their disposition in the above mentioned CPs. In these latter compounds, isomeric 6ani and 2ani ligands establish more rigid hydrogen bonds, particularly in the case of the intramolecular hydrogen bonds found in Zn2ani, whereas the 2-fold interpenetration brings higher flexibility to the crystal building of **3**, explaining the short lifetimes.

Table 6. Lifetime values and corresponding percentages for components obtained from best fittings of decay curves measured at room temperature for compound **3** ($\lambda_{\text{ex}} = 325 \text{ nm}$).

Temperature (K)	$\lambda(\text{nm})$	$\tau_1 (\mu\text{s})$	$\tau_2 (\mu\text{s})$	Chi Sq.
10	411	239(2)		1.118
150	411	18.1(1)	169(4)	1.182
300	411	14.1(1)	121(3)	1.175

2.6. PL Sensing Properties

The flexible porous nature revealed by compound **3**, consisting of a stable doubly interpenetrated metal-organic framework with pores in which small molecules could be exchanged, in addition to the strong blue greenish PL displayed at RT instigated us to study its performance as PL sensing material for various solvents and metal ions. When polycrystalline sample is dispersed in different solvents, solvent@**3** hereafter, the main emission band experiments not only

significant changes regarding the intensity but also slight shifts for the maximum of the emission band (λ_{max}). In a first approach, the analysis of the spectra measured at a representative wavelength ($\lambda_{\text{ex}} = 350$ nm, which falls within the excitation maximum for all suspensions) under the same equipment configuration (identical slit aperture and photomultiplier voltage) revealed that the emission decreases following the expected sequence according to the solvent polarity (note that dielectric constants are shown between brackets): H₂O (80.1) > DMSO (46.7) > DMF (36.7) > MeOH (32.7) > EtOH (24.5) > Ac₂O (20.7) > 2-PrOH (19.2) > THF (7.58).^{16b,55} In other words, the higher the polarity of the solvent the largest its quenching capacity (Figure 19).

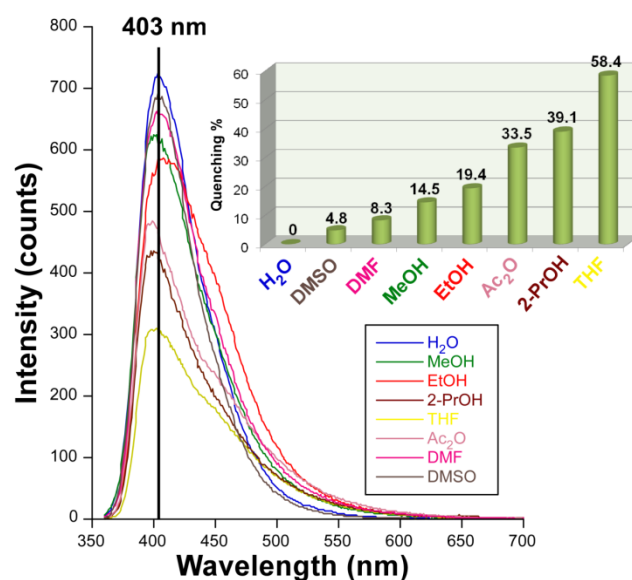


Figure 19. Quenching capacity of solvents based on the emission intensity of **3** under maximum excitation wavelength.

Moreover, the presence of a minor emission peak, in the form of a shoulder peaking at $\lambda_{\text{em}} \approx 450$ nm, was also observed for less polar solvents (Ac₂O, 2-PrOH and THF), which is probably due to the enabling of an electronic transition arising from a less energetic LUMO level derived from solvation effects.⁵⁶ In this sense, it must be recalled that 2ain ligands in the crystal structure possess uncoordinated amino groups exposed to the microchannels, where hydrogen bonding and Van der Waals interactions established with solvent molecules may affect the LCCT mechanism and thus the PL emission.⁵⁷ With the aim of getting insights into the

potential applicability of this material, a further analysis showed that the main emission follows a solvent-dependent excitation, given the drastic changes shown in the excitation spectra monitored at the λ_{max} (where only one wide band or two narrower maxima are observed depending on the selected solvent, Figure 20).

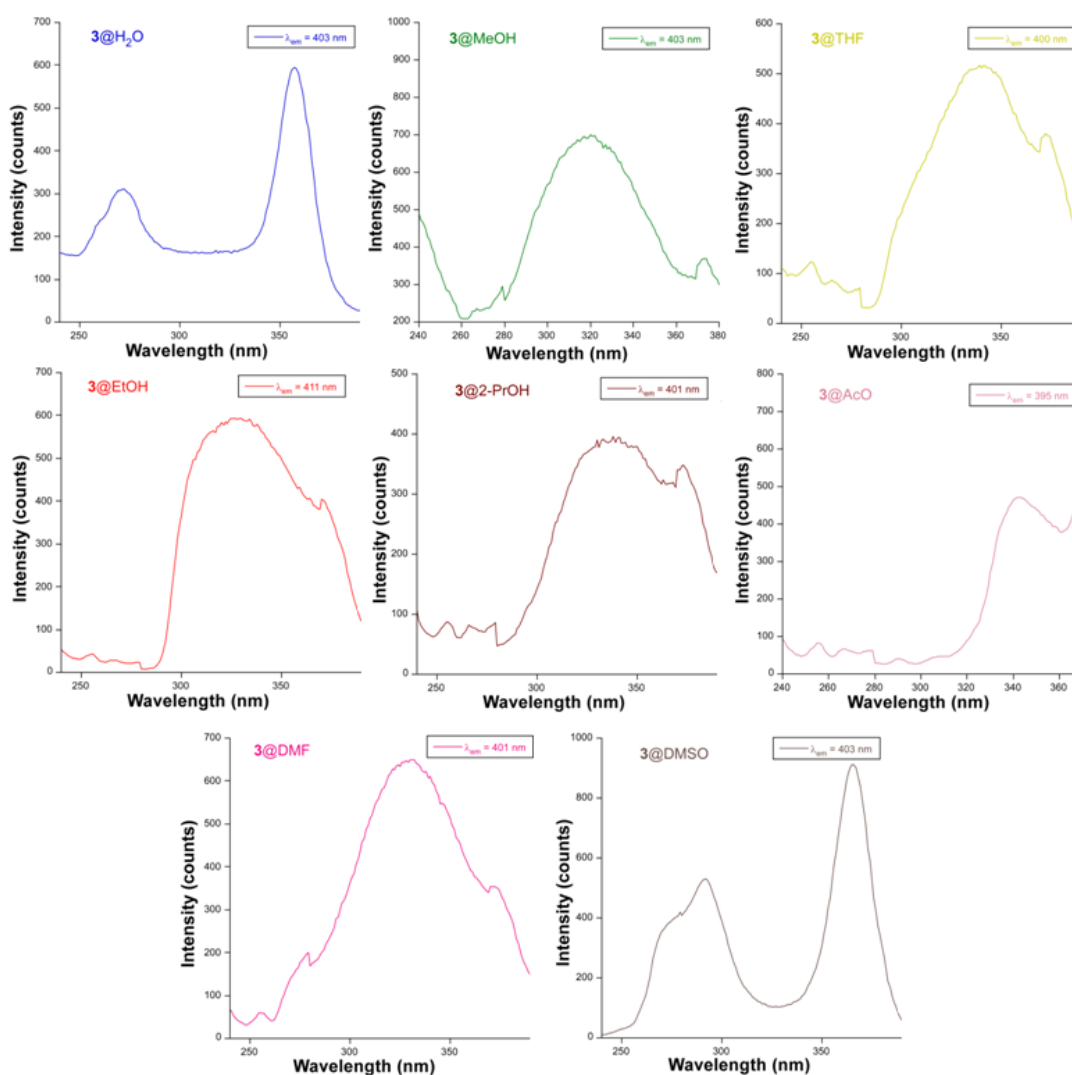


Figure 20. Excitation spectra of compound **3** dispersed on different solvents recorded with the same experimental conditions.

A new set of measurements with variable excitation wavelength in order to maximize the solvent-dependent PL behaviour (focusing at the most intense λ_{ex}) indicates that **3** keeps a strong PL emission in water (note that water itself brings some quenching compared to solid state but it is employed as a reference for the rest

of solvents) whereas, taking water as a reference, the rest of studied solvents cause a large quenching (with a quenching percentage (QP) above 65%, Figure 21).

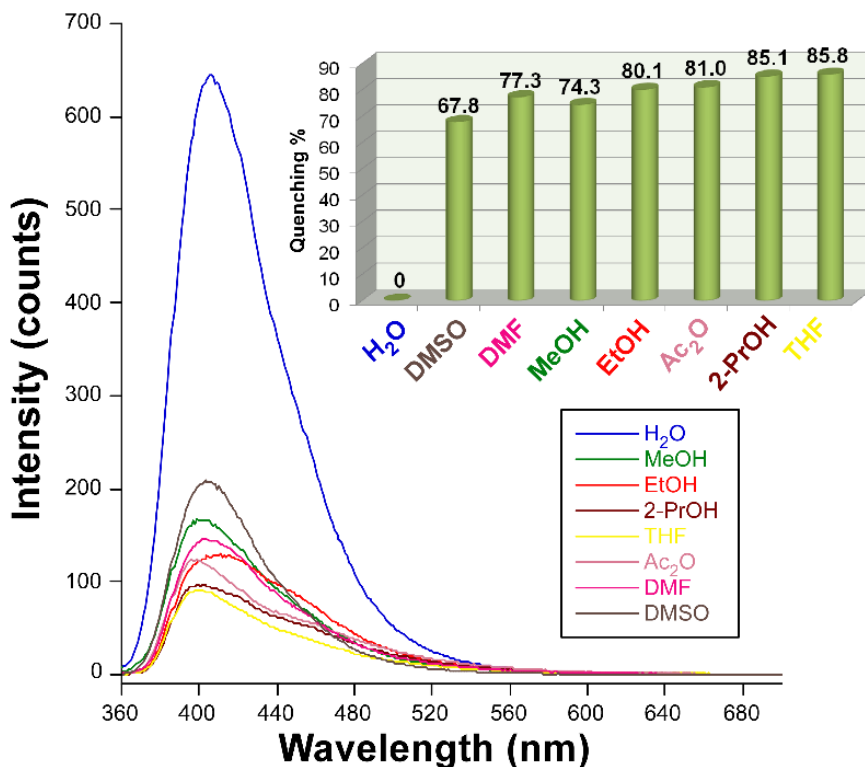


Figure 21. PL emission spectra of dispersion of compound **3** in different solvents at their maximum excitation wavelength. Quenching percentage estimated from the emission intensity relative to H₂O@**3** is reflected in the upper bar chart.

Taking into account that crystal structure of **3** presents no significant change (as corroborated by PXRD collected for samples recovered from solvent@**3** suspensions, Figure 22), it may be assumed that solvents exert a dynamic quenching involving not only solvation processes external surface of the particles in the suspension but also a quenching derived from the particular interactions (enabling competitive absorption and energy transfers)⁵⁸ occurring between solvent molecules and the internal surface of the microchannels, where factors such as size and hydrogen bonding capacity are key factors governing their diffusion throughout the pore system, though .

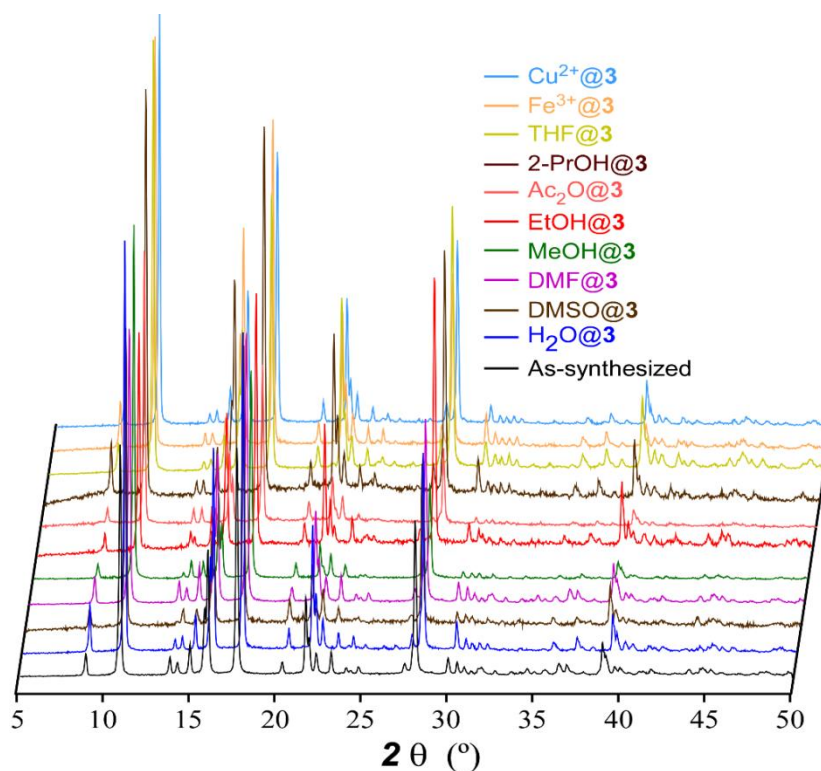


Figure 22. PXRD data of as-synthesized sample and samples collected after suspensions.

In view of the intense PL signal observed for the H₂O@**3** suspension (the least quenching brought by water compared to other solvents), the detection of ions in aqueous solutions was also studied. As inferred from Figure 23, **3** presents a variable sensing capacity to ions according to their quenching capacity that follows the series: Cd²⁺ > NH₄⁺ > Al³⁺ > Ni²⁺ > Co²⁺ > Cr³⁺ > Cu²⁺ > Fe²⁺ > Fe³⁺. It is important to notice that the quenching percentage (QP) at 10 mM is above 90% for both iron cations, among which the most stable oxidation state almost clears the PL emission. This behaviour meets the expected response given that UV-Vis absorption band of these ions overlap substantially well with the excitation band, such that most of the light irradiated does not reach the dispersed solid of **3**.^{32c} More interestingly, the presence of most of studied metal ions promotes a shift of the emission band, most of which cause a blue-shift which can be as large as 15 nm (for Cr³⁺@**3**). However, the strongest quencher of the PL, Fe³⁺ ion, promotes an opposed response by red-shifting the maximum up to ca. $\lambda_{em} = 440$ nm. This overall behaviour seems to indicate that metal ions are able to interact with the ligands of the backbone.

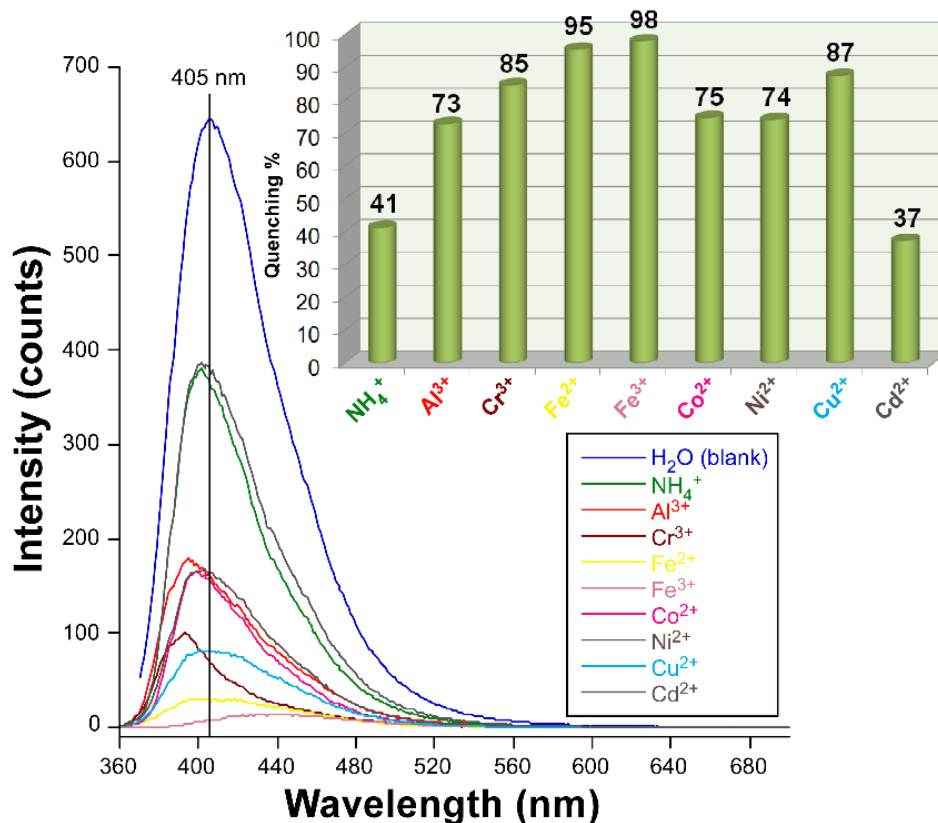


Figure 23. PL response of H₂O@3 against common metal ions ($\lambda_{ex} = 350$ nm) together with the quenching percentage estimated from the maximum emission intensity respect to a blank solution.

Taking into account the previous metal-dependent turn-off results, we decided to explore the PL response of the CP for Fe³⁺ and Cu²⁺ ions, for which an exhaustive evolution of the emission intensity was monitored by gradually increasing the concentration of the metal quencher. Note that no further study was conducted for Fe²⁺ because of its spontaneous oxidation in waste waters. Stern-Volmer plot analyses for the latter two ions exhibit a distinct behaviour. The PL signal exhibits a progressive and polynomial quenching for Fe³⁺ ion from low concentrations on, which points out the coexistence of static and dynamic quenching phenomena. On its part, the quenching by Cu²⁺ ions shows a progressive and linear quenching occurring from null concentration (Q) of 4×10^{-5} M. Instead, fitting of the evolution with the respective expression for both ions gives values of K_{sv} of 1.79×10^4 and 2.12×10^4 M⁻¹ (Figure 24) with calculated limit of detection (LOD) values of 55 μ M and 162 μ M for Fe³⁺ and Cu²⁺ ions, respectively. Note that, despite the relatively high LODs, the estimated K_{sv} value for Fe³⁺ detection can be considered quite promising compared to other reported MOFs with characteristic iron sensing capacity, usually exhibiting

values within the $10^4 - 10^5$ range,^{19,59,60} among which the $K_{sv} = 2.67 \cdot 10^5 \text{ M}^{-1}$ reported for the MOF of $\{[(\text{CH}_3)_2\text{NH}_2]_6[\text{Cd}_3\text{L}(\text{H}_2\text{O})_2] \cdot 12\text{H}_2\text{O}\}_n$ formula deserves to be mentioned.⁶¹ In this regard, despite the dominant dynamic quenching observed for these ions (in view of their large K_{sv}), significant static quenching may be claimed for Fe^{3+} according to the non-linear distribution of the plot, a fact that may be explained according to the accessibility of the carboxylate oxygen atoms of 2ain ligands (which are also involved in hydrogen bonding interactions with exocyclic amino groups of neighbouring 2ain ligands) from the microchannels of the MOF. The recyclability of **3** has been also checked by PXRD measurement on the solid filtered and dried after the experiment. Thinking on a potential use of the compound for sensing applications on polluted wastewaters, an additional analysis was accomplished in order to explore the specific response against similar quenchers, for which the mixed $\text{Fe}^{3+}/\text{Cu}^{2+}$ system was studied. In view of the obtained Stern-Volmer plot, the quenching evolution of the material is not proportional to the sum of both isolated ions, but it shows a linear response after a concentration of $1 \times 10^{-4} \text{ M}$ of each individual ion. Fitting of the linear part gives a K_{sv} of $2.12 \times 10^4 \text{ M}^{-1}$, which allows us concluding that there is a tough competition between both quenchers to interact with the framework.

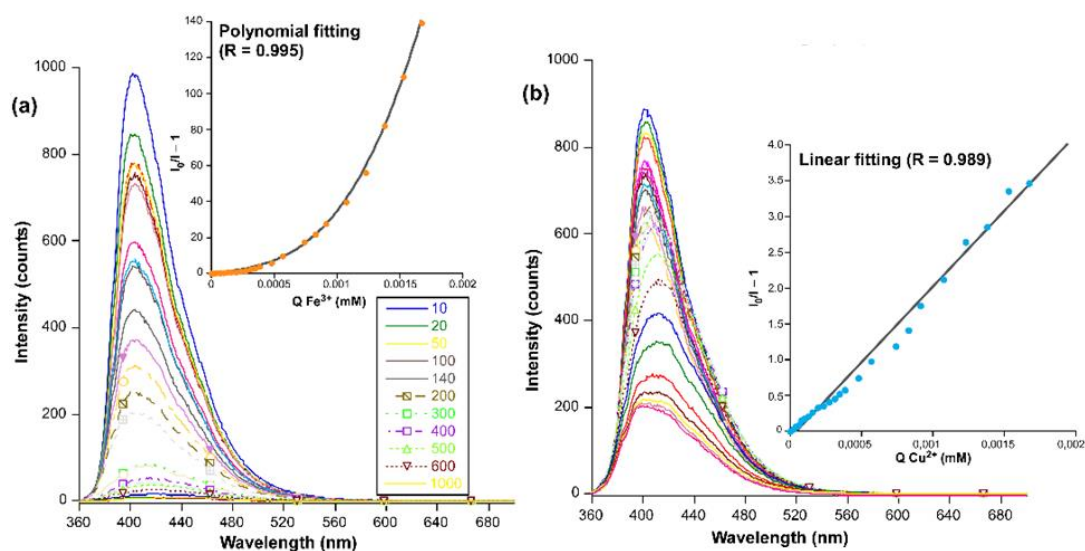


Figure 24. Luminescence quenching of $\text{H}_2\text{O}@3$ with gradual addition (microliters of metal ion solutions added are shown in the capture with different colors of (a) Fe^{3+} and (b) Cu^{2+} ions. Stern-Volmer plots showing the linear fits are also shown.

3. Conclusions

Three metal-organic framework materials, of $\{[M(\mu\text{-}2\text{ain})_2]\cdot\text{DMF}\}_n$ formula, based on first row transition metal ions (Co^{II} , Ni^{II} , and Zn^{II}) and 2-aminoisonicotinate (2ain) ligand have been synthesized and chemically and structurally characterized. Their crystal structure consists of a doubly-interpenetrated three-dimensional open architecture which contains microchannels filled with solvent molecules. Taking advantage of the porosity and their magnetic and/or photoluminescence (PL) properties, their guest-dependent magnetic and PL response has been evaluated. On the one hand, the weak exchange interactions transmitted through the chiral coordination network leads to a spin-glass behaviour that governs the magnetism of the cobalt-based counterpart, though no frequency-dependent signal is observed for the nickel compound. Interestingly, when DMSO and MeOH are loaded within the pores of this MOF, exchanging the pristine DMF molecules, the crystal building undergoes a kind of rearrangement which modulates the magnetic properties of the material. In particular, the glass-like magnetic relaxation gives way to substantial SIM behaviour probably derived from the first-order SOC inherent to cobalt(II) ions, consisting of multiple spin-phonon processes characterized by low blocking temperature but relatively high energy barriers. On another level, solid state PL measurements show that the zinc-based MOF displays strong bright blue emissions arising from a LCCT mechanism (based on $\pi\text{-}\pi^*$ or $n\text{-}\pi^*$ transitions in 2ani) as confirmed by TD-DFT calculations. The vibrational quenching may be efficiently prevented at low temperature (10 K), since a strong gain in integrated emitted intensity (of 55 times) is observed compared to RT. This MOF exhibits clear emission dependence in contact with solvents under a constant excitation wavelength, where the emission quenching increases according to the decreasing polarity of the solvent (moving from $\text{H}_2\text{O} > \text{solvents} > \text{THF}$). With regard to its sensing towards metal ions in aqueous solutions, Cu^{2+} , Fe^{2+} , and Fe^{3+} ions are found to quench the emission to a large extent. Stern-Volmer plots for aqueous Cu^{2+} and Fe^{3+} suspensions containing Zn-2ain reveal a similar detection capacity (K_{sv} of $1.79 \cdot 10^4$ and $2.12 \cdot 10^4 \text{ M}^{-1}$, respectively) but distinct mechanisms, confirming the capacity of these ions to interact with MOF. In fact, the analysis carried out on a mixture of both ions, $\text{Fe}^{3+}/\text{Cu}^{2+}$, shows a quenching evolution distinct to the sum of individual atoms, indicating a competing quenching of both quenchers to interact with the

framework. All in all, the studies confirm that these MOFs modulate their properties according to solvent-exchange and/or capture of metal ions in liquid media, which paves the way to their use as sensors.

4. Experimental Section

4.1. Chemicals

All chemicals were of reagent grade and were used as commercially obtained.

Synthesis of $\{[Co(\mu\text{-}2\text{ain})_2]\cdot\text{DMF}\}_n$ (1). 0.5 mL of a DMF solution containing 0.20 mmol of $\text{Co}(\text{NO}_3)_2\cdot 6\text{H}_2\text{O}$ (0.0582 g) were added dropwise under continuous stirring over 15 mL of a DMF/ H_2O (1:1) solution of H2ain ligand (0.40 mmol, 0.0552 g) at 70°C. The final pH of the solution was 5.6. The dark pink coloured solution was introduced in a Teflon-lined container enclosed into a stainless steel autoclave solution, where it was heated up to 120°C for two days. The mixture was slowly cooled down to room temperature and purple plate shaped single crystals were observed when opening the recipient. Crystals were filtered off and washed several times with water and methanol. Yield 50–60% (based on metal). Homogeneity and purity of samples were checked by means of elemental analysis, FT-IR and X-ray powder diffraction data (Figure 25 y 26). Anal. Calcd for $\text{C}_{15}\text{H}_{19}\text{CoN}_5\text{O}_6$ (%): C, 42.46; H, 4.51; Co, 13.89; N, 16.51. Found: C, 42.32; H, 4.38; Co, 13.83; N, 16.60.

Synthesis of $\{[Ni(\mu\text{-}2\text{ain})_2]\cdot\text{DMF}\}_n$ (2). Well shaped single crystals of compound **2** were collected from a Teflon-lined vessel after carrying out the same experimental procedure reported for **1** but for the use of $\text{Ni}(\text{NO}_3)_2\cdot 6\text{H}_2\text{O}$ (0.0582 g) instead of the cobalt source. Yield of 45–50% (based on metal). Anal. Calcd. for $\text{C}_{15}\text{H}_{19}\text{N}_5\text{NiO}_6$ (%): C, 44.37; H, 4.22; N, 17.25; Ni, 14.45. Found: C, 42.65; H, 4.32; N, 16.45; Ni, 13.74.

Synthesis of $\{[Zn(\mu\text{-}2\text{ain})_2]\cdot\text{DMF}\}_n$ (3). Following the same above mentioned synthetic conditions with $Zn(NO_3)_2\cdot 6H_2O$ (0.0595 g) gave rise to the growth of colourless single crystals of **3**. Yield of 50–55% (based on metal). Anal. Calcd. for $C_{15}H_{17}N_5O_5Zn$ (%): C, 43.65; H, 4.15; N, 16.97; Zn, 15.84. Found: C, 43.25; H, 4.34; N, 16.41; Zn, 15.02.

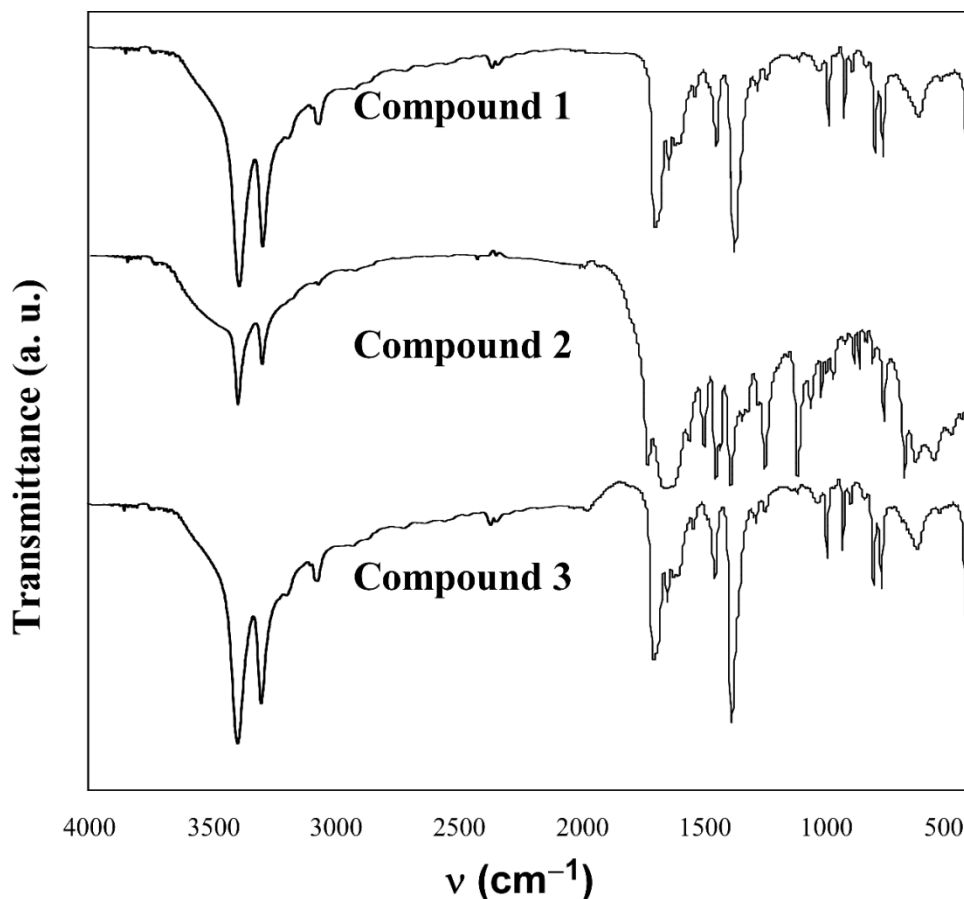


Figure 25. FTIR Spectra for all compounds.

4.2. Physical measurements

Elemental analyses (C, H, N) were performed on an Euro EA Elemental Analyzer and the metal content determined by inductively coupled plasma (ICP-AES) was performed on a Horiba Yobin Yvon Activa spectrometer. IR spectra (KBr pellets) were recorded on a ThermoNicolet IR 200 spectrometer in the 4000–400 cm^{-1} spectral region. Magnetic susceptibility measurements were performed on polycrystalline samples of the complexes with a Quantum Design SQUID MPMS-7T

susceptometer at an applied magnetic field of 1000 G. The susceptibility data were corrected for the diamagnetism estimated from Pascal's Tables,⁶² the temperature-independent paramagnetism, and the magnetization of the sample holder. *Ac* measurements were performed on a Physical Property Measurement System-Quantum Design model 6000 magnetometer under a 3.5 G *ac* field and frequencies ranging from 60 to 10,000 Hz. Thermal analyses (TG/DTA) were performed on Mettler-Toledo TGA/SDTA851 thermal analyser in a synthetic air atmosphere (79% N₂ / 21% O₂) with a heating rate of 5°C·min⁻¹. A closed cycle helium cryostat enclosed in an Edinburgh Instruments FLS920 spectrometer was employed for steady state photoluminescence (PL) and lifetime measurements in the 10–300 K range. All samples are first placed under high vacuum (of *ca.* 10⁻⁹ mbar) to avoid the presence of oxygen or water in the sample holder. For steady-state measurements a Müller-Elektronik-Optik SVX1450 Xe lamp or an IK3552R-G He-Cd continuous laser (325 nm) were used as excitation source, whereas a microsecond pulsed lamp was employed for recording the lifetime measurements. Photographs of irradiated single-crystal and polycrystalline samples were taken at room temperature in a micro-PL system included in an Olympus optical microscope illuminated with a Hg lamp. The PL quantum yield was measured in solid state using a Horiba Quanta-φ F-3029 integrating sphere.

4.3. X-ray Diffraction Data Collection and Structure Determination

X-ray data collection of suitable single crystals was done at 100(2) K on a Bruker VENTURE area detector equipped with graphite monochromated Mo K_α radiation ($\lambda = 0.71073 \text{ \AA}$) by applying the ω -scan method. Data reduction were performed with the APEX2⁶³ software and corrected for absorption using SADABS.⁶⁴ Crystal structures were solved by direct methods using the SIR97 program⁶⁵ and refined by full-matrix least-squares on F^2 including all reflections employing the WINGX crystallographic package.^{66,67} All hydrogen atoms were located in difference Fourier maps and included as fixed contributions riding on attached atoms with isotropic thermal displacement parameters 1.2 times or 1.5 times those of their parent atoms for the organic ligands and the water molecules,

respectively. Lattice solvent molecules placed in the voids of the structures found to be highly disordered due to the high symmetry acquired by the framework. Therefore, the final refinement was made with an hkl file provided by the SQUEEZE routine, which removed the latter electron density. Details of the structure determination and refinement of all compounds are summarized in Table 7. Crystallographic data for the crystal structures have been deposited with the Cambridge Crystallographic Data Center as supplementary publication nos. CCDC 1942731-1942733. Copies of the data can be obtained free of charge on application to the Director, CCDC, 12 Union Road, Cambridge, CB2 1EZ, U.K. (Fax: +44-1223-335033; e-mail: deposit@ccdc.cam.ac.uk or <http://www.ccdc.cam.ac.uk>).

Table 7. Single crystal X-ray diffraction data and structure refinement details of compounds **1**, **2** and **3**.

	1	2	3
Empirical formula	C ₁₅ H ₁₉ CoN ₅ O ₆	C ₁₅ H ₁₉ N ₅ NiO ₆	C ₁₅ H ₁₉ N ₅ O ₆ Zn
Formula weight	424.28	424.04	430.73
Crystal system	orthorhombic	orthorhombic	orthorhombic
Space group	<i>Fddd</i>	<i>Fddd</i>	<i>Fddd</i>
<i>a</i> (Å)	12.693(1)	12.649(1)	12.903(1)
<i>b</i> (Å)	22.776(2)	22.289(2)	22.869(2)
<i>c</i> (Å)	23.847(2)	23.949(2)	23.890(2)
<i>V</i> (Å ³)	6894(1)	6752(1)	7049(1)
<i>Z</i>	16	16	16
Reflections collected	19730	10466	10922
Unique / parameters	2112/96	1998/96	2121/96
R _{int}	0.0597	0.0323	0.314
GoF (S) ^[a]	1.038	1.058	1.077
R ₁ ^[b] /wR ₂ ^[c] [<i>I</i> > 2σ(<i>I</i>)]	0.0344/0.0840	0.0282/0.0746	0.0303/0.0801
R ₁ ^[b] /wR ₂ ^[c] [all]	0.0462/0.0900	0.0318/0.0771	0.0367/0.0835

[a] $S = [\sum w(F_o^2 - F_c^2)^2 / (N_{obs} - N_{param})]^{1/2}$ [b] $R_1 = \sum ||F_o| - |F_c|| / \sum |F_o|$ [c] $wR_2 = [\sum w(F_o^2 - F_c^2)^2 / \sum wF_o^4]^{1/2}$; $w = 1/[\sigma^2(F_o^2) + (aP)^2 + bP]$ where $P = (\max(F_o^2, 0) + 2F_c^2)/3$ with $a = 0.0472$ (**1**), 0.0416 (**2**), 0.0459 (**3**); and $b = 8.1485$ (**1**), 10.0330 (**2**), and 1.3767 (**3**).

The X-ray powder diffraction (XRPD) patterns were collected on a Phillips X'PERT powder diffractometer with Cu-K α radiation ($\lambda = 1.5418 \text{ \AA}$) over the range $5 < 2\theta < 50^\circ$ with a step size of 0.026° and an acquisition time of 2.5 s per step at 25°C . Indexation of the diffraction profiles were made by means of the FULLPROF program (pattern-matching analysis)⁶⁸ on the basis of the space group and the cell parameters found by single crystal X-ray diffraction. The unit cell parameters obtained in the final refinement are listed in Figure 25.

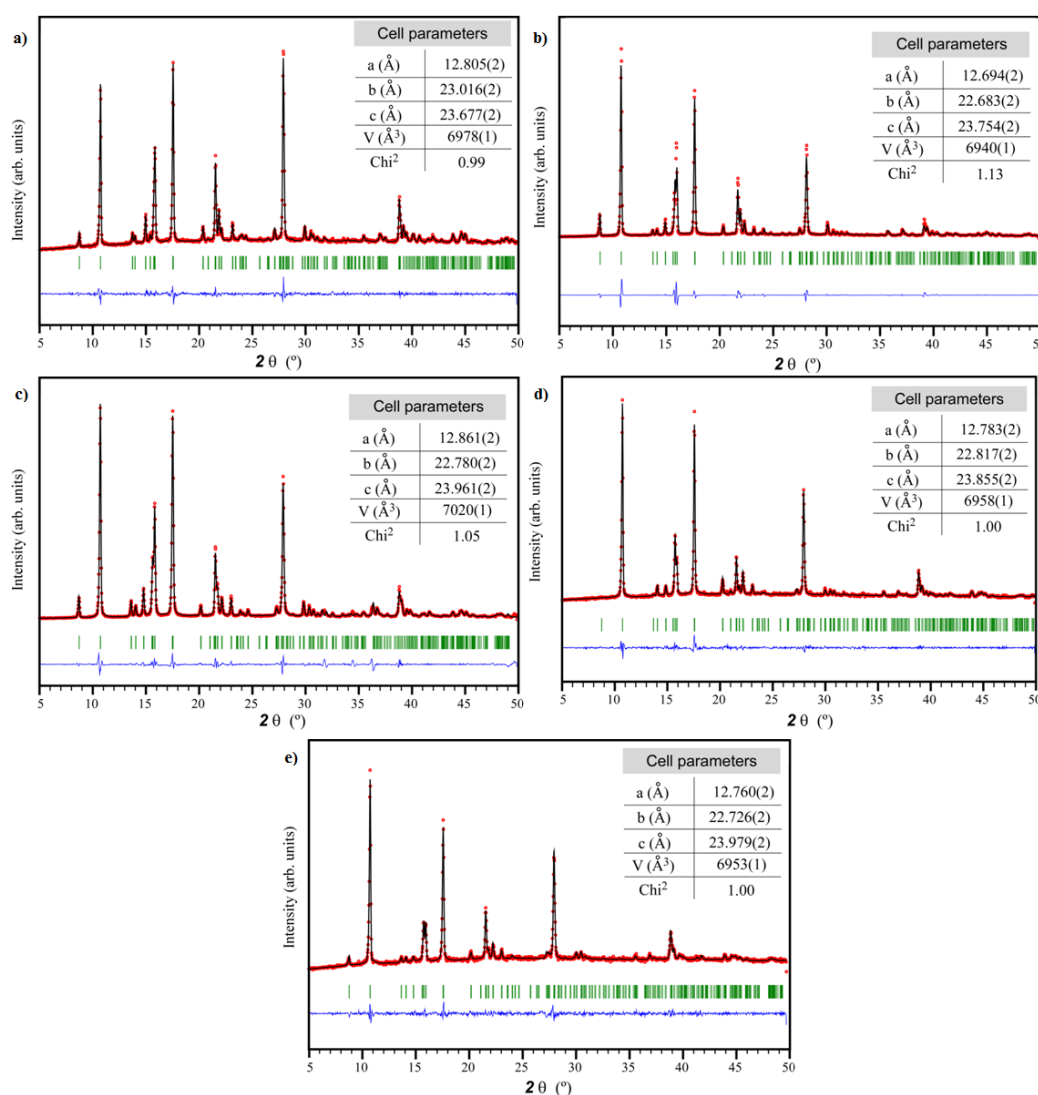


Figure 26. a) Full profile pattern-matching analysis of **1**. b) Full profile pattern-matching analysis of **2**. c) Full profile pattern-matching analysis of **3**. d) Full profile pattern-matching analysis of **1-DMSO**. e) Full profile pattern-matching analysis of **1-MeOH**.

4.4. Computational details

The computational strategy adopted in this work to compute the magnetic coupling constant (J_{calc}) values has been described and validated elsewhere.⁶⁹ One calculation was performed to determine the high-spin state and another to determine the low-spin broken symmetry state. The correctness of the latter state was ensured by means of its spin density distribution. Density functional theory was used to perform two separate calculations to evaluate the coupling constant of each compound, employing the aforementioned hybrid B3LYP functional and Gaussian-implemented 6-311G(d) basis set for all non-metal atoms and the corresponding LANL2DZ pseudopotentials for the metal atoms. Spin-density surfaces were plotted using GaussView 5.⁷⁰

PL spectra were calculated by means of TD-DFT using the Gaussian 09 package,⁷¹ using the Becke three parameter hybrid functional with the non-local correlation functional of Lee-Yang-Parr (B3LYP)^{72,73} along with 6-311G++(d,p) basis set⁷⁴ was adopted for all atoms but for the central zinc cation, for which the LANL2DZ⁷⁵ basis set along with the corresponding effective core potential (ECP) was used. The 40 lowest excitation states were calculated by the TD-DFT method. Results were analysed with GaussSum program package⁷⁶ and molecular orbitals plotted using GaussView 5.

5. References

- 1.- Kreno, L. E., Leong, K., Farha, O. K., Allendorf, M., Van Duyne R. P. & Hupp, J. T. Metal–Organic Framework Materials as Chemical Sensors. *Chem. Rev.* **112**, 110-1125 (2012).
- 2.- Cohen, S. M. Postsynthetic Methods for the Functionalization of Metal–Organic Frameworks. *Chem. Rev.* **112**, 970-1000 (2012).

- 3.- Falcaro, P., Ricco, R., Doherty, C. M., Liang, K., Hill, A. J. & Styles, M. J. MOF positioning technology and device fabrication. *Chem. Soc. Rev.* **43**, 5513-5560 (2014).
- 4.- Meek, S. T., Greathouse, J. A. & Allendorf, M. D. Metal-Organic Frameworks: A Rapidly Growing Class of Versatile Nanoporous Materials. *Adv. Mater.* **23**, 249-267 (2011).
- 5.- Cheetham, A. K. & Rao, C. N. R. Materials science. There's room in the middle. *Science* **318**, 58-59 (2007).
- 6.- Tranchemontagne, D. J., Mendoza-Cortés, J. L., O'Keeffe, M. & Yaghi, O. M. Secondary building units, nets and bonding in the chemistry of metal-organic frameworks. *Chem. Soc. Rev.* **38**, 1257-1283 (2009).
- 7.- Cepeda, J., Beobide, G., Castillo, O., Luque, A. & Pérez-Yáñez, S. Structural diversity of coordination compounds derived from double-chelating and planar diazinedicarboxylate ligands. *Coord. Chem. Rev.* **352**, 83-107 (2017).
- 8.- (a) Eddaoudi, M., Sava, D.F., Eubank, J.F., Adil, K. & Guillemin, V. Zeolite-like metal-organic frameworks (ZMOFs): design, synthesis, and properties. *Chem. Soc. Rev.* **44**, 228-249 (2015). (b) O'Keeffe, M. & Yaghi, O. M. Deconstructing the Crystal Structures of Metal-Organic Frameworks and Related Materials into Their Underlying Nets. *Chem. Rev.* **112**, 675-702 (2012).
- 9.- Janiak, Ch. & Vieth, J. K. MOFs, MILs and more: concepts, properties and applications for porous coordination networks (PCNs). *New J. Chem.* **34**, 2366-2388 (2010).
- 10.- Coronado, E. & Dumbra, K. R. Preface for the Forum on Molecular Magnetism: The Role of Inorganic Chemistry. *Inorg. Chem.* **48**, 3293-3296 (2009).
- 11.- Li, J.-R., Sculley, J. & Zhou, H.-C. Metal-Organic Frameworks for Separations. *Chem. Rev.* **112**, 869-932 (2012).
- 12.- Cepeda, J., Perez-Mendoza, M., Calahorra, A.J., Casati, N., Seco, J.M., Aragonés-Anglada, M., Moghadam, P.Z., Fairen-Jimenez, D. & Rodríguez-Diéguez,

A. Modulation of pore shape and adsorption selectivity by ligand functionalization in a series of “rob”-like flexible metal–organic frameworks. *J. Mater. Chem. A* **6**, 17409-17416 (2018).

13.- Dhakshinamoorthy, A. & Garcia, H. Metal–organic frameworks as solid catalysts for the synthesis of nitrogen-containing heterocycles. *Chem. Soc. Rev.* **43**, 5750- 5765 (2014).

14.- Ma, L., Abney, C. & Lin, W. Enantioselective catalysis with homochiral metal–organic frameworks. *Chem. Soc. Rev.* **38**, 1248-1256 (2009).

15.- Horcajada, P., Gref, R., Baati, T., Allan, P. K., Maurin, G., Couvreur, P., Férey, G., Morris, R. E. & Serre, C. Metal–Organic Frameworks in Biomedicine. *Chem. Rev.* **112**, 1232-1268 (2012).

16.- Lustig, W. P., Mukherjee, S., Rudd, N. D., Desai, A. V., Li, J. & Ghosh, S. K. Metal-organic frameworks: functional luminescent and photonic materials for sensing applications. *Chem. Soc. Rev.* **46**, 3242–3285 (2017).

17.- Kozłowski, H., Janicka-Kłos, A., Brasun, J. Gaggelli, E., Valensin, D. & Valensin, G. Copper, iron, and zinc ions homeostasis and their role in neurodegenerative disorders (metal uptake, transport, distribution and regulation). *Coord. Chem. Rev.* **253**, 2665-2685 (2009).

18.- Mølhave, L., Bach, B. & Pedersen, O. F. Human reactions to low concentrations of volatile organic compounds. *Environ. Int.* **12**, 167-175 (1986).

19.- Yi, F.-Y., Chen, D., Wu, M.-K., Han, L. & Jiang, H.-L. Chemical Sensors Based on Metal–Organic Frameworks. *ChemPlusChem* **81**, 675-690 (2016).

20.- Guo, H., Lee, S. C., Chan, L. Y. & Li, W. M. Risk assessment of exposure to volatile organic compounds in different indoor environments. *Environ. Res.* **94**, 57–66 (2004).

21.- You, L., Zha, D. & Anslyn, E. V. Recent Advances in Supramolecular Analytical Chemistry Using Optical Sensing. *Chem. Rev.* **115**, 7840-7892 (2015).

- 22.-** Allendorf, M. D., Bauer, C. A., Bhaktaa, R. K. & Houk, R. J. T. Luminescent metal–organic frameworks. *Chem. Soc. Rev.* **38**, 1330-1352 (2009).
- 23.-** Lower, S. K. & El-Sayed, M. A. The Triplet State and Molecular Electronic Processes in Organic Molecules. *Chem. Rev.* **66**, 199-241 (1966).
- 24.-** Cepeda, J. & Rodríguez-Diéguez, A. Tuning the luminescence performance of metal–organic frameworks based on d10 metal ions: from an inherent versatile behaviour to their response to external stimuli. *CrystEngComm* **18**, 8556-8573 (2016).
- 25.-** MínguezEspallargas, G. & Coronado, E. Magnetic functionalities in MOFs: from the framework to the pore. *Chem. Soc. Rev.* **47**, 533-557 (2018).
- 26.-** Frost, J. M., Harriman, K. L.M. & Murugesu, M. The rise of 3-d single-ion magnets in molecular magnetism: towards materials from molecules? *Chem. Sci.* **7**, 2470-2491 (2016).
- 27.-** Craig, G. A. & Murrie, M. 3d single-ion magnets. *Chem. Soc. Rev.* **44**, 2135-2147 (2015).
- 28.-** Seco, J. M., Oyarzabal, I., Pérez-Yáñez, S., Cepeda, J. & Rodríguez-Diéguez, A. Designing Multifunctional 5-Cyanoisophthalate-Based Coordination Polymers as Single-Molecule Magnets, Adsorbents, and Luminescent Materials. *Inorg. Chem.* **55**, 11230-11248 (2016).
- 29.-** Murrie, M. Cobalt(II) single-molecule magnets. *Chem. Soc. Rev.*, **39**, 1986–1995 (2010).
- 30.-** Gómez-Coca, S., Aravena, D., Morales, R. & Ruiz, E. Large magnetic anisotropy in mononuclear metal complexes. *Coord. Chem. Rev.*, **289**, 379–392 (2015).
- 31.-** Chen, L., Wang, J., Wei, J. M., Wernsdorfer, W., Chen, X.-T., Zhang, Y.-Q., Song, Y. & Xue, Z.-L. Slow Magnetic Relaxation in a Mononuclear Eight-Coordinate Cobalt(II) Complex. *J. Am. Chem. Soc.* **136**, 12213-12216 (2014).

- 32.-** Cepeda, J., San Sebastian, E., Padro, D., Rodríguez-Diéguez, A., García, J. A., Ugalde, J. M. & Seco, J. M. A Zn based coordination polymer exhibiting long-lasting phosphorescence. *Chem. Commun.* **52**, 8671-8674 (2016).
- 33.-** Pajuelo-Corral, O., Rodríguez-Diéguez, A., Beobide, G., Pérez-Yáñez, S., García, J. A., San Sebastian, E., Seco, J. M. & Cepeda, J. Alkaline-earth and aminonicotinate based coordination polymers with combined fluorescence/long-lasting phosphorescence and metal ion sensing response. *J. Mater. Chem. C* **7**, 6997-7012 (2019).
- 34.-** Rodríguez-Diéguez, A., Pérez-Yáñez, S., Ruiz-Rubio, L., Seco, J.M. & Cepeda, J. From isolated to 2D coordination polymers based on 6-aminonicotinate and 3d-metal ions: towards field-induced single-ion-magnets. *CrystEngComm* **19**, 2229-22242 (2017).
- 35.-** Pachfule, P., Chen, Y., Jiang, J. & Banerjee, R. Experimental and computational approach of understanding the gas adsorption in amino functionalized interpenetrated metal organic frameworks (MOFs). *J. Mater. Chem.* **21**, 17737-17745 (2011).
- 36.-** TOPOS Main Page, <http://www.topos.ssu.samara.ru> (accessed February 14, 2019).
- 37.-** Blatov, V. A., Shevchenko, A. P. & Proserpio, D. M. Applied Topological Analysis of Crystal Structures with the Program Package. *Cryst. Growth Des.* **14**, 3576-3586 (2014).
- 38.-** Lloret, F., Julve, M., Cano, J., Ruiz-Garcia, R. & Pardo, E. Magnetic properties of six-coordinated high-spin cobalt(II) complexes: Theoretical background and its application. *Inorg. Chim. Acta*, **361**, 3432-3445 (2008).
- 39.-** Sakiyama, H., Ito, R., Kumagai, H., Inoue, K., Sakamoto, M., Nishida, Y. & Yamasaki, M. Dinuclear Cobalt(II) Complexes of an Acyclic Phenol-Based Dinucleating Ligand with Four Methoxyethyl Chelating Arms – First Magnetic Analyses in an Axially Distorted Octahedral Field. *Eur. J. Inorg. Chem.* **2001**, 2027-2032 (2001).

- 40.-** Rueff, J.-M., Masciocchi, N., Rabu, P., Sironi, A. & Skoulios, A. Structure and Magnetism of a Polycrystalline Transition Metal Soap – $\text{Co}^{\text{II}}[\text{OOC}(\text{CH}_2)_{10}\text{COO}] \cdot (\text{H}_2\text{O})_2$. *Eur. J. Inorg. Chem.* **2001**, 2843-2848 (2001).
- 41.-** Cui, L., Yang, P. Y., Wu, W.-P., Miao, H.-H., Shi, Q.-Z. & Wang, Y.-Y. Solvents and auxiliary ligands co-regulate three antiferromagnetic Co(II) MOFs based on a semi-rigid carboxylate ligand. *Dalton Trans.* **43**, 5823-5830 (2014).
- 42.-** Lloret, F., Julve, M., Cano, J., Ruiz-García, R. & Pardo, E. Magnetic properties of six-coordinated high-spin cobalt(II) complexes: Theoretical background and its application. *Inorg. Chim. Acta* **361**, 3432-3445 (2008).
- 43.-** Chilton, N. F., Anderson, R. P., Turner, L. D., Soncinea, A. & Murray, K. S. PHI: a powerful new program for the analysis of anisotropic monomeric and exchange-coupled polynuclear d- and f-block complexes. *J. Comput. Chem.* **4**, 1164-1175 (2013).
- 44.-** Boča, R. Zero-field splitting in metal complexes. *Coord. Chem. Rev.*, **248**, 757–815 (2004).
- 45.-** Gómez-Coca, S., Urtizberea, A., Cremades, E., Alonso, P. J., Camón, A., Ruiz, E. & Luis, F. Origin of slow magnetic relaxation in Kramers ions with non-uniaxial anisotropy. *Nat. Commun.*, **5**, 4300 (2014).
- 46.-** Yao, P.-F., Chen, Y.-K., Lai, C.-F., Li, H.-Y., Bian, H.-D., Liu, H.-F., Yao, D. & Huang, F.-P. Hierarchical Assembly of a {Co₂₄} Cluster from Two Vertex-Fused {Co₁₃} Clusters and Their Single-Molecule Magnetism. *Inorg. Chem.* **57**, 9182-9189 (2018).
- 47.-** Liu, Y., Shi, W.-J., Lu, Y.-K., Liu, G., Hou, L. & Wang, Y.-Y. Nonenzymatic Glucose Sensing and Magnetic Property Based On the Composite Formed by Encapsulating Ag Nanoparticles in Cluster-Based Co-MOF. *Inorg. Chem.* **58**, 16743-16751 (2019).
- 48.-** Du, Z.-Y., Zhang, L., Wang, B.-Y., Liu, S.-J., Huang, B., Liu, C.-M. & Zhang, W.-X. Two magnetic Δ -chain-based Mn(II) and Co(II) coordination polymers with

mixed carboxylate-phosphinate and μ_3 -OH⁻ bridges. *CrystEngComm*, **19**, 1052-1057 (2017).

49.- Zhang, X.-M., Li, P., Gao, W., Liu, J.-P. & Gao, E.-Q. 3D Co(II) coordination polymer with ferromagnetic-like layers based on azide and tetrazolate bridges showing slow magnetic dynamics. *Dalton Trans.*, **44**, 511–514 (2015).

50. - García-Valdivia, A. A., Seco, J. M., Cepeda, J. & Rodríguez-Diéguez, A. Designing Single-Ion Magnets and Phosphorescent Materials with 1-Methylimidazole-5-carboxylate and Transition-Metal Ions. *Inorg. Chem.* **56**, 13897-13912 (2017).

51.- Herchel, R., váhová, L., Potocnak, I. & Travnicek, Z. Slow Magnetic Relaxation in Octahedral Cobalt(II) Field-Induced Single-Ion Magnet with Positive Axial and Large Rhombic Anisotropy. *Inorg. Chem.* **53**, 5896-5898 (2014).

52.- Nyokong, T. Effects of substituents on the photochemical and photophysical properties of main group metal phthalocyanines. *Coord. Chem. Rev.* **251**, 1707-1722 (2007).

53.- San Sebastian, E., Rodríguez-Diéguez, A., Seco, J. M. & Cepeda, J. Coordination Polymers with Intriguing Photoluminescence Behavior: The Promising Avenue for Greatest Long-Lasting Phosphors. *Eur. J. Inorg. Chem.* **2018**, 2155-2174 (2018).

54.- Beeby, A., Clarkson, I. M., Dickins, R. S., Faulkner, S., Parker, D., Royle, L., de Sousa, A. S., Gareth Williams, J. A. & Woods, M. Non-radiative deactivation of the excited states of europium, terbium and ytterbium complexes by proximate energy-matched OH, NH and CH oscillators; an improved luminescence method for establishing solution hydration states. *J. Chem. Soc., Perkin Trans. 2*, 493–503 (1999).

55.- Melavanki, R. M., Kusanur, R. A., Dadadevaramath, J. S. & Kulkarni, M. V. Effect of solvent polarity on the fluorescence quenching of biologically active 5BAMC by aniline in binary solvent mixtures. *J. Fluores.* **20**, 1175-1180 (2010).

- 56.-** Ma, D., Wang, W., Li, Y., Li, J., Daignebonne, C., Calvez, G. & Guillou, O. *in situ* 2,5-pyrazinedicarboxylate and oxalate ligands synthesis leading to a microporous europium–organic framework capable of selective sensing of small molecules. *CrystEngComm* **12**, 4372-4377 (2010).
- 57.-** Qiu, Y. C., Deng, H., Mou, J. X., Yang, S. H., Zeller, M., Batten, S. R., Wu, H. H. & Li, J. *In situ* tetrazole ligand synthesis leading to a microporous cadmium–organic framework for selective ion sensing. *Chem. Commun.* **2009**, 5415-5417 (2009).
- 58.-** Liu, X.-J., Zhang, Y.-H., Chang, Z., Li, Z.-L., Tian, D., Yao, Z.-Q., Jia, Y.-Y. & Bu, X.-H. A Water-Stable Metal–Organic Framework with a Double-Helical Structure for Fluorescent Sensing. *Inorg. Chem.* **55**, 7326–7328 (2016).
- 59.-** He, J., Xu, J., Yin, J., Li, N. & Bu, X.-H. Recent advances in luminescent metal–organic frameworks for chemical sensors. *Sci China Mater* **62**, 1655-1678 (2019).
- 60.-** Gao, Q., Xu, J. & Bu, X.-H. Recent advances about metal–organic frameworks in the removal of pollutants from wastewater. *Coord. Chem. Rev.* **378**, 17-31 (2019).
- 61.-** Lu, B. B., Jiang, W., Yang, J., Liu, Y. Y. & Ma, J. F. Resorcin[4]arene-based Microporous Metal-Organic Framework as an Efficient Catalyst for CO₂ Cycloaddition with Epoxides and Highly Selective Luminescent Sensing of Cr²⁺. *ACS Appl. Mater. Interfaces* **9**, 39441-39449 (2017).
- 62.-** Earnshaw, A. in: *Introduction to Magnetochemistry*, Academic Press: London, 1968.
- 63.-** Bruker. Apex2, Bruker AXS Inc: Madison, WI, 2004.
- 64.-** Sheldrick, G. M. *SADABS, Program for Empirical Adsorption Correction*, Institute for Inorganic Chemistry, University of Gottingen: Germany, 1996.
- 65.-** Altomare, A., Burla, M. C., Camalli, M., Cascarano, G. L., Giacovazzo, C., Guagliardi, A., Moliterni, A. G. G., Polidori, G. & Spagna, R. SIR97: a new tool for crystal structure determination and refinement. *J. Appl. Crystallogr.* **32**, 115-119 (1999).

66.- Sheldrick, G. M. *SHELX-2014, Program for Crystal Structure Refinement*, University of Göttingen: Göttingen, Germany, 2014.

67.- Farrugia, L. J. WinGX suite for small-molecule single-crystal crystallography. *J. Appl. Crystallogr.* **32**, 837-838 (1999).

68.- Rodríguez-Carvajal, J. *FULLPROF, version July-2017*, Laboratoire Léon Brillouin (CEA-CNRS), Centre d'Études de Saclay, Gif sur Yvette Cedex: France, 2017.

69.- Ruiz, E., Rodríguez-Forteza, A., Cano, J., Álvarez, S. & Alemany, P. About the calculation of exchange coupling constants in polynuclear transition metal complexes. *J. Comput. Chem.* **24**, 982-989 (2003).

70.- Dennington, R., Keith, T., Millam, J. *GaussView, Version 5*, Semichem Inc: Shawnee Mission, KS, 2009.

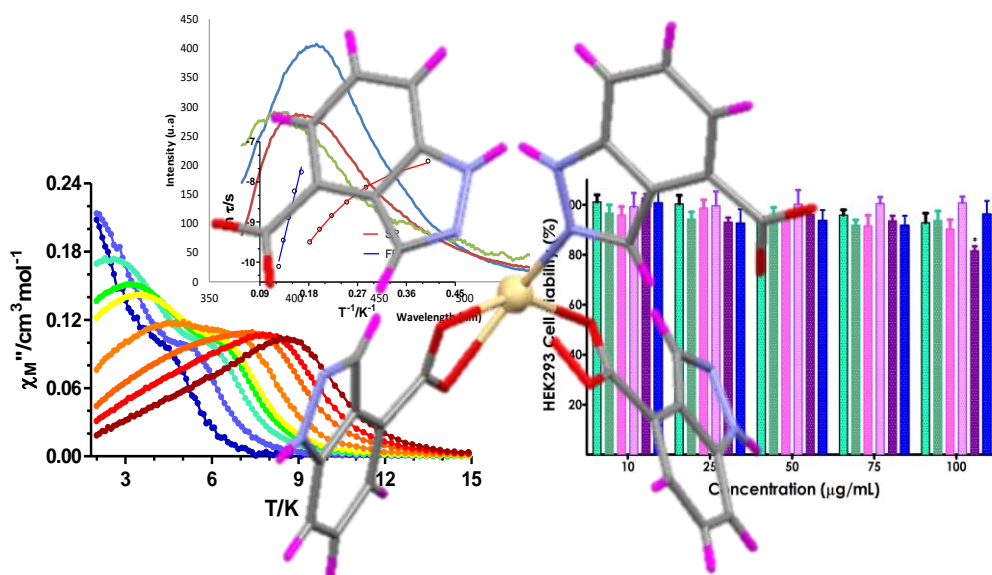
71.- Frisch, M. J., Trucks, G. W., Schlegel, H. B., Scuseria, G. E., Robb, M. A., Cheeseman, J. R., Scalmani, G., Barone, V., Mennucci, B., Petersson, G. A., Nakatsuji, H., Caricato, M., Li, X., Hratchian, H. P., Izmaylov, A. F., Bloino, J., Zheng, G., Sonnenberg, J. L., Hada, M., Ehara, M., Toyota, K., Fukuda, R., Hasegawa, J., Ishida, M., Nakajima, T., Honda, Y., Kitao, O., Nakai, H., Vreven, T., Montgomery Jr., J. A., Peralta, J. E., Ogliaro, F., Bearpark, M., Heyd, J. J., Brothers, E., Kudin, K. N., Staroverov, V. N., Kobayashi, R., Normand, J., Raghavachari, K., Rendell, A., Burant, J. C., Iyengar, S. S., Tomasi, J., Cossi, , Rega, N., Millam, J. M., Klene, M., Knox, J. E., Cross, J. B., Bakken, V., Adamo, C., Jaramillo, J., Gomperts, R., Stratmann, R. E., Yazyev, O., Austin, A. J., Cammi, R., Pomelli, C., Ochterski, J. W., Martin, R. L., Morokuma, K., Zakrzewski, V. G., Voth, G. A., Salvador, P., Dannenberg, J. J., Dapprich, S., Daniels, A. D., Farkas, O., Foresman, J. B., Ortiz, J. V., Cioslowski, J., Fox, D. J. *Gaussian 09, revision A.02*, Gaussian, Inc., Wallingford, CT, 2009.

72.- Becke, A. D. A new mixing of Hartree–Fock and local density-functional theories. *J. Chem. Phys.* **98**, 5648-5652 (1993).

- 73.-** Lee, C., Yang, W.& Parr, R. G. Development of the Colle-Salvetti correlation-energy formula into a functional of the electron density. *Phys. Rev. B* **37**, 785-789 (1988).
- 74.-** Noodleman, L., Case, D. A.&Aizman, A. Broken symmetry analysis of spin coupling in iron-sulfur clusters. *J. Am. Chem. Soc.*, **110**, 1001–1005 (1988).
- 75.-** Hay, P. J.&Wadt, W. R.Ab initio effective core potentials for molecular calculations. Potentials for the transition metal atoms Sc to Hg. *J. Chem. Phys.* **82**, 270 (1985).
- 76.-** O'Boyle, N. M., Tenderholt, A. L.&Langner, K. M. cclib: a library for package-independent computational chemistry algorithms.. *J. Comput. Chem.* **29**, 839-845 (2008).

Capítulo 5

2D-Coordination Polymers based on 1H-Indazole-4-Carboxylic Acid and Transition Metal ions: Magnetic, Luminescent and Biological Properties



2D-Coordination Polymers based on 1H-Indazole-4-Carboxylic Acid and Transition Metal ions: Magnetic, Luminescent and Biological Properties

Antonio A. García-Valdivia,^a Andoni Zabala-Lekuona,^b Gloria B. Ramírez-Rodríguez,^a José M. Delgado-López,^a Belén Fernández,^c Javier Cepeda,^b and Antonio Rodríguez-Diéguez^{a,*}

ACEPTADO: DALTON TRANSACTIONS

^a *Departamento de Química Inorgánica, Facultad de Ciencias, Universidad de Granada, 18071 Granada, Spain.*

^b *Departamento de Química Aplicada, Facultad de Química, Universidad del País Vasco/EuskalHerrikoUnibertsitatea (UPV/EHU), 20018 Donostia-San Sebastian, Spain.*

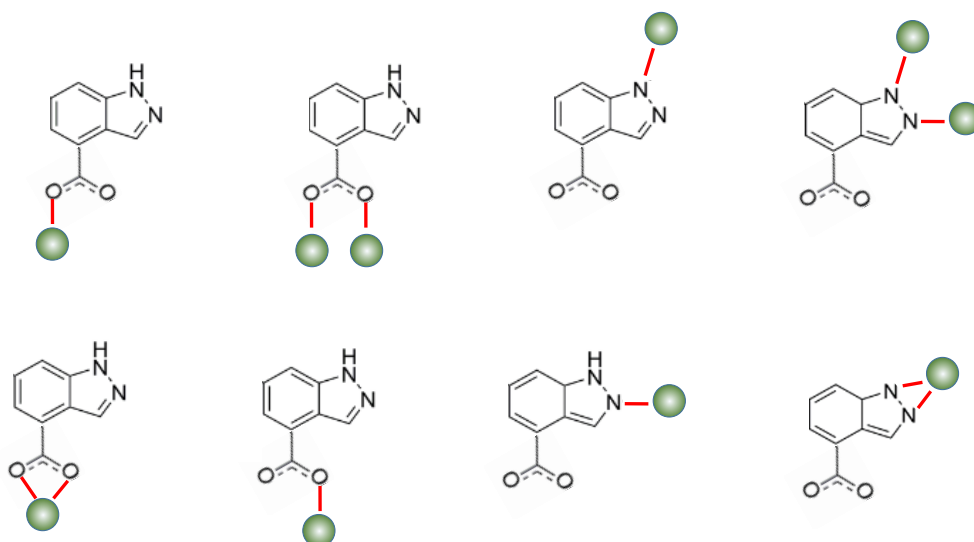
^c *Institute of Parasitology and Biomedicine "López-Neyra", CSIC, Av. Conocimiento s/n, 18600, Granada, Spain.*

Abstract

We report the formation of five novel multifunctional coordination polymers based on 1H-indazole-4-carboxylic acid (HL). To the best of our knowledge, these complexes are the first examples of coordination compounds construct with this novel ligand. These materials were synthesized by soft solvothermal routes, possess different 2D-structures and show interesting magnetic properties due to copper compound shows unusual spin-canted effect while anisotropic cobalt material behaves as a field-induced single molecule magnet. Moreover, cadmium and zinc polymers exhibit luminescent properties, as well as absence of cytotoxicity both in cancer and non-cancer cells, transforming this new family in excellent candidates to be further investigated in the field of luminescent materials with biomedical applications.

1. Introduction

The more than remarkable interest in coordination polymers (CPs), also known as metal-organic frameworks (MOFs), has undergone an exponential growth,¹ derived from their multiple types of verified industrial applications,² such as gas storage and purification, catalysis, luminescence and magnetism, as well as the great possibilities it offers when designing and its great synthetic reproducibility. Of particular interest is the fact that their metal–organic hybrid nature offers potentially limitless arrangement types and topological architectures,³ reinforcing their versatility of use. In particular, the study of transition metal ions-based MOFs has evolved enormously in a great quantity of areas, considering the advantage that ions have fairly predictable coordination spheres, it allows us to design on paper materials with application for virtually all fields. In this sense, in these years, our group and others have worked in the design of novel MOFs to study their properties in luminescence,⁴ gas adsorption,⁵ catalysis,⁶ magnetism,⁷ biology as drug-delivery systems,⁸ cytotoxic agents⁹ and sensing.¹⁰ Bearing in mind the interest of our group in the study of MOFs based on nitrogen linkers with carboxylate groups, we decided to study the properties of this type of materials with the novel 1H-indazole-4-carboxylic acid because, as far as we know, there are no coordination compounds synthesized with it. This ligand is an ideal candidate to form CPs because of its multiple coordination possibilities not only derived from its carboxylate group but also from its indazole ring, being able to show some interesting coordination modes (Scheme I). In addition, the study of the properties of these materials can be very interesting, not only it can enable promising photoluminescence performance resulting from the aromatic rings, but it has also been seen in some recent studies that it can have very interesting anti-cancer properties, turning these CPs into interesting multifunctional materials.¹¹



Scheme I. Plausible coordination modes of 1H-indazole-4-carboxylic acid.

All of the above, in this work we present a new family of 2D-coordination polymers $[\text{Co}(\text{L})_2(\text{H}_2\text{O})_2]_n$ (**1**), $[\text{Ni}(\text{L})_2(\text{H}_2\text{O})_2]_n$ (**2**), $[\text{Cu}(\text{L})_2(\text{H}_2\text{O})]_n$ (**3**), $[\text{Zn}(\text{L})_2]_n$ (**4**) and $[\text{Cd}(\text{L})_2]_n$ (**5**), based on 1H-indazole-4-carboxylic acid and transition metal ions which have been fully characterized from a structural, luminescent and cytotoxic point of view, and highlighting the magnetic properties.

2. Results and discussion

2.1. Description of the structures

Compounds **1** and **2** crystallize in the monoclinic $P2_1/c$ space group and are isostructural materials, therefore, only the structure of **1** is described in detail. The Co(II) ion is located in an inversion center, so that the asymmetric unit contains half cobalt ion, one deprotonated ligand and a coordination water molecule (Figure 1a). The Co1 ion owns a well-defined octahedral CoN_2O_4 coordination environment according to SHAPE values (Table 1).

Table 1. Continuous Shape Measurements for compounds **1** and **2**.

Structure [ML6]	HP-6	PPY-6	OC-6	TPR-6	JPPY-6
Comp1 Co1	32.146	29.617	0.044	16.397	32.961
Comp2 Ni1	31.775	29.505	0.060	16.186	32.854

HP-6 1, D_{6h} Hexagon ; *PPY-6*, 2 C_{5v} Pentagonal pyramid; *OC-6* ,3 Oh Octahedron; *TPR-6* , 4 D_{3h} Trigonal prism; *JPPY-6*, 5 C_{5v}Johnson pentagonal pyramid J2.

The coordinating heteroatoms are all placed in *trans* positions according to its nature (imine N atoms, carboxylate O atoms and water O atoms). Due to the negative charge of the carboxylate oxygen atoms, the shortest bond distances correspond to Co1-O1 (2.0913(9) Å), while Co1-O1W and Co1-N1 distances appear to be somewhat longer (2.1266(9) and 2.1539(11) Å, respectively).

The structure is extended in two directions from each single Co(II) center. Firstly, the indazole derivatives that are coordinated from N1, are inversely oriented so that the carboxylates are located in the opposite sites (Figure 1a). Thus, these carboxylate groups coordinate in a monodentate mode to others Co1' metallic centers in a *zig-zag* fashion (Figure 1b). Secondly, the carboxylates coming from others two main ligands are nearly perpendicular to through imine coordinated indazole derivatives (an angle of 72.68° is formed between two ligands growing in different directions) expanding the structure in a plane. The structures grow in independent 2D layers (Figure 1b), but intermolecular hydrogen bonds play an essential role in stabilizing the structure (Figure 1c). The *trans* water molecules act as donor and acceptor of these bonds. In fact, they form intramolecular hydrogen bonds with the non-coordinating carboxylate O2 atom, forming a distorted six membered ring (Co1-O1W-H1W1...O2-C8-O1) and an intermolecular with O1 (O1W...O1). O1W accepts an extra intermolecular hydrogen bond from a neighbouring imine (N2...O1W). The ionic Co(II) centers are well isolated within the same chain with a distance of 9.104 Å, whereas the intermolecular distances are much shorter, 5.301 Å.

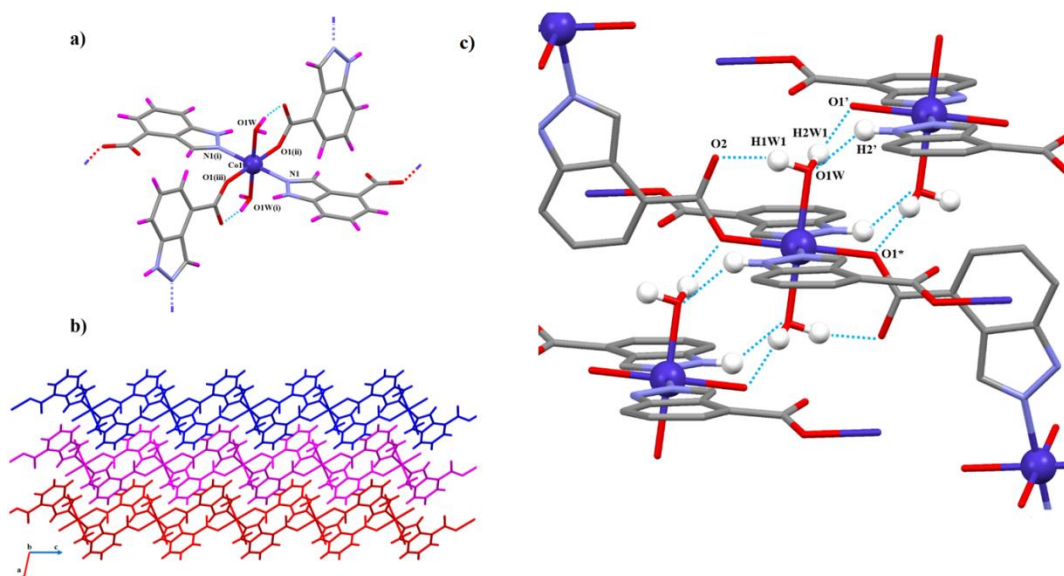


Figure 1. a) Building unit of compound **1** with atom labels for the coordination sphere. Dashed blue lines represent the intramolecular hydrogen bonds. b) View along the *b* axis of the packing of three 2D layers, each of them with a different colour. The same structure was obtained for compound **2**. c) Intra- and intermolecular hydrogen bonds that stabilize the supramolecular structure of compound **1**.

Compound **3** crystallizes in the monoclinic system and $P2_1/c$ space group. Although it is similar to **1-2**, in this case the asymmetric unit is comprised by a single Cu(II) ion coordinated to two crystallographically independent monoanionic ligands (labelled with A and B) and one coordination water molecule (Figure 2). The Cu1 ion possesses a CuN_2O_3 coordination environment (Figure 2a), forming a slightly distorted polyhedron between square pyramid and vacant octahedron according to the SHAPE measurements (Table 2).

Table 2. Continuous Shape Measurements for compound **3**.

Structure [ML5]	PP-5	vOC-5	TBPY-5	SPY-5	JTBPY-5
Comp3 Cu1	30.052	0.945	5.690	0.832	8.668

PP-5, 1 D5h Pentagon; *vOC-5*, 2 C4v Vacant octahedron; *TBPY-5*, 3 D3h Trigonal bipyramid; *SPY-5*, 4 C4v Spherical square pyramid; *JTBPY-5*, 5 D3h Johnson trigonal bipyramid J12.

The two nitrogen N1A and N1B atoms in opposite positions, along with two monodentate carboxylate oxygen atoms belonging to two other main ligands (O1A(i)

and O1B(i)) are nearly coplanar and form the base of the pyramid. The remaining oxygen O1W from the water molecule is coordinated in the apical position completing the polyhedron. The Cu-O_{carboxylate} bonds are the shortest ones (1.948(3) and 1.972(3) Å), whereas Cu-N are slightly longer (1.993(4) and 2.013(4) Å) and Cu-O1W shows the longest distance with 2.361(4) Å.

As well as in **1-2**, the structure is extended in two directions from each Cu(II) center. The inversely oriented indazole derivatives are responsible of the *zig-zag* expansion of the structure. In this case, the intrachain adjacent Cu(II) polyhedra form an angle of 80.71° between the square bases. In addition to the hydrogen bonds, intermolecular $\pi \cdots \pi$ interactions significantly influence the crystal packing of the structure and stabilization of the independent 2D layers (Figure 2b and 2c). In regard to H bonds, the apical water molecule acts again as donor and acceptor. It establishes an intramolecular H bond between O1W \cdots O2B (forming an even more distorted six membered ring due to the longer Cu1-O1W distance), whereas an intermolecular one is formed between O1W \cdots O1A. At the same time, accepts an intermolecular H bond from N2A.

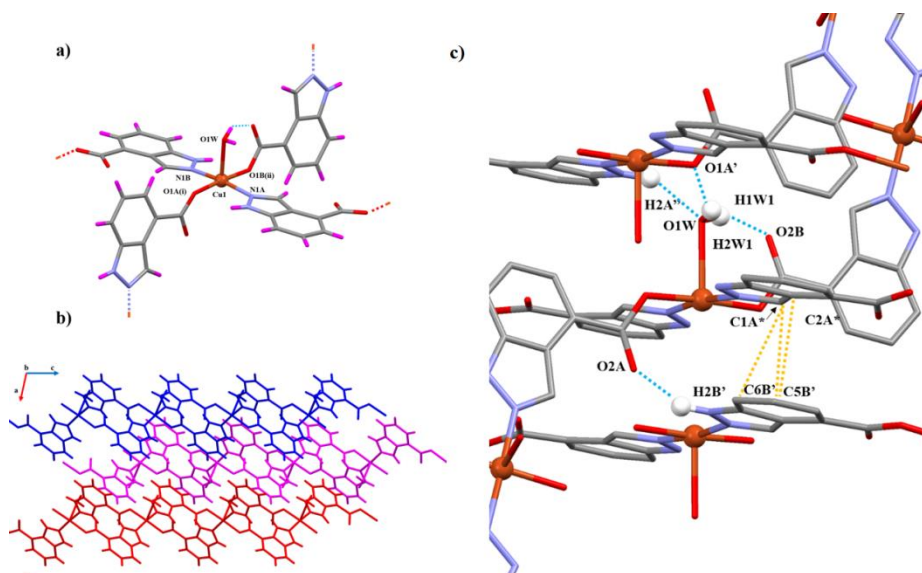


Figure 2. a) Building unit of compound **3** with atom labels for the coordination sphere. Dashed blue lines represent the intramolecular hydrogen bonds. b) View along the *b* axis of the packing of three 2D layers, each of them coloured by a different colour. The same structure was obtained for compound **4**. c) Intra- and intermolecular hydrogen bonds (dashed blue lines) as well as intermolecular $\pi \cdots \pi$ interactions (dashed yellow lines) that stabilize the supramolecular structure of compound **3**.

Because there is not another water molecule *trans* to O1W, the non-coordinating oxygen from the other carboxylate is stabilized by a N2B...O2A hydrogen bond. Moreover, in this case the neighbouring molecules form additional intermolecular $\pi\cdots\pi$ interactions between C1A*...C5B', C1A*...C6B' and C2A*...C5B' that contribute to the long ordering organization of the structure (Figure 2c). Finally, it is worth mentioning that the shortest Cu...Cu distances arise from intermolecular ones (4.743 Å), intramolecular distances are almost the double (8.803 and 8.904 Å).

Relative to compound **4**, single crystals could not be isolated for XR diffraction. However, according to infrared and elemental analysis, we think it is probably an isostructural compound to the cadmium polymer.

Compound **5** crystallizes in the orthorhombic system and *Pccn* space group. The asymmetric unit contains a half Cd(II) ion and a single 1H-indazole-4-carboxylate ligand. As a difference to the previous structures, in this compound water molecules are absent and the CdN₂O₄ coordination sphere is bonded to four different indazole derivatives (Figure 3a). Two of them are coordinated through the imine nitrogen atoms and the others via bidentate carboxylate groups. Thus, the environment of the metal ion is far from an ideal geometry, as all the SHAPE values clearly deviate from zero (Table 3). Alternatively, when considering the second coordination sphere for the carboxylate units and assuming C8 and C8(i) as the vertex of the polyhedron, a slightly distorted tetrahedron shaped fragment is obtained (Table 3).

Table 3. Continuous Shape Measurements for compounds **5** (up). Continuous Shape Measurements for compound **5** considering CdN₂C₂ coordination environment (bottom).

Structure [ML6]	HP-6	PPY-6	OC-6	TPR-6	JPPY-6
Comp5 Cd1	29.641	20.397	5.963	12.968	25.099

Structure [ML4]	SP-4	T-4	SS-4	vTBPY-4
Comp5 Cd1	22.557	2.297	6.480	4.881

PP-5, 1 D_{5h} Pentagon; *vOC-5*, 2 C_{4v} Vacant octahedron; *TBPY-5*, 3 D_{3h} Trigonal bipyramid; *SPY-5*, 4 C_{4v} Spherical square pyramid; *JTBPY-5*, 5 D_{3h} Johnson trigonal bipyramid J12; *SP-4*, 1 D_{4h} Square; *T-4*, 2 Td Tetrahedron; *SS-4*, 3 C_{2v} Seesaw; *vTBPY-4*, 4 C_{3v} Vacant trigonal bipyramid.

In regard to bond distances, Cd1-N1 distances are short (2.267(10) Å), whereas Cd1-O_{carboxylate} bonds vary from shorter (2.291(9) Å) to longer distances (2.448(10) Å).

The structure grows in 2D layers due to the orientation of the four indazole derivatives coordinated to the Cd1. Similar to a propeller, the planes formed by C1-N1-N2 and O1-C8-O2 create open angles in the range of 45.11-78.63° allowing the structure to extend all over the *ab* plane (Figure 3b). In terms of 3D packing, intermolecular hydrogen bonds as well as $\pi \cdots \pi$ interactions are fundamental to stabilize the system. Hydrogen bonds are formed between O2 \cdots N2 of adjacent layers growing in opposite directions. These ones are responsible of the longest Cd1-O_{carboxylate} bond distances. In addition, the indazole rings create $\pi \cdots \pi$ stacking interactions among them (Figure 3c). As it occurs with the other structures, the shortest Cd \cdots Cd interactions are the ones between different molecules (6.194 Å), although intramolecular distances are smaller than in the previous compounds (7.950 Å).

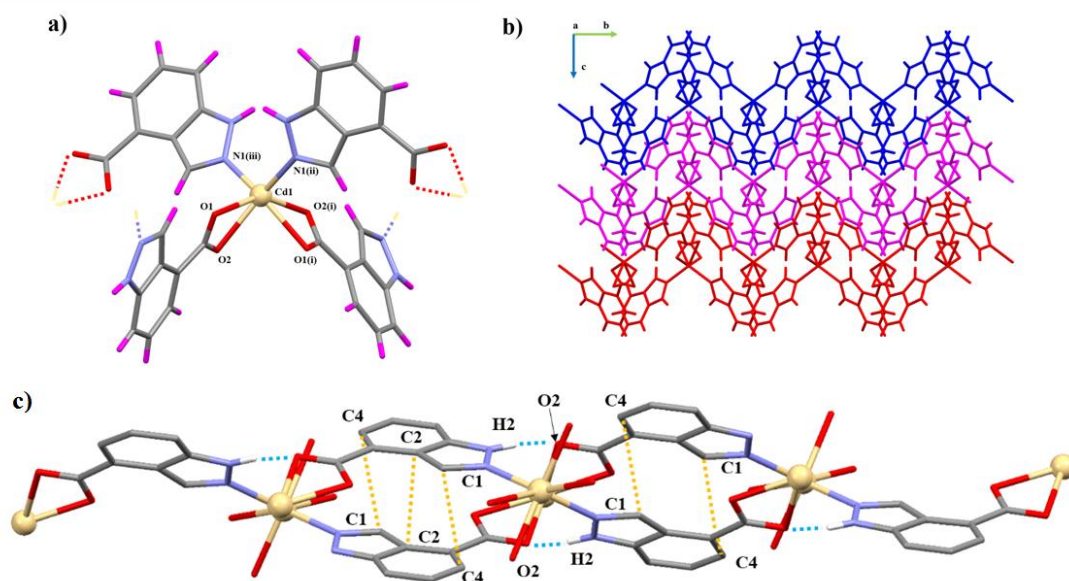


Figure 3. a) Building unit of compound **5** with atom labels for the coordination sphere. b) View along the *a* axis of the packing of three 2D layers, each of them coloured by a different colour. c) Intermolecular hydrogen bonds (dashed blue lines) and $\pi\cdots\pi$ interactions (dashed yellow lines) that are responsible of the packing structure of the 2D layers in compound **5**.

2.2. Magnetic Properties

2.2.1. Static Magnetic Measurements

The temperature dependence of the $\chi_M T$ product for complexes **1-3** (χ_M being the molar paramagnetic susceptibility of the compound) under a constant magnetic field of 0.1 T in the 2-300 K range are displayed in Figures 4, 6 and 7, respectively.

The $\chi_M T$ data of compound **1** is characteristic of anisotropic Co(II) ions. The room temperature value for **1** ($3.07 \text{ cm}^3 \text{ K mol}^{-1}$) is much larger than the spin-only value for a high-spin Co(II) ion ($S = 3/2$, $1.875 \text{ cm}^3 \text{ K mol}^{-1}$ with $g = 2$). This high value indicates a significant orbital contribution to the magnetic moment.

When lowering the temperature, the $\chi_M T$ product decreases gradually reaching a minimum of $1.58 \text{ cm}^3 \text{ K mol}^{-1}$ (Figure 4). The monotonous decrease is mainly associated to spin-orbit coupling (SOC) effects. However, due to the considerably short (5.301 \AA) intermolecular interactions between Co(II) ions, weak

antiferromagnetic interactions could be also involved. To further analyse the magnetic behaviour of **1**, the T state to P state isomorphism (T-P) in the Hamiltonian of equation (1) is an appropriate option, since the magnetic behaviour of octahedral Co(II) complexes is usually induced by first-order spin-orbital coupling.¹²

$$\hat{H} = \sigma\lambda \hat{L}\hat{S} + \Delta[\hat{L}_z^2 - \hat{L}(\hat{L}+1/3)] + \mu_B H(-\sigma \hat{L} + g_i \hat{S}) \text{ (equation 1)}$$

In this equation, λ is the SOC parameter, $\sigma = -A\kappa$ is a combination of the covalency and orbital reduction factor, and Δ is the axial orbital splitting of the T₁ term. The data was fitted using the software PHI¹³ and the following set of parameters was obtained: $\lambda = -183 \text{ cm}^{-1}$, $\sigma = 1.09$, $\Delta = 640 \text{ cm}^{-1}$ and $g = 2.06$ with $R = 6.7 \times 10^{-1}$.

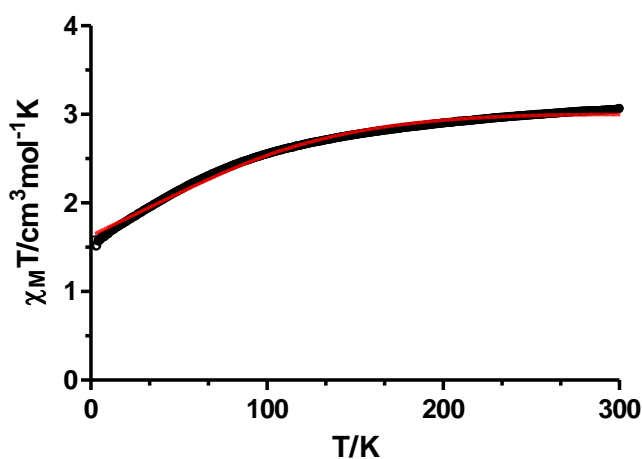


Figure 4. Temperature dependence of the $\chi_M T$ product for **1** in the 2-300 K range. The red solid line is generated from the best fit to the Hamiltonian in equation 1.

The field-dependent magnetization curves at different temperatures that are shown in the Figure 5a confirm the presence of significant magnetic anisotropy, since they are not superimposable. In order to gain information about the magnitude and sign of the anisotropy parameter (D) all the isofield magnetization curves were simultaneously fitted using the PHI program based on the following spin Hamiltonian (2):

$$\hat{H} = g\mu_B\hat{S}\cdot B + D(\hat{S}_z^2 - \hat{S}^2/3) + E(\hat{S}_x^2 - \hat{S}_y^2) \text{ (equation 2)}$$

Where S is the spin ground state, D and E are the axial and transverse magnetic anisotropies, respectively; μ_B is the Bohr magneton, and H the applied magnetic field. The best fit of the data led to the following set of parameters: $D = 50.0 \text{ cm}^{-1}$, $E = 10.0 \text{ cm}^{-1}$, $g_x = g_y = 2.31$, $g_z = 2.60$, $R = 2.52 \times 10^{-1}$. It is worth mentioning that non reasonable set of parameters was obtained by changing the sign of D . The influence of intra- and intermolecular interactions was neglected in the treatment of the magnetic data due to the results that were obtained in the DFT calculations carried out with the broken-symmetry methodology. A dinuclear fragment of **1** was cut from the crystal structure in order to represent the superexchange pathway. The calculation suggests a negligible coupling with very weak ferromagnetism ($J \sim 0.004 \text{ cm}^{-1}$, Figure 5b).

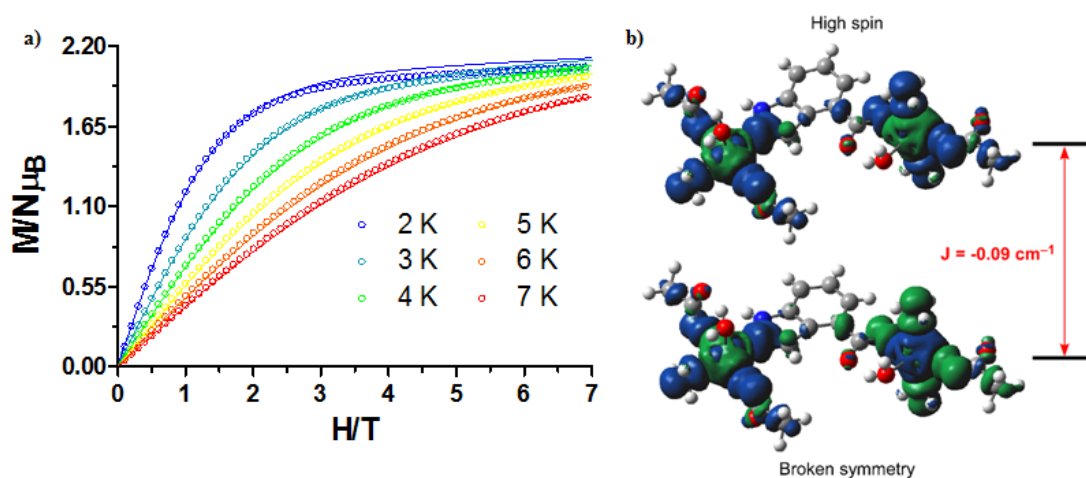


Figure 5. a) Field dependence of the magnetization for **1**. The solid lines are generated from the best fit to the magnetic Parameters. b) Broken-symmetry DFT based calculation on **1** (top) and **3** (down) to account for the value of the exchange parameter. Spin densities are shown for ground and excited states involving the superexchange pathway.

At room temperature the $\chi_M T$ value of $1.04 \text{ cm}^3 \text{ K mol}^{-1}$ for complex **2** is in good agreement with the expected value of $1.00 \text{ cm}^3 \text{ K mol}^{-1}$ for an isolated Ni(II) ion with $g = 2.0$ (Figure 6). Upon cooling, the $\chi_M T$ value remains nearly constant up to 10 K and then abruptly decreases reaching a minimum value of $0.69 \text{ cm}^3 \text{ K mol}^{-1}$. This behaviour is the first evidence of zero-field splitting (ZFS) in Ni(II) compounds.

In addition, the magnetization curve at 2 K saturates below $2\mu_B$, which definitely confirms the presence of this effect (Figure 6, inset).¹⁴ We assume that the long (9.045 Å) intramolecular distances will cause negligible interactions (as it was confirmed for **1** by DFT calculations) in comparison to the mentioned ZFS. Therefore, the *dc* magnetic susceptibility data and magnetization curves at different temperatures were simultaneously analysed with the PHI software and the Hamiltonian from equation 2.

The best fit of the experimental data was obtained with the following set of parameters: $g = 2.04$, $D = -10.58 \text{ cm}^{-1}$, and $E = +0.29 \text{ cm}^{-1}$, with $R = 2.49 \times 10^{-2}$. In view of the short intermolecular distances (5.305 Å) between Ni(II) ions provided by hydrogen bonds, intermolecular interactions were considered in the Hamiltonian. However, the fit to the magnetic data afforded nearly the same values, so they were discarded in order to be coherent with the previous fit of **1**.

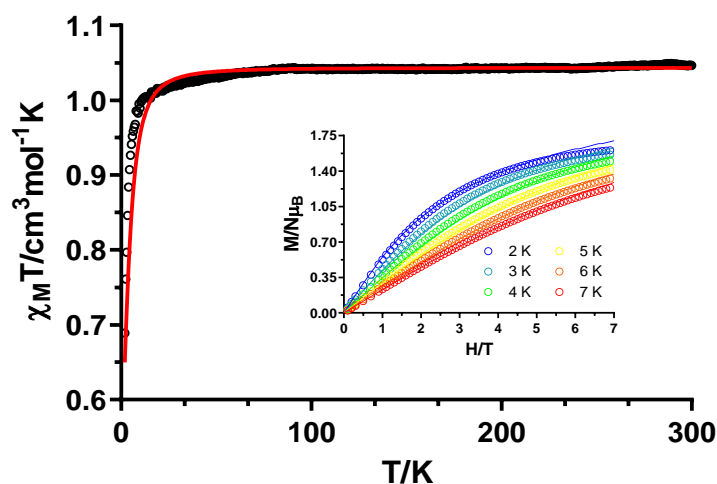


Figure 6. Temperature dependence of the $\chi_M T$ product for **2** in the 2-300 K range. Inset: field dependence of the magnetization for **2**. The solid lines are generated from the best fit to the magnetic parameters.

The temperature dependence of the magnetic susceptibility of **3** in the 2-300 K temperature range under an applied field of 0.1 T is displayed in Figure 7. At room temperature, the $\chi_M T$ value of $0.436 \text{ cm}^3 \text{ K mol}^{-1}$ is higher than the spin only value

expected for an isolated Cu(II) center ($0.375 \text{ cm}^3 \text{ K mol}^{-1}$ with $S = 1/2$ and $g = 2.0$). This occurs when the orbital angular momentum is not completely quenched leading to higher g values and, inherently to higher $\chi_M T$. Upon cooling, the $\chi_M T$ decreases gradually from room temperature reaching the lowest value of $0.355 \text{ cm}^3 \text{ K mol}^{-1}$ at 10 K. Below this temperature, the signal sharply increases to a maximum of $0.467 \text{ cm}^3 \text{ K mol}^{-1}$ at 5 K before it drops rapidly to $0.398 \text{ cm}^3 \text{ K mol}^{-1}$ at 2 K. The maximum displayed at low temperature could be associated to a spontaneous magnetization indicating spin-canted antiferromagnetism that leads at the same time to ferromagnetic ordering.¹⁵ The last drop in $\chi_M T$ could be explained by zero-field-splitting (ZFS) of the ground state.¹⁶

The proposed spin-canted effect can be verified by studying the field-dependence of the $\chi_M T$ in the temperature region that the maximum appears. On the inset of Figure 7 it is evidenced that the $\chi_M T$ value is field-dependent. When intensifying the magnitude of the external magnetic field from 4.5 Oe to 500 Oe, the maximum value at 5 K becomes nearly one order of magnitude smaller. This suggests that the high fields are quenching the effect of the weak antiferromagnetism and confirms the spin canting behaviour.

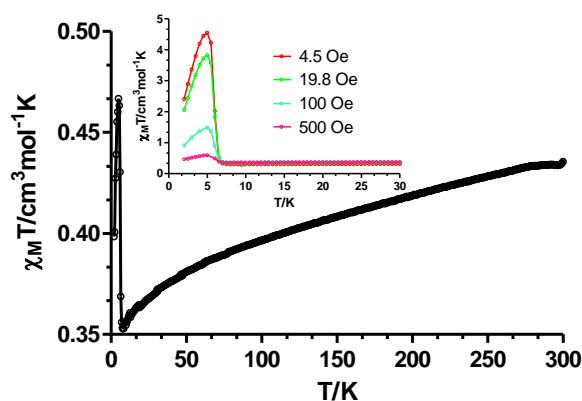


Figure 7. Temperature dependence of the $\chi_M T$ product for **3** in the 2-300 K range. Inset: temperature dependence of the $\chi_M T$ product at the indicated fields in the 2-30 K range.

Moreover, zero-field-cooled (ZFC) and field-cooled (FC) measurements were carried out to continue investigating the aforementioned effect. As it is shown in

Figure 8, both curves show a divergence at 6 K, which it can be indicative of a possible phase transition.¹⁷ Finally, an hysteresis loop was recorded at 2.0 K in the ± 7 T range. Although not obvious, an open loop is seen with a coercive field of 220 Oe and a remnant magnetization of $0.0035 \mu_B$ (Figure 8, inset). The reason to have a small hysteresis loop could arise from a small spin canted effect.

It has been reported that the origin of such spin canted effect might arise from single ion anisotropy or from antisymmetric exchange couplings.¹⁸ In our case, since the metal ion is Cu(II), which is normally considered isotropic, the second hypothesis was considered. In fact, we perform the same DFT calculations such as the ones that were done for **1**, but as it is shown in Figure 5b and as it could be expected from long intramolecular Cu...Cu distances, the interaction appears to be negligible ($J \sim -0.09 \text{ cm}^{-1}$). However, as it was mentioned in the crystal structure description, intermolecular Cu...Cu distances are shorter than the intramolecular ones and this could play an essential role when considering antisymmetric exchange interactions.

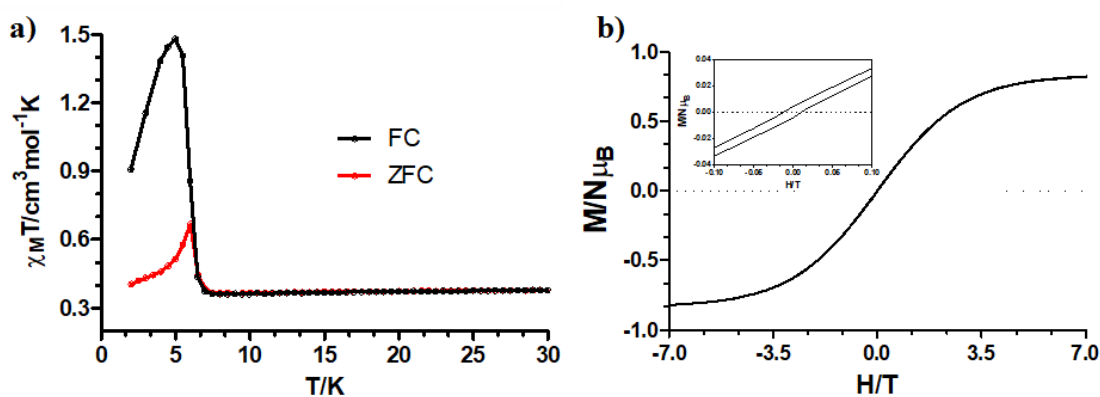


Figure 8. a) ZFC and FC curves at $H = 100$ Oe. b) Hysteresis loop measured at 2 K in the ± 7 T range.

2.2.2. Dynamic Magnetic Properties

With the aim to find out whether compounds **1** and **2** display slow relaxation of the magnetization or not, dynamic magnetic properties were studied with *ac* susceptibility measurements as a function of both temperature and frequency. In the case of **2**, there was no signal in the $\chi_M''(T)$ plot even when applying an external static magnetic field, which confirms that there is not SIM behaviour. In contrast, the

strong spin-orbit coupling of the Co(II) ion makes compound **1** a more promising candidate to behave as a SIM. Indeed, even though maxima could not be observed above 2.0 K due to the fast quantum tunnelling of the magnetization (QTM) in absence of an external magnetic field, when repeating the measurements under an external static field of 1 kOe, frequency dependent maxima could be observed in the $\chi_M''(T)$ up to 9.0 K. This behaviour is not weird in octahedral Co(II) compounds, since they own positive D values as confirmed by the static magnetic measurements and an external magnetic field is required in order to observe slow magnetic relaxation.¹⁹

In the low frequency (60-1000 Hz) and temperature region the presence of two overlapping maxima is observed, which can be attributed to the presence of two thermally activated relaxation processes. When increasing the temperature and the frequency of the oscillating field the intensity of the first maximum is lowered, although the broadness and the low-symmetry shaped maxima indicates the presence of both processes (Figure 9).

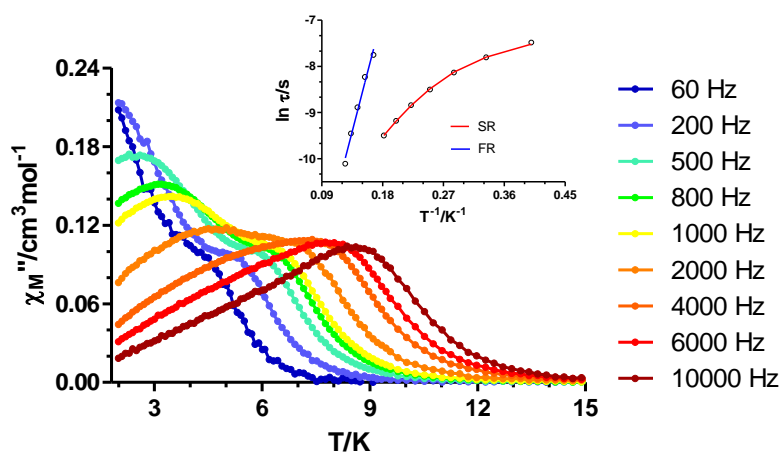


Figure 9. Temperature dependence of the molar out-of-phase ac magnetic susceptibility (χ_M'') for **2** under an applied field of $H_{dc} = 1000$ Oe at different frequencies. Inset: Arrhenius plot (blue and red lines) for the relaxation times.

This can be also seen in the Argand diagram (Cole-Cole plot, Figure 10), where the sum of two semicircles is observed in the 3.6-6.0 K temperature range

confirming the coexistence of fast and slow relaxation processes (FR and SR, respectively).

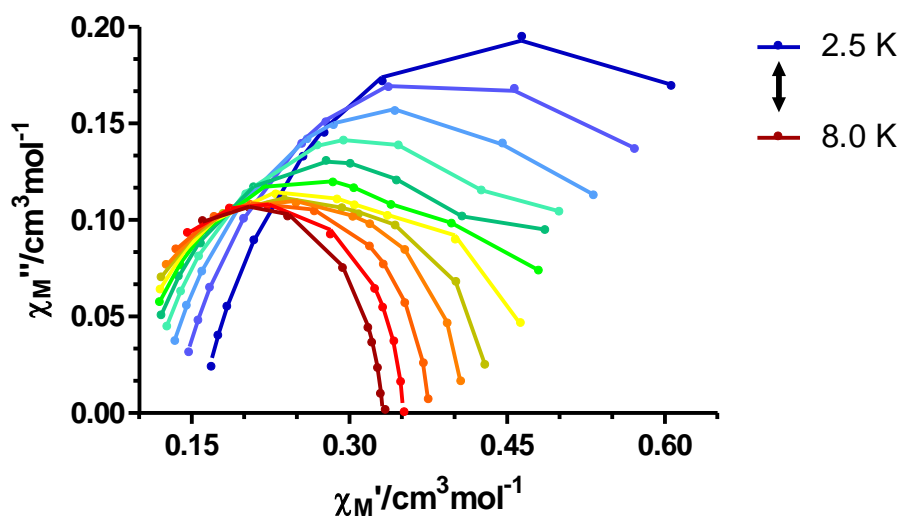


Figure 10. Cole-Cole plots in a dc applied field of 1000 Oe for **1**. Solid lines represent the best fitting of the experimental data to the Debye model.

In view of this, the relaxation times were extracted for each process fitting the data in the 2.5-8.0 K range by using a sum of two modified Debye functions with the CCFIT software.²⁰ It is worth mentioning that the software provides τ and α values for the two processes in the whole temperature range. Nonetheless, taking into account that each process operates or predominates in a certain temperature range, Arrhenius plots were constructed individually in the 2.5-5.5 K and 5.5-8.0 K temperature ranges for SR and FR, respectively. In the case of the slow relaxation process, the non-linearity of the relaxation times along with the relatively wide distribution of the α values (0.22(2.5 K) – 0.19(5.5 K)) are indicative of the presence of simultaneous relaxation mechanisms. Therefore, the data was fitted to following equation:

$$\tau = \tau_0 \exp(-U_{\text{eff}}/k_B T) + AT \text{ (equation 3)}$$

Where the first term accounts for the Orbach mechanism, while the second one accounts the direct process. The fit afforded the next set of parameters: $A = 710.3 \text{ s}^{-1} \text{ K}^{-1}$, $\tau_0 = 1.73 \times 10^{-6} \text{ s}$ and $U_{eff} = 22.6 \text{ K}$. In contrast, the relaxation times of the FR where fitted to the Orbach mechanism, in agreement with the α values ($\sim 0(5.5 \text{ K}) - \sim 0(8.0 \text{ K})$), which suggest the presence of a unique relaxation mode. The fit afforded the following parameters: $\tau_0 = 3.88 \times 10^{-8} \text{ s}$ and $U_{eff} = 56.6 \text{ K}$. The occurrence of two independent relaxations could be explained by the presence of short intermolecular distances between Co(II) centers.²¹ Whereas the paramagnetic ions are well isolated within the 2D layers, the hydrogen bonds connecting these layers provoke short interionic distances that could provide weak, but not negligible, interactions. Therefore, one of the process could be attributed to an exchange coupled system and the other one could arise from each single ion. However, it is worth mentioning that there are other systems in the literature that show the same behaviour even though the paramagnetic ions are well isolated in the structure.²²

2.3. Photoluminescence studies

Due to its extended aromaticity, the 1H-indazole-4-carboxylic acid ligand is a good candidate for enhanced emissive properties. For this reason, we decided to carry out an experimental–theoretical study of the luminescence properties of ligand and d^{10} compounds in solid state and at room temperature (Figure 11). Moreover, recent works have shown that CPs containing d^{10} metal ions enable the stabilization of long-lasting phosphorescence (LLP) or afterglow phenomena.²³ Under excitation at 340 nm, compounds **4** and **5** showed an intense emission at 388 nm and 403 nm, respectively. These emission bands are significantly blue-shifted with respect to the free ligand (415 nm). Emission bands for these types of aromatic ligands generally originate from $\pi^* \rightarrow \sigma$ and/or $\pi^* \rightarrow \pi$ photon relaxation; this energy gap generally decreases (red-shifted emission or bathochromic emission) upon ligand coordination to metals due to the increased rigidity provided to the system.²⁴ The mentioned hypsochromic emission of these materials must therefore arise from either structural and/or electronic features resulting from events other than metal coordination; such an event can cause an increase in the $n \rightarrow \pi^*$ and/or $\pi \rightarrow \pi^*$ energy gap of the light

emitting ligand.²⁵ The existence of π - π stacking interaction between rings of neighboring ligands (3.39 Å) (Figure 3) could explain this effect.

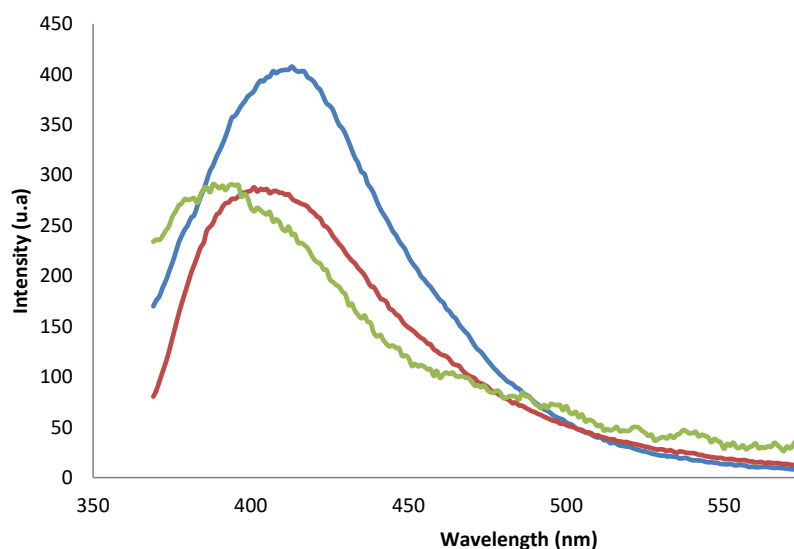


Figure 11. Room temperature solid-state emission spectra of ligand (blue), **4** (green) and **5** (red) upon sample excitation at $\lambda_{ex} = 340$ nm.

2.4. Cytotoxicity of the coordination polymers

We have also evaluated the biological response of the complexes and the ligand through *in vitro* cell viability assays on HEK-293 Human Embryonic Kidney and B16-F10 skin melanoma cell lines (Figure 12). The CPs **1-5** and the ligand exhibited no significant toxicity on HEK-293 cells at any of the analyzed concentrations (Figure 12). Only the compound **5** at the highest concentration ($100 \mu\text{g mL}^{-1}$) prompted to a decrease of HEK-293 cell viability up to 81.6%. B16-F10 cell viability was also reduced up to 80.2% and 81.4% in contact with $100 \mu\text{g mL}^{-1}$ of compound **1** and **2**, respectively (Figure 12).

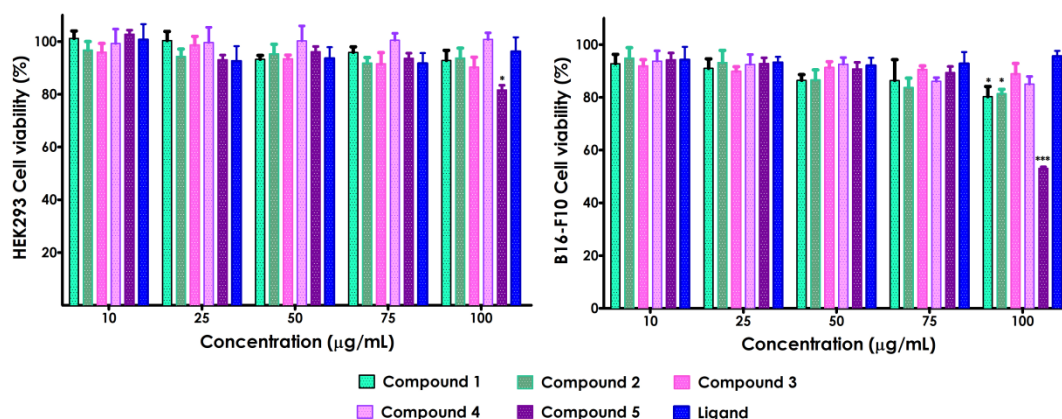


Figure 12. Viability of HEK-293 and B16-F10 cells in contact with compounds 1-5 and the ligand at increasing concentrations (10, 25, 50, 75 and 100 $\mu\text{g mL}^{-1}$). Data are shown as mean \pm SEM ($n = 3$) * $p < 0.05$ and *** $p < 0.001$ compared to untreated cells using One-way Anova followed by Bonferroni comparison test.

Nonetheless, all these values are above the accepted cytocompatibility cut-off (70%, ISO 10993-5:2009).²⁶ On the other hand, compound 5 showed significant cytotoxicity effects on melanoma cells (B16-F10), reducing the viability up to 53% the highest concentration (100 $\mu\text{g mL}^{-1}$). This toxicity was not observed on embryonic cells, indicating that compound 5 selectively kill B16-F10 skin melanoma cells. Indeed, it has been previously reported that cell lines can differ in their sensitivity to external stimuli.²⁷ These preliminary *in vitro* results of compound 5 might be complemented with further experiments on different cell lines to demonstrate such specificity.

3. Conclusion

In summary, a new family of transition metal coordination polymers, with bidimensional structures, have been synthesized with the novel 1H-indazole-4-carboxylic acid: $[\text{Co}(\text{L})_2(\text{H}_2\text{O})_2]_n$ (**1**), $[\text{Ni}(\text{L})_2(\text{H}_2\text{O})_2]_n$ (**2**), $[\text{Cu}(\text{L})_2(\text{H}_2\text{O})]_n$ (**3**), $[\text{Zn}(\text{L})_2]_n$ (**4**) and $[\text{Cd}(\text{L})_2]_n$ (**5**). Static magnetic measurements, as well as DFT calculations performed on **1-3** indicate that 1H-indazole-4-carboxylate ligand provides almost negligible intrachain exchange interactions. However, the quite unusual spin-canted effect in compound **3**, which is normally attributed to anisotropic ions, show that the shorter intramolecular Cu...Cu distances that arise from the

packing of the structure could affect the bulk magnetic properties of the material. The more anisotropic Co based compound **1**, which behaves as a field-induced single molecule magnet, displays two characteristic maxima on the out-of-phase susceptibility data. These two maxima are defined by thermally activated SR and FR, but being different the origin of each process. As it occurs in **3**, the intermolecular Co...Co distances are shorter than the intramolecular ones and this provokes a relaxation that is attributed to a weakly exchange coupled system, whereas the other one appears to be of single ion in origin. On the other hand, **4** and **5** CPs exhibit hypsochromic emission with respect to the ligand free, due to arise from either structural and/or electronic features resulting from events other than metal coordination. Cell viability tests on HEK-293 and B16-F10 cell lines showed non cytotoxic effects with compounds **1-4**. However, compound **5** exhibited toxicity on melanoma B16-F10 cell line. With these studies, we have shown the great versatility shown by the 1H-indazole-4-carboxylic acid to form coordination polymers with multifunctional applications. Currently, more work is being developed in our laboratory to obtain other systems with different dimensionalities using lanthanide ions.

4. Experimental

4.1. Preparation of complexes

All the reagents were purchased commercially and used without any previous purification.

Synthesis of $[M(L)_2(H_2O)_2]_n$ for $\{M = Co(1), Ni(2)\}$. Single orange (**1**) and green (**2**) crystals were obtained following the next synthesis method. 0.047 mmol of 1H-indazole-4-carboxylic acid was solved in 0.5 mL of DMF and 0.5 mL of distilled water. On the other hand, 0.095 mmol of $MCl_2 \cdot 6H_2O$ was solved in 0.5 mL of distilled water and 0.5 mL of DMF. Both solutions were mixed in a closed glass vessel and introduced in an oven at 100°C for 24h. The crystals were washed with

water/methanol. Anal Calcd for $\text{CoC}_{16}\text{H}_{14}\text{N}_4\text{O}_6$ (**1**): C, 46.06; H, 3.38; N, 13.43. Found: C, 46.03; H, 3.36; N, 13.46. Anal Calcd for $\text{NiC}_{16}\text{H}_{14}\text{N}_4\text{O}_6$ (**2**): C, 46.08; H, 3.38; N, 13.44. Found: C, 46.05; H, 3.35; N, 13.47.

Synthesis of $[\text{Cu}(\text{L})_2(\text{H}_2\text{O})]_n$ (3**).** The general procedure described for (**1**) was followed using $\text{CuCl}_2 \cdot 2\text{H}_2\text{O}$ as metal source, which led to green single crystals of (**3**). Yield: 55% based on Cu. Anal Calcd for $\text{CuC}_{16}\text{H}_{12}\text{N}_4\text{O}_5$ (**3**): C, 47.59; H, 2.99; N, 13.87. Found: C, 47.54; H, 2.96; N, 13.90.

Synthesis of $[\text{M}(\text{L})_2]_n$ for $\{\text{M} = \text{Zn}(\mathbf{4}), \text{Cd}(\mathbf{5})\}$. General procedure described for (**1**) was followed using $\text{M}(\text{C}_2\text{H}_3\text{O}_2)_2 \cdot 2\text{H}_2\text{O}$ as metal source, which led to white single crystal of (**4**) and (**5**). Yield: 56% based on metal. Anal Calcd for $\text{ZnC}_{16}\text{H}_{10}\text{N}_4\text{O}_4$ (**4**): C, 49.57; H, 2.60; N, 14.45. Found: C, 49.62; H, 2.56; N, 14.51. Anal Calcd for $\text{CdC}_{16}\text{H}_{10}\text{N}_4\text{O}_4$ (**5**): C, 44.21; H, 2.32; N, 12.89. Found: C, 44.18; H, 2.30; N, 12.91.

In addition to the elemental analyses, all the samples were checked by FT-IR spectra (Figures 13).

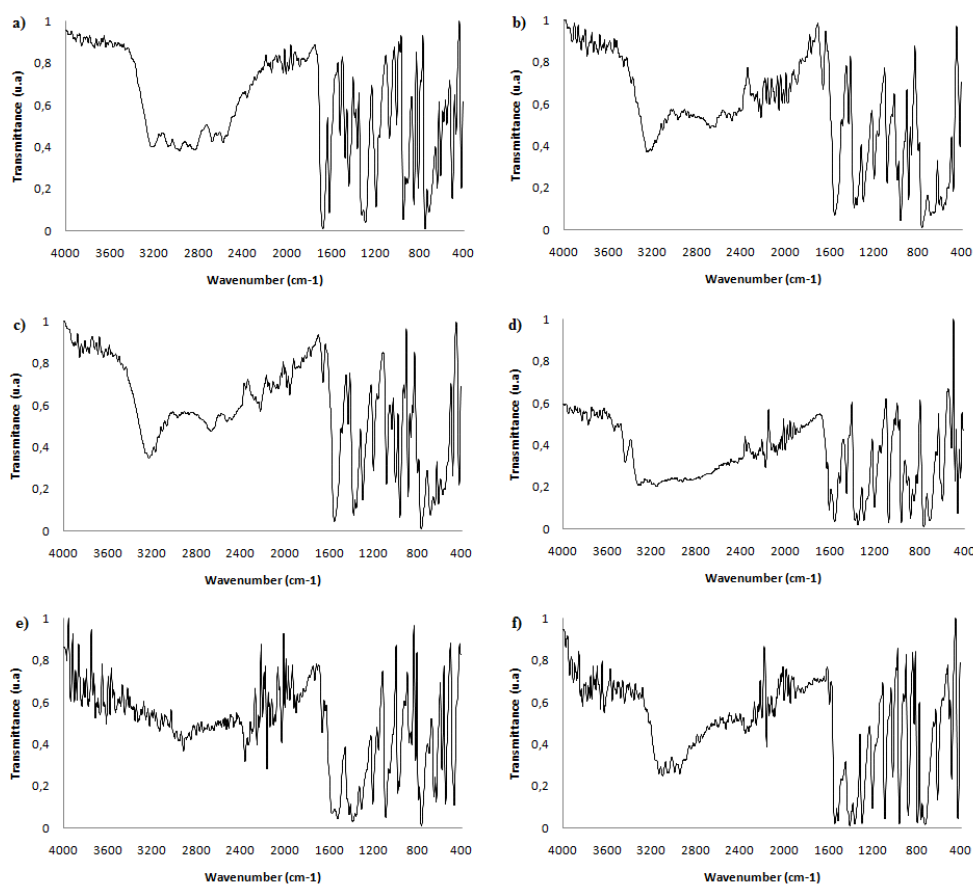


Figure 13. FTIR spectra of a) Ligand 1*H*-indazole-4-carboxylic acid; b) Compound 1; c) Compound 2; d) Compound 3; e) Compound 4; f) Compound 5.

4.2. Physical measurements

Elemental analysis (C, H and N) were carried out at the Centro de Instrumentación Científica (University of Granada) on a Fisons-Carlo Erba analyzer model EA 1108 (Thermo Scientific, Waltham, MA, USA). Infrared (IR) spectra ($400\text{-}4000\text{ cm}^{-1}$) were recorded on a Nicolet FT-IR 6700 spectrometer in KBr pellets. Photoluminescence (PL) measurements were carried out on crystalline samples at room temperature using a Varian Cary-Eclipse fluorescence spectrofluorimeter equipped with a Xe discharge lamp (peak power equivalent to 75 kW), Czerny–Turner monochromators, and an R-928 photomultiplier tube. For the fluorescence measurements, the photomultiplier detector voltage was fixed at 600 V, and the excitation and emission slits were set at 5 and 2.5 nm, respectively. Phosphorescence spectra were recorded with a total decay time of 20 ms, delay time of 0.2 ms and gate time of 5.0 ms. The photomultiplier detector voltage was set at 800 V, and both

excitation and emission slits were open to 10 nm. Alternating current magnetic measurements were performed under zero and 1000 Oe applied static fields on a Quantum Design SQUID MPMS XL-5 device by using an oscillating *ac* field of 3.5 G and *ac* frequencies ranging from 10 to 1400 Hz.

4.3. Cell viability assay

Human Embryonic Kidney (HEK293, ECACC 85120602) and mouse skin melanoma (B16-F10, ATCC® CRL-6322) cell lines were supplied by the Cell Bank of the Scientific Research Center of the University of Granada (Spain). HEK293 cells were cultured in standard tissue culture flask and maintained in Eagle's Minimum Essential Medium (EMEM with EBSS) supplemented with 2 mM Glutamine, 1% Non Essential Amino Acids (NEAA), 1 mM sodium pyruvate (NaP) and 10% Foetal Bovine Serum (FBS) at 37°C with 5% CO₂. B16-F10 cells were cultured in EMEM with EBSS supplemented with 2mM Glutamine and 10% FBS.

Cells were detached from culture flasks by trypsinization, centrifuged and resuspended. The cells were cultured into a 96 flat transparent well (10⁴ cells/well) during 48 hours. Then, the cells were exposed to different concentrations (10, 25, 50, 75 and 100 µg/mL) of compounds **1**, **2**, **3**, **4** and **5** and the corresponding ligand. All the experiments were performed in triplicate. After 48 hours of culture, cell viability was assessed by MTS assay using CellTiter 96® AQueous One Solution Reagent (Promega, Madison, WI), according to the manufacturer's instructions. Twenty microliters of AQueous One Solution Reagent were added to each well and the absorbance at 490 nm was measured with a spectrophotometer (Infinite® 200 PRO NanoQuant) after 2 hours of incubation. This absorbance is proportional to the number of metabolically active cells. The relative cell viability (%) was calculated respect to non-treated cells. Results are expressed as average ± standard error of the mean (S.E.M., as error bars). One-way ANOVA with Bonferroni's post-test was performed using GraphPad Prism software (version 6.0).

4.4. Single-crystal structure determination

Single crystals of suitable dimensions were used for data collection. For compounds **1-3** and **5**, diffraction intensities were collected on a Bruker X8 APEX II and Bruker D8 Venture with a Photon detector equipped with graphite monochromated MoK α radiation ($\lambda = 0.71073 \text{ \AA}$). The data reduction was performed with the APEX2²⁸ software and corrected for absorption using SADABS.²⁹ In all cases, the structures were solved by direct methods and refined by full-matrix least-squares with SHELXL-2018.³⁰ Details of selected bond lengths and angles are given in Tables 4-6.

Table 4. Bond lengths (\AA) and angles ($^\circ$) for compounds **1** and **2**. Symmetry operations: (i) = -x, -y, -z; (ii) = -x, -y+1, -z+1.

Compound	1		2
Co1-O1	2.091(1)	Ni1-O1	2.066(1)
Co1-O1(i)	2.091(1)	Ni 1-O1(ii)	2.066(1)
Co1-O1W	2.126(1)	Ni 1-O1W	2.096(1)
Co1-O1W(i)	2.126(1)	Ni 1-O1W(ii)	2.096(1)
Co1-N1	2.154(1)	Ni 1-N1	2.097(1)
Co1-N1(i)	2.154(1)	Ni 1-N1(ii)	2.097(1)
O1-Co1-O1(i)	180.0	O1-Ni1-O1(I)	180.0
O1-Co1-O1W	90.93(3)	O1-Ni1-O1W	92.02(3)
O1(i)-Co1-O1W	89.07(3)	O1(I)-Ni1-O1W	87.98(3)
O1-Co1-O1W(I)	89.06(3)	O1-Ni1-O1W(I)	87.98(3)
O1(i)-Co1-O1W(i)	90.94(3)	O1(I)-Ni1-O1W(I)	92.02(3)
O1W-Co1-O1W(i)	180.0	O1W-Ni1-O1W(I)	180.0
O1-Co1-N1	87.76(4)	O1-Ni1-N1	92.57(4)
O1(i)-Co1-N1	92.24(4)	O1(I)-Ni1-N1	87.43(4)
O1W-Co1-N1	90.05(4)	O1W-Ni1-N1	89.48(4)
O1W(I)-Co1-N1	89.95(4)	O1W(I)-Ni1-N1	90.52(4)
O1-Co1-N1(i)	92.24(4)	O1-Ni1-N1(I)	87.43(4)
O1(i)-Co1-N1(i)	87.76(4)	O1(I)-Ni1-N1(I)	92.57(4)
O1W-Co1-N1(i)	89.95(4)	O1W-Ni1-N1(I)	90.52(4)
O1W(I)-Co1-N1(i)	90.05(4)	O1W(I)-Ni1-N1(I)	89.48(4)
N1-Co1-N1(i)	180.0	N1-Ni1-N1(I)	180.00(3)

Table 5. Bond lengths (Å) and angles (°) for compound **3**.

Compound	3
Cu1-O1A	1.947(3)
Cu1-O1B	1.972(3)
Cu1-O1W	2.362(4)
Cu1-N1A	2.014(4)
Cu1-N1B	1.993(4)
O1A-Cu1-O1B	175.82(15)
O1A-Cu1-N1B	89.45(16)
O1B-Cu1-N1B	91.26(15)
O1A-Cu1-N1A	90.98(15)
O1B-Cu1-N1A	87.75(15)
N1B-Cu1-N1A	172.18(18)
O1A-Cu1-O1W	87.63(13)
O1B-Cu1-O1W	96.35(14)
N1B-Cu1-O1W	98.14(15)
N1A-Cu1-O1W	89.68(15)

Table 6. Bond lengths (Å) and angles (°) for compound **5**. Symmetry operations: (i) = -x+1, y+1/2, -z+1/2; (ii) = x+1/2, -y+1, -z+1/2; (iii) = -x+3/2, -y+3/2, z.

Compound	5
Cd1-N1(i)	2.267(10)
Cd1-N1(ii)	2.267(10)
Cd1-O1	2.291(9)
Cd1-O1(iii)	2.291(9)
Cd1-O2	2.448(9)
Cd1-O2(iii)	2.448(10)
N1(i)-Cd1-N1(ii)	110.5(5)
N1(i)-Cd1-O1	100.5(3)
N1(ii)-Cd1-O1	97.5(3)
N1(i)-Cd1-O1(iii)	97.5(3)
N1(ii)-Cd1-O1(iii)	100.5(3)
O1-Cd1-O1(iii)	148.3(5)
N1(i)-Cd1-O2(iii)	149.2(3)
N1(ii)-Cd1-O2(iii)	90.6(3)
O1-Cd1-O2(iii)	98.7(3)
O1(iii)-Cd1-O2(iii)	55.4(3)
N1(i)-Cd1-O2	90.6(3)
N1(ii)-Cd1-O2	149.2(3)
O1-Cd1-O2	55.4(3)
O1(iii)-Cd1-O2	98.7(3)
O2(iii)-Cd1-O2	80.7(4)

CCDC reference numbers for the structures are 1940509 – 1940512. Copies of the data can be obtained free of charge on application to the Director, CCDC, 12 Union Road, Cambridge, CB2 1EZ, U.K. (Fax: +44-1223-335033; e-mail: deposit@ccdc.cam.ac.uk or <http://www.ccdc.cam.ac.uk>).

Table 7. Crystallographic data and structural refinement details for all compounds.

Compounds	1	2	3	5
Formula	C ₁₆ H ₁₄ CoN ₄ O ₆	C ₁₆ H ₁₄ NiN ₄ O ₆	C ₁₆ H ₁₂ CuN ₄ O ₅	C ₁₆ H ₁₀ CdN ₄ O ₄
M_r (g mol ⁻¹)	417.24	417.02	403.84	434.68
Crystal system	<i>monoclinic</i>	<i>monoclinic</i>	<i>monoclinic</i>	<i>orthorhombic</i>
Space group (no.)	<i>P</i> 2 ₁ / <i>c</i> (14)	<i>P</i> 2 ₁ / <i>c</i> (14)	<i>P</i> 2 ₁ / <i>c</i> (14)	<i>Pccn</i> (56)
<i>a</i> (Å)	5.3010(2)	5.3050(3)	10.1061(8)	12.3609(15)
<i>b</i> (Å)	10.0099(3)	9.9880(4)	9.8617(7)	9.9856(11)
<i>c</i> (Å)	15.2097(6)	15.0820(7)	14.7053(8)	12.3887(14)
α (°)	90	90	90	90
β (°)	96.8820(10)	97.362(2)	94.716(2)	90
γ (°)	90	90	90	90
<i>V</i> (Å ³)	801.25(5)	792.55(7)	1460.62(17)	1529.1(3)
<i>Z</i>	2	2	4	4
<i>D_c</i> (g cm ⁻³)	1.729	1.747	1.836	1.888
μ (MoK α) (mm ⁻¹)	1.117	1.271	1.537	1.459
<i>T</i> (K)	100	100	100	100
Observed reflections	2068 (1890)	2056 (1869)	3769 (2769)	2010 (1829)
<i>R_{int}</i>	0.0464	0.0400	0.1496	0.0683
Parameters	124	124	225	114
<i>GOF^a</i>	0.989	1.057	1.201	1.496
<i>R₁^{b,c}</i>	0.0284 (0.0246)	0.0254 (0.0223)	0.1269 (0.0868)	0.1192 (0.1130)
<i>wR₂^d</i>	0.0662 (0.0642)	0.0571 (0.0558)	0.1355 (0.1254)	0.2917 (0.2890)
Largest difference in peak and hole (e Å ⁻³)	0.421 and -0.671	0.394 and -0.430	0.663 and -1.303	1.640 and -2.878

[a] $S = [\sum w(F_o^2 - F_c^2)^2 / (N_{\text{obs}} - N_{\text{param}})]^{1/2}$. [b] $R_1 = \sum ||F_o| - |F_c|| / \sum |F_o|$. [c] Values in parentheses for reflections with $I > 2s(I)$. [d] $wR_2 = [\sum w(F_o^2 - F_c^2)^2 / \sum wF_o^2]^{1/2}$; $w = 1/[\sigma^2(F_o^2) + (aP)^2]$ where $P = (\max(F_o^2, 0) + 2F_c^2)/3$ with $a = 5.9161$.

5. Notes and References

- 1.- (a) K. Otsubo, T. Haraguchi and H. Kitagawa, *Coord. Chem. Rev.*, 2017, **346**, 123-138;(b) S. Furukawa, J. Reboul, S. Diring, K. Sumida and S. Kitagawa, *Chem. Soc.Rev.*, 2014, **43**, 5700-5734;(c) F.X. Xamena, I. Llabres and J. Gascon, *RSC Catal.Ser.*, 2013, **12**, 406-424.
- 2.- (a) A. Dhakshinamoorthy and H. Garcia, *Chem. Soc. Rev.*, 2014, **43**, 5750-5765; (b) L. Ma, C. Abney and W. Lin, *Chem. Soc. Rev.*, 2009, **38**, 1248–1256; (c) P. Horcajada, R. Gref, T. Baati, P. K. Allan, G. Maurin, P. Couvreur, G. Ferey, R. E. Morris and C. Serre. *Chem. Rev.*, 2012, **112**, 1232–1268; (d) P. Ramaswamy, N. E. Wong and G. K. H. Shimizu, *Chem. Soc. Rev.*, 2014, **43**, 5913–5932; (e) K. Fujie, R. Ikeda, K. Otsubo, T. Yamada and S. Kitagawa, *Chem. Mater.*, 2015, **27**, 7355–7361; (f) S. Lee, E. A. Kapustin and O. M. Yaghi, *Science*, 2016, **353**, 808–811; (g) Y. Inokuma, S. Yoshioka, J. Ariyoshi, T. Arai, Y. Hitora, K. Takada, S. Matsunaga, K. Rissanen and M. Fujita, *Nature*, 2013, **495**, 461–466;(h) V. Stavila, A. A. Talin and M. D. Allendorf, *Chem. Soc. Rev.*, 2014, **43**, 5994-6010; (i) J. M. Frost, K. L. M. Harriman and M. Murugesu, *Chem. Sci.*, 2016, **7**, 2470–2491; (j) G. A. Craig and M. Murrie, *Chem. Soc. Rev.*, 2015, **44**, 2135–2147; (k) H. S. Quah, W. Chen, M. K. Schreyer, H. Yang, M. W. Wong, W. Ji and J. J. Vital, *Nat. Commun.*, 2015, **6**, 7954–7961;(l) A. Dhakshinamoorthy, M. Alvaro, H. Garcia, *ChemComm*, 2012, **48**, 11275-11288.
- 3.- W. Lu, Z. Wei, Z.-Y. Gu, T.-F. Liu, J. Park, J. Park, J. Tian, M. Zhang, Q. Zhang, T. Gentle, M. Boscha and H.-C. Zhou. *Chem. Soc. Rev.*, 2014, **43**, 5561-559.
- 4.- J. M. Seco, S. Pérez-Yáñez, D. Briones, J. Á. García, J. Cepeda and A. Rodríguez-Diéguez, *Cryst. Growth.Des.*, 2017, **17**, 3893–3906.
- 5.- (a) J.M. Seco, D. Fairen-Jimenez, A.J. Calahorro, L. Méndez-Liñán, M. Pérez-Mendoza, N. Casati, E. Colacio and A. Rodríguez-Diéguez, *Chem.Commun.*, 2013, **49**, 11329-11331;(b) J. Cepeda, M. Pérez-Mendoza, A.J. Calahorro, N. Casati, J.M. Seco, M. Aragonés-Anglada, P.Z. Moghadam, D. Fairen-Jimenez and A. Rodríguez-Diéguez, *J.Mater.Chem.A*, 2018, **6**, 17409-17416.

- 6.- M. Cabrero-Antonino, S. Remiro-Buenamañana, M. Souto, A.A. García-Valdivia, D. Choquesillo-Lazarte, S. Navalón, A. Rodríguez-Diéguez, G. Mínguez Espallargas and H. García, *Chem. Commun.*, 2019, **55**, 10932-10935.
- 7.- A.A. García-Valdivia, J.M. Seco, J. Cepeda and A. Rodríguez-Diéguez, *Inorg. Chem.*, 2017, **56**, 13897-13912.
- 8.- D. Briones, B. Fernández, A.J. Calahorro, D. Fairen-Jimenez, R. Sanz, F. Martínez, G. Orcajo, E. San Sebastián, J.M. Seco, C. SánchezGonzález, J.Llopis and A. Rodríguez-Diéguez, *Cryst.Growth.Des.*, 2016, **16**, 537–540.
- 9.- B. Fernández, I. Oyarzabal, E. Fischer-Fodor, S. Macavei, I. Sánchez, J.M. Seco, S. Gómez-Ruiz and A. Rodríguez-Diéguez, *CrystEngComm*, 2016, **18**, 8718-8721.
- 10.- J.M. Seco, E. San Sebastián, J. Cepeda, B. Biel, A. Salinas-Castillo, B. Fernández, D.P. Morales, M. Bobinger, S. Gómez-Ruiz, F.C. Loghin, A. Rivadeneyra and A. Rodríguez-Diéguez, *Sci.Rep.*, 2018, **8**, 14414.
- 11.- Y.-J. Cui, C.-C. Ma, C.-M. Zhang, L.-Q. Tang and Z.-P. Liu, *Eur. J. Med. Chem.*, 2020, **187**, 111968-111981.
- 12.- F. Lloret, M. Julve, J. Cano and E. Pardo, *Inorg. Chim. Acta*, 2008, **361**, 3432-3445.
- 13.- N. F. Chilton, R. P. Anderson, L. D. Turner, A. Soncini and K. S. Murray, *J. Comput. Chem.*, 2013, **34**, 1164-1175.
- 14.- J. Titiš and R. Boča, *Inorg. Chem.*, 2010, **49**, 3971-3973.
- 15.- M. Hernández-Molina, F. Lloret, C. Ruiz-Pérez and M. Julve, *Inorg. Chem.*, 1998, **37**, 4131-4135.
- 16.- (a) C. D. Zhang, S. X. Liu, C. Y. Sun, F. J. Ma and Z. M. Su, *Cryst. Growth Des.*, 2009, **9**, 3655-3660; (b) S. Z. Li, P. T. Ma, H. Z. Niu, J. W. Zhao and J. Y. Niu, *Inorg. Chem. Commun.*, 2010, **13**, 805-808; (c) J. W. Zhao, D. Y. Shi, L. J. Chen, X. M. Cai, Z. Q. Wang, P. T. Ma, J. P. Wang and J. Y. Niu, *CrystEngComm*, 2012, **14**, 2797-2806.

- 17.- Q. Chen, M. H. Zeng, L. Q. Wei and M. Kurmoo, *Chem. Mater.*, 2010,**22**, 4328-4334.
- 18.- T. Moriya, *Phys. Rev.*, 1960, **120**, 91-98.
- 19.- R. Herchel, L. Váhovská, I. Potočňák and Z. Trávníček, *Inorg. Chem.*, 2014, **53**, 5896-5898.
- 20.- N. F. Chilton, *CCFIT program*, The Chilton Group, Manchester,U.K., 2014, <http://www.nfchilton.com/software.html>.
- 21.- (a) E. A. Buvaylo, V. N. Kokozay, O. Y. Vassilyeva, B. W. Skelton, A. Ozarowski, J. Titiš, B. Vranovičová and R. Boča, *Inorg. Chem.*, 2017, **56**, 6999-7009; b) C. Rajnák, F. Varga, J. Titiš, J. Moncol' and R. Boča, *Eur. J. Inorg. Chem.*, 2017, **13**, 1915-1922; (c) C. Rajnák, J. Titiš, O. Fuhr, M. Ruben and R. Boča, *Inorg. Chem.*, 2014, **53**, 8200-8202.
- 22.- R. Boča, J. Miklovič and J. Titiš, *Inorg. Chem.*, 2014, **53**, 2367-2369.
- 23.- J. Cepeda and A. Rodríguez-Diéguez, *CrystEngComm*, 2016, **18**, 8556-8573.
- 24.- H-Y. Ren, C.-Y. Han, M. Qu and X.-M. Zhang, *RSC Adv.*, 2014, **4**, 49090-49097.
- 25.- (a) S. S. S. Raj, H. K. Fun, J. Zhang, R. G. Xiong and X. Z. You, *Polyhedron*, 2006, **25**, 635-644; (b) A. J. Calahorra, E. San Sebastián, A. Salinas-Castillo, J.M. Seco, C. Mendicute-Fierro, B. Fernández and A. Rodríguez-Diéguez, *CrystEngComm*, 2015, **17**, 3659-3666.
- 26.- X. Liu, D.P. Rodeheaver, J.C. White, A.M. Wright, L.M. Walker, F. Zhang and S. Shannon, *Regul.Toxicol.Pharmacol.*, 2018, **97**, 24-32.
- 27.- (a) M. Khan, A. Mohammad, G. Patil, S.A. Naqvi, L.K. Chauhan and I. Ahmad, *Biomaterials*, 2012, **33**, 1477-1488; (b) B. Fernández, I. Fernández, J. Cepeda, M. Medina-O'Donnell, E.E. Rufino-Palomares, A. Raya-Barón, S. Gómez-Ruiz, A. Pérez-Jiménez, J.A. Lupiáñez, F.J. Reyes-Zurita and A. Rodríguez-Diéguez, *Cryst. Growth Des.*, 2018, **18**, 969-978.

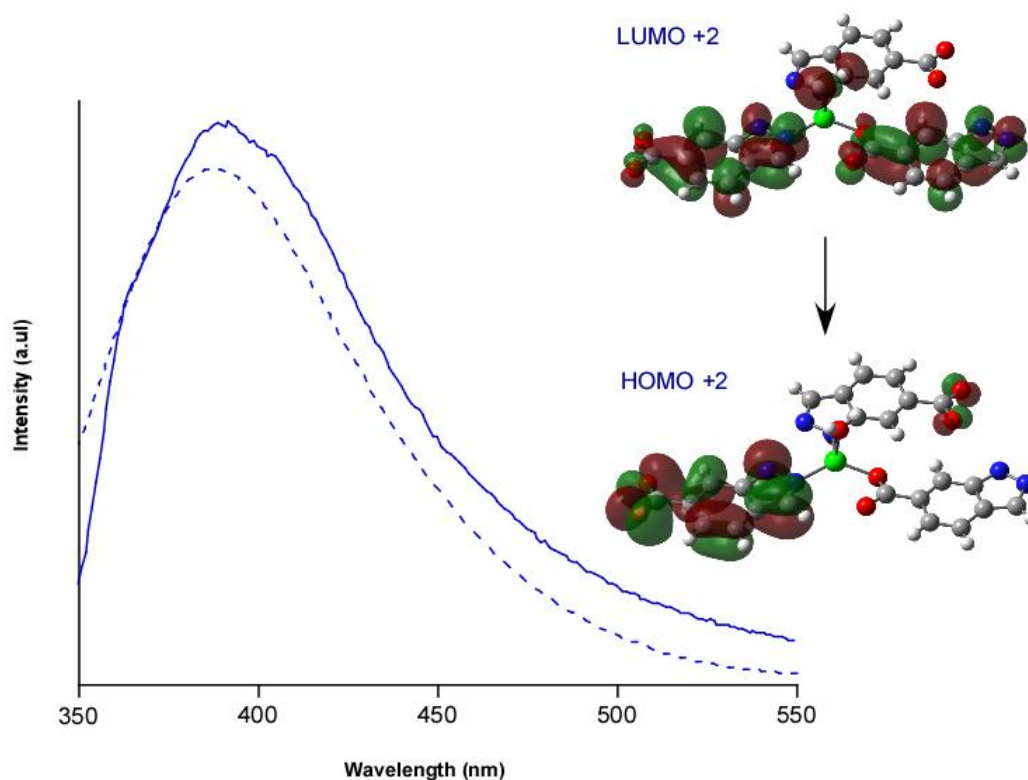
28.- *Bruker Apex2*, Bruker AXS Inc., Madison, Wisconsin, USA, 2004.

29.- G. M. Sheldrick, *SADABS, Program for Empirical Adsorption Correction*, Institute for Inorganic Chemistry, University of Gottingen, Germany, 1996.

30 .- G. M. Sheldrick, *SHELXTL Version 2014/7*. <http://shelx.uni-ac.gwdg.de/SHELX/index>.

Capítulo 6

Photoluminescence and *in vitro* Cytotoxicity in Coordination Polymers based on d^{10} Transition Metals and 1*H*-Indazole-6-Carboxylic Acid



**Photoluminescence and *in vitro* Cytotoxicity in Coordination
Polymers based on d¹⁰ Transition Metals and 1*H*-Indazole-6-
Carboxylic Acid**

A. A. García-Valdivia,^a E. Echenique-Errandonea,^b G.B. Ramírez-Rodríguez,^a J. M. Delgado-López,^a B. Fernández,^c J. Cepeda,^b and A. Rodríguez-Diéguez^{a,*}

ENVIADO A: Inorganica Chimica Acta

^a *Departamento de Química Inorgánica, Facultad de Ciencias, Universidad de Granada, 18071 Granada, Spain.*

^b *Departamento de Química Aplicada, Facultad de Química, Universidad del País Vasco/Euskal Herriko Unibertsitatea (UPV/EHU), 20018 Donostia-San Sebastian, Spain.*

^c *Institute of Parasitology and Biomedicine "López-Neyra", CSIC, Av. Conocimiento s/n, 18600, Granada, Spain.*

Abstract

Two new coordination polymers based on Zn(II) and Cd(II) and 1*H*-indazole-6-carboxylic acid (H₂L) of general formulae [Zn(L)(H₂O)]_n and [Cd₂(HL)₄]_n have been synthesized and fully characterized by elemental analyses, FT-IR spectra and single crystal X-ray diffraction. The results indicate that compound **1** possesses double chains in its structure while **2** exhibits a 3D network. The intermolecular interactions including hydrogen bonds, C–H⋯π and π⋯π stacking interactions stabilise both structures. Photoluminescence properties have been accomplished showing that compounds **1** and **2** present similar emission spectra compared to free-ligand, being the ligand-centred π-π* electronic transition the most relevant transitions which rules compound **1** and **2** emission. Additionally, because of the well-recognised therapeutic properties, anticancer and antioxidant activity of the ligand, the effect on viability of human embryonic kidney cells and mouse melanoma cell lines has been studied for the corresponding ligand and both compounds.

1. Introduction

The study of coordination polymers (CPs) and metal-organic frameworks (MOFs) is at the forefront of modern inorganic chemistry due to the broad range of potential applications spanning from magnetic and luminescent materials, through catalysis and sensing, to gas separation and storage and ending with biomedical applications.¹

It is well known that nitrogen-containing heterocycles are pharmacologically important scaffolds and they are widely present in numerous commercially available drugs. This is the case of 1*H*-indazole-6-carboxylic acid (H₂L), a common moiety in pharmaceutical industry. From the structural point of view, indazole is an aromatic heterocyclic molecule in which a benzene ring is fused with a pyrazole ring.² It shows three tautomeric forms (Figure 1) being tautomer **A** favoured over **B** and **C** because of its higher degree of aromaticity.³

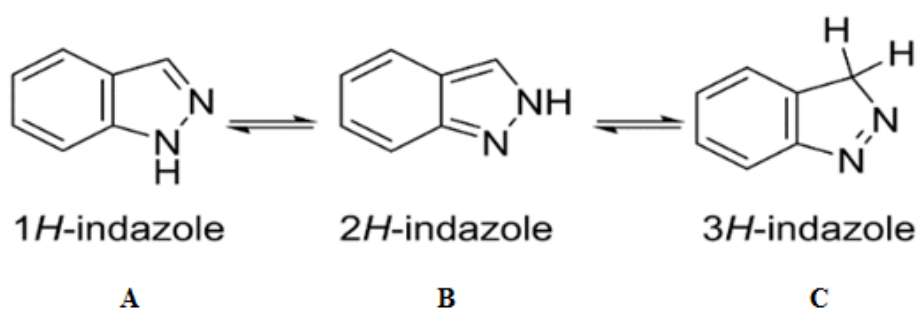


Figure 1. *Indazole tautomerism.*

H₂L is an ideal candidate to form CPs because of its multiple coordination possibilities not only derived from its carboxylate group but also from its pyrazolyl function. A great variety of coordination modes are possible, according to similar ligands containing carboxylate and pyrazole chemical groups (Figure 2). However, only one complex with this ligand has been reported so far.⁴ In this work, the synthesis of four substituted indazole derivatives containing pyridine or carboxylic functionalities, and structural descriptions of their behaviour on coordination to Cu(II) ions in solution and in the solid state was described in detail. Additionally,

H₂L is recognized to have therapeutic properties as well as anticancer or antioxidant activity.⁵

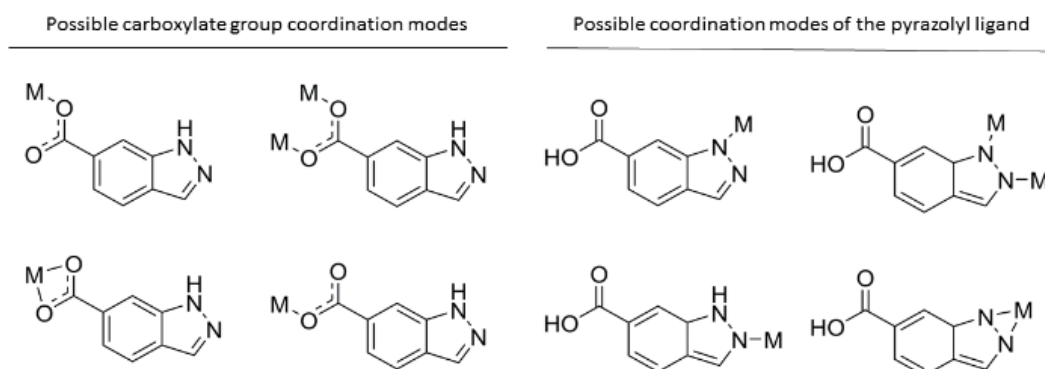


Figure 2. Possible coordination modes of 1*H*-indazole-6-carboxylic acid ligand.

On the other hand, H₂L may also present interesting photoluminescence (PL) properties, due to its aromatic nature and carboxylic functions.⁶ When these ligands are coordinated to metal centres in the crystal structure of a CP, PL tends to be enhanced by means of the well-known crystal-induced luminescence effect.⁷ Among others, metal ions from group 12 are particularly appropriate because of their a priori less quenching effects derived from the banned d-d transitions, consequence of their closed-shell electronic configuration.⁸ Moreover, the presence of these ions may also promote ligand-to-metal charge transfer (LMCT), in the CP provided that empty levels of the metal ions are able to be populated in the excited state, thus modulating the PL emission with regard to the ligand-centred (LC) emissions.⁹

Considering all of the above, in this work we have synthesized two new coordination polymers based on d¹⁰ transition metals and 1*H*-indazole-6-carboxylic acid of general formulae [Zn(L)(H₂O)]_n (**1**) and [Cd₂(HL)₄]_n (**2**) and their structural and photoluminescent properties as well as their *in vitro* cytotoxic activity have been explored.

2. Results and discussion

1*H*-indazole-6-carboxylic acid ligand allowed the formation of two d^{10} transition metal-based complexes with different dimensionalities by varying the metal centre. Thus, the solvothermal reaction of the 1*H*-indazole-6-carboxylic acid ligand with $\text{Zn}(\text{CH}_3\text{COO})_2$ in DMF/ H_2O mixture with a 1:2 molar ratio afforded a double chain complex **1** (Figure 3a). Similarly, for complex **2**, $\text{Cd}(\text{CH}_3\text{COO})_2$ salt was respectively used leading a three dimensional metal-organic framework (Figure 3b).

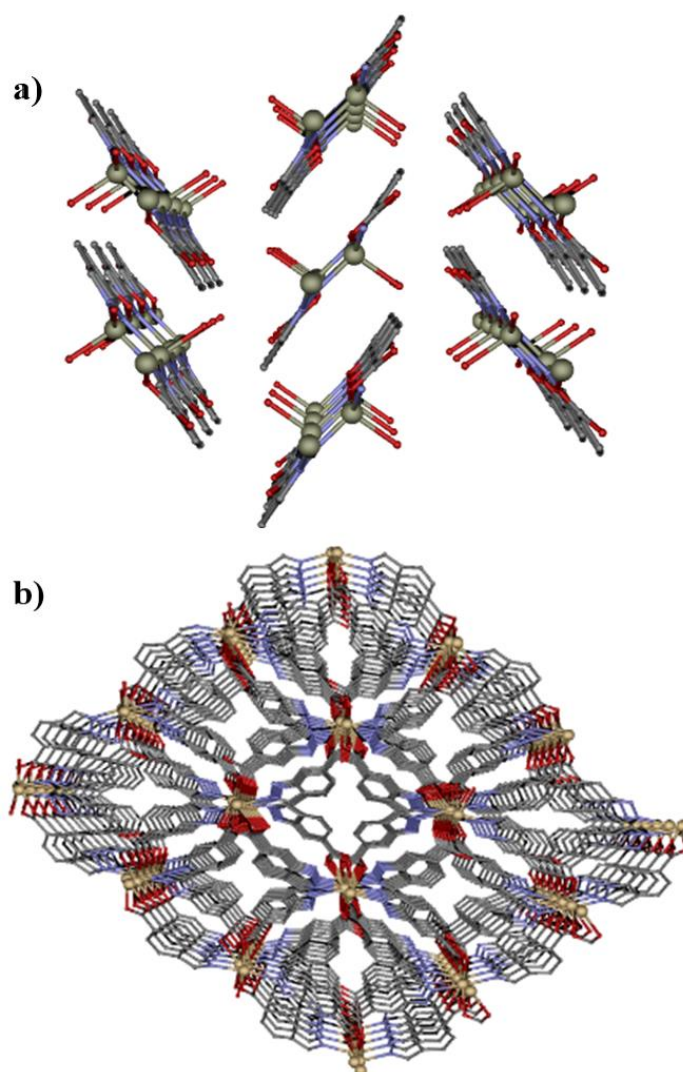


Figure 3. Perspective views of the structures **1** (a) and **2** (b). Colour code: N = blue, O = red, C = grey, Zn = dark grey, Cd = yellow.

2.1. Description of the structures

Structural description of $[\text{Zn}(\text{L})(\text{H}_2\text{O})]_n$ (1**).** Compound **1** consists of a double chain structure that crystallizes in the $P2_1/n$ space group, in which Zn(II) ions are bridged by nitrogen atoms of L^{2-} in a bidentate way giving rise to a stable and in plane Zn_2N_4 six membered ring (Figure 4).

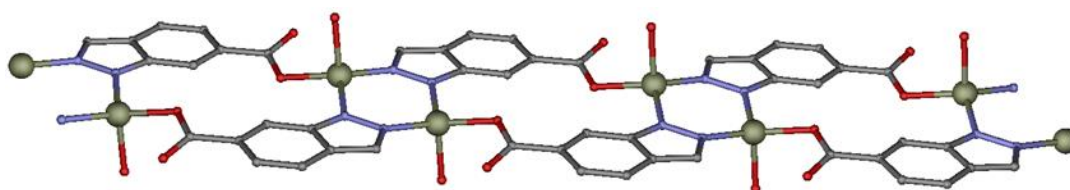


Figure 4. Representation of the Zn_2N_4 planar six membered ring.

The Zn(II) ion is also coordinated to a carboxylate moiety of the indazole derivative ligand in a monodentate way, which extends the dimeric entity into infinite 1D chains. The coordination sphere of the metal is completed by the additional coordination of a water molecule. The ZnN_2O_2 coordination sphere is best described as a tetrahedron, although the zinc ions show a geometry that is close to axially vacant trigonal bipyramid according to continuous-shape-measures (CShMs) using SHAPE software (Table1).¹⁰

Table 1. Continuous Shape Measurements for the ZnN₂O₂ coordination environment.

SP-4	1 D4h	Square
T-4	2 Td	Tetrahedron
SS-4	3 C2v	Seesaw or sawhorse‡ (cis-divacant octahedron)
vTBPY-4	4 C3v	Axially vacant trigonal bipyramid

Complex	SP-4	T-4	SS-4	vTBPY-4
1	29.137	1.086	5.417	1.705

The double chain packing is ruled by the intermolecular interactions. In particular, the coordinated water molecule is involved in hydrogen bonding interactions while the angle formed among neighbouring chains allow establishing C–H... π interactions between aromatic rings (Figure 5).

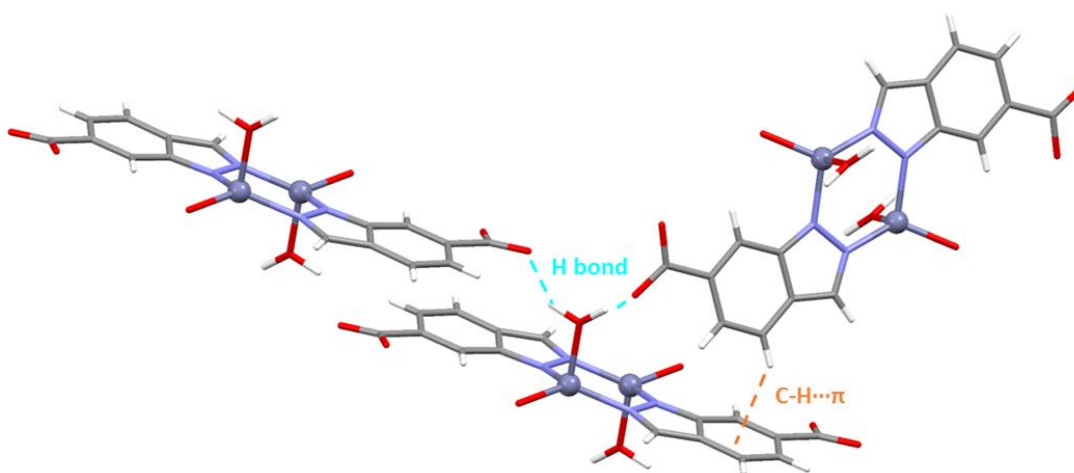


Figure 5. The most representative intermolecular interactions and packing modes for compound **1**. H bonds and C–H... π interactions are shown with dashed blue and orange lines, respectively.

Structural description of [Cd₂(HL)₄]_n (2). Compound **2** crystallizes in the triclinic P-1 space group. The symmetric unit contains two non-equivalent Cd(II) centres and four ligand molecules. Each Cd(II) ion is connected to two monodentate indazole nitrogen atoms and four oxygen atoms of the carboxylate group of the

ligand. Cd1 and Cd2 ions are doubly linked by an ancillary syn-anti carboxylate moiety of 1*H*-indazole-6-carboxylate A, C and D ligands. However, the carboxylate group of ligand B presents a different connection, O1B connects in a monodentate way to both Cd1 and Cd2 atoms giving rise to alternating five and six membered rings along the structure (Figure 6 view along *b* axis) while O2B remains unconnected to any metal centre.

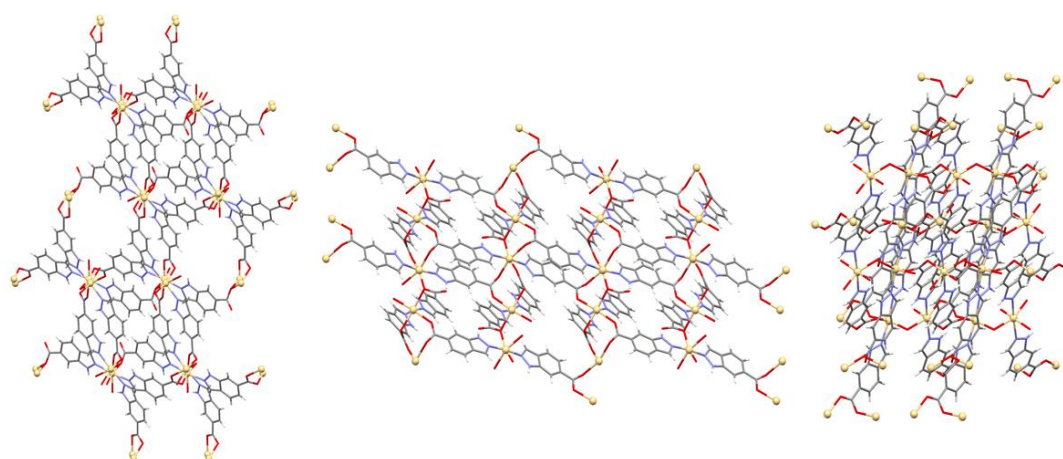


Figure 6. View along *a* (left), *b* (middle) and *c* (right) axis of complex 2.

Continuous-shape-measures (CShMs) indicate that different coordination modes of the ligand affect the coordination environments and yield, as expected, a different crystal structure. The coordination spheres of Cd1 and Cd2 are best described as octahedra according to SHAPE measurements (Table 2).

Table 2. Continuous Shape Measurements for the CdN2O4 coordination environment.

HP-6	1 D6h	Hexagon
PPY-6	2 C5v	Pentagonal pyramid
OC-6	3 Oh	Octahedron
TPR-6	4 D3h	Trigonal prism
JPPY-5	5 C5v	Johnson pentagonal pyramid (J2)

Complex	HP-6	PPY-6	OC-6	TPR-6	JPPY-5
2 -Cd1	28.823	19.153	2.317	9.223	23.163
2 -Cd2	29.031	27.296	1.100	14.572	19.748

M···N2 distances are slightly shorter than in compound **1** (in the 1.969 and 2.293-2.316 Å ranges, respectively), similarly to the M···O1_{carboxylate} bond distances (between 1.935 and 2.320 Å), which follow the same trend.

To end up with the structural description, it is worth mentioning that compound **2** presents significant differences with regard to the supramolecular interactions which build up its packing compared to that of **1**. Unlike to hydrogen bonding interactions and C-H··· π governing the crystal building of **1**, packing of **2** is governed by π ··· π stacking interactions. In particular, the aromatic rings of HL promote strong face-to-face contacts among the whole structure, which directs their packing (Figure 6).

2.2. FT-IR spectrum

The FT-IR spectra of complexes **1** and **2** showed the expected vibrational bands, confirming the coordination to N-containing carboxylate ligand (Figure 7). The main vibrations of 1*H*-indazole-6-carboxylic acid are associated to the U_{C=N} stretching vibration at 1633 cm⁻¹ and the asymmetric and symmetric vibrations of the carboxylate groups at 1683 cm⁻¹ and 1423 cm⁻¹ respectively. The characteristic bands at 1537 cm⁻¹ for complex **1**, 1589 cm⁻¹ for complex **2** can be attributed to the U_{C=N}

stretching vibration of the indazole ring.¹¹ In addition, the strong absorption peak observed at 1558 and 1402 cm^{-1} for **1**, and 1541 and 1411 cm^{-1} for **2** revealed the asymmetric and symmetric vibrations of the carboxylic groups.¹² The strong broad band in the range of 3317–3086 cm^{-1} was assigned to the O–H stretching vibration of the coordinated water molecule in complex **1**.¹³ As can be seen in Figure 7, there is a small displacement in the most characteristic bands due to the coordination of the 1*H*-indazole-6-carboxylic ligand to the metal centers.

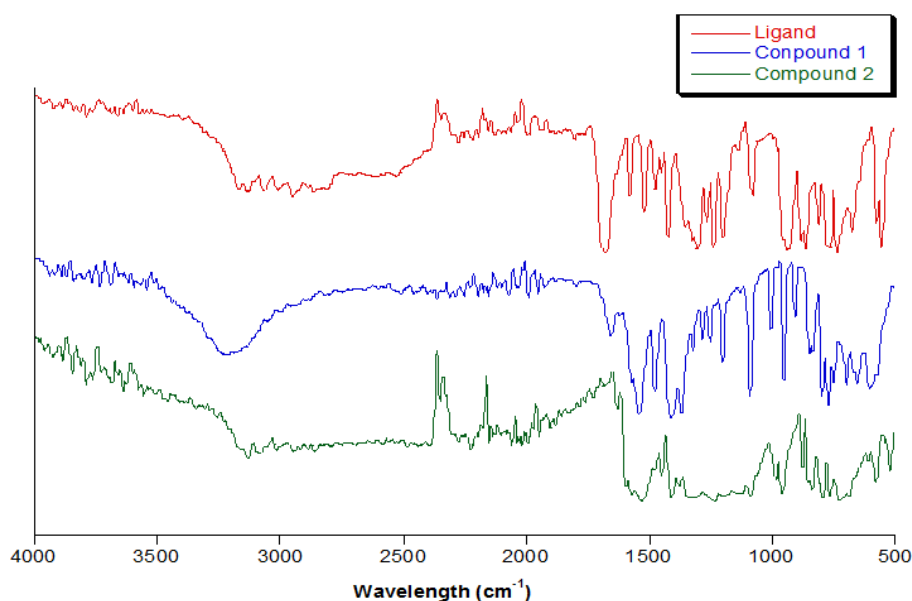


Figure 7. Infrared spectra of the ligand and compounds **1** and **2**.

2.3. Luminescence properties

The solid-state photoluminescence spectra of the complexes recorded at room temperature are shown in Figure 8. It is well known that d^{10} metal complexes yield strong emission because of completely filled d-orbitals that disables ligand field d-d transition through electron/energy transfer, which eliminates fluorescence quenching possibility.⁸ For this reason, these compounds have been of great interest for photochemical, electroluminescence and sensing applications.¹⁴ The extended aromaticity of the 1*H*-indazole-6-carboxylate ligand coordinated to Zn(II) and Cd(II) metallic centres suggests the existence of emissive properties of **1** and **2**. The emission of these compounds are found to be similar to ligand emission, which may

stem from the ligand-centred $\pi\text{-}\pi^*$ electronic transitions, as shown in Figure 5. Consequently, ligand-centred emission process controls emission spectra because of highly conjugated 1*H*-indazole-6-carboxylate ligand.¹⁵ An intense broad band at 350–450 nm dominates the emission spectra of all compounds, the emission peaks of the ligand and compounds **1** and **2** upon 325 nm excitation being in the blue region with maxima at 362 and 388 nm, 363 and 381 nm and 363 and 391 nm, respectively.

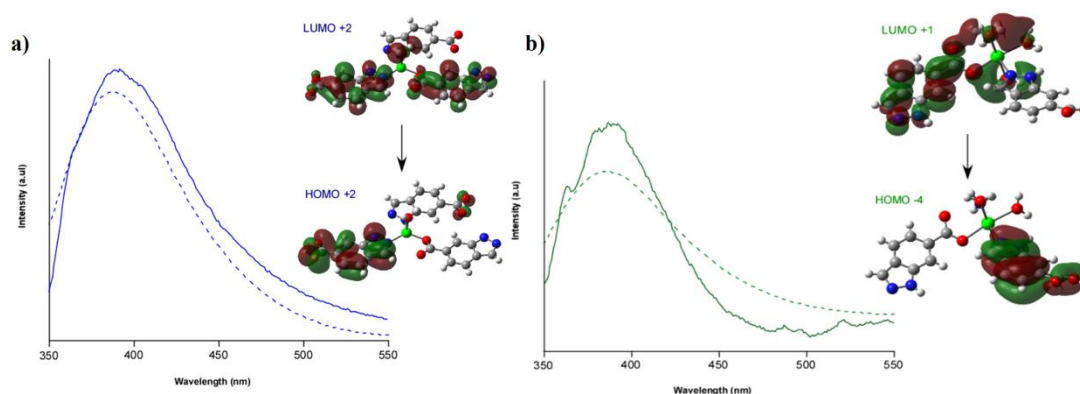


Figure 8. Room temperature TD-DFT computed (dashed lines) and experimental (solid line) photoluminescence emission under $\lambda_{ex} = 325$ nm of CPs. Blue and green lines correspond to compound **1** and **2**, respectively. The insets show the most representative molecular orbitals involved in the electronic transitions.

Among them, the ligand spectrum shows two well-defined maxima and a relatively higher intensity (Figure 9).

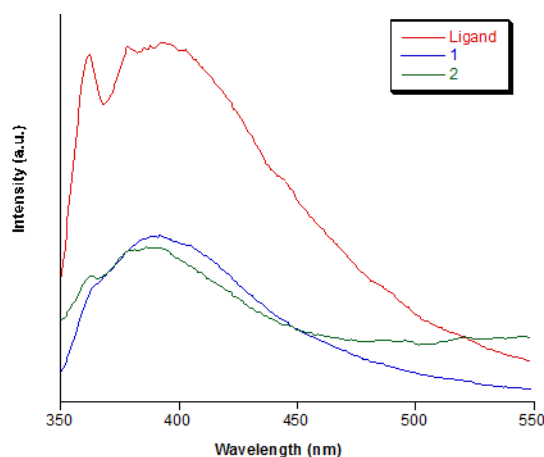


Figure 9. Emission spectra of the ligand and compounds **1** and **2** under $\lambda_{ex} = 325$ nm.

In order to get a deeper insight into the emission mechanism, TD-DFT calculations were performed on a suitable model of compound **1** and **2**. The calculated spectra reproduce fairly well the experimental one, indicating that the process is driven by singlet transitions occurring between the molecular orbitals shown in Figure 8. In both cases, the electron density in HOMO orbitals, HOMO-2 for compound **1** and HOMO-4 for compound **2** respectively extends over the bonds over the whole ligand molecule (signifying a π orbital) while LUMO orbitals, LUMO+2 for compound **1** and LUMO+1 for compound **2** respectively, feature a π^* character. Therefore, by analogy to the experimental data, it can be stated that the transitions involved in the photoluminescence of compound **1** and **2** are mainly of $\pi^* \leftarrow \pi$ nature induced by ligand centred emission.

2.4. *In vitro* cytotoxicity

The cytotoxicity of compounds **1** and **2** and the corresponding ligand has been assessed *in vitro* on human embryonic kidney (HEK-293) and mouse melanoma (B16-F10) cell lines. After two days of incubation any sign of toxicity was observed on compound **1** or the ligand at concentrations ranging from 10 to 100 $\mu\text{g mL}^{-1}$ (Figure 10). On the other hand, compound **2** prompts to a significant decrease of HEK-293 and B16-F10 cell viability for concentrations higher than 20 $\mu\text{g mL}^{-1}$. The mean concentration of this compound required to inhibit cell growth at 50% (IC_{50}) was of 43.2 $\mu\text{g mL}^{-1}$ for HEK-293 cell line and 45 $\mu\text{g mL}^{-1}$ for B16-F10 cell line. This effect could be attributed to the presence of cadmium in this coordination complex. In fact, previous study indicated that Cd has a dose-dependent negative effect on the viability of four different cell lines. In the case of HEK-293 cell line, the IC_{50} for CdCl_2 was of 1.9 $\mu\text{g mL}^{-1}$, much higher than in the case of compound **1**.¹⁶

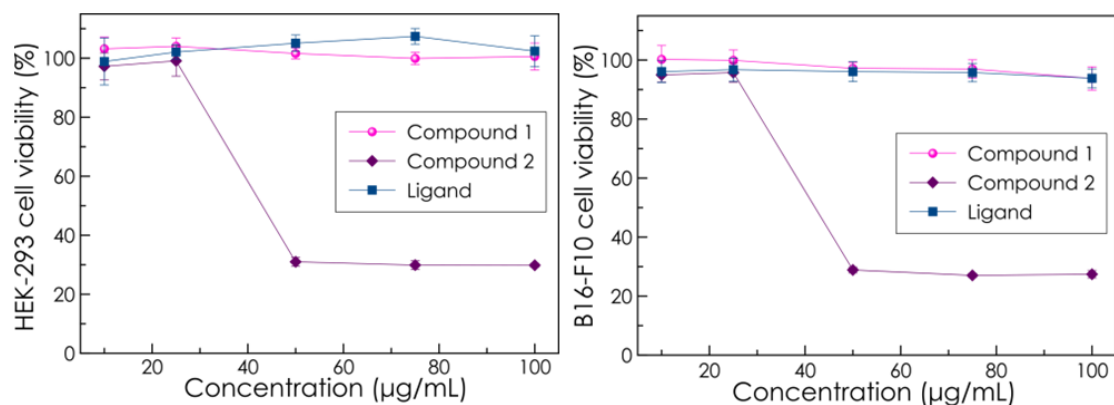


Figure 10. Viability of HEK-293 and B16-F10 cells after 48 hours of incubation with compounds **1**, **2** and the H₂L ligand at increasing concentrations (10, 25, 50, 75 and 100 µg/mL). Cell viability was assessed by MTS assay. Data represent means ± SEM (error bars) of three replicates.

3. Conclusions

The reaction between 1*H*-indazole-6-carboxylic acid ligand with Zn(II) and Cd(II) leads the formation of two new coordination polymers with different dimensionalities. Compound **1** possesses a double chain structure while compound **2** exhibits a 3D structure. Emissive properties of both complexes and the ligand have been studied demonstrating that in both cases the photoluminescent emission is driven by the ligand centred $\pi^* \leftarrow \pi$ emission. Finally, *in vitro* cytotoxicity analysis in human embryonic kidney and mouse melanoma cell lines showed that compound **2** promotes a significant decrease of HEK-293 and B16-F10 cell viability for concentrations higher than 20 µg mL⁻¹. Therefore, this study concludes that these compounds could be good candidates to conduct further *in vivo* analyses owing to their utility as biomedical probes in which the luminescent properties had a special relevance since, so far, it is the first time that the luminescent properties of the ligand and its complexes have been analysed due to only one complex with this ligand has been reported so far. In this sense, we have demonstrated that 1*H*-indazole-6-carboxylic acid is an excellent candidate to the formation of CPs or MOFs materials with different applications. Currently, more materials are being developed in our laboratory with this ligand based on lanthanide ions to enhance its luminescent properties.

4. Experimental Section

4.1. Materials and physical measurements

All the reagents were purchased commercially and used without any previous purification. Elemental analysis (C, H and N) were carried out at the Centro de Instrumentación Científica (University of Granada) on a Fisons-Carlo Erba analyzer model EA 1108 (Thermo Scientific, Waltham, MA, USA). Infrared (IR) spectra ($400\text{-}4000\text{ cm}^{-1}$) were recorded on a Nicolet FT-IR 6700 spectrometer in KBr pellets.

Synthesis of $[\text{Zn}(\text{L})(\text{H}_2\text{O})]_n$, (1). 0.010 g (0.006 mmol) of 1*H*-indazole-6-carboxylic acid (H_2L) was dissolved in 0.5 mL of DMF. Once dissolved, 0.5 mL of water was added to the ligand solution. On the other hand, in a separate vial, 0.0134 g (0.03 mmol) of $\text{Zn}(\text{CH}_3\text{COO})_2$ was dissolved in 0.5 mL of water. Similarly, once metal salt was dissolved, 0.5 mL DMF were added to the solution. Metal solution was added dropwise to the ligand solution and the resulting colourless solution was placed in a closed glass vessel and heated in an oven at 100°C for 24h. X-ray quality crystals were obtained during heating process under autogenous pressure. The obtained white single crystals were washed with water. Yield: 64% based on Zn. Anal Calcd for $\text{ZnC}_8\text{H}_4\text{N}_2\text{O}_3$: C, 39,46; H, 2,48; N, 11,50. Found: C, 39,39; H, 2,41; N, 11,59.

Synthesis of $[\text{Cd}_2(\text{HL})_4]_n$, (2). The same synthetic procedure was carried out to obtain complex **2** but $\text{Zn}(\text{CH}_3\text{COO})_2$ was replaced by 0.01651 g (0.03 mmol) of $\text{Cd}(\text{CH}_3\text{COO})_2$. Single crystals were washed with water. Yield of crystals: 54% based on Cd for **2**. Anal Calcd for $\text{Cd}_2\text{C}_{32}\text{H}_{20}\text{N}_8\text{O}_8$: C, 44,21; H, 2,32; N, 12,89. Found: C, 44,16; H, 2,29; N, 12,91.

In addition to the elemental analyses, the purity of all the samples was checked by FT-IR spectra.

4.2. Crystallographic refinement and structure solution

Single crystals of suitable dimensions were used for data collection. For compound **1** and **2**, diffraction intensities were collected on a Bruker X8 APEX II and Bruker D8 Venture with a Photon detector equipped with graphite monochromated Mo-K α radiation ($\lambda = 0.71073 \text{ \AA}$). The data reduction was performed with the APEX2¹⁷ software and corrected for absorption using SADABS.¹⁸ In all cases, the structures were solved by direct methods and refined by full-matrix least-squares with SHELXL-2018.¹⁹

Table 3. Crystallographic data and structural refinement details for compounds **1** and **2**.

Compound	1	2
Formula	C ₈ H ₆ N ₂ O ₃ Zn	C ₃₂ H ₂₀ N ₈ O ₈ Cd ₂
M_r	243.52	869.36
Crystal system	<i>monoclinic</i>	<i>triclinic</i>
Space group (no.)	<i>P 2₁/n</i>	<i>P-1</i>
a (Å)	9.774(3)	8.7080(4)
b (Å)	5.7633(15)	9.0640(3)
c (Å)	14.592(4)	19.4510(7)
α (°)	90	101.089(1)
β (°)	95.626(7)	90.961(2)
γ (°)	90	98.063(1)
V (Å ³)	818.0(4)	1490.18(1)
Z	4	2
D_c (g cm ⁻³)	1.977	1.937
μ (Mo/CuK α) (mm ⁻¹)	2.979	1.497
T (K)	100	100
Observed reflections	1035 (817)	7671 (5938)
R_{int}	0.1342	0.0722
Parameters	127	451
GoF	1.082	1.107
R ^{a,b}	0.0777 (0.0535)	0.0604 (0.0352)
wR_2 ^c	0.1075 (0.0994)	0.0823 (0.0672)
Largest difference in peak and hole (e Å ⁻³)	0.635 and -0.0656	1.062 and -1.046

^a $R_I = \sum |F_o| - |F_c| / \sum |F_o|$. ^b Values in parentheses for reflections with $I > 2s(I)$. ^c $wR_2 = \{ \sum [w(F_o^2 - F_c^2)^2] / \sum [w(F_o^2)^2] \}^{1/2}$

Details of selected bond lengths and angles are given in Table 4. CCDC reference numbers for the structures are 1948382 and 1948383 for Cd and Zn coordination polymers, respectively.

Table 4. Selected angles (°) and bond lengths (Å) for complexes **1** and **2**.

Complex	1	2	Complex	1	2
N(1)-M(1)-N(2)	113.1(3)		M(1)···N(1)	1.984(6)	
N(1)-M(1)-O(1)	107.7(2)		M(1)···N(2)	1.969(7)	
N(1)-M(1)-O(1W)	101.0(3)		M(1)···N(2A)		2.293(3)
N(2)-M(1)-O(1)	128.7(3)		M(1)···N(2D)		2.329(3)
N(2)-M(1)-O(1W)	103.8(2)		M(1)···O(1)	1.935(6)	
N(2A)-M(1)-N(2D)		173.40(10)	M(1)···O(1W)	2.019(6)	
N(2B)-M(2)-N(2C)		170.76(10)	M(1)···O(2A)		2.332(2)
O(1)-M(1)-O(1W)	97.3(2)		M(1)···O(1B)		2.374(2)
N(2A)-M(1)-O(2A)		90.31(9)	M(1)···O(1C)		2.346(2)
N(2A)-M(1)-O(1B)		95.49(9)	M(1)···O(1D)		2.258(2)
N(2A)-M(1)-O(1C)		78.08(9)	M(1)···O(2D)		2.358(2)
N(2A)-M(1)-O(2D)		103.31(9)	M(2)···N(2B)		2.332(3)
N(2D)-M(1)-O(2A)		83.09(9)	M(2)···N(2C)		2.316(3)
N(2D)-M(1)-O(1B)		85.83(9)	M(2)···O(1A)		2.320(2)
N(2D)-M(1)-O(1C)		102.89(9)	M(2)···O(1B)		2.419(3)
N(2D)-M(1)-O(2D)		83.16(9)	M(2)···O(1C)		2.349(3)
N(2B)-M(2)-O(1A)		79.11(9)	M(2)···O(1D)		2.258(2)
N(2B)-M(2)-O(1B)		91.68(9)	M(1)···N(1)	1.984(6)	
N(2B)-M(2)-O(2C)		98.75(9)	M(1)···N(2)	1.969(7)	
N(2B)-M(2)-O(1D)		108.91(9)	M(1)···N(2A)		2.293(3)
N(2C)-M(2)-O(1A)		92.24(9)	M(1)···N(2D)		2.329(3)
N(2C)-M(2)-O(1B)		91.41(9)	M(1)···O(1)	1.935(6)	
N(2C)-M(2)-O(2C)		78.08(9)	M(1)···O(1W)	2.019(6)	
N(2C)-M(2)-O(1D)		79.57(9)			
O(1C)-M(1)-O(1B)		158.86(9)			
O(1C)-M(1)-O(2D)		73.64(8)			
O(2A)-M(1)-O(1B)		101.09(8)			
O(2A)-M(1)-O(1C)		99.08(8)			
O(2A)-M(1)-O(2D)		162.54(8)			
O(2D)-M(1)-O(1B)		88.58(8)			
O(1A)-M(2)-O(1D)		171.45(8)			
O(1A)-M(2)-O(1B)		88.97(8)			
O(1A)-M(2)-O(2C)		91.70(9)			
O(1B)-M(2)-O(2C)		169.48(8)			
O(1B)-M(2)-O(1D)		93.63(9)			
O(1D)-M(2)-O(2C)		84.27(9)			

4.3. Photophysical measurements

Photoluminescence (PL) measurements were carried out on crystalline samples at room temperature using a Varian Cary-Eclipse fluorescence spectrofluorimeter equipped with a Xe discharge lamp (peak power equivalent to 75 kW), Czerny–Turner monochromators, and an R-928 photomultiplier tube. For the fluorescence measurements, the photomultiplier detector voltage was fixed at 600 V, and the excitation and emission slits were set at 5 and 2.5 nm, respectively. Phosphorescence spectra were recorded with a total decay time of 20 ms, delay time of 0.2 ms and gate time of 5.0 ms. The photomultiplier detector voltage was set at 800 V, and both excitation and emission slits were open to 10 nm.

4.4. *In vitro* cell viability assays

The cytotoxicity of synthesized compounds and the corresponding ligand was evaluated against Human Embryo Kidney cell line (HEK-293, ECACC 85120602) and mouse melanoma cell line (B16-F10, CRL-6322). Both lines were supplied by “Banco de Células del Centro de Instrumentación Científica” of the University of Granada.

HEK-293 cells were maintained in humidified air (5% CO₂) at 37°C in Eagle's Minimum Essential Medium (EMEM with EBSS) supplemented with 2mM Glutamine, 1% Non Essential Amino Acids (NEAA), 1 mM sodium pyruvate (NaP) and 10% Fetal Bovine Serum (FBS). B16-F10 cells were cultured in standard tissue culture flask in EMEM (EBSS) supplemented with 2mM Glutamine and 10% FBS (37°C, 5% CO₂). Before full confluence, cells were detached from culture flasks by trypsinization, centrifuged and resuspended. The cells were seeded at 1.0×10^4 cells/well into a 96 flat transparent well and cultured at 37°C with 5% CO₂. Serial dilutions of the synthesized compounds were prepared in cell culture media up to the final concentrations of 10, 25, 50, 75 and 100 µg/mL. After 48 hours of pre-incubation, the cell culture medium was replaced by the samples. The number of living cells after 48 hours of culture was assessed by MTS assay using CellTiter 96® Aqueous One Solution Reagent (Promega, Madison, WI). The MTS assay is based

on the conversion of a tetrazolium salt into a coloured, aqueous soluble formazan product mediated by mitochondrial activity of viable cells. Briefly, 20 µL of Aqueous One Solution Reagent was added to each well and after 2h of incubation, the absorbance at 490 nm was measured with a spectrophotometer (Infinite® 200 PRO NanoQuant). This absorbance is directly proportional to the number of metabolically active cells. Untreated cells (without synthesized compounds) were used as control. The relative cell viability (%) related to the control was calculated by $[A]_{\text{sample}}/[A]_{\text{control}} \times 100$. Each experiment was done in triplicate. Results are expressed as average \pm standard error of the mean (S.E.M.). The half inhibitory concentrations (IC₅₀) were calculated by the Graph Pad Prism (version 5.0), using the dose-response sigmoidal curves, $p < 0.05$.

Keywords: 1*H*-Indazole-6-Carboxylic Acid • luminescence • anti-cancer activity • Zinc • Cadmium.

5. References

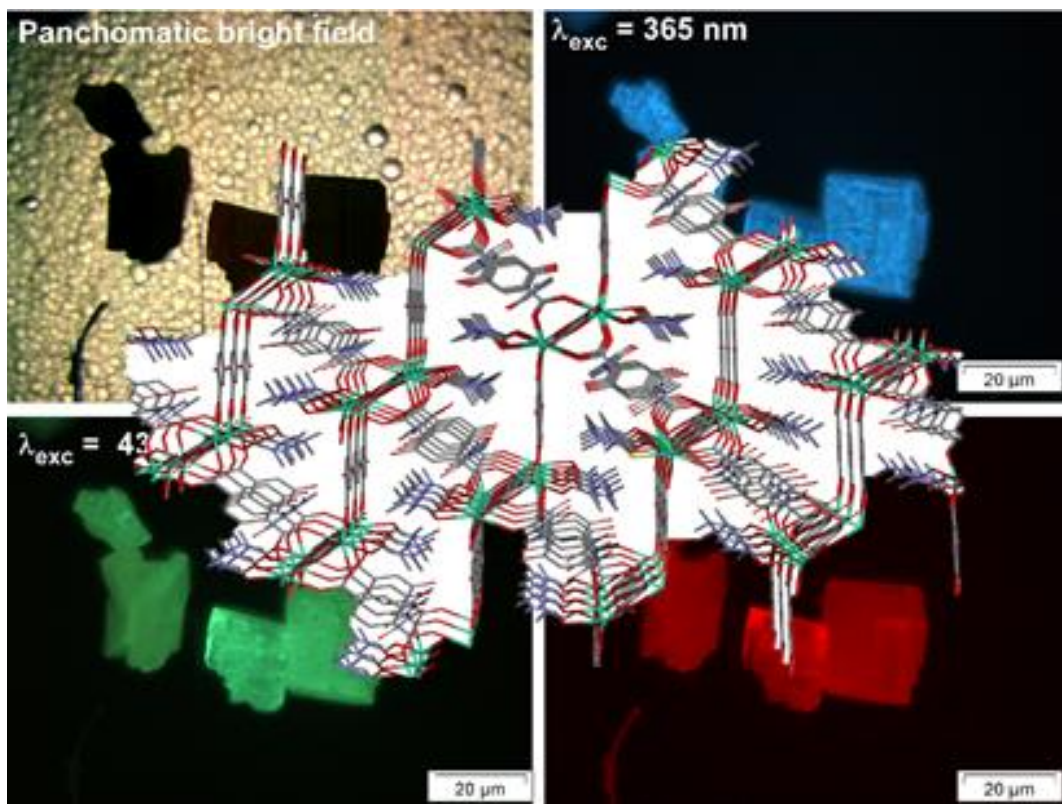
- 1.- a) D. Farrusseng, *Metal–Organic Frameworks: Applications from Catalysis to Gas Storage*, ed., Wiley-VCH, Weinheim, **2011**; b) S. R. Batten, S. M. Neville, D. R. Turner, *Coordination Polymers: Design, Analysis and Application*, RSC Publishing, Cambridge, **2009**; c) L. R. MacGillivray, *Metal–Organic Frameworks Design and Application*, John Wiley and Sons, Hoboken, **2010**; d) C. J. Kepert, in *Porous Materials*, ed. D. W. Bruce, D. O'Hare, R. I. Walton, John Wiley and Sons, Chichester, **2010**; e) D. J. Tranchemontagne, J. L. Mendoza-Cortes, M. O'Keeffe, O. M. Yaghi, *Chem. Soc. Rev.* **2009**, 38, 1257; f) A. C. McKinlay, R. E. Morris, P. Horcajada, G. Ferey, R. Gref, P. Couvreur, C. Serre, *Angew. Chem. Int. Ed.* **2010**, 49, 6260; g) M. Schroder, *Top. Curr. Chem.*, **2010**, 293, 1.
- 2.- J. Dong, Q. Zhang, Z. Wang, G. Huang, S. Li, *ChemMedChem* **2018**, 13, 1490.

- 3.- G. E. Büchel, S. Kossatz, A. Sadique, P. Rapta, M. Zalibera, L. Bucinsky, S. Komorovsky, J. Telser, J. Eppinger, T. Reine, V. B. Arion, *Dalton Trans.* **2017**, *46*, 11925.
- 4.- C. S. Hawes, P. E. Kruger, *Dalton Trans.* **2014**, *43*, 16450.
- 5.- B.-F. Long, Q. Huang, S.-L. Wang, Y. Mi, M.-F. Wang, T. Xiong, S.-C. Zhang, X.-H. Yin, F.-L. Hu, *J. Coord. Chem.* **2019**, *72*, 645.
- 6.- a) J. D. Furman, R. P. Burwood, M. Tang, A. A. Mikhailovsky, A. K. Cheetham, *J. Mat. Chem.* **2011**, *21*, 6595; b) S. K. Lower, M. A. El-Sayed, *Chem. Rev.* **1966**, *66*, 199.
- 7.- W. Z. Yuan, X. Y. Shen, H. Zhao, J. W. Y. Lam, L. Tang, P. Lu, C. Wang, Y. Liu, Z. Wang, Q. Zheng, J. Z. Sun, Y. Ma, B. Z. Tang, *J. Phys. Chem. C* **2010**, *114*, 6090.
- 8.- a) J. Cepeda, A. Rodríguez-Diéguez, *CrystEngComm* **2016**, *18*, 8556; b) K. N. Solov'ev, E. A. Borisevich, *Phys.-Usp.* **2005**, *48*, 231; c) Nyokong, *Coord. Chem. Rev.* **2007**, *251*, 1707.
- 9.- a) R. C. Evans, P. Douglas, C. J. Winscom, *Coord. Chem. Rev.* **2006**, *250*, 2093; b) Q.-D. Liu, R. Wang, S. Wang, *Dalton Trans.* **2004**, 2073; c) A. Barbieri, G. Accorsi, N. Armaroli, *Chem. Commun.* **2008**, 2185.
- 10.- M. Lunell, D. Casanova, J. Cirera, J. M. Bofill, P. Alemany, S. Alvarez, M. Pinsky, D. Avnir, *SHAPE*, v1.1b; Barcelona, Spain, **2005**.
- 11.- M. Bča, P. Baran, R. Boča, H. Fuess, G. Kickelbick, W. Linert, F. Renz, I. Svoboda, *Inorg. Chem.* **2000**, *39*, 3205.
- 12.- H. Xia, X.-B. Li, G. F. Qin, Y. Xia, G. Zho, *J. Iran. Chem. Soc.* **2016**, *13*, 793.
- 13.- K. Ohno, M. Okimura, N. Akai, Y. Katsumoto, *Phys. Chem. Chem. Phys.* **2005**, *7*, 3005.

- 14.- A. Salinas-Castillo, A. J. Calahorro, D. Briones, D. Fairen-Jiménez, F. Gándara, C. Mendicute-Fierro, J. M. Seco, M. Pérez-Mendoza, B. Fernández, A. Rodríguez-Diéguez, *New J. Chem.* **2015**, 39, 3982.
- 15.- M. Pamei, A. Puzari, *Nano-Structures & Nano-Objects*. **2019**, 19, 100364.
- 16.- G. Ravindran, D. Chakrabarty, A. Sarkar, *Animal cells and systems* **2017**, 21, 23.
- 17.- *Bruker Apex2*, Bruker AXS Inc., Madison, Wisconsin, USA, **2004**.
- 18.- G. M. Sheldrick, *SADABS, Program for Empirical Adsorption Correction*, Institute for Inorganic Chemistry, University of Gottingen, Germany, **1996**.
- 19 .- G. M. Sheldrick, *SHELXTL Version 2014/7*. <http://shelx.uni-ac.gwdg.de/SHELX/index>.

Capítulo 7

Dilution Effect on the Slow Relaxation of a Luminescent Dysprosium Metal-Organic Framework based on 2,5-dihydroxyterephthalic Acid



Dilution Effect on the Slow Relaxation of a Luminescent Dysprosium Metal-Organic Framework based on 2,5-dihydroxyterephthalic Acid

Inorganica Chimica Acta 509 (2020) 119687



Contents lists available at ScienceDirect

Inorganica Chimica Acta

journal homepage: www.elsevier.com/locate/ica



Research paper

Dilution effect on the slow relaxation of a luminescent dysprosium Metal-Organic Framework based on 2,5-dihydroxyterephthalic acid



Antonio A. García-Valdivia^a, Andoni Zabala-Lekuona^b, Ainhoa Goñi-Cárdenas^a, Belén Fernández^c, Jose A. García^d, José F. Quílez del Moral^e, Javier Cepeda^{b,*}, Antonio Rodríguez-Diéguez^{a,*}

^a Dept. of Inorganic Chemistry, C/Severo Ochoa s/n, University of Granada, 18071 Granada, Spain

^b Dept. of Applied Chemistry, Chemistry Faculty, University of the Basque Country UPV/EHU, 20018 Donostia-San Sebastián, Spain

^c Institute of Parasitology and Biomedicine "López-Neyra", CSIC, Av. Conocimiento s/n, 18600 Granada, Spain

^d Departamento de Física Aplicada II, Facultad de Ciencia y Tecnología, Universidad del País Vasco (UPV/EHU), 48940 Leioa, Spain

^e Dept. of Organic Chemistry, C/Severo Ochoa s/n, University of Granada, 18071 Granada, Spain

Abstract

A new dysprosium based Metal-Organic Framework with $\{[\text{Dy}(\text{dhbdc})_{1.5}(\text{DMF})_2] \cdot \text{DMF}\}_n$ formula has been obtained from solvothermal reaction with 2,5-dihydroxyterephthalic acid ligand and dysprosium chloride. This coordination polymer has been characterized and its crystal structure has been solved by X-ray diffraction methods elucidating a three-dimensional network. Magnetic studies of this compound reveal the existence of weak antiferromagnetic interactions among the metal ions with θ value of -0.26 K. Dynamic *ac* magnetic susceptibility measurements were carried out under an external *dc* field of 1 kOe, highlighting that at high frequencies two relaxation processes can be observed. However, when studying the diamagnetically diluted analogue **1Y**, a single relaxation process was detected highlighting the effect of the weak but not negligible exchange interactions. Finally, photoluminescence measurements were performed at different temperatures with the aim of getting a more representative characterization of the emissive performance of the material for potential applications in lighting and thermometry.

1. Introduction

The research related to metal-organic frameworks (MOFs) has exponentially increased in the past years mainly due to their multifunctional properties and potential uses in applications such as gas storage/separation, photoluminescence, sensing, magnetism, etc.^[1] These materials are synthesized by combining metal ions or nodes with organic linkers forming three-dimensional structures. Among them, lanthanide based MOFs (Ln-MOFs) have been less studied than transition metal based ones. This is directly related to the large ionic radius of the Ln(III) ions, since they normally present high coordination numbers with distorted symmetries which bring some flexibility to the coordination network, making it more difficult to predict the structure of the compound. However, the large magnetic anisotropy and high spin value of some Ln(III) ions make them potential candidates in order to design ultra-high-density information storage devices^[2]. In fact, some recent advances in the area of Single Molecule Magnets (SMMs) have shown that huge thermal energy barriers that prevent the relaxation of the magnetization, as well as open hysteresis loops up to liquid nitrogen temperature could be obtained by using Dy(III) as anisotropic metal ion^[3]. Moreover, most of Ln(III) ions may display characteristic narrow fluorescence emissions, so they might be good candidates in order to obtain multifunctional magnetic and luminescent materials. Accordingly, even though the absorption coefficients of *f-f* transitions are low, the coordination of strongly absorbing ligands to the metal may be a way to overcome this handicap by an efficient antenna effect, which involves an energy transfer from the ligand to the metal^[4].

The necessity of implementing SMMs within a surface or in a three-dimensional structure is not trivial. Even though high performing SMMs already exist, these are synthesized in bulk without a controlled spatial position and this appears to be a huge problem. When designing an information storage device, all the molecules that are able to preserve information need to be spatially organized. Hence, MOFs might be a good solution to overcome this challenge given that lanthanide ions are intrinsically organized in the three dimensions within the crystal structure of these materials^[5]. In addition, the pores enclosed in the structure of MOFs offer the possibility of intercalating a wide variety of guest molecules that may be able to modulate the magnetic properties^[6]. Moreover, with regard to the multifunctional

character of MOFs, guest molecules could also influence the luminescent emission of the compound so they could be used as sensors.

In view of the mentioned prerequisites and taking into account the great affinity of Ln(III) ions towards oxygen atoms, we have chosen 2,5-dihydroxyterephthalic acid (dhhbc) as main ligand. Carboxylate groups are often used as chemical functions to decorate spacer ligands in MOFs chemistry given their large bridging capacity, as it has been observed for many related aromatic carboxylate based ligands with both transition metal as lanthanide(III) ions^[7]. In particular, the confronted disposition of carboxylate groups in dhhbc ligand is well known to bridge between two and six metal centres with transition metal ions to yield MOFs^[8], while hydroxyl groups adjacent to carboxylate groups, though they do not chelate metal centres, can serve as exceptional groups which can interact with guest molecules. On another level, the aromatic character of the ligand behaves as an appropriate moiety which, in addition to increase the distance among metal ions to dispose them separated for enhancing SMM behaviour, it can also bring large emission brightness centred on the lanthanide due to its strong absorption through π - π^* transitions.

Bearing in mind the latter, we report on the synthesis and structural and chemico-physical characterization of a new MOF with the $\{[\text{Dy}(\text{dhhbc})_{1.5}(\text{DMF})_2] \cdot \text{DMF}\}_n$ formula, which exhibits interesting magnetic and luminescence properties. On the one hand, alternating current magnetic susceptibility measurements reveal the occurrence of subtle slow relaxation of the magnetization that is effectively improved by means of a structural dilution with diamagnetic yttrium(III) ions. On the other hand, photoluminescence studies performed on both solid state and liquid media support a large ligand-to-metal charge transfer (LMCT) which provides the material with an interesting temperature- and solvent-dependent tuneable bright emission.

2. Experimental

2.1. General

2,5-dihydroxyterephthalic acid and all metallic salts used as reagents were purchased from commercial sources (Sigma-Aldrich) and used as received and without further purification.

2.2. Preparation of the complexes

Synthesis of $\{[\text{Dy}(\text{dhbdc})_{1.5}(\text{DMF})_2]\cdot\text{DMF}\}_n$ (1**).** Single crystals of compound **1** were obtained following the next solvothermal procedure. 0.076 mmol (15.00 mg) of 2,5-dihydroxyterephthalic acid and 0.101 mmol (38.05 mg) of $\text{DyCl}_3\cdot 6\text{H}_2\text{O}$ were dissolved in 1 mL of DMF. The resulting solution was placed in a closed glass vessel and introduced in an oven at 95°C for 24h. Yield: 64% based on metal. Anal Calcd for $\text{DyC}_{21}\text{O}_{12}\text{N}_3\text{H}_{27}$: C, 37.31; H, 4.03; N, 6.22. Found: C, 37.34; H, 3.99; N, 6.24.

Synthesis of $\{[\text{Dy}_{0.2}\text{Y}_{1.8}(\text{dhbdc})_3(\text{DMF})_4]\cdot 2\text{DMF}\}_n$ (1Y**).** Single crystals of **1Y** were obtained by carrying out the same general procedure described for **1** but using a Dy:Y molar ratio of 1:9. Yield: 66% based on metal. Anal Calcd for $\text{Dy}_{0.2}\text{Y}_{1.8}\text{C}_{42}\text{O}_{24}\text{N}_6\text{H}_{54}$: C, 41.37; H, 4.46; N, 6.89. Found: C, 41.41; H, 4.42; N, 6.92.

The FT-IR spectra of complexes **1** and **1Y** showed the expected vibrational bands, confirming the coordination to O-containing carboxylate group (Figure 1). The main vibrations of 2,5-dihydroxyterephthalic acid are associated to the stretching vibration at 1643 cm^{-1} and the asymmetric and symmetric vibrations of the carboxylate groups at 1683 cm^{-1} and 1423 cm^{-1} respectively. In addition, the ligand shows a high intensity band 1650 cm^{-1} that in compound **1** and **1Y** lose intensity, probably due to the bond between O-carboxylate and metal centers. As can be seen in Figure 1 there is a small displacement in the most characteristic bands due to the coordination of the 2,5-dihydroxyterephthalic acid ligand to the metal centers.

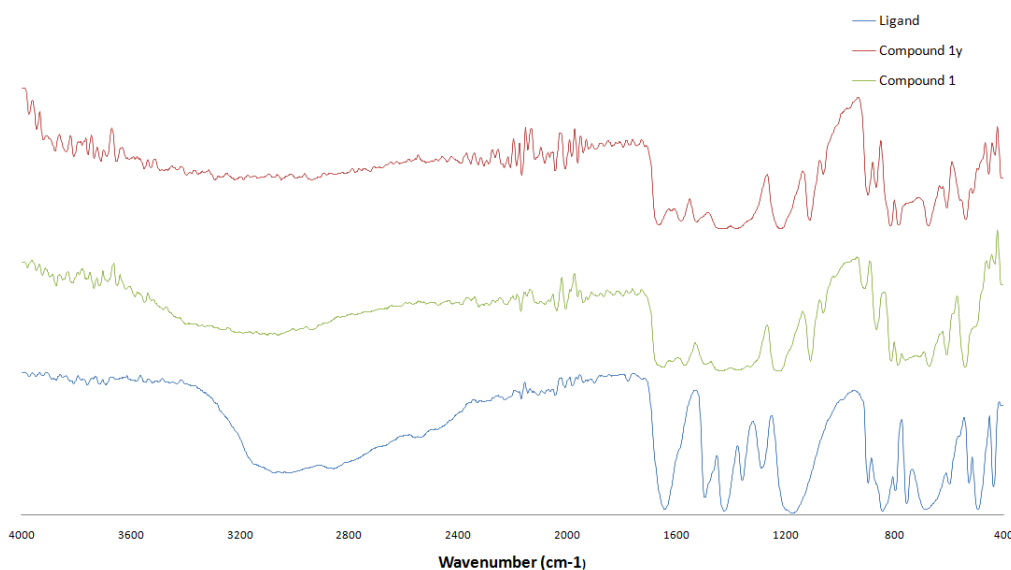


Figure 1. The FT-IR spectra of ligand and complexes **1** and **1y**.

2.3. Physical measurements

Elemental analyses were carried out at the “Centro de Instrumentación Científica” (University of Granada) on a THERMO SCIENTIFIC analyzer model Flash 2000. The IR spectra on powdered samples were recorded with a BRUKER TENSOR 27 FT-IR and OPUS data collection program. Magnetic susceptibility measurements were performed on polycrystalline samples of the complexes with a Quantum Design SQUID MPMS-7T susceptometer at an applied magnetic field of 1000 G. The susceptibility data were corrected for the diamagnetism estimated from Pascal’s Tables [9] the temperature-independent paramagnetism, and the magnetization of the sample holder. *Ac* measurements were performed on a Physical Property Measurement System-Quantum Design model 6000 magnetometer under a 3.5 G *ac* field and frequencies ranging from 1 to 1399 Hz.

2.4. Single-crystal structure determination

Prismatic crystals for **1** were mounted on a glass fibre and used for data collection on a Bruker D8 Venture with Photon detector equipped with graphite

monochromated *Mo-K α* radiation ($\lambda=0.71073$ Å). The data reduction was performed with the APEX2 [10] software and corrected for absorption using SADABS[11]. Crystal structures were solved by direct methods using the SIR97 program [12] and refined by full-matrix least-squares on F^2 including all reflections using anisotropic displacement parameters by means of the WINGX crystallographic package[13]. Several crystals of **1** were measured and the structure was solved from the best data we were able to collect, due to the quality of the crystals was very poor. Final $R(F)$, $wR(F^2)$ and goodness of fit agreement factors, details on the data collection and analysis can be found in Table 1. Selected bond lengths and angles are given in Table 2. CCDC number1985827 contain the supplementary crystallographic data for compound. These data can be obtained free of charge from The Cambridge Crystallographic Data Centre via www.ccdc.cam.ac.uk/data_request/cif.

Table 1. Crystallographic data for compound **1**.

Complex	1
Formula	C ₂₁ H ₂₄ DyN ₃ O ₁₂
M_r	672.93
Crystal system	<i>Triclinic</i>
Space group (no.)	<i>P-1</i>
a (Å)	10.446(2)
b (Å)	10.877(2)
c (Å)	12.503(3)
α (°)	104.644(4)
β (°)	107.329(4)
γ (°)	97.583(4)
V (Å ³)	1278.6(4)
Z	2
D_c (g cm ⁻³)	1.748
μ (MoK α) (mm ⁻¹)	2.988
T (K)	100(2)
Observed reflections	6582 (6086)
R_{int}	0.0495
Parameters	340
GoF	1.086
R_I ^{b,c}	0.0317 (0.0246)
wR_2 ^d	0.0624 (0.0606)
Largest difference in peak and hole (e Å ⁻³)	2.077 and -2.160

^b $R_I = S||F_o| - |F_c||/S|F_o|$. ^cValues in parentheses for reflections with $I > 2s(I)$. ^d $wR_2 = \{S[w(F_o^2 - F_c^2)^2] / S[w(F_o^2)^2]\}^{1/2}$

Table 2. Bond lengths (Å) and angles (°) for compounds **1**.

Symmetry operation for (i): -x,-y,-z.

Bond	Length (Å)	Bond	Angle (°)
Dy1-O1A	2.294(2)	O1A-Dy1-O1B	77.33(7)
Dy1-O1B	2.3224(18)	O1A-Dy1-O2B(i)	75.91(7)
Dy1-O2A(i)	2.375(2)	O1B-Dy1-O2B(i)	126.38(7)
Dy1-O2B(i)	2.3661(19)	O1A-Dy1-O1S	146.26(7)
Dy1-O1C	2.368(2)	O1B-Dy1-O1S	78.81(7)
Dy1-O2C	2.577(2)	O2B(I)-Dy1-O1S	137.82(7)
Dy1-O1S	2.367(2)	O1A-Dy1-O1C	89.05(7)
Dy1-O2S	2.410(2)	O1B-Dy1-O1C	146.07(7)
		O2B(I)-Dy1-O1C	78.35(7)
		O1S-Dy1-O1C	97.80(7)
		O1A-Dy1-O2A(i)	122.12(7)
		O1B-Dy1-O2A(i)	78.36(7)
		O2B(I)-Dy1-O2A(i)	77.99(7)
		O1S-Dy1-O2A(i)	75.19(7)
		O1C-Dy1-O2A(i)	133.93(7)
		O1A-Dy1-O2S	78.23(8)
		O1B-Dy1-O2S	73.94(7)
		O2B(I)-Dy1-O2S	141.31(7)
		O1S-Dy1-O2S	72.45(8)
		O1C-Dy1-O2S	72.91(7)
		O2A(I)-Dy1-O2S	140.64(7)
		O1A-Dy1-O2C	131.24(7)
		O1B-Dy1-O2C	151.23(7)
		O2B(I)-Dy1-O2C	68.07(7)
		O1S-Dy1-O2C	76.23(7)
		O1C-Dy1-O2C	52.93(7)
		O2A(I)-Dy1-O2C	81.59(7)
		O2S-Dy1-O2C	111.23(7)

3. Results and discussion

3.1. Crystal structure of Compound 1

Compound **1** crystallizes in the triclinic *P*-1 space group. A selection of bond distances and angles, as well as crystallographic data are given in Table 2 and Table 1, respectively. The asymmetric unit is composed of a single dysprosium ion, three independent halves of deprotonated dhhbc ligands, two coordinated DMF molecules

and one crystallization DMF molecule. The dysprosium ion is eight-coordinated being bonded to eight oxygen atoms, two of them belonging to two DMF molecules (O1S and O2S) and the rest to carboxylate groups. Whereas O1C and O2C belong to the same chelating carboxylate moiety, O1B, O2B(i), O1A and O2A(i) belong to four carboxylate groups of different dhhdc ligands (two symmetry related A and B ligands), which acquire the local $\mu\text{-}\kappa\text{O}:\kappa\text{O}'$ mode and are responsible for bridging two closest Dy centres forming paddle-wheel dinuclear fragments (Figure 2). In other words, there are different types of L^{2-} depending on the coordination mode. Two of them (the ones with O1A-O2A and O1B-O2B labels) act as double-bridging groups. On the one hand, a carboxylate group in a bimonodentate fashion is bonded to two Dy ions from the same dinuclear entity and, on the other hand, the other carboxylate in the other extreme is bonded to another dinuclear entity. In contrast, the other type of L^{2-} ligand also appears as bridging group, but each carboxylate is only coordinated to a metal ion as a chelate. Every metal centre is coordinated to four ligands of the former type and one of the latter type, thus extending the structure over the 3D.

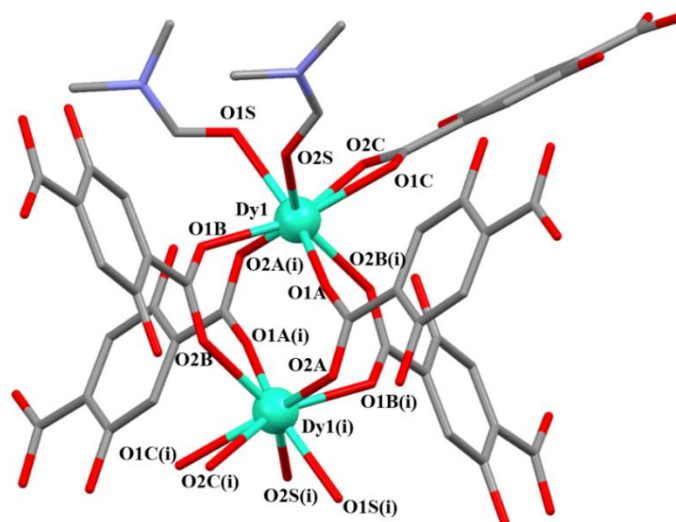


Figure 2. Excerpt of the structure showing the dinuclear entity, where coordination environment of Dy1 along with carboxylate bridged Dy1(i) is shown. Symmetry: (i): $-x, -y, -z$. Colour code: dysprosium, oxygen, nitrogen and carbon are in light green, red, blue and grey, respectively. Hydrogen atoms have been removed for the sake of clarity.

The geometry of the polyhedron was calculated by SHAPE software^[14], indicating that it is a slightly distorted square antiprism (S_{SAPR} value of 1.183). These

entities can be regarded as the repeating secondary building unit (SBU) along the whole structure and are linked to other neighbouring ones by means of both the tetradentate A and B ligands as well as the bis-chelating C ligands (Figure 3). The separation between the Dy ions within the dinuclear entity is 4.187(1) Å whereas it rises up to 10.446(2) Å and 11.421(2) Å between adjacent paramagnetic centres crossing the tetradentate and bidentated hbdc ligands, which indicates that we could expect non-negligible magnetic interactions. Isostructural Metal-Organic Frameworks based on La, Ce, Pr, Nd and Gd have been published^[15]. The Dy-O bond distances do not vary according to the nature of coordinating oxygen. Both the shortest and longest bond distances correspond to Dy1-O_{carboxylate} (2.294(2) and 2.577(2) Å, respectively) bonds, while Dy-O_{DMF} ones display intermediate distances (2.367(2) and 2.410(2) Å). The fact that the coordination sphere is somewhat regular with no notably shorter bond with respect to others might negatively affect the SMM properties. In the case of Dy(III), a well-defined axial ligand field is able to stabilize the highly magnetic $m_J = \pm 15/2$ states as ground levels and separate them from excited states which, in turn, gives rise to high effective energy barriers.

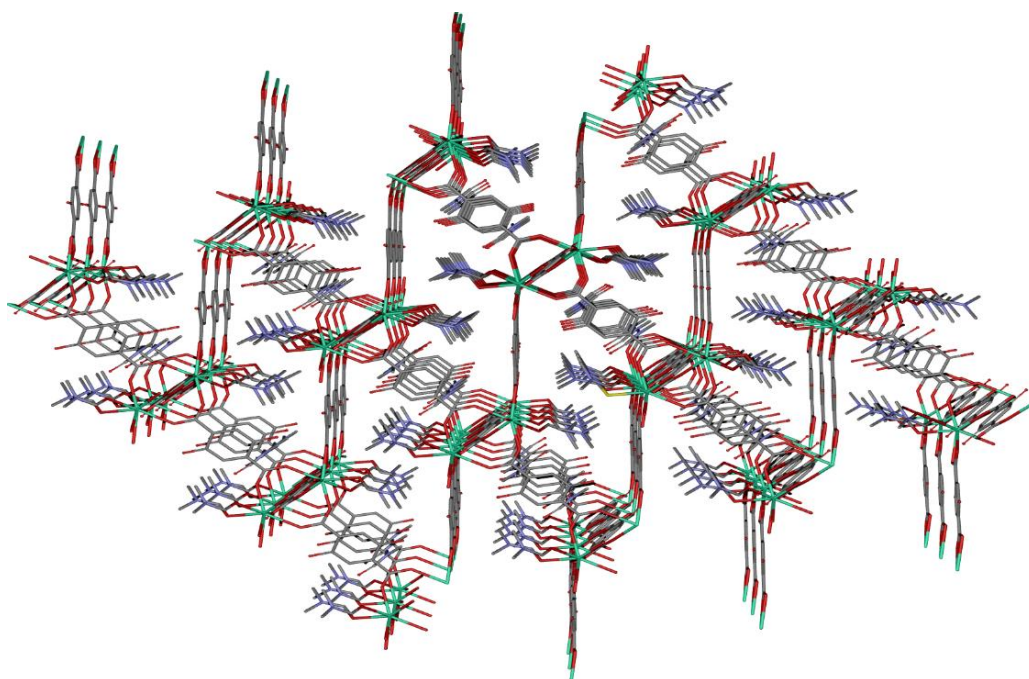


Figure 3. Perspective of Metal-Organic Framework along a axis. Colour code: dysprosium, oxygen, nitrogen and carbon are in light green, red, blue and grey, respectively. Hydrogen atoms have been removed for the sake of clarity.

3.2. Magnetic properties

3.2.1. Static Magnetic Measurements

The direct-current (*dc*) magnetic susceptibility of **1** and **1_Y** were measured in the 2–300 K range under an applied magnetic field of 0.1 T (Figure 4). The $\chi_M T$ value of 14.19 cm³ K mol⁻¹ (calculated for the asymmetric unit) observed in **1** is in good agreement with the calculated theoretical value of 14.17 cm³ K mol⁻¹ for one isolated Dy(III) ion ($4f^9$, $J = 15/2$, $S = 5/2$, $L = 5$, $g = 4/3$ ⁶H_{15/2}). On cooling, the $\chi_M T$ product remains somehow constant until 50 K, where it falls sharply reaching the minimum value of 12.70 cm³ K mol⁻¹ at 2 K. In ions such as the Dy(III), which contain considerable unquenched orbital moment, this drop could be attributed to some different effects: *i*) antiferromagnetic interactions between paramagnetic ions, *ii*) the depopulation of the Stark sublevels of the dysprosium ion, which arise from the splitting of the ground term by the ligand field and *iii*) the presence of magnetic anisotropy. The strong spin-orbit coupling in Dy(III) compounds hinders the possibility to fit the $\chi_M T$ data in order to obtain the exchange coupling constant. However, with the aim of getting a deeper insight into the possible intramolecular interactions between Dy(III) centers, we studied the magnetic data in the range of 2–300 K by the Curie-Weiss law, namely $1/\chi = (T - \theta)/C$.

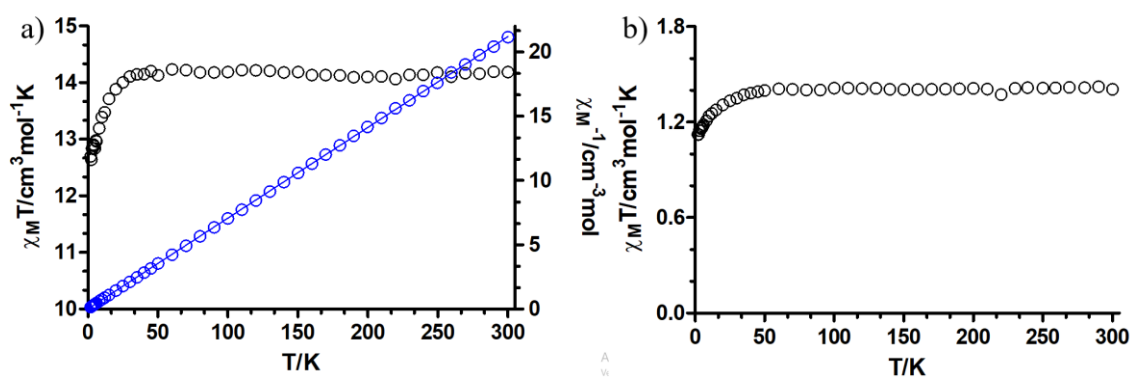


Figure 4. a) Temperature dependence of the $\chi_M T$ product and $1/\chi$ versus T for **1** in the 2–300 K range. The solid line represents the best fitting with the Curie-Weiss law. b) Temperature dependence of the $\chi_M T$ product for **1_Y** in the 2–300 K range.

The best fit afforded the values of $C = 14.17 \text{ cm}^3 \cdot \text{K} \cdot \text{mol}^{-1}$ and $\theta = -0.26 \text{ K}$. The negative value of θ suggests the existence of weak intramolecular antiferromagnetic interactions. This is in good agreement with the previously reported J values for an isostructural Gd(III) analogue^[15]. The isotropic character of Gd(III) provided by the lack of angular momentum enables the analysis of the magnetic data in order to obtain the magnetic coupling constant. The small value of $J = -0.020(2) \text{ cm}^{-1}$ calculated by Nayak and co-authors coincides with our initial prediction, being the dimeric Dy(III) entities weakly antiferromagnetically coupled systems.

With the purpose of supporting the experimental data, DFT calculations with the broken-symmetry methodology were also conducted to better estimate the nature of the magnetic exchange interactions. To that end, dimeric fragments were cut from the crystal structure of **1** in order to represent the three possible superexchange pathways found in the compound: i) that mediated within the paddle-wheel shaped entity involving four carboxylate moieties (which imposes a short bridge of 4.2 \AA between lanthanide(III) atoms); ii) through the bis-chelating dhbdc ligand (involving a Ln...Ln distance of 11.4 \AA); and iii) through the tetradentatedhbdc ligand, which imposes a Ln...Ln distance of ca. 10.9 \AA . Moreover, paramagnetic Dy(III) ions were replaced by isotropic Gd(III) ones to have a good estimate of the J parameter (we were not able to crystallise the Gd(III) analogue). In this case, based on the superexchange path 1, which considers the shortest carboxylate bridged pathways, the calculation suggests an almost negligible coupling among lanthanide(III) ions (weak ferromagnetism with $J \sim 0.02 \text{ cm}^{-1}$ is achieved), which can be considered within the calculation error given the experimental result achieved for the Dy(III) counterpart. Although experimental and theoretical calculations differ in the nature of the exchange interactions, it is evidenced that the carboxylate bridges provide weakly interacting pathways. Therefore, due to the magnetic anisotropy of the Dy(III) ion the contribution of the metal to metal exchange is hidden in **1**.

The magnetization *versus* field plot at 2 K is shown in the Figure 5. It shows an initial rapid increase up to a field of 1 T, followed by an almost linear increase reaching a value of $6.35 N\mu_B$, which is lower than the expected saturation value. This

behaviour can be explained by crystal-field effects leading to significant magnetic anisotropy.

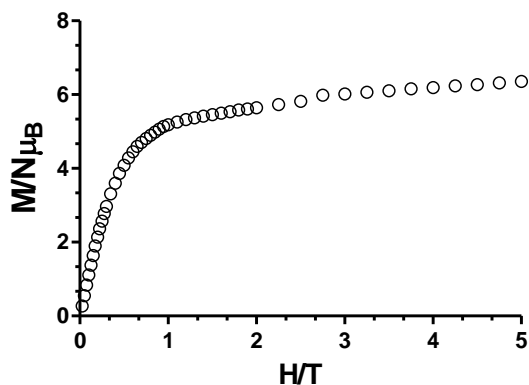


Figure 5. Magnetization versus field plot at 2 K for **1**.

3.2.2. Dynamic Magnetic Properties

Dynamic *ac* magnetic susceptibility measurements as a function of temperature and frequency were carried out on a powder sample of **1**. At zero applied *dc* field, the out-of-phase component (χ_M'') displays non-zero signals at the highest measured frequency (1399 Hz, Figure 6).

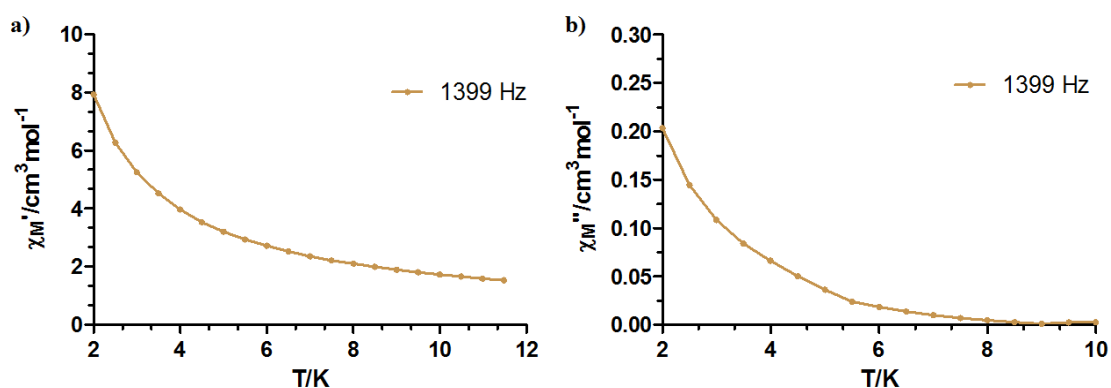


Figure 6. Temperature dependence in-phase (a) and out-of-phase (b) components of the *ac* susceptibility in a zero applied *dc* field for **1**.

However, no maxima could be seen even at the lowest temperature. This behaviour suggests that probably a fast relaxation of the magnetization is occurring through the under-barrier quantum tunnelling of the magnetization process (QTM). Nevertheless, it is well known that an external magnetic field could be a good strategy so as to lift the degeneracy of the ground-state $\pm m_J$ energy levels, thus partially or totally quenching the mentioned effect[¹⁶]. Accordingly, the measurements were carried out again under an external *dc* field of 1 kOe with intriguing results (Figure 7). Although low frequency curves do not display maxima, there is a clear frequency dependence of the χ_M'' product. In addition, at higher frequencies two relaxation processes can be observed, one at lower temperatures (2.0-4.0 K, Fast Relaxation) and the other at notably higher ones (6.0-8.0 K, Slow Relaxation). This result indicates that *i*) the external magnetic field is only able to partially suppress the QTM (since the χ_M'' values do not go to zero below the maxima at lowest temperatures, revealing that QTM still operates) and that *ii*) magnetic exchange or dipolar interactions between the neighbouring Dy ions may play an essential role in the relaxation process due to the appearance of a second maximum. It is worth mentioning, though, that the presence of two maxima could also arise from a single ion[^{2b}],[¹⁷]. Taking into account that the maxima are not well defined, the treatment of the data becomes much more complicated and prevents no further analysis. Indeed, we were not able to fit the data in order to obtain parameters such as the effective energy barrier (U_{eff}), τ_0 or α . Nonetheless, it can be seen that the relaxation mechanisms are not pure Orbach processes.

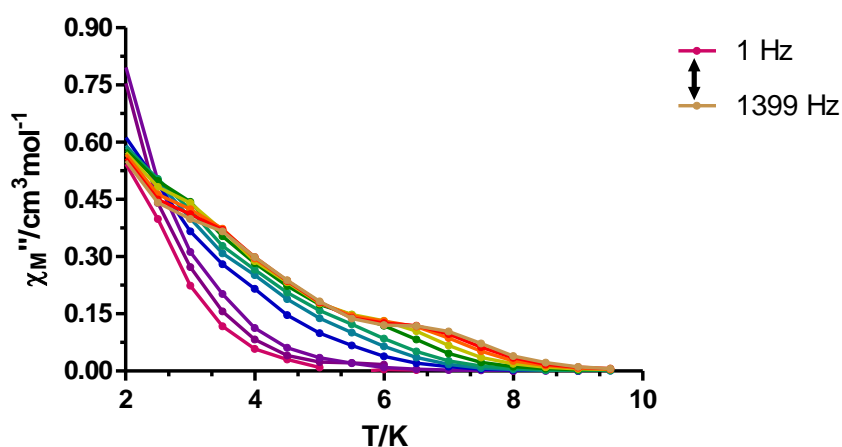


Figure 7. Temperature and frequency dependence of the out-of-phase ac susceptibility of **1** under an external *dc* field of 1 kOe.

To get insight into the role of exchange or dipolar interactions induced by neighbouring metal centres, a diluted sample of **1** was prepared. The compound **1_Y** was synthesized by mixing the diamagnetic analogue Y(III) along with Dy(III) in a Dy/Y molar ratio of 1:9. This procedure allows us to observe the influence of intramolecular interactions in terms of relaxation of the magnetization and, at the same time, is another typical strategy to avoid the fast QTM that could arise from dipolar interactions^[18].

The **1_Y** sample was then measured in the same conditions as the undiluted sample. The results show that *i*) the peaks at the highest temperatures related to the SR have disappeared and *ii*) the peaks at lower temperatures related to FR are now well defined, since both the dilution and the external *dc* field are a good combination to quench QTM (Figure 8).

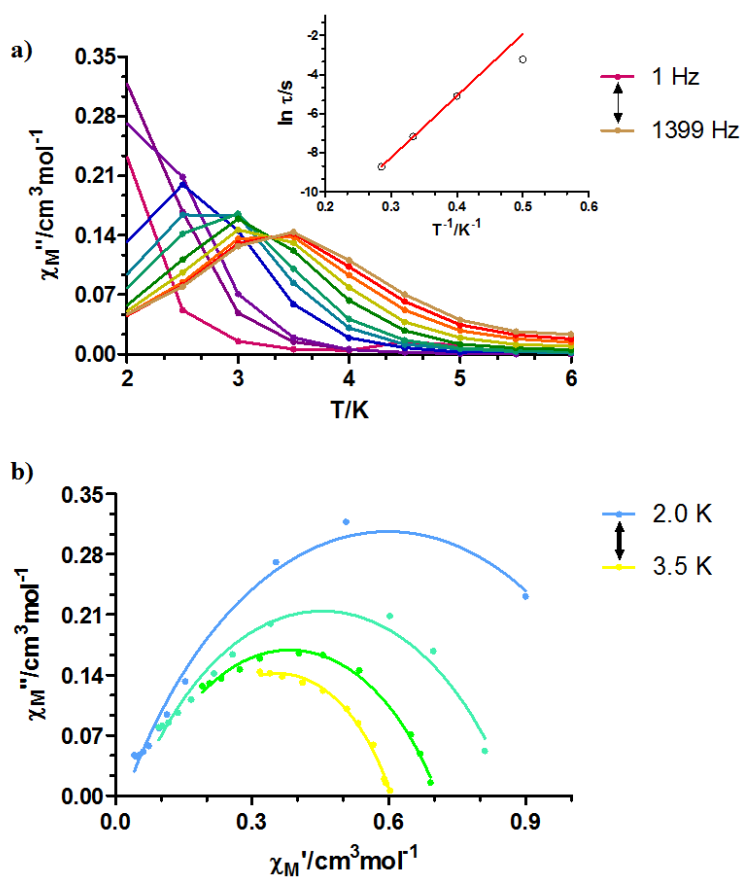


Figure 8. Temperature and frequency dependence of the out-of-phase ac susceptibility of **1_Y** under an external *dc* field of 1 kOe. (a) Arrhenius plot of relaxation time versus temperature for **1_Y** (the solid line represents the best fit to the Arrhenius law, (a) inset). (b) Cole-Cole plots of **1_Y** under 1 kOe *dc* field in the temperature range of 2.0 – 3.5 K.

Regarding to the first consequence, it is now evident that the slowest relaxation in the undiluted sample arose from the effect of the intramolecular exchange interactions and not from single-ion. In fact, when analysing the easy axes of magnetization of an isolated dinuclear entity within the whole structure by the Magellan software^[19], it is demonstrated that the anisotropy axes are completely parallel (which is, in turn, due to the inversion centre, Figure 9). It has been recently reported that the angle between the anisotropy axes plays an essential role in relaxation dynamics with magnetically coupled systems, emphasizing that collinear or almost collinear systems show the slowest relaxation times^[20]. Therefore, this might be the reason why the SR is lost when diluting the sample. In regard to the FR, relaxation times and α parameters were extracted from the frequency-dependent data between 2.0 – 3.5 K. The τ values corresponding to the highest temperature were fitted to the Arrhenius law, $\tau = \tau_0 \exp(U_{\text{eff}}/kT)$, obtaining the following parameters: $U_{\text{eff}} = 31.6$ K and $\tau_0 = 2.0 \cdot 10^{-8}$ s. The obtained τ_0 value lies in the expected range of 10×10^{-6} to 10×10^{-11} s^[21].

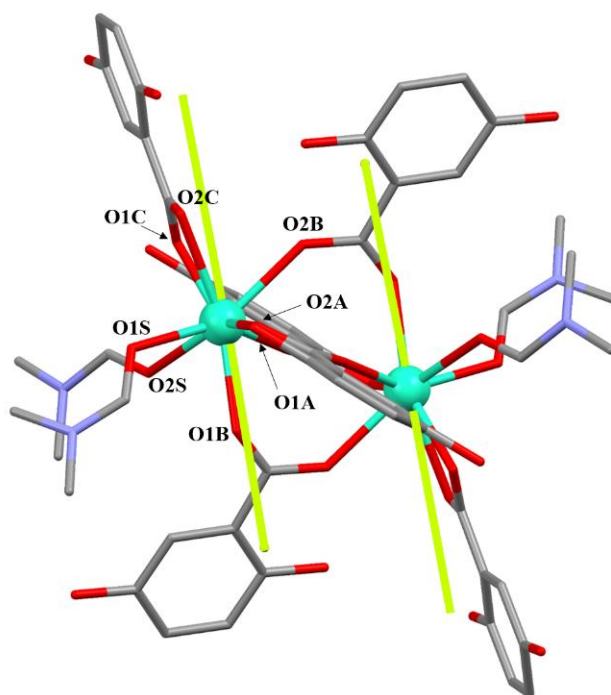


Figure 9. Magnetic axes of the Dy(III) ions calculated with the Magellan software. A neutral reduced dinuclear fragment of the structure was considered in order to obtain a reliable result. Hydrogen atoms were omitted for the sake of clarity, but they were included in the calculation.

The deviation from linearity of the lowest temperature data point, as well as the α values obtained from the Cole-Cole plots (0.38 (2.0 K) – 0.34 (3.5 K)) suggest a quite broad distribution of relaxation processes. However, we were not able to obtain a good fitting assuming the simultaneous presence of different processes.

The relatively poor SMM properties of this system could be explained by an exhaustive study of the ligand field. As aforementioned in the crystal structure description, the coordination environment polyhedron fits well with the square-antiprism geometry. It has been seen in the literature that this kind of geometry is suitable to establish an axial crystal field around the Dy(III) centre^[22]. However, this is not the unique prerequisite to obtain high performance SMMs. In an ideal crystal field, the axially coordinated atoms should have the largest amount of negative charge and they should exhibit the shortest distance towards the metal ion, thus the $m_J = \pm 15/2$ ground state will be well isolated from the excited states. Additionally, the opposite is desired for the equatorial ligand field. Less charged, or neutral, donor atoms will facilitate diminishing the transverse components that favour other relaxing processes that shortcut the always desired through barrier Orbach mechanism. In our case, the anisotropy axes are defined by the chelate carboxylate group (O1 and O2) and one monodentate carboxylate (O4), probably due to the negative charge afforded by the chelate. However, none of these bonds are the shortest ones. Instead, the shortest distance corresponds to Dy1-O8 bond in the equatorial plane, which is counteracting the axial ligand field provided by the chelate. Moreover, another two carboxylate oxygen atoms (O5 and O9) are also located in the equatorial plane with relatively short bond distances. Fortunately, the neutral DMF molecules complete the equatorial field and these ones will not be the maximum responsible of the transverse field. With all this in mind, the none outstanding magnetic properties of our system are not a surprise, but it appears as an interesting model to evaluate the influence of a variety of parameters governing the slow relaxation of the magnetization.

3.3. Luminescence properties

Photoluminescence measurements were performed on polycrystalline sample of compound **1** at different temperatures with the aim of getting a more

representative characterization of the emissive performance of the material for potential applications in lighting and thermometry. It is well-known that lanthanide-based PL constitutes a promising means to develop materials with promising performance for light-emitting, display sensing, optical devices[²³] *in vivo* detection[²⁴]. Despite the fact that organic luminescent compounds are emerging as an alternative source which promotes efficient organic light-emitting diodes (OLEDs)[²⁵], lanthanide based CPs bring the advantages of both classes of materials, affording a more brilliant emission of the organic ligands through the ligand-to-lanthanide energy transfer (antenna effect)[²⁶] or, at least, a significant emission enhancement due to the coordination[²⁷]. At room temperature, the PL emission spectrum measured at $\lambda_{\text{ex}} = 325$ nm (under monochromatic LASER light) shows an intense and somehow broad band centred at 450 nm that possesses significant emission up to 650 nm. Focusing this main emission, the excitation spectrum reveals also a unique band peaking at 350 nm (Figure 10). The shape and width of all bands seem to indicate that they correspond to $\pi \leftarrow \pi^*$ transitions taking place within the aromatic rings of the ligand. It is worth noticing the absence of any of the characteristic transitions attributed to the inner *f* orbitals of the lanthanide atom[²⁸], which makes one guess that the ligand-to-lanthanide energy transfer is poor. This fact may be due to proximity of the hydroxyl groups with regard to the Dy ion, since, occupying the first coordination sphere, could act as effective quenchers of the metal-centred PL emission[²⁹].

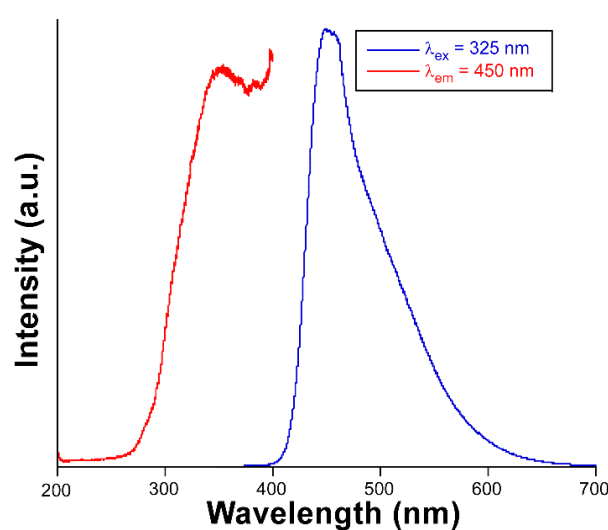


Figure 10. Excitation and emission spectra of compound **1** at room temperature.

In any case, the strong emission observed in the spectrum imbues compound **1** with a remarkable blue emission light, which may be inferred from the photographs taken on single crystals in a microscope under excitation at 365 nm (Figure 11). In fact, the tail observed in the emission spectrum at high wavelength also provides it with a still strong (although comparatively weak) green and even red coloured lights when they are irradiated with less energetic beams (λ_{ex} of 435 and 546 nm).

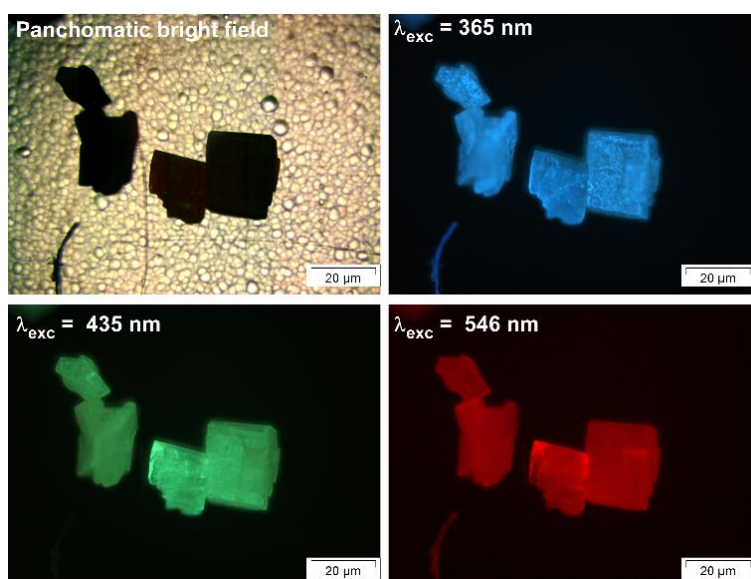


Figure 11. Room temperature micro-PL images taken at different excitation lines.

When the sample is cooled down to 10 K, the emission band shows no remarkable change in its shape yet it undergoes a subtle blue-shift (from 450 to 445 nm) while it also gains intensity compared to room temperature owing to the decrease of the kinetic (thermal) energy of the bond electrons (Figure 12)^[30]. Though the increase in the emission intensity is quite progressive with the temperature, the largest step takes place in the 50 \rightarrow 10 K range, where the intensity shows a quantitative leap. To summarize, the emission intensity at $\lambda_{\text{max}} \approx 450$ nm is much greater for 10 K data compared to RT (about 36% larger in terms of emitted integrated intensity).

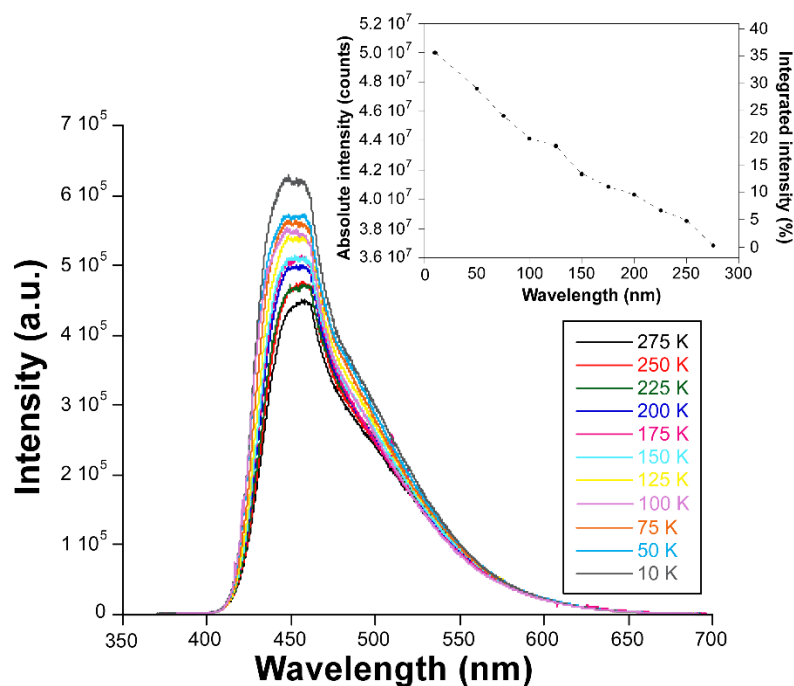


Figure 12. Variable temperature emission spectra. Inset: evolution of the integrated emission intensity.

Additionally, the emission decay curves recorded at the band maximum ($\lambda_{em} = 450$ nm) revealed the occurrence of a fluorescent process below the detection limit of the employed pulse lamp (below $1 \mu s$), given that no reliable long-lived tail could be discerned from the lamp signal.

4. Conclusions

A new dysprosium based Metal-Organic Framework with $\{[Dy(dhbc)_{1.5}(DMF)_2] \cdot DMF\}_n$ formula has been obtained from solvothermal reaction with 2,5-dihydroxyterephthalic acid ligand and dysprosium chloride. This coordination polymer has been characterized and his crystal structure has been solved by X-ray diffraction methods elucidating a three-dimensional network. Magnetic studies of this compound reveal the existence of weak antiferromagnetic interactions among the metal ions with θ value of -0.26 K. Dynamic *ac* magnetic susceptibility measurements were carried out under an external *dc* field of 1 kOe, highlighting that at higher frequencies two relaxation processes can be observed. In order to determine whether both relaxations are of single ion in origin, or intramolecular interactions are

the responsible ones, a diluted sample of **1** was prepared by mixing the diamagnetic analogue Y(III) along with Dy(III) in a Dy/Y molar ratio of 1:9. The *ac* magnetic data of **1**_Y displays a unique relaxation process with an effective energy barrier of $U_{eff} = 31.6$ K, while the SR attributed to the exchange coupled system has disappeared pointing out the influence of the intramolecular interactions. On the other hand, photoluminescence measurements at different temperatures with the aim of getting a more representative characterization of the emissive performance of the material for potential applications in lighting and thermometry. The PL emission spectrum measured at room temperature under monochromatic LASER light ($\lambda_{ex} = 325$ nm) shows an intense and somehow broad band centred at 450 nm that possesses significant emission up to 650 nm, which corresponds to $\pi \leftarrow \pi^*$ transitions taking place within the aromatic rings of the ligand. Cooling the sample down progressively to 10 K brings a subtle blue-shift of the band accompanied by an increase in the integrated intensity of about 36% compared to room temperature. The almost linear progression shown according to the temperature suggests a potential application of the material for lighting and thermometry.

5. References

- [1] a) D. Bradshaw, A. Garai and J. Huo, *Chem. Soc. Rev.*, 41 (2012) 2344–2381; b) A. Betard and R. A. Fischer, *Chem. Rev.*, 112 (2012) 1055–1083; c) E. Coronado and G. Minguez-Espallargas, *Chem. Soc. Rev.*, 42 (2013) 1525–1539; d) M. D. Allendorf, C. A. Bauer, R. K. Bhakta and R. J. T. Houk, *Chem. Soc. Rev.*, 38 (2009) 1330–1352.
- [2] a) M. Wuttig and N. Yamada, *Nat. Mater.*, 6 (2007) 824–832; b) D. Lencer, M. Salinga and M. Wuttig, *Adv. Mater.*, 23 (2011) 2030–2058.
- [3] F.-S. Guo, B. M. Day, Y.-C. Chen, M.-L. Tong, A. Mansikkamäki and R. A. Layfield, *Science*, 362 (2018) 1400–1403.
- [4] a) J. C. G. Bünzli and C. Piguet, *Chem. Soc. Rev.*, 34 (2005) 1048–1077; b) D. Parker, *Chem. Soc. Rev.*, 33 (2004) 156–165; c) J. Heine and K. Müller-Buschbaum, *Chem. Soc. Rev.*, 42 (2013) 9232–9242.

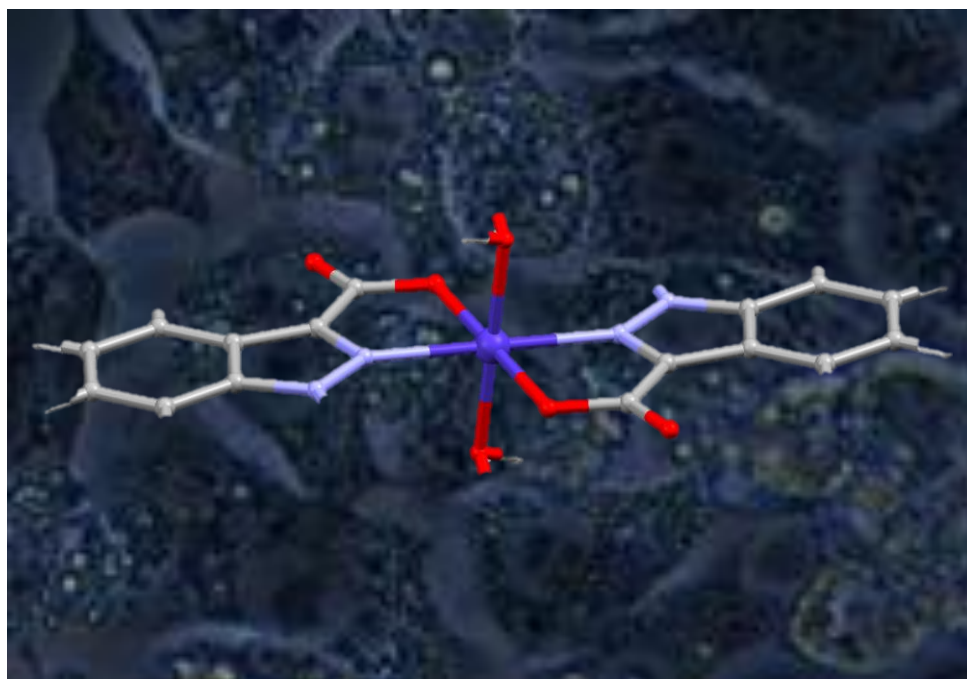
- [5] K. Liu, X. Zhang, X. Meng, W. Shi, P. Cheng and A. K. Powell, *Chem. Soc. Rev.*, 45 (2016) 2423–2439.
- [6] X. Zhang, V. Vieru, X. Feng, J.-L. Liu, Z. Zhang, B. Na, W. Shi, B.-W. Wang, A. K. Powell, L. F. Chibotaru, S. Gao, P. Cheng and J. R. Long, *Angew. Chem., Int. Ed.*, 54 (2015) 9861–9865.
- [7] a) Y.-L. Wang, Y.-L. Jiang, Z.-J. Xiahou, J.-H. Fu and Q.-Y. Liu, *Dalton Trans.*, 41 (2012) 11428–11437; b) D. S. Zhou, F. K. Wang, S. Y. Yang, Z. X. Xie and R. B. Huang, *CrystEngComm*, 11 (2009) 2548–2554; c) I. Oyarzabal, B. Fernández, J. Cepeda, S. Gómez-Ruiz, A. J. Calahorro, J. M. Seco and A. Rodríguez-Diéguez, *CrystEngComm*, 18 (2016) 3055–3063; d) A. J. Calahorro, I. Oyarzabal, B. Fernández, J. M. Seco, T. Tian, D. Fairen-Jimenez, E. Colacio and A. Rodríguez-Diéguez, *Dalton Trans.*, 45 (2016) 591–598.
- [8] a) N. L. Rosi, J. Kim, M. Eddaoudi, B. Chen, M. O’Keeffe and O. M. Yaghi, *J. Am. Chem. Soc.*, 127 (2005) 1504–1518; b) P. D. C. Dietzel, Y. Morita, R. Bloma and H. Fjellvåg, *Angew. Chem., Int. Ed.*, 44 (2005) 6354–6358; c) P. D. C. Dietzel, B. Panella, M. Hirscher, R. Bloma and H. Fjellvåg, *Chem. Commun.*, (2006) 959–961; d) K. Jayaramulu, P. Kanoo, S. J. George and T. K. Maji, *Chem. Commun.*, 46 (2010), 7906–7908; e) T. Devic, P. Horcajada, C. Serre, F. Salles, G. Maurin, B. Moulin, D. Heurtaux, G. Clet, A. Vimont, J.-M. Grenèche, B. L. Ouay, F. Moreau, E. Magnier, Y. Filinchuk, J. Marrot, J. C. Lavalley, M. Daturi and G. Férey, *J. Am. Chem. Soc.*, 132 (2010) 1127–1136.
- [9] A. Earnshaw, Academic Press, London (1968).
- [10] Bruker Apex2, Bruker AXS Inc., Madison, Wisconsin, USA (2004).
- [11] G.M. Sheldrick, SADABS, Program for Empirical Adsorption Correction, Institute for Inorganic Chemistry, University of Göttingen, Germany (1996).
- [12] A. Altomare, M.C. Burla, M. Camilla, G.L. Cascarano, C. Giacovazzo, A. Guagliardi, A.G.G. Moliterni, G. Polidori and R. Spagna, *J. Appl. Cryst.*, 32 (1999) 115–119.
- [13] a) G.M. Sheldrick, SHELX-2014, Program for Crystal Structure Refinement, University of Göttingen, Germany (2014); b) L.J. Farrugia, *J. Appl. Cryst.*, 32 (1999) 837–838.

- [14] M. Llunell, D. Casanova, J. Cirera, J. M. Bofill, P. Alemany, S. Alvarez, M. Pinsky and D. Avnir, *SHAPE*, v1.1b; Barcelona, Spain, 2005.
- [15] S. Nayak, H.P. Nayek, C. Pietzonka, G. Novitchi and S. Dehnen, *J. Mol. Struct.*, 1004 (2011) 82–87.
- [16] a) J. Ruiz, A. J. Mota, A. Rodríguez-Diéguez, S. Tatos, J. M. Herrera, E. Ruiz, E. Cremades, J. P. Costes and E. Colacio, *Chem. Commun.*, 48 (2012) 7916-7918; b) C.-M. Liu, D.-Q. Zhang and D.-B. Zhu, *RSC Adv.*, 4 (2014) 36053-36056.
- [17] S. Das, A. Dey, S. Biswas, E. Colacio and V. Chandrasekhar, *Inorg. Chem.*, 53 (2014) 3417-3426.
- [18] J. Ruiz, A.J. Mota, A. Rodríguez-Diéguez, S. Titos, J.M. Herrera, E. Ruiz, E. Cremades, J.P. Costes and E. Colacio, *Chem. Commun.*, 48 (2012) 7916–7918.
- [19] N. F. Chilton, D. Collison, E. J. L. McInnes, R. E. P. Winpenny and A. Soncini, *Nat. Commun.*, 4 (2013) 2551-2558.
- [20] J. D. Hilgar, M. G. Bernbeck and J. R. Rinehart, *J. Am. Chem. Soc.*, 141 (2019) 1913-1917.
- [21] a) P. F. Shi, Y. Z. Zheng, X. Q. Zhao, G. Xiong, B. Zhao, F. F. Wan and P. Cheng, *Chem. Eur. J.*, 18 (2012) 15086-15091; b) R. Sessoli, D. Gatteschi, A. Caneschi and M. A. Novak, *Nature*, 365 (1993) 141-143; c) R. Vincent, S. Klyatskaya, M. Ruben, W. Wernsdorfer and F. Balestro, *Nature*, 488 (2012) 357-360.
- [22] a) I. Oyarzabal, J. Ruiz, J. M. Seco, M. Evangelisti, A. Camón, E. Ruiz, D. Aravena and E. Colacio, *Chem. Eur. J.*, 20 (2014) 14262-14269; b) I. Oyarzabal, J. Ruiz, E. Ruiz, D. Aravena, J. M. Seco and E. Colacio, *Chem. Commun.*, 51 (2015) 12353-12356; c) N. Ishikawa, M. Sugita, T. Ishikawa, S.-Y. Koshihara and Y. Kaizu, *J. Am. Chem. Soc.*, 125 (2003) 8694-8695.
- [23] a) K. Binnemans, *Chem. Rev.*, 109 (2009) 4283-4374; b) S. V. Eliseeva and J.-C. G. Bünzli, *Chem. Soc. Rev.*, 39 (2010) 189-227; c) J. B. Beck and S. J. Rowan, *J. Am. Chem. Soc.*, 125 (2003) 13922-13923; d) J. Rocha, C. D. S. Brites and L. D. Carlos, *Chem.–Eur. J.*, 22 (2016) 14782-14795; e) J. Heine and K. Müller-Buschbaum, *Chem. Soc. Rev.*, 42 (2013) 9232-9242.

- [24] a) I. Hemmilä, *J. Alloys Compd.*, 225 (1995) 480-485; b) J. Moynagh and H. Schimmel, *Nature*, 400 (1999) 105.
- [25] a) C. Murawski, K. Leo and M. C. Gather, *Adv. Mater.*, 25 (2018) 6801; b) K. Hong and J.-L. Lee, *Chem. Soc. Rev.*, 43 (2014) 5994-6010; c) H. Uoyama, K. Goushi, K. Shizu, H. Nomura and C. Adachi, *Nature*, 492 (2012) 234-238.
- [26] a) J. C. G. Bünzli and C. Piguet, *Chem. Soc. Rev.*, 34 (2005) 1048-1077; b) D. Parker, *Chem. Soc. Rev.*, 33 (2004) 156-165; c) J. Heine and K. Müller-Buschbaum, *Chem. Soc. Rev.*, 42 (2013) 9232-9242.
- [27] a) Q. Zheng, F. Yang, M. Deng, Y. Ling, X. Liu, Z. Chen, Y. Wang, L. Weng, and Y. Zhou, *Inorg. Chem.*, 52 (2013) 10368-10374; b) H.-Y. Ren, C.-Y. Han, M. Qu and X.-M. Zhang, *RSC Adv.*, 4 (2014) 49090-49097.
- [28] a) Y. L. Gai, K.-C. Xiong, L. Chen, Y. Bu, X.-J. Li, F. L. Jiang and M. C. Hong, *Chem.* 51 (2012) 13128-13137; b) S. Quici, M. Cavazzini, G. Marzanni, G. Accorsi, N. Armaroli, B. Ventura and F. Barigelletti, *Inorg. Chem.*, 44 (2005) 529-537; c) J. M. Seco, I. Oyarzabal, S. Pérez-Yáñez, J. Cepeda and A. Rodríguez-Diéguez, *Inorg. Chem.*, 55 (2016) 11230-11248.
- [29] A. Beeby, I. M. Clarkson, R. S. Dickins, S. Faulkner, D. Parker, L. Royle, A. S. de Sousa, J. A. Gareth Williams and M. Woods, *J. Chem. Soc. PerkinTrans.*, 2 (1999) 493-504.
- [30] a) P. C. R. Soares-Santos, L. Cunha-Silva, F. A. Almeida-Paz, R. A. S. Ferreira, J. Rocha, L. D. Carlos and H. I. S. Nogueira, *Inorg. Chem.*, 49 (2010) 3428-3440; b) J. Cepeda, S. Pérez-Yáñez, G. Beobide, O. Castillo, J. A. García, M. Lanchas and A. Luque, *Dalton Trans.*, 44 (2015) 6972-6986; c) J. Rocha, C. D. S. Brites and L. D. Carlos, *Chem. Eur. J.*, 22 (2016) 14782-14795.

Capítulo 8

Anticancer and Anti-inflammatory Activities a new Family of Coordination Compounds based on Divalent Transition Metal Ions and Indazole-3- carboxylic Acid



Anti-Cancer and Anti-Inflammatory Activities of a new Family of Coordination Compounds based on Divalent Transition Metal Ions and Indazole-3-carboxylic Acid

Antonio A. García-Valdivia,^a FatinJannus,^b Amalia García-García,^a Duane Choquesillo-Lazarte,^c Belén Fernández,^d Marta Medina-O'donnell,^e José A. Lupiáñez,^b Javier Cepeda,^f Fernando J. Reyes-Zurita^b, and Antonio Rodríguez-Diéguez^a

ACEPTADO: JOURNAL INORGANIC BIOCHEMISTRY

- a. Departamento de Química Inorgánica, Facultad de Ciencias, Universidad de Granada, Av. Fuentenueva S/N, 18071 Granada, Spain.*
- b. Departamento de Bioquímica y Biología Molecular I, Facultad de Ciencias, Universidad de Granada, Av. Fuentenueva S/N, 18071 Granada, Spain.*
- c. Institute of Parasitology and Biomedicine "López-Neyra", CSIC, Av. Conocimiento s/n, 18600, Granada, Spain.*
- d. Laboratorio de Estudios Cristalográficos, IACT (CSIC-UGR), Avda. de las Palmeras 4, 18100, Armilla, Granada, Spain.*
- e. Departamentode Química Orgánica, Facultad de Ciencias, Universidad de Granada, Av. Fuentenueva S/N, 18071 Granada, Spain*

Abstract

A new family of mononuclear coordination compounds have been synthesized and characterized: $[M(3-ind)_2(H_2O)_2](M=Co$ (**1**), Ni (**2**), Zn(**3**), Fe(**4**), Mn(**5**)). The anti-inflammatory effects of these compounds were assayed in lipopolysaccharide activated RAW 264.7 macrophages by inhibition of NO production. In first time we determined the cytotoxicity of the complex and the ligand in RAW 264.7 cells. The most significative results were obtained for the compounds **4** and **5** reaching values of NO inhibition close to 80% at 48h, and above to 90% at 72h of treatment. The highest inhibitory effects on NO production were showed at the range 7-23 $\mu\text{g/mL}$ for compound **4** and **5**. In conclusion, the compound **4** and **5** could be potential drugs due to the interesting anti-inflammatory properties showed. Also, the anti-cancer potential of these compounds has been tested against different tumor cell lines. The

citotoxicity of the ligand and the compounds **2** and **3** were assayed in three cell lines: HT29, colon cancer cells, Hep-G2, hepatoma cells and B16-F10 melanoma cells. The best results have been achieved with the compound **2** in HepG2 and B16-F10 cell lines, being between 1.5 to 2 times more effective than the ligand in HepG2 cells, and B16-F10 cells. The formation of metal complexes with bioactive ligands is a new and promising strategy to find new compounds with high and enhanced biochemical properties.

1. Introduction

Coordination compounds have been widely studied during years due to the range of properties that could show such as luminescence,[1,2] magnetism[3,4] and/or biological activity.[5,6] Inside this type of materials, specifically, the coordination monomers are very useful in medicinal chemistry to develop new therapeutic agents.[7-9] Since the discovery of cisplatin, platinum-derivative[10,11] and later ruthenium drugs,[12] the research community are trying to create new materials with increased efficacy and reduced toxicity.[13] Although these two families of drugs are the most promising in the fight against cancer, a wide variety of coordination compounds based on different transition metals ions are being developed such as potential therapeutic agents to fight against cancer disease.[14-16]

On the other hand, nitrogen-containing heterocycles are pharmacologically important scaffolds and they are normally present in numerous commercially available drugs. For example, non-steroidal anti-inflammatory drugs comprise a large group of medicines used to inflammation and pain with known side-effects.[17,18] It is for these reasons, that coordination compounds have been broadly studied over recent years as anti-inflammatory drugs.[19,20] During inflammation process different molecular routes are activated, a wide variety of protein kinases are activated, as MAPK (mitogen-activated protein kinases), JAK (Janus-activated kinases), PI3K/AKT (phosphatidylinositol-3-kinase). Disturb in the activation of these transcription factor can produce aberrant cell growth, carcinogenic cell transformation, angiogenesis, and metastasis.

In the last years, our group and others have reported the use of different nitrogen derivative ligands with specific biological activities, with a particular focus on the behaviour of the triazolopyrimidine ligands as antiparasitic therapeutic agents.[21-24] Moreover, other type of therapeutic agents such as anti-inflammatory, anti-diabetic or anti-cancer materials have been synthesized in our laboratory based on this type of organic ligands.[25-27] Based on these previous results, we decided to use a different organic ligand to construct new therapeutic agents to study different properties exhibited for these materials based on transition metal ions. In this sense, we thought that indazole-3-carboxylic acid could be an ideal candidate to form new compounds because its multiple coordination possibilities not only derived from its carboxylate group but also from its pyrazole group. Moreover, to the best of our knowledge, there are few examples of coordination compounds based on this ligand (all examples based on rhenium).[28-29] On the other hand, for the study of biological properties, we wanted to obtain mononuclear compounds, for this reason, to design these materials we decided to use divalent transition metals, in which two monoanionic ligands would coordinate the metal ions and the two free positions would remain where, predictably, molecules would enter solvent.

All of the above in mind, we decided to design novel coordination compounds by using indazole-3-carboxylic acid and transition metal ions to obtain new materials with the aim to study their anti-cancer properties. In this sense, we present here a new family of five coordination compounds with the formulae $[M(3\text{-ind})_2(\text{H}_2\text{O})_2]$ ($M = \text{Co(II)}$ (**1**), Ni(II) (**2**), Zn(II) (**3**), Fe(II) (**4**), Mn(II) (**5**)). We have analysed the structural properties, the cytotoxicity has been assayed for ligand and compounds in three different cell lines, and cell studies on Raw 264.7 were done and the NO-inhibition with the aim to establish the possible potential therapeutic agents of these materials.

2. Experimental Procedures

2.1. Chemicals

All reagents were obtained from commercial sources and used as received. Elemental (C, H, and N) analyses were performed on an Euro EA Elemental Analyzer. The IR spectra of powdered samples were recorded in the 400–4000 cm^{-1} region on a Nicolet 6700 FTIR spectrophotometer using KBr pellets.

The FT-IR spectra of five complexes showed the expected vibrational bands, (Figure 1). The main vibrations of Indazole-3 carboxylic acid are associated to $\nu_{\text{C}=\text{N}}$ vibration at 1654 cm^{-1} and the vibrations of the carboxylate groups at 1525 cm^{-1} and 1484 cm^{-1} . The characteristic band $\nu_{\text{C}=\text{N}}$ displaced at 1628 cm^{-1} for complexes can be due to the stretching vibration of the indazole ring restricted for N-coordinated to metal ions. Further, the double peaks related to asymmetric and symmetric vibrations of the carboxylic groups present on ligand spectra too are displaced at unique wider peak centred at 1464 cm^{-1} . The very similar spectra of 5 compounds bear out that the five compounds are isostructural.

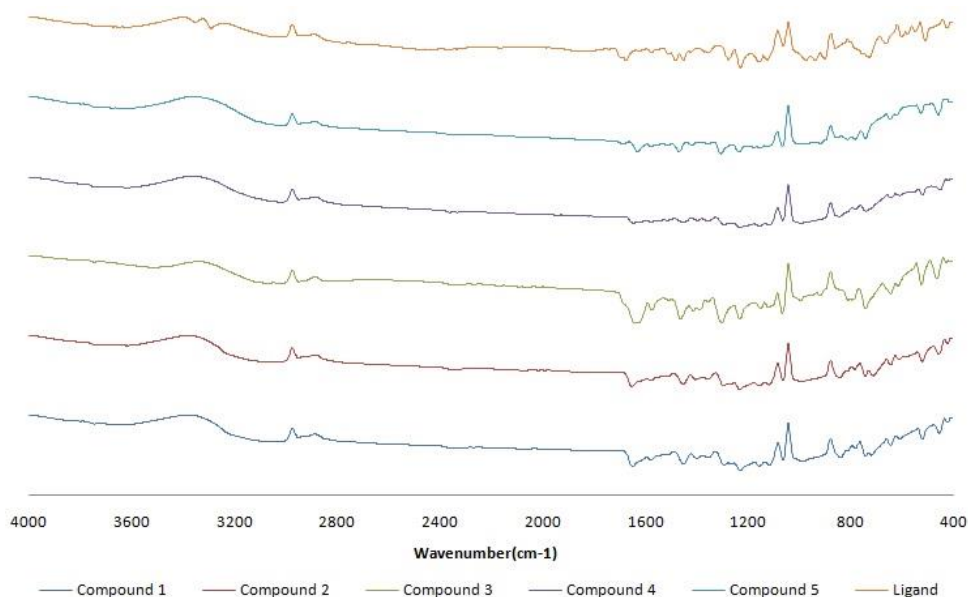


Figure 1. FT-IR spectra of five complexes and ligand.

2.2. Synthesis

Synthesis of $[M(3\text{-ind})_2(\text{H}_2\text{O})_2]$ ($M = \text{Co}$ (1), Ni (2), Zn (3), Fe (4), Mn (5)).

0.06 mmol of Indazole-3-carboxylate were dissolved in 0.5 mL of DMF after 0.5 mL of distilled water was added. In other glass vessel, 0.06 mmol of $\text{MCl}_2 \cdot 6\text{H}_2\text{O}$ was dissolved in 0.5 mL of distilled water and then 0.5 mL of DMF was added. Both solutions were mixed and the resulting solution was placed in a closed glass vessel and introduced in an oven at 95 °C for 24h. Orange (1), bluish green (2), white (3) single crystals and red (4), light-yellow (5) powder were grown during the heating procedure. The final products were washed with distilled water, and dried at room temperature. Anal. Calcd (1) for $\text{CoC}_{16}\text{O}_6\text{N}_4\text{H}_{14}$: C, 46.06; H, 3.38; N, 13.43. Found: C, 46.01; H, 3.30; N, 13.47. Anal Calcd (2) for $\text{NiC}_{16}\text{O}_6\text{N}_4\text{H}_{14}$: C, 46.08; H, 3.38; N, 13.44. Found: C, 45.99; H, 3.32; N, 13.51. Anal Calcd (3) for $\text{ZnC}_{16}\text{O}_6\text{N}_4\text{H}_{14}$: C, 45.36; H, 3.33; N, 13.22. Found: C, 45.29; H, 3.27; N, 13.30. Anal. Calcd (4) for $\text{FeC}_{16}\text{O}_6\text{N}_4\text{H}_{14}$: C, 46.40; H, 3.41; N, 13.53. Found: C, 45.33; H, 3.36; N, 13.59. Anal. Calcd (5) for $\text{MnC}_{16}\text{O}_6\text{N}_4\text{H}_{14}$: C, 46.50; H, 3.41; N, 13.56. Found: C, 45.46; H, 3.38; N, 13.60.

2.3. Crystallographic refinement and structure solution

X-ray data collection of suitable single crystals of compounds were done at 100(2) K on a Bruker VENTURE area detector equipped with graphite monochromated Mo- $\text{K}\alpha$ radiation ($\lambda = 0.71073 \text{ \AA}$) by applying the ω -scan method. The data reduction were performed with the APEX2 software[30] and corrected for absorption using SADABS.[31] Crystal structures were solved by direct methods using the SIR97 program[32-33] and refined by full-matrix least-squares on F^2 including all reflections using anisotropic displacement parameters by means of the WINGX crystallographic package.[34] Several crystals of 1, 2, and 3 were measured and the structures were solved from the best data we were able to collect, due to the quality of crystals were very poor. For this reason, we only submit to the CCDC the crystal data of compound 1. Cif files of 2 and 3 are deposit in supporting information. Details of the structure determination and refinement of compounds are summarized in Table 1. Crystallographic data (excluding structure factors) for the structures

reported in this paper have been deposited with the Cambridge Crystallographic Data Center as supplementary publication no. CCDC 1997814 for compound **1**. Copies of the data can be obtained free of charge on application to the Director, CCDC, 12 Union Road, Cambridge, CB2 1EZ, U.K. (Fax: +44-1223-335033; e-mail: deposit@ccdc.cam.ac.uk or <http://www.ccdc.cam.ac.uk>).

Table 1. Crystallographic data and structure refinement details of compounds **1**, **2** and **3**.

Compound	1	2	3
Formula.	C ₁₆ H ₁₄ N ₄ O ₆ Co	C ₁₆ H ₁₄ N ₄ O ₆ Ni	C ₁₆ H ₁₄ N ₄ O ₆ Zn
Formula weight	417.24	412.99	419.65
CCDC	1997814	Supp.Inf.	Supp.Inf.
Crystalsystem	Monoclinic	Monoclinic	Monoclinic
Spacegroup	<i>P</i> 2 ₁ / <i>c</i>	<i>P</i> 2 ₁ / <i>c</i>	<i>P</i> 2 ₁ / <i>c</i>
<i>a</i> (Å)	4.9786(4)	4.975(3)	4.986(5)
<i>b</i> (Å)	5.3372(4)	5.328(3)	5.347(5)
<i>c</i> (Å)	30.549(3)	30.260(16)	30.593(5)
<i>α</i> (°)	90	90	90
<i>β</i> (°)	93.276(3)	93.55(2)	93.169(5)
<i>γ</i> (°)	90	90	90
<i>V</i> (Å³)	810.42(11)	800.6(8)	814.4(11)
<i>Z</i>	2	2	2
GoF^a	1.293	2.791	1.131
R_{int}	0.068	0.2844	0.0608
R₁^b / wR₂^c [I > 2σ(I)]	0.0856/0.2030	0.2898 / 0.5365	0.0756/0.1864
R₁^b / wR₂^c[all data]	0.0951/0.2070	0.3276/0.5384	0.0853/0.1887

^a $R_I = S||F_o| - |F_c||/S|F_o|$. ^b Values in parentheses for reflections with $I > 2s(I)$. ^c $wR_2 = \{S[w(F_o^2 - F_c^2)^2] / S[w(F_o^2)^2]\}^{1/2}$

2.4. Cell culture

Human colorectal adenocarcinoma cell line HT29 (ECACC no. 9172201; ATCC no. HTB-38), human hepatocarcinome cell line HepG2 (ECACC no. 85011430), and mouse melanoma cells B16-F10 (ATCC no. CRL-6475) were cultured in DMEM supplemented with 2 mM glutamine, 10% heat-inactivated FBS, 10,000 units/mL of penicillin and 10 mg/mL of streptomycin, being incubated at

37°C in an atmosphere of 5% CO₂ and 95% humidity. Subconfluent monolayer cells were used in all experiments. All cell lines used were provided by the cell bank of the University of Granada, Spain.

RAW 264.7 macrophage/monocyte murine cells (ECACC no; ATCC no) were cultured in DMEM medium supplemented with 2 mM glutamine, 10% heat-inactivated FCS, 10,000 units/mL of penicillin and 10 mg/mL of streptomycin, being incubated at 37°C in an atmosphere of 5% CO₂ and 95% humidity. Cells were grown to 80-90% of confluence in sterile cell culture flasks. Subconfluent monolayer cells were used in all experiments. The cell line was provided by cell bank of the University of Granada, Spain.

2.5. Cell viability assay

The effect of each treatment with ligand and compounds **1**, **2**, **3**, **4** and **5** in RAW 264.7 macrophage/monocyte murine cells, and the ligand and compounds **2** and **3** in HT29 colon cancer cells, Hep-G2 hepatome cells and B16-F10 murine melanome cells, was measured using the MTT (3-(4,5-dimethylthiazol-2-yl)-2,5-diphenyltetrazolium bromide) proliferation assay (Sigma, MO, USA), which is based on the ability of live cells to cleave the tetrazolium ring, thus producing formazan, which absorbs at 570 nm.

Cell viability was determined by measuring the absorbance of MTT dye staining of living cells. For this assay, 6×10³ HT29 cells, 15×10³ Hep G2 cells, 5×10³ B16-F10 cells and 6×10³ RAW 264.7 cells were grown on a 96-well plate and incubated with the different concentrations of ligand and compounds (0-160 µg/ml). Lately, after 72h of incubation, 100 µL of MTT solution (0.5 mg/mL) in 50% of PBS 50% of medium was added to each well. After 1.5h of incubation, formazan was resuspended in 100 µL of DMSO. Relative cell viability, with respect to untreated control cells, was measured by absorbance at 570 nm on an ELISA plate reader (Tecan Sunrise MR20-301, TECAN, Austria).

2.6. Determination of nitrite concentration

Nitrite concentration was used as indicator of NO production. NO determination was based on Griess reaction.[35]

For complex compound treatment test, cells were plated at a 6×10^4 RAW 264.7 cells/well in 24-well cell culture plates, supplemented with 10 $\mu\text{g}/\text{mL}$ of LPS. After 24h of plated, the cells were incubated for 24h with the test compounds at $\frac{3}{4} \cdot \text{IC}_{50}$, $\frac{1}{2} \cdot \text{IC}_{50}$, $\frac{1}{4} \cdot \text{IC}_{50}$ concentrations determined by MTT proliferation assay. The supernatants were collected at 24h, 48h and 72h to determine nitrite concentration and/or stored at -80°C for further use.

Griess reaction was performed taking 150 μL of supernatant test samples or sodium nitrite standard (0-120 μM) and mixed with 25 μL of Griess reagent A (0.1% N-N-(1-naphthyl)-ethylenediaminedihydrochloride) and 25 μL of Griess reagent B (1% sulfanilamide in 5% of phosphoric acid), in a 96-well plate. After 15 min at room temperature, the absorbance was measure at 540 nm on ELISA plate reader (Tecan Sunrise MR20-301, TECAN, Austria). The absorbance was referred to nitrite standard curve to determine the concentration of nitrite in the supernatant. The percentage of NO production was determined, assigning 100% at the increase between negative control (untreated cells) and positive control (cells only treated with 10 $\mu\text{g}/\text{mL}$ of LPS).

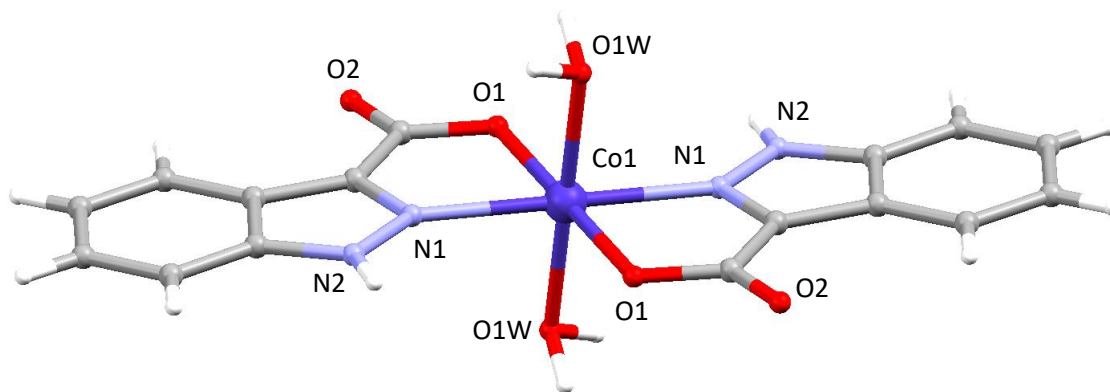
3. Structural description

Structural description of $[\text{Co}(\text{3-ind})_2(\text{H}_2\text{O})_2]$. Compound **1**, crystallizes in the $P2_1/c$ and consists of mononuclear coordination compounds generating a two-dimensional coordination network by strong hydrogen bonds. The centrosymmetric monomer consists in two ligands coordinated to Co(II) ions in a antiparallel form and two coordination water molecules. The ligands are coordinated through the nitrogen (N1) pertaining to the pyrazole ring and one oxygen (O1) from the carboxylate group (Figure 2). The oxygen bonds occupying the basal plane of octahedron while nitrogen bonds are situated at the apical position. The distances bond of the coordination sphere are collected on Table 2.

Table 2. Selected bond lengths (Å) and angles (°) for compound **1**.^a

Bond	Distance	Angle	Degree
Co1–N1	2.174(6)	O1W–Co1–OW1(iii)	180.0
Co1–N1(iii)	2.174 (6)	O1W–Co1–O1	89.1(2)
Co1–O1	2.063(6)	O1W–Co01–O1(iii)	90.9(2)
Co1–O1(iii)	2.063(6)	O1W–Co01–N1	88.1(2)
Co1–O1w	2.061(6)	O1W–Co01–N1(iii)	91.9(2)
Co1–O1w(iii)	2.061(6)	O1–Co01–N1	101.1(2)
		O1–Co01–N1(iii)	78.9(2)
		O1W(iii)–Co01–N1(iii)	88.1(2)
		O1W(iii)–Co01–N1	91.9(2)
		O1W(iii)–Co01–O1	90.9(2)
		O1W(iii)–Co01–O1(iii)	89.1(2)
		O1–Co01–O1(iii)	180.0
		N1–Co01–N1(iii)	180.0
		N1(iii)–Co01–O1(iii)	101.1(2)
		O1(iii)–Co01–N1	78.9(2)

^aSymmetry operations (iii)='-x, -y, -z'

**Figure 2.** View of complex **1** showing the atoms that shapes the coordination polyhedron.

These mononuclear coordination compounds interact among them thanks to strong hydrogen bonds forming a two-dimensional supramolecular structure which is showed in Figure 3. These monomers are linked by two different types of hydrogen bonds. The first of them is through N2–H2···O2, with a value of 2.781(9) Å, and

other that involves O1W-H1WA...O1 and O1W-H1WB...O1 with distances of 2.684 (9) Å and 2.693(9) Å, respectively (Table 3).

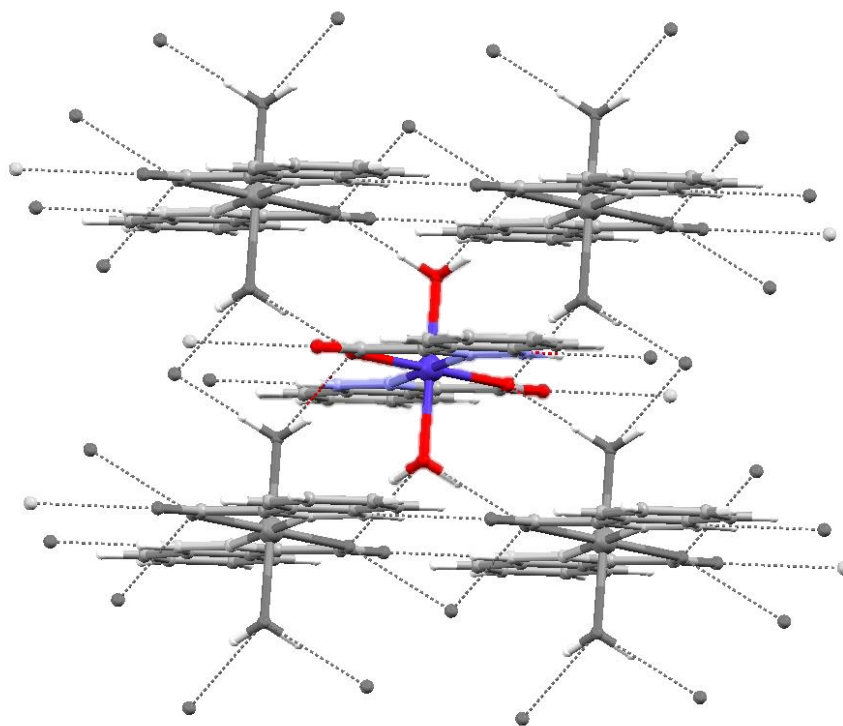


Figure 3. View of plane of compound **1** generated by hydrogen bonds.

Table 3. Selected H-bonds lengths (Å) and angle (°) for compound **1**.^a

D-H...A	Distances (D-H)	Distances (H...A)	Distances(D-H...A)	Angles
N2-H2...O2(i)	0.88	2.01	2.781(9)	146.0
O1W-H1WA...O1(iii)	0.91	1.84	2.684 (8)	153.3
O1W-H2WB...O1(ii)	0.92	1.92	2.693(8)	141.5

^aSymmetry operations (i)= $x-1, y+1, z$; (ii) = $-x+2, -y+1, -z+1$; (iii)= $x, y+1, z$.

The crystalline structures of compounds **2** and **3** are not described due to they are isostructural materials to compound **1**. Their distances and angles of coordination sphere are collected in Table 4 and 5. The compound **4** and **5** has been characterized by DXR-Powder.

Table 4. Selected bond lengths (Å) and angles (°) for compound **2**.^a

Bond	Distance	Angle	Degree
Ni01–N1	2.13(3)	O1W–Ni01–OW1(iii)	180.000(16)
Ni01–N1 (iii)	2.13(3)	O1W–Ni01–O1	92.5(10)
Ni01–O1	2.01(3)	O1W–Ni01–O1(iii)	87.5(10)
Ni01–O1(iii)	2.01(3)	O1W–Ni01–N1	88.9(10)
Ni01–O1w	2.06(2)	O1W–Ni01–N1(iii)	91.1(10)
Ni01–O1w(iii)	2.06(2)	O1–Ni01–N1	79.5(10)
		O1–Ni01–N1(iii)	100.5(10)
		O1W(iii)–Ni01–N1(iii)	88.9(10)
		O1W(iii)–Ni01–N1	91.1(10)
		O1W(iii)–Ni01–O1	87.5(10)
		O1W(iii)–Ni01–O1(iii)	92.5(10)
		O1–Ni01–O1(iii)	180.0
		N1–Ni01–N1(iii)	180.0(14)
		N1–Ni01–O1(iii)	100.5(10)
		O1(iii)–Ni01–N1(iii)	79.5(10)

^a Symmetry operations (iii) = '-x, -y, -z'**Table 5.** Selected bond lengths (Å) and angles (°) for compound **3**.^a

Bond	Distance	Angle	Degree
Zn01–N1	2.177(9)	O1W–Zn01–OW1(iii)	180.0
Zn01–N1 (iii)	2.177(9)	O1W–Zn01–O1	87.9(3)
Zn01–O1	2.063(8)	O1W–Zn01–O1(iii)	92.1(3)
Zn01–O1(iii)	2.063(8)	O1W–Zn01–N1	86.7(3)
Zn01–O1w	2.091(8)	O1W–Zn01–N1(iii)	93.3(3)
Zn01–O1w(iii)	2.091(8)	O1–Zn01–N1	77.9(3)
		O1–Zn01–N1(iii)	102.1(3)
		O1W(iii)–Zn01–N1(iii)	86.7(3)
		O1W(iii)–Zn01–N1	93.3(3)
		O1W(iii)–Zn01–O1	92.1(3)
		O1W(iii)–Zn01–O1(iii)	87.9(3)
		O1–Zn01–O1(iii)	180.0
		N1–Zn01–N1(iii)	180.0(7)
		N1–Zn01–O1(iii)	102.1(3)
		O1(iii)–Zn01–N1(iii)	77.9(3)

^a Symmetry operations (iii) = '-x, -y, -z'

4. Biological Properties

4.1. Cytotoxicity cancer cells

The cytotoxicity has been assayed for ligand and compounds **2** and **3** in three different cancer cell lines, B16-F10 murine melanoma cells, HT29 colon cancer cells, and HepG2 hepatome cells. Cell viability was tested by MTT assay, which is transformed to formazan into peroxisomes from viable cells. The products were added at increased concentrations (range from 0 to 100 $\mu\text{g/mL}$) and IC_{50} (concentration required for 50% inhibition in vitro) were determinate for these two compounds and the ligand (Table 6). Also, IC_{20} and IC_{80} were calculated to analyze the range of cytotoxicity.

Table 6. Growth-inhibitory effects of ligand and compounds **2** and **3** on the viability of HT29, HepG2 and B16-F10 cancer cells, after treatment with the compounds for 72h in a range of 0 to 100 $\mu\text{g/mL}$, each point represents the mean value \pm SD of at least two independent experiments performed in triplicate.

Cell line	Compound	IC_{20}	$\text{IC}_{\text{Lig}}/\text{IC}_{\text{comp}}$	IC_{50}	$\text{IC}_{\text{Lig}}/\text{IC}_{\text{comp}}$	IC_{80}	$\text{IC}_{\text{Lig}}/\text{IC}_{\text{comp}}$
HT29	L	52,08 \pm 3,94	1,00	79,06 \pm 5,14	1,00	123,53 \pm 8,51	1,00
	2	60,06 \pm 7,05	0,87	84,11 \pm 6,37	0,94	N/A	-
	3	90,24 \pm 8,96	0,58	116,81 \pm 5,87	0,68	148,08 \pm 2,65	0,83
HepG2	L	42,27 \pm 4,88	1,00	80,56 \pm 9,12	1,00	N/A	-
	2	21,91 \pm 3,29	1,93	62,64 \pm 5,57	1,29	120,87 \pm 1,29	-
	3	72,24 \pm 4,38	0,59	96,24 \pm 1,23	0,84	122,49 \pm 5,63	-
B16-F10	L	62,74 \pm 4,24	1,00	89,36 \pm 1,52	1,00	107,91 \pm 1,86	1,00
	2	45,94 \pm 9,13	1,37	69,07 \pm 7,93	1,29	95,12 \pm 3,07	1,13
	3	63,77 \pm 6,07	0,98	92,17 \pm 2,98	0,97	127,36 \pm 3,02	0,85

For HepG2 cells and B16-F10 the compound **2** was the most cytotoxic with IC_{50} values of $62,64 \pm 5,57 \mu\text{g/mL}$ and $69,07 \pm 7,93 \mu\text{g/mL}$ (Figure 4). Compound **2** was the higher cytotoxic compound being between 1.5 to 2 times more effective than the ligand in HepG2 cells, and B16-F10 cells. However, on HT29 the ligand was the more effective with $IC_{50}=52,08 \pm 3,94 \mu\text{g/mL}$, while the compound **3** is the least cytotoxic with IC_{50} value of $116,81 \pm 5,87 \mu\text{g/mL}$. In general terms, the compound **3** is the least cytotoxicity data between 92,17 to $116,81 \mu\text{g/mL}$. It should be noted that compound **2** is the most effective on HepG2 as the IC_{20} is half of the other samples.

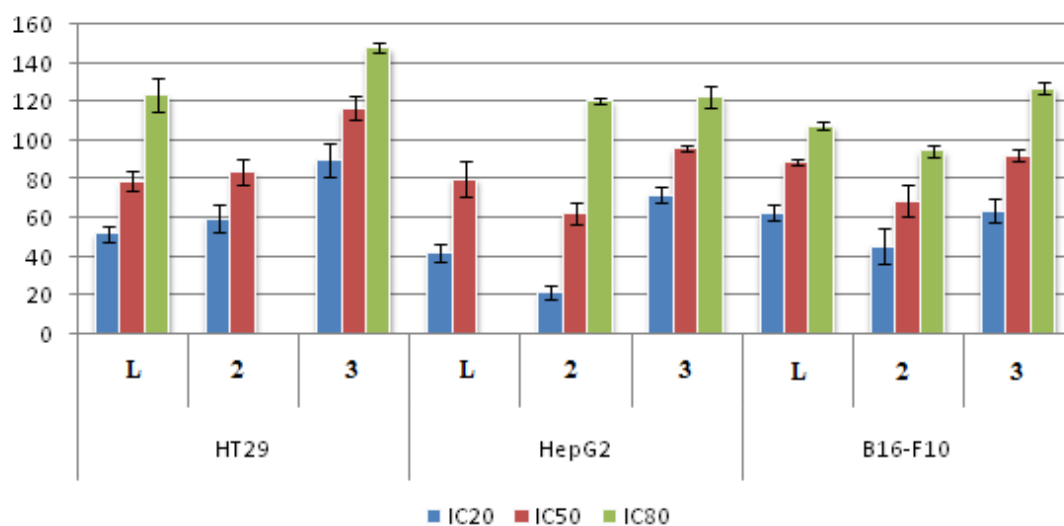


Figure 4. Growth-inhibitory effects (IC_{20} , IC_{50} , and IC_{80} , $\mu\text{g/mL}$) of ligand and compounds **2** and **3** on the three cancer cell lines HT29, HepG2 and B16-F10.

4.2. Raw 264.7 cell viability

Cytotoxicity of ligand and all compounds were determined on RAW 264.7 murine monocyte/ macrophage cells to establish infra-cytotoxic work concentrations and to assure that anti-inflammatory effects were due to an inflammatory process and not due to their cytotoxicity (Table 7). The cytotoxicity range was determined by MTT assay, at increased concentrations (range from 0 to $160 \mu\text{g/mL}$) and IC_{50} (concentration required for 50% inhibition in vitro) were determinate (Figure 5).

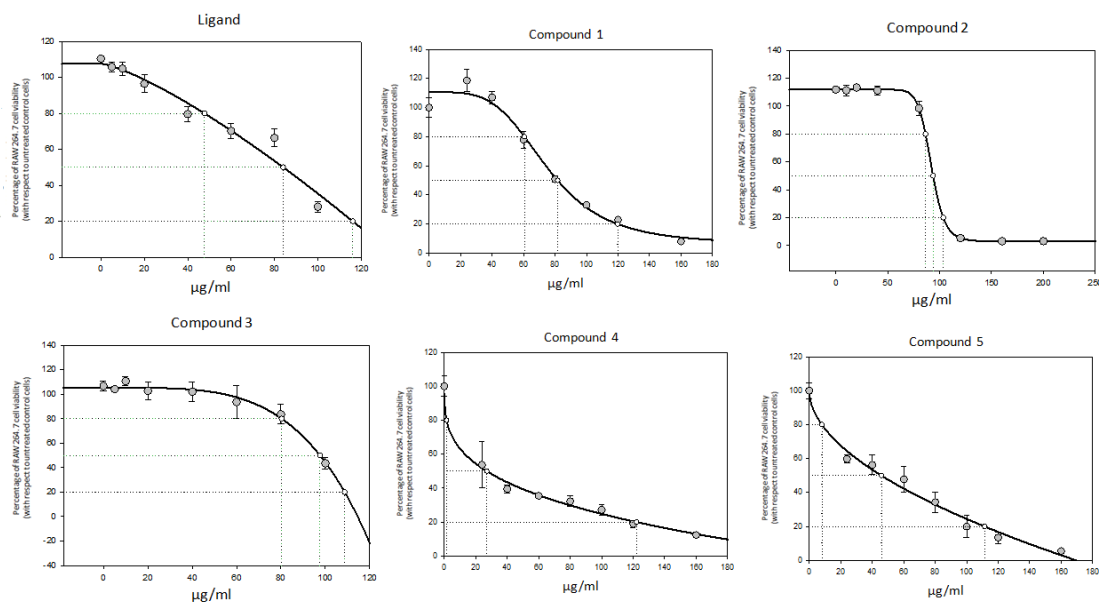


Figure 5. Effect of ligand and all compounds on cell proliferation of RAW 264.7 macrophage murine cells, after treatment with the compounds for in the range of concentration from 0 to 100 µg/mL, each point represents the mean value ± S.D. of at least two independent experiments performed in triplicate. By a dashed line are marked the IC₂₀, IC₅₀, and IC₈₀, which are the concentrations required for growth inhibition of 20%, 50% and 80%, respectively.

Table 7. Growth-inhibitory effects of ligand, and compound **1**, **2**, **3**, **4** and **5** on RAW 264.7 monocyte/ macrophage murine cells.

Compound	IC ₂₀	IC ₅₀	IC ₈₀
L	78,10 ± 1,02	97,09 ± 2,56	110,57 ± 2,21
1	9,50 ± 3,45	46,29 ± 9,34	109,87 ± 11,89
2	47,62 ± 6,93	83,77 ± 4,52	115,85 ± 0,94
3	78,10 ± 10,16	97,09 ± 2,56	110,57 ± 2,21
4	60,33 ± 3,14	81,50 ± 1,89	119,69 ± 1,66
5	10,41 ± 0,61	27,04 ± 1,20	122,38 ± 7,56

4.3. Nitro Oxide Production

In the inflammatory response process, nitric oxide, NO, is release as intermediate or second messenger. The enzymatic production of NO is cell type specific, with cytokine-driven inducible nitric-oxide synthase (iNOS) noted initially for the burst of higher levels as part of the inflammatory activation process. RAW 264.7 murine macrophage cells produce the highest release of NO during the inflammatory response, being an especially indicated model in anti-inflammatory

compounds screening studies. Macrophages were activated with LPS during 24h after the samples were added. As the nitrite concentration is proportional to the NO release, in this study the anti-inflammatory potential of the compounds assayed was analysed by measuring of nitrites in cell culture medium at 24h, 48h and 72h of incubation with the compounds.

After 24h of incubation, the higher anti-inflammatory effect was produced by compound **5**, with approximately a 55% of NO-inhibition with respect to the positive control (only LPS treated control cells) and negative control (untreated control cells) followed by compound **3** with 50%. Also, the compound **5** is the only one that shows values of inhibition close or lower to 50% for $\frac{3}{4}$ IC₅₀, at this time ligand not produce inhibition in the NO release. However, after 48h the inhibition clearly occurred for the ligand and all compounds in proportional form with respect to concentration, except to the compound **5**. The ligand produce a 60% of NO release inhibition, the inhibition generated by compounds **1** and **2** was lower that the ligand. The compounds **3** and **4** produces a 75% of inhibition at $\frac{3}{4}$ ·IC₅₀ concentration, and at $\frac{1}{2}$ ·IC₅₀ concentration in compound **4** case. The compound **5** produced a 85% of at all concentrations assayed. Finally, after 72h of incubation while the compounds **1**, **2** and **3** showed similar variations in NO-inhibition, whereas compounds **4** and **5** displayed values greater than 90% at all concentrations assayed (Figure 6).

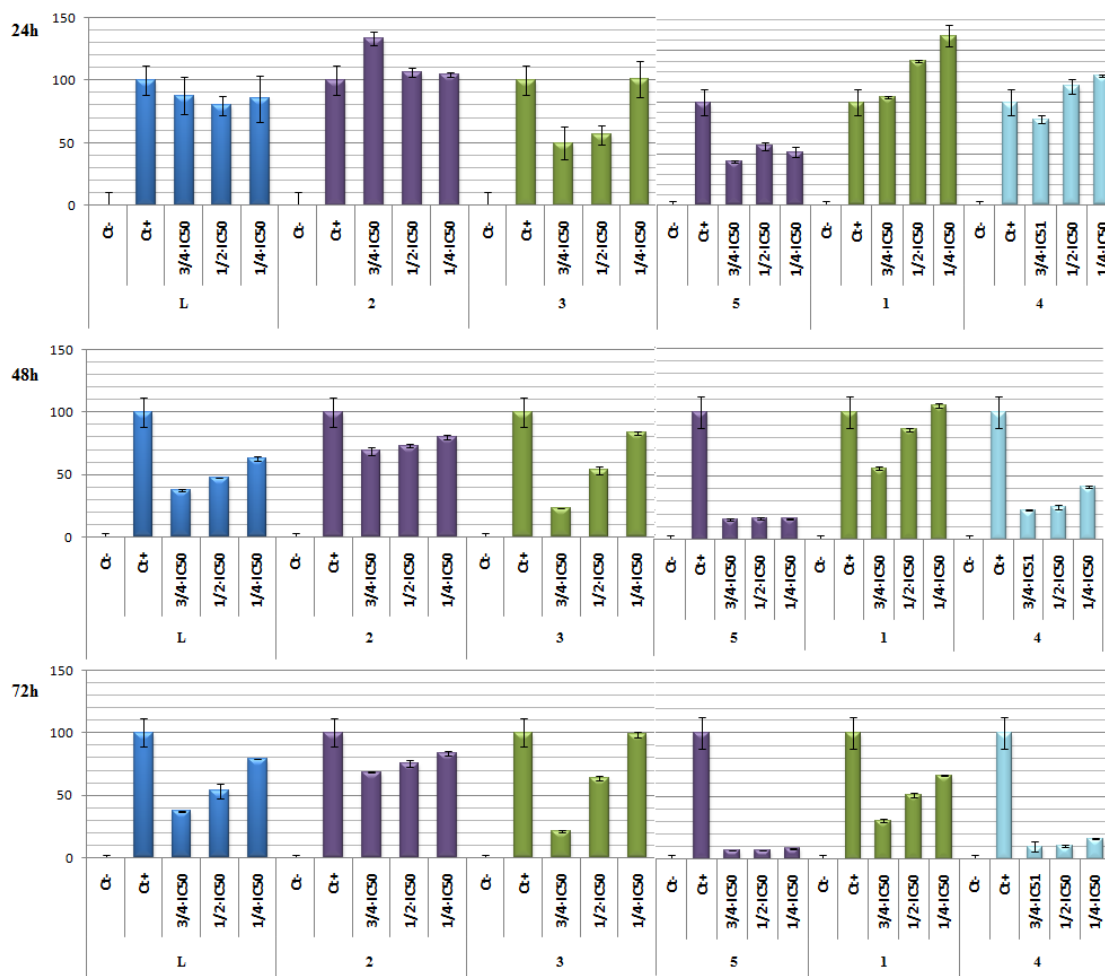


Figure 6. Effect of Ligand and all compounds on the release of nitrites in RAW 264.7 murine macrophage cells. After activation of the inflammatory process by incubation with LPS for 24h, the compounds were incubated for 24, 48, 72h at concentrations of $3/4\text{-IC}_{50}$, $1/2\text{-IC}_{50}$ and $1/4\text{-IC}_{50}$. The data represent the mean \pm S.D. of at least two independent experiments performed in triplicate.

5. Conclusions

In summary, five novel isostructural monomeric coordination compounds based on Indazole-3-carboxylic acid (H3-ind) have been synthesized: $[\text{M}(3\text{-ind})_2(\text{H}_2\text{O})_2]$ ($\text{M}=\text{Co}$ (1), Ni (2), Zn(3), Fe(4), Mn(5)). We assayed the comportment of several metal complexes and the indazole derivative ligand. The NO release is an event that occurred during the inflammatory respond, all product assayed reduced the production of NO at 48h and 72h. At 24h only the compound 5 was able to lower this production. Also the treatment with compound 5 result in the highest NO reduction at all times assayed reaching values close to 85-90% or NO release inhibition.

Compound **5** was, between 6 (24h) to 2 times (48h and 72h) more effective than ligand in this process. Compound **3** and **4** were too more effective than the ligand, between 5, at 24h for compound **3**, to 2 times for compound **4** at 72h. At this time the compounds **4** and **5** reaching percentage of NO release inhibition greater than 90% at all concentrations assayed $\frac{3}{4}\cdot IC_{50}$, $\frac{1}{2}\cdot IC_{50}$, $\frac{1}{4}\cdot IC_{50}$. Only ligand and compounds **2** and **3** were assayed with respect to its anti-cancer properties in HT29 colon cancer cells, HepG2 hepatome cells and B16-F10 murine melanome cells. The compound with highest cytotoxic compound was the compound **2**, in HepG2 and B16-F10 cells. The development of new compounds with more potential properties than its precursors is an important strategy for find compound that could be used as new, safe, and effective anti-inflammatory and/or anti-cancer drugs.

6. References

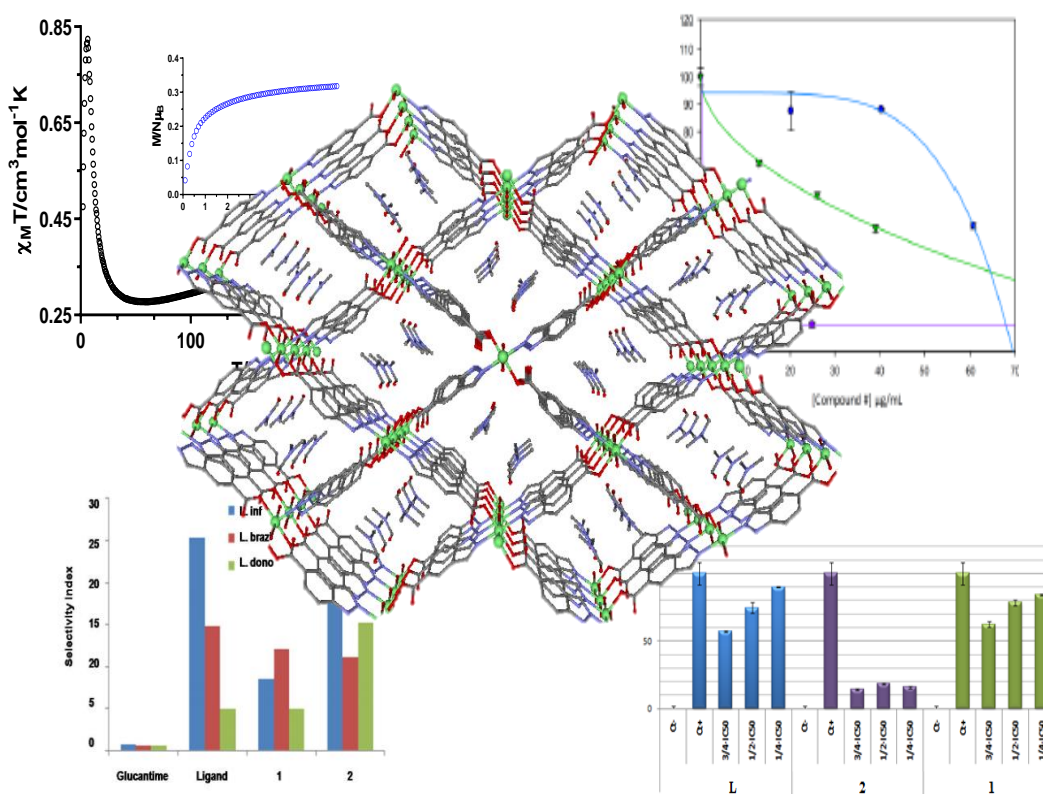
- [1] J. Cepeda, S. Pérez-Yáñez, G. Beobide, O. Castillo, J.A. García, M. Lanchas, A. Luque, Dalton Trans, 44 (2015) 6972–6986.
- [2] R.-B. Lin, S. Y. Liu, J. W. Ye, X. Y. Li, J. P. Zhang, Adv. Sci., 3 (2016) 1500434–1500454.
- [3] A. J. Calahorro, A. Salinas-Castillo, J. M. Seco, J. Zuñiga, E. Colacio, A. Rodríguez-Diéguez, CrystEngComm., 15 (2013) 7636-7639.
- [4] A. Rodríguez-Diéguez, S. Pérez-Yáñez, L. Ruiz-Rubio, J. M. Seco, J. Cepeda, CrystEngComm., 19 (2017) 2229-2242.
- [5] V. Oliveri, A. Puglisi, G. Vecchio, Dalton Trans., 40 (2011) 2913-2919.
- [6] Ibrahim, M.; Sabouni, R.; Hussein, G. A. J. Nanosci. Nanotechnol., 18 (2018) 5266-5273.
- [7] Kumar, D.; Kumar, A.; Sharma, J. J. Chem-Ny., 2012, 2013, 1-7.
- [8] R. Trondl, P. Heffeter, C. R. Kowol, M. Jakupec, W. Berger, B. K. Keppler, Chem. Sci., 5 (2014) 2925–2932.

- [9] S. I. Büyükeksi, M. Erkisa, A. Sengül, E. Ulukaya, Oral, A. Y. *Appl. Organomet. Chem.*, 32 (2018) e4406.
- [10] B. Rosenberg, L. van Camp, J. E. Trosko, V. H. Mansour, *Nature*, 222 (1969) 385-386.
- [11] E. Wong, C. M. Giandomenico, *Chem. Rev.*, 99 (1999) 2451–2466.
- [12] E. S. Antonarakis, A. Emadi, *Cancer Chemother. Pharmacol.*, 66 (2010)1–9.
- [13] B. W. J. Harper, J. R. Aldrich-Wright, *Dalton Trans.*, 44 (2015) 87-96.
- [14] M. Jabeen, S. Ali, S. Shahzadi, M. Shahid, S. K. Sharma, K. Qanungo, *Russ. J. Gen. Chem.*, 87(2017) 530-538.
- [15] M. Hanif, C. G. Hartinger, *Future Med. Chem.*, 10 (2018) 6115-617.
- [16] S. Xianchao, H. Fang, Y. Guo, H. Yuan, Z. Gou, W. J. Wang, *Inorg. Biochem.*, 190 (2019) 38-44.
- [17] G. Psomas, D. P. Kessissoglou, *Dalton Trans.*, 42 (2013) 6252-6276.
- [18] C. N. Banti, S. K. Hadjikakou, *Eur. J. Inorg. Chem.*, 19 (2016) 3048–3071.
- [19] L. Sun, L-Y. Sha, J. Jiang, *Biomed. Res.-India*, 28 (2017)2152-2155.
- [20] Y. Zeng, T. Xu, *Lat Am J Pharm*, 35 (2016) 1228-1233.
- [21] J. M. Méndez-Arriaga, I. Oyarzabal, G. Escolano, A. Rodríguez-Diéguez, M. Sánchez-Moreno and J. M. Salas, *J. Inorg. Biochem*, 180 (2018) 26–32.
- [22] A. B. Caballero, A. Rodríguez-Diéguez, L. Lezama, and J. M. Salas, *Cryst. Growth Des*, 12 (2012) 3583–3593.
- [23] A. B. Caballero, A. Rodríguez-Diéguez, M. Quirós, J. M. Salas, O. Huertas, I. Ramírez-Macías, F. Olmo, C. Marín, G. Chaves-Lemaur, R. Gutierrez-Sanchez, M. Sanchez-Moreno, *Eur. J. Med. Chem.* 85 (2014) 526-534.
- [24] A. B. Caballero, J. K. MacLaren, A. Rodríguez-Diéguez, I. Vidal, J. A. Dobado, J. M. Salas, C. Janiak, *Dalton Trans*, 40 (2011) 11845–11855.

- [25] A. B. Caballero, A. Rodríguez-Diéguez, E. Barea, M. Quiros, J. M. Salas, *CrystEngComm*. 12 (2010) 3038–3045.
- [26] B. Fernández, A. Gómez-Vílchez, C. Sánchez-González, J. Bayón, E. San Sebastian, S. Gómez-Ruiz, C. López-Chaves, P. Aranda, J. Llopis, A. Rodríguez-Diéguez. *New J. Chem.* 40 (2016) 5387-5393
- [27] D. Briones, B. Fernández, A.J. Calahorro, D. Fairen-Jimenez, R. Sanz, F. Martínez, G. Orcajo, E.S. Sebastián, J.M. Seco, C.S. González, J. Llopis and A. Rodríguez-Diéguez, *CrystGrowth Des.* 16 (2016) 537–540.
- [28] B. Machura, A. Świetlicka, M. Wolff, R. Kruszynski, *Polyhedron* 29(2010) 2061-2069.
- [29] I. Gryca, B. Machura, J. G. Małecki, L. S. Shul'pina, A. J. L. Pombeiro, and G.B. Shul'pin, *Dalton Trans.*, 2014,43, 5759-5776.
- [30] Bruker Apex2, Bruker AXS Inc., Madison, Wisconsin, USA, 2004.
- [31] Sheldrick, G.M. SADABS, Program for Empirical Adsorption Correction, Institute for Inorganic Chemistry, University of Gottingen, Germany, 1996.
- [32] Sheldrick, G. M. SHELX-2014, Program for Crystal Structure Refinement, University of Göttingen, Göttingen, Germany, 2014.
- [33] L. J. J. Farrugia, *Appl. Cryst.*, 32 (1999) 837–838.
- [34] A. Altomare, M. C. M. Burla, G. L. Cascarano, C. Giacovazzo A. Guagliardi, A. G. G. Moliterni, G. Polidori, R. Spagna, *J. Appl. Crystallogr.*, 32 (1999) 115–119.
- [35] N. S. Bryan, M. B. Grisham, *Free RadicBiol Med.*, 43 (2007) 645-657.

Capítulo 9

Antiparasitic, Anti-inflammatory and Cytotoxic Activities of 2D Coordination Polymers based on 1H-indazole-5-carboxylic Acid



Antiparasitic, Anti-inflammatory and Cytotoxic Activities of 2D Coordination Polymers based on 1H-indazole-5-carboxylic Acid

Journal of Inorganic Biochemistry 208 (2020) 111098



Contents lists available at ScienceDirect

Journal of Inorganic Biochemistry

journal homepage: www.elsevier.com/locate/jinorgbio



Antiparasitic, anti-inflammatory and cytotoxic activities of 2D coordination polymers based on 1H-indazole-5-carboxylic acid



Antonio A. García-Valdivia^a, Amalia García-García^a, Fatin Jannus^b, Andoni Zabala-Lekuona^c, José M. Méndez-Arriaga^d, Belén Fernández^{e,*}, Marta Medina-O'donnell^f, Gloria B. Ramírez-Rodríguez^a, José M. Delgado-López^a, Luisa M. Pastrana-Martínez^a, Javier Cepeda^c, José A. Lupiáñez^b, Fernando J. Reyes-Zurita^{b,*}, Antonio Rodríguez-Diéguez^{a,*}

^a Departamento de Química Inorgánica, Facultad de Ciencias, Universidad de Granada, Av. Puentenueva s/n, 18071 Granada, Spain

^b Departamento de Bioquímica y Biología Molecular I, Facultad de Ciencias, Universidad de Granada, Av. Puentenueva s/n, 18071 Granada, Spain

^c Departamento de Química Aplicada, Facultad de Química, Universidad del País Vasco (UPV/EHU), Paseo Manuel Lardizabal, no 3, 20018 Donostia-San Sebastián, Spain

^d Department of Biology and Geology, Physics and Inorganic Chemistry, Calle Tulipán s/n, 28933 Móstoles, Madrid, Spain

^e Institute of Parasitology and Biomedicine "López-Neyra", CSIC, Av. Conocimiento s/n, 18600 Granada, Spain

^f Departamento de Química Orgánica, Facultad de Ciencias, Universidad de Granada, Av. Puentenueva s/n, 18071 Granada, Spain

Abstract

We report on the formation of two novel multifunctional isomorphous (4,4) square-grid 2D coordination polymers based on 1H-indazole-5-carboxylic acid. To the best of our knowledge, these complexes are the first examples of 2D-coordination polymers constructed with this novel ligand. We have analysed in detail the structural, magnetic and anti-parasitic properties of the resulting materials. In addition, the capability of inhibiting nitric oxide production from macrophage cells has been measured and was used as an indirect measure of the anti-inflammatory response. Finally, the photocatalytic activity was measured with a model pollutant, i.e. vanillic acid (phenolic compound), with the aim of further increasing the functionalities and applicability of the compounds.

1. Introduction

In the last decades, the study of coordination polymers (CPs) has increased exponentially because of their potential applications in different areas of science owing to the continuous advances shown by these multifunctional materials.[1-5]

Experimental conditions such as temperature, solvent, stoichiometry and pH need to be carefully controlled during the synthesis of CPs.[6-9] These conditions play a major role in the intrinsic characteristics of the structural components, which in turn make the difference to generate advanced materials with fascinating functionalities.[10,11] Aromatic ligands with carboxylate groups are widely used owing to rigidity as well as high coordination capacity, resulting in different binding modes and interesting crystal packings.[12-14] On the other hand, first row transition metal ions are a perfect choice for obtaining new materials with excellent physical properties.[14-17] In fact, it has been observed that family of indazole-carboxylic acids together with first row transition metals have a great potential for the construction of new coordination compounds with a wide range of traits.[18-22]

In the last years, our group and others have reported the use of different nitrogen derivative ligands with specific antiparasitic activities, with a particular focus on the behaviour of the triazolopyrimidine ligands.[23-26] In addition, materials with anti-inflammatory or anti-diabetic activity have been synthesized in our laboratory with this class of organic ligands.[27-29] Based on these previous results, we decided to use a novel organic linker to construct new CPs and to study different physical properties of these materials based on transition metal ions. In this sense, we chose the 1H-indazole-5-carboxylic acid due to, to the best of our knowledge, there is only one example of coordination compound based on this ligand, specifically, this compound is based on copper and consists of two interpenetrated networks with hysteretic carbon dioxide sorption.[30] Therefore, in addition to the biological properties, we will be able to characterize the synthesized materials by studying other properties such as magnetism or photocatalysis, or even other very interesting properties could be studied in case the materials show superparamagnetism.[31] In this sense, the use of transition metal ions generates the possibility of the study of magnetic properties [32,33] while, on the other hand, nitrogen aromatic ligands are widely employed in the preparation of news CPs that show excellent photocatalytic degradation of organic wastes,[34,35] principally the Ni-CPs are very attractive in this field.[36]

However, the main objective of this work is the study of the biological properties that these materials may exhibit, such as anti-parasitic or anti-

inflammatory activities. Bioinorganic and medicinal chemists have focused on the design and synthesis of new metal-based agents with better biological activity, lower toxicity and different mechanisms of action to overcome the unresolved clinical problems of some current therapeutic agents.[37,38] For example, non-steroidal anti-inflammatory drugs comprise a large group of medicines used to inflammation and pain with known side-effects.[39,40] For this reason CPs have been broadly studied over recent years as anti-inflammatory drugs.[41,42] Nitric oxide (NO) is a very important mediator in acute or chronic inflammation. This radical compound is produced by constitutive and inducible nitric oxide synthases. The inducible enzyme is activated in response to pro-inflammatory signals as LPS (either bacterial lipopolysaccharide), enterotoxin, or cytokines as TNF α (tumor necrosis factor α) or INF- γ (interferon- γ) in macrophages, hepatocytes, and endothelial cells. The reduction of NO can be produced by directly scavenger action of NO radicals, iNOS inhibition enzyme activity, and/or iNOS (inducible nitric oxide synthase) gene expression inhibition.

As a complement to these biological studies, numerous investigations have demonstrated the activity of indazole derivatives against Leishmaniasis.[43,44] In humans, the disease is presented as three clinical forms, depending on the involved species of *Leishmania*. Actually, there are more than 12 million of cases and 350 million people at risk, also 2 million new cases are estimated each year.[45,46] The current therapies are inadequate due to several factors such as the high toxicity, pernicious side effects, high prices and the emergence of drug-resistant parasites.[47] Therefore, looking for new effective therapeutic agents against this disease should be considered by new CPs based on 1H-indazole-5-carboxylic acid.

All of the above in mind, in this work, we have synthesized two new coordination polymers based on first row transition metals and 1H-indazole-5-carboxylic acid (5-inca) with the formula $\{[M(5\text{-inca})_2(\text{H}_2\text{O})_2]\cdot(\text{DMF})_2\}_n$ (M = Ni (**1**) and Cu (**2**)). We have analysed in detail the structural, magnetic and anti-parasitic properties of these materials. In addition, the capability of inhibiting NO production from LPS RAW macrophage cells has been also measured. This was used as an indirect proof of the anti-inflammatory response.[48] Finally, the photocatalytic activity was measured with a model pollutant, i.e. vanillic acid (phenolic compound),

with the aim of further increasing the functionalities and applicability of the compounds.

2. Experimental

2.1. Materials and physical measurements

All reagents were obtained from commercial sources and used as received. Elemental (C, H, and N) analyses were performed on an Euro EA Elemental Analyzer. The IR spectra of powdered samples were recorded in the 400–4000 cm^{-1} region on a Nicolet 6700 FTIR spectrophotometer using KBr pellets (Figure 1). Alternating current magnetic measurements were performed under zero and 1000 Oe applied static fields on a Quantum Design SQUID MPMS XL-5 device by using an oscillating *ac* field of 3.5 G and *ac* frequencies ranging from 10 to 1400 Hz.

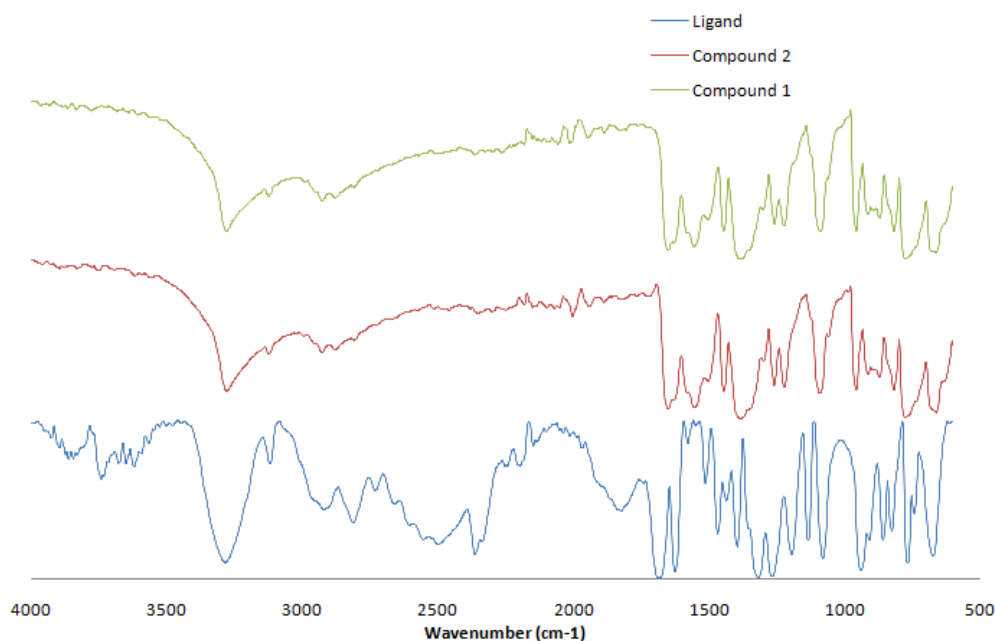


Figure 1. IR spectrum of ligand and compounds 1 and 2.

2.2. Synthesis of complexes

Synthesis of $\{[M(5\text{-inca})_2(\text{H}_2\text{O})_2] \cdot (\text{DMF})_2\}_n$ ($M = \text{Ni}$ (1**), Cu (**2**)).** Green and orange single crystals of compound **1** and **2**, respectively, were obtained following the next solvothermal procedure: 0.06 mmol (10.00 mg) of 1H-indazole-5-carboxylate were dissolved in 0.5 mL of DMF and then 0.5 mL of distilled water was added. Then 0.03 mmol of $\text{MCl}_2 \cdot x\text{H}_2\text{O}$ for different compounds was dissolved in 0.5 mL of distilled water and afterward 0.5 mL of DMF was added. Both solutions were mixed and the resulting solution was placed in a closed glass vessel and introduced in an oven at 95°C for 24h. Yield (**1**): 54% based on Ni. Yield (**2**): 48% based on Cu. Anal. Calcd. for $\text{NiC}_{22}\text{H}_{28}\text{N}_6\text{O}_8$: C, 46.92; H, 5.01; N, 14.92. Found: C, 46.88; H, 4.99; N, 14.98. Anal. Calcd. for $\text{CuC}_{22}\text{H}_{28}\text{N}_6\text{O}_8$: C, 46.52; H, 4.97; N, 14.79. Found: C, 46.50; H, 4.93; N, 14.84.

2.3. Crystallographic refinement and structure solution

X-ray data collection of suitable single crystals of the compounds were conducted at 100(2) K on a Bruker VENTURE area detector equipped with a graphite monochromated Mo-K α radiation source ($\lambda = 0.71073 \text{ \AA}$) by applying the ω -scan method. The data reduction was performed with the APEX2 software [49] and corrected for absorption using SADABS.[50] Crystal structures were solved by direct methods using the SIR97 program [51] and refined by full-matrix least-squares on F^2 including all reflections using anisotropic displacement parameters by means of the WINGX crystallographic package.[52] Details of the structure determination and refinement of compounds **1** and **2** are summarized in Table 1. Crystallographic data (excluding structure factors) for the structures reported in this paper have been deposited with the Cambridge Crystallographic Data Center as supplementary publication nos. CCDC 1987070 and 1987071. Copies of the data can be obtained free of charge on application to the Director, CCDC, 12 Union Road, Cambridge, CB2 1EZ, U.K. (Fax: +44-1223-335033; e-mail: deposit@ccdc.cam.ac.uk or <http://www.ccdc.cam.ac.uk>).

Table 1. Crystallographic data and structure refinement details of all compounds.

Compound	1	2
Chem. form.	NiC ₂₂ H ₂₈ N ₆ O ₈	CuC ₂₂ H ₂₈ N ₆ O ₈
CCDC	1987070	1987071
Form. weight	563.21	568.04
Cryst. system	Monoclinic	Monoclinic
Space group	<i>P</i> 2 ₁ / <i>n</i>	<i>P</i> 2 ₁ / <i>n</i>
<i>a</i> (Å)	6.5605(12)	6.5541(4)
<i>b</i> (Å)	17.9705(3)	18.0179(11)
<i>c</i> (Å)	10.970(2)	10.9212(7)
<i>α</i> (°)	90	90
<i>β</i> (°)	93.970(5)	94.027(2)
<i>γ</i> (°)	90	90
<i>V</i> (Å³)	1290.2(3)	1286.51(14)
<i>Z</i>	2	2
GoF^a	1.170	1.131
R_{int}	0.1338	0.0787
R₁^b / wR₂^c [I>2σ(I)]	0.0455/0.1108	0.0275/0.0418
R₁^b / wR₂^c[all data]	0.0840/0.1610	0.0446/0.0448

$$[a] S = [\sum w(F_0^2 - F_c^2)^2 / (N_{\text{obs}} - N_{\text{param}})]^{1/2}$$

$$[b] R_1 = \sum |F_0| - |F_c| / \sum |F_0| \quad [c] wR_2 = [\sum w(F_0^2 - F_c^2)^2 / \sum wF_0^2]^{1/2}$$

$$w = 1/[\sigma^2(F_0^2) + (aP)^2 + bP] \quad \text{where } P = (\max(F_0^2, 0) + 2F_c^2)/3$$

2.4. Parasite culture and *in vitro* activity

Promastigote forms of *L. infantum* (MCAN/ES/2001/UCM-10), *L. braziliensis* (MHOM/BR/1975/M2904) and *L. donovani* (MHOM/PE/84/LC26) were grown *in vitro* in trypanosomal liquid medium (MTL) [Hank's Balanced Salt Solution-HBSS (Gibco), NaHCO₃, lactalbumin, yeast extract, bovine hemoglobin and antibiotics] with 10% inactivated fetal bovine serum being stored in an air atmosphere at 28°C, in Roux flasks (Corning, USA) with a surface area of 25 cm², according to the methodology described by Gonzalez et al.[53] The extracellular promastigote forms were screened using 24-well plates with MTL medium and 5×10⁴ parasites per well. Different concentrations of the compounds (1, 10, 25 and 50 μM) were tested preparing three replicas of each one and maintaining some wells without drugs as control. They were incubated at 28°C during 72h before determining the leishmanicidal activity counting the final parasite population using a Neubauer chamber. Finally, the leishmanicidal effect was expressed as the IC₅₀ (concentration

required to obtain 50% inhibition, calculated through a linear regression analysis from the Kc values at the concentration employed).

2.5. Cell culture and cytotoxicity test

RAW 264.7 monocyte/macrophage murine cell line (ATCC no. TIB-71) is a murine leukemia virus-induced tumor cell line from mouse *Mus musculus*. This cell line does not produce detectable retrovirus. Cells were cultured in DMEM (Dulbecco's Modified Eagle's medium) supplemented with 2 mM glutamine, 10% heat-inactivated FCS (Fetal Calf Serum), 0,5 µg/mL of gentamicin, being incubated at 37°C, in an atmosphere of 5% CO₂ and 95% humidity. Subconfluent monolayer cells were used in all experiments.

The cytotoxicity tests for macrophages were carried out in 96-well plates. The growth inhibition of mammalian cells was studied testing the compounds in a concentration range from 0 to 100 µg/ml.

First, the cells were cultured in the plates to a volume of 100 µL at 6.0×10³cells/mL and were incubated at 37°C with 5% CO₂ during 24h. The compounds were dissolved in the cell growth medium and then were added in another 100 µL (only adding medium in the control wells) to the corresponding wells. After that, the plates were incubated at 37°C with 5% CO₂ for 72h.

Cell viability was determined by measuring the absorbance of MTT (3-(4,5-dimethylthiazol-2-yl)-2,5-diphenyltetrazolium bromide) dye staining of living cells. After 72h of incubation, the medium with the compounds was removed, and 100 µL of MTT solution (0.5 mg/mL) in 50% of PBS 50% of medium was added to each well. After 1.5h of incubation formazan was resuspended in 100 µL of DMSO. Relative cell viability, with respect to untreated control cells, was measured by absorbance at 570 nm on an ELISA (enzyme linked immunosorbent assay) plate reader (Tecan Sunrise MR20-301, TECAN, Austria).

Experimental data were fitted to a sigmoidal function ($y = y_{max}/(x/a)^{-b}$) by non-linear regression. IC₅₀ values (*i.e.*, concentration causing a 50% of cell viability)

were obtained by interpolation. These analyses were performed with SigmaPlot statistical software (Version 12.5). Similar analyses were performed to obtain the $IC_{50\ NO}$ (vide infra).

2.6. Determination of nitrite concentration

Nitrite concentration was used as indicator of NO production. NO determination was based on Griess reaction.[54]

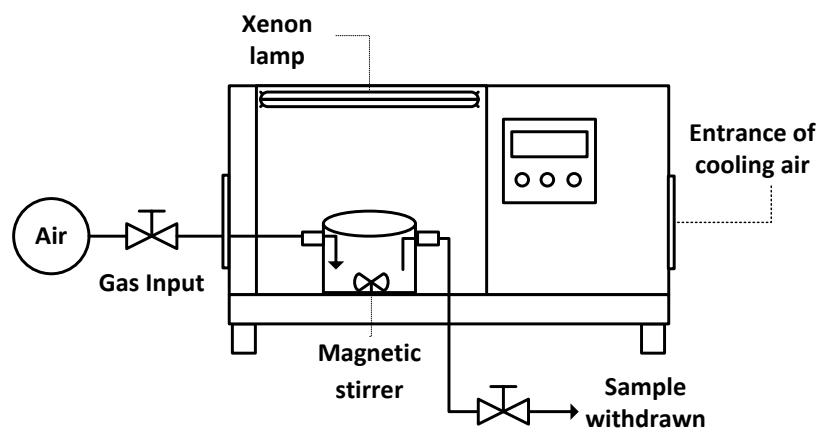
Cells were plated at 6×10^4 cells/well in 24-well cell culture plates and supplemented with 10 $\mu\text{g/mL}$ of lipopolysaccharide (LPS). After 24h of plated, cells were incubated for 72h with ligand and compounds **1**, and **2** at $\frac{3}{4} IC_{50}$, $\frac{1}{2} IC_{50}$ and $\frac{1}{4} IC_{50}$ concentrations. The supernatants were collected at 24h, 48h and 72h to determine their nitrite concentration and/or stored at -80°C for further use.

Griess reaction was performed taking 150 μL of supernatant test samples or sodium nitrite standard (0-120 μM) and mixed with 25 μL of Griess reagent A (0.1% N-N-(1-naphthyl)-ethylenediaminedihydrochloride) and 25 μL of Griess reagent B (1% sulfanilamide in 5% of phosphoric acid), in a 96-well plate. After 15 min of incubation at room temperature, the absorbance was measure at 540 nm in an ELISA plate reader (Tecan Sunrise MR20-301, TECAN, Austria). The absorbance was referred to nitrite standard curve to determine the concentration of nitrite in the supernatant of each experimental sample. The percentage of NO production was determined, assigning 100% at the increase between negative control (untreated cells) and positive control (cells only treated with 10 $\mu\text{g/mL}$ of LPS).

2.7. Photocatalytic performance measurements

The photocatalytic experiments using MOF materials (Compound **1** and Compound **2**) were performed in a 50 mL Pyrex batch reactor loaded with a 20 mg L^{-1} vanillic acid (VA) solution ($\text{C}_8\text{H}_8\text{O}_4$), under simulated solar light irradiation for 60 min. The irradiation source consisted of a 1500 W xenon lamp min using a CofomegraSolarBox 1500e (Scheme II). The material load was fixed at 1 g L^{-1} and the

suspensions were magnetically stirred and continuously saturated with an air flow. The temperature was maintained at 303 K. The concentration of VA was monitored using a UV-spectrophotometer model UV-1800 Shimadzu.



Scheme I. *Experimental set-up for photocatalytic experiments.*

3. Results and Discussion

3.1. Structural descriptions

Structural description of $\{[\text{Ni}(\text{5-inca})_2(\text{H}_2\text{O})_2] \cdot (\text{DMF})_2\}_n$ (1). Compound **1** crystallizes in $P2_1/n$ and grows from the piling of neutral 2D layers held together by hydrogen bonds. Each metallic center (Ni1), which is situated at a centre of symmetry, is coordinated to four 5-inca ligands and two water molecules, shaping a slightly octahedron as a coordination polyhedron (Figure 2). The polyhedron basal plane is formed by two O1W coordination water molecules and two O1A atoms from carboxylate groups, whereas the slightly elongated axis is occupied by N1A atoms pertaining to indazole aromatic rings. Besides, the asymmetric unit includes a DMF molecule. A square-grid 2D coordination polymer is formed with DMF molecules located at square holes, as the result of strong hydrogen bond interactions.

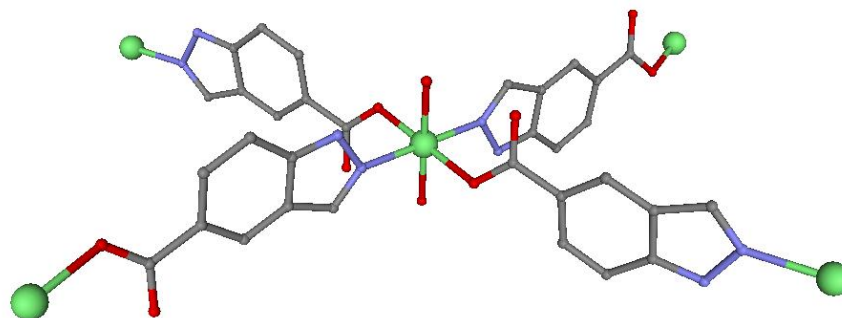


Figure 2. View of complex **1** showing the coordination polyhedron. Nickel (green), nitrogen (blue), oxygen (red), carbon (grey). Hydrogen atoms are been omitted for clarity.

Within these sheets, nickel(II) ions are bridged by four 1H-indazole-5-carboxylate ligands which are coordinated to the metal ions through the pyrazol and carboxylate groups pertaining to the ligand with Ni-N and Ni-O bond distances of about 2 Å (Table 2).

Table 2. Bond distances for coordination environment in compound **1**.^a

Ni1-O1W	2.057(4)	Ni1-O1A(iii)	2.069(5)
Ni1-O1W(iii)	2.057(4)	Ni1-N1A	2.093(5)
Ni1-O1A	2.069(5)	Ni1-N1A(iii)	2.093(5)

^aSymmetry operation (iii) = '-x, -y, -z'

The layers grow on the diagonal of the unit cell (Figure 3a) and are connected by hydrogen bond interactions (Table 3, 2.795(8) Å) involving nitrogen atoms from pyrazol rings and oxygen atoms pertaining to the carboxylate groups of adjacent sheets (Figure 3b).

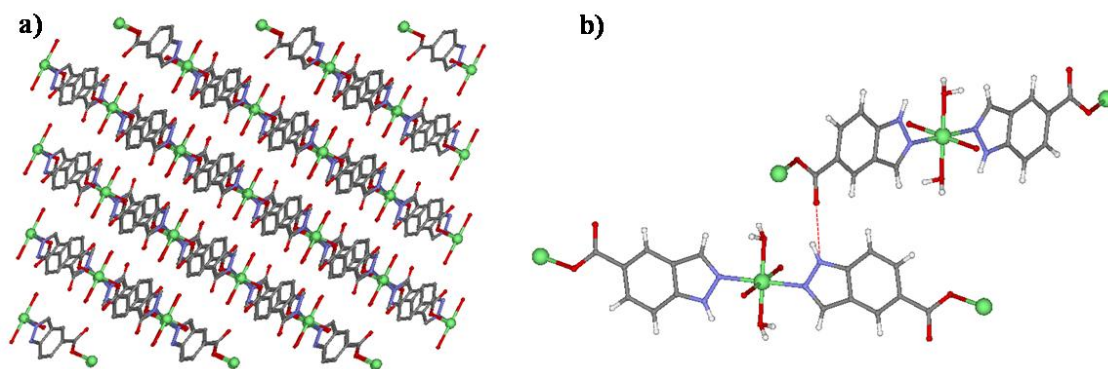


Figure 3. (a) Views of the packing of compound **1** along *b* axis in which hydrogen atoms have been omitted for clarity. (b) Strong hydrogen bond interaction involving nitrogen and oxygen atoms of different layers. Nickel (green), nitrogen (blue), oxygen (red), carbon (grey) and hydrogen (white).

Table 3. Selected H-bonds lengths (Å) and angle (°) for compound **1**.^b

<i>D-H...A</i> ^b	<i>D-H</i>	<i>H...A</i>	<i>D...A</i> ^b	<i>Angle</i>
N2A-H2A...O2A(ii)	0.86	2.02	2.795(8)	148.8
N2A-H2A...O1W	0.86	2.30	2.803(7)	117.9
O1W-H1W1...O2A	0.82	1.88	2.626(6)	149.9
O1W-H2W1...O1D(iv)	0.82	1.95	2.747(7)	162.4

^bSymmetry operations (ii) = '-x-1, -y, -z'; (iv) = 'x-3/2, -y+1/2, z-1/2'

Accordingly, the linkage of these units gives rise to flattened open 2D layers showing square holes. Owing to this, the structure presents channels along *a* axis occupied by crystallization DMF molecules (Figure 4). These DMF molecules are there located due to strong hydrogen bond interactions involving the oxygen pertaining to DMF molecules and the water molecules coordinated to nickel ions with a value of 2.748 Å.

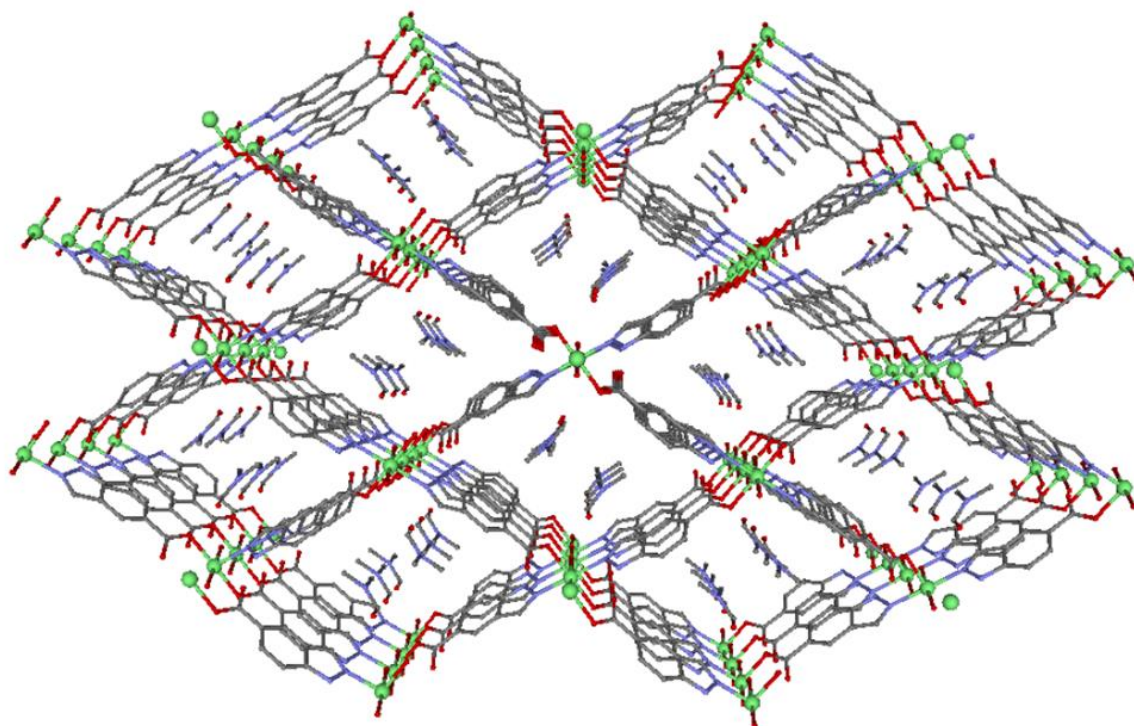


Figure 4. View of the channels in network compound **1** along a axis showing the crystallization DMF molecules. Hydrogen atoms have been omitted for clarity.

Structural description of $\{[\text{Cu}(\text{5-inca})_2(\text{H}_2\text{O})_2] \cdot (\text{DMF})_2\}_n$ (2**).** The compound **2** is isostructural to compound **1**, crystallizes in $P2_1/n$ and grows from the piling of neutral 2D layers held together in the same way that previous Ni-CP. The same type of description applies to compound **2**, except that Cu-N and Cu-O bond distances in **2** that are slightly smaller than in **1** (Table 4 and Figure 5), which is consistent with the larger atomic radio of nickel. Likewise, in this Cu-CP there are hydrogen interactions that are involved in the packaging of the layers in CP and in the presence of crystallization DMF molecules in channels generated (Figure 5). These interactions (Table 5) are in the range 2.626(17) - 2.803(18) Å

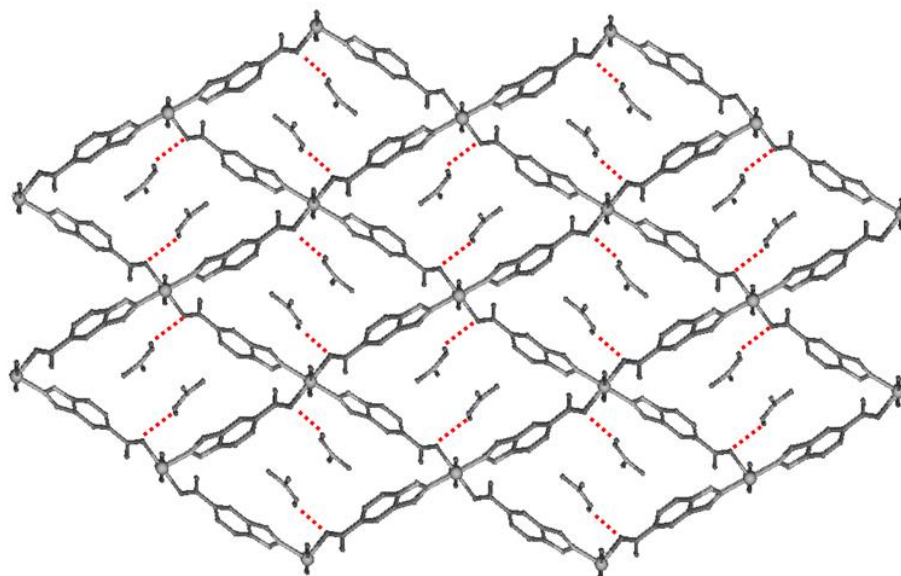


Figure 5. Hydrogen bonds involving crystallization DMF molecules and 2D-CP.

Table 4. Bond distances for coordination environment in compound **2**.

Cu1-O1W	2.0567(13)	Cu1-O1A(iii)	2.0672(12)
Cu1-O1W(iii)	2.0567(13)	Cu1-N1A(iv)	2.0855(14)
Cu1-O1A	2.0672 (12)	Cu1-N1A(ii)	2.0855(14)

Table 5. Selected H-bonds lengths (Å) and angle (°) for compound **2**.^b

<i>D-H...A</i> ^b	<i>D-H</i>	<i>H...A</i>	<i>D...A</i>	<i>Angle</i>
N2A-H2A...O2A(iv)	0.86	2.02	2.7905(18)	148.8
N2A-H2A...O1W(ii)	0.86	2.29	2.803(18)	117.9
O1W-H1W1...O2A	0.81	1.83	2.626(17)	164.9
O1W-H2W1...O1D(iv)	0.81	1.94	2.747(2)	168.6

^b Symmetry operations (ii) = '-x-1/2, y+1/2, -z-1/2'; (iv) = 'x+1/2, -y+1/2, z-1/2'

3.2. Magnetic Properties

Magnetic properties of the compounds have been studied in order to complete the physico-chemical characterization and ensure the purity of the samples. At room temperature the $\chi_M T$ value of 1.02 cm³ K mol⁻¹ for compound **1** is in good agreement

with the expected value of $1.00 \text{ cm}^3 \text{ K mol}^{-1}$ for one isolated Ni(II) ion with $g = 2.0$ (Figure 6). Upon cooling, the $\chi_M T$ value remains nearly constant up to 15 K and then abruptly decreases reaching a minimum value of $0.79 \text{ cm}^3 \text{ K mol}^{-1}$ at 2.5 K. This thermal dependence is the first evidence of zero-field splitting (ZFS) in Ni(II) compounds. Assuming that the long intramolecular Ni...Ni distances (10.913 \AA) will provide negligible interactions in comparison to the mentioned ZFS, the $\chi_M T$ data were analysed with the PHI software and the following Hamiltonian:

$$\hat{H} = g\mu_B\hat{S}\cdot B + D(\hat{S}_z^2 - \hat{S}^2/3) + E(\hat{S}_x^2 - \hat{S}_y^2) \quad (\text{Equation 1})$$

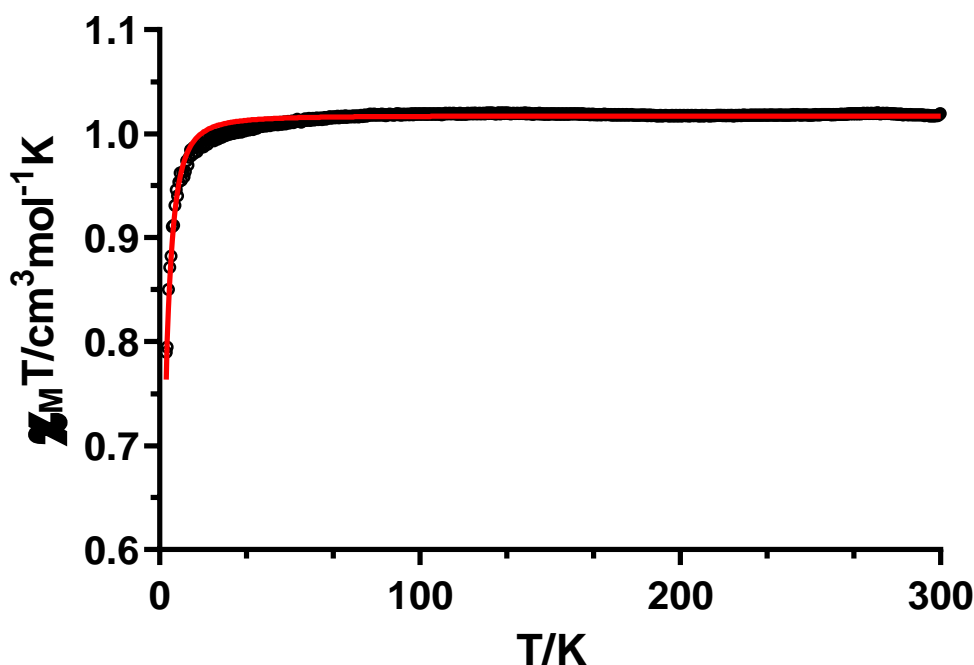


Figure 6. Temperature dependence of the $\chi_M T$ product for compound **1** in the 2.5-300 K range. The solid line is generated from the best fit to the magnetic parameters.

The first term accounts for the Zeeman interaction with the local magnetic field (B), which is parametrized through the Landé g tensor, and the second and third terms correspond to axial (D) and rhombic (E) anisotropic ZFS parameters. Finally, \hat{S} represents the spin operator with x , y or z components. The best fit of the experimental data afforded the following set of parameters: $g = 2.02$, $D = -6.53 \text{ cm}^{-1}$, and $E = +0.19 \times 10^{-3} \text{ cm}^{-1}$, with $R = 9.74 \times 10^{-3}$. The small value of E indicates a weak influence of rhombicity in the ZFS, however the values are consistent with other previously reported similar compounds.[55]

The temperature dependence of the magnetic susceptibility of compound **2** in the 2-300 K temperature range under an applied field of 0.1 T is displayed in Figure 6. At room temperature, the $\chi_M T$ value of $0.439 \text{ cm}^3 \text{ K mol}^{-1}$ is higher than the spin only value expected for an isolated Cu(II) center ($0.375 \text{ cm}^3 \text{ K mol}^{-1}$ with $S = 1/2$ and $g = 2.0$). This occurs when the orbital angular momentum is not completely quenched leading to higher g values and, inherently to higher $\chi_M T$. When lowering the temperature, the $\chi_M T$ value decreases gradually until 54 K reaching the lowest $\chi_M T$ value of $0.28 \text{ cm}^3 \text{ K mol}^{-1}$. At this point, the signal sharply increases reaching $0.82 \text{ cm}^3 \text{ K mol}^{-1}$ at 6.5 K before falling to $0.48 \text{ cm}^3 \text{ K mol}^{-1}$ at 2.0 K.

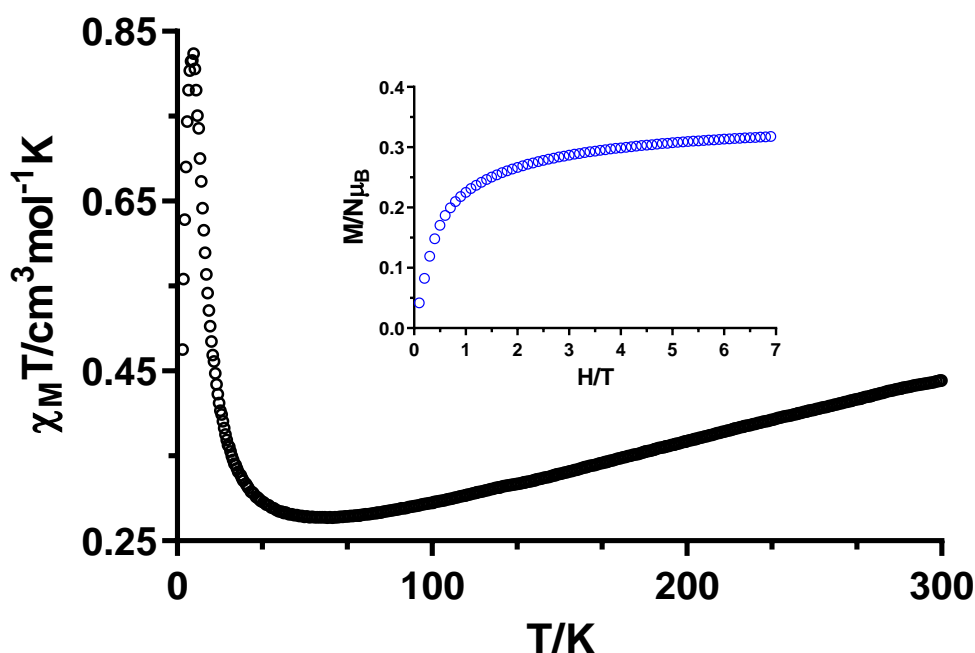


Figure 7. Temperature dependence of the $\chi_M T$ product for compound **2** in the 2-300 K range. Inset: field dependence of the magnetization for **2**.

Similar results were previously obtained for other Cu(II) compounds.[56] Indeed, we associated these magnetic properties to a spin-canted antiferromagnetism, which at the same time leads to a ferromagnetic ordering that causes the abrupt increase in the *dc* data. This phenomenon is known to occur for acentric and chiral structures but the proposed antisymmetric exchange pathways for the previous systems might not be comparable to this particular system, since compound **2** owns an inversion center. Instead, this phenomenon may be also derived from a canted

arrangement between the individual spins of the metal ions in the layer with regard to the packing orientation, as it is the case for the present compound. We are currently studying this system by measuring the field-dependence of the $\chi_M T$ in the temperature region that the maximum appears, hysteresis loops, ZFC-FC measurements and dynamic magnetic properties, which will shed light in the origin of these magnetic properties.

3.3. Photocatalytic degradation of vanillic acid

Heterogeneous photocatalysis appears as one of the most destructive processes for organic contaminants under ambient conditions and by using solar energy. Preliminary tests were carried out over CPs materials as photocatalysts for the degradation of vanillic acid, VA (phenolic compound) in aqueous solution under UV-Vis irradiation. The results showed a higher absorption of the VA spectra at 60 min after UV-Vis irradiation (VA after irradiation, Compound 1 and VA after irradiation Compound 2, respectively) in comparison to the VA spectrum before irradiation (see Figure 8). More studies/strategies will be further required to promote the photocatalytic performance of these compounds such as modulation of their organic linkers/metal or integration with semiconductors, photosensitizers and so on.

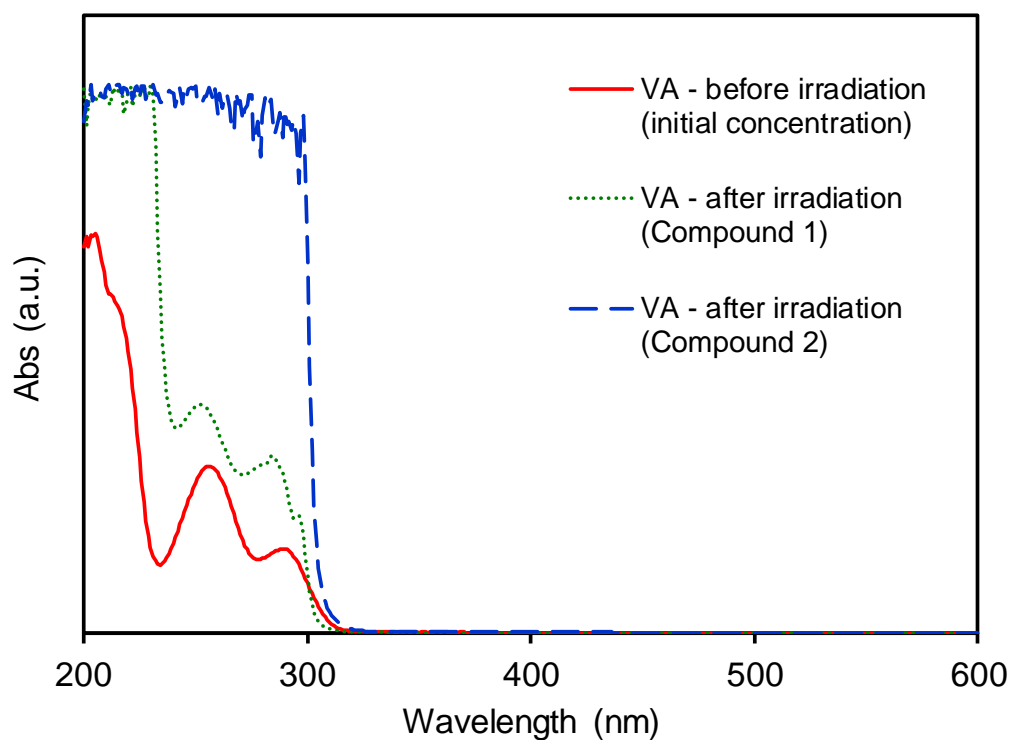


Figure 8. UV-visible absorption spectra of vanillic acid (VA) before irradiation and after UV-Vis irradiation at 60 min over both CPs materials.

3.4. *In vitro* antiparasitic activity

Taking into account the urgent need to find novel and effective drugs and the exploration of new paths in the search of improved therapies to fight Leishmaniasis, we have compared the activity of the two mentioned complexes (and the ligand) against several *Leishmania* spp. strains to that obtained with the commercial drug Glucantime (Table 6).

Table 6. *In vitro* activity of ligand (5-inca) and complex **1** and **2** against promastigote forms of *Leishmania* spp. and J774.2 macrophages after 72h of incubation.

Compound	IC ₅₀ (μM) ^a ± SD			Toxicity IC ₅₀ Macrophage (μM)	SI ^b		
	<i>L. infantum</i>	<i>L. braziliensis</i>	<i>L. donovani</i>		<i>L. infantum</i>	<i>L. braziliensis.</i>	<i>L. donovani</i>
Glucantime	18.0±3.1	25.6±1.7	26.6±5.4	15.2±1.0	0.8	0.6	0.6
Ligand	39.5±3.6	67.7±5.4	>200	>1000	25.3(32)	14.8(25)	5(8)
1	115.7±21.6	82.8±6.3	>200	>1000	8.6(11)	12.1(20)	5(8)
2	36.9±2.9	90.8±6.2	65.9±4.7	>1000	27.1(34)	11.1(18)	15.2(25)

The results presented are averages of three separate determinations. In brackets: number of times that ligand SI exceed the reference drug SI. ^aThe concentration required to obtain 50% inhibition, calculated through a linear regression analysis from the Kc values at the concentration employed (1, 10, 25 and 50 μM for promastigote forms of *Leishmania* spp. and 50, 100, 200 and 400 μM for macrophage host cells). ^bSelectivity index = IC₅₀ against J774.2 macrophages / IC₅₀ parasite (promastigote forms).

Regarding the antiproliferative assays against the promastigote forms of *Leishmania*, the two compounds and the ligand exhibited less inhibitory activity than the reference drug, Glucantime. It is indeed necessary at least to duplicate the concentration of the compounds to reduce by 50 % the parasite population, in comparison to the drug (Table 4 and Figure 7). Nevertheless, the excellent cytotoxicity data obtained with macrophage host cells resulted in very good SI coefficients in many of the studied cases. Focusing on *L. infantum* values, ligand and compound **2** present similar SI, increasing in more than 30 folds the Glucantime coefficients, which make them the best candidates to further biological tests *in vivo*. *L. braziliensis* turns out to be the more homogeneous series, with very similar SI results for the ligand and the two compounds. In the case of *L. donovani*, the ligand and complex **1** exhibited identical moderate activities while compound **2** showed very high efficacy. All the SI coefficients are also represented in Figure 9.

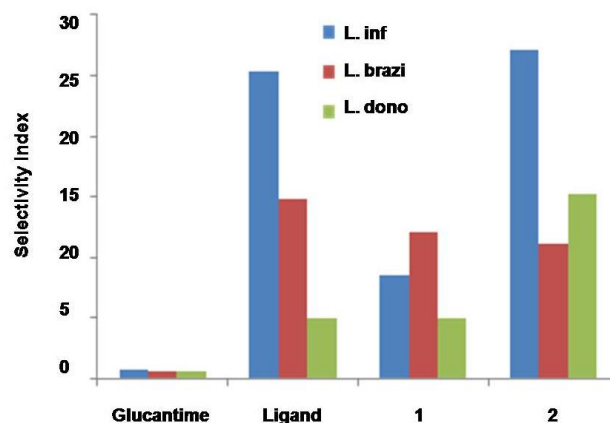


Figure 9. Comparative of SI values between Glucantime, ligand and complexes **1** and **2**. Selectivity index = IC_{50} against J774.2 macrophages / IC_{50} parasite (promastigote forms).

3.5. Cytotoxicity on Raw 264.7 cell line

Cytotoxicity (cell viability) of the ligand or compounds **1** and **2** was evaluated on RAW 264.7 murine macrophage cells to establish infra-cytotoxic concentrations. This is needed to assure that anti-inflammatory effects were due to an inflammatory process and not due to their intrinsic cytotoxicity. IC_{50} concentration (concentration causing 50% reduction growth) were $81,11 \pm 3,36$ for ligand, $54,07 \pm 6,95$ for compound **1** and $33,38 \pm 1,52$ for compound **2**. Also we have determined the compound concentrations required for 20% and 80% of growth inhibition (IC_{20} and IC_{80}) to analyse the complete range of cytotoxicity (Table 7).

Table 7. Growth-inhibitory effects of ligand, and compound **1** and **2** on RAW 264.7 monocyte/ macrophage murine cells.

Compound	IC_{20}	IC_{50}	IC_{80}
Ligand	$54,86 \pm 2,34$	$81,11 \pm 3,36$	$114,34 \pm 8,59$
1	$13,91 \pm 3,56$	$54,07 \pm 6,95$	$120,87 \pm 3,89$
2	$14,23 \pm 0,14$	$33,38 \pm 1,52$	$80,48 \pm 10,28$

The results showed that the compound **2** is more toxic than **1** and the free-ligand for the explored concentration range (0 to 100 $\mu\text{g}/\text{mL}$) (Figure 10).

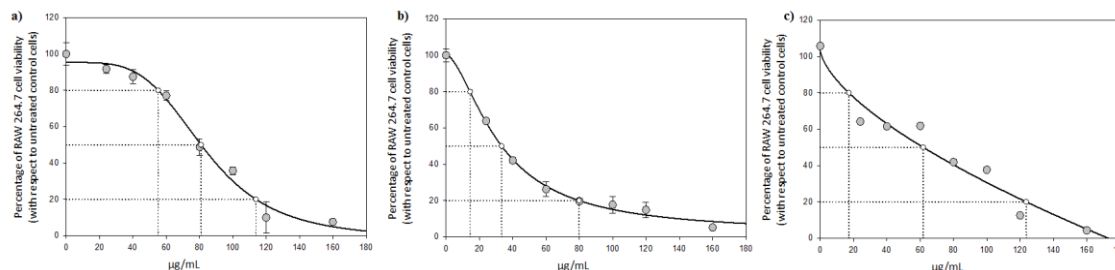


Figure 10. Effect of ligand (a), compound **2** (b) and compound **1** (c) on cell proliferation of RAW 264.7 macrophage murine cells. After treatment with the compounds in the range of concentration from 0 to 100 $\mu\text{g}/\text{mL}$, each point represents the mean value \pm S.D. of at least two independent experiments performed in triplicate. IC₂₀, IC₅₀, and IC₈₀ are the concentrations required for growth inhibition of 20%, 50% and 80%.

3.6. Nitro Oxide Production

In the inflammatory response process, nitric oxide, NO, is released as intermediate or second messenger. The enzymatic production of NO is cell-type specific, with cytokine-driven inducible nitric-oxide synthase (iNOS) noted initially for the burst of higher levels as part of the inflammatory activation process. RAW 264.7 murine macrophage cells produce the highest release of NO during the inflammatory response, being usually used a cell model for determining the anti-inflammatory activity of drug candidates (Figure 11). The anti-inflammatory activity of the compounds was analysed by measuring the nitrite concentration (which is proportional to the released NO) in the cell culture medium by the Griess method. Macrophages were activated with LPS during 24h after the addition of the compounds. Sub-cytotoxic concentrations corresponding to $\frac{3}{4}$ IC₅₀, $\frac{1}{2}$ IC₅₀, and $\frac{1}{4}$ IC₅₀ were used.

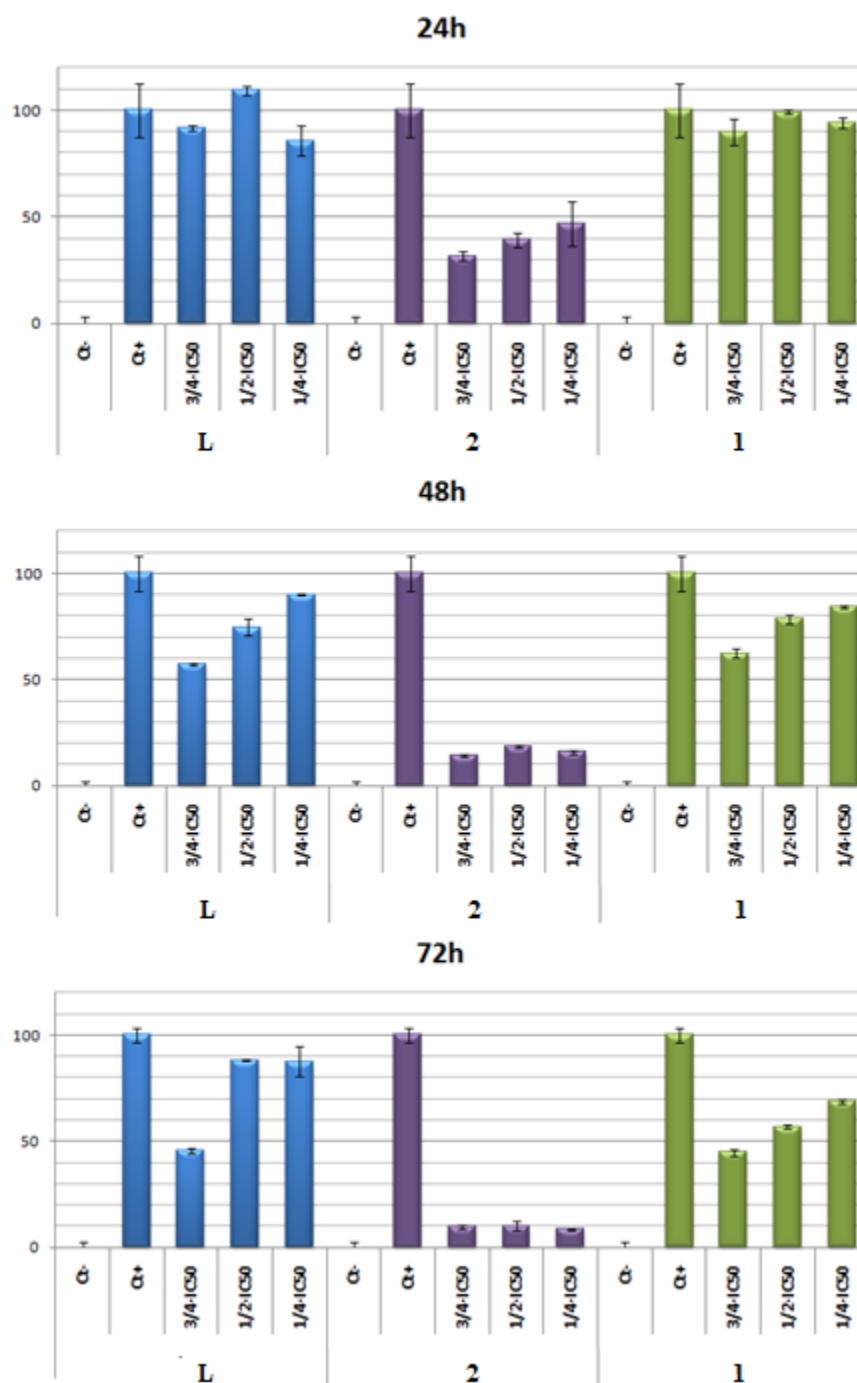


Figure 11. Effect of the ligand (L) and compounds 1 and 2 on the release of nitrites in RAW 264.7 macrophage murine cells. After activation of the inflammatory process by incubation with LPS for 24h, the compounds were incubated for 24, 48, 72h at concentrations of $3/4 \cdot IC_{50}$, $1/2 \cdot IC_{50}$, $1/4 \cdot IC_{50}$. The data represent the mean \pm S.D. of at least two independent experiments performed in triplicate.

After 24h of incubation, the higher anti-inflammatory effect was produced by compound 2, with a 68.35% of NO-inhibition with respect to the positive control (only LPS treated control cells) and negative control (untreated control cells), while

the ligand and compound **1** only showed 8.44% and 11.13% of NO-inhibition at 25 $\mu\text{g}/\text{mL}$ ($\frac{3}{4}$ IC_{50} concentration). At 48h of incubation the compound **2** produced high inhibition of NO production, being around 85% in all the concentrations assayed. At this time point, the ligand produced inhibited by 40% at $\frac{3}{4}$ IC_{50} concentration. The inhibition effects of compound **1** were very similar to those of the ligand. After 72h, the inhibition was, in general, more pronounced than at 48 hours, the compound **2** producing an inhibition of 90% irrespectively of the concentration. The treatment with the ligand inhibited by 60% the NO release at $\frac{3}{4}$ IC_{50} concentration, and the compound **1** also produced NO release inhibition similar to the ligand at the same concentration.

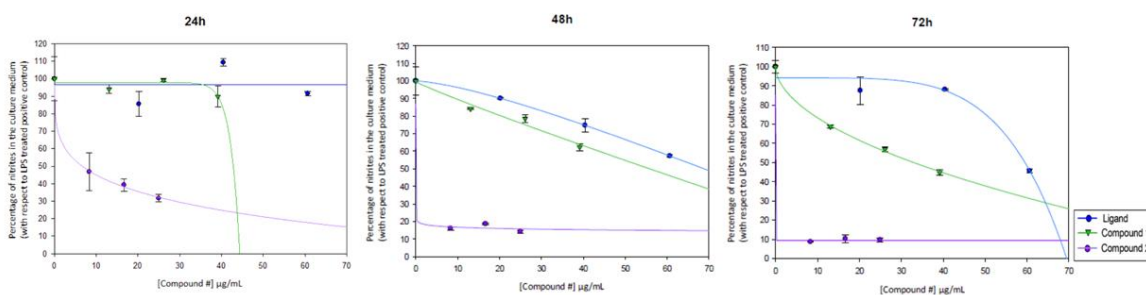


Figure 12. Sigmoidal curves of the effect of the ligand and compounds **1** and **2** on the release of nitrites in RAW 264.7 macrophage murine cells. It can be seen that the curves corresponded to metal compound complex **2** ($\text{IC}_{50\text{24h NO}} = 7.74 \pm 3.78 \mu\text{g}/\text{mL}$; $\text{IC}_{50\text{48h NO}} = 1.15 \pm 0.01 \mu\text{g}/\text{mL}$; $\text{IC}_{50\text{72h NO}} = 0.57 \pm 0.18 \mu\text{g}/\text{mL}$) are below to the ligand and the compound **1**. The data represent the mean \pm S.D. of at least two independent experiments performed in triplicate.

To complete the anti-inflammatory effect of compound **2**, we calculated the concentration to reduce by 50% the production of NO ($\text{IC}_{50\text{NO}}$) at the time assayed (Figure 12). The results showed that the $\text{IC}_{50\text{NO}}$ of the compound **2** were lower than the $\text{IC}_{50\text{NO}}$ of the compound **1** and the ligand. The $\text{IC}_{50\text{NO}}$ for the compound **2** were $7.74 \pm 3.78 \mu\text{g}/\text{mL}$ at 24h, $1.15 \pm 0.01 \mu\text{g}/\text{mL}$ at 48h, and $0.57 \pm 0.18 \mu\text{g}/\text{mL}$ at 72h. For compound **1** values of $42.59 \pm 0.42 \mu\text{g}/\text{mL}$ at 24h, $55.8 \pm 4.7 \mu\text{g}/\text{mL}$ at 48h and $32.99 \pm 1.53 \mu\text{g}/\text{mL}$ at 72h. The $\text{IC}_{50\text{NO}}$ of the ligand was only measurable at 48h ($68.83 \pm 4.22 \mu\text{g}/\text{mL}$) and 72h ($59.51 \pm 0.16 \mu\text{g}/\text{mL}$). In summary, the compound **2** was more effective than the ligand and compound **1** at all the times and concentrations assayed (Figure 10 and Figure 13). Significant differences ($p \leq 0.001$)

were found between the IC_{50NO} of the ligand and the compound **2** at 48 and 72h, and with the ligand and compound **1** at 72h of treatment (Figure 13).

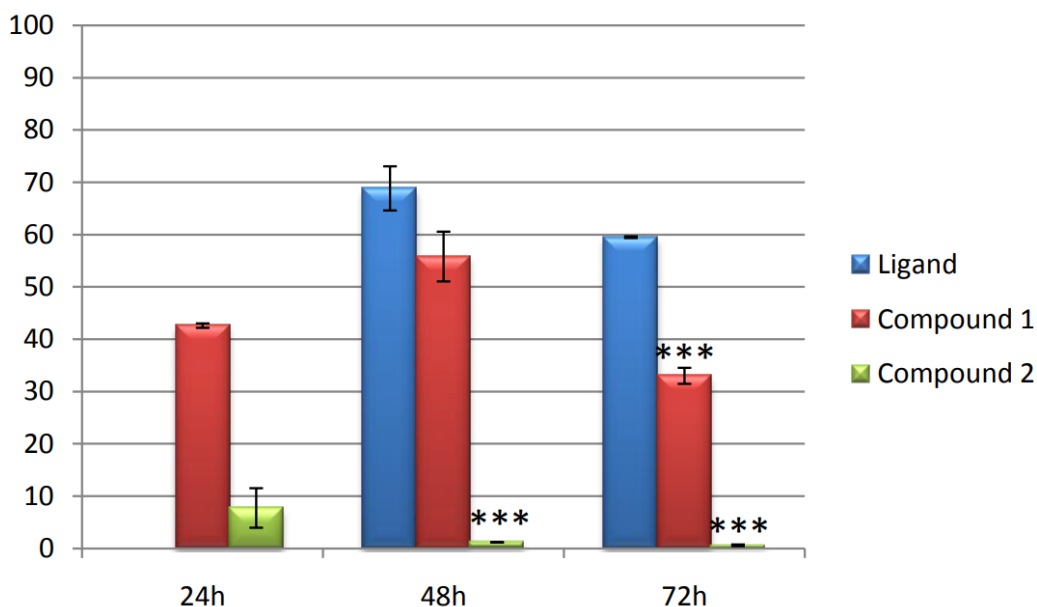


Figure 13. IC_{50NO} values for the ligand and the compound 1 and 2 at 24h, 48h and 72h of treatment. Key: $p < 0.05$ (*), $p \leq 0.01$ (**), and $p \leq 0.001$ (***) , respect to results obtained for the ligand.

4. Conclusion

We report the formation of two novel multifunctional isomorphous (4,4) square-grid 2D coordination polymers based on 1H-indazole-5-carboxylic acid. To the best of our knowledge, these complexes are the second and third examples of coordination compounds construct with this novel ligand. These materials were synthesized by soft solvothermal routes, possess different 2D-structures and show interesting magnetic and biological properties. Despite no synergetic effect was observed in the antiparasitic selectivity, ligand and complex **2** show promising values against *L. braziliensis* and *L. donovani* respectively, and especially against *L. infantum* in both cases, making them good candidates for further intracellular studies. Compound **2** produced anti-inflammatory effects at all the assayed times, 24, 48, 72h, with the higher percentage of NO inhibition release being close to 90%. Compound **1**

and ligand only induced anti-inflammatory effects after 72h of treatment, with a NO inhibition release of the 60%, being the compound **1** a little more effective than the ligand. With respect to the IC_{50NO} the concentration found for the compound **2** were one or two orders lower than concentrations found for the compound **1** and the ligand. In conclusion the compound **2** was more effective as anti-inflammatory than the ligand or compound **1**. The formation of metal complexes with bioactive ligands is a new and promising strategy to find new compounds with high and enhanced biochemical properties.

5. References

- [1] H.-Y. Li, Y.-L. Wei, X.-Y. Dong, S.-Q. Zang and T. C. W. Mak, *Chem. Mater.* 27 (2015) 1327–1331.
- [2] J.-Z. Gu, Y. Cai, Z.-Y. Qian, M. Wen, Z.-F. Shi, D.-Y. Lv, A. M. Kirillov, *Dalton Trans.* 47 (2018) 7431-7444.
- [3] E. San Sebastian, A. Rodríguez-Diéguez, J. M. Seco, J. Cepeda, *Eur. J. Inorg. Chem.* 2018 (2018) 2155-2174.
- [4] S. N. Nobar, *Mater. Chem. Phys.* 213 (2018) 343-351.
- [5] I. Abánades-Lázaro, R. S. Forgan, *Coordin. Chem. Rev.* 380 (2019) 230-259.
- [6] O. Abuzalat, D. Wong, M. Elsayed, S. Park, S. Kim, *Ultrason. Sonochem.* 45 (2018) 180-188.
- [7] J. Cepeda, S. Pérez-Yáñez, G. Beobide, O. Castillo, J. A. García, A. Luque, *Eur. J. Inorg. Chem.* 2015 (2015) 4318-4328.
- [8] N. Stock, S. Biswas, *Chem. Rev.* 112 (2012) 933-969.
- [9] P. Cubillas, M. W. Anderson, M. P. Attfield, *Chem. Eur. J.* 18 (2012) 15406-1541.
- [10] L. J. Murray, M. Dinca, J. R. Long, *Chem. Soc. Rev.* 38 (2009) 1294–1314.

- [11] C. Ruiz, A. A. García-Valdivia, B. Fernandez, J. Cepeda, I. Oyarzaval, E. Abas, M. Laguna, J. A. García, I. Fernandez, E. San Sebastián, A. Rodríguez-Diéguez, *CrystEngComm*. 21 (2019) 3881-3890.
- [12] F. A. Alemida-Paz, J. Klinowski, S. M. F. Vilela, J. P. C. Tomé, J. A. S. Cavaleiro, J. Rocha, *Chem. Soc. Rev.* 41(2012) 1088–1110.
- [13] I.-H. Choi, Y. Kim, D. Lee, S. Huh, *Polyhedron*. 155(2016) 96-103.
- [14] J.-H. Gu, W.-X. Li, H.-X. Li, H.-Y. Li, J.-P. Lang, *Polyhedron*. 154 (2018) 47-53.
- [15] M. Kurmoo, *Chem. Soc. Rev.* 38 (2009) 1353–1379.
- [16] B.V. De Voorde, B. Bueken, J. Denayer, J. Vos, *Chem. Soc. Rev.* 43 (2014) 5766-5788.
- [17] J. Cepeda, A. Rodríguez-Diéguez, *CrystEngCom*. 18 (2016) 8556–8573.
- [18] A. A. García-Valdivia, J. M. Seco, J. Cepeda, A. Rodríguez-Diéguez, *Inorg. Chem.* 56 (2019) 13897-13912.
- [19] C. S. Hawes, R. Babarao, M. R. Hill, K. F. White, B. F. Abrahams, P. E. Kruger, *Chem. Commun.* 48 (2012) 11558-11560.
- [20] C. S. Hawes and P. E. Kruger, *Dalton Trans.* 43(2014) 16450-16458.
- [21] C. S. Hawes, P. E. Kruger, *RSC Adv.* 4 (2014) 15770-15775.
- [22] H. Xiao, X.-B. Li, G.-F. Qin, Y. Xia, G. Zhou, *J. Iran. Chem. Soc.* 13 (2016) 793-802.
- [23] J. M. Méndez-Arriaga, I. Oyarzabal, G. Escolano, A. Rodríguez-Diéguez, M. Sánchez-Moreno and J. M. Salas, *J. Inorg. Biochem.* 180 (2018) 26–32.
- [24] A. B. Caballero, A. Rodríguez-Diéguez, L. Lezama, and J. M. Salas, *Cryst. Growth Des.* 12 (2012) 3583–3593.

- [25]. A.B. Caballero, A. Rodríguez-Diéguez, M. Quirós, J.M. Salas, O. Huertas, I. Ramírez-Macías, F. Olmo, C. Marín, G. Chaves-Lemaur, R. Gutierrez-Sanchez, M. Sanchez-Moreno, *Eur. J.Med.Chem.* 85 (2014) 526-534.
- [26] A.B. Caballero, J.K. MacLaren, A. Rodríguez-Diéguez, I. Vidal, J.A. Dobado, J.M. Salas, C. Janiak, *Dalton Trans*, 40 (2011) 11845–11855.
- [27] A.B. Caballero, A. Rodríguez-Diéguez, E. Barea, M. Quiros, J.M. Salas, *CrystEngComm*.12 (2010) 3038–3045.
- [28] B. Fernández, A. Gómez-Vílchez, C. Sánchez-González, J. Bayón, E. San Sebastian, S. Gómez-Ruiz, C. López-Chaves, P. Aranda, J. Llopis, A. Rodríguez-Diéguez. *New J. Chem.*40 (2016) 5387-5393.
- [29] D. Briones, B. Fernández, A.J.Calahorro, D.Fairen-Jimenez, R.Sanz, F.Martínez, G. Orcajo, E.S. Sebastián, J.M. Seco, C.S. González, J. Llopis and A. Rodríguez-Diéguez, *CrystGrowth Des.*16 (2016) 537–540.
- [30] C.S.Hawes, R.Babarao, M.R.Hill, K.F.White, B.F.Abrahams, P.E.Kruger, *Chem.Commun.* 48 (2012) 11558-11560.
- [31] A.A. Mieloch, M. Zurawek, M. Giersig, N. Rozwadowska and J.D. Rybka, *Sci. Rep.*, 10 (2020), 2725.
- [32] L. Botana, J. Ruiz, J.M. Seco, A.J. Mota, A. Rodríguez-Diéguez, R.Sillanpääand E.Colacio, *Dalton Trans*, 40 (2011), 12462-12471.
- [33] M.A. Palacios, A. Rodríguez-Diéguez, A. Sironi, J.M. Herrera, A.J. Mota, J. Cano and E. Colacio, *Dalton Trans*, (2009) 8538-8547.
- [34] Q.-Q. Xiao, D. Liu, Y.-L. Wei, G.-H. Cui, *Polyhedron*. 158 (2019) 342-351.
- [35] J. Huo, D. Yu, H. Li, B. Luo, N. Arusamy, *RSC Adv.* 9 (2019) 39323-39333.
- [36] Y.-H. Qu, Y.-J. Yang, G.-Y- Dong. *Polyhedron*.180 (2020) 114431-114438.
- [37] J. Jansen, W. Karges, L. Rink, *J. Nutr. Biochem.* 20 (2019) 399–417.
- [38] X.-T. Xin, X.-K. Wang, *J. Struct. Chem.* 60 (2019) 1850-1856.

- [39] G. Psomas, D. P. Kessissoglou, *Dalton Trans.* 42 (2013) 6252-6276.
- [40] C. N. Banti, S. K. Hadjikakou, *Eur. J. Inorg. Chem.* 2016 (2016) 3048-3071.
- [41] L. Sun, L-Y. Sha, J. Jiang, *Biomed. Res.-India.* 28 (2017) 2152-2155.
- [42] Y. Zeng, T. Xu, *Lat Am J Pharm.* 35 (2016) 1228-1233.
- [43] L. Boiani, A. Gerpe, V. J. Arán, S. Torres de Ortiz, E. Serna, N. Vera de Bilbao, L. Sanabria, G. Yaluff, H. Nakayama, A. Rojas de Arias, J. D. Maya, J. A. Morello, H. Cerecetto, M. González, *Eur. J. Med. Chem.* 44 (2009) 1034-1040.
- [44] C. Marín, I. Ramírez-Macías, M. J. Rosales, B. Muro, F. Reviriego, P. Navarro, V. J. Arán, M. Sánchez-Moreno, *Acta Trop.* 148 (2015) 170-178.
- [45] A. Cavalli, M.-L. Bolognesi, *J. Med. Chem.* 52 (2009) 7339-7359.
- [46] Y. C. Ong, S. Roy, P. C. Andrews, G. Gasser, *Chem. Rev.* 119 (2019) 730-796.
- [47] S. Espuelas, D. Plano, P. Nguewa, M. Font, J. A. Palop, J. M. Irache, C. Sanmartín, *Curr. Me. Chem.* 19 (2012) 4259-4288.
- [48] H. Yki-Järvinen, R. Bergholm, M. Leirisalo-Repo, *Ann Rheum Dis* 62 (2003) 630-634.
- [49] Bruker Apex2, Bruker AXS Inc., Madison, Wisconsin, USA, 2004.
- [50] G. M. Sheldrick, SADABS, Program for Empirical Adsorption Correction, Institute for Inorganic Chemistry, University of Göttingen, Germany, 1996.
- [51] G. M. Sheldrick, SHELX-2014, Program for Crystal Structure Refinement, University of Göttingen, Göttingen, Germany, 2014.
- [52] L. J. Farrugia, *J. Appl. Crystallogr.* 32 (1999) 837-838.
- [53] P. González, C. Marín, I. Rodríguez-González, A.B. Hitos, M.J. Rosales, M. Reina, J.G. Díaz, A. González-Coloma, M. Sánchez-Moreno, *Int. J. Antimicrob. Agent.* 25 (2005) 136-141.
- [54] N.S. Bryan, M.B. Grisham, *Free Radic Biol Med.* 43 (2007) 645-657.

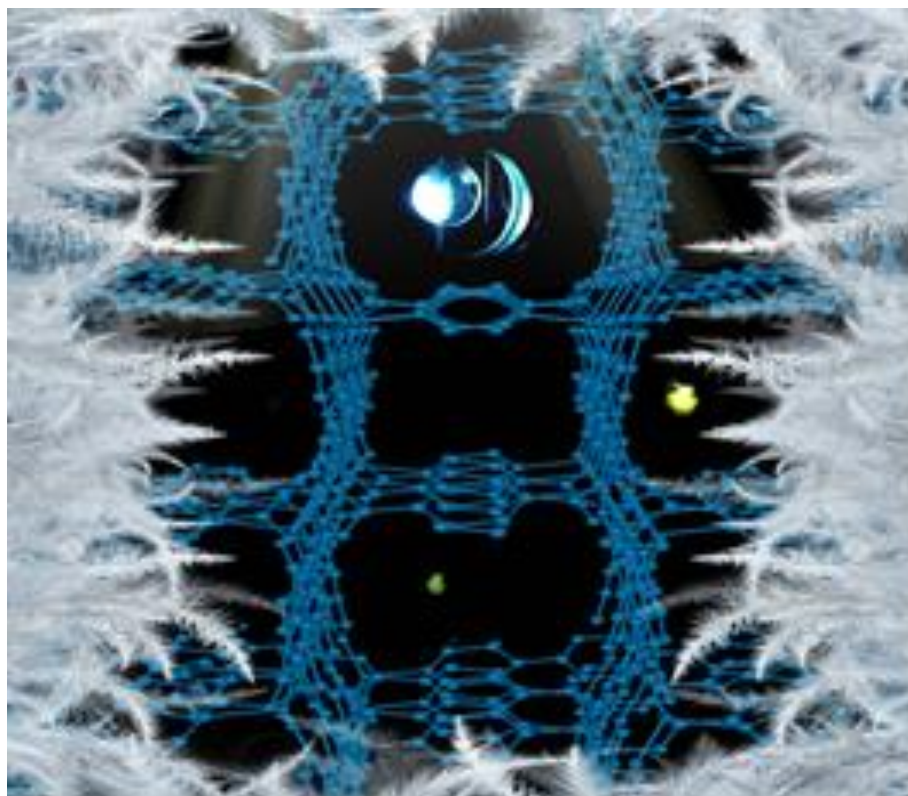
ANTONIO ANDRÉS GARCÍA VALDIVIA

[55] R. Boca, *Coord. Chem. Rev.* 248 (2004) 757–815.

[56] T. Moriya, *Phys. Rev.* 120 (1960) 91.

Capítulo 10

Interpenetrated Luminescent Metal-Organic Frameworks based on 1H-Indazole-5-Carboxylic Acid



Interpenetrated Luminescent Metal–Organic Frameworks based on 1H-Indazole-5-Carboxylic Acid



pubs.acs.org/crystal

Article

1 Interpenetrated Luminescent Metal–Organic Frameworks based on 2 1H-Indazole-5-carboxylic Acid

³ Antonio A. García-Valdivia, Manuel Pérez-Mendoza, Duane Choquesillo-Lazarte, Javier Cepeda,*

⁴ Belén Fernández, Manuel Souto, Marcos González-Tejero, Jose A. García,

⁵ Guillermo Mínguez Espallargas,* and Antonio Rodríguez-Diéguez*



Cite This: <https://dx.doi.org/10.1021/acs.cgd.0c00345>



Read Online

Abstract

Herein we report the formation and characterization of two novel Zn-based multifunctional metal-organic frameworks (MOFs) based on 1H-indazole-5-carboxylic acid and bipyridine-like linkers, synthesized by soft solvothermal routes. These materials possess isorecticular two-fold interpenetrated 3D-structures which afford a flexible character and allow porosity modulation of the MOFs as confirmed by CO₂ sorption measurements. Apart from this attractive structural feature, the MOFs exhibit fascinating luminescent properties involving both luminescence thermometry and long-lasting phosphorescence.

1. Introduction

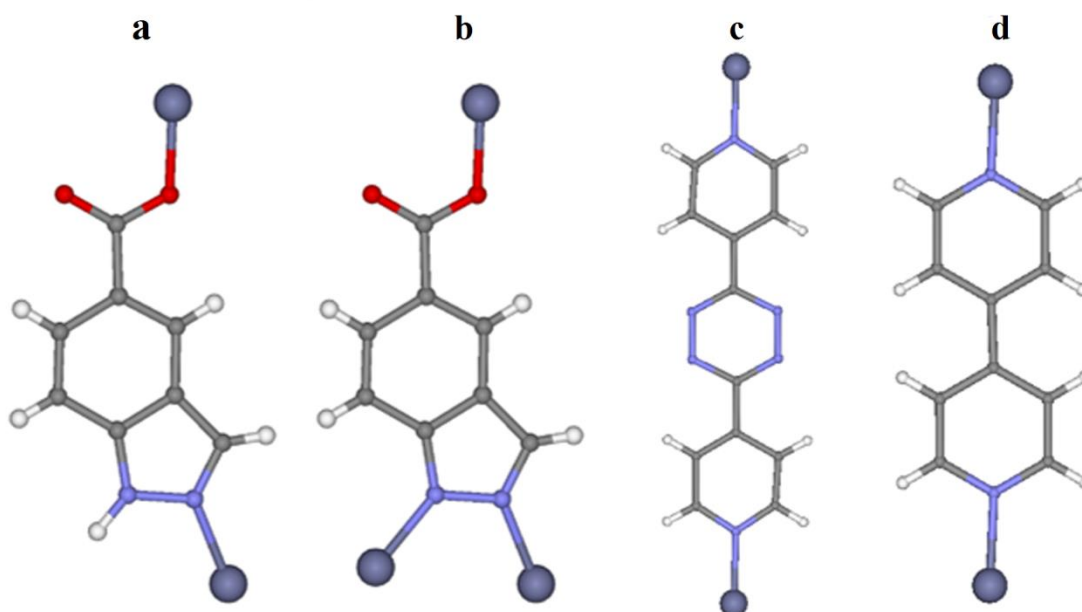
The development of novel functional porous materials is one major point towards the sustainable development of our society and should deal with an optimum performance for the capture, separation and storage of different types of gases at industrial level.¹⁻³ In this sense, much efforts have been devoted to produce selective adsorbents for purifying and separating CO₂ in the mixture resulting from a gasification process.⁴⁻⁹ One important research field that has emerged during the last

two decades has mainly focused on the design and synthesis of new metal-organic frameworks (MOFs), also called porous coordination polymers (PCPs), which are materials constituted by organic ligands coordinated to metal ions or clusters defining a porous and crystalline network with structural diversities as a consequence of their modular nature and, consequently, functional properties. Therefore, MOFs cover multiple fields of applications in addition to adsorption, such as magnetism, luminescence, electronics, catalysis or medicine.^{10,11} An interesting synthetic strategy to achieve an optimal structure to enhance the gas storage or separation performance is based on the modulation of the size and type of pore in a rational way, by using different ligands that present small structural changes (i.e. the size or shape) to yield topologically similar polymeric materials but with small pore changes. In this sense, the resulting materials may present small modifications that could be, in turn, related to other properties such as luminescence.¹² The enormous family of excellent porous materials synthesized from bipyridine ligands are good examples of such precise pore design and control.^{13,14}

Photoluminescence (PL) properties of MOFs have received a lot of interest during the last decade not only because of their large applicability in solid-state lighting materials (light-emitting devices (LEDs), long lasting phosphors (LLPs), and so on)¹⁵⁻¹⁷ but also towards sensing applications due to the celerity of the process. In this last particular case, when luminescent emission is coupled to a physical change such as the temperature, MOFs allow for a rapid detection of that magnitude.¹⁸⁻²⁰ A main reason for such behaviour is due to the fact that temperature is a key factor in MOFs that governs the non-radiative quenching originated at the molecular vibrations of ligands and, in turn, it brings structural changes of variable magnitude depending on the flexibility of the framework. PL in MOFs takes advantage of their hybrid metal-organic structure since the emissions may involve different components: ligand centred (LC) and metal centred (MC) charge transfer (CT) processes between them, or related to the adsorption of guest molecules (which could be exploited for PL detection).²¹ However, most of luminescent MOFs used as thermometers are based on lanthanide metals,¹⁸⁻²² which present some disadvantages such as reduced resources availability and environmental concerns. For this reason, another promising strategy for the design on luminescent MOFs for thermometry argues for the use of organic ligands with strong absorption (usually molecules with

chemical functions containing heteroatoms with lone-pairs) combined with metal ions with closed-shell electronic configuration, which avoid non-radiative quenching.^{23,12}

Taking these considerations into account, we selected two different bipyridine ligands and 1H-indazole-5-carboxylic acid (5-incaH₂) as main ligand, with the aim of obtaining new three-dimensional MOFs. In relation to the latter ligand, there are only few examples of coordination polymers based on copper in which this ligand is acting as a bidentate ligand participating as monoanionic linker (Scheme I, left).²⁴ Regarding the bipyridine ligands, we have chosen the 4,4-bipyridyl (4,4-bipy) and the 3,6-bis(4-pyridyl)-1,2,4,5-tetrazine (pbptz) as linkers due to the presence of pyridine and tetrazine rings that favor the enhancement of the luminescent properties of the resulting coordination polymers,^{25,26} and due to their high potential to build open architectures as a result of the length of the spacer and the disposition of the donor atoms. On the other hand, the linkage of the ligands to metal atoms with a high coordination plasticity, such as zinc (II), opens the way to synthesize materials with not only possible dynamics in the crystal structures but also interesting photoluminescence properties.¹² Moreover, the existence of a second type of ligand that combines benzene with pyrazole rings may modify the initial properties of these systems, generating MOFs with tunable luminescent properties in which the emission of the materials in response to the temperature can be analyzed in order to study their potential use as thermometers, as seen in previous studies conducted on zinc and pyrazole based coordination polymers.²⁷



Scheme I. Coordination modes of (5-inca)⁻ (a) (5-inca)²⁻ (b), pbptz (c) and 4,4-bipy (d).

Therefore, we report herein the synthesis and characterization of a novel family of Zn²⁺ coordination polymers based on the novel 1H-indazole-5-carboxylic acid, {[Zn(5-inca)(pbptz)_{0.5}]·1.5DMF}_n (**1**) and {[Zn(5-inca)(4,4-bipy)_{0.5}]·DMF}_n (**2**). In these compounds, (5-inca)²⁻ ligand shows a new coordination mode (Scheme I, right), by which is coordinated to Zn ions through two nitrogen and one oxygen pertaining to the pyrazole ring and the carboxylate group, respectively. Both materials possess open structures despite the occurrence of interpenetration and are able to adsorb CO₂ with tunable sorption capacities. Photoluminescence measurements together with TD-DFT calculations have been performed in order to verify the origin of the emissions occurring when these ligands are coordinated to d¹⁰ transition metal ion in the MOFs. Moreover, the emission of the materials in response to the temperature has been analyzed in order to study their potential utility as thermometers due to the presence of pyrazole rings and zinc ions in the frameworks.²⁷

2. Experimental Procedures

Chemicals. All the chemicals were of reagent grade and were used as commercially obtained.

Synthesis of $\{[\text{Zn}(\text{5-inca})(\text{pbptz})_{0.5}]\cdot 1.5 \text{ DMF}\}_n$ (1**).** 0.12 mmol (20.00 mg) of 1H-indazole-5-carboxylate and 0.06 mmol (14.17 mg) of 3,6-di(4-pyridinyl)-1,2,4,5-tetrazine were dissolved in 0.5 mL of DMF and then 0.5 mL of distilled water was added. On the other hand, 0.12 mmol (22.02 mg) of zinc acetate was dissolved in 0.5 mL of distilled water and afterward 0.5 mL of DMF was added. Both solutions were mixed and the resulting solution was placed in a closed glass vessel and heated in an oven at 95°C for 24h. Pink single crystals were grown during the heating procedure under autogenous pressure, which were filtered off and collected at open atmosphere and washed with water. Yield: 38% based on zinc. Anal. Calcd. for $\text{ZnC}_{17}\text{H}_{15}\text{N}_6\text{O}_3$: C, 49.00; H, 3.63; N, 20.17. Found: C, 48.23; H, 3.31; N, 20.49%.

Synthesis of $\{[\text{Zn}(\text{5-inca})(\text{4,4-bipy})_{0.5}](\text{DMF})\}_n$ (2**).** Well-shaped yellow single crystals of **2** were obtained after carrying out the same general procedure described for **1** but replacing 3,6-di(4-pyridinyl)-1,2,4,5-tetrazine by 4,4'-bipyridil (9.37 mg). Yield: 45% based on zinc. Anal. Calcd. for $\text{ZnC}_{16}\text{H}_{15}\text{N}_4\text{O}_3$: C, 51.01; H, 4.01; N, 14.87. Found: C, 50.86; H, 3.98; N, 14.95%.

Physical Measurements. Elemental analyses (C, H, N) were performed on an Euro EA Elemental Analyzer. FTIR spectra (KBr pellets) were recorded on a Nicolet IR 6700 spectrometer in the 4000–400 cm^{-1} spectral region. Thermogravimetric analysis was carried out using a Mettler Toledo TGA/SDTA 851 apparatus in the 25–600°C temperature range with a 10°C min^{-1} scan rate and a N_2 flow of 30 mL min^{-1} . High pressure adsorption isotherms have been measured in a non-commercial volumetric adsorption instrument (University of Granada) equipped with two Baratron absolute pressure transducers (MKS type 627B). Their pressure ranges are from 0 to 133.33 kPa and from 0 to 3333.25 kPa, respectively, and the reading accuracy is 0.05% of the usable measurement range. Prior to measurement, powder samples were heated at 393 K for 12h and outgassed to 10^{-5} Torr. All gases

employed were supplied by Air Liquide with a purity of at least 99.998%. A closed cycle helium cryostat enclosed in an Edinburgh Instruments FLS920 spectrometer was employed for steady state photoluminescence (PL) and lifetime measurements at variable temperature. All samples were first placed under high vacuum (of ca. 10^{-9} mbar) to avoid the presence of oxygen or water in the sample holder. For steady-state measurements a Müller-Elektronik-Optik SVX1450 Xe lamp or an IK3552R-G He-Cd continuous laser (325 nm) were used as excitation source, whereas a microsecond pulsed lamp was employed for recording the lifetime measurements. Photographs of irradiated single-crystals and polycrystalline samples were taken at room temperature in a micro-PL system included in an Olympus optical microscope illuminated with a Hg lamp. Time-resolved emission spectra were recorded using excitation and emission band-pass of 5 nm and 2.5 nm, respectively.

X-ray Diffraction. The X-ray intensity data were collected on a Bruker D8 Venture diffractometer using Mo-K α radiation at 100(2) K. The data were integrated with SAINT²⁸ and corrected for absorption effects with SADABS.²⁹ The crystal structures were solved with SHELXT³⁰ and refined with SHELXL.³¹ The OLEX2 software was used as a graphical interface.³² Anisotropic atomic displacement parameters were introduced for all non-hydrogen atoms. Hydrogen atoms were placed at geometrically calculated positions and refined with the appropriate riding model, with $U_{iso}(H) = 1.2 U_{eq}(C)$. Even though crystal data was collected up to 0.77Å, crystals still diffracted quite weakly at high angle due to their rather low quality and data were cut off according to intensity statistics (compound **1**), using restraints and constraints during refinement. In compound **1**, the 4-pyridyl moiety of pbptz ligand was found disordered over two alternative positions (0.56:0.44 ratio), and was refined with rigid groups and restraints on geometry and displacement parameters. In the case of compound **2**, the 4-pyridyl moiety of 4,4-bipy ligand also was found disordered over two alternative positions (0.56:0.44 ratio), and was refined with rigid groups and restraints on geometry and displacement parameters. Disorder of the ligands was modeled using AFIX (compound **1**) or FLAT (compound **2**) commands. For all compounds, a number of RIGU and ISOR restraints had to be used to obtain reasonable displacement parameters for selected non hydrogen atoms.

Their U_{ij} values were therefore restrained to be approximately spherical. In both compounds, severely disordered DMF molecules could not be modeled reasonably and were therefore removed from the diffraction data (using the OLEX2 Mask tool) but considered for calculation of empirical formula, formula weight, density, linear absorption coefficient and $F(000)$. Crystal data and refinement details are listed in Table 1. Crystallographic data for the structures reported in this paper have been deposited with the Cambridge Crystallographic Data Center as supplementary publication nos. CCDC 1942013-14 for compounds. Copies of the data can be obtained free of charge on application to the Director, CCDC, 12 Union Road, Cambridge, CB2 1EZ, U.K. (Fax: +44-1223-335033; e-mail: deposit@ccdc.cam.ac.uk or <http://www.ccdc.cam.ac.uk>).

Table 1. Crystallographic data and structure refinement details for all compounds.

Compound	1	2
Chemical formula	$C_{17}H_{15}N_6O_3Zn$	$C_{16}H_{15}N_4O_3Zn$
CCDC	1942013	1942014
M/g mol⁻¹	452.27	376.69
T/K	100	100
Cryst. syst.	Monoclinic	Orthorhombic
Spacegroup	$C2/c$	$Pccn$
<i>a</i> (Å)	16.6227 (11)	16.8684 (9)
<i>b</i> (Å)	17.9748 (13)	12.9147 (7)
<i>c</i> (Å)	13.8372 (10)	14.8470 (7)
β (°)	98.135 (3)	90
<i>V</i> Å³	4092.8 (14)	3234.4 (3)
<i>Z</i>	8	8
ρ/g cm⁻³	1.471	1.547
μ/mm⁻¹	1.236	1.541
<i>S</i>(GOF)	1.046	1.162
<i>R</i>[1>2σ(I)]^a	0.0729	0.0729
<i>wR</i>² [1>2σ(I)]^b	0.1858	0.1376

[a] $S = [\sum w(F_o^2 - F_c^2)^2 / (N_{obs} - N_{param})]^{1/2}$ [b] $R_1 = \sum ||F_o| - |F_c|| / \sum |F_o|$ [c] $wR_2 = [\sum w(F_o^2 - F_c^2)^2 / \sum wF_o^2]^{1/2}$
 $w = 1/[\sigma^2(F_o^2) + (aP)^2 + bP]$ where $P = (\max(F_o^2, 0) + 2F_c^2)/3$

Computational details. PL spectra were calculated by means of TD-DFT using the Gaussian 09 package,³³ using the Becke three parameter hybrid functional with the non-local correlation functional of Lee-Yang-Parr (B3LYP)³⁴⁻³⁶ along with 6-311G++(d,p) basis set³⁷ was adopted for all atoms but for the central zinc cation, for which the LANL2DZ³⁸⁻⁴⁰ basis set along with the corresponding effective core potential (ECP) was used. The 40 lowest excitation states were calculated by the TD-DFT method. Results were analyzed with GaussSum program package⁴¹ and molecular orbitals plotted using GaussView 5.⁴²

3. Results and Discussion

The solvothermal reaction between 1-H-indazole-5-carboxylic acid and the corresponding pyridine derivative ligand, with zinc acetate in H₂O:DMF, produces two new MOF materials (**1** and **2**) based on dimeric Secondary Building Units, in which the structures present interpenetration. Activation of MOFs **1** and **2** was performed by heating the washed material at 150 °C for 2h. Crystallinity of desolvated materials was confirmed by Powder X-ray Diffraction (PXRD) (Figs. 1a and 1b) whereas thermogravimetric analysis (TGA) was consistent with the elimination of solvent molecules (Figs. 2a and 2b).

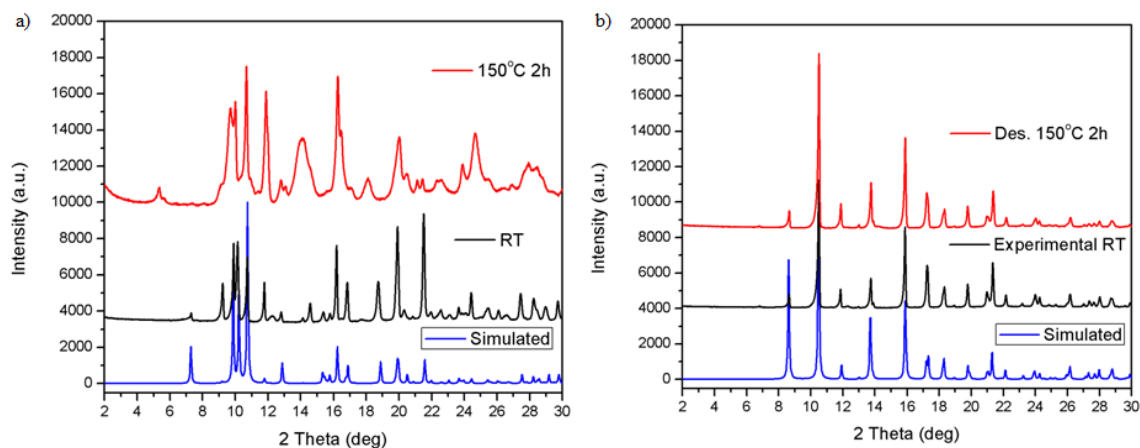


Figure 1. (a) Powder X-ray diffraction patterns of simulated, experimental and desolvated sample (2h at 150 °C) of **1**. (b) Powder X-ray diffraction patterns of simulated, experimental and desolvated sample (2h at 150 °C) of **2**.

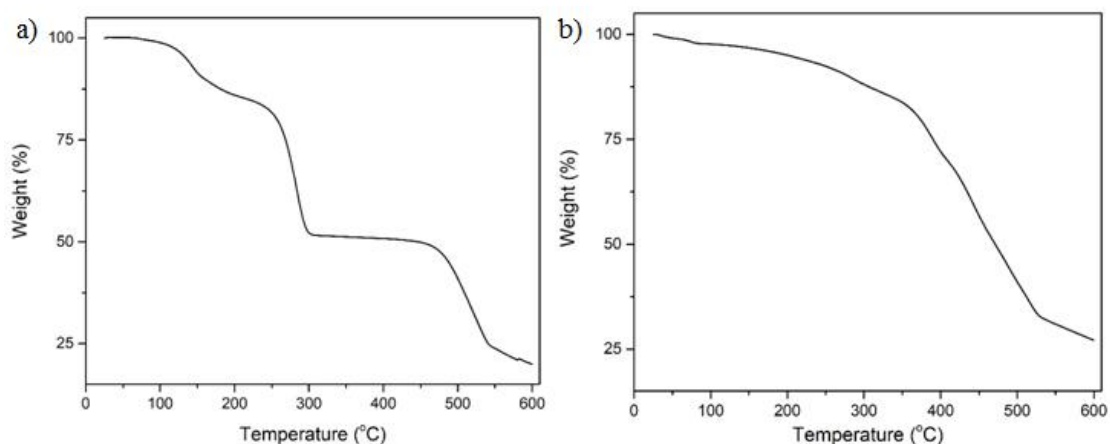


Figure 2. (a) Thermogravimetric analysis (TGA) profile of **1** at a heating rate of 5 °C/min under a constant stream of N₂. (b) Thermogravimetric analysis (TGA) profile of **2** at a heating rate of 5 °C/min under a constant stream of N₂.

3.1. Structural description of {[Zn(5-inca)(pbptz)_{0.5}](DMF)}_n (**1**).

Compound **1** crystallizes in the *C2/c* monoclinic space group, and the crystal structure consists on zinc(II) atoms linked through pbptz and (5-inca)²⁻ co-ligands, which afford large connectivity resulting in an open 3D framework.

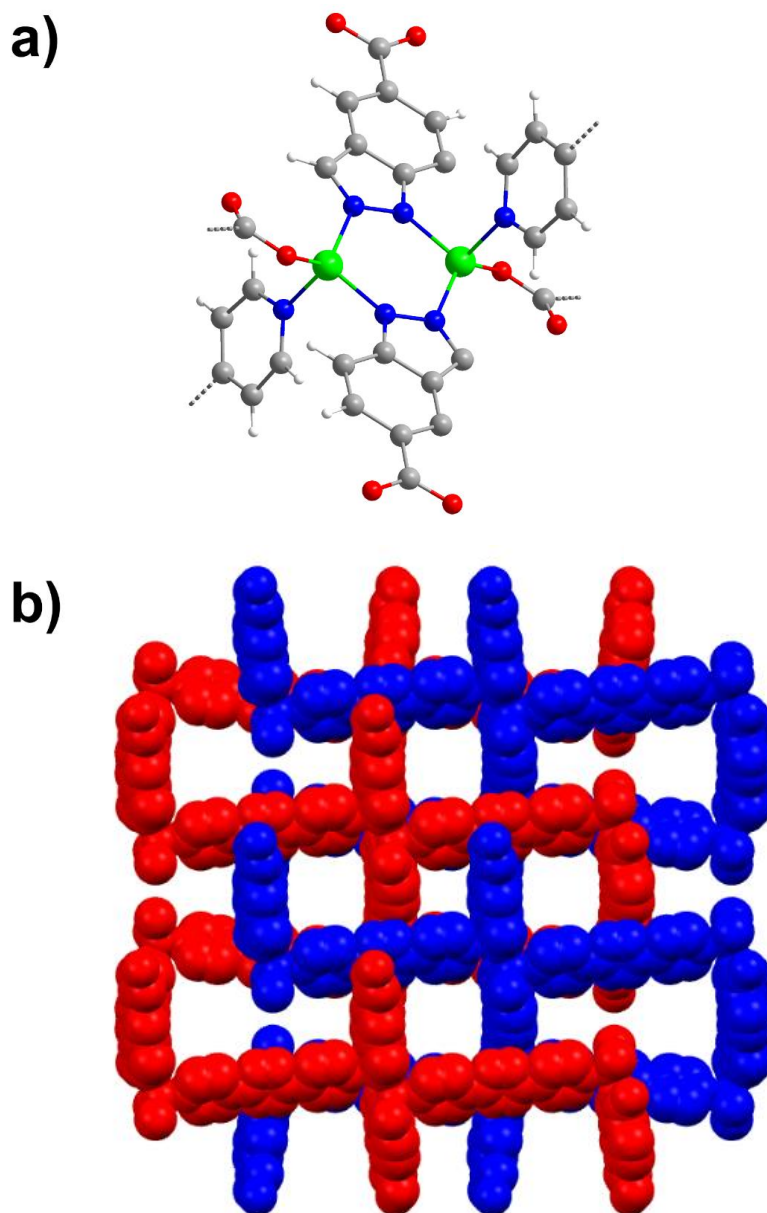


Figure 3. Crystal structure of compound **1**: a) fragment containing the SBU and b) perspective view showing the perpendicular disposition of the pillaring pbptz linkers with regard to $\text{Zn}/(5\text{-inca})^{2-}$ layers. Colour code: zinc, green; oxygen, red; nitrogen, blue; carbon, grey; hydrogen, white.

The asymmetric unit of the crystal structure consists of a Zn1 atom, one (5-inca)²⁻ ligand and half of pbptz linker. The metal centre exhibits a N₃O tetrahedral coordination environment (Figure 1a) that is established by two nitrogen atoms from two symmetry related indazole rings, one nitrogen atom pertaining to pbptz ligand and one oxygen from the carboxylate group of a third (5-inca)²⁻ ligand. Continuous

Shape Measures performed corroborate the low distorted tetrahedral shape ($S_T = 0.67$) of the coordination shell (Table 2).

Table 2. CShMs for ZnO_4 coordination environment for compound **1** and **2**. The lowest SHAPE values for each ion are shown highlighted in grey, indicating best fits.

Structure [ML4]	SP-4	T-4	SS-4	vTBPY-4
Comp 1	29.717	0.668	6.289	2.802
Comp 2	31.630	0.413	7.418	2.371

$(5\text{-inca})^{2-}$ exhibits the novel tridentate coordination mode showed in Scheme 1 (right), which allows it linking to two zinc(II) atoms through the nitrogen atoms pertaining to the indazole ring to eventually form dinuclear secondary building units (SBUs). Within these units, the metal atoms are slightly placed out of the planes delimited by indazole moieties (0.073 \AA), in such a way that the resulting six-member ring imposes a $Zn \cdots Zn$ distance of 3.548 \AA . Each building dinuclear unit connects to six neighbouring ones through both $(5\text{-inca})^{2-}$ ligands and pbptz linkers. On the one hand, the SBU joins to two adjacent units through the carboxylate moieties of four $(5\text{-inca})^{2-}$ ligands, two of which are coplanar and define the SBU of reference whereas the remaining two belong to other SBUs, yielding $Zn/(5\text{-inca})^{2-}$ layers along the crystallographic bc plane. On the other hand, two pbptz pillaring linkers that arise almost perpendicularly from the central six-member ring of the SBU (with an angle of 76.5°) connect to the two remaining SBUs, thus establishing the 3D structure of the MOF (Figure 3b). Taking into account the connectivity achieved among SBUs, which may be considered as 6-connected nodes from the topological point of view, the framework resembles that exhibited by the well-known isorecticular family of MOF-5, in good agreement with the topological analysis performed with TOPOS software which confirms that herein described MOF possesses a *pcu* network with the $(4^{12} \cdot 6^3)$ point symbol (Figure 4).^{43,44}

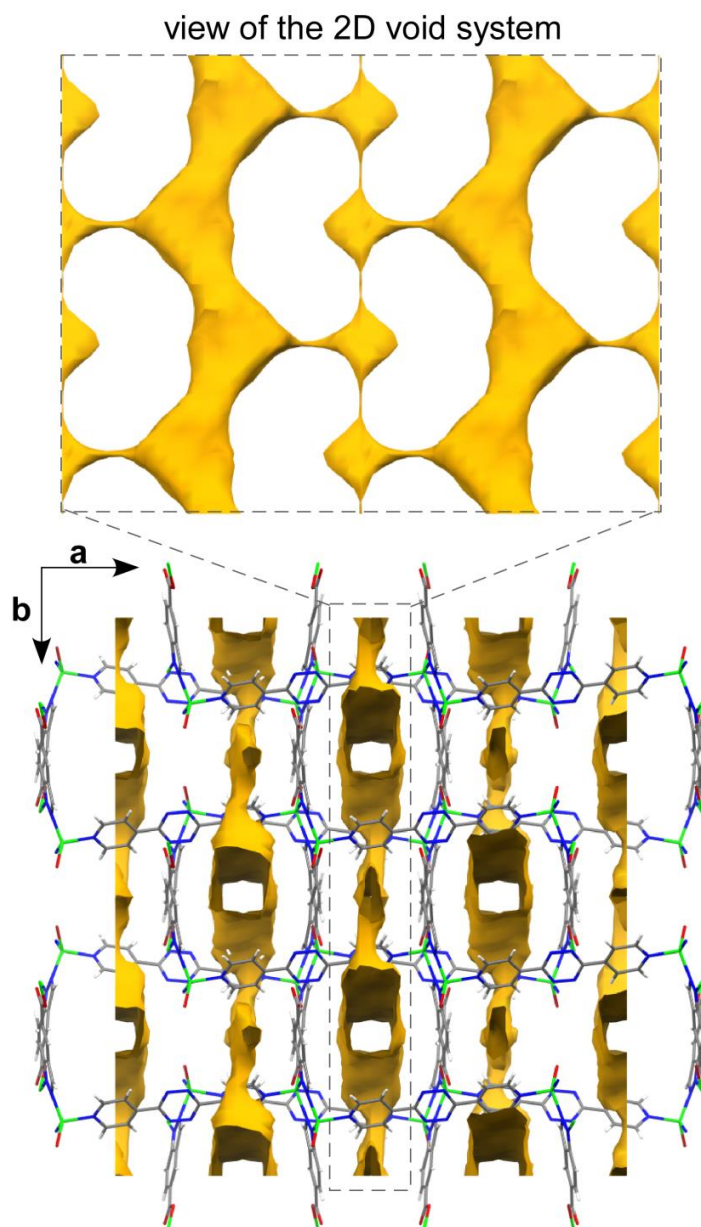


Figure 4. Perspective view of compound **1** showing the solvent-accessible surface.

The length of both connectors and the topology of the framework drive the growth of an almost empty architecture with so large accessible volume that admits the occurrence of a second network in the crystallization. Therefore, the porosity of the resulting two-fold interpenetrated structure is reduced though it still leaves a substantially large 2D void system in within that accounts for the 44.1% of the unit cell volume.⁴⁵ Despite the large solvent accessible volume contained in the structure, it must be highlighted that the pore network is not regular, but it contains large tubular channels with an approximate section of 7 Å, whereas they are cross-linked

through narrow windows with apertures of 1.7–2.7 Å. This fact explains the limited gas adsorption capacity of the MOF, involving no N₂ adsorption capacity at low pressures. Instead, the microporous nature of the MOF was confirmed by CO₂ sorption isotherms (Figure 5), revealing that compound **1** adsorbs 0.9 mmol/g of CO₂ at 273 K and 600 kPa a value which are lower than those of other recently reported MOFs.^{46,47} Interestingly, this value decreases to 0.34 mmol/g upon increasing the CO₂ pressure to 2570 kPa. The shape of the isotherm, showing the above mentioned negative gas sorption during the pressure increase, in line with some previous works by Kaskel et al.,⁴⁸ is characteristic of a sudden hysteretic structural deformation and pore contraction probably derived from a subnetwork displacement occurring in the interpenetrated framework. A careful analysis of the interpenetration occurring in the structure reveals that both frameworks are weakly bound to each other, finding no remarkable interactions apart from C–H··· π interactions between indazole and pbptz ligands involving some kind of lateral interactions among their π clouds, which should be translated into a flexible character.

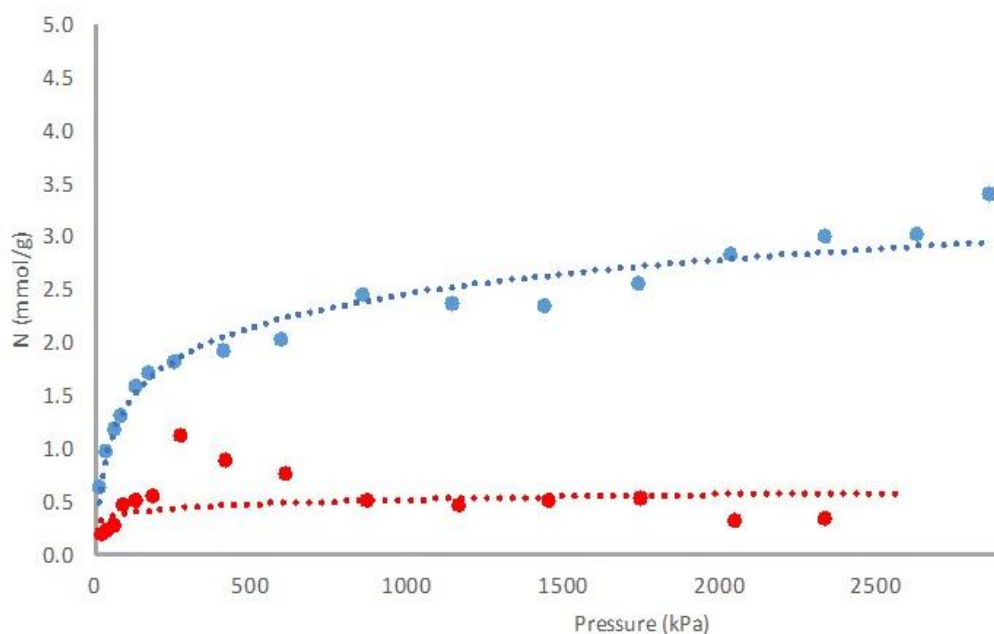


Figure 5. Carbon dioxide adsorption at 273 K on Compound **2** (blue) and **1** (red). Trend lines are just guides for eyes.

3.2. Structural description of $\{[\text{Zn}(\text{5-inca})(\text{4,4-bipy})_{0.5}](\text{DMF})\}_n$ (2).

Compound **2** crystallizes in the orthorhombic *Pccn* space group and possesses an isorecticular 3D framework where pbptz linkers are replaced by 4,4-bipy. (5-inca)²⁻ exhibits a similar coordination pattern detailed for the previous material (right-hand side of Scheme I), which forms dinuclear SBUs owing to the coordination of nitrogen atoms pertaining to the indazole ring to two zinc(II) atoms (Figure 6a). Three significant differences are found in this dinuclear unit compared to that of the previous compound: i) the carboxylate moiety of (5-inca)²⁻ ligand is slightly moved to bite the zinc atom (bringing a semi-coordination of O2A atom, $\text{Zn}\cdots\text{O2A}$ of 2.73 Å), despite of which the coordination environment is best described as a tetrahedron in view of the low distortion with regard to the ideal polyhedron ($S_T = 0.413$, see Table 2); ii) Zn atoms are more coplanar with regard to the plane established by the aromatic rings (which is dropped to 0.029 Å) and iii) the intradinuclear $\text{Zn}\cdots\text{Zn}$ distance is enlarged to 3.657 Å. It must be highlighted that both changes are clearly derived from the change of the pillaring linker which, being considerably shorter than pbptz (the $\text{Zn}\cdots\text{Zn}$ bond distance is reduced from 15.2 to 11.2 Å), modulates the flexibility of the framework.

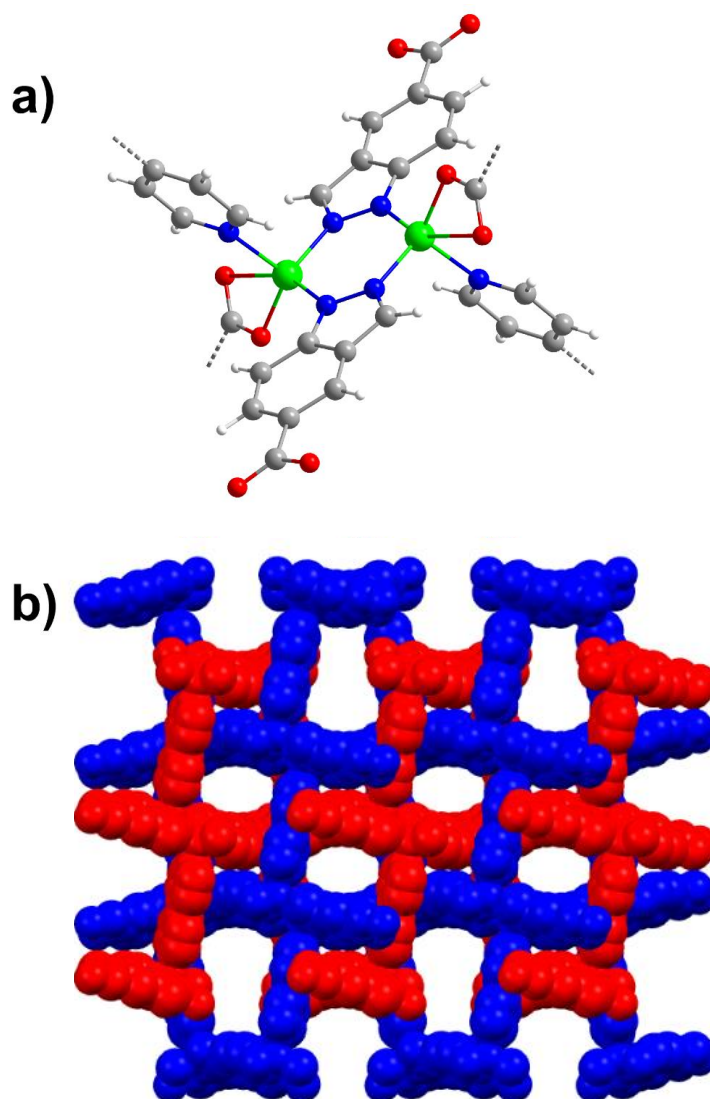


Figure 6. *a) SBU of the structure of compound 2 and b) crystal packing of the compound showing the two-fold interpenetration.*

As a consequence of the mutual displacement between the subnets, the free volume enclosed in the structure is shaped in the form of one-dimensional microchannels (with an irregular tubular shape containing wide and narrow sections of 4.3 and 1.6 Å) and accounts for 32.4% of the unit cell volume (Figure 7). The microporous nature of the MOF was confirmed by CO₂ sorption (Figure 5), revealing that compound **2** adsorbs more CO₂ than compound **1**: 2.0 mmol/g CO₂ at 273 K and 600 kPa and 3.01 mmol/g CO₂ at 273 K and 2570 kPa.

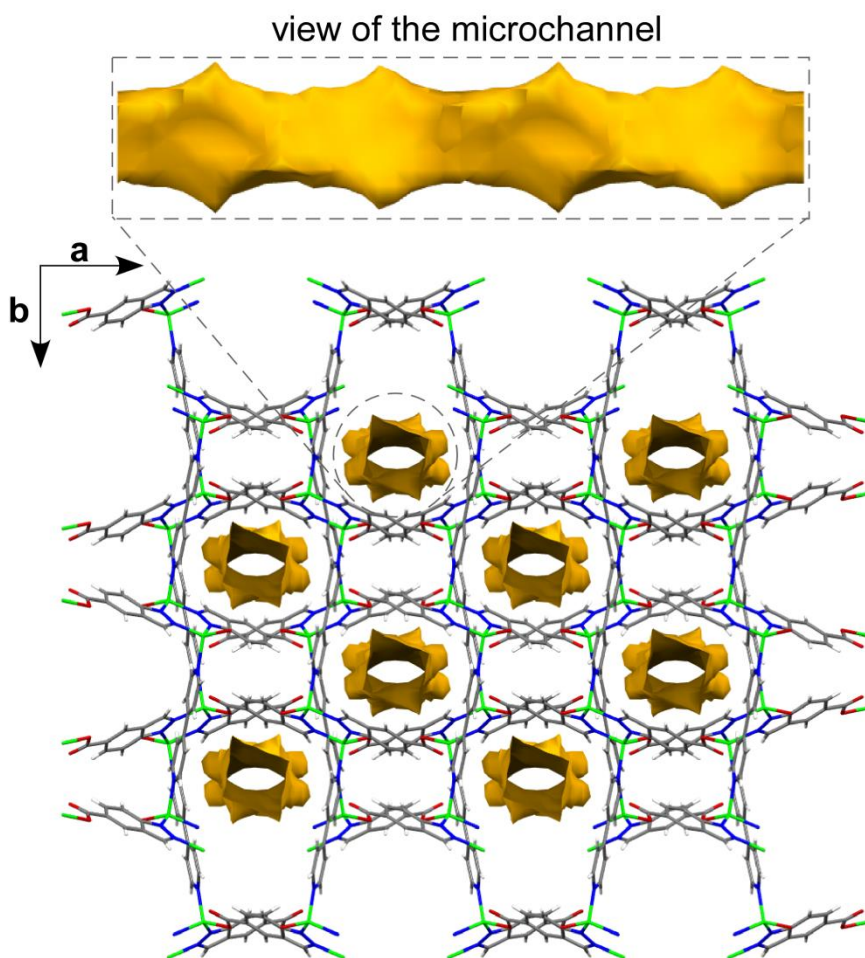


Figure 7. Perspective view of compound **2** showing the solvent-accessible surface. Colour code: zinc, light steel blue; oxygen, red; nitrogen, blue; carbon, grey; chloride, green.

3.3. Photoluminescence Properties

The metal-organic nature of these materials, based on 3D frameworks containing ligands with π -conjugated systems (some of which are also decorated with carboxylate groups that are coordinated to closed-shell metal ions such as zinc(II)) make them suitable to exhibit photoluminescence (PL) in solid state. Under monochromatic UV light excitation ($\lambda_{\text{ex}} = 325$ nm), the room temperature emission spectrum of compound **1** consists of two main and one minor broad bands. A first main band is centred at 374 nm, followed by that located at 440 nm with a shoulder at 420 nm, which dominates the entire spectrum (Figure 8a). Finally, a less intense band is shown to peak at ca. 620 nm. It is worth mentioning that the two main bands are similar to the bands corresponding to each individual ligand, since free (5-*inca*H₂)

and pbptz show emission bands at $\lambda_{\text{em}} = 371$ and 430/460 nm, respectively. Instead, the last less intense band, not directly related with the emissions centred on the ligands, may be ascribed to the formation of an exciplex among the π clouds of the aromatic rings of (5-inca)²⁻ and pbptz ligands pertaining to different subnets, although the participation of non-localized DMF molecules should not be discarded.^{21,49} The subtle shifts observed for the bands with respect to free ligands can be attributed to the coordination effect, as previously observed for other zinc-based MOFs.^{50,51}

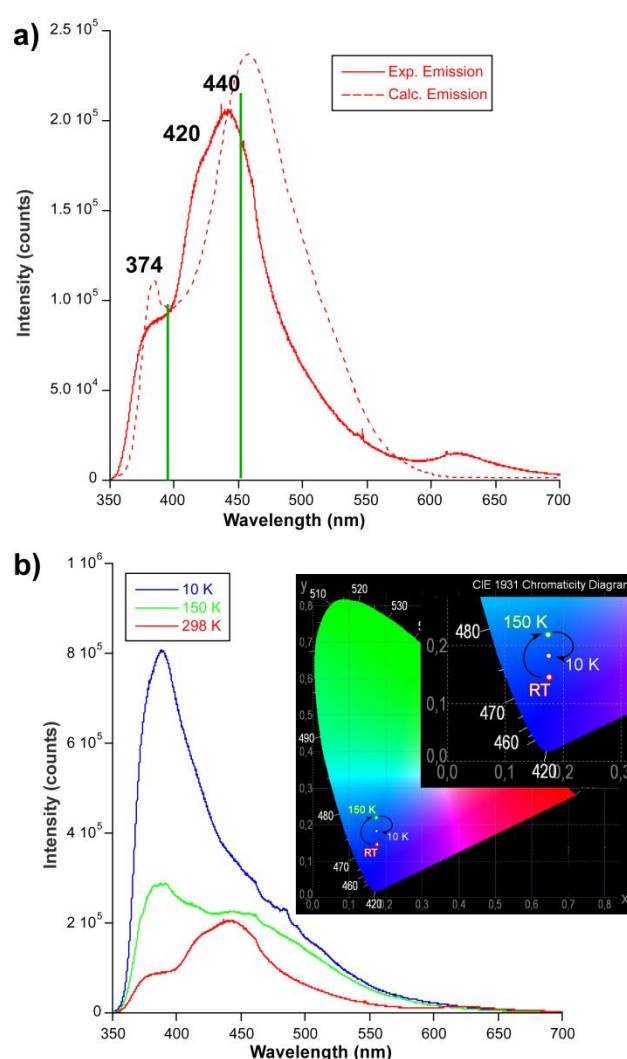


Figure 8. a) Room temperature experimental (solid red line) and TD-DFT calculated (dotted red line) steady-state emission spectra of compound **1**. Black numbers account for experimental emission maxima whereas main calculated main lines are represented as vertical green lines. b) Experimental emission spectra of **1** at variable temperature together with the thermochromic emission. Inset shows luminescent thermochromism represented in the CIE1931 chromaticity color coordinates.

In order to get deeper insights into the PL emission of **1**, TD-DFT calculations were conducted on a suitable model taken from its X-ray structure (model 1 hereafter, Figure 9).

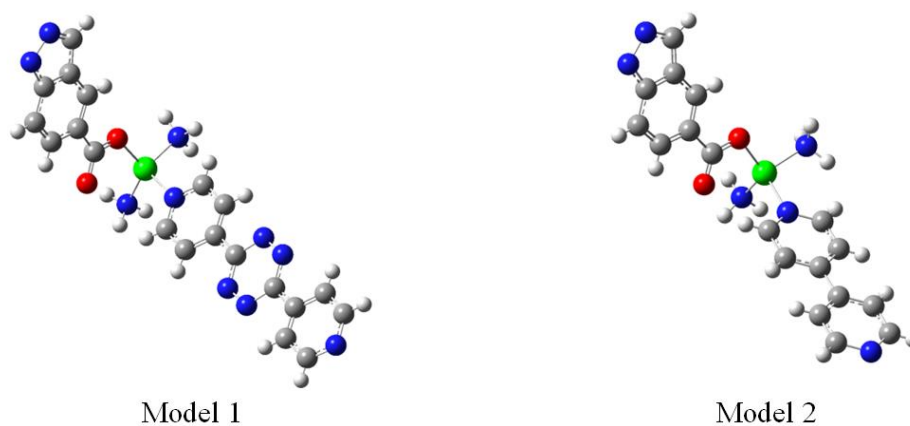


Figure 9. Models 1 and 2 employed for TD-DFT calculations of compounds **1** and **2**.

As shown in Figure 8a, after a vertical excitation at 320 nm proceeding through the HOMO – 5 \rightarrow LUMO + 2 electronic transition (which represents the main excitation line and resembles the experimental λ_{ex} of 325 nm, see Figure 10), the calculated emission spectrum reproduces fairly well the experimental one, showing a wide band with two maxima peaking at 398 and 451 nm ascribed to HOMO – 1 \leftarrow LUMO + 1 and HOMO \leftarrow LUMO + 1.

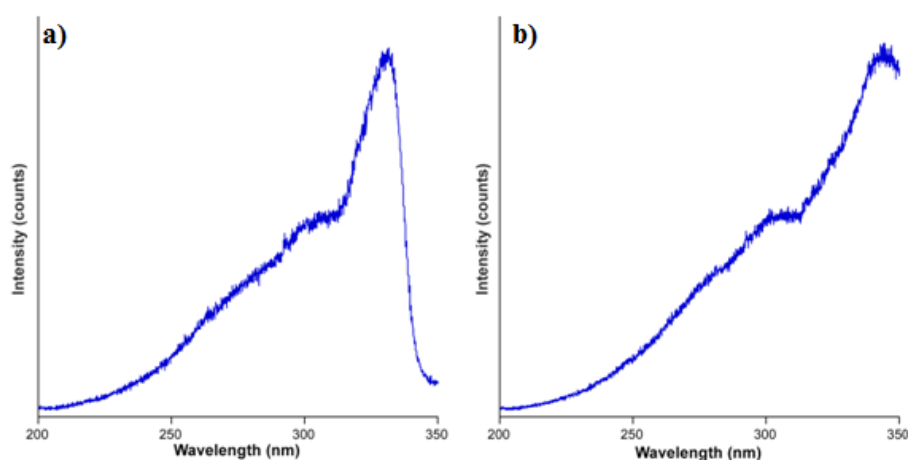


Figure 10. Excitation spectra of compound **2** monitored under (a) $\lambda_{\text{em}} = 380$ nm and (b) $\lambda_{\text{em}} = 535$ nm.

It is worth noticing that this model, based on a monomeric molecule, is not able to reproduce the minor less-energetic band peaking at ca. 625 nm. Nonetheless, a model consisting of a (5-inca)²⁻ and a pbptz ligand pertaining to different subnets (model 3, Figures 11) suggests that the latter emission might be derived from their weak interaction, confirming the occurrence of excimer. The emission of compound 1 at room temperature shows the occurrence of an excimer formation between the (5-inca)²⁻ ligand belonging to a subnet and the pbptz ligand of the second subnet. As shown in Figure 11, the excimer shows a main absorption maxima at ca. 500 nm, ascribed to the HOMO – 13 → LUMO transition of the complex, in such a way that this excited state could be populated during the LC emission occurring within each subnetwork (which governs the PL of the sample). On its part, once the complex is relaxed, it emits with a band centred at 615 nm, attributed to the HOMO – 1 → LUMO transition, which is very close to the experimental band ($\lambda_{em} = 625$ nm) and thus confirms the nature of the emission.

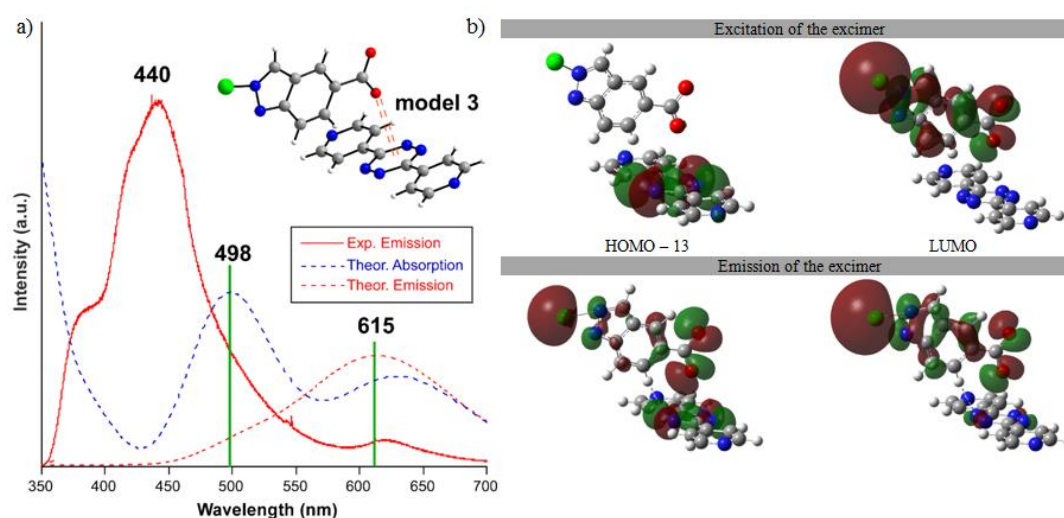


Figure 11. (a) Calculated excitation and emission spectra of model 3 (based on comp. 1) compared to the experimental emission. (b) Molecular orbitals involved in the main excitation and emission line of model 3.

Taking into account the dominant π and π^* character of these electronic transitions in addition to the participation of molecular orbitals extending over both (5-inca)²⁻ and pbptz ligands, the PL scenario of **1** is accurately described as LLCT.

Figure 12 summarizes the global PL scenario for a better understanding of their main electronic transitions. As it is well known, the luminescence in MOFs is known to be quenched by the coupling of non-radiative molecular vibrations, such as aromatic C–H bonds present in both ligands,^{52,53} with excited-to-ground state energy difference. Therefore, the sample was cooled down to low temperature to study such effect. Keeping the experimental setting unchanged for comparative purposes, the emission spectrum was measured at the lowest possible temperature (10 K) as well as at an intermediate temperature (150 K). Interestingly, apart from an obvious increase of the emitted signal, which rises by a 43% at 150 K and by a 300% at 10 K considering the absolute emission maxima, the two main bands ($\lambda_{em} = 374$ and 440 nm) invert progressively their relative intensity as the temperature is dropped since at 10 K the 374 nm band at RT is covering most of the spectrum whereas that at 440 nm is nearly undistinguishable and becomes a shoulder (Figure 8b). On its part, the minor band ($\lambda_{em} = 625$ nm) is not observed anymore, meaning that the excimer is disrupted as the temperature drops probably due to a relative displacement between subnets. Especially at 10 K, the emission band extends up to 600 nm showing a long tail and is shifted to $\lambda_{em} = 388$ nm in such a way that it can be considered to occupy an intermediate wavelength between those of free ligands. The evolution of the emission spectra brings a remarkable luminescent thermochromism in the compound, since the emission varies among different tones of blue.

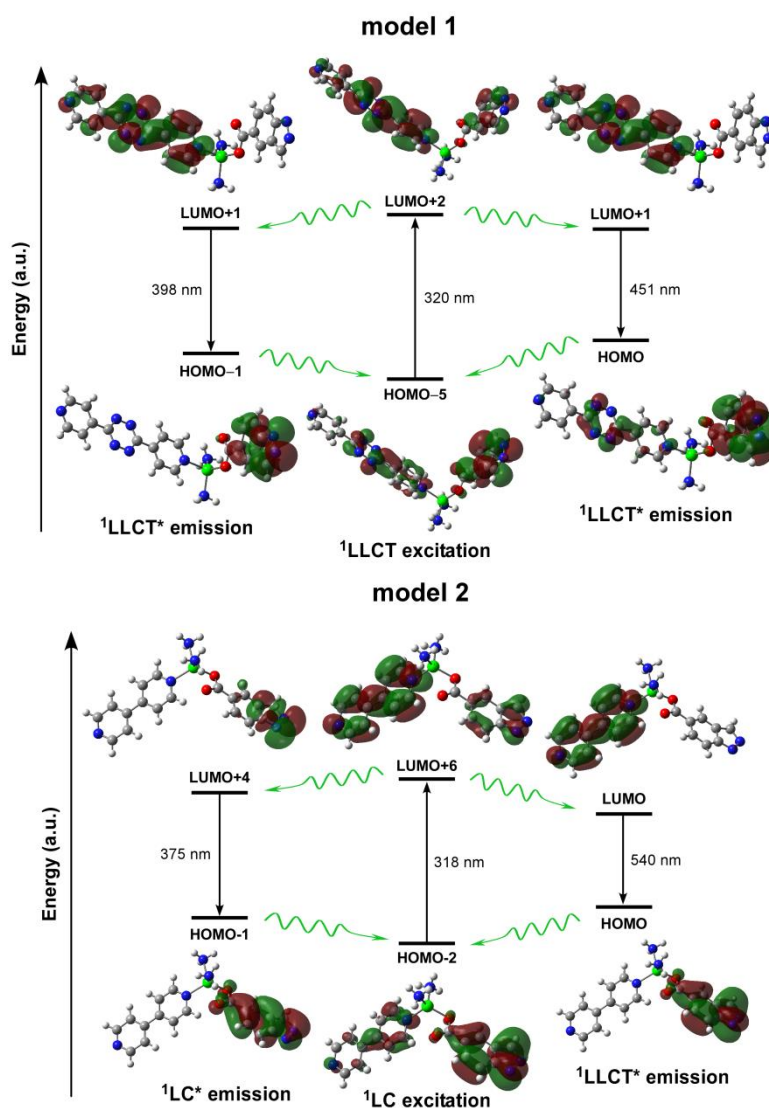


Figure 12. Diagram of the dominant MOs involved in the PL excitation and emission of models 1 and 2. Note that red and blue straight lines represent excitation and emission transitions, whereas undulated green lines account for vibrational relaxation processes.

On the other hand, under $\lambda_{\text{ex}} = 325$ nm excitation with a laser at RT, compound **2** shows two perfectly separated emission bands with their maximum centred at 380 and 535 nm, respectively (Figure 13a). Conversely to **1**, compound **2** does not show any significant thermochromic effect (there is no change in the relative intensity of the maxima) but a strong increase in the absolute emission (integrated intensity) with the lowering of the temperature, which experiments an increment of 700% (Figure 13b). Despite the fact that one could a priori attribute the presence of two bands to the intra-ligand emission of (5-inca)²⁻ and bipy molecules, a similar band is only observed for the first ligand ($\lambda_{\text{em}} = 380$ for **2** and 371 nm for (5-

$\text{inca})^{2-}$, whereas the second band appears to be deeply red-shifted compared to the free bipy ligand emission ($\lambda_{\text{em}} = 535$ for **2** and 430 nm for bipy).⁵⁴

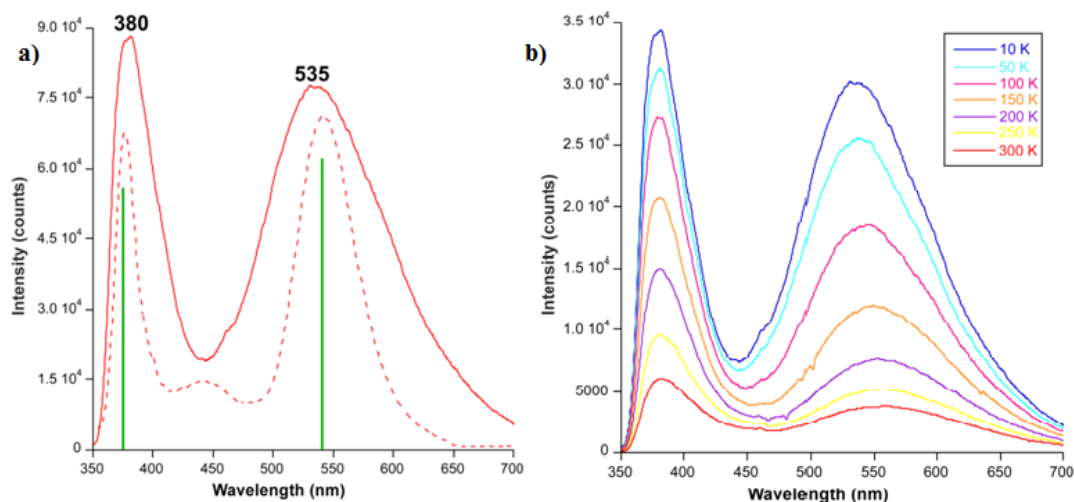


Figure 13. a) Comparison between room temperature experimental and calculated emission spectra of compound **2**. Black numbers and green lines represent the main experimental emission maxima and calculated vertical main lines, respectively. b) Emission spectra of compound **2** monitored under $\lambda_{\text{ex}} = 325$ nm recorded at different temperatures.

A detailed analysis with TD-DFT methodology on a suitable model of **2** (model 2 hereafter) reveals a somewhat different PL scenario for this compound despite the similar nature of its ligands. On the one hand, the system is excited through two similar lines: a minor band at 302 nm corresponding to the $\text{HOMO} - 5 \rightarrow \text{LUMO} + 2$ transition and the major band located at 318 nm described by the $\text{HOMO} - 2 \rightarrow \text{LUMO} + 6$ transition. Given that the experimental spectrum is recorded with a $\lambda_{\text{ex}} = 325$ nm, it may be assumed that the excitation proceeds mainly through the latter transition. On the other hand, the radiative relaxation of **2** is governed by $\text{HOMO} - 1 \leftarrow \text{LUMO} + 4$ and $\text{HOMO} \leftarrow \text{LUMO}$ transitions peaking at 375 and 540 nm, which fairly represent the two main emission bands. In agreement with the previous speculations, the first band is centred on the $(5\text{-inca})^{2-}$ ligand, which explains why it resembles the emission band displayed by the free ligand. Instead, the second band clearly corresponds to ligand-to-ligand charge transfer (LLCT) process involving the empty molecular orbitals (MOs) of the bipy and the filled MOs of $(5\text{-inca})^{2-}$.

Though there is no previous report on LLP behaviour for CPs based on (5-*inca*)²⁻ ligand, in view of the long-lived phosphorescent emissions shown by zinc compounds based on similar aromatic ligands found in the literature, we decided to measure decay curves on both compounds.¹⁷ To that end, the most representative emission wavelengths of the spectrum of **1** were monitored, i.e. the emission maxima ($\lambda_{em} = 374$ and 440 nm). The decay curves show a very rapid decrease of the signal, indicating that the emission proceeds through a fluorescent process. Though the decay at 374 nm is too rapid as to be analyzed (with a lifetime below the pulse of the lamp \approx few μ s), a weak but larger process could be discerned from the curve measured at 440 nm. The analysis by means of an exponential expression gives a lifetime of about 4150 μ s (Figure 14), which may be regarded within the low limit of LLP (below the arbitrary value of 20 ms).⁵⁵

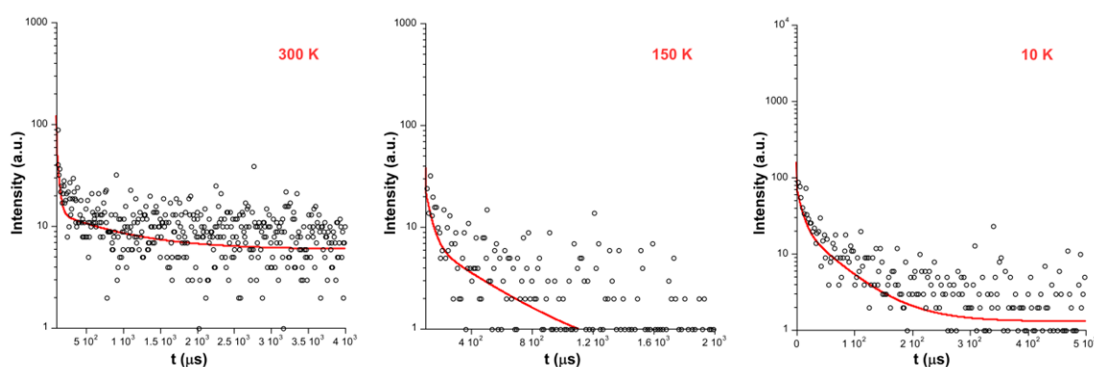


Figure 14. Decay curves with best fitting at selected temperatures for compound **1** ($\lambda_{ex} = 325$ and $\lambda_{em} = 440$ nm).

It was observed that lowering the temperature keeps the lifetime almost constant, where the subtle enlargement may be related with afore mentioned decrease of vibrational quenching ($\tau_{150\text{ K}} \approx 6040$ and $\tau_{10\text{ K}} \approx 8590$ μ s). Instead, compound **2** presents a wavelength dependent emission scenario composed of a persistent fluorescent emission ($\tau_{fl} \approx 170$ μ s) around the maximum of the first band ($\lambda_{em} = 380$ nm) and a phosphorescence emission ($\tau_{ph} \approx 200$ ms) around the high-wavelength band ($\lambda_{em} \approx 535$ nm) (Figure 15 and Table 3).

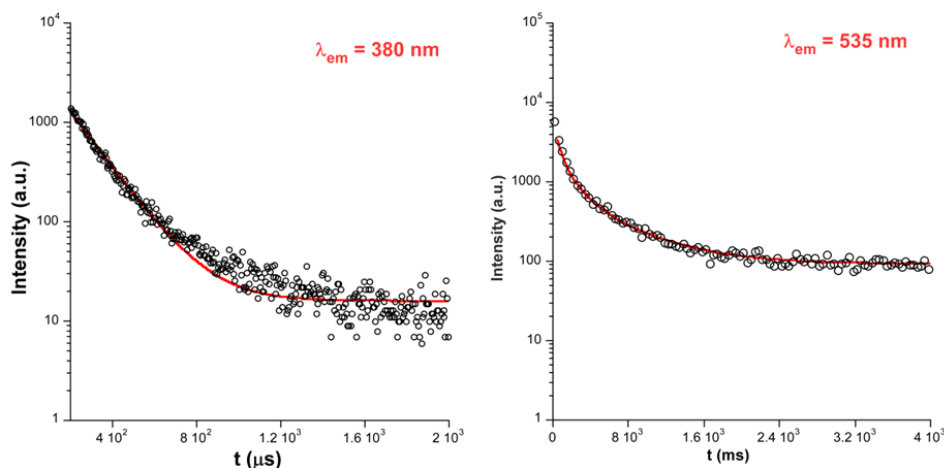


Figure 15. Decay curves with best fitting at room temperature for compound **2** ($\lambda_{ex} = 325$).

Table 3. Best fitting results from decay curves measured at variable temperature for compound **2** ($\lambda_{ex} = 325$ nm, $\lambda_{em} = 535$ nm) at selected emission wavelengths.

Temperature	τ_1 (ms)	τ_2 (ms)	Chi Sq.
10	244(17) / 28%	948(29) / 72%	1.212
50	172(15) / 34%	797(36) / 66%	1.236
70	156(13) / 38%	605(22) / 62%	1.143
100	210(28) / 28%	552(33) / 72%	1.185
150	102(11) / 42%	348(19) / 58%	1.078
200	98(3) / 35%	301(11) / 65%	1.192
250	50(6) / 44%	252(60) / 56%	1.275
300	5886 / 50%	199(10) / 50%	1.265

Given their curvi-linear shape, all phosphorescence decay curves were fitted with two lifetime components so they were analysed with a multi-exponential expression [$I_t = A_0 + A_1 \exp(-t/\tau_1) + A_2 \exp(-t/\tau_2)$] that considers two lifetimes. The T_1-S_0 energy difference, which corresponds to the main phosphorescent emission line, has been estimated from vertical excitation performed for the optimized geometry of the lowest lying excited triplet state (T_1). The triplet state geometry optimisation and frequencies calculation was performed on models 1 and 2 with Gaussian 09 package, using the Becke three parameter hybrid functional with the non-local correlation functional of Lee-Yang-Parr (B3LYP) with the 6-311G++(d,p) basis set for all atoms. A fact about these MOs calculated at triplet state geometry

that must be emphasized is that they show a similar shape regarding their singlet counterparts, with a π and π^* character respectively for HOMO and LUMO (Figure 16).

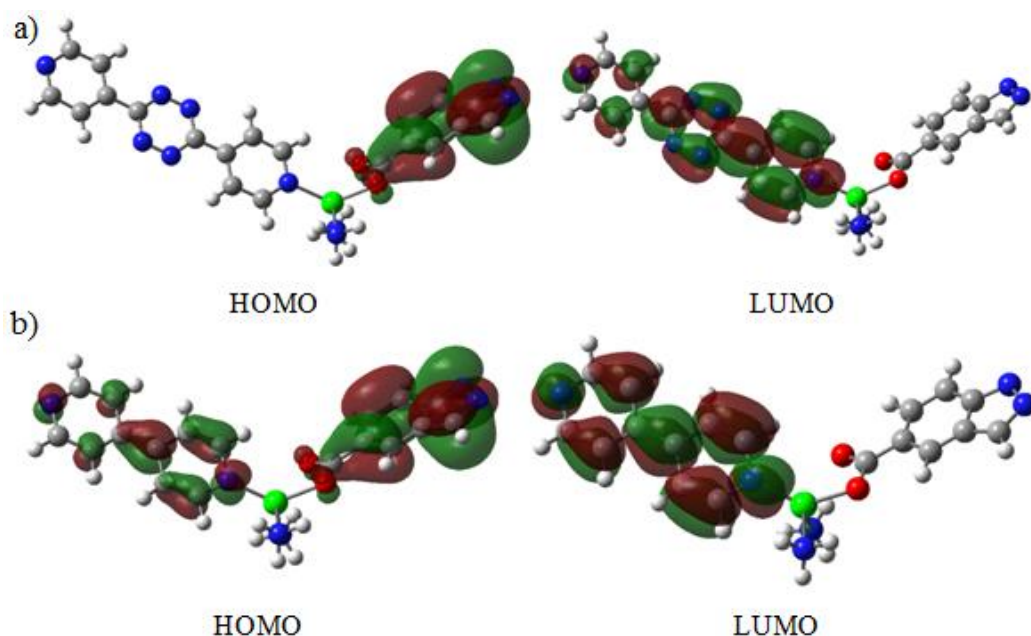


Figure 16. (a) Highest Occupied and Lowest Uoccupied (single-occupied alpha) Molecular Orbitals covered at first excited triplet state geometry for model 1. (b) Highest Occupied and Lowest Uoccupied (single-occupied alpha) Molecular Orbitals covered at first excited triplet state geometry for model 2.

The pale blue and yellowish green colours displayed by **2** in the micro-PL photographs taken on crystals are a good indication of the fluorescent and phosphorescent emissions (Figure 17). As observed in these photographs, the fluorescent signal observed under irradiation with UV light ($\lambda_{\text{ex}} \approx 365$ nm in the present case) shows a kind of luminescent waveguiding effect, since the emitted colour is only seen depending on the orientation of the crystals. This effect is not so common although it has already been described for other luminescent materials, for which crystals with an adequate refraction index and morphology as well as strong luminescence emission are required, in such a way that most of the light is confined within the crystal and emitted through a particular face.⁵⁶⁻⁶⁰

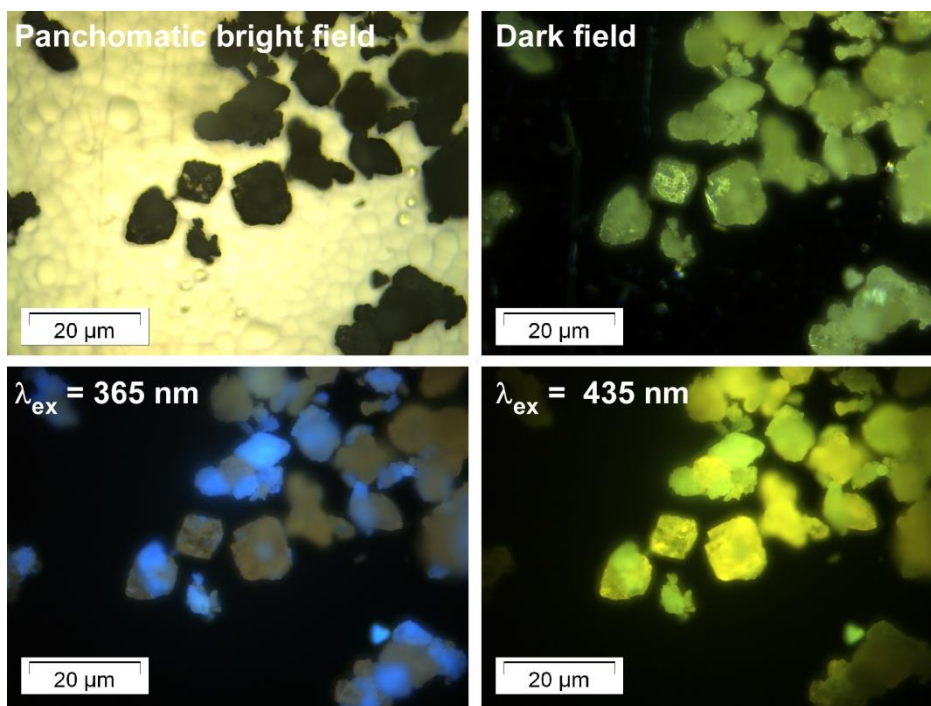


Figure 17. Room temperature micro-PL images for single-crystals of compound **2**.

The recorded lifetime of **2** is large enough as to be referred to as room temperature phosphorescence (RTP), which provides this compound with a very subtle greenish afterglow that is glimpsed when turning off laser beam. Dropping the temperature off to save non-radiative quenching does not bring any substantial on decay curves measured at the first emission maxima $\lambda_{em} = 380$ nm, but it promotes a substantial lengthening of the lifetime associated with the phosphorescent emission. In particular, at $\lambda_{em} = 535$ nm the lifetime enlarges progressively, mainly below 150 K, until it achieves a value of ca. 950 ms, which can be considered as an intermediate-to-large value for the CPs presenting LLP reported so far (Figure 18).⁵⁶⁻

60

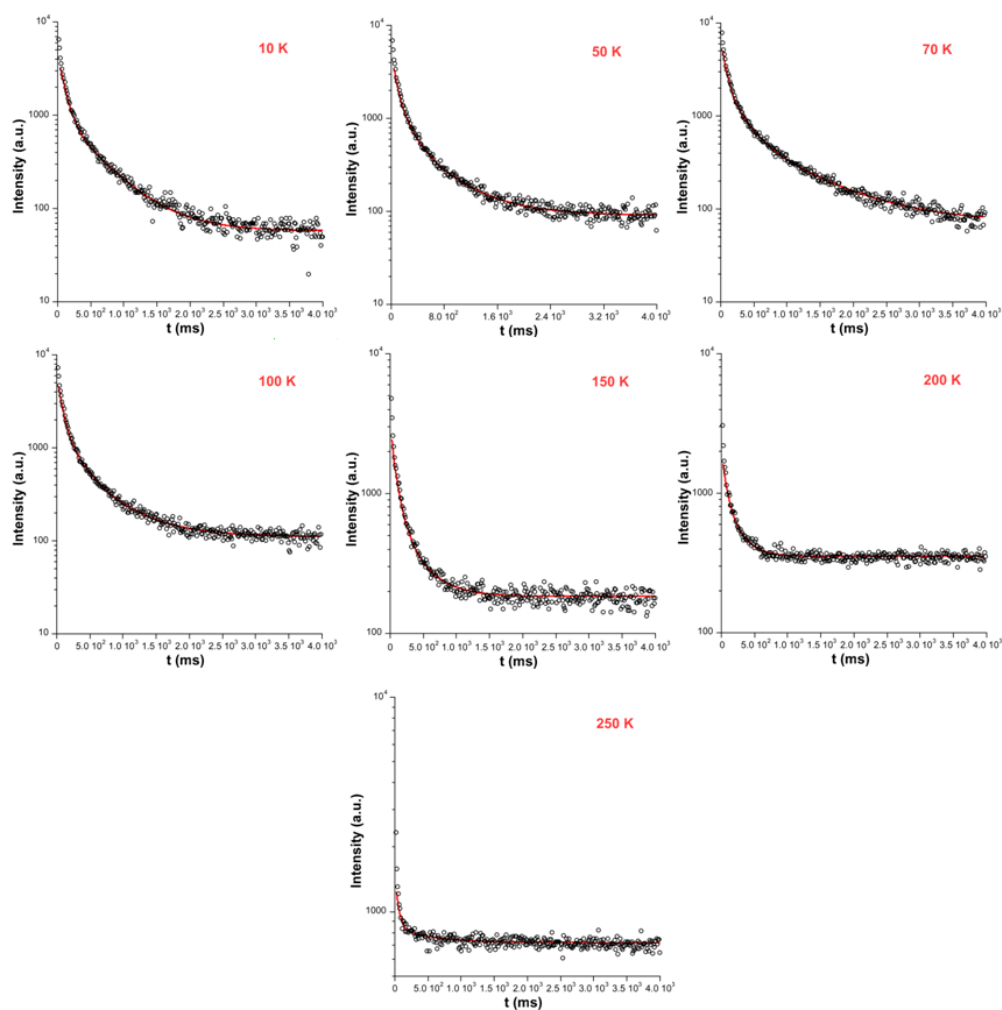


Figure 18. Decay curves with best fitting at selected temperatures for compound 2 ($\lambda_{ex} = 325$ and $\lambda_{em} = 535$ nm).

These results evidence the fluorescent/phosphorescent character of the MOF at low temperature, a fact that confirms that LCCT process occurring at the ligand is stabilized in the framework of the MOF such that both $S_0 \leftarrow S_1$ and $S_0 \leftarrow T_1$ transitions are enabled and enhanced. With the aim of better characterizing the phosphorescent emission, time-resolved emission spectra (TRES) were recorded for 2 at low temperature, which confirmed that the persistent emission consists of a wide band centred at $\lambda_{em} = 550$ nm, close to the band measured at steady-state, thus explaining well the green-yellowish afterglow shown when the UV excitation source is turned off (Figure 19). It is worth highlighting that the emitted light, yet it is weak as to be captured by a common camera, can be perfectly traced by the naked eye 4 seconds after having turned off the excitation source.

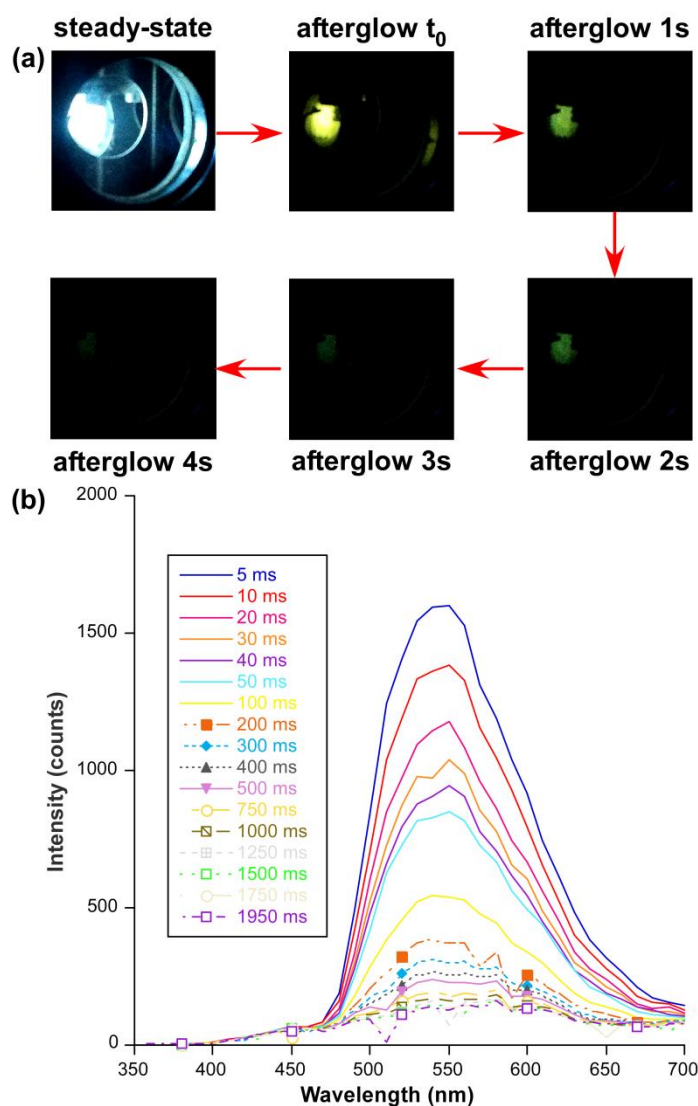


Figure 19. (a) Photographs of the steady-state and afterglow emissions of compound **2**. (b) TRES of compound **2** at 10 K at selected delays ($\lambda_{ex} = 325$ nm).

A calculation of the phosphorescent emission estimated from the DFT computed T_1 and S_0 electronic states (usually denoted as vertical excitation phosphorescent energy)⁶¹ on model **2** gives a very good estimate of the experimentally measured band for compound **2** ($\lambda_{vert-phosp} = 507$ vs $\lambda_{ph} = 550$ nm). This value can be taken as an approach to estimate the energy of the T_1 state in the compound assuming that the compound follows Kasha's rule.⁶² A similar calculation performed on model **1** renders a $\lambda_{vert-phosp} = 470$ nm, meaning that the T_1 state in compound **1**, conversely to **2**, is less energetic than the lowest-lying excited singlet state from which a radiative emission takes place ($S_0 \leftarrow S_1 \approx 440$ nm). Therefore, this fact could a priori inhibit an intersystem crossing to populate the T_1 state that enables

the occurrence of phosphorescence in **1** and, hence, explains why LLP is solely enhanced in compound **2**. Moreover, it cannot be discarded that weaker phosphorescence shown by **1** is also related to the less rigidity of pbptz ligand in the MOF, which clearly possesses more degrees of freedom compared to bipy ligand in **2**.

4. Conclusions

Two novel porous zinc based metal-organic frameworks consisting of indazole-5-carboxylate and 3,6-di(4-pyridinyl)-1,2,4,5-tetrazine for compound **1** or 4,4'-bipyridine like for **2** have been synthesized and characterized. Both MOFs present an isorecticular architecture with **pcu** topology that crystallizes as a doubly interpenetrated structure. This structural feature affords some flexibility to the frameworks and permits to modulate their porosity obtaining a 2D void system with narrow pore sections and 1D microchannels for **1** and **2**, respectively. Solid state photoluminescence measurements reveal that both compounds provide intense blue emissions under irradiation with UV light which arise from charge transfers occurring between (5-inca)²⁻ and bipyridyl-like ligands as confirmed by TD-DFT calculations. Variable-temperature data indicate that compound **1** shows a remarkable thermochromism, which modulates the tonality of the emitted blue light provoked by the change in the relative intensity of the two main emission bands and an excimer formation/disruption between ligands belonging to different interpenetrated subnetworks. On its part, dropping down the temperature in **2** has no such effect yet it largely enhances its emission capacity, a fact that is particularly inferred from the occurrence of long-lasting phosphorescence that may be perceived by the naked eye (with an associated lifetime of ca. 950 ms) below the temperature of liquid nitrogen. DFT calculations performed on these compounds point out to the relative energy of the excited singlet and triplet states as a probable source in the origin of sizeable phosphorescence solely in compound **2**, although the less rigidity of pbptz ligand of compound **1** compared to bipy in **2** may also have some influence.

5. References

- (1) Chen, B.; Ma, S.; Zapata, F.; Fronczek, F. R.; Lobkovsky, E. B.; Zhou, H.-C. Rationally Designed Micropores within a Metal–Organic Framework for Selective Sorption of Gas Molecules. *Inorg. Chem.* **2007**, *46*, 1233-1236.
- (2) Jeazet, H. B. T.; Staudt, C.; Janiak, C. A method for increasing permeability in O₂/N₂ separation with mixed-matrix membranes made of water-stable MIL-101 and polysulfone. *Chem. Commun.* **2012**, *48*, 2140-2142.
- (3) Li, J.-R.; Sculley, J.; Zhou, H.-C. Metal-organic frameworks for separations. *Chem. Rev.* **2012**, *112*, 869-932
- (4) Shang, J.; Li, G.; Singh, R.; Gu, Q.; Nairn, K. M.; Bastow, T. J.; Medhekar, N.; Doherty, C. M.; Hill, A. J.; Liu, J. Z.; Webley, P. A. Discriminative Separation of Gases by a “Molecular Tramdoor” Mechanism in Chabazite Zeolites. *J. Am. Chem. Soc.* **2012**, *134*, 19246-19253.
- (5) Bourrelly, S.; Llewellyn, P. L.; Serre, C.; Millange, F.; Loiseau, T.; Fèrey, G. Different Adsorption Behaviors of Methane and Carbon Dioxide in the Isotypic Nanoporous Metal Terephthalates MIL-53 and MIL-47. *J. Am. Chem. Soc.* **2005**, *127*, 13519-13521.
- (6) Yan, Y.; Yang, S. H.; Blake A. J.; Schroder, M. Studies on Metal-Organic Frameworks of Cu(II) with Isophthalate Linkers for Hydrogen Storage. *Acc. Chem. Res.* **2014**, *47*, 296-307.
- (7) Pérez-Yáñez, S.; Beobide, G.; Castillo, O.; Fischer, M.; Hoffman, F.; Fröba, M.; Cepeda J.; Luque, A. Gas Adsorption Properties and selectivity in Cu^{II}/adeninato/carboxilato metal-Biomolecule Frameworks *Eur. J. Inorg. Chem.* **2012**, *2012*, 5921-5933.
- (8) Farha, O. K.; Eyazici, I.; Jeong, N. C.; Hauser, B. G.; Wilmer, C. E.; Sarjeant, A. A.; Snurr, R. Q.; Nguyen, S. T.; Yazaydin, A.; Hupp, J. T. Metal-Organic Framework

Materials with Ultra-High Surface Areas: Is the Sky the Limit? *J. Am. Chem. Soc.* **2012**, *134*, 15016-15021.

(9) Li, J.-R.; Kuppler, R. J.; Zhou, H.-C. Selective gas adsorption and separation in metal-organic frameworks. *Chem. Soc. Rev.* **2009**, *38*, 1477-1504.

(10) Zhou, H.-C.; Kitagawa, S. Metal-Organic Frameworks (MOFs). *Chem. Soc. Rev.* **2014**, *43*, 5415-5418.

(11) Maurin, G.; Serre, C.; Cooper, A.; Férey, G. The new age of MOFs and of their porous-related solids. *Chem. Soc. Rev.* **2017**, *46*, 3104-3107.

(12) Cepeda, J.; Rodríguez-Diéguez, A. Tuning the luminescence performance of metal-organic frameworks based on d^{10} metal ions: from an inherent versatile behaviour to their response to external stimuli. *CrystEngComm.* **2016**, *18*, 8556-8573.

(13) Seco, J.M.; Fairen-Jimenez, D.; Calahorra, A.J.; Méndez-Liñán, L.; Pérez-Mendoza, M.; Casati, N.; Colacio E.; Rodríguez-Diéguez, A. Modular structure of a robust microporous MOF based on Cu_2 paddle-wheels with high CO_2 selectivity. *Chem. Commun.* **2013**, *49*, 11329-11331.

(14) Cepeda, J.; Pérez-Mendoza, M.; Calahorra, A.J.; Casati, N.; Seco, J.M.; Aragonés-Anglada, M.; Moghadam, P.Z.; Fairen-Jimenez, D.; Rodríguez-Diéguez, A. Modulation of Pore shape and adsorption selectivity by ligand functionalization in a series of “rob”-like flexible metal-organic frameworks. *J. Mater. Chem. A.* **2018**, *6*, 17409-17416.

(15) Li, H.-Y.; Wei, Y.-L.; Dong, X.-Y.; Zang, S.-Q.; Mak, T. C. W. Novel Tb-MOF Embedded with Viologen Species for Multi-Photofunctionality: Photochromism, Photomodulated Fluorescence, and Luminescent pH Sensing. *Chem. Mater.* **2015**, *27*, 1327-1331.

(16) Barbieri, A.; Accorsi, G.; Armaroli, A. Luminescent complexes beyond the platinum group: the d^{10} avenue. *Chem. Commun.* **2008**, 2185-2193.

(17) San Sebastian, E.; Rodríguez-Diéguez, A.; Seco, J. M.; Cepeda, J. Coordination Polymers with Intriguing Photoluminescence Behavior: The Promising Avenue for Greatest Long-Lasting Phosphors. *Eur. J. Inorg. Chem.* **2018**, 2155-2174.

(18) Rocha, J.; Brites, C. D. S.; Carlos, L. D. Lanthanide Organic Framework Luminescent Thermometers. *Chem.–Eur. J.* **2016**, *22*, 14782-14795.

(19) Han, Y.-H.; Tian, C.-B.; Li, Q.-H.; Du, S.-W. Highly chemical and thermally stable luminescent $\text{Eu}_x\text{Tb}_{1-x}$ MOF materials for broad-range pH and temperature sensors. *J. Mat. Chem. C* **2014**, *2*, 8065-8070.

(20) Brites, C. D. S.; Lima, P.; Silva, N. J. O.; Millán, A.; Amaral, V. S.; Palacio, F.; Carlos, L. D. Lanthanide-based luminescent molecular thermometers. *New J. Chem.* **2011**, *35*, 1177-1183.

(21) Allendorf, M. D.; Bauer, C. A.; Bhaktaa, R. K.; Houk, R. J. T. Luminescent metal–organic frameworks. *Chem. Soc. Rev.* **2009**, *38*, 1330-1352.

(22) Cui, Y.; Zhu, F.; Chen, B.; Qian, G. Metal–organic frameworks for luminescence thermometry. *Chem. Commun.* **2015**, *51*, 7420-7431.

(23) Lower, S. K.; El-Sayed, M. A. The Triplet State and Molecular Electronic Processes in Organic Molecules. *Chem. Rev.* **1966**, *66*, 199-241.

(24) Hawes, C.S.; Babarao, R.; Hill, M. RR.; White, K. F.; Abrahams, B. F.; Kruger, P.E. Hysteretic carbon dioxide sorption in a novel copper(II)-indazole-carboxylate porous coordination polymer. *Chem. Commun.* **2012**, *48*, 11558-11560.

(25) Botana, L.; Ruiz, J.; Seco, J.M.; Mota, A. J.; Rodríguez-Diéguez, A.; Sillanpää, R.; Colacio, E. Influence of the anions on the structure and magnetic properties of a series of bis(μ -diphenoxo)-bridged linear trinuclear copper(II) complexes: an experimental and theoretical study. *Dalton Trans.* **2011**, *40*, 12462-12471.

(26) Seco, J. M.; Pérez-Yáñez, S.; Briones, D.; García, J. A.; Cepeda, J.; Rodríguez-Diéguez, A. Combining Polycarboxylate and Bipyridyl-like Ligand in the Design of luminescent Zinc and Cadmium Based Metal-Organic Frameworks. *Cryst. Growth Des.* **2017**, *17*, 3893-3906.

- (27) Qi, Y.-J.; Wang, Y.-J.; Li, X.-X.; Zhao, D.; Sun, Y.-Q.; Zheng, S.-T. Two d¹⁰ Metal–Organic Frameworks as Low-Temperature Luminescent Molecular Thermometers. *Cryst. Growth Des.* **2018**, *18*, 7383-7390.
- (28) SAINT v8.40A, Bruker AXS Inc., Madison, Wisconsin, USA, 2016.
- (29) Krause, L.; Herbst-Irmer, R.; Sheldrick, G.M.; Stalke, D. Comparison of silver and molybdenum microfocus X-ray sources for single-crystal structure determination. *J. Appl. Cryst.* **2015**, *48*, 3-10.
- (30) Sheldrick, G.M. SHELXT - Integrated space-group and crystal-structure determination. *Acta Cryst.* **2015**, *A71*, 3-8.
- (31) Sheldrick, G.M. Crystal structure refinement with SHELXL. *Acta Cryst.* **2015**, *C71*, 3-8.
- (32) Dolomanov, O. V.; Bourhis, L. J.; Gildea, R. J.; Howard, J. A. K.; Puschmann, H. OLEX2: a complete structure solution, refinement and analysis program. *J. Appl. Crystallogr.* **2009**, *42*, 339-341.
- (33) Frisch, M. J.; Trucks, G. W.; Schlegel, H. B.; Scuseria, G. E.; Robb, M. A.; Cheeseman, J. R.; Scalmani, G.; Barone, V.; Mennucci, B.; Petersson, G. A.; Nakatsuji, H.; Caricato, M.; Li, X.; Hratchian, H. P.; Izmaylov, A. F.; Bloino, J.; Zheng, G.; Sonnenberg, J. L.; Hada, M.; Ehara, M.; Toyota, K.; Fukuda, R.; Hasegawa, J.; Ishida, M.; Nakajima, T.; Honda, Y.; Kitao, O.; Nakai, H.; Vreven, T.; Montgomery Jr. J. A.; Peralta, J. E.; Ogliaro, F.; Bearpark, M.; Heyd, J. J.; Brothers, E.; Kudin, K. N.; Staroverov, V. N.; Kobayashi, R.; Normand, J.; Raghavachari, K.; Rendell, A.; Burant, J. C.; Iyengar, S. S.; Tomasi, J.; Cossi, M.; Rega, N.; Millam, J. M.; Klene, M.; Knox, J. E.; Cross, J. B.; Bakken, V.; Adamo, C.; Jaramillo, J.; Gomperts, R.; Stratmann, R. E.; Yazyev, O.; Austin, A. J.; Cammi, R.; Pomelli, C.; Ochterski, J. W.; Martin, R. L.; Morokuma, K.; Zakrzewski, V. G.; Voth, G. A.; Salvador, P.; Dannenberg, J. J.; Dapprich, S.; Daniels, A. D.; Farkas, O.; Foresman, J. B.; Ortiz, J. V.; Cioslowski, J.; Fox, D. J. *Gaussian 09, revision A.02*, Gaussian, Inc., Wallingford, CT, **2009**.

- (34) Becke, A. D. Density-functional thermochemistry. III. The role of exact exchange. *J. Chem. Phys.* **1993**, *98*, 5648-5652.
- (35) Miehlich, B.; Savin, A.; Stoll, H; Preuss, H. Results obtained with the correlation energy density functional of becke and Lee, Yang and Parr. *Chem. Phys. Lett.* **1989**, *157*, 200-206.
- (36) Lee, C.; Yang, W.; Parr, R. G. Development of the Colle-Salvetti correlation-energy formula into a functional of the electron density. *Phys. Rev. B.* **1988**, *37*, 785-789.
- (37) Noodleman, L.; Case, D. A.; Aizman, A. Broken symmetry analysis of spin coupling in iron-sulfur clusters. *J. Am. Chem. Soc.* **1988**, *110*, 1001-1005.
- (38) Hay, P. J.; Wadt, W. R. Ab initio effective core potentials for molecular calculations. Potentials for the transition metal atoms Sc to Hg. *J. Chem. Phys.* **1985**, *82*, 270-283.
- (39) Wadt, W. R.; Hay P. J. Ab initio effective core potentials for molecular calculations. Potentials for main group elements Na to Bi. *J. Chem. Phys.* **1985**, *82*, 284-298.
- (40) Hay, P. J.; Wadt, W. R. Ab initio effective core potentials for molecular calculations. Potentials for K to Au including the Outermost core orbitals. *J. Chem. Phys.* **1985**, *82*, 299-310.
- (41) O'Boyle, N. M.; Tenderholt, A. L.; Langner, K. M. cclib: A library for package-independent computational chemistry algorithms. *J. Comput. Chem.* **2008**, *29*, 839-845.
- (42) Dennington, R.; Keith, T.; Millam, J. *GaussView, Version 5*, Semichem Inc., Shawnee Mission: KS, **2009**.
- (43) *TOPOS Main Page*, <http://www.topos.ssu.samara.ru> (accessed February 14, 2019).

- (44) Blatov, V.A.; Shevchenko, A. P.; Proserpio, D. M. Applied Topological Analysis of Crystal Structures with the program Package ToposPro. *Cryst. Growth Des.* **2014**, *14*, 3576-3586.
- (45) Spek, A. L. Structure validation in chemical crystallography. *Acta Cryst.* **2009**, *D65*, 148-155.
- (46) Ding, M.; Flaig, R.W.; Jiang, H.-L.; Yaghi, O.M. Carbon capture and conversion using metal–organic frameworks and MOF-based materials. *Chem. Soc. Rev.* **2019**, *48*, 2783-2828.
- (47) Boyd, P.G.; Chidambaram, A.; García-Díez, E.; Ireland, C.P.; Daff, T.D.; Bounds, R.; Gładysiak, A.; Schouwink, P.; Moosavi, S.M.; Maroto-Valer, M.; Reimer, J.A.; Navarro, J.A.R.; Woo, T.K.; Garcia, S.; Stylianou, K.C.; Smit, B. Data-driven design of metal–organic frameworks for wet flue gas CO₂ capture. *Nature*, **2019**, *576*, 253-256.
- (48) Krause, S.; Bon., V.; Senkowska, I.; Stoeck, U.; Wallacher, D.; Töbrens, D. M.; Zander, S.; Pillai, R. S.; Maurin, G.; Coudert, F.-X.; Kaskel, S. A pressure-amplifying framework material with negative gas adsorption transitions. *Nature* **2016**, *532*, 348-352.
- (49) Wagner, B. D.; McManus, G. J.; Moulton, B.; Zaworotko, M. J. *Chem. Commun.* **2002**, 2176–2177.
- (50) Zheng, Q.; Yang, F.; Deng, M.; Ling, Y.; Liu, X.; Chen, Z.; Wang, Y.; Zhou, Y. A Porous Metal-Organic Framework Constructed from Carboxylate-Pyrazolate Shared Heptanuclear Zinc Clusters: Synthesis, Gas Adsorption, and Guest-Dependent Luminescent Properties. *Inorg. Chem.* **2013**, *52*, 10368-10374.
- (51) Ren, H.-Y.; Han, C.-Y.; Qu, M.; Zhang, X.-M. Luminescent group 12 metal tetracarboxylate networks as probe for metal ions. *RSC Adv.* **2014**, *4*, 49090-49097.
- (52) Eliseeva, S. V.; Pleshkov, D. N.; Lyssenko, K. A.; Lepnev, L. S.; Bünzli, J. C.; Kuzmina, N. P. Highly Luminescent and Triboluminescent Coordination Polymers Assemble from Lanthanide β -Diketonates and Aromatic Bidentate O-donor Ligands. *Inorg. Chem.* **2010**, *49*, 9300-9311.

(53) De Bettencourt-Dias, A.; Barber, P. S.; Viswanathan, S.; de Lill, D. T.; Rollett, A.; Ling, G.; Altun, S. Para-derivatized Pybox Ligands As Sensitizers in Highly Luminescent Ln(III) Complexes. *Inorg. Chem.* **2010**, *49*, 8848-8861.

(54) Mendiratta, S.; Lee, C.-H.; Lee, S.-Y.; Kao, Y.-C.; Chang, B.-C.; Lo, Y.-H.; Lu, K.-L. Structural Characteristics and Non-Linear Optical Behaviour of a 2-Hydroxynicotinate-containing Zinc-Based Metal-Organic Framework. *Molecules* **2015**, *20*, 8941-8951.

(55) Xue, P.; Wang, P.; Chen, P.; Yao, B.; Gong, P.; Sun, J.; Zhang, Z.; Lu, R. Bright persistent luminescence from pure organic molecules through a moderate intermolecular heavy atom effect. *Chem. Sci.* **2017**, *8*, 6060-6065.

(56) Cepeda, J.; Pérez-Yáñez, S.; Beobide, G.; Castillo, O.; García, J. A.; Lanchas, M.; Luque, A. Enhancing luminescence properties of lanthanide(III)/pyrimidine-4,6-dicarboxylato system by solvent-free approach. *Dalton Trans.* **2015**, *44*, 6972-6986.

(57) Yang, X.; Lin, X.; Zhao, Y.; Zhao Y. S.; Yan, D. Lanthanide Metal-Organic Framework Microrods: Colored Optical Waveguides and Chiral Polarized Emission *Angew. Chem., Int. Ed.* **2017**, *56*, 7853-7857.

(58) Geburt, S., Lorke, M.; da Rosa, A. L.; Frauenheim, T.; Röder, R.; Voss, T.; Kaiser, U.; Heimbrod, W.; Ronning, C. Intense Intrashell Luminescence of Eu-Doped Single ZnO nanowires at Room Temperature by Implantation Created Eu-O_i complexes. *Nano Lett.* **2014**, *14*, 4523-4528.

(59) Pajuelo-Corral, O.; Rodríguez-Diéguez, A.; García, J. A.; San Sebastian, E.; Seco, J. M.; Cepeda, J. Chiral coordination polymers based on d¹⁰ metal and 2-aminonicotinate with blue fluorescent/green phosphorescent anisotropic emissions. *Dalton Trans.* **2018**, *47*, 8746-8754.

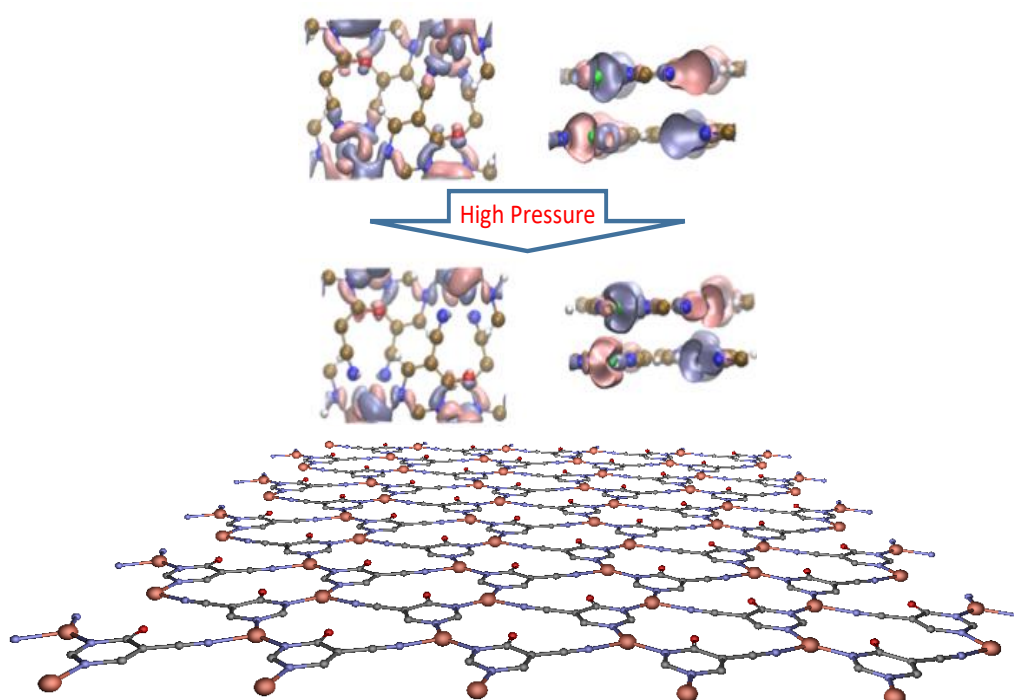
(60) Gu F.; Yu, H.; Wang, P.; Yang, Z.; Tong, L. Light-Emitting Polymer Single Nanofibers via Waveguiding Excitation. *ACS Nano* **2010**, *4*, 5332-5338.

(61) Adamo C.; Jacquemin, D. The calculations of Excited-state properties with Time-Dependent Density Functional Theory. *Chem. Soc. Rev.* **2013**, *42*, 845-856.

(62) Kasha, M. Characterization of electronic transitions in complex molecules.
Discuss. Faraday Soc. **1950**, 9, 14-19.

Capítulo 11

Rational Design of an unusual 2D-MOF based on Cu(I) and 4-hydroxypyrimidine-5-carbonitrile as Linker with Conductive Capabilities. A Theoretical Approach based on High-Pressure XRD



Rational Design of an unusual 2D-MOF based on Cu(I) and 4-hydroxypyrimidine-5-carbonitrile as Linker with Conductive Capabilities. A Theoretical Approach based on High-Pressure XRD

Antonio A. García-Valdivia,^a Francisco J. Romero,^b Javier Cepeda,^c Diego P. Morales,^b Nicola Casati,^d Antonio J. Mota,^a Linda A. Zotti,^e Juan J. Palacios,^f Duane Choquesillo-Lazarte,^g José F. Salmerón,^b Almudena Rivadeneyra^b and Antonio Rodríguez-Diéguez,^a

ENVIADO: CHEMICAL COMMUNICATIONS

- a. Departament of Inorganic Chemistry, Faculty of Science, University of Granada, 18071, Granada, Spain.*
- b. Pervasive Electronic Advanced Research Laboratory (PEARL) Departament Electronics and Computer Technology, University of Granada, 18071, Granada, Spain.*
- c. Departament of Applied Chemistry, Faculty of Chemistry, University of The Basque Country UPV/EHU, Paseo Manuel Lardizabal 3, 20018, Donostia-san Sebastián, Spain.*
- d. Laboratory for Synchrotron Radiation- Condensed Matter, Paul Scherrer Institute, Forschungstrasse 111, 5232 Villigen, Switzerland.*
- e. Departamentode Física Aplicada I, Escuela politécnica Superior, Universidad de Sevilla, Seville, E-41011, Spain.*
- f. Departamento de Física de la Materia Condensada, Condensed Matter Physics Center (IFIMAC), and Instituto Nicolás Cabrera (INC), Universidad Autónoma de Madrid; Madrid, 28049, Spain.*
- g. Crystallographic Studies Laboratoryru, IACT (CSIC-UGR), Avda. de las Palmeras 4, 18100, Armilla, Granada, Spain.*

Abstract

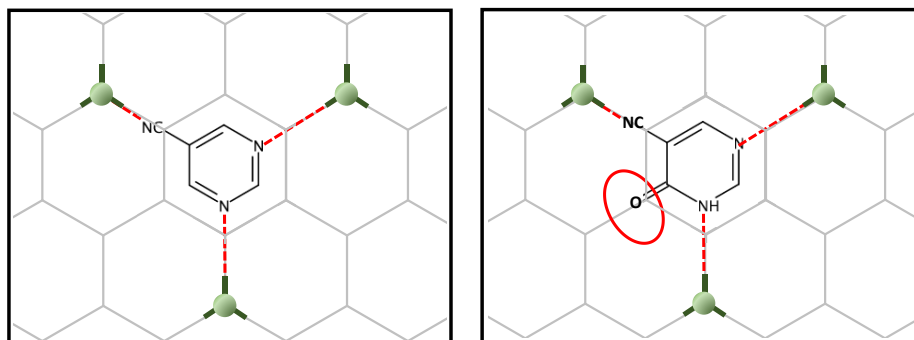
Herein we present, for the first time, a 2D-MOF based on copper and 4-hydroxypyrimidine-5-carbonitrile as linker. Each MOF layer is perfectly flat and neutral, as is the case for grapheme. High pressure XR diffraction measurements reveal that such layered structure can be modulated between 3.01 to 2.78 Å interlayer separation, with an evident piezochromism and varying conductive properties. An analysis of the band structure indicates that this material is conductive along different directions depending on the application of preasure or

H doping. These results pave the way to developing novel layered materials with tunable and efficient properties for pressure-based sensors.

1. Introduction

The design and synthesis of new materials that have high electrical conductivity and switchable properties is of great interest due to the current demand in the field of devising sensors.^{1,2} Some of the most interesting materials applicable in this respect metal-organic frameworks (MOFs), materials constituted by organic ligands coordinated to metal ions or clusters defining a porous and crystalline network,³ have received great interest due to their structural tunability as well as the properties that arise from their topological features.⁴ In particular, the study of transition metal ions-based MOFs has evolved enormously in many areas.⁵ The great advantage of coordination chemistry is that, thanks to its simple synthetic routes, it allows us to design materials with applications in virtually all fields. In this sense, in recent years, several groups have worked in the design of novel MOFs to explore their properties in luminescence,⁶ gas adsorption,⁷ optical storage,⁸ magnetism⁹ and biology as drug-delivery systems,¹⁰ cytotoxic agents¹¹ and sensing.¹² However, the use of MOFs to construct materials for pressure-based sensors is almost unexplored.¹³

Taking into account the above, we set out minds to design a novel 2D-MOF with a potentially large number of applications. For this, and inspired by multilayer graphene, we generate graphene-like layers as a template, promoting coordination links at 120 degree angles. To generate some asymmetry in the network, we could have used pyrimidine-5-carbonitrile as ligand, however, we decided to use 4-hydroxypyrimidine-5-carbonitrile as this linker possesses an oxygen atom in para position that can be an excellent alternative to increase the extended aromaticity and introduce electronic density in the channels of the possible MOF (Scheme I).



Scheme I. Design of 2D-MOF by using 4-hydroxypyrimidine-5-carbonitrile and copper metal ions.

Finally, we must choose the ideal metal ion. In this case, we decided to use copper(II) because of its easy plasticity in the coordination sphere which would allow you to display a trigonal bipyramid geometry. Moreover, another possibility could be that within the solvothermal reaction, Cu(II) could be reduced to Cu(I) with a flat trigonal geometry, as it should have to maintain the desired graphene type network. The choice of copper as a metal ion is the perfect choice that would favour the formation of the desired two-dimensional network, thereby achieving graphene-like networks. The copper-ligand linkage, moreover, enables π -d conjugation in a 2D plane.

As a result, we present in this work a novel MOF based on 2D-coordination polymers (CPs) with formula $[\text{Cu}(4\text{hypymca})]_n$ (hereafter compound **1**) that shows a distorted honeycomb-like structure and shares some features with graphene. Moreover, we report on its structural and electronic properties under pressure and doping, both promising strategies to improve the material conductivity.

2. Results

When we carried out the reaction between the above ligand and the copper chloride we obtained a bidimensional CP that crystallizes in the orthorhombic system, in the $Pbcm$ space group. The geometry around copper(I) may be described as a distorted trigonal planar environment that involves the N atoms pertaining to three independent 4hypymca linkers (Figure 1). These three nitrogen atoms

correspond to two nitrogen atoms from the pyrimidine rings of 4hypymca and one nitrogen pertaining to the cyanide group. The Cu-N_{pyr} bond distances are 1.935(5) and 1.955(5) Å, while the Cu-N_{cyno} distance has a value of 2.009(6) Å. These distances lie within the expected range.¹⁴

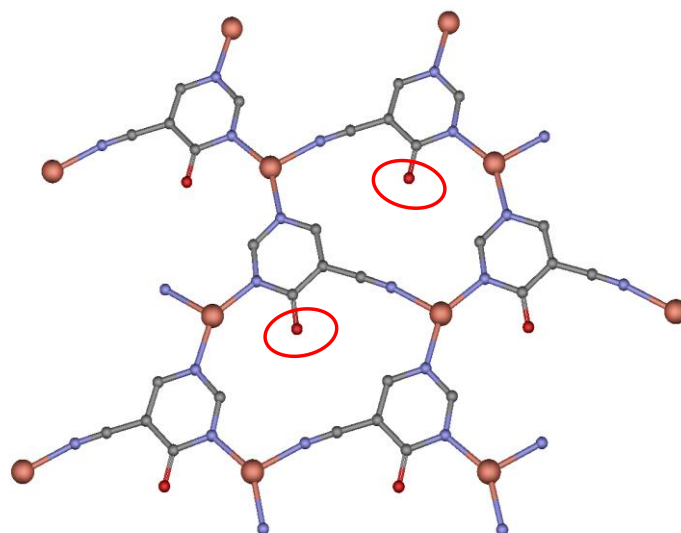


Figure 1. Perspective of coordination mode of the 4-hydroxypyrimidine-5-carbonitrile and distorted trigonal environment of copper ions.

The perfectly planar **hcb** network is formed from tiled neutral Cu₃(4hypymca)₃ units running parallel to the *ab* plane (Figure 2). In these sheets, Cu(I) ions exhibit a CuN₃ coordination polyhedron with distorted trigonal geometry. The equatorial positions are occupied by three nitrogen atoms belonging to three different bridging ligands, which adopt a planar conformation. Each layer is therefore neutral, as is the case of graphene, and can be conceived as a self-standing monolayer material.

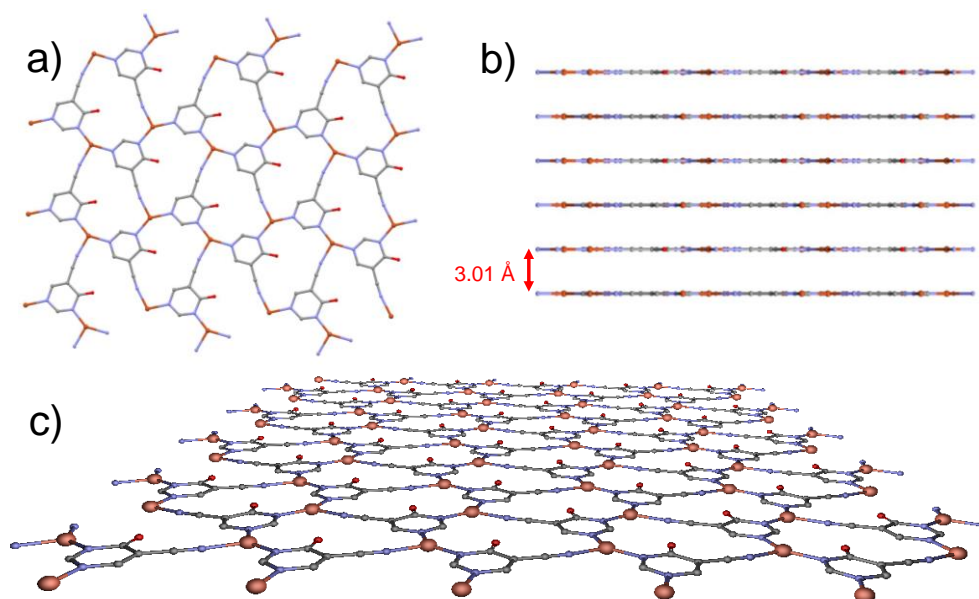


Figure 2. *a) Perspective of 2D plane in MOF. b) Separation among sheets in MOF. c) Projection in perspective of MOF.*

Compound **1** exhibits unsupported cuprophilic interactions among layers (Figure 3), featuring infinite $(\text{Cu}\cdots\text{Cu})_n$ chains spanning the crystal lattice with identical intermolecular $\text{Cu}\cdots\text{Cu}$ distances ($3.0160(9)\text{\AA}$), which is close to the separation found in paddle-wheel shaped dimeric entities or 1D CPs.¹⁵ Nonetheless, a search of the structures deposited in the CSD database looking for similar arrangements did not yield any results. Instead, the linkers are, from a layer to the next, staggered in the *c* direction. Thus, we can describe the complete structure as a 2D-dimensional network formed by metal-organic layers, joined by weak $\text{Cu}\cdots\text{Cu}$ metal interactions along *c* axis.

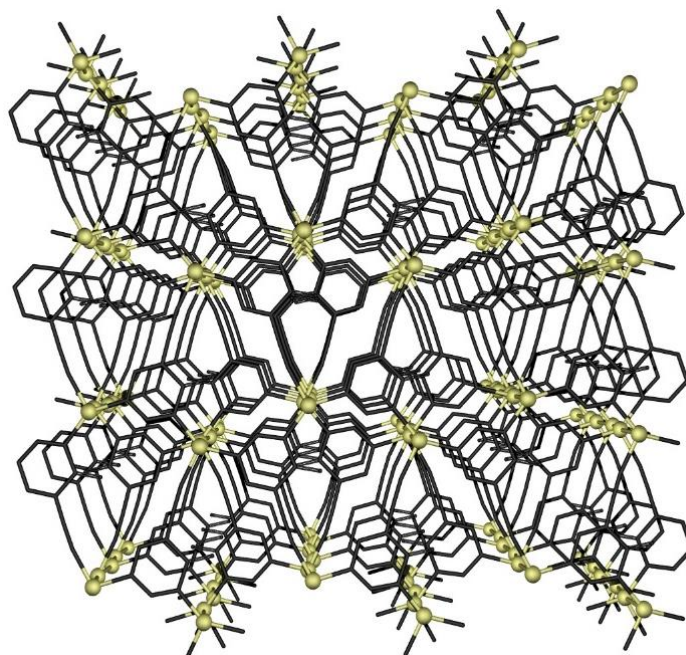


Figure 3. *Three-dimensional network formed by C...Cu metal interactions.*

Subsequently, the material was also subjected to high pressure diffraction measurements so as to study the potential flexibility of the 3D packing. In this sense, we have managed to apply 0.9, 2.75 and 4.2 GPa to the sample and we have measured the crystalline structure by XRD (structure 2 = 4.2 GPa). In general, the layers of this compound under pressure preserve the original topology, without distortion of the flat arrangement, although the interlayer distance is observed to be reduced from 3.01 to 2.78 Å (Figure 4).

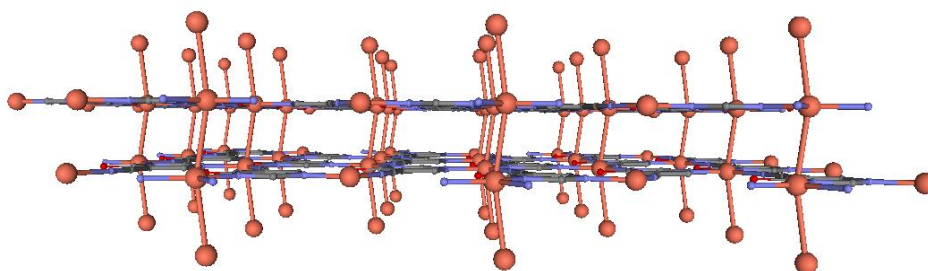


Figure 4. *Perspective of 2D plane in compound 2 in which the reduction in the separation distance between the layers is observed.*

Further details about bond lengths and angles are reported in Table 1. This, in turn, brings a radical change in the colour of the crystal from yellow to red, as previously reported for other Cu-based systems.¹⁶ We also found that the linear (Cu \cdots Cu)_n chains are not completely straight anymore in **2**, a fact that is not surprising in view of observations for other metallic chains.¹⁷

Table 1. Bond lengths (Å) and angles (deg) in the original and compressed materials.

	Original compound	0.9 GPa	2.7 GPa	4.2 GPa
Cu-N1	1.935(5)	1.93(3)	1.92(2)	1.93(3)
Cu-N2	1.955(5)	1.96(4)	1.94(3)	1.91(3)
Cu-N3	2.009(6)	2.01(2)	2.012(19)	1.996(19)
Cu1 \cdots Cu1	3.0160(9)	2.9549(11)	2.8333(10)	2.7786(13)
N1-Cu-N2	143.3(2)	145.6(13)	145.9(10)	147.9(11)
N1-Cu-N3	112.3(2)	110.0(17)	109.5(14)	107.6(14)
N2-Cu-N3	104.4(2)	104.4(12)	104.6(9)	104.5(9)
Cu1-N3-C5	170.4(5)	166(3)	166(3)	166(3)
Cu1 \cdots Cu1 \cdots Cu1	170.04(5)	168.5(4)	166.1(3)	164.4(4)

In order to get a deeper insight into the physical properties of the layered structure, we decided to perform theoretical (DFT) calculations on a Cu₃L₆³⁻ unit in order. The π electronic density is obtained by means of the Electron Localization Function (ELF) calculated by the Multiwfn suite of programs,¹⁸ see Figure 5, indicating a highly extended π electronic structure on each sheet. This insight can be further extended by performing band structure calculations as implemented in the OpenMX code.¹⁹

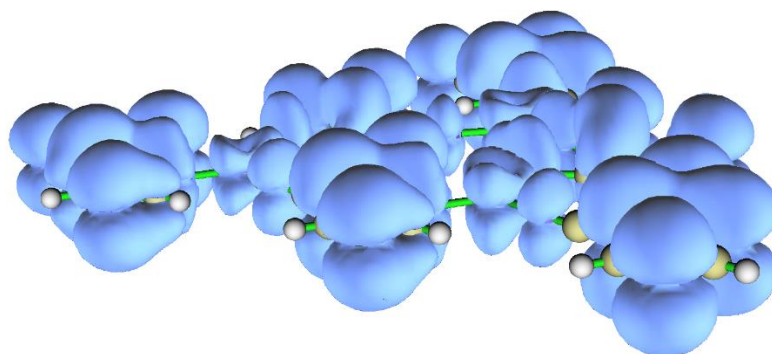


Figure 5. *Electron localization function representation.*

We employed the PBE functional²⁰ and a triple-zeta basis set for all atoms. Figure 6 gathers the band structure obtained for the original compound (panel a) and the one obtained upon compression (panel b) along selected paths in the orthorhombic cell of the reciprocal space (see inset c for a representation of the Brillouin zone). The curvature of an energy band is known to be related to the effective mass, which in turns determines the mobility inside a crystal. The final conductivity obviously depends on the position of the chemical potential. This is determined by the type of free carriers generated upon doping the material. However, analysing the shape of a band can provide important information on how good the conductivity in that specific band can be, once it becomes energetically accessible by carriers. In the case of both structures shown in Figure 6, conductivity seems to be possible in the conduction band and especially along the GZ and GX direction. This is suggested by the parabolic (free-electron like) behaviour of the band shape observed along these two directions. The same applies to the GY direction, albeit not to the same extent.

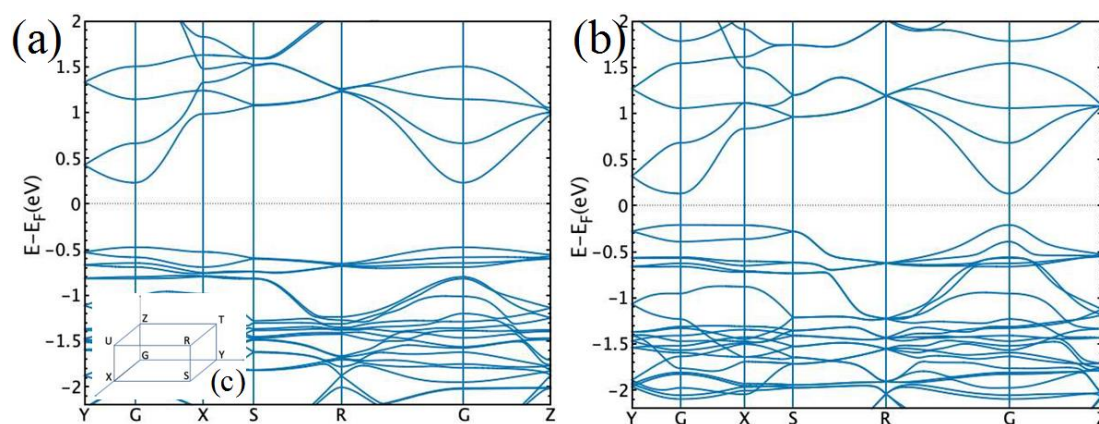


Figure 6. Band structure for the original compound (a) and compressed structure (b). The inset (c) contains a representation of the Brillouin Zone.

In Figure 7, the spatial distribution of the wavefunction for both structures is shown at the G point for the lowest unoccupied (conduction band) and highest occupied (valence band) states (henceforth called LUMO and HOMO, in analogy with the molecular-orbital terminology). In the LUMO top-view representation of both compounds, we observe a higher amount of overlap along the GX direction than in the GY, which agrees with the difference in band curvature observed between these two paths in the conduction band. In addition, the corresponding side view reveals that the conductivity along the z axis can take place either along the Cu-Cu chains normal to the planes or along the overlap formed between pz orbitals of C (or N) atoms belonging to two different planes (and not necessarily aligned perpendicularly to the plane).

As for the HOMO, the top view shows, overall, a lower degree of overlap with respect to the LUMO (consistent with the flatness observed for the valence band in the GY and GX directions). Nevertheless, the side view reveals that, in the compressed structure **2**, the distribution of the wavefunction in the z direction (normal to the planes) seems to be slightly more delocalized across the planes, which could give rise to higher conductive properties. This again agrees well with the different behaviour observed for the valence band around the G point in the compressed compound with respect to the original structure.

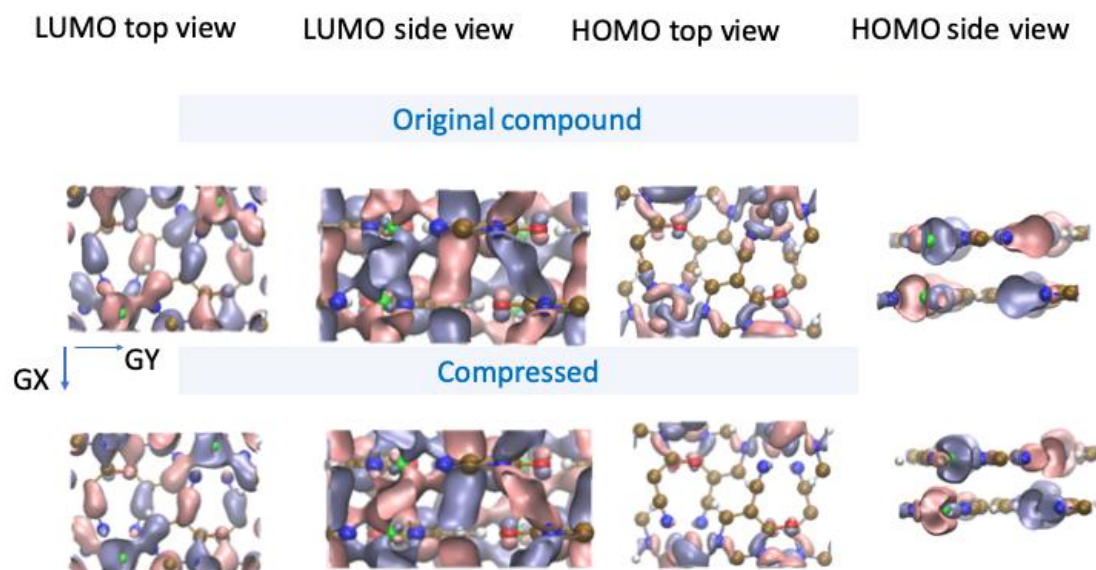


Figure 7. Wavefunction spatial distribution in the G point for the lowest unoccupied and highest occupied states. Copper, carbon, oxygen, nitrogen and hydrogen atoms are displayed in green, brown, red, blue and white, respectively. The arrows indicate the direction of the GX and GY paths in the reciprocal space.

To understand the effect on the electronic structure of piling multiple layers as compared to a single layer or two layers, we have analysed the band structure of these two systems (Figure 8). The valence band is found to be rather flat in both cases along all the reciprocal paths, whereas a more free-electron behaviour is observed in the conduction band at the G point for the monolayer (barely visible) and for the bilayer (noticeable), albeit not as much as in the 3D structure.

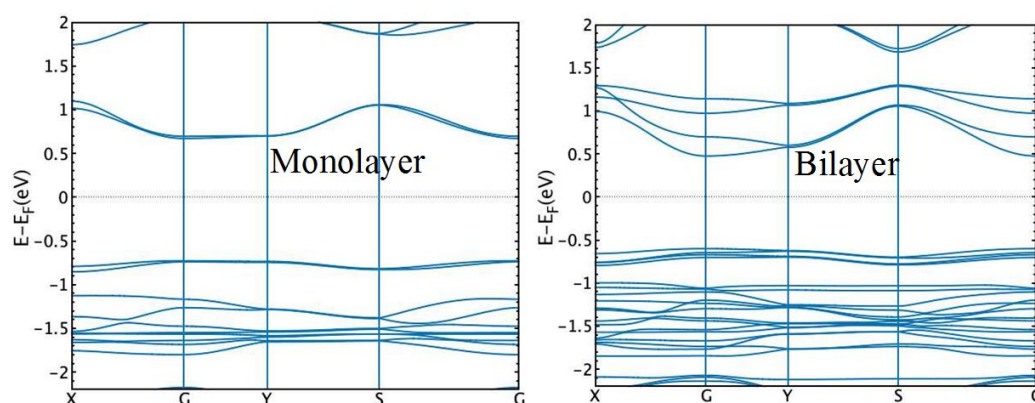


Figure 8. Band structure for an isolated single layer and for two consecutive layers.

Finally, one must bear in mind that the conductivity will be ultimately determined by the position of the chemical potential, which in turn will be dependent on the kind of free carriers (i.e. kind of doping). In the case of the initial structure of 1 (before compression), doping strategies which could a priori shift the conduction band towards the Fermi level should be adopted. This would allow one to take advantage of the conductive properties of the conduction band discussed above. As an example, in Figure 9 we show how the band structure of the 3D MOF before compression changes upon replacement of 1:4 oxygen with a hydrogen atom. We observe that indeed such a strategy makes the conduction band accessible for charge carriers.

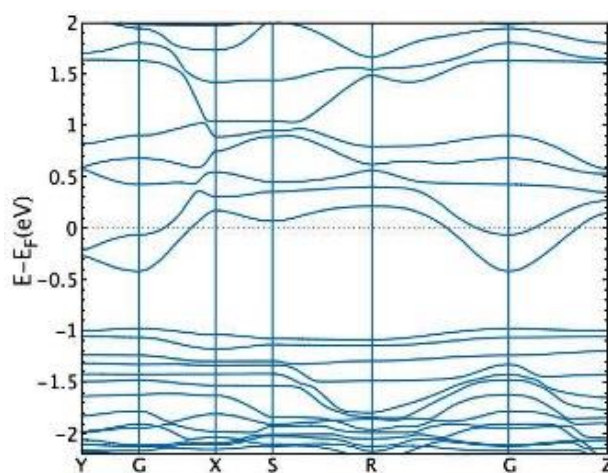


Figure 9. Band structure for 3D material upon replacement of 1:4 oxygen with a hydrogen atom.

Further research would be needed to study how doping may affect the chemical stability of this MOF and consequently, what the right concentration and best type of replacement are in order to achieve the highest performance. In general, replacing oxygen with any atom having a lower number of valence electrons would generate an excess of electrons and bring the chemical potential closer to the conduction band. Obviously, the lower the valence the closer the chemical potential will get to this band. Below we show two examples: energy band structure obtained by replacing 1:4 O with 1 C atom (Figure 10a) and with 1 Li atom (Figure 10b). Employing C, which has only two electrons less than O, affects the shape of the conduction band but it does not locate the chemical

potential close enough to it. Conversely, using Li, which has the same valence as H, results into a similar shift as that observed for H. This goes beyond the scope of the present work and will be pursued in future studies.

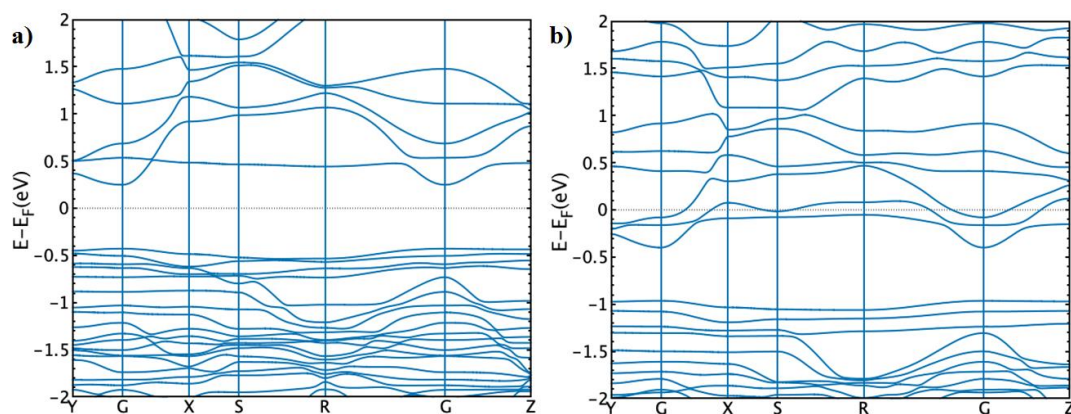


Figure 10. a) O replaced by C. b) O replaced by Li.

3. Conclusions

In summary, we have described for the first time a 2D-MOF based on copper and 4-hydroxypyrimidine-5-carbonitrile as linker. High pressure XRD measurements reveal that the layers of this material may be brought from 3.01 to 2.78 Å, changing the colour of the crystal and (according to our DFT-based results) varying the conductive properties of the material. We have analysed the band structure which indicates that this material shows different conduction properties depending on whether pressure is applied or not. In the case of compound **1**, the band structure indicates that this material is conductive in the conduction band, along perpendicular direction to the sheets as well as within the sheet plane. Instead, the gap becomes narrower in the compressed structure **2** and the material becomes conductive also in the valence band along the z direction. Analysing the 3D structure, we concluded that n-type doping could be a good strategy to improve the conductivity of this material. These results pave the way to developing novel layered materials, which can be deposited as single layers or engineered in the 3D structure for specific properties such as efficient materials for pressure sensors. New studies in these directions are currently being carried out in our laboratory

focusing, for instance, on the possible employment of different types of similar ligands.

4. Experimental Procedures

Chemicals. All the chemicals were of reagent grade and were used as commercially obtained.

Synthesis of [Cu(4hypymca)]_n (1). 0.09 mmol (10.00 mg) of 4-hydroxypyrimidine-5-carbonitrile were dissolved in 0.5 mL of DMF afterwards 0.5 mL of distilled water was added. In another glass vessel 0.06 mmol (15.59 mg) of CuCl₂·2H₂O was dissolved in 0.5 mL of distilled water and then 0.5 mL of DMF was added. Both solutions were mixed in a closed glass vessel and introduced in an oven at 100°C for 24h. Dark-green single crystals were grown during the heating procedure. The final product was washed with distilled water, and dried in open atmosphere. Yield: 71% based on metal. Anal Calcd for CuC₅H₂N₃O: C, 32.70; H, 1.10; N, 22.88. Found: C, 32.65; H, 1.06; N, 22.94.

Physical Measurements. Elemental analyses (C, H, N) were performed on an Euro EA Elemental Analyzer. FTIR spectra (KBr pellets) were recorded on a Nicolet IR 6700 spectrometer in the 4000–400 cm⁻¹ spectral region.

X-ray Diffraction. X-ray data collection of suitable single crystal of compound **1** was done at 100(2) K on a Bruker VENTURE area detector equipped with graphite monochromated Mo-K α radiation ($\lambda = 0.71073 \text{ \AA}$) by applying the ω -scan method. The data reduction were performed with the APEX2 software²¹ and corrected for absorption using SADABS.²² Crystal structures were solved by direct methods using the SIR97 program²³ and refined by full-matrix least-squares on F^2 including all reflections using anisotropic displacement parameters by means of the WINGX crystallographic package.²⁴ All hydrogen atoms were included as fixed contributions riding on attached atoms with isotropic thermal displacement parameters 1.2 times or 1.5 times those of their parent atoms for the organic ligands. Details of the structure determination and refinement of compounds are summarized in Table 2. Crystallographic data for the structures reported in this

paper have been deposited with the Cambridge Crystallographic Data Center as supplementary publication nos. CCDC 1942013-14 for compounds. Copies of the data can be obtained free of charge on application to the Director, CCDC, 12 Union Road, Cambridge, CB2 1EZ, U.K. (Fax: +44-1223-335033; e-mail: deposit@ccdc.cam.ac.uk or <http://www.ccdc.cam.ac.uk>).

Table 2. Crystallographic data and structure refinement details for all compounds.

Compound	1	0.9 GPa	2.75 GPa	2 (4.2 GPa)
Chemical formula	C ₅ H ₂ N ₃ OCu			
CCDC	1942013			
M/g mol⁻¹	183.64	183.64	183.64	183.64
T/K	100 K	293 K	293 K	293 K
Cryst. syst.	Orthorhombic	Orthorhombic	Orthorhombic	Orthorhombic
Space group	Pbcm	Pbcm	Pbcm	Pbcm
a (Å)	8.056 (3)	8.0286(8)	7.9702(8)	7.9478 (16)
b(Å)	10.787 (3)	10.776(10)	10.714(9)	10.61 (2)
c(Å)	6.0093 (18)	5.8800(5)	5.6247(4)	5.5058 (12)
V/ Å³	522.2 (3)	508.7(5)	480.3(4)	464.3 (9)
Z	4	4	4	4
ρ/g cm⁻³	2.336	2.398	2.539	2.627
μ/mm⁻¹	4.082	4.191	4.439	4.592
R[1>2σ(I)]a	0.0303	0.0645	0.0672	0.0443
wR2 [1>2σ(I)]b	0.0618	0.2066	0.2069	0.1222

$$[a] S = [\sum w(F_o^2 - F_c^2)^2 / (N_{obs} - N_{param})]^{1/2} [b] R_1 = \sum ||F_o| - |F_c|| / \sum |F_o| [c] wR_2 = [\sum w(F_o^2 - F_c^2)^2 / \sum wF_o^2]^{1/2}$$

$$w = 1/[\sigma^2(F_o^2) + (aP)^2 + bP] \text{ where } P = (\max(F_o^2, 0) + 2F_c^2)/3$$

5. High-Pressure X-Ray Diffraction

High pressure single crystal study was undertaken using a custom made Diamond Anvil Cell equipped with 0.5 mm culets and a ~40° opening. A small crystal of the sample was loaded in the pre-pressed and drilled steel gasket along with a methanol-ethanol mixture (4:1) and a small ruby sphere for pressure calibration. Data were collected using a single phi scan in the Extreme conditions beamline at Diamond Light Source, using a focused beam of 40 keV as defined by a 20 μm pinhole. Short acquisitions were performed to avoid large radiation

damage, anyway visible at the end of the experiment in the form of a brown spot in the center of the crystal. Data were collected using an Agilent Atlas CCD calibrated with a NIST ruby sphere and integrated using the CrysAlis package and its high pressure dedicated abilities. Diamond overlapping peaks were masked out of the integration. Despite attempts no lower or higher symmetry were identified for the given data sets up to 4.5 GPa.

6. Notes and References

- 1 P. Dechambenoit, J.R. Long, *Chem. Soc. Rev.* 2011, **40**, 3249–3265.
- 2 T. Dietl and H. Ohno, *H. Rev. Mod. Phys.* 2014, **86**, 187–251.
- 3 S.-N. Zhao, Y. Zhang, S.-Y. Song, H.J. Zhang, *Coordin. Chem. Rev.*, 2019, **398**, 113007.
- 4 H. Furukawa, K.E. Cordova, M. O'Keeffe, O.M. Yaghi, *Science*, 2013, **341**, 974.
- 5 B. Li, M. Chrzanowski, Y. Zhang, S. Ma, *Coord. Chem. Rev.*, 2016, **307**, 106–129.
- 6 J. Cepeda, E. San Sebastian, D. Padro, A. Rodríguez-Diéguez, J.A. García, J.M. Ugalde and J.M. Seco, *Chem. Commun.*, 2016, **52**, 8671–8674.
- 7 a) J.M. Seco, D. Fairen-Jimenez, A.J. Calahorro, L. Méndez-Liñán, M. Pérez-Mendoza, N. Casati, E. Colacio and A. Rodríguez-Diéguez, *Chem. Commun.*, 2013, **49**, 11329–11331. b) J. Cepeda, M. Perez-Mendoza, A.J. Calahorro, N. Casati, J.M. Seco, M. Aragonés-Anglada, P.Z. Moghadam, D. Fairen-Jimenez and A. Rodríguez-Diéguez, *J. Mat. Chem. A*, 2018, **6**, 17409–17416.
- 8 J. Cepeda and A. Rodríguez-Diéguez, *CrystEngComm*, 2016, **18**, 8556–8573.
- 9 A.J. Calahorro, I. Oyarzabal, B. Fernández, J.M. Seco, T. Tian, D. Fairen-Jimenez, E. Colacio and A. Rodríguez-Diéguez, *Dalton Trans*, 2016, **45**, 591–598.

- 10** D. Briones, B. Fernández, A.J. Calahorro, D. Fairen-Jimenez, R. Sanz, F. Martínez, G. Orcajo, E. San Sebastián, J.M. Seco, C. SánchezGonzález, J. Llopis and A. Rodríguez-Diéguez, *Cryst. Growth Des.* 2016, **16**, 537-540.
- 11** B. Fernández, I. Fernández, J. Cepeda, M. Medina-O'Donnell, E.E. Rufino-Palomares, A. Raya-Barón, S. Gómez-Ruiz, A. Pérez-Jiménez, J. Antonio Lupiáñez, F.J. Reyes-Zurita and A. Rodríguez-Diéguez, *Cryst. Growth Des.*, 2018, **18**, 969–978.
- 12** J.M. Seco, E. San Sebastián, J. Cepeda, B. Biel, A. Salinas-Castillo, B. Fernández, D.P. Morales, M. Bobinger, S. Gómez-Ruiz, F.C. Loghin, A. Rivadeneyra and A. Rodríguez-Diéguez, *Sci. Rep-UK.*, 2018, **8**, 14414-14423.
- 13** R. Dong, Z. Zhang, D.C. Tranca, S. Zhou, M. Wang, P. Adler, Z. Liao, F. Liu, Y. Sun, W. Shi, Z. Zhang, E. Zschech, S.C.B. Mannsfeld, C. Felser and X. Feng, *Nat. Commun.*, 2018, **9**, 2637, DOI: 10.1038/s41467-018-05141-4.
- 14** J. Troyano, E. Zapata, J. Perles, P. Amo-Ochoa, V. Fernández-Moreira, J. I. Martínez, F. Zamora and S. Delgado, *Inorg. Chem.*, 2019, **58**, 3290-3301.
- 15** M. Köberl, M Cokoja, W. A. Herrmann and F. E. Kühn, *Dalton Trans.*, 2011, **40**, 6384-6859.
- 16** Q. Benito, B. Baptiste, A. Polian, L. Delbes, L. Martinelli, T. Gacoin, J.-P. Boilot and S. Perruchas, *Inorg. Chem.*, 2015, **54**, 9821-9825.
- 17** S. You, Z. Li, L. Yang, C. Dong, L. Chen, C. Jin, J. Hu, G. Shen, H. Mao, *J. Solid State Chem.*, 2009, **182**, 3085-3090.
- 18** T. Lu, F. Chen, *J. Comput. Chem.* 2012, **33**, 580-592.
- 19** T. Ozaki, K. Nishio and H. Kino, *Phys. Rev. B*, 2010, **81**, 035116.
- 20** J.P. Perdew, K. Burke and M. Ernzerhof, *Phys. Rev. Lett*, 1997, **78**, 1396.
- 21** Bruker Apex2, Bruker AXS Inc., Madison, Wisconsin, USA, 2004.
- 22** Sheldrick, G.M. SADABS, Program for Empirical Adsorption Correction, Institute for Inorganic Chemistry, University of Gottingen, Germany, 1996.

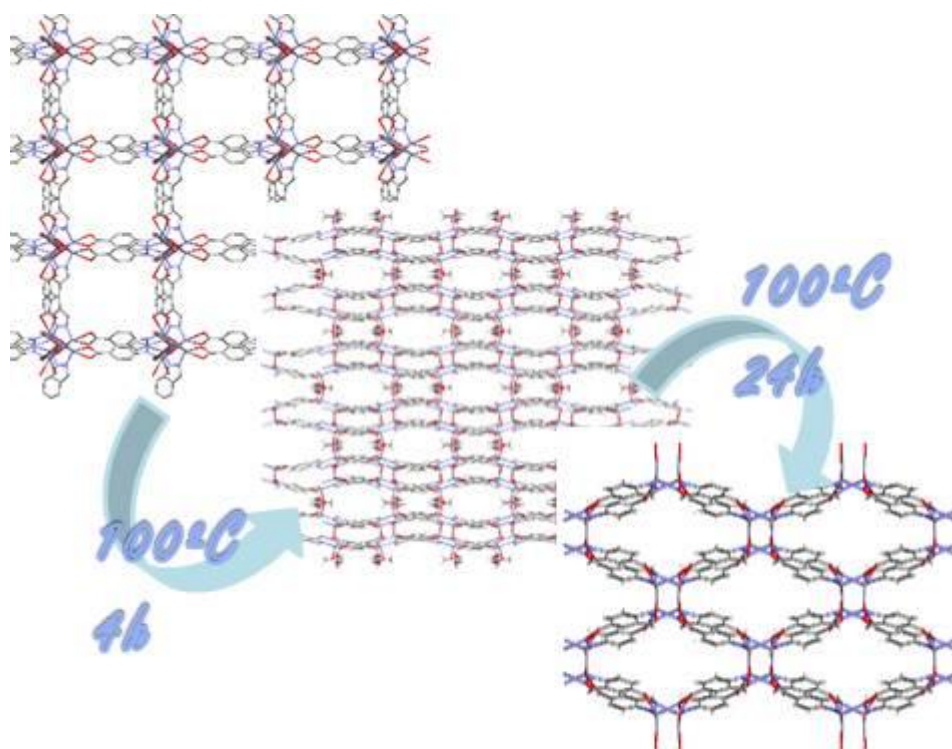
23 Altomare, A.; Burla, M. C.; Camilla, M.; Cascarano, G. L.; Giacovazzo, C.; Guagliardi, A. Moliterni A. G. G.; Polidori, G.; Spagna, *J. Appl. Cryst.*, 1999, **32**, 115-119.

24 (a) Sheldrick, G. M. SHELX-2014, Program for Crystal Structure Refinement, University of Göttingen, Göttingen, Germany, 2014. (b) Farrugia, *J. Appl. Cryst.*, 1999, **32**, 837-838.

ANEXOS

Anexo 1

Time-induced Single Crystal to Single Crystal Transformation and Luminescence of a Dynamic 3D Metal-Organic Framework based on Zn(II) and 1H-Indazole-5-Carboxylic Acid



Time-induced Single Crystal to Single Crystal Transformation and Luminescence of a Dynamic 3D Metal-Organic Framework based on Zn(II) and 1H-Indazole-5-Carboxylic Acid

Abstract

We report the formation of three novel metal-organic frameworks based on 1H-indazole-5-carboxylic acid. To the best of our knowledge, these complexes are the first examples of coordination compounds based on Zinc construct with this novel ligand. Must be highlighted that a time-induced transformation is produced generating different metal-organic frameworks with great topological diversity. These materials were synthesized by soft solvothermal routes and show interesting luminescent properties corroborates by theoretical calculations.

1. Introduction

The more than remarkable interest in metal-organic frameworks (MOFs) has undergone an exponential growth,¹ derived from their multiple types of verified industrial applications,² such as gas storage and purification, catalysis, luminescence and magnetism, as well as the great possibilities it offers when they are designed and synthesized. Their metal-organic hybrid nature offers potentially limitless arrangement types and topological architectures,³ reinforcing their versatility of use. In particular, the study of transition metal ions-based MOFs has evolved enormously in a great quantity of areas, considering the advantage that ions have fairly predictable coordination spheres, it allows us to design on paper materials with application for virtually all fields. In this sense, in these years, our group and others have worked in the design of novel MOFs to study their properties in luminescence,⁴ gas adsorption,⁵ catalysis,⁶ magnetism,⁷ biology as drug-delivery systems,⁸ cytotoxic agents⁹ and sensing.¹⁰ Bearing in mind the interest of our groups in the study MOFs based on nitrogen linkers with carboxylate groups, we decided to study the properties of this type of materials with the novel 1H-indazole-5-carboxylic acid because, as far as we know, there are few examples of coordination compounds synthesized with it.

This ligand is an ideal candidate to form CPs because of its multiple coordination possibilities not only derived from its carboxylate group but also from its indazole ring, being able to show some interesting coordination modes. Moreover, promising photoluminescence performance may as well be assumed to be developed because of the aromatic rings.

For all the above, in this work we present a new family of multidimensional zinc metal-organic frameworks based on 1H-Indazole-5-carboxylic acid which has been fully characterized from a structural and luminescent point of view.

2. Crystal Structures

Compound **1** consists of a three dimensional structure that crystallizes in the $A b a 2$ space group, in which Zn(II) ions are bridged by nitrogen atoms of H₂L in a bidentate way. The ZnN₂O₃ coordination sphere is completed by the coordination to the carboxylate moiety of the indazole derivative ligand in a bidentate way; in addition to a water molecule, which bridges the three Zn atoms of the asymmetric unit.

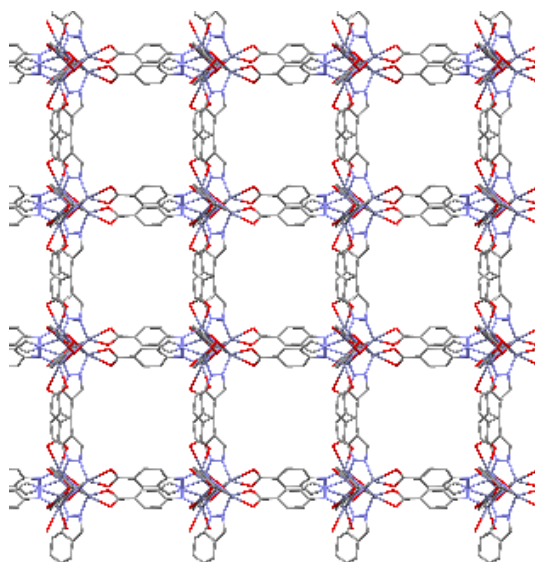


Figure 1. View along *a* axis of complex **1**.

The metal coordination sphere is best described as a square bipyramid, although the zinc ions show a geometry that is close to Johnson trigonal bipyramid

according to continuous-shape-measures (CShMs) using SHAPE software (Tables 1).¹¹

Tables 1. Continuous Shape Measurements for the ZnN₂O₃ coordination environment.

PP-5	1 D5h	Pentagon
vOC-5	2 C4v	Vacant octahedron [‡] (Johnson square pyramid, J1)
TBPY-5	3 D3h	Trigonal bipyramid
SPY-5	4 C4v	Square pyramid §
JTBPY-5	5 D3h	Johnson trigonal bipyramid (J12)

Complex	PP-5	vOC-5	TBPY-5	SPY-5	JTBPY-5
1-Zn 1	30.097	7.502	3.110	5.500	3.994
1-Zn 2	31.134	6.960	3.515	5.116	4.228
1-Zn 3	31.963	7.487	3.140	5.664	4.049

The 3D network presents potential solvent accessible volume along the cell axis, 75.3 % per unit cell volume concretely.

Compound **2** crystallizes in the orthorhombic *Pbcn* space group in which Zn(II) ions are bridged by nitrogen atoms of H₂L in a bidentate way giving rise to a stable and in plane M₂N₄ six membered ring. The Zn(II) ion is also coordinated to a carboxylate moiety of the indazole derivative ligand in a monodentate way, which extends the entity into infinite 2D layers. The coordination sphere of the metal is completed by the additional coordination of a water molecule. The ZnN₂O₂ coordination sphere is best described as a tetrahedron according to continuous-shape-measures (CShMs) using SHAPE software (Tables 1). The asymmetric unit contains a disordered dimethylformamide solvent molecule. This structure is derived by single-crystal to single-crystal transformation of compound **1**.

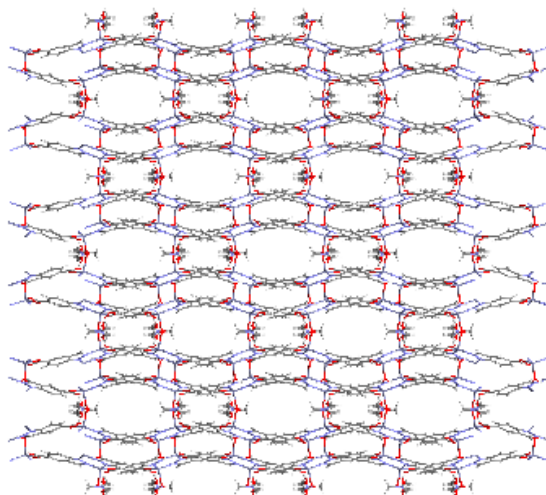


Figure 2. View along *c* axis complex **2**.

In regard to the supramolecular interactions which build up the structure it is worth mentioning the involvement of the coordinated water molecule in hydrogen bonding interactions while the angle formed among neighbouring ligands allow establishing C–H··· π interactions between aromatic rings (Figure 3).

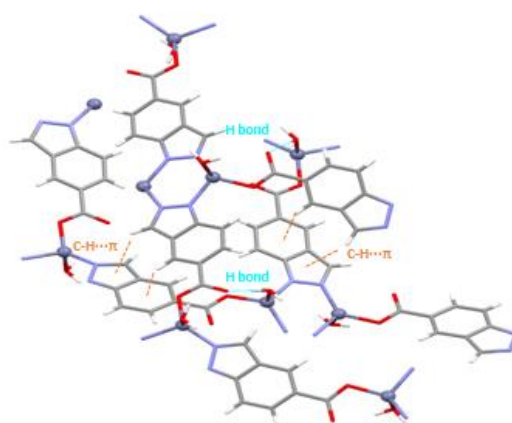


Figure 3. The most representative intermolecular interactions and packing modes for complex **2**.

Compound **3** is the result of the single-crystal-to-single-crystal transformation of compound **2**. It is derived from the desolvation of the disordered

dimethylformamide molecule of the unit cell as well as the coordination rearrangement of H₂L. Compound **3** crystallizes in the orthorhombic $C222_1$ space group in which Zn(II) ions are bridged by nitrogen atoms of H₂L in a bidentate way giving rise to an out of plane M₂N₄ six membered ring. In this case, the Zn(II) ion coordinated to a carboxylate moiety of the indazole derivative ligand in a bidentate way extending the structure into three dimensional coordination polymer. The structure presents narrow porous along *c* axis which are accessible to solvent (5.9% per unit cell volume).

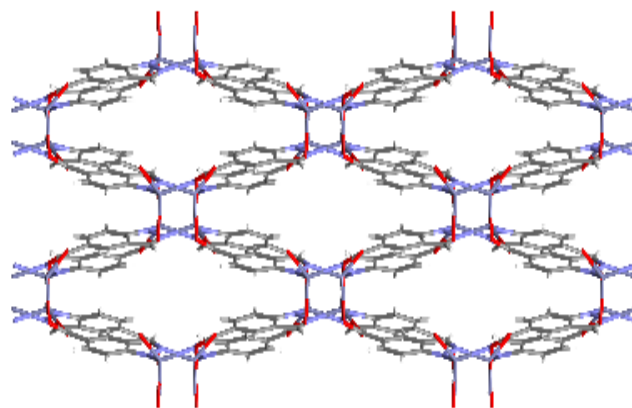


Figure 4. View along *c* axis complex **3**.

Continuous-shape-measures (CShMs) indicate that Zn1 coordination sphere is best described as tetrahedron according to SHAPE measurements (Tables 1).

To end up with the structural description, weak $\pi \cdots \pi$ interactions with high lateral offset among adjacent aromatic rings governs the crystal building in compound **3** (Figure 5).

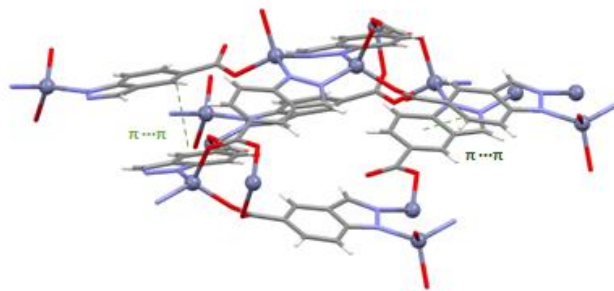


Figure 5. The most representative intermolecular interactions and packing modes for complex **3**.

Details of the structure determination and refinement of compounds are summarized in Table 2.

Table 2. Crystallographic data and structural refinement details for compounds.

Compound	1	2	3
Formula	C ₂₄ H ₁₂ N ₆ O ₇ Zn ₃	C ₃₅ H ₃₅ N ₉ O ₁₅ Zn ₄	C ₈ H ₄ N ₂ O ₂ Zn
<i>M_r</i>	692.51	1083.20	225.50
Crystal system	<i>orthorhombic</i>	<i>orthorhombic</i>	<i>orthorhombic</i>
Space group (no.)	<i>A b a 2 (41)</i>	<i>P b c n (60)</i>	<i>C 2 2 21 (20)</i>
<i>a</i> (Å)	24.293(3)	18.3981(12)	6.5467(16)
<i>b</i> (Å)	24.400(2)	17.7573(5)	17.711(5)
<i>c</i> (Å)	24.470(3)	14.1320(5)	13.5779(18)
<i>α</i> (°)	90	90	90
<i>β</i> (°)	90	90	90
<i>γ</i> (°)	90	90	90
<i>V</i> (Å ³)	14504(3)	4616.9(4)	1574.3(6)
<i>Z</i>	8	4	8
<i>D_c</i> (g cm ⁻³)	0.634	1.558	1.903
<i>μ</i> (Mo/CuK _α) (mm ⁻¹)	1.004	2.125	3.079
<i>T</i> (K)	100	100	100
Observed reflections	7597 (7130)	2421 (1743)	835 (650)

3. References

- 1.- a) K. Otsubo, T. Haraguchi and H. Kitagawa, *Coordination Chemistry Reviews*, 2017, **346**, 123-138. b) S. Furukawa, J. Reboul, S. Diring, K. Sumida and S. Kitagawa, *Chemical Society Reviews*, 2014, **43**, 5700-5734. c) F.X. Xamena, I. Llabres and J. Gascon, *RSC Catalysis Series*, 2013, **12**, 406-424.
- 2.- a) A. Dhakshinamoorthy and H. Garcia, *Chem. Soc. Rev.*, 2014, **43**, 5750-5765. b) L. Ma, C. Abney and W. Lin, *Chem. Soc. Rev.*, 2009, **38**, 1248–1256. c) P. Horcajada, R. Gref, T. Baati, P. K. Allan, G. Maurin, P. Couvreur, G. Ferey, R. E. Morris and C. Serre. *Chem. Rev.*, 2012, **112**, 1232–1268. d) P. Ramaswamy, N. E. Wong and G. K. H. Shimizu, *Chem. Soc. Rev.*, 2014, **43**, 5913–5932. e) K. Fujie, R. Ikeda, K. Otsubo, T. Yamada and S. Kitagawa, *Chem. Mater.*, 2015, **27**, 7355–7361. f) S. Lee, E. A. Kapustin and O. M. Yaghi, *Science*, 2016, **353**, 808–811. g) Y. Inokuma, S. Yoshioka, J. Ariyoshi, T. Arai, Y. Hitora, K. Takada, S. Matsunaga, K. Rissanen and M. Fujita, *Nature*, 2013, **495**, 461–466. h) V. Stavila, A. A. Talin and M. D. Allendorf, *Chem. Soc. Rev.*, 2014, **43**, 5994-6010. i) J. M. Frost, K. L. M. Harriman and M. Murugesu, *Chem. Sci.*, 2016, **7**, 2470–2491. j) G. A. Craig and M. Murrie, *Chem. Soc. Rev.*, 2015, **44**, 2135–2147. k) H. S. Quah, W. Chen, M. K. Schreyer, H. Yang, M. W. Wong, W. Ji and J. J. Vital, *Nat. Commun.*, 2015, **6**, 7954–7961. l) A. Dhakshinamoorthy, M. Alvaro, H. Garcia, *Chem. Commun.*, 2012, **48**, 11275-11288.
- 3.- W. Lu, Z. Wei, Z.-Y. Gu, T.-F. Liu, J. Park, J. Park, J. Tian, M. Zhang, Q. Zhang, T. Gentle, M. Boscha and H.-C. Zhou. *Chem. Soc. Rev.*, 2014, **43**, 5561-559.
- 4.- J.M. Seco, S. Pérez-Yáñez, D. Briones, J.Á. García, J. Cepeda and A. Rodríguez-Diéguez, *Cryst.Growth.Des.*, 2017, **17**, 3893–3906.
- 5.- a) J.M. Seco, D. Fairen-Jimenez, A.J. Calahorro, L. Méndez-Liñán, M. Pérez-Mendoza, N. Casati, E. Colacio and A. Rodríguez-Diéguez, *Chem. Commun.*, 2013, **49**, 11329-11331. b) J. Cepeda, M. Pérez-Mendoza, A.J. Calahorro, N. Casati, J.M. Seco, M. Aragonés-Anglada, P.Z. Moghadam, D. Fairen-Jimenez and A. Rodríguez-Diéguez, *J.Mater.Chem.A*, 2018, **6**, 17409-17416.

- 6.- M. Cabrero-Antonino, S. Remiro-Buenamañana, M. Souto, A.A. García-Valdivia, D. Choquesillo-Lazarte, S. Navalón, A. Rodríguez-Diéguez, G. Mínguez Espallargas and H. García, *Chem. Commun.*, 2019, **55**, 10932-10935.
- 7.- A.A. García-Valdivia, J.M. Seco, J. Cepeda and A. Rodríguez-Diéguez, *Inorg.Chem.*, 2017, **56**, 13897-13912.
- 8.- D. Briones, B. Fernández, A.J. Calahorro, D. Fairen-Jimenez, R. Sanz, F. Martínez, G. Orcajo, E. San Sebastián, J.M. Seco, C. SánchezGonzález, J.Llopis and A. Rodríguez-Diéguez, *Cryst.Growth.Des.*, 2016, **16**, 537–540.
- 9.- B. Fernández, I. Oyarzabal, E. Fischer-Fodor, S. Macavei, I. Sánchez, J.M. Seco, S. Gómez-Ruiz and A. Rodríguez-Diéguez, *CrystEngComm*, 2016, **18**, 8718-8721.
- 10.- J.M. Seco, E. San Sebastián, J. Cepeda, B. Biel, A. Salinas-Castillo, B. Fernández, D.P. Morales, M. Bobinger, S. Gómez-Ruiz, F.C. Loghin, A. Rivadeneyra and A. Rodríguez-Diéguez, *Sci. Rep.*, 2018, **8**, 14414.
- 11.- M. Lunell, D. Casanova, J. Cirera, J.M. Bofill, P. Alemany, S. Alvarez, M. Pinsky and D. Avnir, SHAPE, v1.1b; Barcelona, Spain, 2005.

Conclusiones Generales



Esta Tesis doctoral ha tenido como objetivo general sintetizar y estudiar las propiedades de nuevos materiales multifuncionales basados en ligandos nitrogenados con grupos carboxilato. Se han recogido 33 compuestos de coordinación multifuncionales con interesantes estructuras cristalinas de aplicación en varios campos de interés (magnetismo, luminiscencia, adsorción, conductividad, sensores y actividad biológica) recogidos en 11 artículos científicos. Además, se está trabajando en 1 artículo que contiene 3 compuestos más, recogidos en el apartado Anexos de esta Tesis.

Las conclusiones generales a las que se ha llegado durante la realización de esta Tesis han sido:

1. La síntesis solvotermal sigue siendo un método excelente para la obtención de nuevos materiales. Más en concreto la utilización de viales de vidrio permite un mejor seguimiento de la reacción. La utilización de estos viales ha facilitado la síntesis de la gran mayoría de los compuestos presentes en esta Tesis.
2. Se ha sintetizado 4 compuestos de coordinación de diferentes dimensiones utilizando el ligando ácido 1-metilimidazol-5-carboxílico (mimc) e iones metálicos de la primera serie de transición con fórmulas $[\text{Ni}(\text{mimc})_2(\text{H}_2\text{O})_4]$, $[\text{Co}(\mu\text{-mimc})_2]_n$, $\{[\text{Cu}_2(\mu\text{-mimc})_4(\text{H}_2\text{O})] \cdot 2\text{H}_2\text{O}\}_n$ y $[\text{Cd}(\mu\text{-mimc})_2(\text{H}_2\text{O})]_n$, demostrando así, la gran versatilidad de unión de este ácido. El compuesto de cobalto(II) es de los pocos polímeros de coordinación 2D de este metal que presentan una relajación lenta de la magnetización a causa de una anisotropía magnética moderada de signo positivo ($D = +12.9 \text{ cm}^{-1}$, $E = +0.5 \text{ cm}^{-1}$). Además el análisis dinámico de espín a través de medidas en *ac* muestra la aparición de un túnel cuántico de la magnetización que puede suprimirse con la aplicación de un campo magnético, permitiendo identificar dos procesos de relajación: (i) uno más rápido referido a la relajación de los iones aislados en la estructura mediante múltiples mecanismos (directo, Orbach y Raman) dada la combinación de anisotropía magnética axial positiva, con una barrera térmica de 26 K y (ii) otro más lento debido a interacciones de

intercambio débiles a través de la red 2D o interacciones de *stacking* tipo π - π . Otro punto destacable de dicho compuesto es la temperatura de *blocking* de aproximadamente 14K, la cual se encuentra entre las más altas para SIMs de Co(II). Por otro lado, el compuesto de cadmio(II) presenta una interesante emisión verde caracterizada por una fosforescencia persistente con una remanencia de aproximadamente 1 segundo a baja temperatura tras retirar la fuente de UV. Las medidas revelan tres emisiones fluorescentes/fosforescentes de diferentes tiempos de vida medios: persistentes (0.25-0.43 s), intermedios (0.05-0.23 s) y cortos (6-39 ms). Los cálculos TD-DFT combinados con una estrategia computacional estiman que la emisión de fosforescencia está regida por un mecanismo LCCT (singlete-singlete y triplete-singlete).

3. Han sido sintetizados cuatro nuevos compuestos de coordinación basados en lantánidos y el ácido 5-bromonicotínico (5-BrNic) con las siguientes fórmulas moleculares: $[\text{Dy}(\text{5-BrNic})_3(\text{H}_2\text{O})_4]$, $[\text{Tb}(\text{5-BrNic})_2(\text{H}_2\text{O})_4] \cdot [\text{Tb}(\text{5-BrNic})_4(\text{H}_2\text{O})_2] \cdot (\text{5-HBrNic})_2$, $[\text{Yb}(\text{5-BrNic})_2(\text{H}_2\text{O})_4] \cdot [\text{Yb}(\text{5-BrNic})_4(\text{H}_2\text{O})_2] \cdot (\text{5-HBrNic})_2$ y $\{[\text{Nd}(\text{5-BrNic})_3(\text{H}_2\text{O})_3] \cdot \text{H}_2\text{O}\}_n$. Las medidas de magnetismo confirman la presencia de centros metálicos aislados debido a que las interacciones antiferromagnéticas presentes son despreciables incluso en el compuesto monodimensional de Nd. Por otra parte, las medidas de susceptibilidad magnética *ac* revelan una U_{eff} de 33K para el compuesto de Dy. Los espectros de fotoluminiscencia en estado sólido de esta familia de compuestos han demostrado la existencia de efecto antena ejercido por el ligando 5-BrNic. En relación a los estudios de fosforescencia, éstos indican estados de excitación de corta duración para el compuesto de Dy, mientras que la emisión del compuesto de Tb mostró vidas más largas (aproximadamente 1ms). Por su parte, los estudios de viabilidad celular manifiestan una completa ausencia de toxicidad tanto en células sanas como en células cancerosas Caco-2 en los cuatro compuestos.

4. Han sido sintetizados cinco compuestos basados en Terbio, Erblio, Yterbio, Cobalto y Cobre y en el ácido 5-aminopiridin-2-carboxílico (Hampy) con fórmulas: $[MNa(ampy)_4]_n$ ($M= Tb(III), Er(III)$ e $Yb(III)$), $\{[CoK(ampy)_3(H_2O)_3] \cdot (H_2O)_3\}_n$ y $[Cu(ampy)_2]_n$. Los estudios de magnetismo muestran para el compuesto de Erblio una señal fuera de fase dependiente de la frecuencia, mientras que el compuesto de Yterbio presenta relajación lenta de la magnetización mediante varios mecanismos de relajación, dotándolo de características propias de SIM. Por otro lado, los estudios anticancerígenos han revelado que mientras los compuestos de lantánidos no son muy activos, en el caso del compuesto de Cobalto los valores de IC_{50} en células HT29 son 2, 3-5 y 9 veces más bajos que para los compuestos de Terbio, Yterbio y Cobre, respectivamente.
5. Se han obtenido tres MOFs (red tridimensional abierta doblemente interpenetrada) basados en el ligando 2-aminoisonicotinato (2ain) y diferentes metales de transición con fórmula: $\{[M(\mu-2ain)_2] \cdot DMF\}_n$ ($M^{II} = Co, Ni, Zn$). Estos materiales porosos, junto a sus propiedades magnéticas y/o fotoluminiscentes han sido evaluados como sensores frente a varios disolventes e iones metálicos. El compuesto de cobalto presenta un comportamiento magnético “*glass-like*” derivados del antiferrmagnetismo y el ordenamiento de largo alcance, que al sustituir las moléculas de DMF por DMSO y MeOH, el ligero desplazamiento que surge en la estructura es suficiente para causar una variación en sus propiedades magnéticas, llegando a presentar un comportamiento más parecido a un SIM. Por su parte para el compuesto de Cinc, la intensidad de la banda principal a 405 nm se ve afectada tanto por el solvente en el que se encuentre como por la presencia de cationes (disoluciones acuosas). Ambos compuestos, por tanto, presentan potencial en su uso como sensores.
6. La utilización del ligando ácido 1H-indazol-4-carboxílico (L) y varios metales de la primera serie de transición ha dado como resultado la obtención de cinco compuestos bidimensionales: $[Co(L)_2(H_2O)_2]_n$,

$[\text{Ni}(\text{L})_2(\text{H}_2\text{O})_2]_n$, $[\text{Cu}(\text{L})_2(\text{H}_2\text{O})]_n$, $[\text{Zn}(\text{L})_2]_n$ y $[\text{Cd}(\text{L})_2]_n$. Las mediciones magnéticas así como los cálculos DFT realizados para los compuestos de Co, Ni y Cu indican que el ligando proporciona interacciones intracadena casi insignificantes. Sin embargo, las distancias Cu...Cu interlaminares al ser más cortas que las distancias intramoleculares debido al empaquetamiento, confieren al material un efecto *spin-canted* inusual relacionado con un intercambio antisimétrico. El compuesto de Co, que se comporta como molécula imán aislada inducida por el campo, muestra dos máximos en los datos de susceptibilidad definidos por una relajación lenta y rápida activada térmicamente. De forma similar las distancias Co...Co entre capas son más cortas que la intramoleculares lo que nos permite atribuir los procesos de relajación a un intercambio débil y, a su vez, a los propios iones aislados. Los compuestos de Zn y Cd exhiben una emisión luminiscente hipsocrómica originada por causas estructurales y/o electrónicas. Finalmente las pruebas de viabilidad celular no han mostrado efectos citotóxicos salvo para el compuesto de Cd en la línea celular B16-F10.

7. Teniendo en cuenta los resultados mostrados por el ligando 1H-indazol-4-carboxílico, se han logrado sintetizar dos compuestos de diferentes dimensionalidades con el 1H-indazol-6-carboxílico (L): $[\text{Zn}(\text{L})(\text{H}_2\text{O})]_n$ y $[\text{Cd}_2(\text{HL})_4]_n$. Los estudios de luminiscencia realizados en los compuestos demuestran que la emisión fotoluminiscente en ambos compuestos está impulsada por la transiciones π - π^* centrada en el ligando. Los estudios de viabilidad en diferentes líneas celulares mostraron que el compuesto de Cd presenta una disminución significativa para HEK-293 y B16-F10 para concentraciones superiores a 20 $\mu\text{g}/\text{ml}$.
8. Con la idea de dar importancia a la existencia de los grupos carboxilato a la hora de conseguir compuestos con excelentes propiedades, se han sintetizado dos compuestos de coordinación basados en el ácido 2,5-dihidroxitereftálico (dhbdc) e iones metálicos

trivalentes como el Dy^{III} y el Y^{III} con fórmulas: $\{[\text{Dy}(\text{dhbdc})_{1.5}(\text{DMF})_2] \cdot \text{DMF}\}_n$ y $\{[\text{Dy}_{0.2}\text{Y}_{1.8}(\text{dhbdc})_3(\text{DMF})_4] \cdot 2\text{DMF}\}_n$. Los estudios magnéticos realizados sobre el primer compuesto revelan la existencia de interacciones antiferromagnéticas débiles con $\theta = -0.26\text{K}$. Las medidas de susceptibilidad magnética dinámicas *ac* destacan que a frecuencias más altas se pueden observar dos procesos de relajación. Con la idea de determinar si dichas relajaciones tenían origen en iones aislados o interacciones intramoleculares se preparó una muestra diluida de Y (análogo diamagnético) junto al Dy en un ratio molar Dy:Y de 1:9. Las medidas realizadas sobre este segundo compuesto reflejan un único proceso de relajación con energía de barrera efectiva de 31.6 K, puesto que la relajación lenta atribuida a los procesos intramoleculares ha desaparecido. Las medidas de fotoluminiscencia realizadas ($\lambda_{\text{ex}} = 325 \text{ nm}$) muestran una banda intensa centrada a 450 nm que posee una emisión significativa alrededor de los 650 nm correspondiente a transiciones $\pi-\pi^*$ de los anillos aromáticos del ligando. La realización de la medida a temperaturas de 10K produce un desplazamiento hacia el azul de la banda junto con un aumento de intensidad del 36%, dotando al material de potencial para su aplicación en termometría.

9. Con el objetivo de ampliar el estudio a otros ligandos de la familia de los ácidos indazol-carboxílicos se ha llevado a cabo la síntesis de cinco compuestos de coordinación monoméricos basados en el ácido indazol-3-carboxílico (3-ind) con fórmulas $[\text{M}(\text{3-ind})_2(\text{H}_2\text{O})_2]$ (M=Co, Ni, Zn, Fe, Mn). Los ensayos de citotoxicidad realizados en tres líneas celulares diferentes, B16-F10, HT29 y HepG2, sobre el ligando y los compuestos de Ni y Zn revelan que ambos materiales son menos tóxicos que el ligando para las células HT29. Sin embargo, el compuesto de Ni es más tóxico que el ligando y el compuesto de Zn para el resto de líneas celulares, con un IC_{50} de $62,64 \pm 5,57 \mu\text{g/mL}$ para HepG2 y de $69,07 \pm 7,93 \mu\text{g/mL}$ para B16-F10. Por otro lado, los estudios de viabilidad realizados en células RAW 264.7 sobre los

cinco materiales arrojan unos resultados interesantes. El compuesto de Co presenta una inhibición de NO cercana al 50% a las 24 horas para la fracción $\frac{3}{4}$ IC₅₀. Mientras que, por otra parte, los compuestos de Fe y Mn no muestran una inhibición significativa hasta pasadas 48 horas (cerca al 80% de media) y 72 horas (con una reducción casi del 90%). Esto hace a los compuestos [Fe(3-ind)₂(H₂O)₂] y [Mn(3-ind)₂(H₂O)₂] candidatos potenciales para su uso como agentes anti-inflamatorios.

10. Siguiendo con los ligandos derivados del indazol, se han obtenido dos polímeros de coordinación isoestructurales “*square-grid*” basados en el ácido 1H-indazol-5-carboxílico (5-inca): [M(5-inca)₂(H₂O)₂](DMF)₂ (M= Ni(II), Cu(II)). Ambos compuestos muestran interesantes propiedades magnéticas y biológicas. Los estudios en macrófagos RAW 264.7 exhiben una inhibición de NO de 68.35% para la concentración $\frac{3}{4}$ IC₅₀ en 24h, llegando en 72h a un porcentaje del 90% para las tres concentraciones ($\frac{1}{4}$ IC₅₀, $\frac{1}{2}$ IC₅₀ y $\frac{3}{4}$ IC₅₀). Los estudios realizados en parásitos muestran que ambos compuestos presentan potencial como agentes antiparasitarios, con unos índices de selectividad para *L. Infantum* 30 veces mayor a la Glucantime. También, a partir de este ligando, se ha logrado sintetizar un compuesto 3D de Zn con estructura muy similar al famoso MOF-5 que sufren una transformación en sólido inducida por la temperatura.
11. Se han sintetizado dos nuevos MOFs porosos de Zinc basados en 1H-indazol-5-carboxílico y 3,6-di(4-piridil)-1,2,4,5-tetrazina (pbptz) para uno, y 4,4'-bipiridina (4,4-bipy) para el otro: {[Zn(5-inca)(pbptz)_{0.5}](DMF)}_n y {[Zn(5-inca)(4,4-bipy)_{0.5}](DMF)}_n, respectivamente. Ambos presentan una arquitectura isorreticular con tipología *pcu* que cristaliza formando una doble red interpenetrada. Su flexibilidad estructural permite modular su porosidad y obtener un sistema 2D vacío para el primero y microcanales 1D para el segundo. Los estudios de fosforescencia en estado sólido revelan para ambos una intensa emisión azul bajo luz UV, debido a la transferencia de

carga entre el indazol y el biperidin/tetrazina confirmado por TD-DFT. Por su parte, el compuesto de tetrazina revela un remarcable termocromismo, lo cual modula la tonalidad de la emisión azul debido al cambio entre la intensidad relativa entre las dos bandas principales. Cabe resaltar que el compuesto de biperidina exhibe una fosforescencia perceptible al ojo con un tiempo de vida media asociado de 950 ms. Los cálculos DFT señalan estados de energía excitados singlete y triplete como fuente del origen de la fosforescencia.

12. Con la idea de aunar las propiedades de los ligandos piridina e indazol, se optó por probar ligandos tipo pirimidina, puesto que presentan, a nivel estructural, el mismo número de nitrógenos en los anillos aromáticos pero con distinta disposición. Se utilizó, a partir de esta premisa, el ligando 4-hidroxipirimidina-5-carbonitrilo lográndose sintetizar un compuesto bidimensional plano de Cu(I), donde el entorno de coordinación del Cu junto a su estructura laminar podrían dotar al material de propiedades conductoras en la banda de conducción, en la dirección perpendicular a las láminas y en el plano laminar. Además, el compuesto sometido a alta presión presenta conductividad en la banda de valencia a lo largo de la dirección z. Esta nueva conductividad influida por la presión dota al material de potencial como sensor de presión.
13. Se ha corroborado nuevamente que los ligandos aromáticos nitrogenados con grupos carboxilato son excelentes unidades de construcción en el diseño de compuestos de coordinación, tanto por la diversidad estructural conseguida como por la gran variedad de propiedades exhibidas por estos materiales.

Artículos relacionados con la Tesis

Artículos relacionados e incluidos en la Memoria de la Tesis.

Los resultados de la investigación realizados durante el desarrollo de esta Tesis Doctoral se recogen en los siguientes artículos ya publicados.

1- Designing Single-Ion Magnets and Phosphorescent Materials with 1-Methylimidazole-5-carboxylate and Transition-Metal Ions, Antonio A. García-Valdivia, Jose M. Seco, Javier Cepeda and Antonio Rodríguez-Diéguez, *Inorg. Chem.*, **2017**, 56, 22, 13897-13912, DOI: 10.1021/acs.inorgchem.7b02020.

2- Multifunctional coordination compounds based on lanthanide ions and 5-bromonicotinic acid: magnetic, luminescence and anti-cancer properties, Cristina Ruiz, Antonio A. García-Valdivia, Belén Fernández, Javier Cepeda, Itziar Oyarzabal, Elisa Abas, Mariano Laguna, Jose A. García, Ignacio Fernández, Eider San Sebastian and Antonio Rodríguez-Diéguez, *CrystEngComm*, **2019**, 21,3881 DOI: 10.1039/c9ce00292h.

3- 5-aminopyridine-2-carboxylic acid as Appropriate Ligand for Constructing Coordination Polymers with Luminescence, Slow Magnetic Relaxation and Anti-Cancer Properties, Antonio A. García-Valdivia, Javier Cepeda, Belén Fernández, Marta Medina Odonnell, Itziar Oyarzabal, Jerónimo Parra, Fatin Jannus, Duane Choquesillo-Lazarte, Jose A. García, José Antonio Lupiáñez, Santiago Gómez-Ruiz, Fernando Reyes-Zurita and Antonio Rodríguez-Diéguez, *J. Inorg. Biochem.* **2020**, 207,111051 DOI: 10.1016/j.jinorgbio.2020.111051.

4- Magnetic and Photoluminescent Sensors Based on Metal-Organic Frameworks Built up from 2-aminoisonicotinate, Antonio A. García-Valdivia, Sonia Pérez-Yáñez, José A. García, Belén Fernández, Javier Cepeda and Antonio Rodríguez-Diéguez, *Sci. Rep.* **2020**, 10, 8843 DOI: 10.1038/s41598-020-65687-6.

5- 2D-Coordination Polymers based on 1H-Indazole-4-carboxylic acid and Transition Metal ions: Magnetic, Luminescent and Biological Properties, Antonio A. García-Valdivia, Andoni Zabala-Lekuona, Gloria B. Ramírez-Rodríguez, José M. Delgado-López, Belén Fernández, Javier Cepeda and Antonio Rodríguez-Diéguez, *Dalton Trans.* **(Aceptado)**.

6- Photoluminescence and *in vitro* Cytotoxicity in Coordination Polymers based on d¹⁰ Transition Metals and 1H-Indazole-6-carboxylic Acid. Antonio A. García-Valdivia, Estitxu Echenique-Errandonea, Gloria B. Ramírez-Rodríguez, José M. Delgado-López, Belén Fernández, Javier Cepeda and Antonio Rodríguez-Diéguez, *Inorg. Chim. Acta* (**Enviado**).

7- Dilution effect on the slow relaxation of a luminescent Dysprosium Metal-Organic Framework based on 2,5-dihydroxyterephthalic acid. Antonio A. García-Valdivia, Andoni Zabala, Ainhoa Goñi, Belén Fernández, José A. García, Javier Cepeda and Antonio Rodríguez-Diéguez, *Inorg. Chim. Acta* **2020**, 509, 119687 DOI: 10.1016/j.ica.2020.119687.

8- Anti-Cancer and Anti-Inflammatory Activities of a new Family of Coordination Compounds based on Divalent Transition Metal Ions and Indazole-3-carboxylic acid Antonio A. García-Valdivia, Fatin Jannus, Amalia García-García, Duane Choquesillo-Lazarte, Belén Fernández, Marta Medina-O'donnell, José A. Lupiáñez, Javier Cepeda, Fernando J. Reyes-Zurita and Antonio Rodríguez-Diéguez, *J. Inorg. BioChem.* (**Aceptado**).

9- Antiparasitic, anti-inflammatory and cytotoxic activities of 2D coordination polymers based on 1H.indazole-5-carboxylic acid. Antonio A. García-Valdivia, AmaliaGarcía-García, Fatin Jannus, Andoni Zabala-Lekuona, José M.Méndez-Arriaga, Belén Fernández, Marta Medina-O'donnell, Gloria B. Ramírez-Rodríguez, José M. Delgado-López, Luisa M. Pastrana-Martínez, Javier Cepeda, José A. Lupiáñez, Fernando J. Reyes-Zurita, Antonio Rodríguez-Diéguez *J. Inorg. BioChem.* **2020**, 208, 111098. DOI: 10.1016/j.jinorgbio.2020.111098.

10- Interpenetrated Luminescent Metal-Organic Frameworks based on 1H-Indazole-5-carboxylic Acid. Antonio A. García-Valdivia, Manuel Perez-Mendoza, Duane Choquesillo-Lazarte, Javier Cepeda, Belén Fernández, Manuel Souto, Marcos González-Tejero, Jose A. García, Guillermo Minguez Espallargas and Antonio Rodríguez-Diéguez, *Cryst. Growth Des.* **2020** DOI: 10.1021/acs.cgd.0c00345

11- Rational Design of an unusual 2D-MOF based on Cu(I) and 4-hydroxypyrimidine-5-carbonitrile as Linker with Conductive Capabilities. A theoretical approach based on High-Pressure XRD. Antonio A. García-Valdivia, Francisco J. Romero, Javier Cepeda, Diego P. Morales, Nicola Casati, Antonio J. Mota, Linda A. Zotti, Juan J. Palacios, Duane Choquesillo-Lazarte, José F. Salmerón, Almudena Rivadeneyra and Antonio Rodríguez-Diéguez, *Chem. Commun.* (**Enviado**).

Además, también se han incluido otros resultados pendientes de publicar que serán mandados a diferentes revistas y que quedan recogidos en los Anexos.

Time-induced Single Crystal to Single Crystal Transformation and Luminescence of a Dynamic 3D Metal-Organic Framework based on Zn(II) and 1H-Indazole-5-carboxylic Acid.

Artículos relacionados pero no incluidos en la Memoria de la Tesis.

Design of cost-efficient and photocatalytically active Zn-based MOFs decorated with Cu₂O nanoparticles for CO₂ methanation, María Cabrero-Antonino, Sonia Remiro-Buenamañana, Manuel Souto, Antonio A. García-Valdivia, Duane Choquesillo-Lazarte, Sergio Navalón, Antonio Rodríguez-Diéguez, Guillermo Mínguez, Espallargas Hermenegildo García, *Chem. Commun.*, **2019**, 55, 10932. DOI: 10.1039/c9cc04446a.

Artículos no relacionados y no incluidos en la Memoria de la Tesis.

1- Slow Relaxation of Magnetization and Luminescence Properties of a Novel Dysprosium and Pyrene-1,3,6,8-tetrasulfonate Based MOF, Amalia García-García, Itziar Oyarzabal, Javier Cepeda, Jose M. Seco, Antonio A. Garcia-Valdivia, Santiago Gomez-Ruiz, Alfonso Salinas-Castillo, Duane Choquesillo-Lazarte, and Antonio Rodriguez-Dieguez, *New J. Chem.*, **2018**, 42, 832-837. DOI: 10.1039/c7nj02935g.

2- Design and synthesis of a family of 1D lanthanide coordination polymers showing luminescence and slow relaxation of the magnetization, Ana Belén Ruiz-Muelle, Amalia García-García, Antonio A. García-Valdivia, Itziar Oyarzabal, Javier

ANTONIO ANDRÉS GARCÍA VALDIVIA

Cepeda, José M. Seco, Enrique Colacio, Antonio Rodríguez-Diéguez and Ignacio Fernández, *Dalton Trans.*, **2018**, 47,12783. DOI: 10.1039/c8dt02592d.

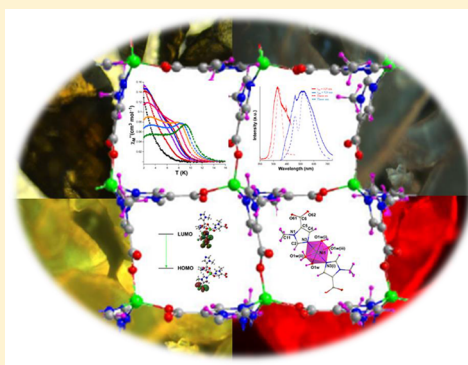
Artículos Publicados

Designing Single-Ion Magnets and Phosphorescent Materials with 1-Methylimidazole-5-carboxylate and Transition-Metal Ions

Antonio A. García-Valdivia,[†] Jose M. Seco,[‡] Javier Cepeda,^{*,‡,†} and Antonio Rodríguez-Diéguez^{*,†,†}[†]Departamento de Química Inorgánica, Universidad de Granada, 18071 Granada, Spain[‡]Departamento de Química Aplicada, Facultad de Química, Universidad del País Vasco/Euskal Herriko Unibertsitatea, UPV/EHU, 20018 San Sebastián, Spain

Supporting Information

ABSTRACT: Detailed structural, magnetic, and photoluminescence (PL) characterization of four new compounds based on 1-methylimidazole-5-carboxylate (mimc) ligand and transition metal ions, namely [Ni(mimc)₂(H₂O)₄] (1), [Co(μ-mimc)₂]_n (2), {[Cu₂(μ-mimc)₄(H₂O)]·2H₂O}_n (3), and [Cd(μ-mimc)₂(H₂O)]_n (4) is reported. The structural diversity found in the family of compounds derives from the coordination versatility of the ligand, which coordinates as a terminal ligand to give a supramolecular network of monomeric entities in 1 or acts as a bridging linker to build isorecticular 2D coordination polymers (CPs) in 2–4. Magnetic direct-current (dc) susceptibility data have been measured for compounds 1–3 to analyze the exchange interactions among paramagnetic centers, which have been indeed supported by calculations based on broken symmetry (BS) and density functional theory (DFT) methodology. The temperature dependence of susceptibility and magnetization data of 2 are indicative of easy-plane anisotropy ($D = +12.9 \text{ cm}^{-1}$, $E = +0.5 \text{ cm}^{-1}$) that involves a bistable $M_s = \pm 1/2$ ground state. Alternating-current (ac) susceptibility curves exhibit field-induced single-ion magnet (SIM) behavior that occurs below 14 K, which is characterized by two spin relaxation processes of distinct nature: fast relaxation of single ions proceeding through multiple mechanisms ($U_{\text{eff}} = 26 \text{ K}$) and a slow relaxation attributed to interactions along the polymeric crystal building. Exhaustive PL analysis of compound 4 in the solid state confirms low-temperature phosphorescent green emission consisting of radiative lifetimes in the range of 0.25–0.43 s, which explains the afterglow observed during about 1 s after the removal of the UV source. Time-dependent DFT and computational calculations to estimate phosphorescent vertical transitions have been also employed to provide an accurate description of the PL performance of this long-lasting phosphor.



INTRODUCTION

The construction of coordination polymers (CPs) is a hot topic in crystal engineering that is receiving increasing interest from many different areas of science owing to the continuous advances shown by these multifunctional materials.^{1–4} The success of CPs is mainly due to their intriguing architectures and topologies resulting from the self-assembly of bridging organic ligands with appropriate metal ions or clusters, which offers endless possibilities, given the large list of both components and their combinations obeying the principles of reticular chemistry.^{5–8} In this regard, an important aspect to exert control toward the desired crystalline frameworks lies in controlling synthetic conditions (temperature, solvent, stoichiometry, pH, and so on);^{9–14} the selection of adequate metal ions and organic ligands, indeed, is not of less importance in tuning the structures. Although the particular subclass of metal–organic frameworks (MOFs), enclosing impressive surface areas and versatile pores, occupies an important part of this research area,^{15–23} a wide variety of equally fascinating properties arise from nonporous CPs, among which optical storage, drug delivery, catalysis, magnetism, or luminescence may be highlighted.^{24–33} It is at this point, in fact, where the

intrinsic characteristics of the structural components (ions and ligands) make the difference in imbue these metal–organic materials with outstanding functionalities. On the one hand, ligands containing carboxylate groups are widely employed owing to their high coordination capacity as well as flexibility that permits them to adopt different binding modes to fit into most first-row transition-metal environments and crystal packing requirements.^{34,35} Moreover, the chemical nature of the spacer is not a less important concern, since, for example, aromatic spacers afford greater rigidity than aliphatic spacers owing to their limited geometric characteristics that may restrict the structural variability, a fact of major importance when only one ligand is employed. On the other hand, first-row transition-metal ions are undoubtedly a great choice in seeking materials with best-in-class magnetic and photoluminescent (PL) properties.^{36–41}

Particularly for molecular magnetism, actual scientific efforts are focused on understanding the physics governing the slow magnetic relaxation behavior of molecular systems with only

Received: August 6, 2017

Published: November 9, 2017

Table 1. Crystallographic Data and Structure Refinement Details of All Compounds

	1	2	3	4
chem formula	C ₁₀ H ₁₈ N ₄ NiO ₈	C ₁₀ H ₁₀ CoN ₄ O ₄	C ₂₀ H ₂₆ Cu ₂ N ₈ O ₁₁	C ₁₀ H ₁₂ CdN ₄ O ₅
formula wt	380.97	309.15	681.56	380.64
cryst syst	monoclinic	monoclinic	monoclinic	monoclinic
space group	C2/m	P2 ₁ /c	P2/c	P2 ₁ /n
a (Å)	14.7901(8)	12.492(2)	12.885(1)	8.0827(4)
b (Å)	6.9602(3)	13.417(2)	5.604(1)	12.2183(6)
c (Å)	7.6649(4)	7.390(1)	18.544(1)	12.9795(6)
α (deg)	90	90	90	90
β (deg)	113.977(2)	100.04(1)	93.17(4)	95.100(2)
γ (deg)	90	90	90	90
V (Å ³)	720.95(6)	1219.6(10)	1337.0(2)	1266.9(1)
Z	2	4	2	4
GOF ^a	1.142	1.168	1.036	1.047
R _{int}	0.0340	0.1044	0.0891	0.0577
R1 ^b /wR2 ^c [I > 2σ(I)]	0.0198/0.0199	0.0842/0.2079	0.0522/0.1197	0.0241/0.0274
R1 ^b /wR2 ^c (all data)	0.0500/0.0500	0.1039/0.2208	0.0853/0.1309	0.0626/0.0608

^aGOF = $S = [\sum w(F_o^2 - F_c^2)^2 / (N_{obs} - N_{param})]^{1/2}$. ^bR1 = $\sum ||F_o| - |F_c|| / \sum |F_o|$. ^cwR2 = $[\sum w(F_o^2 - F_c^2)^2 / \sum wF_o^4]^{1/2}$; $w = 1 / [\sigma^2(F_o^2) + (aP)^2 + bP]$, where $P = (\max(F_o^2, 0) + 2F_c^2) / 3$ with $a = 0.0163$ (1), 0.0573 (2), 0.0571 (3), 0.0298 (4) and $b = 0.9304$ (1), 26.7323 (2), 18.5744 (3), 0.9904 (4).

one spin carrier, large magnetic anisotropy, and no intermetallic exchange interactions of the so-called single-ion magnets (SIMs).^{42,43} In this regard, as already corroborated by many works since Chang and Long et al. first proved the concept in 2010,^{44,45} slow magnetic relaxation is achieved for mononuclear transition-metal-based compounds provided that they afford ground states with high spin (*S*) and magnetic anisotropy consisting of zero-field splitting *D* and *E* parameters (denoting axial and transverse anisotropy, respectively).⁴⁶ More recently, it could be demonstrated that SIM behavior was not exclusively manifested in mononuclear species and so has rapidly been extended over polymeric species and the first SIM-CPs have been reported.^{47–52} At first sight, Co(II) is clearly the most acknowledged ion among first-row transition metals to build SIM-CPs, given that its noninteger spin ground state, according to the Kramers theorem, reduces the probability of fast quantum tunneling of the magnetization process that bypasses the desired slow relaxation.^{53–55} Although different coordination geometries and donor environments are available for Co(II)-based SIMs, the vast majority contain tetrahedral or pseudotetrahedral geometries.^{56–60} The main reason lies in the fact that a low coordination number is beneficial for designing SIMs, given that first-order orbital angular momentum is largely quenched by the ligand field so that spin–orbit coupling may be compensated.^{61,62} In this sense, a low coordination number is able to afford a weak ligand field, thus preventing the quenching up to a point.

Regarding the photoluminescent performance, recent research works have shifted the attention toward CPs containing d¹⁰ metal ions^{63–68} owing to their capacity to stabilize long-lasting phosphorescence (LLP) or afterglow phenomena in the resulting materials so that they could bring a significant advancement in the field of enhanced organic light-emitting diodes (OLEDs).^{69,70} This fact is derived from the intrinsic characteristics of these metal ions (namely the absence of potential quenching processes owing to their closed-shell configuration) which, in combination with the appropriate fluorescent organic ligands, promotes the reorganization of the energy levels in the compounds that leads to stronger and brighter emission (via ligand-centered (LCCT) or ligand to

metal charge transfers (LMCT)) in comparison to that of a free organic molecule.^{71,72}

All in all, we have made use of the latter considerations to design new CPs showing SIMs and LLP behaviors, for which adequate transition-metal ions have been reacted with 1-methylimidazole-5-carboxylate (mimc). The selection of this ligand, not yet employed in the construction of CPs so far, is due to its ability to play two essential roles while it sequentially bridges metal ions: serve as spacer between spin carriers spatially in the network by favoring metal ions to adopt low coordination numbers, which promotes slow relaxation phenomena, and act as an effective fluorescent molecule that allows for intense photoluminescent transitions.

EXPERIMENTAL SECTION

Chemicals. All the chemicals were of reagent grade and were used as commercially obtained.

Synthesis of [Ni(mimc)₂(H₂O)₄] (1). A 0.08 mmol portion (10.00 mg) of Hmimc was dissolved in 0.5 mL of DMF and mixed with a distilled water solution containing 0.04 mmol of Ni(NO₃)₂·6H₂O (11.63 mg). Then, 1 mL of DMF was added to the mixture and stirred until homogeneity. The resulting solution was placed in a closed glass vessel and introduced in an oven at 95 °C for 24 h. Light green single crystals were grown during the heating procedure under autogenous pressure, which were filtered off and collected at open atmosphere and washed with water and methanol. Yield: 30% based on metal. Anal. Calcd for C₁₀H₁₈N₄NiO₈: C, 31.53; H, 4.76; N, 14.71. Found: C, 31.65; H, 4.58; N, 14.52.

Synthesis of [Co(μ-mimc)₂]_n (2). Well-shaped purple single crystals of **2** were obtained after carrying out the same general procedure described for **1** but replacing Ni(NO₃)₂·6H₂O by Co(NO₃)₂·6H₂O (11.65 mg). Yield: 43% based on metal. Anal. Calcd for C₁₀H₁₀CoN₄O₄: C, 38.85; H, 3.26; N, 18.12. Found: C, 38.71; H, 3.18; N, 18.15.

Synthesis of [Cu₂(μ-mimc)₄(H₂O)]_n·2H₂O (3). The general procedure described for **1** was followed using Cu(NO₃)₂·H₂O (9.66 mg) as the metal source, which led to single crystals of **3**. Yield: 25% based on metal. Anal. Calcd for C₂₀H₂₆Cu₂N₈O₁₁: C, 35.24; H, 3.84; N, 16.44. Found: C, 35.42; H, 3.64; N, 16.53.

Synthesis of [Cd(μ-mimc)₂(H₂O)]_n (4). The general procedure described for **1** was followed using Cd(NO₃)₂·4H₂O (15.88 mg) as the metal source, which led to well-shaped single crystals of **4**. Yield: 23% based on metal. Anal. Calcd for C₁₀H₁₂CdN₄O₅: C, 31.55; H, 3.18; N, 14.72. Found: C, 31.37; H, 3.10; N, 14.62.

Physical Measurements. Elemental analyses (C, H, N) were performed on an Euro EA Elemental Analyzer. FTIR spectra (KBr pellets) were recorded on a Nicolet IR 6700 spectrometer in the 4000–400 cm^{-1} spectral region. Magnetic susceptibility measurements were performed on polycrystalline samples of the complexes with a Quantum Design SQUID MPMS-7T or MPMS-XL5 (only for compound 3) susceptometer at an applied magnetic field of 1000 G. The susceptibility data were corrected for the diamagnetism estimated from Pascal's tables,⁷³ the temperature-independent paramagnetism, and the magnetization of the sample holder. Magnetization and alternating-current (ac) susceptibility measurements were carried out on a PPMS (Physical Property Measurement System)-Quantum Design Model 6000 magnetometer under a 3.5 Oe ac field and frequencies ranging from 60 to 10000 Hz. Thermal analyses (TG/DTA) were performed on a TA Instruments SDT 2960 thermal analyzer in a synthetic air atmosphere (79% N_2 /21% O_2) with a heating rate of 5 $^\circ\text{C min}^{-1}$. A closed-cycle helium cryostat enclosed in an Edinburgh Instruments FLS920 spectrometer was employed for recording photoluminescence (PL) measurements of polycrystalline samples of **4** in the 10–250 K range. For steady-state measurements an IK3552R-G HeCd continuous laser (325 nm) and a Müller-Elektronik-Optik SVX1450 Xe lamp were used as excitation sources. Photographs of irradiated single-crystal and polycrystalline samples were taken at room temperature in a micro-PL system included in an Olympus optical microscope illuminated with a HeCd laser or a Hg lamp. Lifetime measurements were performed under excitation at the maximum (325 nm) for selected emission wavelengths in the 350–650 nm range. Decay curves were recorded with microsecond pulse lamps as excitation sources employing exposure times so as to achieve 10^4 counts in the pulse of reference, and they were analyzed by tail fitting.

X-ray Diffraction. X-ray data collection of suitable single crystals of all compounds were done at 100(2) K on a Bruker VENTURE area detector equipped with graphite-monochromated Mo $K\alpha$ radiation ($\lambda = 0.71073 \text{ \AA}$) by applying the ω -scan method. The data reduction was performed with the APEX2⁷⁴ software and corrected for absorption using SADABS.⁷⁵ Crystal structures were solved by direct methods using the SIR97 program⁷⁶ and refined by full-matrix least squares on F^2 including all reflections using anisotropic displacement parameters by means of the WINGX crystallographic package.^{77,78} All hydrogen atoms were located in difference Fourier maps and included as fixed contributions riding on attached atoms with isotropic thermal displacement parameters 1.2 times or 1.5 times those of their parent atoms for the organic ligands and the water molecules, respectively. Details of the structure determination and refinement of compounds **1–4** are summarized in Table 1. During the refinement of compound **1**, it was observed that single crystals consist of nonmerohedral twins; therefore, the structure was refined with the (1 0 0.59/0–1 0/0 0–1) twin law, giving a value of 8% for the minor domain. On the other hand, the structure of **3** presents small pseudosymmetry caused by a lattice O2w water molecule because it does not fit the symmetry of the whole framework. This forces symmetry-related O2w to form hydrogen-bonding interactions in which hydrogen atoms clash with each other, and so they were not refined. Moreover, the coordinated O1w molecule is disordered into two symmetry-related dispositions; therefore, an occupation of 50% has been employed for each position. Crystallographic data (excluding structure factors) for the structures reported in this paper have been deposited with the Cambridge Crystallographic Data Center as supplementary publication nos. CCDC 1566132–1566135. Copies of the data can be obtained free of charge on application to the Director, CCDC, 12 Union Road, Cambridge, CB2 1EZ, U.K. (fax, +44-1223-335033; e-mail, deposit@ccdc.cam.ac.uk; web, <http://www.ccdc.cam.ac.uk>).

Powder X-ray diffraction (PXRD) patterns were collected on a Phillips X'PERT powder diffractometer with Cu $K\alpha$ radiation ($\lambda = 1.5418 \text{ \AA}$) over the range $5 < 2\theta < 50^\circ$ and using a fixed slit, a step size of 0.026° , and an acquisition time of 2.5 s per step at 25 $^\circ\text{C}$. Pattern-matching analyses of the diffractograms were done by means of the FULLPROF program (pattern-matching analysis)^{79,80} on the basis of the space group and the cell parameters found for single-crystal X-ray diffraction.

Computational Details. TD-DFT theoretical calculations were performed at 10 K using the Gaussian 09 package,⁸¹ using the Becke three-parameter hybrid functional with the nonlocal correlation functional of Lee–Yang–Parr (B3LYP),^{82–84} the 6-311G(d)^{85–87} basis set was adopted for all atoms except for the central cadmium cation, where the LANL2DZ^{88–90} basis set along with the corresponding effective core potential (ECP) was used. The latter strategy has proven successful in describing the luminescence performance of cadmium-based coordination compounds.^{91,92} A detailed description of a suitable model (model 4) can be found in the Supporting Information. The 40 lowest excitation and emission energies were calculated on model 4 by the TD-DFT method. Results were analyzed with the GaussSum program package,⁹³ and molecular orbitals were plotted using GaussView 5.⁹⁴ A detailed description of the computational strategy adopted in this work to compute the magnetic coupling constant (J_{calc}) value of **2** and **3** consists of Noddemann's broken symmetry approach.^{95,96} One calculation was performed to determine the high-spin state and another to determine the low-spin broken symmetry state, employing the dispersion-corrected B97D functional⁹⁷ and Gaussian implemented 6-311G++(d,p) basis set⁹⁸ for all nonmetallic atoms or LANL2DZ pseudopotentials for the cobalt(II) atoms. The correctness of this method is supported by the work of Singh and Rajaraman,⁹⁹ whereas the nature of both spin states was confirmed by means of the spin density distribution.

RESULTS AND DISCUSSION

Structural Description of $[\text{Ni}(\text{mimc})_2(\text{H}_2\text{O})_4]$ (1**).** Compound **1** crystallizes in the space group $C2/m$ and consists of a supramolecular crystal structure in which neutral monomers of the title formula are linked together by means of hydrogen-bonding and π – π interactions. In the centrosymmetric complex, four water molecules occupy the basal plane that crosses the Ni1 atom while two $\text{mimc-}\kappa\text{N3}$ terminal ligands are coordinated at the apical positions, thus rendering a slightly compressed octahedron, as confirmed by continuous shape measures (CShMs) calculated by the SHAPE ($S_{\text{OC}} = 0.04$) program (Figure 1 and Table 2).^{100–103} The monomeric entity

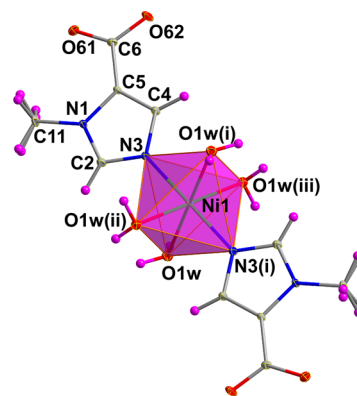


Figure 1. View of complex **1** (ellipsoids 50% of probability) showing the coordination polyhedron and numbering scheme used.

Table 2. Selected Bond Lengths for Compound **1**^a

Ni1–N3	2.064(2)	Ni1–O1w(i)	2.102(2)
Ni1–N3(i)	2.064(2)	Ni1–O1w(ii)	2.102(2)
Ni1–O1w	2.102(2)	Ni1–O1w(iii)	2.102(2)

^aSymmetry operations: (i) $-x - 1, -y, -z$; (ii) $x, -y, z$; (iii) $-x - 1, y, -z$.

resembles that contained in the recently reported compound $[\text{Cd}(\text{HMPCA})_2(\text{H}_2\text{O})_4]$ (where HMPCA = 3-methyl-1*H*-pyrazole-4-carboxylate), in which apical mimic ligands are replaced by HMPCA ligands.¹⁰⁴ Within the molecule, carboxylate groups of mimic ligands remain completely planar and are exposed outward so as to act as receptors of $\text{Ow}-\text{Hw}\cdots\text{Ocarb}$ hydrogen-bonding interactions starting at coordination water molecules of adjacent monomers. First, a sort of supramolecular array is established along the crystallographic *c* axis by successive double hydrogen bonds formed between two coordination waters in a *cis* arrangement and an O62 atom, where mimic ligands are forced to remain coplanar by means of weak $\text{C}-\text{H}\cdots\text{O}$ interactions. Hereafter, additional $\text{Ow}-\text{Hw}\cdots\text{Ocarb}$ bonds are set to join the monomers along the remaining directions (Figure S1 in the Supporting Information), such that the resulting 3D structure is completed and sustained by relatively strong face to face $\pi-\pi$ stacking interactions among the aromatic rings of mimic ligands (Tables S1 and S2 in the Supporting Information). As a matter of fact, considering that all supramolecular interactions cause each complex molecule to be surrounded by six other molecules, it is concluded that they are organized in a *pcu* topological framework as confirmed by the TOPOS program.^{105–107}

Structural Description of $[\text{Co}(\mu\text{-mimc})_2]_n$ (2). The crystal structure of compound 2 grows from the piling of neutral 2D layers held together by $\pi-\pi$ stacking interactions. In the asymmetric unit, Co1 is coordinated to four mimic ligands through two imidazole nitrogen atoms and two carboxylate oxygen atoms, since the O62B atom (at a distance of ca. 2.85 Å) cannot be considered to be coordinated (Table 3), which

Table 3. Bond Lengths for Coordination Environment of Compound 2^a

Co1–O61A	1.931(6)	Co1–N3A(ii)	2.000(8)
Co1–O61B(i)	1.956(7)	Co1–N3B	2.028(8)

^aSymmetry operations: (i) $-x, y - 1/2, -z + 1/2$; (ii) $x, y, z + 1$.

gives a coordination polyhedron that resembles a distorted tetrahedron ($S_T = 0.72$, Figure 2). It is worth noting that the two crystallographically independent mimic ligands remain essentially planar (carboxylate groups rotate ca. 1.5 and 4.6° with regard to the imidazole ring, respectively, for ligands A and B) to bridge Co1 atoms one another by acquiring the $\mu-\kappa\text{N1}:\kappa\text{O61}$ mode, which imposes Co \cdots Co distances of ca. 7.8 and 11.5 Å for the edge and square diagonal, respectively. Taking into account that each metal center is surrounded by four ligands and that they acquire parallel dispositions in pairs (ligands A and B on their part), the resulting $\text{Co}(\text{N})_2(\text{CO}_2)_2$ building unit may be considered as a pseudo-square-planar node from a topological point of view. The parallel arrangement between symmetry-related A ligands seems to come from an intramolecular $\text{C2A}-\text{H2A}\cdots\text{O62A}$ hydrogen bond between the aromatic ring and nonbonding carboxylate oxygen atom, which in turn prevents the latter atom from coordinating to the Co1 atom. Accordingly, the linkage of these units with one another gives rise to somewhat corrugated open 2D layers showing square windows and, thus, the *sql* topological class and ($4^4\cdot 6^2$) point symbol.

These kinds of layers are frequently found for CPs resulting from the combination of tetrahedral nodes with ligands capable of acting as $\mu-\kappa\text{N}:\kappa\text{O}$ linkers since four-membered $\text{M}-\text{O}-\text{C}-\text{O}-\text{M}$ chelating rings are prevented, as is the case for the

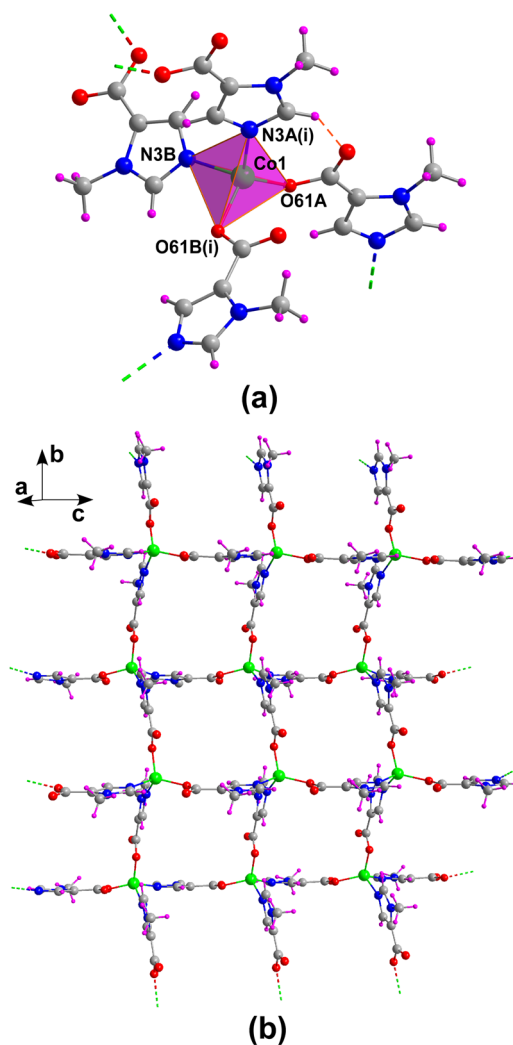


Figure 2. (a) Building unit of compound 2 with atom labels for the coordination sphere. Note that labels A and B stand for ligands A and B and that orange dashed line represents the intramolecular hydrogen bond. (b) 2D layer showing the square grid.

compound $\{[\text{Co}(\mu\text{-6ani})_2]\cdot\text{H}_2\text{O}\}_n$ based on a 6-aminonicotinato ligand.⁵¹ Probably as a consequence of the large section of the square windows within the layers of compound 2, mimic ligands are allowed to cross through the windows, which brings a 2-fold interpenetration in the overall crystal building. Within the entangled layers, the second subnet is placed close to the first one in order to favor strong face to face $\pi-\pi$ interactions (Figure 3) between the aromatic rings of mimic B ligands when crossing the rings of the first subnet in addition to comparatively weak stacking interactions among A ligands (Table S3 in the Supporting Information). These entangled layers are packed with one another along the *a* axis in the absence of any remarkable interaction unless there are very weak contacts involving the methyl groups and aromatic rings of mimic ligands that belong to different subnets. Moreover, the entangled layers show no offset along the packing directions, such that the overall building contains no voids (see the Supporting Information).

Structural Description of $\{[\text{Cu}(\mu\text{-mimc})_2(\text{H}_2\text{O})]\cdot 2\text{H}_2\text{O}\}_n$ (3). Compound 3 crystallizes in the space group *P2/c* and consists of a compact framework built up from 2D layers similar to those described for 2 that are held together by means of

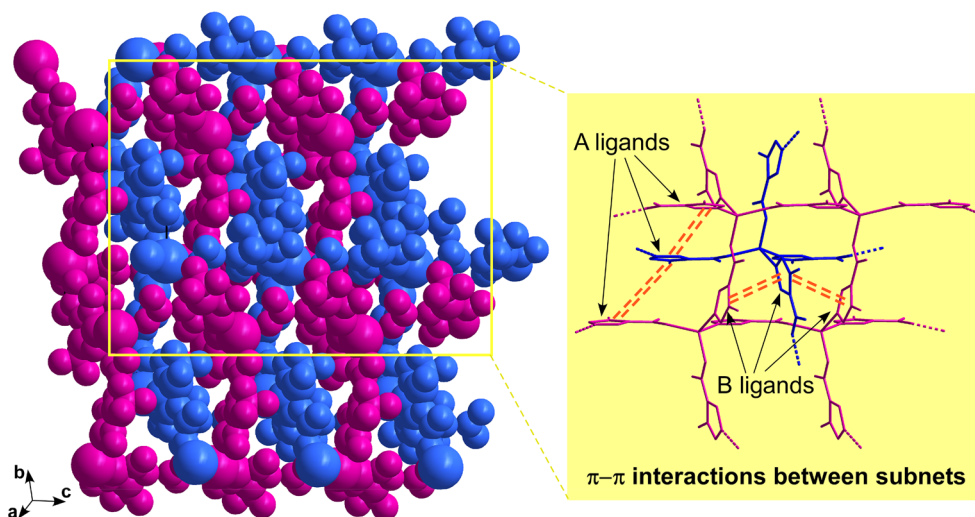


Figure 3. View of the 2-fold interpenetrated building of compound 2 (red and blue layers represent independent subnets) showing π - π interactions among mimc ligands.

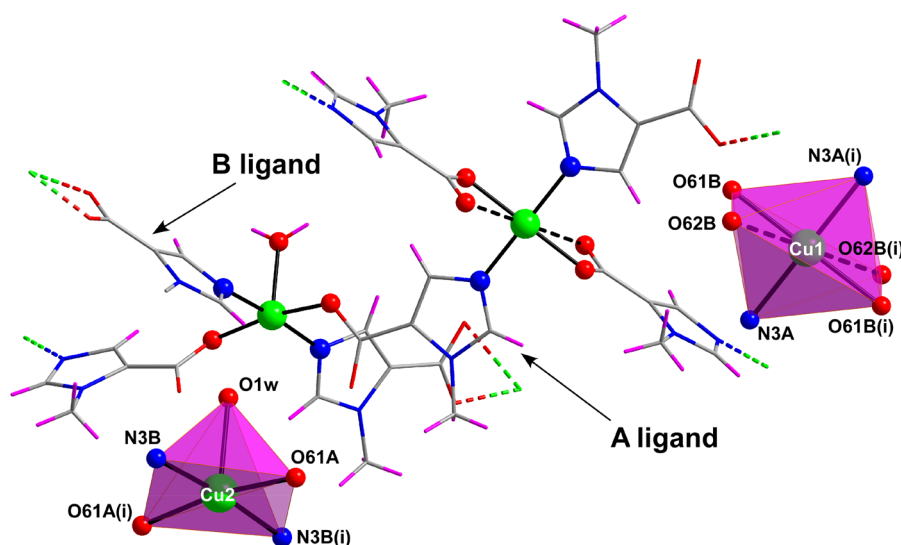


Figure 4. Portion of the crystal structure of compound 3 showing the coordination polyhedra of Cu1 and Cu2 atoms and the numbering scheme of donor atoms.

hydrogen-bonding interactions. The asymmetric unit contains two crystallographically independent copper(II) atoms (both of which are sited on a binary axis), a coordination water molecule, two mimc bridging ligands, and a lattice water molecule (Figure 4). Cu1 lies on an inversion center and describes a severely distorted 4 + 2 octahedron ($S_{OC} = 9.70$) in which the basal plane is formed by two O61B carboxylate oxygen atoms and two N3A imidazole atoms, whereas the elongated axis is occupied by O62B atoms pertaining to the chelating carboxylate group. Cu2 displays an almost ideal square-pyramidal (SPY) environment ($S_{SPY} = 0.48$) established by two monodentate carboxylate oxygen atoms and two N3B atoms of mimc ligands, whereas an apically elongated water molecule completes the coordination shell (Table 4). Note that while O1w is disordered into two equivalent dispositions close to the main axis of the square pyramid, CShMs were performed on the ideal model without disorder (i.e., O1w on the special site contained in the main axis).

Hence, copper(II) atoms are sequentially joined by two types of mimc ligands describing slightly different coordination

Table 4. Bond Lengths for Coordination Environment of Compound 3^a

Cu1–N3A	1.980(3)	Cu2–N3B(ii)	1.969(3)
Cu1–N3A(i)	1.980(3)	Cu2–N3B(iii)	1.969(3)
Cu1–O61B	1.960(2)	Cu2–O61A	2.001(2)
Cu1–O61B(i)	1.960(2)	Cu2–O61A(iv)	2.001(2)
Cu1–O62B	2.768(2)	Cu2–O1w	2.188(6)
Cu1–O62B(i)	2.768(2)		

^aSymmetries: (i) $-x + 1, -y + 2, -z + 1$; (ii) $-x, -y + 2, -z + 1$; (iii) $x, -y + 2, z - 1/2$; (iv) $-x, y, -z + 1/2$.

modes, i.e. μ -mimc- κ N3A: κ O61A (A ligand) and μ -mimc- κ N3B: κ^2 O61B,O62B (B ligand), imposing Cu1...Cu2 distances of ca. 7.79 and 8.21 Å. The nonequality of those bridges promotes substantial distortion on the square grid of the 2D layers that spread along the crystallographic ac plane. Moreover, mimc ligands are forced to be folded, as required by the coordination shells, and are thus arranged in a non-perpendicular disposition (angles of 55.2 and 52.5° for A and

B ligands, respectively, with respect to the mean plane of the 2D layer), although the 2D network preserves the **sql** topology (Figure 5). This structural feature closes to a large extent the

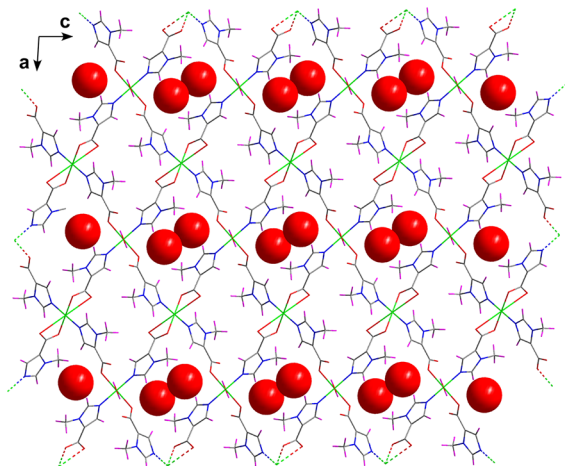


Figure 5. Packing of compound 3 along the *b* axis showing the lattice water molecules occupying the voids of the structure.

accessibility of the square rings thereby preventing any possible π - π stacking interaction among mimc ligands belonging to adjacent layers. Instead, layers are packed in a parallel fashion along the *b* axis in such a way that layers become mutually eclipsed, which is achieved by means of hydrogen-bonding interactions provided by the coordination O1w water molecule (Table S4 in the Supporting Information). As a consequence, very narrow pores, filled with crystallization water molecules, are left within the framework.

Structural Description of $[\text{Cd}(\mu\text{-mimc})_2(\text{H}_2\text{O})]_n$ (4). Compound 4 presents a 2D-layered framework that can be considered as another variant of square grid networks shown by compounds 2 and 3. The Cd1 atom is placed in the center of a severely distorted octahedron ($S_{\text{OC}} = 3.02$) established by two nitrogen atoms of two independent mimc ligands, two oxygen atoms from a chelating carboxylate group, a monodentate carboxylate oxygen atom, and a water molecule (Figure 6 and Table 5).

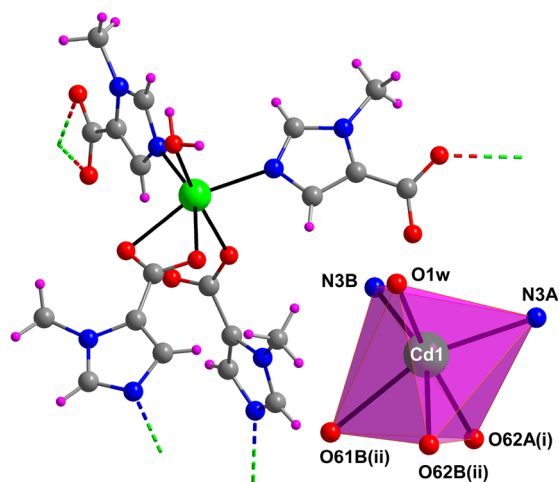


Figure 6. Relative disposition of square rings within the layer, hydrogen-bonding interactions between layers, and their mutual packing in compound 4.

Table 5. Selected Bond Lengths for Compound 4^a

Cd1–N3A	2.258(2)	Cd1–O61B(ii)	2.437(2)
Cd1–N3B	2.243(2)	Cd1–O62B(ii)	2.345(2)
Cd1–O62A(i)	2.282(2)	Cd1–O1w	2.355(3)

^aSymmetry operations: (i) $-x + 1/2, y - 1/2, -z + 3/2$; (ii) $x + 1/2, -y + 1/2, z + 1/2$.

The disposition of the four mimc ligands (two showing the $\mu\text{-}\kappa\text{N}:\kappa\text{O}$ mode (A ligands) and two the $\mu\text{-}\kappa\text{N}:\kappa^2\text{O},\text{O}'$ mode (B ligands)) coordinated to Cd1 atoms is such that the junction of the $[\text{Cd}(\text{N}_{\text{mimc}})_2(\text{CO}_2)_2]$ four-connected nodes by the linear linkers gives rise to a highly corrugated square grid. In fact, considering the mean plane formed by metal centers, adjacent four-membered rings are largely folded to acquire a relatively perpendicular disposition (80.6°). An important structural feature concerns the relative disposition of mimc ligands within the four-membered rings, since it allows π - π stacking interactions in the overall building of 4 among consecutive layers in spite of their lack of planarity (Figure 7). Furthermore,

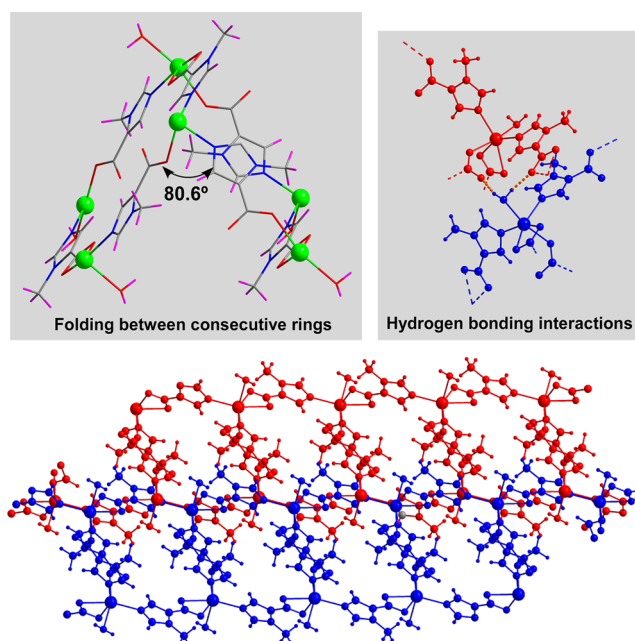


Figure 7. Relative disposition of square rings within the layer, hydrogen-bonding interactions between layers, and their mutual packing in compound 4.

strong hydrogen bonds are established between the layers through $\text{O1w}\cdots\text{Ocarboxylate}$ interactions, which reinforce the cohesiveness and lead to a dense 3D packing that leaves no voids (Table S6 in the Supporting Information).

Static Magnetic Measurements. The temperature-dependent magnetic susceptibility data were measured on polycrystalline samples of compounds 1–3 under an applied magnetic field of 1000 Oe in the 5–300 K range. The magnetic behavior of compound 1 in the form of $\chi_M T$ vs T (where χ_M stands for the magnetic susceptibility per nickel(II) ion) exhibits a $\chi_M T$ value at room temperature which is close to that expected for an isolated spin doublet ($1.00 \text{ cm}^3 \text{ mol}^{-1} \text{ K}$ with $g = 2.01$, see Figure S10 in the Supporting Information and Table 6). Upon cooling, the $\chi_M T$ product remains almost constant up to 40 K, where it decreases abruptly and reaches a value of $0.74 \text{ cm}^3 \text{ mol}^{-1} \text{ K}$ probably as a consequence of the occurrence of

Table 6. Best Least-Squares Fits of the Experimental Curves and Theoretically or Computationally Calculated Magnetic Data

compound	$\chi_M T$ (300 K) ^a		J (cm ⁻¹) ^b		g^b	$10^6 R^b$
	exptl	calcd	exptl	DFT		
2	2.670	1.870		-0.2	2.17/2.36	
3	0.389	0.375	-6.4(1)	-5.8	2.13	1.75

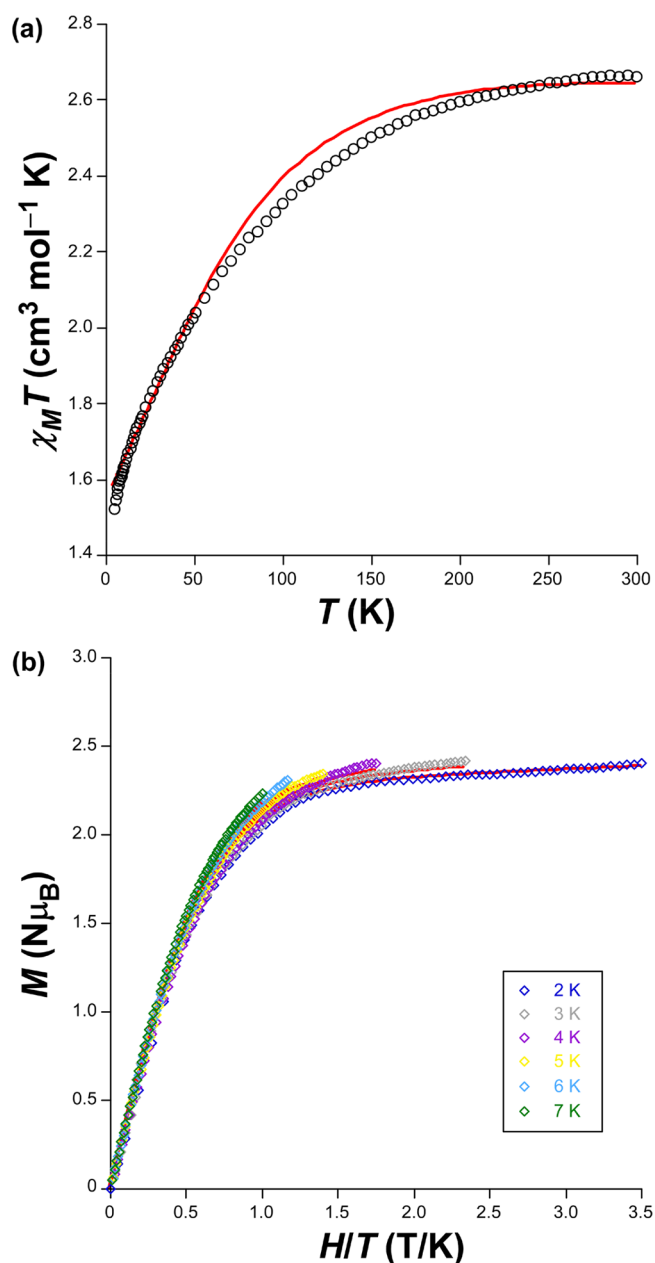
^a $R = \sum_i [(\chi_M T)_{\text{obsd}}(i) - (\chi_M T)_{\text{calcd}}(i)]^2 / \sum_i [(\chi_M T)_{\text{obsd}}(i)]^2$. ^bExperimental and calculated room-temperature $\chi_M T$ values expressed in cm³ K mol⁻¹. ^cCoupling constants from best fitting of experimental curves and BS-DFT calculations.

zero-field splitting (ZFS) considering the large Ni...Ni distances mediating through hydrogen bonding (ca. 7.7 Å) and face to face π - π (ca. 8.9 Å) interactions among monomeric complexes in the crystal structure of compound **1**. In fact, computational calculations have shown the occurrence of negligible anti-ferromagnetic couplings through similar face to face π - π stackings in a recent work.¹⁰⁸ The dc magnetic susceptibility data and magnetization curves (Figure S11 in the Supporting Information) were simultaneously analyzed using the PHI program¹⁰⁹ with the effective spin Hamiltonian (eq 1)

$$\hat{H} = D(\hat{S}_z^2 - \hat{S}^2/3) + E(\hat{S}_x^2 + \hat{S}_y^2) + \mu_B \bar{B} \cdot g \cdot \hat{S} \quad (1)$$

where the first and second terms stand for axial and rhombic anisotropic ZFS interactions parametrized by D and E , respectively, \hat{S} is the spin operator with x , y , or z components, and the last term accounts for the Zeeman interaction with the local magnetic field (\bar{B}), parametrized through the Landé g tensor. Best fitting of the experimental curve was achieved with the following set of parameters: $g = 2.08$, $D = +2.41$ cm⁻¹, and $E < +0.1$ cm⁻¹ with $R = 9.3 \times 10^{-4}$. The weak rhombicity signified by the E parameter and the value of D are consistent with the magnetostructural correlation of this parameter on the basis of Ni(II) complexes containing a {NiN₂O₄} chromophore with a compressed tetragonal-bipyramidal geometry.^{110,111} Although it is true that most of the latter compounds present an experimental negative sign for the D parameter, the present case fits well the predicted positive sign of D by CASSCF calculations.¹¹²

The $\chi_M T$ vs T plot for **2** (Figure 8) shows that the room-temperature $\chi_M T$ product (2.67 cm³ mol⁻¹ K) is within the range expected for one high-spin d^7 Co^{II} ion ($S = 3/2$) with some orbital angular momentum contribution.^{113,114} $\chi_M T$ exhibits a continuous decrease as the sample is cooled, which is indicative of significant spin-orbit coupling (SOC) that makes the fitting of these data somewhat tricky. In particular, the drop is more abrupt below 50 K (where it reaches a value of 1.51 cm³ mol⁻¹ K) probably owing to intrinsic magnetic anisotropy of the Co^{II} ions, taking into account the large Co...Co distance along μ -mimc bridges (ca. 7.8 Å) in the structure. Fitting of the χ_M^{-1} vs T curve to the Curie-Weiss law in the 50–300 K range gives values of $C = 2.88$ cm³ K mol⁻¹ and $\Theta = -22.6$ K. Despite the apparent antiferromagnetic nature of compound **2**, an estimation of the exchange interactions with the phenomenological equation proposed by Rueff et al.^{115,116} (eq 2, see the Supporting Information) that gives $A + B = 2.93$ cm³ K mol⁻¹ (very close to the Curie parameter), $E_1/\kappa = +49(1)$ K (within the range for similar cobalt(II) compounds),^{117–119} and $-E_2/\kappa = -0.56(3)$ K suggests the presence

**Figure 8.** (top) χ_M vs T plot (O) and (bottom) M vs H/T curves showing best fits for compound **2**.

of almost negligible antiferromagnetic interactions (Figure S12 in the Supporting Information).

$$\chi_M T = A \exp(-E_1/\kappa T) + B \exp(-E_2/\kappa T) \quad (2)$$

BS-DFT calculations performed on a suitable dimeric model of **2** confirm the occurrence of very weak antiferromagnetic exchange in **2**, allowing us to consider it as a 2D network of isolated Co^{II} ions. Magnetization data were collected at several temperatures (2–7 K) under an applied field ranging from 0 to 3.5 T. At first glance, the value of M at 2 K (2.23 $N\mu_B$) does not reach the theoretical saturation for $S = 3/2$ ($M_{\text{sat}} = 3.3$, with $g = 2.2$). Moreover, isothermal curves do not collapse in a single master curve, which supports the presence of significant magnetic anisotropy. The simultaneous fitting of both data with the spin Hamiltonian that includes the ZFS term and electron Zeeman interaction (eq 1) by means of the PHI

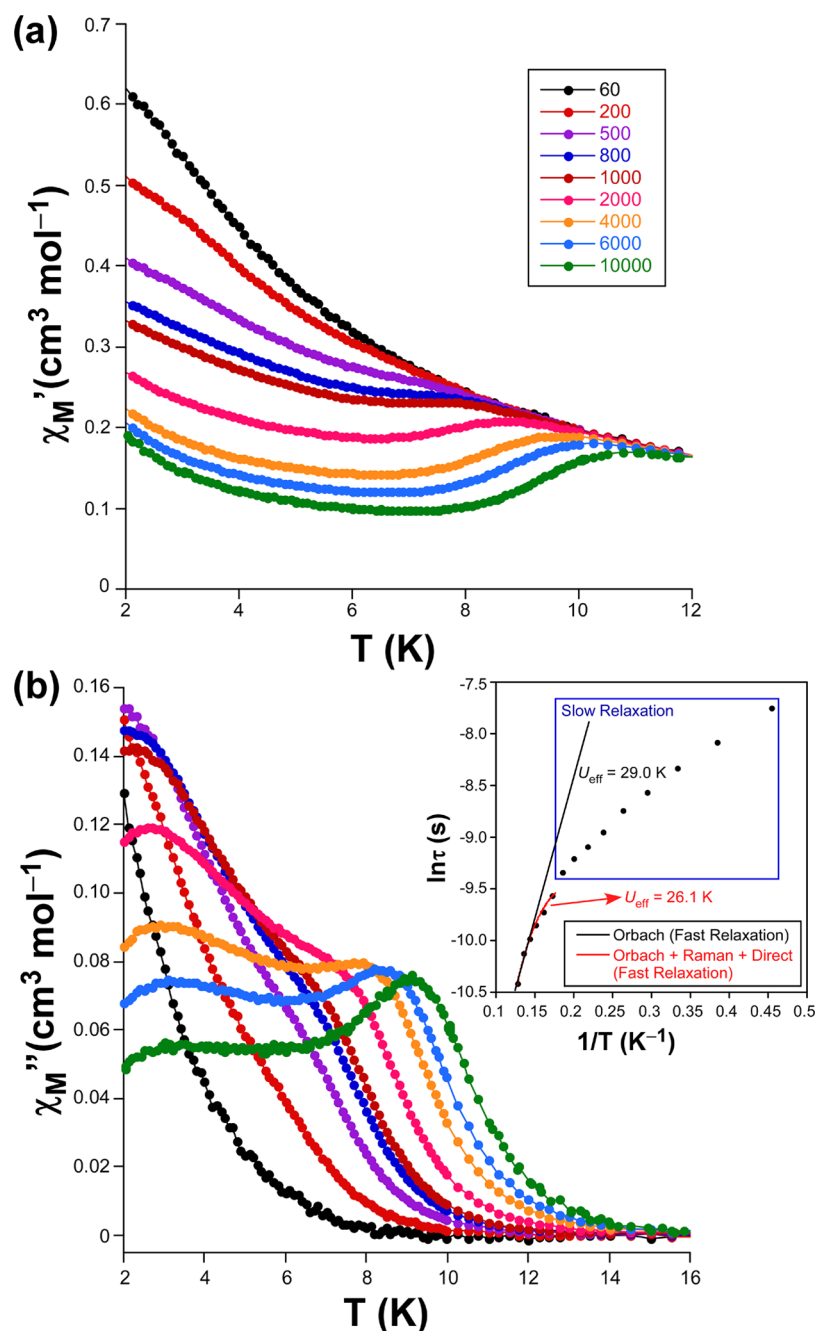


Figure 9. Temperature dependence of (a) in-phase and (b) out-of-phase ac magnetic susceptibilities under an applied field of 1000 Oe for compound **2**. Inset: Arrhenius plot of relaxation times with best fittings.

program allowed us to estimate the value and sign of the magnetic anisotropy: $D = +12.9 \text{ cm}^{-1}$, $E = +0.5 \text{ cm}^{-1}$ with $R = 8.6 \times 10^{-3}$. Note that the fit required a slight anisotropy in the gyromagnetic tensor: $g_x = g_y = 2.17$, $g_z = 2.36$. Although these parameters should be taken with care given the limitations of the Hamiltonian employed,¹²⁰ a deep analysis of the residual obtained along the fitting according to the magnitude and sign of D and E (through the survey mode of PHI) clearly suggests a positive sign for the axial magnetic anisotropy parameter (so-called easy-plane anisotropy). Although the existence of positive D is limited to a few recent works,^{61,121–124} the high-spin d^7 configuration, especially with a pseudo-tetrahedral environment, appears to be very promising in giving moderate D values and, in turn, promising SIM behavior.^{125,126} Possible

reasons explaining such a moderate value of D point to both the low distortion of the metal environment on compound **2** ($S_T = 0.72$) and its inherent positive sign. While it is true that the larger the distortion (less symmetry) the larger the magnetic anisotropy, positive D parameters tend to be smaller than those of negative sign.¹²⁵

The $\chi_M T$ value at room temperature for **3** is close to that expected for a magnetically isolated copper(II) ion (see Table 6). The $\chi_M T$ curve shows a very slight decrease upon cooling up to 60 K, below which it describes a sharper drop to reach an almost null value (Figure S13 in the Supporting Information). The thermal evolution of the magnetic susceptibility exhibits a maximum around 5 K. This behavior is indicative of dominant weak antiferromagnetic interactions among Cu(II) atoms. In

spite of the fact that the square grid of the 2D layer contains two crystallographically independent copper(II) atoms joined through two almost equivalent types of μ -mimc bridges (A and B ligands with μ - κ N: κ O and μ - κ N: κ^2 O, O' modes), the magnetic network is adequately described as a regular quadractic layer. Accordingly, fitting of the curve by means of a magnetic model based on an $H = -JS_1 \cdot S_2$ spin-only Hamiltonian, in which a high-temperature series expansion above a possible Néel temperature is considered, gave a reliable estimate of the exchange coupling.¹²¹ The goodness of the result is indeed corroborated by the DFT computed coupling constant (see the Supporting Information). This type of antiferromagnetic interaction results from a poor magnetic exchange between neighboring copper(II) atoms through long superexchange pathways (ca. 7.8–8.2 Å), which has been previously observed for systems containing similar μ - κ N: κ O bridges.^{51,121,122}

Dynamic Magnetic Properties. Spin dynamics were evaluated for cobalt-based compound **2** by means of alternating-current (ac) susceptibility measurements. No frequency-dependent signals could be observed in the lack of an external dc field, which is not surprising for a compound with easy-plane anisotropy.^{61,124,127,128} According to the Kramers theorem,⁵³ spin–lattice relaxation in easy-plane ($D > 0$) half-integer systems is allowed to occur directly between the ground $M_S = \pm 1/2$ levels in the absence of transverse, hyperfine, and dipolar interactions, in such a way that fast relaxation is expected even under an applied field. Nonetheless, if the existing spin–phonon coupling is weak or if there are very few phonons of the appropriate frequency, the relaxation could be slowed down, an effect known as phonon bottleneck, in such a way that direct relaxation is somewhat hindered as to enable an Orbach relaxation through the higher energy $M_S = \pm 3/2$ levels.⁶¹ At any rate, this fact does not necessarily discard the existence of additional relaxation mechanisms involved in the spin reversal. When an external dc field of 1000 Oe is applied, compound **2** exhibits SIM behavior below 14 K with two out-of-phase maxima peaking in the 2.3 K (2000 Hz) to 3.2 K (10000 Hz) and 7.3 K (2000 Hz) to 9.1 K (10000 Hz) ranges, which can be attributed to the occurrence of slow (SR) and fast relaxation (FR) processes, respectively (Figure 9). The presence of two maxima is a quite uncommon phenomenon^{33,127–130} that could not be anticipated, considering the fact that the crystal structure contains a unique independent Co(II) ion. In any case, fast tunneling at low temperatures is not to be fully discarded, given the divergence in the out-of-phase signal below the blocking temperature.

Cole–Cole plots were generated each 0.4 K in the 2–9 K range to cover the whole frequency-dependent region (below the high-frequency maximum; see Figure S16 in the Supporting Information). The semicircular distributions seem to confirm the thermal evolution and coexistence of SR and FR processes. The semicircle at 2.2 K, attributed to the SR, suffers a progressive widening with increasing temperature in such a way that a broad semicircle is observed at 3.0 K, suggesting that a mixture of both processes could be taking place (superposition of two semicircles). The comparatively narrower semicircles shown above 3.8 K may be related to the FR process, in good agreement with the progressive decrease in α value estimated from fitting with the generalized Debye model.¹³¹ Accordingly, the Arrhenius-like diagram (in the form of $\ln \tau$ vs $1/T$) possesses two branches that were individually analyzed.^{129,130,132–135} The faster relaxation was processed with

eq 3, which accounts for spin reversal through Orbach but also direct and Raman mechanisms.

$$\tau = \tau_0 \exp(-U_{\text{eff}}/k_{\text{B}}T) + A_{\text{direct}}T + B_{\text{Raman}}T^n \quad (3)$$

where $A_{\text{direct}} = 257 \text{ s}^{-1} \text{ K}^{-1}$, $B_{\text{Raman}} = 4.2 \text{ s}^{-1}$, $n = 7.1$, $\tau_0 = 9.98 \times 10^{-7} \text{ s}$, and $U_{\text{eff}} = 26.1 \text{ K}$ are estimated. It is remarkable that parameters associated with direct and Raman processes are comparable to each other, while τ_0 falls within the typical range found for cobalt(II)-based SIMs (between 1.0×10^{-6} and 1.0×10^{-11}).⁴⁷ At the three highest-temperature points the obtained U_{eff} (29.0 K, which equals 20.2 cm^{-1} , with $\tau_0 = 3.36 \times 10^{-7} \text{ s}$) is in good agreement with the gap between $M_S = \pm 1/2$ and $M_S = \pm 3/2$ (equivalent to $2D = 25.8 \text{ cm}^{-1}$). The occurrence of the second much slower relaxation could be due to weak exchange interactions among spin carriers through both the 2D network itself and/or strong π – π stackings between mimc ligands belonging to adjacent metal–organic layers (with C...C as short as 3.59 Å).¹³⁶ Within this assumption, the SR process could originate in the formation of a polymeric array, whereas the FR corresponds to the relaxation of single ions, both of which may coexist at a certain temperature.

Photoluminescence Properties. CPs built from closed-shell d^{10} metal centers and aromatic ligands are known to exhibit PL in the solid state, covering interesting behaviors such as dual fluorescent/phosphorescent emissions and/or tunable emission colors according to the temperature.^{38,137,138} Therefore, PL measurements were carried out on a polycrystalline sample of compound **4** with the temperature varied in the 10–250 K range. At 10 K, **4** shows a broad and intense band that extends over the whole visible spectrum (400–700 nm) on excitation with monochromatic 325 nm light, which corresponds to the excitation maximum (Figure 10). Within the emission band, the maximum is centered at 520 nm, though an additional and sharper peak at 460 nm is also distinguished, which is responsible for the pale green emission of **4** under continuous excitation. The band progressively loses intensity as the temperature is increased whereas it keeps a similar shape, in such a way that, at room temperature, the emission of the

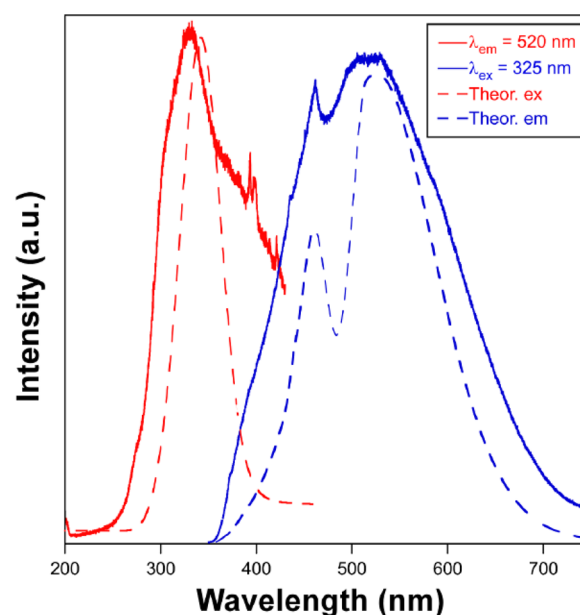


Figure 10. Experimental (solid line) and calculated (dotted line) excitation and emission spectra of compound **4**.

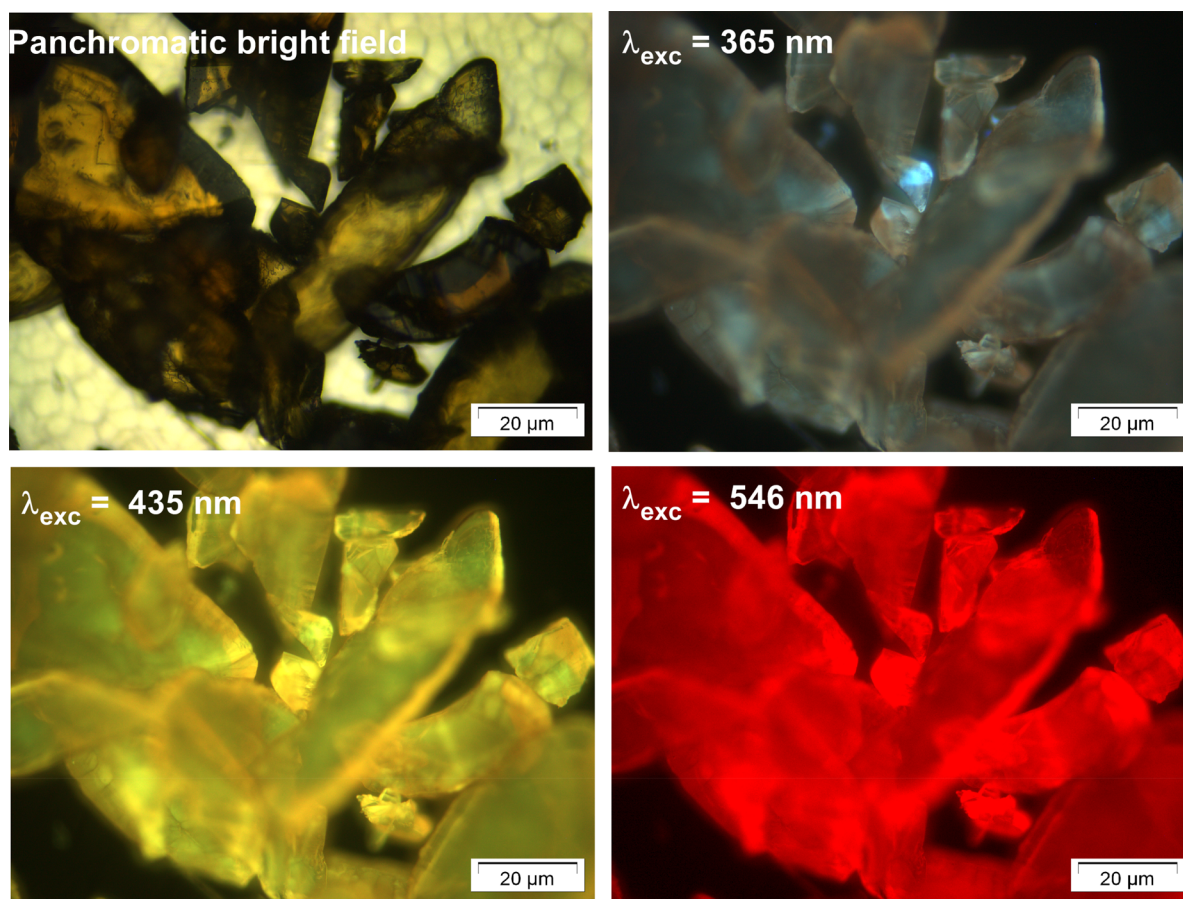


Figure 11. Room-temperature micro-PL images taken at different excitation lines.

material is comparatively weak (Figure S19 in the Supporting Information).

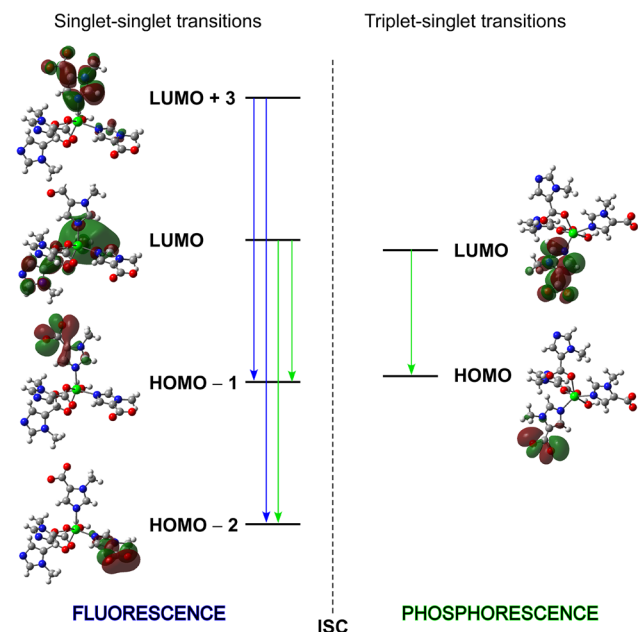
This fact is in good agreement with the micro-PL photographs taken at room temperature on crystals of **4** (Figure 11). As observed, a negligible emission is shown when λ_{ex} 365 nm is used, whereas bright greenish yellow emission can be clearly inferred from the micrograph taken with the 435 nm excitation line. Moreover, crystals exhibit red emission when they are exposed to the green (546 nm) excitation line, which confirms the multicolored emission of this material. In comparison to the emission of the free Hmimc ligand, compound **4** shows a large bathochromic shift (of ca. 110 nm) that seems to be related to its coordination to cadmium atoms (Figure S18 in the Supporting Information).^{139,140} TD-DFT calculations were carried out on a suitable model of **4** (Figure S22 in the Supporting Information) to provide further insights into the PL performance of this compound. As inferred from Figure 10, the calculated spectra reproduce fairly well the experimental spectra, with very small shifts between their maxima. The two main $S_0 \rightarrow S_1$ excitations (at 328 and 335 nm) that conform the band stand for HOMO-4 \rightarrow LUMO+2 and HOMO-3 \rightarrow LUMO+2 transitions, meaning that the compound is excited via $\sigma \rightarrow \pi^*$ and $\pi \rightarrow \pi^*$ transitions between different ligands (LLCT) (see Figure S23 in the Supporting Information). After these singlet excitations, the emission proceeds through similar processes for both bands. The first one (centered at 460 nm) contains three transitions: HOMO-2 \rightarrow LUMO, HOMO-1 \rightarrow LUMO+3, and HOMO-2 \rightarrow LUMO+3; whereas the main band with a maximum at 520

nm results from several HOMO-1 \rightarrow LUMO transitions involving different vibrational states of the latter levels (see Table S8 in the Supporting Information). As observed in Scheme 1, HOMO- n levels show a predominant σ character and lie mainly on the carboxylate groups of the ligands; therefore, taking into account the π nature of LUMO+ n molecular orbitals, it can be concluded that the singlet emission of this compound is again of the LLCT type.

During the PL characterization of this compound at low temperature, it was observed that the solid sample preserves a significant pale green afterglow when the excitation beam is turned off, indicating that it exhibits LLP. This fact prompted us to further investigate the phosphorescent emission of the material, for which decay curves were recorded for some representative wavelengths (each 20 nm) over the emission spectrum. At first sight, two opposite regions were distinguished according to the profile of the curves, indicative of rapid or slow deactivation processes (Table 7).

On the one hand, curves measured for λ_{em} included within 350–400 and 640–750 nm ranges reveal very short emission processes (on the order of a few nanoseconds). On the other hand, slow and gradual decays derived from the occurrence of successive long-lived processes are described for the curves corresponding to the central and most representative region of the emission band (420–620 nm). The analysis of these curves with a multiexponential ($I_t = A_0 + A_1 \exp(-t/\tau_1) + A_2 \exp(-t/\tau_2) + A_3 \exp(-t/\tau_3)$) expression revealed the presence of three kinds of components: persistent emissions of 0.25–0.43 s, intermediate lifetimes of 0.05–0.23 s, and very short processes

Scheme 1. Energy Diagram of the Orbitals onto Model 4 Involved in the Electronic Transitions of 4 Resulting in Fluorescent and Phosphorescent Blue and Green Emissions^a



^aISC denotes intersystem crossing.

Table 7. Best-Fit Results of Decay Curves Measured at 10 K for Compound 4 (λ_{ex} 325 nm; λ_{em} 400–340 nm)^a

wavelength (nm)	τ_1 (ms)	τ_2 (ms)	τ_3 (ms)	χ^2
400	51(6)/100%			1.544
420	6(2)/4%	46(7)/27%	245(18)/69%	1.538
440	39(1)/30%	227(5)/70%		1.517
460	9(1)/4%	67(3)/37%	318(8)/59%	1.435
480	14(1)/7%	78(4)/38%	369(13)/55%	1.522
500	16(2)/9%	76(6)/34%	320(14)/57%	1.389
520	19(1)/9%	97(3)/36%	427(9)/56%	1.431
540	15(2)/9%	75(7)/35%	321(17)/56%	1.476
560	34(2)/32%	195(6)/68%		1.255
580	26(1)/27%	179(14)/73%		1.515
600	28(2)/30%	171(5)/70%		1.769
620	22(1)/30%	148(5)/70%		1.658
640	68(5)/100%			1.613

^aNote that, accompanying the lifetime values, percentages for each component are also given.

attributed to the lamp pulse (6–39 ms). Despite the fact that some Cd^{II}-based compounds showing green phosphorescence have been recently reported,^{63–68} all of them display mixed blue to green emission as the fluorescent signal under UV excitation turns into a green phosphorescent afterglow, which differs from the bright green to pale green transition described for compound 4. Among the few reported materials, the structure of 4 resembles the recently characterized LLP with formula $[\text{Cd}(\mu\text{-6-aminonicotinato})_2]_n$, which presents the longest emission lifetimes (of above 0.8 s).⁶⁸ Taking into account the close similarity between both ligands (N/O donor ligands), the more modest lifetimes achieved for this compound may be tentatively attributed to the presence of coordination water molecules, whose O–H bonds act as efficient quenchers on radiative processes through a vibronic coupling mecha-

nism.^{141–143} In any case, the occurrence of such behavior seems to indicate that, according to the well-established Kasha rule,¹⁴⁴ the phosphorescent emission should proceed via a spin-forbidden $T_1 \rightarrow S_0$ transition. This involves, in turn, that the triplet state of the complex is accessible through an intersystem crossing phenomenon facilitated by the spin–orbit coupling of the d^{10} metal atom, in addition to the absence of efficient quenchers that could be coupled to the $T_1 \rightarrow S_0$ emission. In order with the latter hypothesis, the lowest-lying T_1 state was geometrically optimized, from which the vertical emission energy ($\lambda_{\text{vert-phosp}}$ as described by Adamo et al.¹⁴⁵) was estimated to be 478 nm. This value is quite close to 520 nm, the wavelength of the emission maximum that corresponds to the longest lifetime recorded, which confirms that phosphorescent emission proceeds through a $T_1 \rightarrow S_0$ transition (see Scheme 1). Nonetheless, it cannot be discarded that the emitted signal is indeed also composed of fluorescent emission, as revealed by singlet–singlet transitions studied by TD-DFT. On another level, the long-lasting emission remains stable up to 100 K (Table S7 and Figure S21 in the Supporting Information), whereas it is practically prevented at higher temperatures owing to the increase of molecular vibrations that bring a significant nonradiative quenching, such that only the fluorescent emission takes place.

CONCLUSIONS

A family of four new compounds grown from the coordination of 1-methylimidazole-5-carboxylate (mimc) ligand to first-row transition-metal(II) ions has been synthesized under solvothermal conditions. Single-crystal X-ray analysis reveals the largest possible structural diversity in the family despite the limited coordination versatility of the ligand. In fact, mimc coordinates as a terminal ligand to nickel(II) atoms and forms monomeric entities in 1, whereas it acts as a bridging linker among metal ions to give 2D CPs of sql topology in 2–4. The structural dissimilarities of the latter (small distortions of the topological network) may be attributed to subtle changes occurring in the coordination shells owing to the features imposed by cobalt(II), copper(II), and cadmium(II) ions (ion radii and preferred geometries) on coordination to the carboxylate moiety of the ligand, forcing it to adopt different modes that maintain the metal to ligand connectivity. Measurements of the magnetic susceptibility under static conditions indicate that mimc ligands show almost negligible exchange interactions among metal centers, also confirmed by DFT computed values of the coupling parameter, which allow considering these systems as networks of magnetically isolated spins. This fact is particularly interesting for the Co(II)-based CP (2) because it shows field-induced slow magnetic relaxation arising from a moderate magnetic anisotropy of positive sign ($D = +12.9 \text{ cm}^{-1}$, $E = +0.5 \text{ cm}^{-1}$) estimated from simultaneous fitting of $\chi_M T(T)$ and $M(H)$ curves, which may in turn be attributed to the pseudo-tetrahedral environment. The analysis of the spin dynamics of 2 through ac measurements show the occurrence of fast quantum tunneling of the magnetization that can be partially suppressed by applying a dc field, allowing two relaxation processes to be identified. The faster process refers to the relaxation of single ions in the structure which proceeds through multiple mechanisms (i.e., Orbach, direct, and Raman) given the combination of positive axial and low transverse magnetic anisotropy, from which a thermally activated barrier of ca. 26 K is estimated. In contrast, the slower relaxation is assigned to weak exchange interactions through the 2D

network or π - π stackings among mimic ligands belonging to adjacent metal-organic layers. In any case, the blocking temperature (of ca. 14 K) deserves to be highlighted, since it lies on the high edge found for cobalt(II)-based SIMs.

On another level, the cadmium(II)-based CP presents an interesting bright green emission which is characterized by a long-persisting phosphorescence that is responsible for the low-temperature afterglow observed for at least 1 s after the removal of the UV source. In fact, measurements of the decay curves reveal the occurrence of fluorescent/phosphorescent emissions, consisting of several lifetimes that account for persistent (0.25–0.43 s), intermediate (0.05–0.23 s), and short (6–39 ms) components. TD-DFT calculations combined with a computational strategy to estimate the vertical transitions related to the phosphorescent emission not only allow surmising the LCCT mechanism governing both singlet-singlet and triplet-singlet transitions but also give an accurate description of the photoluminescent performance of the compound.

■ ASSOCIATED CONTENT

● Supporting Information

The Supporting Information is available free of charge on the ACS Publications website at DOI: 10.1021/acs.inorgchem.7b02020.

Additional crystal structures and data, FT-IR spectroscopy, thermogravimetric analysis, powder X-ray diffraction analyses, dc and ac magnetic susceptibility data, spin density distributions, photoluminescence spectra and lifetimes, and TD-DFT computational results (PDF)

Accession Codes

CCDC 1566132–1566135 contain the supplementary crystallographic data for this paper. These data can be obtained free of charge via www.ccdc.cam.ac.uk/data_request/cif, or by emailing data_request@ccdc.cam.ac.uk, or by contacting The Cambridge Crystallographic Data Centre, 12 Union Road, Cambridge CB2 1EZ, UK; fax: +44 1223 336033.

■ AUTHOR INFORMATION

Corresponding Authors

*E-mail for J.C.: javier.cepeda@ehu.es.

*E-mail for A.R.-D.: antonio5@ugr.es.

ORCID

Javier Cepeda: 0000-0002-0147-1360

Antonio Rodríguez-Diéguez: 0000-0003-3198-5378

Notes

The authors declare no competing financial interest.

■ ACKNOWLEDGMENTS

Red Guipuzcoana de Ciencia, Tecnología e Innovación (OF215/2016 and OF188/2017), and University of the Basque Country (GIU14/01, EHUA16/32), Junta de Andalucía (FQM-1484), and Ministerio de Economía, Industria y Competitividad of Spain (Projects CTQ2014-56312-P) are acknowledged for support. The authors acknowledge technical and human support provided by SGIker of UPV/EHU and European funding (ERDF and ESF).

■ REFERENCES

(1) Li, M.; Li, D.; O'Keeffe, M.; Yaghi, O. M. Topological Analysis of Metal-Organic Frameworks with Polytopic Linkers and/or Multiple

Building Units and the Minimal Transitivity Principle. *Chem. Rev.* **2014**, *114*, 1343–1370.

(2) Batten, S. R.; Murray, K. S. Structure and magnetism of coordination polymers containing dicyanamide and tricyanomethanide. *Coord. Chem. Rev.* **2003**, *246*, 103–130.

(3) Hoskins, B. F.; Robson, R. Infinite polymeric frameworks consisting of three dimensionally linked rod-like segments. *J. Am. Chem. Soc.* **1989**, *111*, 5962–5964.

(4) Allendorf, M. D.; Stavila, V. Crystal engineering, structure–function relationships, and the future of metal–organic frameworks. *CrystEngComm* **2015**, *17*, 229–246.

(5) Chen, C. T.; Suslick, S. One-dimensional coordination polymers: Applications to material science. *Coord. Chem. Rev.* **1993**, *128*, 293–322.

(6) Kawata, S.; Kitagawa, S.; Kondo, M.; Furuchi, L.; Munakata, M. Two-Dimensional Sheets of Tetragonal Copper(II) Lattices: X-Ray Crystal Structure and Magnetic Properties of $[\text{Cu}(\text{C}_6\text{O}_4\text{Cl}_2)(\text{C}_4\text{H}_4\text{N}_2)]_n$. *Angew. Chem., Int. Ed. Engl.* **1994**, *33*, 1759–1761.

(7) Furukawa, S.; Reboul, J.; Diring, S.; Sumida, K.; Kitagawa, S. Structuring of metal-organic frameworks at the mesoscopic/macroscopic scale. *Chem. Soc. Rev.* **2014**, *43*, 5700–5734.

(8) Colacio, E.; Rodríguez-Diéguez, A. Possibilities with 2-pyrimidinecarbonitrile to design MOFs. *Polyhedron* **2014**, *80*, 173–179.

(9) Ma, S.; Sun, D.; Ambrogio, M.; Fillinger, J. A.; Parkin, S.; Zhou, H.-C. Framework-catenation isomerism in metal–organic frameworks and its impact on hydrogen uptake. *J. Am. Chem. Soc.* **2007**, *129*, 1858–1859.

(10) Zhang, J.; Wotjas, L.; Larsen, R. W.; Eddaoudi, M.; Zaworotko, M. J. Temperature and concentration control over interpenetration in a metal–organic material. *J. Am. Chem. Soc.* **2009**, *131*, 17040–17041.

(11) Wang, J. H.; Li, M.; Li, D. A dynamic, luminescent and entangled MOF as a qualitative sensor for volatile organic solvents and a quantitative monitor for acetonitrile vapour. *Chem. Sci.* **2013**, *4*, 1793–1801.

(12) Cepeda, J.; Pérez-Yáñez, S.; Beobide, G.; Castillo, O.; García, J. A.; Luque, A. Photoluminescence modulation in lanthanide(III)/pyrazine-2,5-dicarboxylate/nitrato frameworks. *Eur. J. Inorg. Chem.* **2015**, *2015*, 4318–4328.

(13) Takashima, Y.; Martínez, V. M.; Furukawa, S.; Kondo, M.; Shimomura, S.; Uehara, H.; Nakahama, M.; Sugimoto, K.; Kitagawa, S. Molecular decoding using luminescence from an entangled porous framework. *Nat. Commun.* **2011**, *2*, 168.

(14) Stock, N.; Biswas, S. Synthesis of metal-organic frameworks (MOFs): routes to various MOF topologies, morphologies, and composites. *Chem. Rev.* **2012**, *112*, 933–969.

(15) Loiseau, T.; Serre, C.; Huguenard, C.; Fink, G.; Taulelle, F.; Henry, M.; Bataille, T.; Férey, G. A Rationale for the Large Breathing of the Porous Aluminum Terephthalate (MIL-53) Upon Hydration. *Chem. - Eur. J.* **2004**, *10*, 1373–1382.

(16) Murray, L. J.; Dinca, M.; Long, J. R. Hydrogen storage in metal–organic frameworks. *Chem. Soc. Rev.* **2009**, *38*, 1294–1314.

(17) Millward, A. R.; Yaghi, O. M. Metal–Organic Frameworks with Exceptionally High Capacity for Storage of Carbon Dioxide at Room Temperature. *J. Am. Chem. Soc.* **2005**, *127*, 17998–17999.

(18) Llewellyn, P. L.; Bourrelly, S.; Serre, C.; Vimont, A.; Daturi, M.; Hamon, L.; De Weireld, G.; Chang, J. S.; Hong, D. Y.; Hwang, Y. K.; Jhung, S. H.; Férey, G. High Uptakes of CO₂ and CH₄ in Mesoporous Metal–Organic Frameworks MIL-100 and MIL-101. *Langmuir* **2008**, *24*, 7245–7250.

(19) Farha, O. K.; Yazaydin, A. Ö.; Eryazici, I.; Malliakas, C. D.; Hauser, B. G.; Kanatzidis, M. G.; Nguyen, S. T.; Snurr, R. Q.; Hupp, J. T. De novo synthesis of a metal-organic framework material featuring ultrahigh surface area and gas storage capacities. *Nat. Chem.* **2010**, *2*, 944–948.

(20) Pérez-Yáñez, S.; Beobide, G.; Castillo, O.; Cepeda, J.; Fröba, M.; Hoffmann, F.; Luque, A.; Román, P. Improving the performance of a poorly adsorbing porous material: template mediated addition of

microporosity to a crystalline submicroporous MOF. *Chem. Commun.* **2012**, *48*, 907–909.

(21) Jiang, H.-L.; Makal, T. A.; Zhou, H.-C. Interpenetration control in metal–organic frameworks for functional applications. *Coord. Chem. Rev.* **2013**, *257*, 2232–2249.

(22) Seco, J. M.; Fairén-Jimenez, D.; Calahorra, A. J.; Méndez-Liñán, L.; Pérez-Mendoza, M.; Casati, N.; Colacio, E.; Rodríguez-Diéguez, A. Modular structure of a robust microporous MOF based on Cu₂ paddle-wheels with high CO₂ selectivity. *Chem. Commun.* **2013**, *49*, 11329–11331.

(23) Spanopoulos, I.; Bratsos, I.; Tampaxis, C.; Kourtellaris, A.; Tasiopoulos, A.; Charalambopoulou, G.; Steriotis, T. A.; Trikalitis, P. N. Enhanced gas-sorption properties of a high surface area, ultramicroporous magnesium formate. *CrystEngComm* **2015**, *17*, 532–539.

(24) Russell, S. E.; Gosset, C.; Agache, X.; Volkringer, C.; Henry, N.; Decadt, R.; Van, D. R.; Visseaux, M.; Loiseau, T. A new series of trivalent lanthanide (Ce, Pr, Nd, Sm, Eu, Gd, Tb, Dy) coordination polymers with a 1,2-cyclohexanedicarboxylate ligand: synthesis, crystal structure, luminescence and catalytic properties. *CrystEngComm* **2016**, *18*, 3594–3605.

(25) Quah, H. S.; Chen, W.; Schreyer, M. K.; Yang, H.; Wong, M. W.; Ji, W.; Vittal, J. J. Multiphoton harvesting metal–organic frameworks. *Nat. Commun.* **2015**, *6*, 7954–7961.

(26) Li, H.-Y.; Wei, Y.-L.; Dong, X.-Y.; Zang, S.-Q.; Mak, T. C. W. Novel Tb-MOF Embedded with Viologen Species for Multi-Photofunctionality: Photochromism, Photomodulated Fluorescence, and Luminescent pH Sensing. *Chem. Mater.* **2015**, *27*, 1327–1331.

(27) Baldoví, J. J.; Coronado, E.; Gaita-Ariño, A.; Gamer, C.; Giménez-Marqués, M.; Mínguez-Espallargas, G. A SIM-MOF: Three-Dimensional Organisation of Single-Ion Magnets with Anion-Exchange Capabilities. *Chem. - Eur. J.* **2014**, *20*, 10695–10702.

(28) Shi, P.-F.; Zhao, B.; Xiong, G.; Hou, Y.-L.; Cheng, P. Fast capture and separation of, and luminescent probe for, pollutant chromate using a multi-functional cationic heterometal-organic framework. *Chem. Commun.* **2012**, *48*, 8231–8233.

(29) Wu, M.-X.; Yang, Y.-W. Metal–Organic Framework (MOF)-Based Drug/Cargo Delivery and Cancer Therapy. *Adv. Mater.* **2017**, *29*, 1606134.

(30) Cepeda, J.; Pérez-Yáñez, S.; Beobide, G.; Castillo, O.; García, J. A.; Lanchas, M.; Luque, A. Enhancing luminescence properties of lanthanide(III)/pyrimidine-4,6-dicarboxylate system by solvent-free approach. *Dalton Trans.* **2015**, *44*, 6972–6986.

(31) Rocha, J.; Brites, C. D. S.; Carlos, L. D. Lanthanide Organic Framework Luminescent Thermometers. *Chem. - Eur. J.* **2016**, *22*, 14782–14795.

(32) Lin, R.-B.; Liu, S.-Y.; Ye, J.-W.; Li, X.-Y.; Zhang, J.-P. Photoluminescent Metal–Organic Frameworks for Gas Sensing. *Adv. Sci.* **2016**, *3*, 1500434–1500454.

(33) Calahorra, A. J.; Oyarzabal, I.; Fernández, B.; Seco, J. M.; Tian, T.; Fairén-Jimenez, D.; Colacio, E.; Rodríguez-Diéguez, A. Rare earth anthracenedicarboxylate metal–organic frameworks: slow relaxation of magnetization of Nd³⁺, Gd³⁺, Dy³⁺, Er³⁺ and Yb³⁺ based materials. *Dalton Trans.* **2016**, *45*, 591–598.

(34) Ma, L. F.; Wang, L. Y.; Du, M.; Batten, S. R. Unprecedented 4- and 6-connected 2D coordination networks based on 44-subnet tectons, showing unusual supramolecular motifs of rotaxane and helix. *Inorg. Chem.* **2010**, *49*, 365–367.

(35) Chen, S. P.; Ren, Y. X.; Wang, W. T.; Gao, S. L. Nanoporous lanthanide-carboxylate frameworks based on 5-nitroisophthalic acid. *Dalton Trans.* **2010**, *39*, 1552–1557.

(36) Almeida Paz, F. A.; Klinowski, J.; Vilela, S. M. F.; Tomé, J. P. C.; Cavaleiro, J. A. S.; Rocha, J. Ligand design for functional metal–organic frameworks. *Chem. Soc. Rev.* **2012**, *41*, 1088–1110.

(37) Heine, J.; Müller-Buschbaum, K. Engineering metal-based luminescence in coordination polymers and metal–organic frameworks. *Chem. Soc. Rev.* **2013**, *42*, 9232–9242.

(38) Cepeda, J.; Rodríguez-Diéguez, A. Tuning the luminescence performance of metal–organic frameworks based on d¹⁰ metal ions:

from an inherent versatile behaviour to their response to external stimuli. *CrystEngComm* **2016**, *18*, 8556–8573.

(39) Wiers, B. M.; Foo, M.-L.; Balsara, N. P.; Long, J. R. A Solid Lithium Electrolyte via Addition of Lithium Isopropoxide to a Metal–Organic Framework with Open Metal Sites. *J. Am. Chem. Soc.* **2011**, *133*, 14522–14525.

(40) Férey, G.; Millange, F.; Morcrette, M.; Serre, C.; Doublet, M. L.; Grenèche, J.-M.; Tarascon, J.-M. Mixed-valence li/fe-based metal-organic frameworks with both reversible redox and sorption properties. *Angew. Chem., Int. Ed.* **2007**, *46*, 3259–3263.

(41) Kurmoo, M. Magnetic metal–organic frameworks. *Chem. Soc. Rev.* **2009**, *38*, 1353–1379.

(42) Meng, Y.-S.; Jiang, S.-D.; Wang, B.-W.; Gao, S. Understanding the Magnetic Anisotropy toward Single-Ion Magnets. *Acc. Chem. Res.* **2016**, *49*, 2381–2389.

(43) Fernández, B.; Oyarzabal, I.; Fischer-Fodor, E.; Macavei, S.; Sánchez, I.; Seco, J. M.; Gómez-Ruiz, S.; Rodríguez-Diéguez, A. Multifunctional applications of a dysprosium based metal–organic chain with single-ion magnet behavior. *CrystEngComm* **2016**, *18*, 8718–8721.

(44) Freedman, D. E.; Harman, W. H.; Harris, T. D.; Long, G. J.; Chang, C. J.; Long, J. R. Slow Magnetic Relaxation in a High-Spin Iron(II) Complex. *J. Am. Chem. Soc.* **2010**, *132*, 1224–1225.

(45) Harman, W. h.; Harris, T. D.; Fong, H.; Chang, A.; Rinehart, J. D.; Ozarowski, A.; Sougrati, M. T.; Grandjean, F.; Long, G. J.; Long, J. R.; Chang, C. J. Slow Magnetic Relaxation in a Family of Trigonal Pyramidal Iron(II) Pyrrolide Complexes. *J. Am. Chem. Soc.* **2010**, *132*, 18115–18126.

(46) Huang, X.-C.; Zhou, C.; Shao, D.; Wang, X.-Y. Field-Induced Slow Magnetic Relaxation in Cobalt(II) Compounds with Pentagonal Bipyramid Geometry. *Inorg. Chem.* **2014**, *53*, 12671–12673.

(47) Frost, J. M.; Harriman, K. L. M.; Murugesu, M. The rise of 3-d single-ion magnets in molecular magnetism: towards materials from molecules? *Chem. Sci.* **2016**, *7*, 2470–2491.

(48) Craig, G. A.; Murrie, M. 3d single-ion magnets. *Chem. Soc. Rev.* **2015**, *44*, 2135–2147.

(49) Ion, A. E.; Nica, S.; Madalan, A. M.; Shova, S.; Vallejo, J.; Julve, M.; Lloret, F.; Andruh, M. Two-Dimensional Coordination Polymers Constructed Using, Simultaneously, Linear and Angular Spacers and Cobalt(II) Nodes. New Examples of Networks of Single-Ion Magnets. *Inorg. Chem.* **2015**, *54*, 16–18.

(50) Mondal, A. K.; Khatua, S.; Tomar, K.; Konar, S. Field-Induced Single-Ion-Magnetic Behavior of Octahedral Co^{II} in a Two-Dimensional Coordination Polymer. *Eur. J. Inorg. Chem.* **2016**, *2016*, 3545–3552.

(51) Rodríguez-Diéguez, A.; Pérez-Yáñez, S.; Ruiz-Rubio, L.; Seco, J. M.; Cepeda, J. From isolated to 2D coordination polymers based on 6-aminonicotinate and 3d-metal ions: towards field-induced single-ion-magnets. *CrystEngComm* **2017**, *19*, 2229–2242.

(52) Palion-Gazda, J.; Klemens, T.; Machura, B.; Vallejo, J.; Lloret, F.; Julve, M. Single ion magnet behaviour in a two-dimensional network of dicyanamide-bridged cobalt(II) ions. *Dalton Trans.* **2015**, *44*, 2989–2992.

(53) Kramers, H. A. Théorie générale de la rotation paramagnétique dans les cristaux. *Proc. R. Acad. Sci. Amsterdam* **1930**, *33*, 959–972.

(54) Atherton, N. M. In *Principles of Electron Spin Resonance*; Ellis Horwood: Chichester, U.K., 1993.

(55) Ishikawa, N.; Sugita, M.; Wernsdorfer, W. Quantum tunneling of magnetization in lanthanide single-molecule magnets: bis-(phthalocyaninato)terbium and bis-(phthalocyaninato)dysprosium anions. *Angew. Chem., Int. Ed.* **2005**, *44*, 2931–2935.

(56) Zadrozny, J. M.; Long, J. R. Slow Magnetic Relaxation at Zero Field in the Tetrahedral Complex [Co(SPh)₄]²⁻. *J. Am. Chem. Soc.* **2011**, *133*, 20732–20734.

(57) Cucos, P.; Tuna, F.; Sorace, L.; Matei, I.; Maxim, C.; Shova, S.; Gheorghie, R.; Caneschi, A.; Hillebrand, M.; Andruh, M. Magnetic and Luminescent Binuclear Double-Stranded Helicates. *Inorg. Chem.* **2014**, *53*, 7738–7747.

- (58) Cao, D.-K.; Feng, J.-Q.; Ren, M.; Gu, Y.-W.; Song, Y.; Ward, M. D. A mononuclear cobalt(II)–dithienylethene complex showing slow magnetic relaxation and photochromic behavior. *Chem. Commun.* **2013**, *49*, 8863–8865.
- (59) Rechkemmer, Y.; Breitgoff, F. D.; van der Meer, M.; Atanasov, M.; Hakl, M.; Orlita, M.; Neugebauer, P.; Neese, F.; Sarkar, B.; van Slageren, J. A four-coordinate cobalt(II) single-ion magnet with coercivity and a very high energy barrier. *Nat. Commun.* **2016**, *7*, 10467.
- (60) Carl, E.; Demeshko, S.; Meyer, F.; Stalke, D. Triimidodisulfonates as Acute Bite-Angle Chelates: Slow Relaxation of the Magnetization in Zero Field and Hysteresis Loop of a Co^{II} Complex. *Chem. - Eur. J.* **2015**, *21*, 10109–10115.
- (61) Zadrozny, J. M.; Liu, J.; Piro, N. A.; Chang, C. J.; Hill, S.; Long, J. R. Slow magnetic relaxation in a pseudotetrahedral cobalt(II) complex with easy-plane anisotropy. *Chem. Commun.* **2012**, *48*, 3927–3929.
- (62) Orchard, A. F. In *Magnetochemistry*; Oxford University Press: Oxford, U.K., 2003.
- (63) Calahorra, A. J.; Salinas-Castillo, A.; Fairen-Jimenez, D.; Seco, J. M.; Mendicutie-Fierro, C.; Gómez-Ruiz, S.; López-Viseras, M.; Rodríguez-Diéguez, A. Long lifetime photoluminescence emission of 3D cadmium metal–organic frameworks based on the 5-(4-pyridyl)-tetrazole ligand. *Inorg. Chim. Acta* **2015**, *427*, 131–137.
- (64) Yuan, S.; Deng, Y.-K.; Sun, D. Unprecedented Second-Timescale Blue/Green Emissions and Iodine-Uptake-Induced Single-Crystal-to-Single-Crystal Transformation in Zn^{II}/Cd^{II} Metal–Organic Frameworks. *Chem. - Eur. J.* **2014**, *20*, 10093–10098.
- (65) Cepeda, J.; San Sebastian, E.; Padro, D.; Rodríguez-Diéguez, A.; García, J. A.; Ugalde, J.; Seco, J. M. A Zn based coordination polymer exhibiting long-lasting phosphorescence. *Chem. Commun.* **2016**, *52*, 8671–8674.
- (66) Yang, X.; Yan, D. Strongly Enhanced Long-Lived Persistent Room Temperature Phosphorescence Based on the Formation of Metal–Organic Hybrids. *Adv. Opt. Mater.* **2016**, *4*, 897–905.
- (67) Yang, Y.; Wang, K.-Z.; Yan, D. Ultralong Persistent Room Temperature Phosphorescence of Metal Coordination Polymers Exhibiting Reversible pH-Responsive Emission. *ACS Appl. Mater. Interfaces* **2016**, *8*, 15489–15496.
- (68) Seco, J. M.; Rodríguez-Diéguez, A.; Padro, D.; García, J. A.; Ugalde, J. M.; San Sebastian, E.; Cepeda, J. Experimental and Theoretical Study of a Cadmium Coordination Polymer Based on Aminonicotinate with Second-Timescale Blue/Green Photoluminescent Emission. *Inorg. Chem.* **2017**, *56*, 3149–3152.
- (69) Murawski, C.; Leo, K.; Gather, M. C. Efficiency roll-off in organic light-emitting diodes. *Adv. Mater.* **2013**, *25*, 6801–6827.
- (70) Hong, K.; Lee, J.-L. Review paper: Recent developments in light extraction technologies of organic light emitting diodes. *Electron. Mater. Lett.* **2011**, *7*, 77–91.
- (71) McClenaghan, N. D.; Leydet, Y.; Maubert, B.; Indelli, M. T.; Campagna, S. Excited-State Equilibration: A Process Leading to Long-Lived Metal-to-Ligand Charge Transfer Luminescence in Supramolecular Systems. *Coord. Chem. Rev.* **2005**, *249*, 1336–1350.
- (72) Indelli, M. T.; CGhirotti, M.; Prodi, A.; Chiorboli, C.; Scandola, F.; MacClenaghan, N. D.; Puntoriero, F.; Campagna, S. Solvent Switching of Intramolecular Energy Transfer in Bichromophoric Systems. Photophysics of (2,2'-Bipyridine)tetracyanoruthenate(II)/Pyrenyl Complexes. *Inorg. Chem.* **2003**, *42*, 5489–5497.
- (73) Earnshaw, A. In *Introduction to Magnetochemistry*; Academic Press: London, 1968.
- (74) Bruker Apex2; Bruker AXS Inc., Madison, WI, USA, 2004.
- (75) Sheldrick, G. M. *SADABS, Program for Empirical Adsorption Correction*; Institute for Inorganic Chemistry. University of Göttingen: Göttingen, Germany, 1996.
- (76) Altomare, A.; Burla, M. C.; Camilla, M.; Cascarano, G. L.; Giacovazzo, C.; Guagliardi, A.; Moliterni, A. G. G.; Polidori, G.; Spagna, R. SIR97: a new tool for crystal structure determination and refinement. *J. Appl. Crystallogr.* **1999**, *32*, 115–119.
- (77) Sheldrick, G. M. *SHELX-2014, Program for Crystal Structure Refinement*; University of Göttingen, Göttingen, Germany, 2014.
- (78) Farrugia, L. J. WinGX suite for small-molecule single-crystal crystallography. *J. Appl. Crystallogr.* **1999**, *32*, 837–838.
- (79) Rodríguez-Carvajal, J. FULLPROF, Program Rietveld for Pattern Matching Analysis of Powder Patterns. *Abstracts of the Satellite Meeting on Powder Diffraction of the XV Congress of the IUCr*, Toulouse, France, 1990; p 127.
- (80) Rodríguez-Carvajal, J. *FULLPROF 2000, version 2.5d*; Laboratoire Léon Brillouin (CEA-CNRS), Centre d'Études de Saclay, Gif sur Yvette Cedex, France, 2003.
- (81) Frisch, M. J.; Trucks, G. W.; Schlegel, H. B.; Scuseria, G. E.; Robb, M. A.; Cheeseman, J. R.; Scalmani, G.; Barone, V.; Mennucci, B.; Petersson, G. A.; Nakatsuji, H.; Caricato, M.; Li, X.; Hratchian, H. P.; Izmaylov, A. F.; Bloino, J.; Zheng, G.; Sonnenberg, J. L.; Hada, M.; Ehara, M.; Toyota, K.; Fukuda, R.; Hasegawa, J.; Ishida, M.; Nakajima, T.; Honda, Y.; Kitao, O.; Nakai, H.; Vreven, T.; Montgomery, J. A., Jr.; Peralta, J. E.; Ogliaro, F.; Bearpark, M.; Heyd, J. J.; Brothers, E.; Kudin, K. N.; Staroverov, V. N.; Kobayashi, R.; Normand, J.; Raghavachari, K.; Rendell, A.; Burant, J. C.; Iyengar, S. S.; Tomasi, J.; Cossi, M.; Rega, N.; Millam, J. M.; Klene, M.; Knox, J. E.; Cross, J. B.; Bakken, V.; Adamo, C.; Jaramillo, J.; Gomperts, R.; Stratmann, R. E.; Yazyev, O.; Austin, A. J.; Cammi, R.; Pomelli, C.; Ochterski, J. W.; Martin, R. L.; Morokuma, K.; Zakrzewski, V. G.; Voth, G. A.; Salvador, P.; Dannenberg, J. J.; Dapprich, S.; Daniels, A. D.; Farkas, O.; Foresman, J. B.; Ortiz, J. V.; Cioslowski, J.; Fox, D. J. *Gaussian 09, revision A.02*; Gaussian, Inc., Wallingford, CT, 2009.
- (82) Becke, A. D. Density-functional thermochemistry. III. The role of exact exchange. *J. Chem. Phys.* **1993**, *98*, 5648–5652.
- (83) Miehlich, B.; Savin, A.; Stoll, H.; Preuss, H. Results obtained with the correlation energy density functionals of Becke and Lee, Yang and Parr. *Chem. Phys. Lett.* **1989**, *157*, 200–206.
- (84) Development of the Colic–Salvetti correlation-energy formula into a functional of the electron density: Lee, C.; Yang, W.; Parr, R. G. *Phys. Rev. B: Condens. Matter Mater. Phys.* **1988**, *37*, 785–789.
- (85) Rassolov, V. A.; Ratner, M. A.; Pople, J. A.; Redfern, P. C.; Curtiss, L. A. 6-31G* basis set for third-row atoms. *J. Comput. Chem.* **2001**, *22*, 976–984.
- (86) Francl, M. M.; Pietro, W. J.; Hehre, W. J.; Binkley, J. S.; DeFrees, D. J.; Pople, J. A.; Gordon, M. S. Self-consistent molecular orbital methods. XXIII. A polarization-type basis set for second-row elements. *J. Chem. Phys.* **1982**, *77*, 3654–3665.
- (87) Hariharan, P. C.; Pople, J. A. Accuracy of AHn equilibrium geometries by single determinant molecular orbital theory. *Mol. Phys.* **1974**, *27*, 209–214.
- (88) Hay, P. J.; Wadt, W. R. Ab initio effective core potentials for molecular calculations. Potentials for the transition metal atoms Sc to Hg. *J. Chem. Phys.* **1985**, *82*, 270–283.
- (89) Wadt, W. R.; Hay, P. J. Ab initio effective core potentials for molecular calculations. Potentials for main group elements sodium to bismuth. *J. Chem. Phys.* **1985**, *82*, 284–298.
- (90) Hay, P. J.; Wadt, W. R. Ab initio effective core potentials for molecular calculations. Potentials for potassium to gold including the outermost core orbitals. *J. Chem. Phys.* **1985**, *82*, 299–310.
- (91) Xu, S.; Wang, C.; Wang, Z.; Cui, Y. Theoretical and experimental investigation of stability and spectra of doped Ag:ZnSe nanocrystals. *J. Mol. Model.* **2014**, *20*, 2184.
- (92) Zheng, K.; Liu, X.; Deng, H.; Chao, H.; Yun, F.; Ji, L. Theoretical and experimental studies on electron transfer among complexes [M(phen)₃]²⁺ [M = Os(II), Ru(II), Co(III) and Zn(II)] binding to DNA. *J. Mol. Struct.: THEOCHEM* **2003**, *626*, 295–304.
- (93) O'Boyle, N. M.; Tenderholt, A. L.; Langner, K. M. cclib: A library for package-independent computational chemistry algorithms. *J. Comput. Chem.* **2008**, *29*, 839–845.
- (94) Dennington, R.; Keith, T.; Millam, J. *GaussView, Version 5*; Semicem Inc., Shawnee Mission, KS, 2009.
- (95) Ruiz, E.; Cano, J.; Álvarez, S.; Alemany, P. Broken symmetry approach to calculation of exchange coupling constants for

homobinuclear and heterobinuclear transition metal complexes. *J. Comput. Chem.* **1999**, *20*, 1391–1400.

(96) Ruiz, E.; Rodríguez-Fortea, A.; Cano, J.; Álvarez, S.; Alemany, P. About the calculation of exchange coupling constants in polynuclear transition metal complexes. *J. Comput. Chem.* **2003**, *24*, 982–989.

(97) Grimme, S. Semiempirical GGA-type density functional constructed with a long-range dispersion correction. *J. Comput. Chem.* **2006**, *27*, 1787–1799.

(98) Noodleman, L.; Case, D. A.; Aizman, A. Broken symmetry analysis of spin coupling in iron-sulfur clusters. *J. Am. Chem. Soc.* **1988**, *110*, 1001–1005.

(99) Singh, Kumar M.; Rajaraman, G. Can CH \cdots p Interactions Be Used To Design Single-Chain Magnets? *Chem. - Eur. J.* **2015**, *21*, 980–983.

(100) Lluell, M.; Casanova, D.; Cirera, J.; Bofill, J. M.; Alemany, P.; Alvarez, S.; Pinsky, M.; Avnir, D. *SHAPE (1.7)*; University of Barcelona, Barcelona, Spain, 2010.

(101) Alvarez, S.; Alemany, P.; Casanova, D.; Cirera, J.; Lluell, M.; Avnir, D. Shape Maps and Polyhedral Interconversion Paths in Transition Metal Chemistry. *Coord. Chem. Rev.* **2005**, *249*, 1693–1708.

(102) Alvarez, S.; Lluell, M. Continuous symmetry measures of penta-coordinate molecules: Berry and non-Berry distortions of the trigonal bipyramid. *J. Chem. Soc., Dalton Trans.* **2000**, 3288–3303.

(103) Alvarez, S.; Avnir, D.; Lluell, M.; Pinsky, M. Continuous symmetry maps and shape classification. The case of six-coordinated metal compounds. *New J. Chem.* **2002**, *26*, 996–1009.

(104) Liu, J.; Cheng, M.-L.; Yu, L.-L.; Chen, S.-C.; Shao, Y.-L.; Liu, Q.; Zhai, C.-W.; Yin, F.-X. Three metal complexes derived from 3-methyl-1H-pyrazole-4-carboxylic acid: synthesis, crystal structures, luminescence and electrocatalytic properties. *RSC Adv.* **2016**, *6*, 52040–52047.

(105) TOPOS Main Page: <http://www.topos.ssu.samara.ru> (accessed September 6, 2016).

(106) Blatov, V. A.; O'Keeffe, M.; Proserpio, D. M. Vertex-, face-, point-, Schläfli-, and Delaney-symbols in nets, polyhedra and tilings: recommended terminology. *CrystEngComm* **2010**, *12*, 44–48.

(107) Alexandrov, E. V.; Blatov, V. A.; Kochetkov, A. V.; Proserpio, D. M. Underlying nets in three-periodic coordination polymers: topology, taxonomy and prediction from a computer-aided analysis of the Cambridge Structural Database. *CrystEngComm* **2011**, *13*, 3947–3958.

(108) Singh, M. K.; Rajaraman, C. G. CH \cdots π Interactions Be Used To Design Single-Chain Magnets. *Chem. - Eur. J.* **2015**, *21*, 980–983.

(109) Chilton, N. F.; Anderson, R. P.; Turner, L. D.; Soncini, A.; Murray, K. S. PHI: A powerful new program for the analysis of anisotropic monomeric and exchange-coupled polynuclear d- and f-block complexes. *J. Comput. Chem.* **2013**, *34*, 1164–1175.

(110) Boča, R. Zero-field splitting in metal complexes. *Coord. Chem. Rev.* **2004**, *248*, 757–815.

(111) Titiš, J.; Boča, R. Magnetostructural D Correlation in Nickel(II) Complexes: Reinvestigation of the Zero-Field Splitting. *Inorg. Chem.* **2010**, *49*, 3971–3973.

(112) Singh, S. K.; Gupta, T.; Badkur, P.; Rajaraman, G. Magnetic Anisotropy of Mononuclear Ni^{II} Complexes: On the Importance of Structural Diversity and the Structural Distortions. *Chem. - Eur. J.* **2014**, *20*, 10305–10313.

(113) Lloret, F.; Julve, M.; Cano, J.; Ruiz-Garcia, R.; Pardo, E. Magnetic properties of six-coordinated high-spin cobalt(II) complexes: Theoretical background and its application. *Inorg. Chim. Acta* **2008**, *361*, 3432–3445.

(114) Sakiyama, H.; Ito, R.; Kumagai, H.; Inoue, K.; Sakamoto, M.; Nishida, Y.; Yamadasaki, M. Dinuclear cobalt(II) complexes of an acyclic phenol-based dinucleating ligand with four methoxyethyl chelating arms - first magnetic analyses in an axially distorted octahedral field. *Eur. J. Inorg. Chem.* **2001**, *2001*, 2027–2032.

(115) Rueff, J.-M.; Masciocchi, N.; Rabu, P.; Sironi, A.; Skoulios, A. Structure and Magnetism of a Polycrystalline Transition Metal Soap –

Co^{II}[(OOC(CH₂)₁₀COO)](H₂O)₂. *Eur. J. Inorg. Chem.* **2001**, *2001*, 2843–2848.

(116) Rabu, P.; Rueff, J.-M.; Huang, Z. L.; Angelov, S.; Souletie, J.; Drillon, M. Copper(II) and cobalt(II) dicarboxylate-based layered magnets: influence of π electron ligands on the long range magnetic ordering. *Polyhedron* **2001**, *20*, 1677–1685.

(117) Cui, L.; Yang, P. Y.; Wu, W.-P.; Miao, H.-H.; Shi, Q.-Z.; Wang, Y.-Y. Solvents and auxiliary ligands co-regulate three antiferromagnetic Co(II) MOFs based on a semi-rigid carboxylate ligand. *Dalton Trans.* **2014**, *43*, S823–S830.

(118) García-Couceiro, U.; Castillo, O.; Luque, A.; García-Terán, J. P.; Beobide, G.; Román, P. Rational Design of 2D Magnetic Metal-Organic Coordination Polymers Assembled from Oxalato and Dipyriddy Spacers. *Cryst. Growth Des.* **2006**, *6*, 1839–1847.

(119) Si, C.-D.; Hu, D.-C.; Fan, Y.; Dong, X.-Y.; Yao, X.-Q.; Yang, Y.-X.; Liu, J.-C. Three-Dimensional Supramolecular Architectures with Co^{II} Ions Assembled from Hydrogen Bonding and $\pi\cdots\pi$ Stacking Interactions: Crystal Structures and Antiferromagnetic Properties. *Cryst. Growth Des.* **2015**, *15*, 5781–5793.

(120) Palii, A. V.; Clemente-Juan, J. M.; Coronado, E.; Klokishner, S. I.; Ostrovsky, S. M.; Reu, O. S. Role of Orbital Degeneracy in the Single Molecule Magnet Behavior of a Mononuclear High-Spin Fe(II) Complex. *Inorg. Chem.* **2010**, *49*, 8073–8077.

(121) Šebová, M.; Jorík, V.; Moncol, J.; Kožíšek, J.; Boča, R. Structure and magnetism of Co(II) complexes with bidentate heterocyclic ligand Hsalbim derived from benzimidazole. *Polyhedron* **2011**, *30*, 1163–1170.

(122) Petit, S.; Pilet, G.; Luneau, D.; Chibotaru, L. F.; Ungur, L. A dinuclear cobalt(II) complex of calix[8]arenes exhibiting strong magnetic anisotropy. *Dalton Trans.* **2007**, 4582–4588.

(123) Vaidya, S.; Tewary, S.; Singh, S. K.; Langley, S. K.; Murray, K. S.; Lan, Y.; Wernsdorfer, W.; Rajaraman, G.; Shanmugam, M. What Controls the Sign and Magnitude of Magnetic Anisotropy in Tetrahedral Cobalt(II) Single-Ion Magnets? *Inorg. Chem.* **2016**, *55*, 9564–9578.

(124) Ziegenbalg, S.; Hornig, D.; Görls, H.; Plass, W. Cobalt(II)-Based Single-Ion Magnets with Distorted Pseudotetrahedral [N₂O₂] Coordination: Experimental and Theoretical Investigations. *Inorg. Chem.* **2016**, *55*, 4047–4058.

(125) Gomez-Coca, S.; Cremades, E.; Alaga-Alcalde, N.; Ruiz, E. Mononuclear Single-Molecule Magnets: Tailoring the Magnetic Anisotropy of First-Row Transition-Metal Complexes. *J. Am. Chem. Soc.* **2013**, *135*, 7010–7018.

(126) Boča, R. Zero-field splitting in metal complexes. *Coord. Chem. Rev.* **2004**, *248*, 757–815.

(127) Huang, W.; Liu, T.; Wu, D.; Cheng, J.; Ouyang, Z. W.; Duan, C. Field-induced slow relaxation of magnetization in a tetrahedral Co(II) complex with easy plane anisotropy. *Dalton Trans.* **2013**, *42*, 15326–15331.

(128) Gomez-Coca, S.; Urtizberea, A.; Cremades, E.; Alonso, P. J.; Camon, A.; Ruiz, E.; Luis, F. Origin of slow magnetic relaxation in Kramers ions with non-uniaxial anisotropy. *Nat. Commun.* **2014**, *5*, 4300.

(129) Ruiz, J.; Mota, A. J.; Rodríguez-Diéguez, A.; Titos, S.; Herrera, J. M.; Ruiz, E.; Cremades, E.; Costes, J. P.; Colacio, E. Field and dilution effects on the slow relaxation of a luminescent DyO₉ low-symmetry single-ion magnet. *Chem. Commun.* **2012**, *48*, 7916–7918.

(130) Habib, F.; Korobkov, I.; Murugesu, M. Exposing the intermolecular nature of the second relaxation pathway in a mononuclear cobalt(II) single-molecule magnet with positive anisotropy. *Dalton Trans.* **2015**, *44*, 6368–6373.

(131) Cole, K. S.; Cole, R. H. Dispersion and Absorption in Dielectrics I. Alternating Current Characteristics. *J. Chem. Phys.* **1941**, *9*, 341–351.

(132) Cucinotta, G.; Perfetti, M.; Luzon, J.; Etienne, M.; Car, P.-E.; Caneschi, A.; Calvez, G.; Bernot, K.; Sessoli, R. Magnetic Anisotropy in a Dysprosium/DOTA Single-Molecule Magnet: Beyond Simple Magneto-Structural Correlations. *Angew. Chem., Int. Ed.* **2012**, *51*, 1606–1610.

(133) Jiang, S. D.; Liu, S.-S.; Zhou, L.-N.; Wang, B. W.; Wang, Z. M.; Gao, S. Series of Lanthanide Organometallic Single-Ion Magnets. *Inorg. Chem.* **2012**, *51*, 3079–3087.

(134) Meihaus, K. R.; Rinehart, J. R.; Long, J. R. Dilution-Induced Slow Magnetic Relaxation and Anomalous Hysteresis in Trigonal Prismatic Dysprosium(III) and Uranium(III) Complexes. *Inorg. Chem.* **2011**, *50*, 8484–8489.

(135) Wang, Y.-L.; Chen, L.; Liu, C.-M.; Du, Z.-Y.; Chen, L.-L.; Liu, Q.-Y. 3D chiral and 2D achiral cobalt(II) compounds constructed from a 4-(benzimidazole-1-yl)benzoic ligand exhibiting field-induced single-ion-magnet-type slow magnetic relaxation. *Dalton Trans.* **2016**, *45*, 7768–7775.

(136) Miklovič, J.; Valigura, D.; Boča, R.; Titiš, J. A mononuclear Ni(II) complex: a field induced single-molecule magnet showing two slow relaxation processes. *Dalton Trans.* **2015**, *44*, 12484–12487.

(137) Beck, J. B.; Rowan, S. J. Multistimuli, Multiresponsive Metallo-Supramolecular Polymers. *J. Am. Chem. Soc.* **2003**, *125*, 13922–13923.

(138) Uchiyama, S.; Prasanna de Silva, A.; Iwai, K. Luminescent Molecular Thermometers. *J. Chem. Educ.* **2006**, *83*, 720–727.

(139) Zheng, Q.; Yang, F.; Deng, M.; Ling, Y.; Liu, X.; Chen, Z.; Wang, Y.; Weng, L.; Zhou, Y. A porous metal-organic framework constructed from carboxylate-pyrazolate shared heptanuclear zinc clusters: synthesis, gas adsorption, and guest-dependent luminescent properties. *Inorg. Chem.* **2013**, *52*, 10368–10374.

(140) Ren, H.-Y.; Han, C.-Y.; Qu, M.; Zhang, X.-M. Luminescent group 12 metal tetracarboxylate networks as probe for metal ions. *RSC Adv.* **2014**, *4*, 49090–49097.

(141) Eliseeva, S. V.; Pleshkov, D. N.; Lyssenko, K. A.; Lepnev, L. S.; Bünzli, J. C.; Kuzmina, N. P. Highly luminescent and triboluminescent coordination polymers assembled from lanthanide β -diketonates and aromatic bidentate O-donor ligands. *Inorg. Chem.* **2010**, *49*, 9300–9311.

(142) de Bettencourt-Dias, A.; Barber, P. S.; Viswanathan, S.; de Lill, D. T.; Rollett, A.; Ling, G.; Altun, S. Paraderivatized pybox ligands as sensitizers in highly luminescent Ln(III) complexes. *Inorg. Chem.* **2010**, *49*, 8848–8861.

(143) Beeby, A.; Clarkson, I. M.; Dickins, R. S.; Faulkner, S.; Parker, D.; Royle, L.; de Sousa, A. S.; Gareth Williams, J. A.; Woods, M. Non-radiative deactivation of the excited states of europium, terbium and ytterbium complexes by proximate energy-matched OH, NH and CH oscillators: an improved luminescence method for establishing solution hydration states. *J. Chem. Soc., Perkin Trans. 2* **1999**, *2*, 493–504.

(144) Kasha, M. Characterization of electronic transitions in complex molecules. *Discuss. Faraday Soc.* **1950**, *9*, 14–19.

(145) Adamo, C.; Jacquemin, D. The calculations of excited-state properties with Time-Dependent Density Functional Theory. *Chem. Soc. Rev.* **2013**, *42*, 845–856.



Cite this: *CrystEngComm*, 2019, 21, 3881

Multifunctional coordination compounds based on lanthanide ions and 5-bromonicotinic acid: magnetic, luminescence and anti-cancer properties†

Cristina Ruiz,^a Antonio A. García-Valdivia,^a Belén Fernández,^b Javier Cepeda,^c Itziar Oyarzabal,^c Elisa Abas,^d Mariano Laguna,^d Jose Angel García,^e Ignacio Fernández,^f Eider San Sebastian^{*c} and Antonio Rodríguez-Diéguez^{*a}

We report the formation of four novel multifunctional coordination compounds based on 5-bromonicotinic acid and different lanthanide(III) ions (Dy, Tb, Yb and Nd), synthesized by simple hydrothermal routes. These materials possess different structures and dimensionalities and show interesting magnetic and luminescence properties, as well as a complete absence of cytotoxicity both in cancer and non-cancer Caco-2 cells, transforming these new compounds into excellent candidates to be further investigated in the field of luminescence materials with biomedical applications.

Received 1st March 2019,
Accepted 21st May 2019

DOI: 10.1039/c9ce00292h

rsc.li/crystengcomm

1. Introduction

The interest in coordination polymers (CPs), also known as metal–organic frameworks (MOFs), has grown exponentially,¹ derived from their multiple types of verified industrial applications, such as gas storage and purification, catalysis, luminescence and magnetism,² as well as their ease of synthesis. Of particular interest is the fact that their metal–organic hybrid nature offers potentially limitless arrangement types and topological architectures,³ reinforcing their versatility of use. The latter is particularly true for Ln(III)-based CPs, where large

coordination numbers (8–12) are usually observed for the central cation, yielding fancy structures that, conversely, are hardly anticipated *via* a rational design process. Still, the adequacy of the selection of Ln(III) ions for the generation of multifunctional CPs in the field of new magnetic and/or luminescent materials is well supported by their intrinsic features such as large intrinsic magnetic anisotropy and large magnetic moment in the ground state (key to generating molecular magnets). On the other hand, due to the open-shield character of the trivalent lanthanide ions as well as the efficient shielding of their valence f-orbitals, all lanthanide ions (but La³⁺ and Lu³⁺) emit highly pure-colored light, with long-lived emissions and large quantum yield values,⁴ from the ultraviolet (UV) to the visible region (Eu³⁺, Tb³⁺, Sm³⁺ and Tm³⁺) as well as in the near infrared (NIR) region (Yb³⁺, Nd³⁺ and Er³⁺).⁵ Unfortunately, the forbidden character of the f–f transitions in lanthanide ions prevents the latter from being able to efficiently absorb light. The solution to the latter issue lies in the use of organic linkers that promote the well-known antenna effect,⁶ where the light absorbed by the ligand is efficiently transferred to the outermost orbitals in the metal, increasing the efficiency of the light emitted by the latter.

The attention in the present study was focused on the synthesis, structural and functional characterization of Ln(III) based coordination complexes and CPs using 5-bromonicotinic acid (5-HBrNic) as a linker ligand. With one carboxyl group and one N atom as potential metal coordination groups, 5-HBrNic possesses, in addition, a Br atom capable of potentially establishing N⋯Br or O⋯Br halogen bonds, as well as additional Br⋯π and Br⋯Br interactions.

^a Dept. of Inorganic Chemistry, University of Granada, C/Severo Ochoa s/n, 18071, Granada, Spain. E-mail: antonio5@ugr.es

^b Institute of Parasitology and Biomedicine “López-Neyra”, Consejo Superior de Investigaciones Científicas (CSIC), Avda. del Conocimiento s/n, 18016, Granada, Spain

^c Department of Applied Chemistry, Chemistry Faculty, University of the Basque Country (UPV/EHU), 20018 San Sebastian, Spain. E-mail: eider.sansebastian@ehu.es

^d Dept. of Inorganic Chemistry, University of Zaragoza, C/Pedro Cerbuna 12, 50009, Zaragoza, Spain

^e Departamento de Física Aplicada II, Facultad de Ciencia y Tecnología, University of the Basque Country (UPV/EHU), 20018 San Sebastian, Spain

^f Department of Chemistry and Physics, Research Center for Agricultural and Food Biotechnology (BITAL), University of Almería, Ctra. Sacramento s/n, 04120 Almería, Spain

[‡] Univ. Bordeaux, CNRS, Centre de Recherche Paul Pascal, UMR5031, F-33600, Pessac, France

† Electronic supplementary information (ESI) available. CCDC 1882984–1882987. For ESI and crystallographic data in CIF or other electronic format see DOI: 10.1039/c9ce00292h

Few examples have been reported where 5-HBrNic coordinates to a Ln(III) ion to generate coordination complexes or CPs. Still, this ligand has shown its potential to form meta-organic compounds of different dimensionalities with luminescence, magnetic and absorptive properties.⁷ In addition, 5-bromonicotinate (5-BrNic) possesses a wide variety of coordination modes to metal cations (see Scheme 1), yielding multiple types of molecular architectures. We hereby report the synthesis as well as structural and functional characterization of four novel Ln(III)- and 5-BrNic-based coordination compounds of different dimensionalities, with dual magnetic and luminescence properties. Additionally, the antitumor activity of this family of compounds has been tested with the aim of characterizing their cytotoxic behavior in potential biomedical applications.

2. Experimental

2.1. Materials and physical measurements

All reagents were obtained from commercial sources and used as received. Elemental (C, H, and N) analyses were performed on a Leco CHNS-932 microanalyzer. The IR spectra of powdered samples were recorded in the 400–4000 cm⁻¹ region on a Nicolet 6700 FTIR spectrophotometer using KBr pellets. Alternating current magnetic measurements were performed under zero and 1000 Oe applied static fields on a Quantum Design SQUID MPMS XL-5 device by using an oscillating ac field of 3.5 G and ac frequencies ranging from 10 to 1400 Hz. A Varian Cary-Eclipse Fluorescence spectrofluorimeter was used to obtain the fluorescence spectra at room temperature. The spectrofluorimeter is equipped with a xenon discharge lamp (peak power equivalent to 75 kW), Czerny–Turner monochromators, and an R-928 photomultiplier tube which is red sensitive (even 900 nm) with manual or automatic voltage. The photomultiplier detector voltage was 600 V and the instrument excitation and emission slits were set at 5 nm. A closed cycle helium cryostat enclosed in an Edinburgh Instruments FLS920 spectrometer was employed for steady state photoluminescence (PL) and lifetime measurements carried out at 10 K. All samples were set under high vacuum (of ca. 10⁻⁷ mbar) to avoid the presence of oxygen or water in the sample holder. Steady-state spectra were measured with an IK3552R-G He–Cd continuous laser (325 nm) as an excitation source, whereas a microsecond pulsed lamp was employed for recording the lifetime measurements. The

photographs of irradiated single-crystal and polycrystalline samples were taken at room temperature in a micro-PL system included in an Olympus optical microscope illuminated with a Hg lamp.

2.2. Preparation of complexes

Synthesis of [Dy(5-BrNic)₃(H₂O)₄] (1). Compound 1 was obtained by hydrothermal routes through the following procedure: a mixture of DyCl₃·6H₂O (0.24 mmol), 5-HBrNic (0.24 mmol) and 10 mL of distilled water was sealed in a Teflon reactor and heated at 95 °C under autogenous pressure for 48 h. The reaction vessel was then slowly cooled down to room temperature during a period of about 3 h, yielding yellow crystals of 1. Yield: 47%, based on Dy. Anal. calcd. C₁₈H₁₇Br₃DyN₃O₁₀: C 25.81, H 2.04, N 5.01. Found: C 25.63, H 2.19, N 4.83.

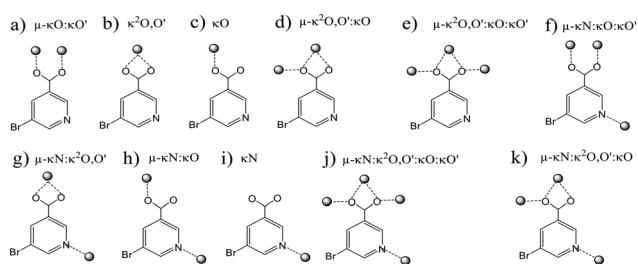
Synthesis of [Tb(5-BrNic)₂(H₂O)₄][Tb(5-BrNic)₄(H₂O)₂](5-HBrNic)₂ (2). Yellow crystals of compound 2 were obtained following a procedure similar to that used in the synthesis of 1, with the following modifications: the reactor was left in an oven for 96 h and crystals only appeared 24 h after cooling down the sample slowly. Yield: 51%, based on Tb. Anal. calcd. for C₂₄H₁₉Br₄N₄O₁₁Tb: C 28.32, H 1.88, N 5.50. Found: C 29.01, H 1.92, N 5.66.

Synthesis of [Yb(5-BrNic)₂(H₂O)₄][Yb(5-BrNic)₄(H₂O)₂](5-HBrNic)₂ (3). Colorless crystals of 3 were obtained following the same procedure as the one used for the synthesis of 2. Yield: 57%, based on Yb. Anal. calcd. for C₂₄H₁₉Br₄N₄O₁₁Yb: C 27.93, H 1.86, N 5.43. Found: C 28.75, H 1.85, N 5.99.

Synthesis of {[Nd(5-BrNic)₃(H₂O)₃·H₂O]}_n (4). Pink crystals of 4 were obtained following the same procedure as the one used for the synthesis of 2. Yield: 47%, based on Nd. Anal. calcd. C₁₈H₁₇Br₃NdN₃O₁₀: C 26.39, H 2.09, N 5.13. Found: C 28.01, H 2.12, N 5.61.

2.3. Crystallographic refinement and structure solution

X-ray data collection of suitable single crystals of the compounds were conducted at 100(2) K on a Bruker VENTURE area detector equipped with a graphite monochromated Mo-K α radiation source ($\lambda = 0.71073$ Å) by applying the ω -scan method. The data reduction was performed with the APEX2 software⁸ and corrected for absorption using SADABS.⁹ Crystal structures were solved by direct methods using the SIR97 program¹⁰ and refined by full-matrix least-squares on F^2 including all reflections using anisotropic displacement parameters by means of the WINGX crystallographic package.¹¹ Compound 4 contains one lattice water molecule which presents a significantly prolate shaped ellipsoid so it has been disordered into two equivalent positions (each with an occupancy of 50%). All hydrogen atoms were included as fixed contributions riding on attached atoms with isotropic thermal displacement parameters 1.2 times or 1.5 times those of their parent atoms for the organic ligands. The details of the structure determination and refinement of the compounds are summarized in Table S1.†



Scheme 1 Eleven plausible coordination modes (a–k) of 5-BrNic.

2.4. Growth inhibition assay

The human Caco-2 cell line (TC7 clon) was kindly provided by Dr. Edith Brot-Laroche (Université Pierre et Marie Curie-Paris 6, UMR S 872, Les Cordeliers, France). Caco-2 cells were maintained in a humidified atmosphere of 5% CO₂ and 95% of air at 37 °C. Cells (passages 32–42) were grown in Dulbecco's modified Eagle's medium (DMEM; Gibco Invitrogen, Paisley, U.K.) with high glucose concentration (4.5 g L⁻¹) supplemented with 20% fetal bovine serum (FBS) previously decomplexed (30 min at 56 °C), 1% non-essential amino acids, 1% penicillin (1000 U mL⁻¹), 1% streptomycin (1000 µg mL⁻¹), and 2% L-glutamine (200 mM). Stock solutions of the complexes in DMSO were diluted in a medium without FBS to the required concentration. DMSO was also tested at the same concentrations and no effects on the cytotoxicity were shown. Cells were seeded in 96-well plates at a density of 20 × 10³ cells per well. Experiments were performed 48 h postseeding and the culture medium was replaced with a fresh medium (without FBS) containing the complexes at concentrations varying from 0 to 20 µM, with an exposure time of 72 h.

For cell viability studies of differentiated (enterocyte-like) cells, Caco-2/TC7 cells were seeded in 96-well plates at a density of 4 × 10³ cells per well and incubated for 12 days, with the culture medium changed every 3 days, up to confluence, and the cells were treated with the complexes and at the same concentrations explained before. Thereafter, cell survival was measured using the 3-(4,5-dimethyl-2-thiazoyl)-2,5-diphenyltetrazolium bromide (MTT, Merck) test as previously described. The assay is dependent on the cellular reduction of MTT by the mitochondrial dehydrogenase of viable cells to a blue formazan product, which can be measured spectrophotometrically. Following appropriate incubation of the cells, with or without metallic complexes, MTT was added to each well in an amount equal to 10% of the culture volume, and incubation was continued at 37 °C for 2.5 h. Afterwards, the medium and MTT were removed, and DMSO was added to each well. At the end, the results were obtained by measuring the absorbance with a scanning multiwell spectrophotometer (BIOTEX SINERGY HT SIAFRTD) at a wavelength of 575 nm and compared to the values of control cells incubated in the absence of complexes. Experiments were conducted in quadruplicate wells and repeated three times.

3. Results and discussion

3.1. Description of the structures

Compound 1, of general formula [Dy(5-BrNic)₃(H₂O)₄], crystallizes in the *P* $\bar{1}$ space group (see ESI† Table S1). As observed in Fig. 1, the lanthanide ion coordinates to three 5-BrNic ligands, one of which establishes a chelating ring (O1C/O2C, coordination mode b in Scheme 1) whereas the remaining two bind in a monodentate mode (O1A and O1B, coordination mode c in Scheme 1). Besides, four water molecules complete the octacoordinated (DyO₈) sphere of the Dy ion, which displays a triangular dodecahedral shape (see the ESI†

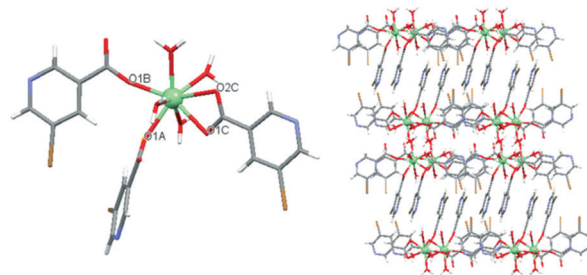


Fig. 1 Left: Structure of the monomeric entity of compound 1. Right: Perspective view of the packing of compound 1 along the *a** axis. Color code: dysprosium, green; oxygen, red; nitrogen, blue; carbon, grey; bromine, brown; hydrogen, white.

for shape measurements). Dy–O distances in the mononuclear compound fall within the range of 2.280(2)–2.515(2) Å (see the ESI†).

Coordination water molecules are involved in a complex hydrogen-bond network in which non-bonding carboxylate oxygen and pyridine nitrogen atoms act as acceptors to sequentially bring the monomers along the *a* axis. In the same line, π – π stacking interactions established between the aromatic pyridine rings of adjacent monomers along the *b* axis, further stabilize the packing of 1 (see additional details in the ESI†).

Compounds 2 and 3, of general formula [Ln(5-BrNic)₂(H₂O)₄][Ln(5-BrNic)₄(H₂O)₂] \cdot (5-HBrNic)₂, where Ln stands for Tb or Yb in 2 and 3, respectively, are isostructural and crystallize in the monoclinic *P*2/*c* space group (see the ESI†). The description of compound 2 found in the lines below will therefore be equivalent to that of 3 (omitted).

The unit cell of 2 contains four distinct entities (Fig. 2), consisting of a monomeric complex with a Tb(III) cation (Tb1) coordinated to four 5-BrNic ligand units and two water molecules, a second monomeric complex with a Tb(III) cation (Tb2) coordinated to two 5-BrNic ligand units and four water molecules and, lastly, two protonated crystallization 5-HBrNic ligand molecules. Both Tb1 and Tb2 units show TbO₈ distorted polyhedra resembling less habitual snub disphenoid and square antiprism, respectively (see the ESI†

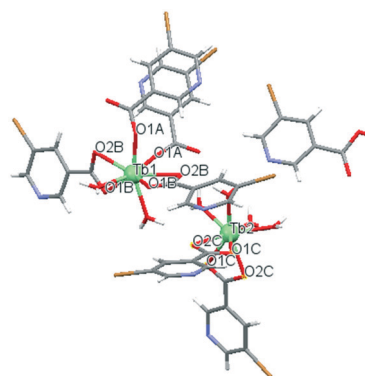


Fig. 2 Asymmetric unit of compound 2. Color code: terbium, green; oxygen, red; nitrogen, blue; carbon, grey; bromine, brown; hydrogen, white.

for shape measurements), derived from the coordination of i) two perpendicular 5-BrNic ligands bound to Tb1 in a bidentate fashion, two copies of a monodentate ligand parallel to each other along the *b* axis, and two water molecules in the case of the Tb1 unit, and ii) four water molecules and two bidentate copies of the ligand in the Tb2 unit. The remaining two units consist of protonated 5-HBrNic crystallization ligands. It is worth noticing that the two monodentate 5-BrNic ligands establish quite strong π - π stacking interactions, a fact that sets their orientation outwards the monomeric entity. The packing of the structure reveals a unit cell containing two $[\text{Tb}(5\text{-BrNic})_4(\text{H}_2\text{O})_2]^-$ (Tb1) units, two $[\text{Tb}(5\text{-BrNic})_2(\text{H}_2\text{O})_4]^+$ (Tb2) units and four copies of a 5-HBrNic crystallization ligand. Notwithstanding the fact that monomeric complexes are hydrogen bonded with each other along the packing, the crystallization 5-HBrNic molecule serves as an effective supramolecular glue by acting as both a hydrogen-bonding donor and acceptor as well as an intermediate to extend π - π stacking all along the crystal. The same type of description applies to compound 3, except that Ln(III)-O distances in 2 are larger than in 3 (see ESI† Table S2), which is consistent with the larger nuclear charge of the former. Additional details on the packing of compounds 2 and 3 can be found in the ESI.†

Compound 4 is nearly isostructural to the Tb compound reported by Song *et al.*^{7a} Our compound, of general formula $\{[\text{Nd}(\mu\text{-}5\text{-BrNic})_2(5\text{-BrNic})(\text{H}_2\text{O})_3]\cdot\text{H}_2\text{O}\}_m$, crystallizes in the $P\bar{1}$ space group (see ESI† Table S1), and consists of a racemic mixture of linear chains of Nd(III) atoms bridged by means of two 5-BrNic ligands along the crystallographic *a* axis. Lanthanide ions show a NdO_8 environment where an almost ideal triangular dodecahedron is generated (Fig. 3) when five 5-BrNic ligands each bind to the lanthanide through a deprotonated carboxylic oxygen (O1A, O2A, O2B, O1C and O2C). The metal ion completes its coordination sphere with three water molecules (O1W, O2W and O3W), the last of which plays a key role in the generation of the H-bond network in the crystal, and particularly with a crystallization water molecule found in the structure (which is disordered into

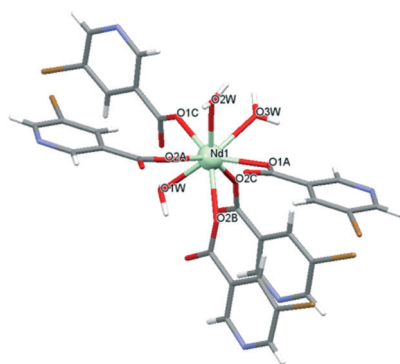


Fig. 3 Fragment of 4 showing complete ligands around the coordination sphere of the Nd1 atom. Color code: neodymium, green; oxygen, red; nitrogen, blue; carbon, grey; bromine, brown; hydrogen, white.

two equivalent dispositions). All Nd-O distances are in the 2.386(2)–2.518(2) Å range (see ESI† Table S2 for details).

1D chains of 4 are generated along the *a* axis *via* the sequential coordination of A and C copies of 5-BrNic ligands to Nd1 atoms (Fig. 4), where carboxylate oxygen atoms link nearby neodymium(III) cations adopting one of the characteristic binding modes of the ligand (mode a), as shown in Scheme 1. It is worth mentioning that each pair of Nd1...Nd1 atoms are doubly bridged by two crystallographically related (by the inversion center) 5-BrNic ligands (A/A and C/C bridges sequentially along the chain), which in turn are almost perpendicularly oriented to each other along the chain (displaying a mutual angle between mean planes of A and C ligands of 85.9°). The B ligand, which remains essentially planar and coordinated as a terminal ligand, emerges from the chain by staying parallel to the C ligand with which it forms face-to-face π - π stacking.

The so-generated 1-D chains are held together by strong hydrogen bonding interactions established among crystallization water molecules and non-coordinated pyridine nitrogen atoms, in such a way that surrounding 5-BrNic ligands belonging to the chains in the vicinity are able to form weaker yet significant interchain π - π interactions (see the ESI† for additional details).

3.2. Magnetic measurements

The experimental $\chi_M T$ values at room temperature are close to those expected for the ground states with all Stark levels equally populated (Table 1).¹² Cooling down the temperature causes a progressive drop in the $\chi_M T$, as expected for the selective depopulation of the excited Stark sublevels (see the ESI†). However, this magnetic response could also involve a

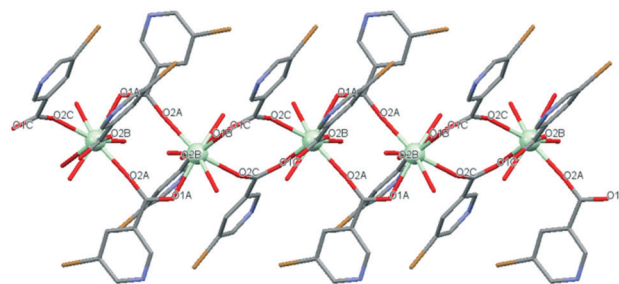


Fig. 4 Elongation of an infinite linear chain of 4 along the c^* axis. Color code: neodymium, green; oxygen, red; nitrogen, blue; carbon, grey; bromine, brown; hydrogen, white.

Table 1 Comparison between best least-squares fitting results of the experimental curves and theoretically calculated magnetic data

Comp.	g_J (exp./theor.)	$\chi_M T$ (exp./theor.)	Δ (cm^{-1})
1(Dy)	1.32(1)/1.33	14.32/14.17	0.34
2(Tb)	1.49(1)/1.5	11.38/11.76	0.10
3(Er)	1.22(1)/1.2	11.57/11.53	0.48
4(Nd)	0.70(1)/0.73	1.61/1.67	2.31

significant contribution from antiferromagnetic exchange interactions between lanthanide ions, especially for compounds in which there are short ligand mediated pathways,¹³ as is the case of carboxylate bridges in **4**. The χ_M^{-1} vs. T curves for these compounds follow the Curie–Weiss law almost in the whole temperature range, finding only small deviations for **3** below 30 K (see the ESI†). As far as we are aware, there is no available expression to determine the magnetic susceptibilities of 3D systems with large anisotropy, so $\chi_M T$ vs. T curves were fitted in the high temperature range (50–300 K) with expressions (eqn (1)–(4)) that assume only a splitting of the m_j energy levels ($H = \Delta Jz^2$) in an axial crystal field.¹⁴

$$\chi_{Dy} = \frac{Ng^2\beta^2}{kT} \left(\frac{0.5e^{-0.25\Delta/kT} + 4.5e^{-2.25\Delta/kT} + 12.5e^{-6.25\Delta/kT} + 24.5e^{-12.25\Delta/kT}}{1 + 2e^{-\Delta/kT} + 2e^{-2\Delta/kT} + 2e^{-9\Delta/kT} + 2e^{-16\Delta/kT} + 2e^{-25\Delta/kT} + 2e^{-36\Delta/kT}} + \frac{40.5e^{-20.25\Delta/kT} + 60.5e^{-30.25\Delta/kT} + 84.5e^{-42.25\Delta/kT} + 112.5e^{-56.25\Delta/kT}}{1 + 2e^{-\Delta/kT} + 2e^{-2\Delta/kT} + 2e^{-9\Delta/kT} + 2e^{-16\Delta/kT} + 2e^{-25\Delta/kT} + 2e^{-36\Delta/kT}} \right) \quad (1)$$

$$\chi_{Tb} = \frac{Ng^2\beta^2}{kT} \frac{2e^{-\Delta/kT} + 4e^{-2\Delta/kT} + 18e^{-9\Delta/kT} + 32e^{-16\Delta/kT} + 50e^{-25\Delta/kT} + 72e^{-36\Delta/kT}}{1 + 2e^{-\Delta/kT} + 2e^{-2\Delta/kT} + 2e^{-9\Delta/kT} + 2e^{-16\Delta/kT} + 2e^{-25\Delta/kT} + 2e^{-36\Delta/kT}} \quad (2)$$

$$\chi_{Er} = \frac{Ng^2\beta^2}{kT} \left(\frac{0.5e^{-0.25\Delta/kT} + 4.5e^{-2.25\Delta/kT} + 12.5e^{-6.25\Delta/kT} + 24.5e^{-12.25\Delta/kT}}{1 + 2e^{-\Delta/kT} + 2e^{-2\Delta/kT} + 2e^{-9\Delta/kT} + 2e^{-16\Delta/kT} + 2e^{-25\Delta/kT} + 2e^{-36\Delta/kT}} + \frac{40.5e^{-20.25\Delta/kT} + 60.5e^{-30.25\Delta/kT} + 84.5e^{-42.25\Delta/kT} + 112.5e^{-56.25\Delta/kT}}{1 + 2e^{-\Delta/kT} + 2e^{-2\Delta/kT} + 2e^{-9\Delta/kT} + 2e^{-16\Delta/kT} + 2e^{-25\Delta/kT} + 2e^{-36\Delta/kT}} \right) \quad (3)$$

$$\chi_{Nd} = \frac{Ng^2\beta^2}{4kT} \frac{81e^{-81\Delta/4kT} + 49e^{-49\Delta/4kT} + 25e^{-25\Delta/4kT} + 9e^{-9\Delta/4kT} + e^{-9\Delta/4kT}}{e^{-81\Delta/4kT} + e^{-49\Delta/4kT} + e^{-25\Delta/4kT} + e^{-9\Delta/4kT} + e^{-9\Delta/4kT}} \quad (4)$$

In these expressions, Δ is the zero-field splitting and the Zeeman splitting was treated isotropically for the sake of simplicity. Additionally, a zJ' parameter based on the molecular field approximation to account for the magnetic interaction between Ln(III) ions did not improve the fitting and brought almost negligible values (*ca.* -0.01 cm^{-1}), meaning that lanthanide(III) ions may be considered as magnetically isolated centers in all cases.

With the aim of obtaining insights into the magnetic properties of these Ln(III) complexes, dynamic alternating current magnetic measurements were carried out on **1**, which revealed (Fig. 5) that **1** does not show any significant frequency dependency of the out-of-phase signals (χ_M''). This could be a consequence of either a lack of a slow relaxation of the magnetization or the presence of quantum tunneling of the magnetization (QTM). With the aim of suppressing the possible QTM effect, measurements were repeated in the presence of an external field of 1000 Oe, and as derived from Fig. 5, compound **1** showed frequency dependent signals; since χ_M' and χ_M'' still remained above zero at low temperatures, it was therefore concluded that QTM was not completely removed.

The latter is consistent with the α values derived from the Cole–Cole plots (in the range of 0.38 (2.8 K)–0.13 (4 K)), compatible with the existence of more than one relaxation processes (Fig. 6).

The linear portion of the relaxation times was fitted to the Arrhenius equation, obtaining an effective energy barrier of 33.1 K with $\tau_0 = 5.90 \times 10^{-8} \text{ s}$ (Fig. 5, inset). In general, Dy(III) ions with the highest symmetric coordination environments ($C_{\infty v}$, $D_{\infty h}$, S_8 (I_4), D_{5h} , and D_{4d} symmetries) show better single molecule magnet (SMM) properties than the ones with lower symmetry, due to the reduction of QTM.¹⁵ Thus, the triangular dodecahedral coordination environment of the Dy(III) ions (D_{2d} symmetry),¹⁶ together with the hydrogen bonding inter-

actions (known to suppress the SMM behavior), explains the modest energy barrier observed for this compound. Despite the fact that other electronic effects are known to strongly modulate the SMM behavior,¹⁷ a trend of the symmetry of the coordination environment may be inferred by analyzing the results for those selected reported complexes shown in Table 2.

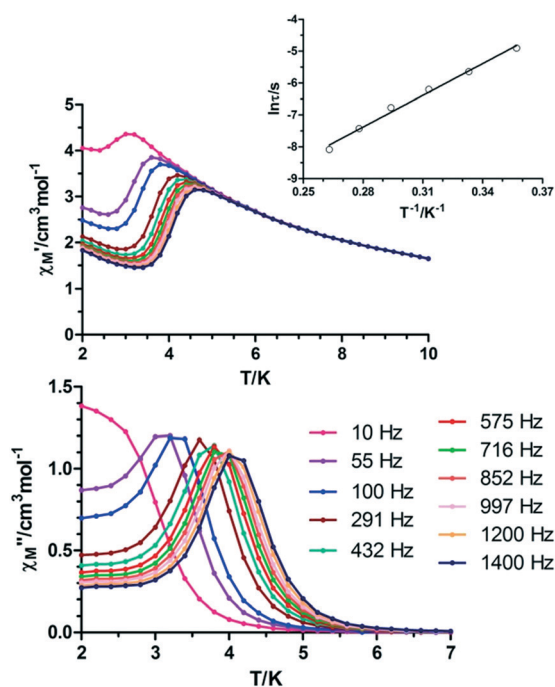


Fig. 5 Temperature dependence of in-phase (top) and out-of-phase (bottom) components of the ac susceptibility of compound **1** measured under 1000 Oe dc field. Inset: Arrhenius plots for the relaxation times. The black line corresponds to the best fits to the Orbach process.

3.3. Photoluminescence studies

Solid state photoluminescence measurements were performed on the polycrystalline samples of compounds 1–4, both at room temperature and 50 K, with the aim of achieving a more representative characterization of the emissive performance of the materials for potential applications as light-emitting diodes and chemical sensors. In this sense, the excitation spectra of compound 1 (see ESI† Fig. S8) monitored around the metal's more intense emission lines ($\lambda_{em} = 484$ nm and 575 nm, respectively) revealed, among others, a wide and relatively intense maximum around 300 nm and multiple narrower signals centered around 370 nm, which can be attributed to typical $\pi \leftarrow \pi^*$ transitions inside the ligand. The emission spectrum of 1 was then recorded at room temperature (Fig. 7) using two distinct excitation wavelengths ($\lambda_{ex} = 300$ nm and 370 nm, respectively) centered at the ligand. In addition to the wide emission bands in the 360–400 nm (with a peak at 393 nm) and in the 420–460 nm regions (attributed to ligand-to-ligand electronic relaxation processes), the intense emission peaks observed at 486 and 577 nm, respectively, are clearly ascribed to $^4F_{9/2} \rightarrow ^6H_J$ transitions in the metal, confirming the existence of a significant antenna effect.²⁶

The emission spectra of a solid sample of 1, which was also excited with a monochromatic beam of 325 nm, both at low (50 K) and room temperatures (see Fig. S8 in the ESI†), show in both cases an equivalent behavior to that observed in Fig. 7. To gain further insight into the main luminescence processes described so far, the decay curves (50 K) of the

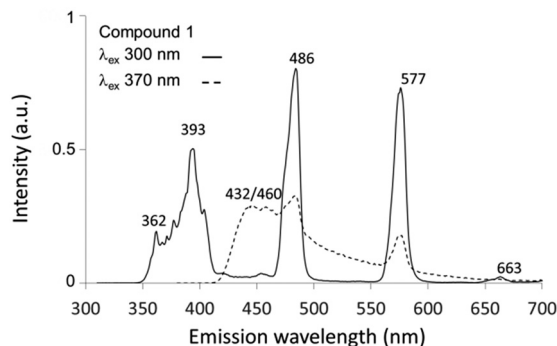


Fig. 7 Room temperature solid state emission spectra of 1 upon sample excitation at $\lambda_{ex} = 300$ nm (solid line) and $\lambda_{ex} = 370$ nm (dashed line).

mentioned main transitions were monitored at the most intense line of the main transitions, *i.e.*, at 432 nm, 460 nm, 486 nm and 577 nm, respectively (Fig. 8). The emission decay curve for the process with a maximum at $\lambda_{em} = 432$ nm was well fitted by a single-exponential function [$I_t = A_0 + A_1 \exp(-t/\tau)$], τ being the luminescence lifetime, A_0 the background and A_1 the weighting parameter. As summarized in Table 2, the lifetime of the mentioned transition was in the range of a few microseconds, which indicates that the process is fluorescent in nature. In contrast, other signals in the emission spectrum displayed a decay curve with two components and where therefore fitted to equations of the form [$I_t = A_0 + A_1 \exp(-t/\tau) + A_2 \exp(-t/\tau')$], where A_n are the two weighting parameters. Observed lifetimes (few microseconds) were equally indicative of the existence of associated fluorescence processes.

The photoluminescence properties of 2 were studied following the same procedure as in 1. The room temperature excitation spectra of 2 were monitored around the metal's (Tb^{3+}) most intense emission lines (ESI† Fig. S9), which revealed multiple signals in the 300–410 nm range arising from electronic transitions inside the ligand. The two emission spectra of 2 (Fig. 9) were then recorded at room temperature and 50 K, respectively, upon exciting the ligand with $\lambda_{ex} = 325$

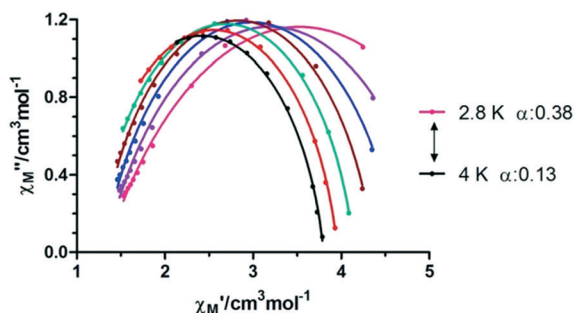


Fig. 6 Cole-Cole plots for 1 under 1000 Oe dc field.

Table 2 Comparison between best least-squares fitting results of the experimental curves and theoretically calculated magnetic data

Dy-SMM	Pseudo local symmetry	U_{eff} (K)	Ref.
[Dy(DOTA)(H ₂ O)]	C_{4v}	59	18
1	D_{2d}	38	This work
[Dy(FTA) ₃ (BBO)]	D_{2d}	53	19
[Dy(acac) ₃ (1,10-phen)]	D_{4d}	62	20
[DyPc ₂]	D_{4d}	40	21
[Dy(acac) ₃ (H ₂ O) ₂]	σ_h	66	22
[Dy(OPCy ₃) ₂ (H ₂ O) ₅] ³⁺	C_{5h}/D_{5h}	543	23
[Dy(BIPMTMS) ₂] ⁻	S_4/D_{2d}	721	24
[Dy(Cp ^{ttt}) ₂] ⁺	C_{∞}	1837	25

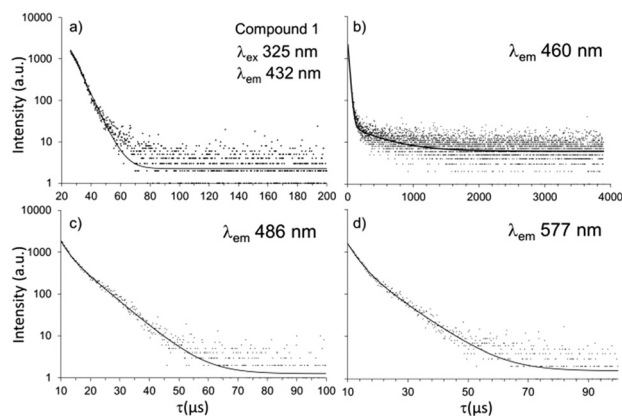


Fig. 8 Luminescence decay curves for the main transitions in 1 (50 K, $\lambda_{ex} = 325$ nm). a) $\lambda_{em} = 432$ nm; b) $\lambda_{em} = 460$ nm; c) $\lambda_{em} = 486$ nm; d) $\lambda_{em} = 577$ nm.

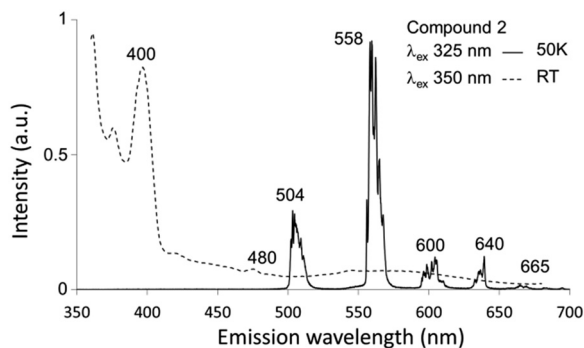


Fig. 9 Room temperature (dashed line) and 50 K (solid line) solid state emission spectra of **2** upon sample excitation with a laser beam of $\lambda_{\text{ex}} = 350$ nm and $\lambda_{\text{ex}} = 325$ nm, respectively.

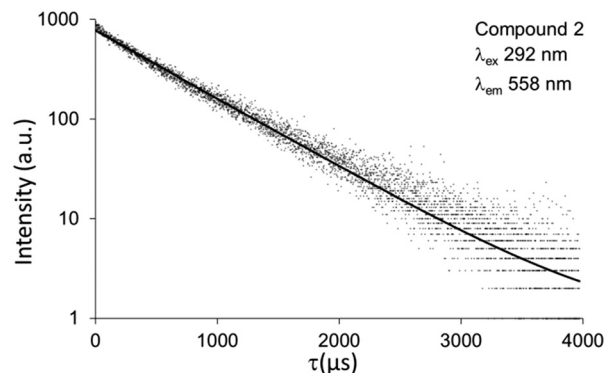


Fig. 10 Luminescence decay curve for the emission of **2** centered at 558 nm, measured at 50 K ($\lambda_{\text{ex}} = 292$ nm).

nm. Whereas at room temperature, the signals derived from electronic transitions inside the ligand (centered around 400 nm) were significantly more intense than those ascribed to the metal–metal electronic transition (weak wide band centered around 550 nm), at low temperature, relative intensities were inverted, which permitted a clear visualization of narrow multiplet signals derived from the well-known transitions of Tb(III) (Table 3).

The latter results are consistent with the existence of a significant antenna effect. The most intense signal among the latter, centered around 558 nm and attributed to $^5D_4 \rightarrow ^7F_5$ transitions, was characterized by the acquisition of corresponding decay curves. As observed in Fig. 10 and summarized in Table 3, the emission decay curve for the luminescence process characterized by a $\lambda_{\text{em}} = 558$ nm was well fitted to a single-exponential function, which yielded an emission lifetime of 938(3) μs . The latter value, in the border between classical lifetimes for fluorescence and phosphorescence processes, suggests that there is an efficient phosphorescence charge transfer from the ligand-based triplet state to the 5D_4 level of the Tb³⁺ ion as a consequence of the antenna effect, which provides such a long-lived intraionic emission in **2**.

The solid-state photoluminescence spectra of a polycrystalline sample of **3** at room temperature revealed, upon sample (ligand) excitation with $\lambda_{\text{ex}} = 339$ nm (dashed line in Fig. 11), two intense emission bands centered around 391 and 495 nm, respectively, and multiple weaker signals (461, 534, and 605 nm, for instance). Whereas the signal at 391 nm might be ascribed to electronic processes involving the ligand only, additional signals in the spectrum might be derived from

electronic relaxation processes involving the central Yb(III) metal cation. Equivalent maxima were revealed when **3** was excited with $\lambda_{\text{ex}} = 444$ nm.

The behavior of **4** upon excitation of a polycrystalline sample with a 325 nm laser beam at 50 K was equivalent to the one at room temperature (Fig. 12), and was characterized by a wide band centered around 540 nm, attributed to $\pi \leftarrow \pi^*$ transitions inside the 5-BrNic ligands, similar to those shown by compounds **1** and **2**. Unfortunately, compounds **3** and **4** did not display emissive properties in the NIR region (data not shown).

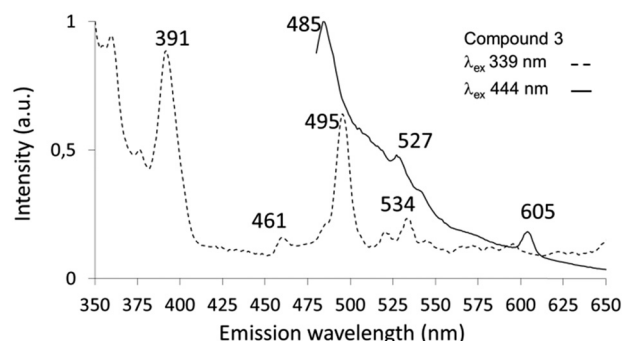


Fig. 11 Room temperature solid state emission spectra of **3** upon sample excitation with a laser, $\lambda_{\text{ex}} = 339$ nm (dashed line) or $\lambda_{\text{ex}} = 444$ nm (solid line).

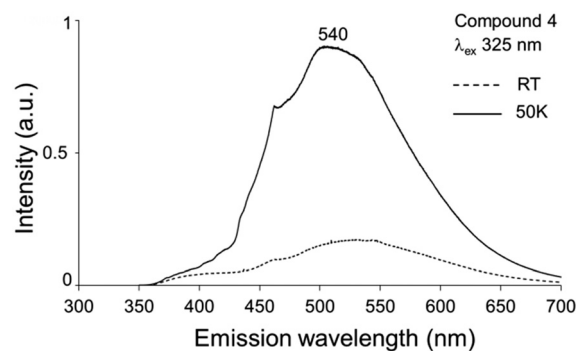


Fig. 12 RT (dashed line) and 50 K (solid line) emission spectra of **4** ($\lambda_{\text{ex}} = 325$ nm).

Table 3 Lifetime values for the main luminescence processes in compounds **1** and **2**, measured at 50 K

Comp.	$\lambda_{\text{ex}}/\lambda_{\text{em}}$	Assign.	τ exp (μs)
1	325/432	I-I	5.62(2)
	325/460	L-L	5.42(3)/115(4)
	325/486	$^4F_{9/2} \rightarrow ^6H_{15/2}$	2.29(3)/7.32(7)
	325/577	$^4F_{9/2} \rightarrow ^6H_{13/2}$	2.97(4)/8.7(1)
2	292/558	$^5D_4 \rightarrow ^7F_5$	938(3)

The room temperature photoluminescence behavior of **1** and **2** was also studied in solution (water), which revealed that metal derived emission processes are quenched significantly by the solvent (see the ESI†), as opposed to the ligand related emission bands, which were observed to be equivalent to the ones described before for the solid state emission spectra.

With the aim of achieving a more representative characterization of the emissive performance of the materials for potential applications as light-emitting diodes and chemical sensors, photographs were taken on single crystals of **1** (Fig. 13) and a polycrystalline sample of **2** (Fig. 14) using an optical microscope.

Excitation of **1** crystals with UV light of 365 nm (ligand) revealed a blue emission ascribed to $\pi \leftarrow \pi^*$ electronic transitions of the aromatic ring of the ligand, implying that the Dy(III) ion is not yet effectively sensitized at that excitation line (as shown in Fig. 7). Still, the relatively strong $^4F_{9/2} \rightarrow ^6H_{13/2}$ transition provokes the emission of an intense green light when crystals are irradiated with blue light (435 nm), whereas

excitation with green light (546 nm) reveals a red color arising from the metal. In this sense, it must be specified that the observed bright red emission should be taken with care and cannot be directly compared to previous emissions because the latter is a much more powerful excitation source.

Optical microscopy images of **2** (Fig. 14) revealed a weak emission when excited with UV light of 365 nm at RT, whereas excitation at 435 nm (centered on a region where the lanthanide ion exhibits various intraionic transitions), revealed a yellow/orange emission derived from the mixture of blue (ligands fluorescence) and green (Tb(III) fluorescence). In the same line, if the sample is irradiated with wavelengths larger than intraionic emissions (546 nm), a red light is emitted, which arises from the emission of the compound in the 550–700 nm range (see also Fig. 9).

3.4. Cytotoxicity of the lanthanide complexes

With the aim of obtaining insight into potential applications of compounds **1–4** in biological/cellular environments, cell viability studies (3-(4,5-dimethyl-2-thiazoyl)-2,5-diphenyltetrazolium bromide, MTT assay, see the Experimental section for details), were carried out on the human colon cancer cell line Caco-2 as well as human healthy (differentiated) Caco-2/TC7 cells, both in the presence and absence of increasing concentrations (0–20 μM) of each of the compounds. Fig. 15 shows the viability results for Caco-2 cancer cells; as observed, incubation with compound **1** provoked a very modest inhibition of cell growth at 15 μM concentration, decreasing the cell viability by 30% with respect to the control experiment. Still, growth inhibition did not show a clear relationship with compound **1** concentration. On the other hand, Caco-2 cell incubation with compounds **2–4** provoked no clear inhibition of cell growth.

Similarly, the effect of compounds **1–4** on non-neoplastic cells was studied by the analysis of their effect on the viability of Caco-2/TC7 cells, which consist of a monolayer of polarized and confluent Caco-2 cells that mimic a healthy human small-intestinal tissue both in terms of architecture and molecular environment (see the ESI† for additional details).

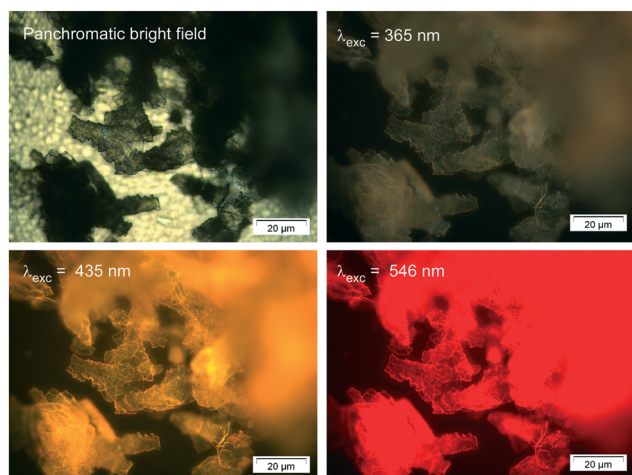


Fig. 13 Micro-PL images taken on single crystals of **1**.

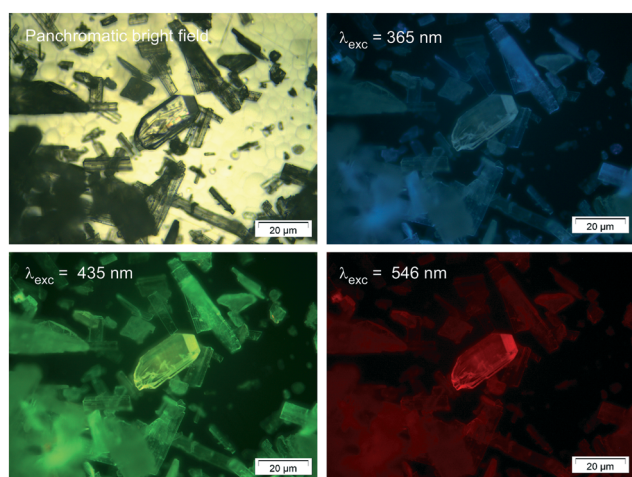


Fig. 14 Micro-PL images taken on a polycrystalline sample of **2**.

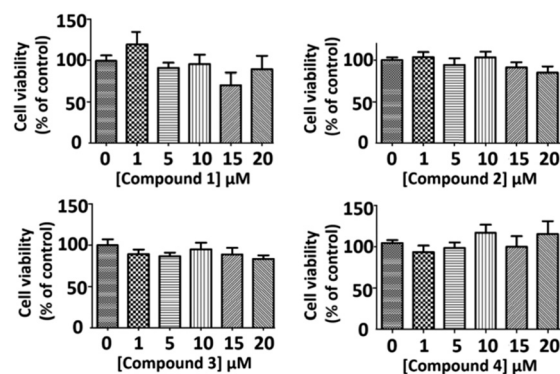


Fig. 15 Cell viability study on Caco-2 cells upon incubation with increasing concentrations of compounds **1–4**.

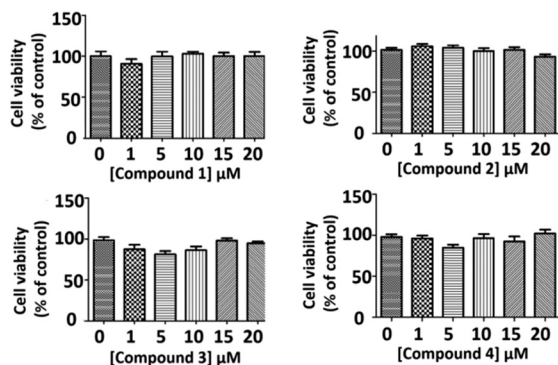


Fig. 16 Cell viability study on Caco-2/TC7 (under confluence) cells upon incubation with increasing concentrations of compounds 1–4.

As derived from the results plotted in Fig. 16, incubation of healthy cells with increasing concentrations of compounds 1–4 resulted in no significant change on cell viability.

The absence of any significant toxicity effect of our compounds over either cancer or non-cancerous cells strengthens the chances of success of this group of Ln(III) complexes when used either in biosensing or bioimaging applications.

Conclusions

In summary, 4 novel lanthanide coordination compounds, with three types of crystal structures, have been crystallized: [Dy(5-BrNic)₃(H₂O)₄] (1), [Tb(5-BrNic)₂(H₂O)₄][Tb(5-BrNic)₄(H₂O)₂](5-HBrNic)₂ (2), [Yb(5-BrNic)₂(H₂O)₄][Yb(5-BrNic)₄(H₂O)₂](5-HBrNic)₂ (3) and {[Nd(5-BrNic)₃(H₂O)₃·H₂O]_n} (4). Magnetic measurements confirm the presence of isolated lanthanide centers given the negligible antiferromagnetic interactions existing even in the case of 1D Nd-carboxylate chains of 4. On its part, alternating current magnetic susceptibility measurements carried out on 1 have been accomplished by means of revealing a U_{eff} of 33 K. Solid state photoluminescence spectra of compounds 1–4 showed the relevance of the antenna effect exerted by the 5-BrNic ligand. Decay lifetime measurements indicate short-lived excitation states in 1, whereas the yellow/orange colored emission of 2 showed larger lifetimes (approx. 1 ms). Cell viability studies on both cancer and non-cancer Caco-2 cells revealed a complete absence of cell growth inhibition exerted by compounds 1–4. In conclusion, four new non-toxic luminescent Ln(III) compounds have been generated with the 5-BrNic ligand with interesting magnetic and luminescence properties, accompanied by a complete absence of toxicity in cellular assays.

Conflicts of interest

There are no conflicts to declare.

Acknowledgements

Financial support was given by Spanish Ministerio de Ciencia e Innovación y Universidades (MCIU/AEI/FEDER/UE) projects RTC-2016-5239-2, CTQ2017-84334-R, PGC2018-102052-A-C22

and PGC2018-102052-B-C21, Red Guipuzcoana de Ciencia, Tecnología e Innovación (OF188/2017), Gobierno Vasco/Eusko Jaurlaritz (IT1005-16), Junta de Andalucía (P12-FQM-1484 and P12-FQM-2668) and University of the Basque Country (GIU 17/13). The authors acknowledge the technical and human support provided by SGIker of UPV/EHU and European funding (ERDF and ESF).

Notes and references

- E. San Sebastian, A. Rodríguez-Diéguez, J. M. Seco and J. Cepeda, *Eur. J. Inorg. Chem.*, 2018, 2155–2174.
- (a) A. Dhakshinamoorthy and H. Garcia, *Chem. Soc. Rev.*, 2014, 43, 5750–5765; (b) L. Ma, C. Abney and W. Lin, *Chem. Soc. Rev.*, 2009, 38, 1248–1256; (c) P. Horcajada, R. Gref, T. Baati, P. K. Allan, G. Maurin, P. Couvreur, G. Férey, R. E. Morris and C. Serre, *Chem. Rev.*, 2012, 112, 1232–1268; (d) P. Ramaswamy, N. E. Wong and G. K. H. Shimizu, *Chem. Soc. Rev.*, 2014, 43, 5913–5932; (e) K. Fujie, R. Ikeda, K. Otsubo, T. Yamada and S. Kitagawa, *Chem. Mater.*, 2015, 27, 7355–7361; (f) S. Lee, E. A. Kapustin and O. M. Yaghi, *Science*, 2016, 353, 808–811; (g) Y. Inokuma, S. Yoshioka, J. Ariyoshi, T. Arai, Y. Hitora, K. Takada, S. Matsunaga, K. Rissanen and M. Fujita, *Nature*, 2013, 495, 461–466; (h) V. Stavila, A. A. Talin and M. D. Allendorf, *Chem. Soc. Rev.*, 2014, 43, 5994–6010; (i) J. M. Frost, K. L. M. Harriman and M. Murugesu, *Chem. Sci.*, 2016, 7, 2470–2491; (j) G. A. Craig and M. Murrie, *Chem. Soc. Rev.*, 2015, 44, 2135–2147; (k) H. S. Quah, W. Chen, M. K. Schreyer, H. Yang, M. W. Wong, W. Ji and J. J. Vital, *Nat. Commun.*, 2015, 6, 7954–7961.
- (a) V. Guillerme, D. Kim, J. F. Eubank, R. Luebke, X. Liu, K. Adil, M. S. Lah and M. Eddaoudi, *Chem. Soc. Rev.*, 2014, 43, 6141–6172; (b) M. Eddaoudi, D. F. Sava, J. F. Eubank, K. Adil and V. Guillerme, *Chem. Soc. Rev.*, 2015, 44, 228–249.
- (a) Y. Cui, B. Chen and G. Qian, *Coord. Chem. Rev.*, 2012, 112, 1126–1162; (b) J. Rocha, L. D. Carlos, F. A. A. Paz and D. Ananias, *Chem. Soc. Rev.*, 2011, 40, 926–940; (c) B. Li, H.-M. Wen, Y. Cui, G. Qian and B. Chen, *Prog. Polym. Sci.*, 2015, 48, 40–84; (d) B. Chen, L. Wang, Y. Xiao, F. R. Fronczek, M. Xue, Y. Cui and G. Qian, *Angew. Chem., Int. Ed.*, 2009, 48, 500–503.
- (a) S. V. Eliseeva and J.-C. G. Bünzli, *Chem. Soc. Rev.*, 2010, 39, 189–227; (b) L. D. Carlos, R. A. S. Ferreira, V. de Zea Bermudez, B. Julián-López and P. Escrivano, *Chem. Soc. Rev.*, 2011, 40, 536–549; (c) J.-C. G. Bünzli and C. Piguet, *Chem. Rev.*, 2002, 102, 1897–1928; (d) J.-C. G. Bünzli, *Chem. Rev.*, 2010, 110, 2729–2755; (e) K. Binnemans, *Chem. Rev.*, 2009, 109, 4283–4374; (f) E. G. Moore, A. P. S. Samuel and K. N. Raymond, *Acc. Chem. Res.*, 2009, 42, 542–552; (g) Y. Cui, J. Zhang, B. Chen and G. Qian, *Lanthanide Metal-Organic Frameworks for Luminescent Applications, Handbook on the Physics and Chemistry of Rare Earths*, Elsevier, 1999, vol. 26, pp. 243–268.
- E. G. Moore, A. P. S. Samuel and K. N. Raymond, *Acc. Chem. Res.*, 2009, 42, 542–552.
- (a) Y.-S. Song, B. Yan and Z.-X. Chen, *J. Solid State Chem.*, 2004, 177, 3805–3814; (b) J.-Z. Gu, J. Wu, A. M. Kirillov, D.-Y.

- Lv, Y. Tang and J.-C. Wu, *J. Solid State Chem.*, 2014, **213**, 256–267; (c) A. J. Calahorra, M. E. López-Viseras, A. Salinas-Castillo, D. Fairen-Jimenez, E. Colacio, J. Cano and A. Rodríguez-Diéguez, *CrystEngComm*, 2012, **14**, 6390–6393.
- 8 Bruker Apex2, Bruker AXS Inc., Madison, Wisconsin, USA, 2004.
- 9 G. M. Sheldrick, *SADABS, Program for Empirical Adsorption Correction*, Institute for Inorganic Chemistry, University of Göttingen, Germany, 1996.
- 10 (a) G. M. Sheldrick, *SHELX-2014, Program for Crystal Structure Refinement*, University of Göttingen, Göttingen, Germany, 2014; (b) L. J. Farrugia, *J. Appl. Crystallogr.*, 1999, **32**, 837–838.
- 11 A. Altomare, M. C. Burla, M. Camilla, G. L. Cascarano, C. Giacovazzo, A. Guagliardi, A. G. G. Moliterni, G. Polidori and R. Spagna, *J. Appl. Crystallogr.*, 1999, **32**, 115–119.
- 12 (a) R. Sessoli and A. K. Powell, *Coord. Chem. Rev.*, 2009, **253**, 2328–2341; (b) P. Díaz-Gallifa, O. Fabelo, J. Pasán, L. Cañadillas-Delgado, F. Lloret, M. Julve and C. Ruiz-Pérez, *Inorg. Chem.*, 2014, **53**, 6299–6308.
- 13 (a) D. Aguilà, L. A. Barrios, V. Velasco, L. Arnedo, N. Aliaga-Alcalde, M. Menelaou, S. J. Teat, O. Roubeau, F. Luis and G. Aromí, *Chem. – Eur. J.*, 2013, **19**, 5881–5891; (b) N. W. Waggoner, B. Saccoccia, I. A. Ibarra, V. M. Lynch, P. T. Wood and S. M. Humphrey, *Inorg. Chem.*, 2014, **53**, 12674–12676.
- 14 (a) I. A. Kahwa, J. Selbin, C. J. O'Connor, J. W. Foise and G. L. McPherson, *Inorg. Chim. Acta*, 1988, **148**, 265–272; (b) H. Ke, L. Zhao, G.-F. Xu, Y.-N. Guo, J. Tang, X.-Y. Zhang and H.-J. Zhang, *Dalton Trans.*, 2009, 10609–10613; (c) J. Cepeda, R. Balda, G. Beobide, O. Castillo, J. Fernández, A. Luque, S. Pérez-Yáñez, P. Román and D. Vallejo-Sánchez, *Inorg. Chem.*, 2011, **50**, 8437–8451; (d) C. J. O'Connor, *Prog. Inorg. Chem.*, 1982, **29**, 203.
- 15 B. Yao, B. Gu, M. Su, G. Li, Y. Ma, L. Li, Q. Wang, P. Cheng and X. Zhang, *RSC Adv.*, 2017, **7**, 2766–2772.
- 16 (a) Q.-W. Xie, S.-Q. Wu, W.-B. Shi, C.-M. Liu, A.-L. Cui and H.-Z. Kou, *Dalton Trans.*, 2014, **43**, 11309–11316; (b) Y. Li, C. Zhang, J.-W. Yu, E.-C. Yang and X.-J. Zhao, *Inorg. Chim. Acta*, 2016, **445**, 110–116; (c) J. P. Costes, S. Titos-Padilla, I. Oyarzabal, T. Gupta, C. Duhayon, G. Rajaraman and E. Colacio, *Inorg. Chem.*, 2016, **55**, 4428–4440; (d) P.-Y. Shan, H.-F. Li, P. Chen, Y.-M. Tian, W.-B. Sun and P.-F. Yan, *Z. Anorg. Allg. Chem.*, 2015, **641**, 1119–1124.
- 17 (a) J.-L. Liu, Y.-C. Chen and M.-L. Tong, *Chem. Soc. Rev.*, 2018, **47**, 2431–2453; (b) D. N. Woodruff, R. E. P. Winpenny and R. A. Layfield, *Chem. Rev.*, 2013, **113**, 5110–5148.
- 18 P. E. Car, M. Perfetti, M. Mannini, A. Favre, A. Caneschi and R. Sessoli, *Chem. Commun.*, 2011, **47**, 3751–3753.
- 19 D. Li, T. Wang, C. Li, D. Liu, Y. Li and X. You, *Chem. Commun.*, 2010, **46**, 2929–2931.
- 20 G. Chen, C. Gao, J. Tian, J. Tang, W. Gu, X. Liu, S. Yan, D. Liao and P. Cheng, *Dalton Trans.*, 2011, **40**, 5579–5583.
- 21 N. Ishikawa, M. Sugita, T. Ishikawa, S.-Y. Koshihara and Y. Kaizu, *J. Am. Chem. Soc.*, 2003, **125**, 8694–8695.
- 22 S. Jiang, B. Wang, G. Su, Z. Wang and S. Gao, *Angew. Chem., Int. Ed.*, 2010, **49**, 7448–7451.
- 23 Y.-C. Chen, J.-L. Liu, L. Ungur, J. Liu, Q.-W. Li, L.-F. Wang, Z.-P. Ni, L. F. Chibotaru, X.-M. Chen and M.-L. Tong, *J. Am. Chem. Soc.*, 2016, **138**, 2829–2837.
- 24 M. Gregson, N. F. Chilton, A.-M. Ariciu, F. Tuna, I. F. Crowe, W. Lewis, A. J. Blake, D. Collison, E. J. L. McInnes, R. E. P. Winpenny and S. T. Liddle, *Chem. Sci.*, 2016, **7**, 155–165.
- 25 (a) C. A. P. Goodwin, F. Ortu, D. Reta, N. F. Chilton and D. P. Mills, *Nature*, 2017, **548**, 439–442; (b) F.-S. Guo, B. M. Day, Y.-C. Chen, M.-L. Tong, A. Mansikkamaki and R. A. Layfield, *Angew. Chem., Int. Ed.*, 2017, **56**, 11445–11449.
- 26 (a) M. D. Allendorf, C. A. Bauer, R. K. Bhakta and R. J. T. Houk, *Chem. Soc. Rev.*, 2009, **38**, 1330–1352; (b) J. Cepeda, S. Pérez-Yáñez, G. Beobide, O. Castillo, J. A. García, M. Lanchas and A. Luque, *Dalton Trans.*, 2015, **44**, 6972–6986; (c) K. Müller-Buschbaum, S. G. Torres, P. Larsen and C. Wickleder, *Chem. Mater.*, 2007, **19**, 655–659.



5-Aminopyridine-2-carboxylic acid as appropriate ligand for constructing coordination polymers with luminescence, slow magnetic relaxation and anti-cancer properties[☆]



Antonio A. García-Valdivia^a, Javier Cepeda^b, Belén Fernández^{c,*}, Marta Medina-O'donnell^d, Itziar Oyarzabal^b, Jerónimo Parra^a, Fatin Jannus^e, Duane Choquesillo-Lazarte^g, José A. García^h, José Antonio Lupiáñez^e, Santiago Gómez-Ruiz^f, Fernando Reyes-Zurita^{e,*}, Antonio Rodríguez-Diéguez^{a,*}

^a Department of Inorganic Chemistry, University of Granada, 18071 Granada, Spain

^b Department of Applied Chemistry, Faculty of Chemistry, University of The Basque Country UPV/EHU, Paseo Manuel Lardizabal 3, 20018 Donostia-San Sebastián, Spain

^c Institute of Parasitology and Biomedicine "López-Neyra", CSIC, Av. Conocimiento s/n, 18600 Granada, Spain

^d Department of Organic Chemistry, University of Granada, 18071 Granada, Spain

^e Dept. of Biochemistry and Molecular Biology I, Severo Ochoa s/n, University of Granada, 18071 Granada, Spain

^f Department of Biology and Geology, Physics and Inorganic Chemistry, E.S.C.E.T., Rey Juan Carlos University, c/ Tulipán s/n, 28933 Móstoles, Spain

^g Laboratorio de Estudios Cristalográficos, IACT (CSIC-UGR), Avda. de las Palmeras 4, 18100 Armilla, Granada, Spain

^h Departamento de Física Aplicada II, Facultad de Ciencia y Tecnología, Universidad del País Vasco (UPV/EHU), 48940 Leioa, Spain

ARTICLE INFO

Keywords:

Coordination polymers
CPs
Lanthanides
Transition metals
Slow relaxation of magnetization
SMM
Luminescence properties
Anticancer activity

ABSTRACT

Five new coordination polymers (CPs) constructed of aminopyridine-2-carboxylate (ampy) ligand have been synthesized and fully characterized. Three of them correspond to metal-organic chains built from the coordination of ampy to sodium and lanthanides with formulae $[MNa(ampy)_4]_n$ ($M = \text{terbium (2), erbium (1) and ytterbium (3)}$) resembling a previously reported dysprosium material which shows anticancer activity. On another level, the reaction of Hampy with cobalt and copper ions ($\{[CoK(ampy)_3(H_2O)_3](H_2O)_3\}_n$ (4) and $[Cu(ampy)_2]_n$ (5)) lead to CPs with variable dimensionalities, which gives the opportunity of analyzing the structural properties of this new family. Lanthanide materials display solid state intense photoluminescent emissions in both the visible and near-infrared region and exhibit slow relaxation of magnetization with frequency dependence of the out-of-phase susceptibility. More interestingly, in our search for multifunctional materials, we have carried out antitumor measurements of these compounds. These multidisciplinary studies of metal complexes open up the possibility for further exploring the applications in the fields of metal-based drugs.

1. Introduction

In the last years, mononuclear Single-Molecule Magnets (M-SMMs) have been intensively studied due to their potential applications in quantum-computing devices [1] and molecular spintronics [2]. In the same time, coordination polymers (CPs) have received great interest due to their structural diversity as well as the properties that arise from their topological features [3]. In particular, the study of lanthanide-based CPs has evolved enormously in areas such as luminescence [4], gas adsorption [5], optical storage [6], magnetism [7] and biology as drug-delivery systems [8] or cytotoxic agents [9]. Coordination

polymers are obtained by the self-assembly of metal ions with appropriate bridging organic ligands generating multidimensional materials with different properties. During the recent years, we have also focused on designing novel organic ligands to construct M-SMMs [10] and Lanthanides-CPs based on carboxylic linkers [11] that display slow relaxation of the magnetization. It is worth noting that there are not many examples of mixed 3s-4f systems, so the synthesis and study of these systems could provide materials with interesting properties, reason why we decided to focus on this type of systems. In this line, our research group has recently obtained and characterized an interesting metal-organic chain (MOC) based on dysprosium which, to the best of

[☆] In memoriam of Professor Juan Manuel Salas Peregrín and his contribution to the research on bioinorganic chemistry in Spain. Without you, science will never be the same.

* Corresponding authors.

E-mail addresses: belenfernandez@ipb.csic.es (B. Fernández), ferjes@ugr.es (F. Reyes-Zurita), antonio5@ugr.es (A. Rodríguez-Diéguez).

<https://doi.org/10.1016/j.jinorgbio.2020.111051>

Received 5 August 2019; Received in revised form 23 February 2020; Accepted 2 March 2020

Available online 17 March 2020

0162-0134/ © 2020 Published by Elsevier Inc.

our knowledge, can be regarded as the first example of a material showing slow relaxation of the magnetization, magnetic field dependent cytotoxicity and modulation of the multidrug resistance [12]. In this work, the cytotoxicity of both the ligand and complexes was quantified by the IC_{50} values, showing that the complexes and their ligand exert a mild cytotoxic activity against HT-29 and DLD-1 colon carcinoma cells, while complex has a very weak cytotoxicity against Caco-2 cells as none of the concentrations, not even 20 mM, inhibited 100% of the living cells.

In the development of biological applications, this type of metal-organic compounds could be used for variable purposes with different points of view. These systems can be used as bioluminescent markers [13] when present a low cytotoxicity or, alternatively, they can be used as cytotoxic compounds with a cytotoxicity modulated by an external magnetic field or by the structural properties [14]. These properties feature a wide range of potential uses such as allow determining the organism distribution of the compound, and once reached the target tumor area, its toxicity could be activated in response to a magnetic field and minimize nonspecific interactions as it happens with other anticancer agents such as terpenic acids derivatives [15].

Due to the potential application of these materials, we have synthesized similar coordination polymers based on terbium, erbium and ytterbium ions that show slow relaxation of magnetization with the aim of studying their cytotoxic properties with different cancer cell lines. In these studies, we have observed that the cytotoxic activity varies depending on the lanthanide ion used, which opens up the possibility of switching the biological activity of the compound while its multifunctional character is adapted. Moreover, we have synthesized two new multidimensional coordination polymers based on cobalt and copper with the same ligand to study the modification of the anticancer properties by the use of transition metal ions. On this occasion, we have used ligand 5-aminopyridine-2-carboxylic acid (Hampy), due to there was only one coordination compound in the literature [16]. In this case, the ligand showed a different coordination mode than the one shown in the previous work and in this manuscript.

Herein, we report the synthesis and structure of five novel coordination polymers based on 5-aminopyridine-2-carboxylic acid as linker, three MOCs with formulae $[TbNa(ampy)_4]_n$ (1), $[ErNa(ampy)_4]_n$ (2), $[YbNa(ampy)_4]_n$ (3), and two multidimensional CPs $\{[CoK(ampy)_3(H_2O)_3](H_2O)_3\}_n$ (4) and $[Cu(ampy)_2]_n$ (5) that present interesting magnetic, luminescence and biological properties. Thanks to its aromaticity, Hampy is a good candidate for enhanced emissive properties, which are tunable by coordination to metal with different coordination modes (Scheme I). These materials corroborate the potential of this pyridine derivative linker to construct new coordination polymers with interesting physical and biological properties. Moreover, in this work we assayed the cytotoxicity effects of five metal complexes, in three cellular lines: B16-F10 murine melanoma cells, Hep-G2 human hepatocarcinoma cells, and HT29 human colon cancer cells. Our results showed that the compounds were especially cytotoxic in the carcinoma

cells HT29 or Hep-G2, whereas no results were found in B16-F10 melanoma cells. Compound 4 seemed to be the more cytotoxic complex (including B16-F10 melanoma cells), whereas compound 1 did not have effects on any of the cancer cell lines assayed. One of our main objectives in this study is to search for new anticancer-drugs with new biochemical properties rather than improving actual anti-cancer drugs. In this sense the synthesis of new families of coordination compounds could be a new strategy with new applications, which may represent a useful mechanistic approach to both chemoprevention and chemotherapy in different types of cancer.

2. Experimental section

2.1. General procedures

Unless stated otherwise, all reactions were conducted under solvothermal conditions, with the reagents purchased commercially and used without further purification.

2.2. Preparation of complexes

2.2.1. $[TbNa(ampy)_4]_n$ (1)

This reaction is achieved via the soft solvothermal reaction of terbium nitrate (1 mmol), NaOH (0.1 mmol) and 5-aminopyridine-2-carboxylic acid (4 mmol) in dimethylformamide (10 mL) at 95 °C for 24 h to give prismatic crystals of compound 1. Yield: ca. 45% based on terbium. Anal. calcd $C_{24}H_{20}N_8NaO_8Tb$: C 39.47, H 2.76, N 15.34. Found: C 39.43, H 2.67, N 15.41.

2.2.2. $[ErNa(ampy)_4]_n$ (2) and $[YbNa(ampy)_4]_n$ (3)

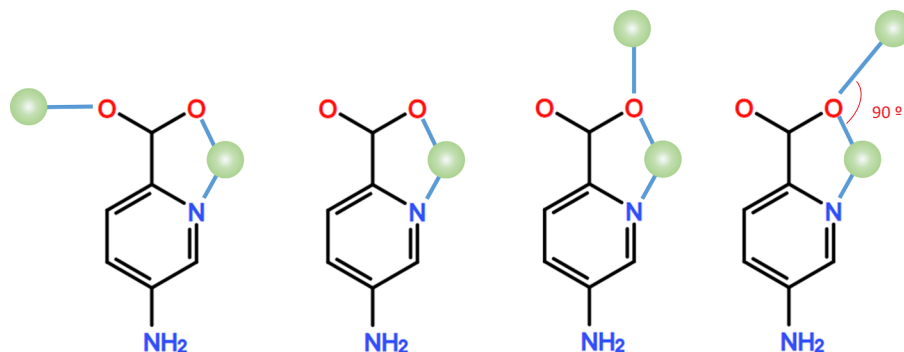
Complexes 2 and 3 were synthesized following the same reaction as in the above compound but using erbium nitrate and ytterbium nitrate, respectively. Yield: ca. 38% and 43% based on metal ions for 2 and 3, respectively. Anal. calcd $C_{24}H_{20}N_8NaO_8Er$: C 39.02, H 2.73, N 15.17. Found: C 38.94, H 2.65, N 15.21. Anal. calcd $C_{24}H_{20}N_8NaO_8Yb$: C 38.72, H 2.71, N 15.05. Found: C 38.64, H 2.63, N 15.11.

2.2.3. $\{[CoK(ampy)_3(H_2O)_3](H_2O)_3\}_n$ (4)

This reaction is achieved via the soft solvothermal reaction of cobalt nitrate (1 mmol), KOH (0.1 mmol) and 5-aminopyridine-2-carboxylic acid (3 mmol) in dimethylformamide (10 mL) at 95 °C for 24 h to give prismatic crystals of compound 4. Yield: ca. 15% based on cobalt. Anal. calcd $C_{18}H_{33}CoKN_6O_{15}$: C 32.19, H 4.95, N 12.51. Found: C 32.06, H 4.83, N 12.67.

2.2.4. $[Cu(ampy)_2]_n$ (5)

This reaction is achieved via the soft solvothermal reaction of copper nitrate (1 mmol) and 5-aminopyridine-2-carboxylic acid (2 mmol) in dimethylformamide (10 mL) at 95 °C for 24 h to give prismatic crystals of compound 5. Yield: ca. 41% based on copper. Anal.



Scheme I. Different known coordination modes of Hampy ligand.

calcd $C_{12}H_{10}CuN_4O_4$: C 42.67, H 2.98, N 16.59. Found: C 42.49, H 2.82, N 16.74.

2.3. Physical measurements

Elemental analyses were carried out at the Centro de Instrumentación Científica (University of Granada) on a Fisons-Carlo Erba analyser model EA 1108. FTIR spectra were recorded on a Nicolet IR 6700 spectrometer in the $4000\text{--}400\text{ cm}^{-1}$ spectral region. The spectra of compounds show bands around 1710 cm^{-1} (C=O, carboxylate) and 3350 cm^{-1} and 1550 cm^{-1} (N–H, amine group) with little displacement compared to 5-aminopyridine-2-carboxylic acid spectra's bands.

2.4. Single-crystal structure determination

The crystal structure of compounds 1–5 were determined by single crystal X-ray crystallography. Suitable crystals of these materials were mounted on a glass fibre and used for data collection on a Bruker D8 Venture diffractometer using $MoK\alpha$ radiation ($\lambda = 0.71073\text{ \AA}$). Absorption correction was applied using SADABS software [17]. The structure was solved by direct methods and refined with full-matrix least-squares calculations on F^2 using the program SHELXL [18] and Olex2 as the graphical interface [19]. Anisotropic temperature factors were assigned to all atoms except for hydrogen atoms, which are riding their parent atoms with an isotropic temperature factor chosen as 1.2 times or 1.5 times those of their parent atoms. Attempts to solve disorder problems with crystallization water molecules failed in compound 4. During the structure refinement, regions of electron density were identified as highly disordered water molecules. Attempts to model these electron densities as water were not successful due to the extent of the disorder. In the final structure model, the contribution of the electron density from three water molecules per formula unit has been removed from the intensity data using the solvent mask tool in Olex2. The structure exhibits disorder of the coordinated ampy ligand, which was successfully refined using a two-site model with a 0.54:0.46 occupancy ratio. Compound 5 was refined as a pseudo-merohedral twin. From the original HKLF file, a modified file was prepared by means of the TWINROT option (twin matrix $-1\ 0\ 0\ 0\ 1\ 0\ 0\ 0\ 1$) in PLATON software [20] in such a way that final refinement gave twin fractions of 0.22 and 0.78. Details of the structure determination and refinement of the studied compounds are summarized in Table S1. Crystallographic data (excluding structure factors) for the structure reported in this paper have been deposited with the Cambridge Crystallographic Data Centre as supplementary publication nos. CCDC 1519675, 1519676 and 1944059–1944061. Copies of the data can be obtained free of charge on application to the Director, CCDC, 12 Union Road, Cambridge, CB2 1EZ, U.K. (Fax: +44-1223-335033; e-mail: deposit@ccdc.cam.ac.uk or <http://www.ccdc.cam.ac.uk>).

2.5. Luminescence measurements

Lifetime and steady-state photoluminescence (PL) measurements were carried out on crystalline samples at 10 K using a close cycle helium cryostat enclosed in an Edinburgh Instruments FLS920 spectrometer. All samples are first placed under high vacuum (of ca. 10^{-9} mbar) to avoid the presence of oxygen or water in the sample holder. For recording steady-state emission spectra an IK3552R-G HeCd continuous laser (325 nm) was used as excitation source. A Hamamatsu NIR-PMT PicoQuant FluoTime 200 detector was employed for collecting the spectra in the NIR region.

2.6. Magnetic measurements

Magnetization and variable-temperature (1.9–300 K) magnetic susceptibility measurements on polycrystalline samples were carried out

with a Quantum Design SQUID MPMS XL-5 device operating at different magnetic fields. The experimental susceptibilities were corrected for the diamagnetism of the constituent atoms by using Pascal's tables. Ac susceptibility measurements under different applied static fields were performed by using an oscillating ac field of 3.5 Oe on a PPMS 6000 magnetometer.

2.7. Antiproliferative activity

The effect of treatment with the three 1D-coordination polymers (compound 1, 2 and 3) and two coordination polymer materials (compounds 4 and 5) on cancer cell proliferation were assayed by MTT (3-(4,5-dimethylthiazol-2-yl)-2,5-diphenyltetrazolium bromide) assay, on HT29 colon cancer cells, HepG2 hepatoma cells and B16-F10 melanoma cells. The three cancer cell lines were treated with increasing concentration of the compounds (range from 0 to $100\text{ }\mu\text{g/mL}$). MTT is transformed by viability cells to formazan, therefore its concentration is proportional to the number of life cells. The percentage of viability cells were expressed with respect to untreated control cells. In all cells lines we determined the concentration of compounds required for 20%, 50%, and 80% of inhibition cell growth, IC_{20} , IC_{50} and IC_{80} , concentrations respectively.

3. Results and discussion

The solvothermal reactions of the appropriate metallic salts at $95\text{ }^\circ\text{C}$ for 24 h produced prismatic crystals of these coordination polymers. The crystal structures of terbium, erbium, ytterbium, cobalt and copper compounds were determined using single crystal X-ray crystallography.

3.1. Description of the structures

3.1.1. Structural descriptions of Tb-MOC (1), Er-MOC (2) and Yb-MOC (3)

The preparation of $[TbNa(ampy)_4]_n$ is very simple and is achieved via the soft hydrothermal reaction of the terbium nitrate (1 mmol), NaOH (0.1 mmol) and 5-aminopyridine-2-carboxylic acid (4 mmol) in dimethylformamide (10 mL) at $95\text{ }^\circ\text{C}$ for 24 h to give prismatic crystals of this Tb-MOC (1). Compounds 1 ($M = Tb$), 2 ($M = Er$) and 3 ($M = Yb$) are isostructural materials, and therefore we will only describe the latter. These compounds crystallize in the tetragonal space group $I4_1/a$. The 1D structure of 3 (Fig. 1) is described by ytterbium and sodium ions bridged by four different $(ampy)^{1-}$ linkers. The $(ampy)^{-}$ ligand shows a chelating coordination mode that involves the coordination of the oxygen atom pertaining to the carboxylate group and the nitrogen atom from the pyridine ring.

The Yb^{III} atom exhibits a YbN_4O_4 coordination environment which is made of four oxygen atoms pertaining to four different $(ampy)^{-}$

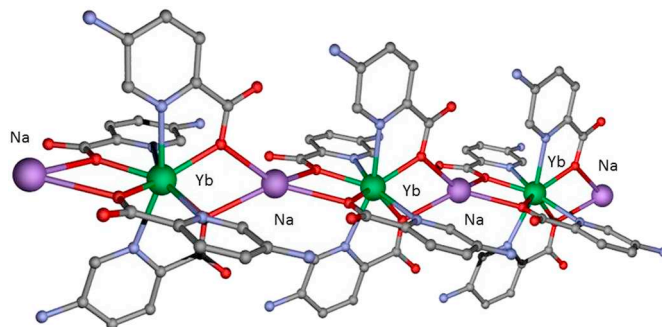


Fig. 1. Perspective view of the ytterbium-sodium chain. Hydrogen atoms have been omitted for clarity. Colour code: Ytterbium, green; sodium, purple; oxygen, red; nitrogen, blue; carbon, grey. (For interpretation of the references to colour in this figure, the reader is referred to the web version of this article.)

Table 1
Selected bond lengths and angles for compounds 1–3.

Tb1-O1	2.318(4)	Er1-O1	2.308(3)	Yb1-O1	2.282(2)
Tb1-N1	2.556(4)	Er1-N1	2.529(4)	Yb1-N1	2.518(3)
Tb1-Na1	4.253(8)	Er1-Na1	4.272(7)	Yb1-Na1	4.280(9)
Tb1-Tb1	8.507(9)	Er1-Er1	8.543(7)	Yb1-Yb1	8.560(10)

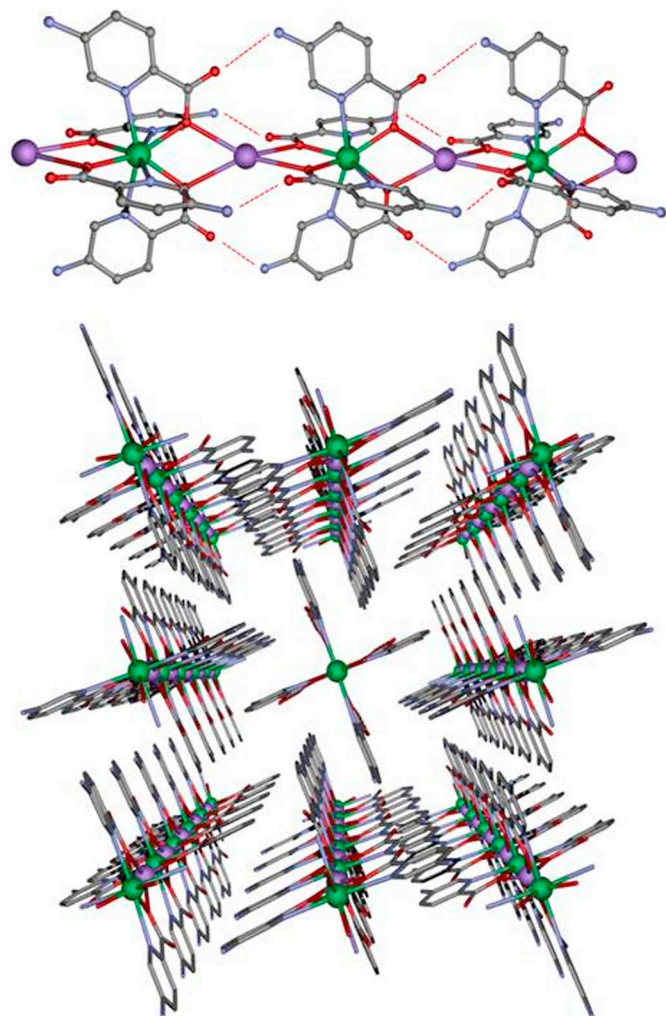


Fig. 2. Top: Hydrogen bonds present in the chains pertaining to Yb-MOC. Bottom: Perspective view of packing in **3** along *c* axis in which π - π interactions among pyridine rings pertaining to the ligand can be observed.

ligands and four nitrogen atoms belonging to four pyridine rings. Calculations by SHAPE software [21] indicate that the YbN₄O₄ coordination sphere is close to the triangular dodecahedron ideal polyhedron (SHAPE value of 1.693, Table S2). The Yb–O_{carb} bond distance has a value of 2.282(2) Å whereas the Yb–N_{pyr} distance is 2.518(3) Å (see Table 1). Within the one-dimensional coordination polymer, the intrachain Yb⋯Yb distance is of 8.560(10) Å, while the shortest interchain Yb⋯Yb distance is of 9.254(10) Å. These chains can be described by [Yb(ampy)₄][−] units bridged by Na⁺ ions, in which chains are packed thanks to an interesting hydrogen bond network (Fig. 2, top) that involves the oxygen pertaining to carboxylate group and the amino group of the ligand with a distance of 2.972(6) Å.

In these three structures, Na⁺ ions show a very distorted tetrahedral coordination geometry of type NaO₄, in which the bond distances Na–O are 2.736, 2.753 and 2.762 Å for **1**, **2** and **3**, respectively.

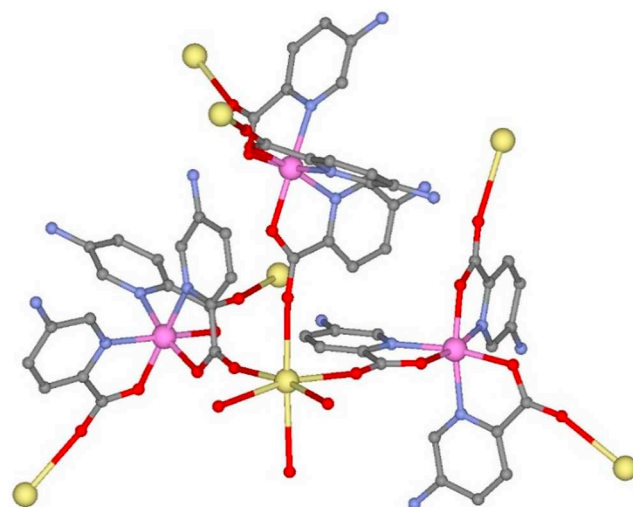


Fig. 3. Perspective of a fragment of Co-CP in which [Co(ampy)₃][−] units are connected by K⁺ ions. Hydrogen atoms have been omitted for clarity. Colour code: Cobalt, pink; potassium, yellow; oxygen, red; nitrogen, blue; carbon, grey. (For interpretation of the references to colour in this figure, the reader is referred to the web version of this article.)

3.1.2. Structural description of Co-CP (**4**)

Compound **4** crystallizes in the cubic *P*2₁3 space group. The cobalt (II) ion resides in a 3-fold axis, adopting an octahedral coordination polyhedron and is tris chelated by three ampy ligands which supply six donor atoms in a CoN₃O₃ coordination environment in *fac* disposition (Fig. 3). The overall assembly consists of a three-dimensional coordination polymer that can be described as [Co(ampy)₃][−] units connected by K⁺ ions.

The potassium centres exhibit six-coordinate environments consisting of three bridging carboxylate O atoms and three terminal water molecules. It is observed that the K–O_{ampy} distances (2.686(4) Å) are shorter than that of the K–O_{water} (2.844(8) Å), indicating that the former bridges may play a more important role in stabilizing the network (Fig. 4). Hydrogen bonding interactions involving –NH₂ groups reinforce the supramolecular architecture. Terminal water ligands also participate in a hydrogen network pointing towards the interior of cavities (26.9% of unit cell volume). These cavities are occupied by highly disordered water molecules that were masked by the Olex2 mask tool (see Experimental section).

3.1.3. Structural description of Cu-CP (**5**)

The structure of **5** is made of planar [Cu(ampy)₂] units connected by weak Cu–O axial interactions to afford linear chains parallel to the *a* axis (Fig. 5). This compound crystallizes in the *P*2₁/*c* monoclinic space group in which Cu(II) ions exhibit a CuN₂O₄ coordination polyhedron with tetragonally distorted octahedral geometry. The equatorial positions are occupied by two nitrogen atoms and two oxygen atoms from two carboxylate groups belonging to two different ampy bridging ligands, which adopt a *trans*-planar configuration. Two carboxylate oxygen atoms, O1, are situated in axial positions at a longer distance of 2.961(3) Å. Neighbouring [Cu(ampy)₂] units are held together by a pair of complementary weak Cu–O1 interactions, which lead to the chain structure with *syn*-anti carboxylate bridges. The Cu⋯Cu distance along the chain is 3.628(4) Å, whereas the shortest interchain Cu⋯Cu distance is 8.936(4) Å.

These chains generate a three-dimensional network by means of strong hydrogen bonds (2.911 Å) involving the O2 atoms from the carboxylate groups and the N2 atoms from the amino groups pertaining to the ampy ligand (Fig. S1).

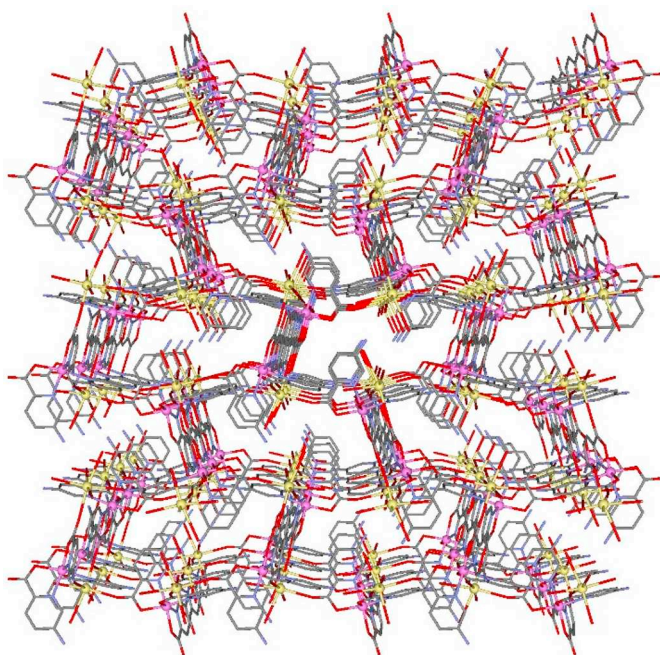


Fig. 4. Perspective of the three-dimensional structure in Co-CP. Hydrogen atoms have been omitted for clarity. Colour code: Cobalt, pink; potassium, yellow; oxygen, red; nitrogen, blue; carbon, grey. (For interpretation of the references to colour in this figure, the reader is referred to the web version of this article.)

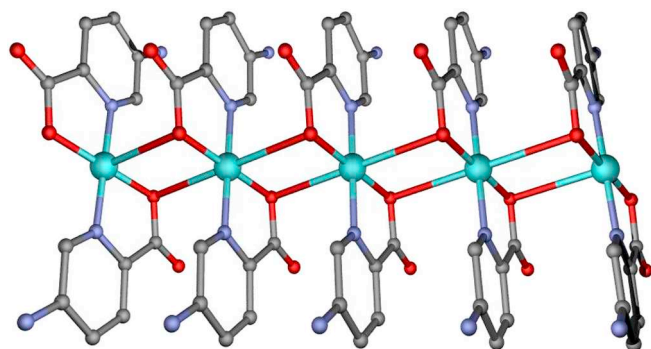


Fig. 5. Perspective of one chain pertaining to Cu-CP parallel to *a* axis. Hydrogen atoms have been omitted for clarity. Colour code: Copper, cyan; oxygen, red; nitrogen, blue; carbon, grey. (For interpretation of the references to colour in this figure, the reader is referred to the web version of this article.)

3.2. Luminescence properties

Among lanthanide ions, Tb(III) is one of the most strongly emitting members and accordingly, it has been widely employed for the characterization of the active metal environments in many macromolecules of biological interest [22]. Lanthanide luminophores present sharp emission bands and their luminescent lifetimes are often long, which allows easily discriminating their emission from background fluorescence, identifying it through time-resolved measurements and performing a selected detection when they are mixed with other emitting lanthanide cations [10]. On the other hand, a major drawback for lanthanide(III) ions is derived from their low absorption coefficients, since being based on Laporte forbidden *f-f* transitions, hinders their direct excitation. This inconvenient may be bypassed by the so-called “antenna effect”, in which ligands consisting of aromatic chromophores and possessing a reasonably large molar absorption cross section mediate in the process, thus generating more efficient emissions originated at the lanthanides. The polycrystalline sample of compound 1

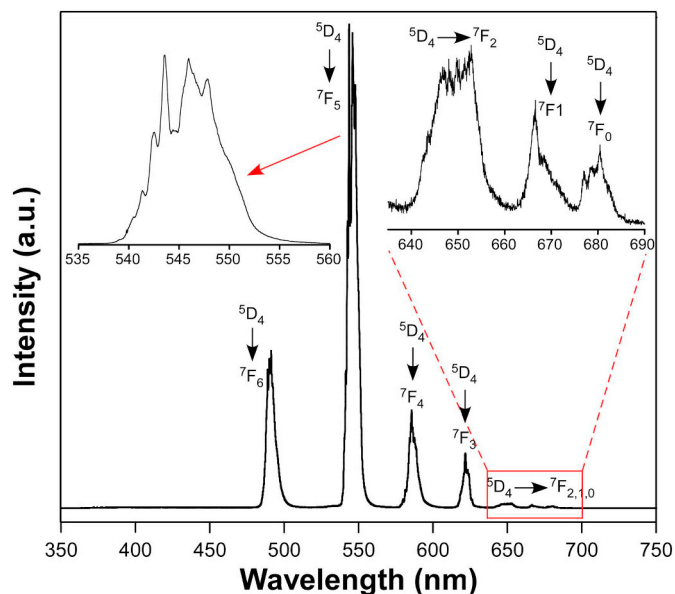


Fig. 6. 10 K emission spectrum of compound 1 collected under excitation at 325 nm showing the characteristic transitions of the corresponding lanthanide (III) ion.

shows a brilliant green emission upon laser excitation at 325 nm. The emission spectrum shows seven multiplets assigned to the $^5D_4 \rightarrow ^7F_J$ ($J = 6, 5, 4, 3, 2, 1,$ and 0) transitions (Fig. 6), among which the $^5D_4 \rightarrow ^7F_5$ (called hypersensitive transition) is the strongest one owing to its large probability being both electric-dipole and magnetic-dipole induced transition. Moreover, as observed in the spectrum, no remarkable emission is observed in the 350–450 nm region (characteristic of ligand fluorescence), so it may be assumed that the ligand acts as an effective antenna for the terbium(III) centre.

In the case of NIR emitters, the sensitization via ligands antenna effect is often more difficult to be achieved given the large energy difference between the excited levels of the ligands and the emissive levels of the lanthanide, which favours the occurrence of non-radiative processes to govern the deactivation process. Accordingly, the examples of NIR emitters based on CPs are somewhat scarce. As previously observed for other compounds based on amino substituted pyridinecarboxylate, these ligands have proven an effective UV light absorption capacity, so they could behave as sensitizers for lanthanide emission. In fact, as depicted in Fig. 7, compounds 2 and 3 exhibit intense characteristic emission when the polycrystalline samples are excited at monochromatic 325 nm laser irradiation. In the emission spectrum of compound 2, the very narrow band centred at 1542 nm shows a quite symmetric profile in which a fine-structure may be distinguished. These emission maxima are attributed to the $^4I_{13/2} \rightarrow ^4I_{15/2}$ transition of the intraionic levels of the Er^{III} ion, which are of particular interest in the field of amplification since 1540 nm is an appropriate wavelength in the third telecommunication window. When ampy ligand is introduced to sensitize Yb^{III} ion, the emission spectrum of 3 exhibits the characteristic emission bands sited around 980 nm assigned to the $^2F_{5/2} \rightarrow ^2F_{7/2}$ transition. It is worth mentioning that this emission is not a single sharp line but, in addition to the most intense one at 983 nm, it consists of an envelope of bands peaking at 975, 1004 and 1032 nm. The occurrence of those bands seems to correspond to the crystal-field splitting at the emitting and/or fundamental states as a consequence of the growth of the crystalline complex.

3.3. Magnetic measurements

Dynamic alternating current (*ac*) magnetic measurements showed that in the absence of an external field none of these complexes exhibit

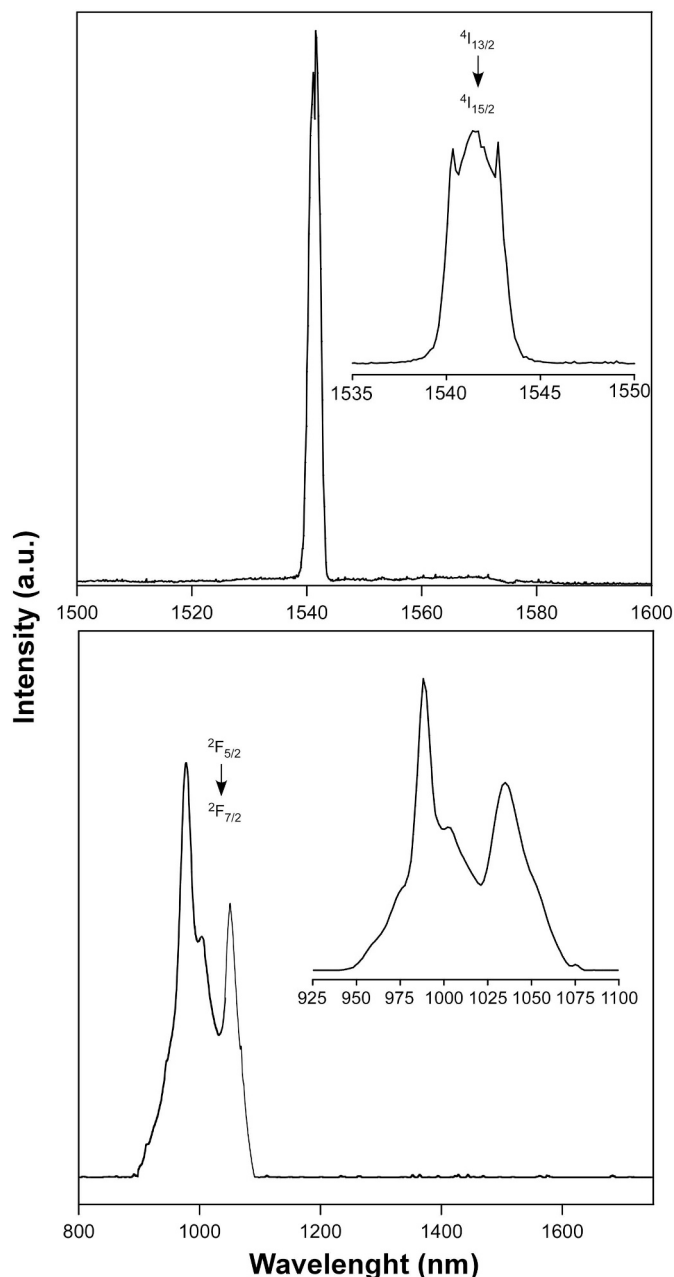


Fig. 7. 10 K emission spectra of compounds **2** and **3** collected under excitation at 325 nm showing the characteristic transitions of the corresponding lanthanide(III) ion.

frequency dependence of the out-of-phase susceptibility signals, which could be due to the lack of slow relaxation of magnetization or to the presence of quantum tunnelling of magnetization (QTM). When a small external dc field of 1000 Oe was applied to suppress QTM, the Er (**2**) counterpart showed slight frequency dependent signals (Fig. S2), whereas the Yb compound (**3**) showed characteristic signals of SMM behaviour with maxima below 6 K (Fig. 8). The fact that the terbium based compound does not show slow magnetic relaxation in contrast to isostructural Er and Yb counterparts is not surprising, but it could be attributed to the different shape of the electron density of the employed lanthanide(III) ions. In particular, Tb(III) presents an oblate density whereas Er(III) and Yb(III) ions show a prolate distribution, which fits better the coordination environment described in **1–3** [23].

However, the applied dc field of 1000 Oe is not enough to completely suppress the QTM for the Yb compound, as both χ_M' and χ_M''

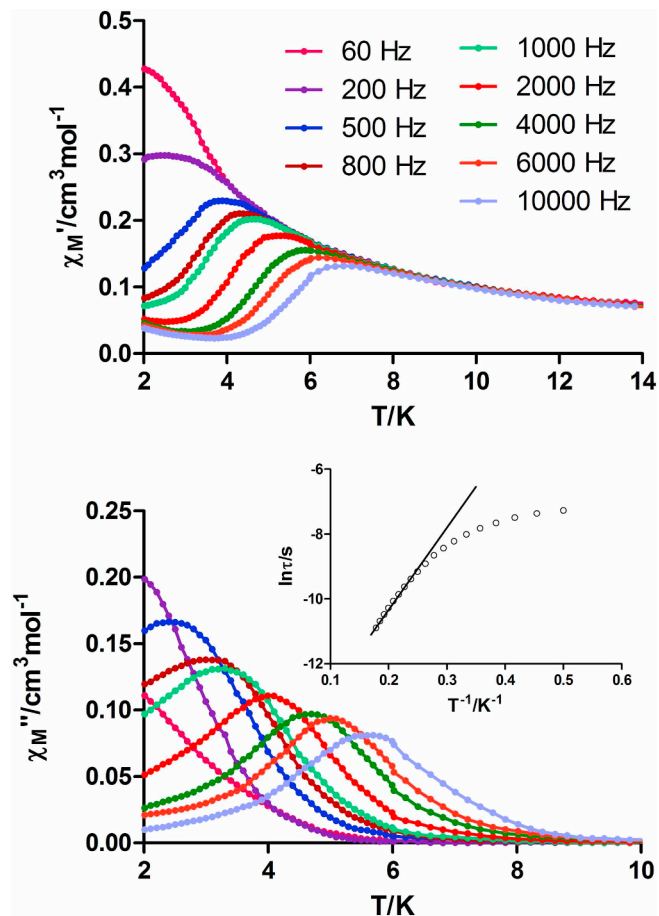


Fig. 8. Temperature dependence of in-phase (top) and out-of-phase (bottom) components of the ac susceptibility measured under 1000 Oe applied dc field for **3**. Inset: Arrhenius plots for the relaxation times.

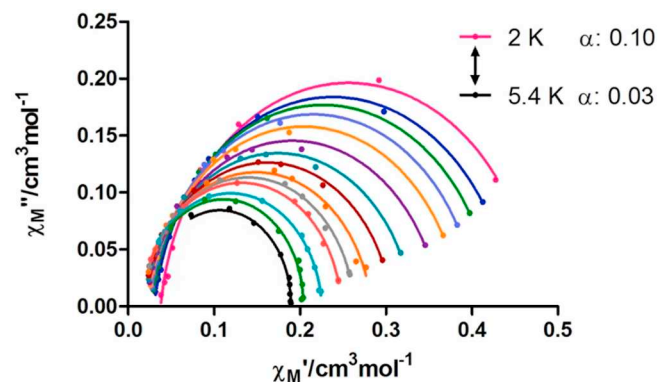


Fig. 9. Cole-Cole plots for complex **3** under an external dc field of 1000 Oe.

components of the ac signals of the highest frequencies do not go to zero below the maxima at low temperature. The Cole-Cole plots (Fig. 9), with α values in the 0.10 (2 K)–0.03 (5.4 K) range, also suggest the existence of multiple relaxation processes at least at the lowest temperatures.

The Arrhenius plot of the relaxation times affords U_{eff} and τ_0 values of 25 K and $2.2 \cdot 10^{-7}$ s, respectively, for the Orbach process (Fig. 8, inset). The obtained energy barrier is much lower than the energy gap between the ground and first excited states extracted from the photoluminescence spectra (Fig. 7), which is of 120 K. This value is obtained from the position of the first two bands in the spectra (975 and 983 nm), as these bands are related to the emissions from the $^2F_{5/2}$ multiplet to

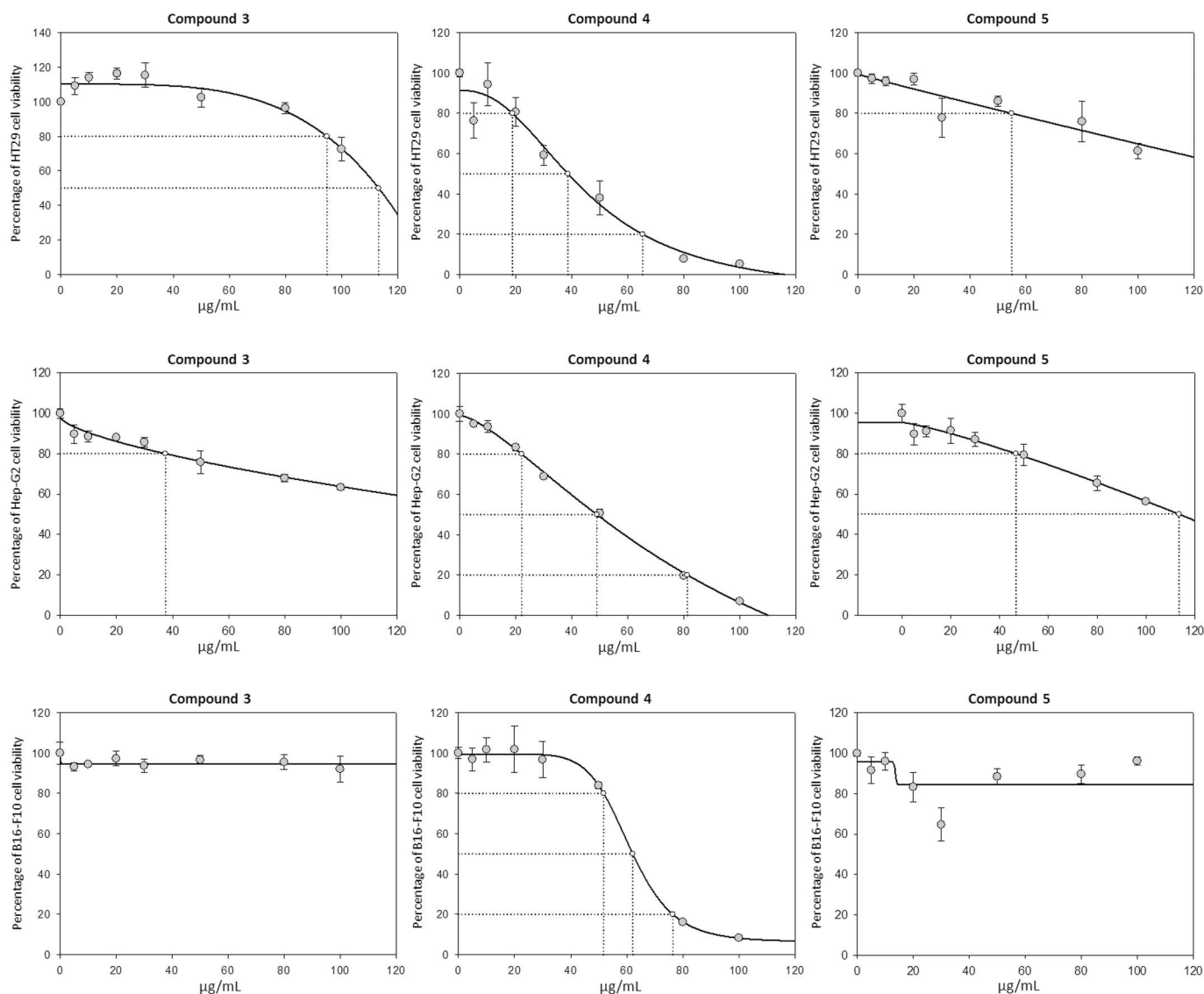


Fig. 10. Effects of compounds 3, 4 and 5, on the viability of B16-F10, HT29, and HepG2 cancer cells, after treatment with the compounds for 72 h in a range of 0 to 100 µg/mL, each point represents the mean value \pm SD of at least two independent experiments performed in triplicate.

Table 2
Growth-inhibitory effects of compound 1–5 on the three cancer cell lines.

Cell line	Comp. #	IC ₂₀	IC ₅₀	IC ₈₀
HT29	1	N/A	N/A	N/A
	2	108,75 \pm 6,37	228,64 \pm 0,00	N/A
	3	92,66 \pm 3,06	110,86 \pm 3,33	122,88 \pm 3,90
	4	18,44 \pm 5,84	38,57 \pm 4,77	65,03 \pm 4,90
	5	56,30 \pm 19,27	137,21 \pm 7,33	221,56 \pm 35,03
Hep-G2	1	N/A	N/A	N/A
	2	37,08 \pm 8,29	212,97 \pm 15,14	N/A
	3	37,55 \pm 9,25	167,10 \pm 1,34	353,44 \pm 28,27
	4	21,89 \pm 0,88	48,68 \pm 1,26	80,96 \pm 1,28
	5	46,03 \pm 12,34	113,44 \pm 0,96	174,61 \pm 18,69
B16F10	1	N/A	N/A	N/A
	2	N/A	N/A	N/A
	3	N/A	N/A	N/A
	4	51,72 \pm 0,31	62,22 \pm 0,45	76,40 \pm 0,58
	5	N/A	N/A	N/A

the ground and first excited states of the $^2F_{7/2}$ multiplet. The differences between U_{eff} and the energy gap, together with the deviation of the relaxation times from linearity, clearly suggest the presence of

additional relaxation mechanisms such as the Raman process in this compound [24].

3.4. Potential antiproliferative activities

The results showed that compound 1 does not display cytotoxicity at any assayed conditions, in any cell lines. Compounds 2 and 3 showed relative cytotoxicity in HT29 and Hep G2 cells (not in B16-F10 cells) with IC₅₀ data range between 110 and 228 µg/mL, IC₂₀ data between 37 and 108 µg/mL, and IC₈₀ data between 123 and 353 µg/mL (Fig. 11). Only Cu-complex was cytotoxic in all three cell lines assayed with IC₅₀ data between 38 and 62 µg/mL, IC₂₀ data between 18 and 51 µg/mL, and IC₈₀ between 65 and 81 µg/mL (Fig. 11). The effectiveness showed for these coordination complexes in the three cell lines assayed was similar in HT29 and HepG2 cell lines with cytotoxic effects for all compounds except for compound 1. On the other hand, in B16-F10 melanoma cells any compounds assayed showed cytotoxicity but for compound 4 (Fig. 10). The best results were obtained for compound 4 with the lowest IC₅₀ values, especially in HT29, with IC₅₀ values between 2.3 and 5.9 fold lower than the compounds 2, 3, and 5, in both HT29 and HepG2 cells. In HT29 cell line, compound 4 displays cytotoxicity at lower concentrations than compounds 2, 3 and 5, whereas in

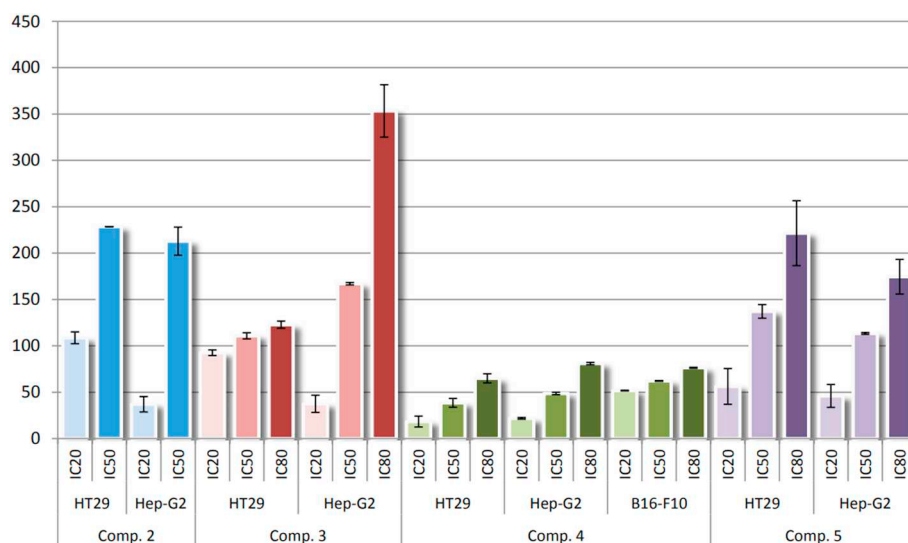


Fig. 11. Growth-inhibitory effects (IC20, IC50, and IC80, µg/mL) of compounds 2, 3, 4, and 5 on the three cancer cell lines.

HepG2 cells the onset of the cytotoxic effect were similar for all compounds (except 1), with concentrations closed 35 µg/mL (see IC20 values, Table 2). The highest cytotoxic effect was reached before for the compound 4, in both HT29 and HepG2 cells, with a concentration around 70 µg/mL, being between 1,9 to 4,3 fold lower than the rest of compounds (see IC80 values, Table 2).

In general terms, we found that the complexes with lower IC₅₀ were the materials 4 and 5 with respect to MOC complexes, with Co²⁺ and Cu²⁺ ions. MOC complexes showed a moderate cytotoxicity, with similar results for complexes with Yb³⁺ and Er³⁺ metals, in both HT29 and HepG2 cells. Nevertheless not cytotoxicity results were found for the Tb³⁺-MOC complex. With respect to cell lines only Cobalt compound produced cytotoxicity in B16-F10 murine melanoma cell line, the rest of compounds did not produce any effects on this cell line.

The fact of the relatively low cytotoxicity of several of these compounds is not a handicap, because these compounds could be used as in vivo biological probes, with the option to active or increase its cytotoxicity in respond to external magnetic field [13]. Future studies will be necessary to confirm this point. To determine the organism distribution of the compounds thinking of them as biological probes, the incident radiation must be able to penetrate the tissues to reach the chromophore, which rules UV light and part of visible spectrum [25]. Therefore it is desirable to design NIR-luminescent lanthanide complexes that produce luminescence after absorption of light at longer wavelengths. As consequence of the biological compartment of this type of compounds, which show clearly cytotoxicity in two of the three cancer cell lines assayed, that can be modulated externally with a magnetic field, and have intrinsic luminescent properties. These compounds could afford important and effective new tools for potential treatment from cancer, although more depth studies will be necessary to characterize completely its possible use as anti-cancer compounds.

4. Conclusions

We have succeeded in the design, synthesis, and characterization of the physical properties of a new family of coordination polymers based on terbium, erbium, ytterbium, cobalt and copper with the interesting 5-aminopyridine-2-carboxylic acid ligand. These lanthanide coordination polymers show isostructural 1D-structures and display intense photoluminescence properties in the solid state that have been fully characterized. The erbium material displays slightly frequency-dependent out-of-phase signals, whereas the ytterbium compound presents slow magnetic relaxation that proceeds through various relaxation

mechanisms. The absence of SMM-type behaviour in the terbium based compound seems to be related with its oblate shape, in contrast to the prolate shape of other lanthanides. The luminescence signal and potential magnetic properties of the compounds instigate their utility as multifunctional materials. On the other hand, the anti-cancer properties of these materials have been measured by MTT which show, in general, lanthanide compounds are not very active, while cobalt material (4) shows the lowest IC₅₀ values, especially in HT29, with IC₅₀ values between 2,3 to 5,9 fold all of them lower that values showed by compounds 2, 3, and 5, in both HT29 and HepG2 cells, whereas in HepG2 cells the onset of the cytotoxic effect were similar for all compounds. In conclusion, this new family of compounds could suppose important and effective new tools for potential treatment from cancer, although more depth studies will be necessary to improve its possible use as anti-cancer drugs.

Declaration of competing interest

There is not any conflict of interest.

Acknowledgements

This work has been funded by Red Guipuzcoana de Ciencia, Tecnología e Innovación (OF188/2017), University of the Basque Country (GIU 17/13), Gobierno Vasco/Eusko Jaurlaritz (IT1005-16), Junta de Andalucía (FQM-1484 and FQM-394) and the Spanish Ministry of Economy and Competitiveness (MCIU/AEI/FEDER, UE) (PGC2018-102052-A-C22, PGC2018-102052-B-C21). The authors thank for technical and human support provided by SGiker of UPV/EHU and European funding (ERDF and ESF).

Appendix A. Supplementary data

Supplementary data to this article can be found online at <https://doi.org/10.1016/j.jinorgbio.2020.111051>.

References

- [1] M.N. Leuenberger, D. Loss, *Nature* 410 (2001) 789–793.
- [2] S. Sanvito, *Chem. Soc. Rev.* 40 (2011) 3336–3355.
- [3] O.K. Farha, A.O. Yazaydn, I. Eryazici, C.D. Malliakas, B.D. Hauser, M.G. Kanatzidis, S.T. Nguyen, R.Q. Snurr, J.T. Hupp, *Nat. Chem.* 2 (2010) 944–948.
- [4] H.-Y. Li, Y.-L. Wei, X.-Y. Dong, S.-Q. Zang, T.C.W. Mak, *Chem. Mater.* 27 (2015) 1327–1334.
- [5] S. Biswas, H.S. Jena, S. Goswami, S. Sanda, S. Konar, *Cryst. Growth Des.* 14 (2014)

- 1287–1295.
- [6] P.-F. Shi, B. Zhao, G. Xiong, Y.-L. Hou, P. Cheng, *Chem. Commun.* 48 (2012) 8231–8232.
- [7] J.J. Baldov, E. Coronado, A. Gaita-Ariño, C. Gamer, M. Giménez-Marqués, G. Mínguez-Espallargas, *Chem. Eur. J.* 20 (2014) 10695–10702.
- [8] a) S. Rojas, A. Arenas-Vivo, P. Horcajada, *Coord. Chem. Rev.* 388 (2019) 202–226;
b) M. Gimenez-Marques, T. Hidalgo, C. Serre, P. Horcajada, *Coord. Chem. Rev.* 307 (2016) 342–360.
- [9] a) K.J. Haxton, H.M. Burt, *J. Pharm. Sci.* 98 (2009) 2299–2316.
- [10] J. Ruiz, A.J. Mota, A. Rodríguez-Diéguez, S. Titos, J.M. Herrera, E. Ruiz, E. Cremades, J. Pierre Costes, E. Colacio, *Chem. Commun.* 48 (2012) 7916–7918.
- [11] a) A.J. Calahorra, I. Oyarzabal, B. Fernández, J.M. Seco, T. Tian, D. Fairen-Jimenez, E. Colacio, A. Rodríguez-Diéguez, *Dalton Trans.* 45 (2016) 591–598;
b) I. Oyarzabal, B. Fernández, J. Cepeda, S. Gómez-Ruiz, A.J. Calahorra, J.M. Seco, A. Rodríguez-Diéguez, *CrystEngComm* 18 (2016) 3055–3063;
c) A.A. García-Valdivia, J.M. Seco, J. Cepeda, A. Rodríguez-Diéguez, *Inorg.Chem* 56 (2017) 13897–13912.
- [12] B. Fernandez, I. Oyarzabal, E. Fischer-Fodor, S. Macavei, I. Sanchez, J.M. Seco, S. Gomez-Ruiz, A. Rodríguez-Diéguez, *Crystengcomm* 18 (2016) 8718–8721.
- [13] A. Mayer, S. Neuenhofer, *Angew. Chem. Int. Ed.* 33 (1994) 1044–1072.
- [14] B. Fernández, I. Fernández, J. Cepeda, M. Medina-O'Donnell, E.E. Rufino-Palomares, A. Raya-Barón, S. Gómez-Ruiz, A. Pérez-Jiménez, J. Antonio Lupiáñez, F.J. Reyes-Zurita, A. Rodríguez-Diéguez, *Cryst.GrowthDes* 18 (2018) 969–978.
- [15] a) E.E. Rufino-Palomares, A. Perez-Jimenez, F.J. Reyes-Zurita, L. Garcia-Salguero, K. Mokhtari, A. Herrera-Merchan, P.P. Medina, J. Peragon, J.A. Lupianez, *Curr. Org. Chem.* 19 (2015) 919–947;
b) M. Medina-O'Donnell, F. Rivas, F.J. Reyes-Zurita, A. Martinez, S. Martin-Fonseca, A. Garcia-Granados, R.M. Ferrer-Martin, J.A. Lupianez, A. Parra, *Eur. J. Med. Chem.* 118 (2016) 64–78.
- [16] B. Fernández, A. Gómez-Vílchez, C. Sánchez-González, J. Bayón, E. San Sebastián, S. Gómez-Ruiz, C. López-Chaves, P. Aranda, J. Llopis, A. Rodríguez-Diéguez, *New J. Chem.* 40 (2016) 5387–5393.
- [17] L. Krause, R. Herbst-Irmer, G.M. Sheldrick, D. Stalke, *J. Appl. Crystallogr.* 48 (2015) 3–10.
- [18] G.M. Sheldrick, *Acta Cryst A* 64 (2008) 112–122.
- [19] O.V. Dolomanov, L.J. Bourhis, R.J. Gildea, J.A.K. Howard, H. Puschmann, *J. Appl. Crystallogr.* 42 (2009) 339–341.
- [20] A.L. Spek, *Acta Cryst D* 65 (2009) 148–155.
- [21] M. Llunell, D. Casanova, J. Girera, J.M. Bofill, P. Alemany, S. Alvarez, M. Pinsky, D. Avnir, SHAPE, v1.1b; Barcelona, Spain, (2005).
- [22] D. Josse, W.H. Xie, P. Masson, L.M. Schopfer, O. Lockridge, *Chem. Biol. Interact.* 119 (1999) 79–84.
- [23] a) A. Gorzynski, D. Marcinkowski, M. Kubicki, M. Loffler, M. Korabik, M. Karbowiak, P. Wisniewski, C. Rudowicz, V. Patroniak, *Inorg. Chem. Front.* 5 (2018) 605–618;
b) K.R. Vignesh, S.K. Langley, A. Swain, B. Moubaraki, M. Damjanovic, W. Wernsdorfer, G. Rajaraman, K.S. Murray, *Angew. Chem. Int. Ed.* 57 (2018) 779–784.
- [24] a) J. Ruiz, G. Lorusso, M. Evangelisti, E.K. Brechin, S.J. Pope, E. Colacio, *Inorg. Chem.* 53 (2014) 3586–3594;
b) I. Oyarzabal, B. Artetxe, A. Rodríguez-Diéguez, J.A. García, J.M. Seco, E. Colacio, *Dalton Trans.* 45 (2016) 9712–9726;
c) A. Zabala, J. Cepeda, I. Oyarzabal, A. Rodríguez-Diéguez, J.A. Garcia, J.M. Seco, E. Colacio, *CrystEngComm* 19 (2017) 256–264.
- [25] N.M. Shavaleev, G. Accorsi, D. Virgili, Z.R. Bell, T. Lazarides, G. Calogero, N. Armaroli, M.D. Ward, *Inorg. Chem.* 44 (2005) 61–72.



OPEN

Magnetic and Photoluminescent Sensors Based on Metal-Organic Frameworks Built up from 2-aminoisonicotinate

Antonio A. García-Valdivia¹, Sonia Pérez-Yáñez², Jose A. García³, Belén Fernández⁴, Javier Cepeda⁵✉ & Antonio Rodríguez-Diéguez¹✉

In this work, three isostructural metal-organic frameworks based on first row transition metal ions and 2-aminoisonicotinate (2ain) ligands, namely, $[[M(\mu\text{-}2\text{ain})_2]\cdot\text{DMF}]_n$ [$M^{\text{II}} = \text{Co}$ (1), Ni (2), Zn (3)], are evaluated for their sensing capacity of various solvents and metal ions by monitoring the modulation of their magnetic and photoluminescence properties. The crystal structure consists of an open diamond-like topological 3D framework that leaves huge voids, which allows crystallizing two-fold interpenetrated architecture that still retains large porosity. Magnetic measurements performed on 1 reveal the occurrence of field-induced spin-glass behaviour characterized by a frequency-independent relaxation. Solvent-exchange experiments lead successfully to the replacement of lattice molecules by DMSO and MeOH, which, on its part, show dominating SIM behaviour with low blocking temperatures but substantially high energy barriers for the reversal of the magnetization. Photoluminescence studied at variable temperature on compound 3 show its capacity to provide bright blue emission under UV excitation, which proceeds through a ligand-centred charge transfer mechanism as confirmed by time-dependent DFT calculations. Turn-off and/or shift of the emission is observed for suspensions of 3 in different solvents and aqueous solutions containing metal ions.

The multifunctionalization of metal-organic frameworks (MOFs) has recently become one of the main research strategies of inorganic and materials chemistry to guide the construction of materials with sensing capacities^{1–3}. This is a consequence of the capacity of these materials to allow for multiple physical properties which may coexist or even cooperate in a synergistic way^{4,5}. As it is well known, MOFs are a class of potentially porous materials comprised of single metal ions or metal ion clusters linked one another by organic ligands to give an extended crystalline architecture^{6–8}. The variety of metal ions and organic ligands opens up an infinite number of possible combinations which allow designing MOFs almost at will in such a way that their structure responds to a particular commitment^{9–15}. In particular, the rapid detection of toxic species in environmental and ecological systems is gaining increasing interest because of the large overlap existing between residential and surrounding industrial areas, which already causes many diseases in human being and tends to be expanded in near future¹⁶. For instance, various salts containing Fe^{3+} and Cu^{2+} ions, usually employed in industry, are eventually found in rivers and streams damaging those ecosystems¹⁷. The same applies for some common solvents referred to as volatile organic compounds (VOCs) that are air and water pollutants and cause severe environmental problems¹⁸. In this regard, MOFs are good candidates to drive the detection of all above mentioned molecules in liquid media owing to their specific functions bearing on the surface of the pores, since they are known to show interactions able to provide a reversible load/unload on the material and, hence, a significant change in a property^{19,20}.

¹Departamento de Química Inorgánica, Facultad de Ciencias, Universidad de Granada, 18071, Granada, Spain.

²Departamento de Química Inorgánica, Facultad de Farmacia, Universidad del País Vasco/Euskal Herriko Unibertsitatea (UPV/EHU), 01006, Vitoria, Spain. ³Departamento de Física Aplicada II, Facultad de Ciencia y Tecnología, Universidad del País Vasco/Euskal Herriko Unibertsitatea (UPV/EHU), 48940, Leioa, Spain. ⁴Institute of Parasitology and Biomedicine "López-Neyra", CSIC, Av. Conocimiento s/n, 18600, Granada, Spain. ⁵Departamento de Química Aplicada, Facultad de Química, Universidad del País Vasco/Euskal Herriko Unibertsitatea (UPV/EHU), 20018, Donostia-San Sebastian, Spain. ✉e-mail: javier.cepeda@ehu.es; antonio5@ugr.es

Focusing on the sensor activity of the MOFs, the transduction mechanism by which the material manifests a change in a property when the target analyte is uploaded is undoubtedly a key point. Most of the systems studied so far are based on luminescence detection because, making use of the changes (increase/decrease on the intensity or shift of the emission signal) in the photoluminescence (PL) of a probe MOF provoked by the presence of the analyte, is very desired for its relative ease of use, technical simplicity and broad adaptability²¹. Moreover, PL in MOFs can have multiple origins which proceed through a complex electronic excitation/emission scenario in which different parts of the hybrid structure are involved: ligand centred (LC) and metal centred (MC) luminescence, charge transfers (CT) processes with different electron pathways, such as ligand-to-ligand (LLCT), ligand-to-metal (LMCT), metal-to-ligand (MLCT), or even guest molecules centred (GC) charge transfers²². To that end, a promising strategy argues for the use of organic ligands with strong absorption (usually aromatic molecules with functionalities containing heteroatoms with lone-pairs) combined with metal ions with closed-shell electronic configuration, which avoid non-radiative quenching^{23,24}. Although comparatively less explored than PL sensing, a magnetic response dependent on different guest molecules, that is the change of the magnetic molecular properties of the MOF as a consequence of the analyte loaded in the voids, is an already plausible alternative despite the more complex technical requirements implied²⁵. MOFs behaving as single-molecule magnets (SMMs) below a blocking temperature (T_B) consist of isolated spin carriers with large magnetic anisotropy which present no (or negligible) magnetic ordering by means of weak intermetallic exchange interactions^{26–28}. For transition metals, spin-reversal barrier that promotes slow magnetic relaxation is $U = |D| (S^2 - 1/4)$, where D and S stand for the ground state half-integer spin and axial parameter of the zero-field splitting (zfs). That is the reason why cobalt(II) systems, with not only high and non-integer ground state ($S = 3/2$) which reduces the probability of the quantum tunnelling of magnetization (QTM) but also large magnetic anisotropy, have been most widely studied during the last years^{29–31}.

In our continuous quest for metal-organic materials showing enhanced PL and magnetic properties, such as those recently reported based on aminonicotinic ligands^{32–34}, we are now giving a step forward and combining one of the latter properties with the porosity afforded by the family of isostructural MOFs of $\{[M(\mu\text{-}2\text{ain})_2]\cdot\text{DMF}\}_n$ (where $M^{\text{II}} = \text{Co}, \text{Ni}$ and Zn and $2\text{ain} = 2\text{-aminoisonicotinate}$) formulae. In particular, given that the porous nature of these materials was already confirmed by gas adsorption capacity and the fact that in those previous reports these MOFs crystallized with different solvents occupying the voids³⁵, magnetic behaviour of the cobalt(II) counterpart and PL performance of the zinc(II) counterpart have been deeply analysed, focusing on their modulation by solvent-exchange experiments and/or capture of metal ions.

Results and Discussion

Structural description of $\{[M(\mu\text{-}2\text{ain})_2]\cdot\text{DMF}\}_n$ [$M^{\text{II}} = \text{Co}$ (1), Ni (2), Zn (3)]. Title compounds are isostructural and crystallize in the orthorhombic $Fddd$ space group so their structure will be described using compound **2** as a reference. The crystal structure consists of an entangled 3D open framework. Ni1 exhibits a N_2O_4 donor set exerted by its coordination to four symmetry related 2ain ligands by means of two pyridine nitrogen and four carboxylate oxygen atoms (Table 1 and Fig. 1). Given that the latter establish two four-member chelating rings with the metal centre, the resulting coordination polyhedron is severely distorted with regard to a perfect octahedron ($S_{\text{OC}} = 3.43$). It must be highlighted that bond distances are clearly more irregular in the coordination shell of compounds **1** and **3**, which translates into more distorted octahedra ($S_{\text{OC}} = 4.41$ and 4.96 for **1** and **3**, respectively; see ESI).

2ain anions acquire the $\mu\text{-}\kappa\text{NIA}:\kappa^2\text{O71A}, \text{O72A}$ bridging mode in such a way that the central Ni1 atom is connected to four neighbouring ones at a distance of *ca.* 8.77 Å. This coordination mode makes the ligands be somewhat twisted by breaking the planarity of the carboxylate group with respect to the aromatic ring (significantly rotated with an angle of *ca.* 15.9°), which, in turn, gives rise to a tetrahedral building unit from the topological point of view. This arrangement is supported by strong N–H...O hydrogen bonds established among amino and carboxylate groups of 2ain ligands. The junction of building units leads to an open 3D framework of **dia** topological class and (6^6) point symbol^{36,37} which contains very large cavities where a sphere of 8 Å fits in within (Fig. S2). Nonetheless, the occurrence of such a large free volume allows the crystallization of an identical subnet, which drops the porosity of the eventual doubly-interpenetrated framework to a 36.1% of the unit cell volume (Fig. 2). Both subnets are mutually sustained by means of hydrogen bonding interactions among the exocyclic amino and carboxylate groups belonging to different subnets (see Table S1 and Fig. S3). These supramolecular interactions allows for the occurrence of a stable porous system which consists of narrow microchannels running along the crystallographic a axis. Despite the large disorder affecting the lattice solvent molecules occupying the voids, a careful analysis by both TGA/DTA and SQUEEZE routine results confirm that the content of the voids may be determined as one DMF molecule per formula unit (see sections S4 and S5 in the ESI for further detail)³⁸. A further analysis of the compound by means of thermogravimetry shows that the release of solvent molecules does not bring any relevant structural change, as confirmed by the similar shape of the diffractograms recorded according to the increasing temperature.

Static magnetic properties. Variable temperature dependence of the magnetic susceptibility data were analysed in the 2–300 K range on polycrystalline samples of compounds **1** and **2**. Room temperature $\chi_M T$ product of **1** is $3.22 \text{ cm}^3 \text{ K mol}^{-1}$, which is significantly higher than that expected for a magnetically isolated spin triplet ($g = 2.01$) in octahedral coordination geometry ($1.87 \text{ cm}^3 \text{ K mol}^{-1}$). Upon cooling, $\chi_M T$ value experiments a slight and progressive decrease up to 50 K, below which it subtly drops off to reach $1.85 \text{ cm}^3 \text{ K mol}^{-1}$ at low temperature. This behaviour may be mainly attributed to the zfs that may cause a high intrinsic magnetic anisotropy arising from the first order spin-orbit coupling (SOC) usually present in Co(II) atoms derived from its $^4T_{1g}$ ground state in high-spin octahedral geometry^{39,40}, though the occurrence of weak antiferromagnetic interactions cannot be discarded. Taking into account the absence of an appropriate mathematical expression to estimate the

Compound 1					
Co1–N1A	2.073(1)	Co1–O71A(v)	2.314(1)	Co1–O72A(v)	2.060(1)
Co1–N1A(iv)	2.073(1)	Co1–O71A(vi)	2.314(1)	Co1–O72A(vi)	2.060(1)
Compound 2					
Ni1–N1A	2.060(1)	Ni1–O71A(ii)	2.075(1)	Ni1–O72A(ii)	2.178(1)
Ni1–N1A(i)	2.060(1)	Ni1–O71A(iii)	2.075(1)	Ni1–O72A(iii)	2.178(1)
Compound 3					
Zn1–N1A	2.063(1)	Zn1–O71A(v)	2.034(1)	Zn1–O72A(v)	2.472(1)
Zn1–N1A(iv)	2.063(1)	Zn1–O71A(vi)	2.034(1)	Zn1–O72A(vi)	2.472(1)

Table 1. Selected bond lengths for all compound. [a] Symmetries: (i) $-x - 1/4, y, -z + 3/4$; (ii) $x + 1/4, y + 1/4, -z + 1$; (iii) $-x - 1/2, y + 7/4, z - 1/4$; (iv) $-x + 5/4, y, -z + 1/4$; (v) $x + 7/4, y + 7/4, -z$; (vi) $-x, y + 7/4, z + 7/4$.

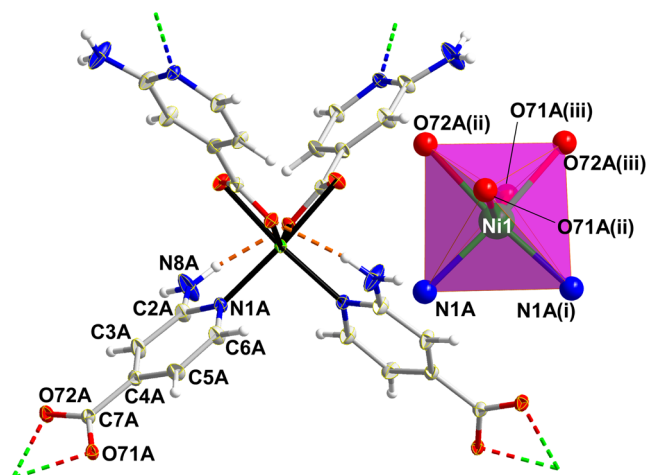


Figure 1. Fragment of crystal structure of compound 2 showing labelling mode and the distorted octahedral coordination environment (inset). Connectivity of the structure is inferred by dashed double-colour lines whereas dashed orange lines stand for hydrogen bonds.

nature of the magnetic interactions for 3D networks containing cobalt(II) ions, the data were analysed with the Curie–Weiss law. Given the fact that compound 1 follows Curie–Weiss law in the whole temperature range, χ_M^{-1} vs T was fitted giving the results shown in Table 2 (see also ESI). Moreover, the data were also fitted to the phenomenological equation proposed by Rueff and co-workers⁴¹ (Eq. 1) in view of the SOC present, from which the antiferromagnetic exchange interactions were estimated:

$$\chi_M T = A \exp(-E_1/\kappa T) + B \exp(-E_2/\kappa T) \quad (1)$$

The fact that the sum of A and B parameters equals the Curie constant and that “activation energies” of SOC (E_1) and (E_2) exchange interactions (see Table 2) fall in the range of related Co(II) compounds⁴², weak antiferromagnetic interactions may be claimed to occur among Co(II) ions in the 3D network.

DFT calculations performed on a suitable model of compound 1 (see Fig. S21) give a value of the coupling constant (J) of -0.07 cm^{-1} , which concords well with the mentioned negligible magnetic interactions. Accordingly, cobalt(II) spin carriers may be considered to be isolated by the regular bridging ligands, bearing in mind that the shortest distance among them is of about 8.8 \AA , thus allowing us to analyse the SOC effects by means of fitting of the magnetic susceptibility with the Hamiltonian given in Eq. 2⁴³:

$$\hat{H} = \sigma \lambda (L_{Co} S_{Co}) + \Delta [L_{z, Co}^2 - L_{Co} (L_{Co} + 1)]/3 + \mu_B H \cdot (-\sigma L_{Co} + g S_{Co}) \quad (2)$$

where all parameter have their usual meaning. The calculated curve using the PHI program⁴⁴ reproduces quite well the experimental one, though a slight deviation is found mainly for the high temperature data (see Table 2 and Fig. 3a).

Among the estimated parameters, it deserves to be mentioned the large and positive value of Δ , which suggests that only the two lowest Kramers doublets of the 4A_2 ground term are thermally populated, in turn meaning that the axial zfs within the quartet state matches well with the energy gap existing between them. Therefore, the magnetic properties may be interpreted by means of the spin Hamiltonian of Eq. 3 (Fig. 3b):

$$\hat{H} = D(\hat{S}_z^2 - \hat{S}^2/3) + E(\hat{S}_x^2 + \hat{S}_y^2) + \mu_B \vec{B} \cdot g \cdot \hat{S} \quad (3)$$

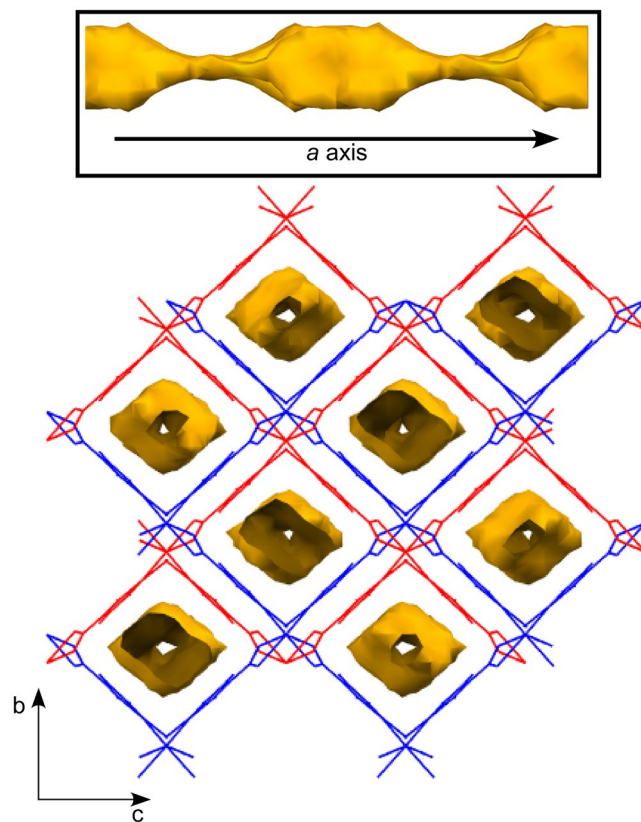


Figure 2. Crystal packing of compound 2 showing the two-fold interpenetrated structure and the microchannels.

Curie-Weiss law fitting ^a							
<i>C</i>	3.27	θ	-7.52 K				
Rueff phenomenological fitting (Eq. 1)							
<i>A</i>	0.93(4)	<i>B</i>	2.34(5)	E_1/κ	23(2)	$-E_2/\kappa$	-0.80(9)
Hamiltonian SOC (Eq. 2) ^b							
λ	-110	σ	-1.12	Δ	188	<i>g</i>	2.10
Hamiltonian <i>zfs</i> (Eq. 3) ^c							
g_x/g_y	2.36	g_z	3.26	<i>D</i>	-11.9		

Table 2. Best fitting results for compound 1. [a] Units: *C* constant and θ are given in $\text{cm}^3 \text{K mol}^{-1}$ and K, respectively. [b] λ and Δ parameters are expressed in cm^{-1} . [c] *D* parameter is given in cm^{-1} .

in which *S* is the spin of the ground state ($S = 3/2$), *D* and *E* are the axial and rhombic magnetic anisotropies, and *H* is the applied magnetic field. On its part, magnetization curves collected at several temperatures (2–7 K) under an applied field ranging from 0 to 7 T do not reach the theoretical saturation for $S = 3/2$ ($M_{\text{sat}} = 3.3$, with $g = 2.2$), but they show a value of ca. $2.45 N_{\mu_B}$ at 2 K. This behaviour together with the fact that isothermal curves do not collapse in a single master curve are indicative of magnetic anisotropy. A simultaneous fitting of susceptibility and magnetization data with PHI using Eq. 3 gives $D = -16.1 \text{ cm}^{-1}$, $E = -0.1 \text{ cm}^{-1}$, and $g = 2.29$, whereas the fitting was substantially improved by allowing a slightly anisotropic gyromagnetic tensor, such that the values found in Table 2 were achieved with an $R = 8.5 \times 10^{-4}$. Assuming an axial anisotropy, being $E \approx 0$, the energy separation between $\pm 1/2$ and $\pm 3/2$ doublets equals $2D$ due to the second-order SOC present in the distorted octahedral Co(II) ion.

$\chi_M T$ vs *T* plot of compound 2 shows a room temperature $\chi_M T$ value ($1.11 \text{ cm}^3 \text{ mol}^{-1} \text{ K}$) close to that expected for an isolated ion ($1.00 \text{ cm}^3 \text{ mol}^{-1} \text{ K}$ with $g = 2.01$, see Fig. 4). This curve shows a plateau from room temperature up to 25 K, where it experiments an abrupt drop up to $0.85 \text{ cm}^3 \text{ K mol}^{-1}$ at 5 K, probably due to the occurrence of *zfs* and weak antiferromagnetic interactions, which may be assumed given that the shortest 2ain mediated Ni...Ni distance along the network is of the same order of the cobalt(II) counterpart (larger than 8.7 Å) and the absence of significant π - π stacking interactions between the subnets (where Ni...Ni separations of ca. 8 Å are found). In this sense, the computed broken symmetry procedure upon model 2 supports the weak antiferromagnetic nature of

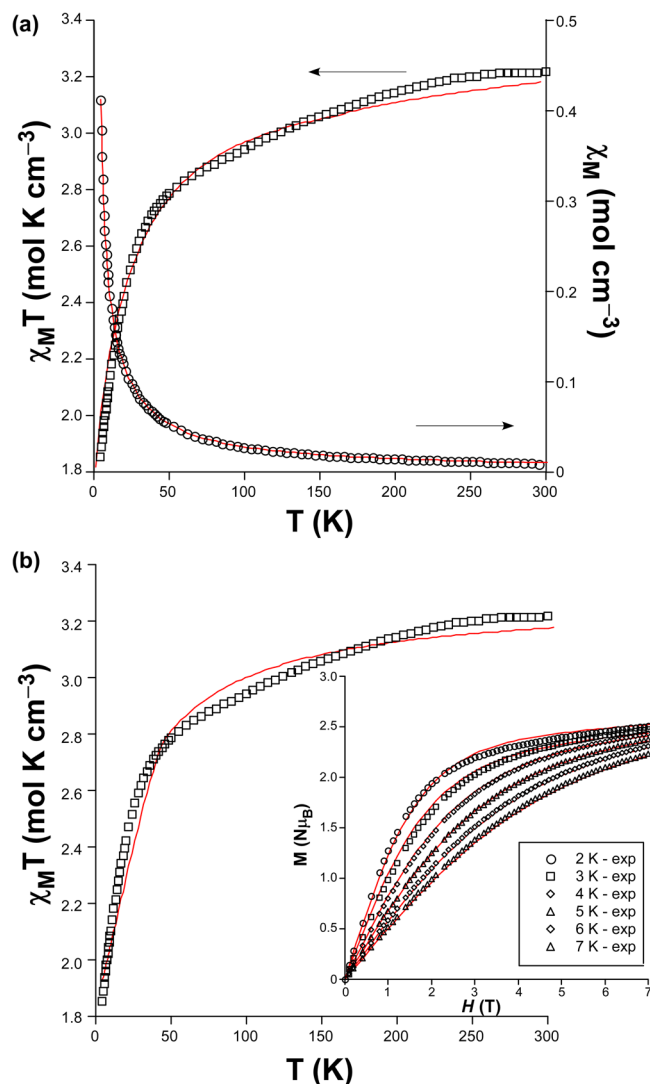


Figure 3. (a) χ_M (o) and $\chi_M T$ (\square) vs T plots of **1** with best fit according to Eq. 2. (b) Simultaneous fitting of the $\chi_M T$ vs T and M vs H (inset) plots using Eq. 3.

the intramolecular exchange interaction ($J = -0.55$). Accordingly, the experimental $\chi_M T$ vs T data were fitted with the Hamiltonian shown in Eq. 3 with PHI, from which the following set of parameters were achieved: $g_{\text{iso}} = 2.11$ and $D = -4.4 \text{ cm}^{-1}$ (with a negligible value of $E < 0.1 \text{ cm}^{-1}$) with $R = 4.6 \times 10^{-5}$. It is worth noticing that the value of D lies within the range found for similar octahedral Ni^{II} complexes⁴⁵.

Dynamic magnetic properties. The magnetic anisotropy found for compounds **1** and **2** prompted us to study their spin dynamics by means of *ac* magnetic susceptibility measurements (using an alternating field of 3.5 Oe). Compound **1** exhibited a slight frequency-dependent signal although the maxima remained below 2 K when applying a zero *dc* field, which did not allow further fitting of the data (Fig. S16). This behaviour seems to indicate that magnetic relaxation proceeds through a fast quantum tunnelling (QTM) derived from intramolecular and/or strong hyperfine interactions occurring with the $I = 7/2$ nuclear spin of the Co(II) atom^{29d,46}. Interestingly, when a *dc* field of 1 kOe is applied, compound **1** shows temperature-dependent in-phase (χ_M') and out-of-phase (χ_M'') signals (Fig. 5), whereas QTM could not be suppressed for compound **2** so no frequency dependence was observed. A first inspection of the *ac* data of **1** reveals that χ_M'' signals peaking at ca. 10 K present a remarkable width, mainly for the low frequency regime (60–1000 Hz), which makes one suspect about the occurrence of two consecutive and overlapped maxima. In any case, the most remarkable feature of the *ac* signals is clearly the fact both peaks (χ_M' and χ_M'') are weakly dependent of the frequency. In fact, the frequency shift calculated as $\phi = \Delta T_p / [T_p \Delta(\log f)]$ (where T_p corresponds to the peak of $\chi_M''(T)$ curve and f to the frequency) gives a low value of 0.03, which is a common value for spin glasses ($\phi < 0.1$)^{47,48}. Accordingly, relaxation times (τ) estimated from the $\tau = 1/(2\pi f_{\text{max}})$ expression based on $\chi_M''(T)$ peak give thermally activated relaxations with $\tau_0 = 9.4 \times 10^{-33}$ s and $U = 660$ K, values that agree well with those recorded for other reported spin-glass materials with slow dynamics^{49,50}. At this point, it must be highlighted that this sort of glass-like magnetic behaviour is

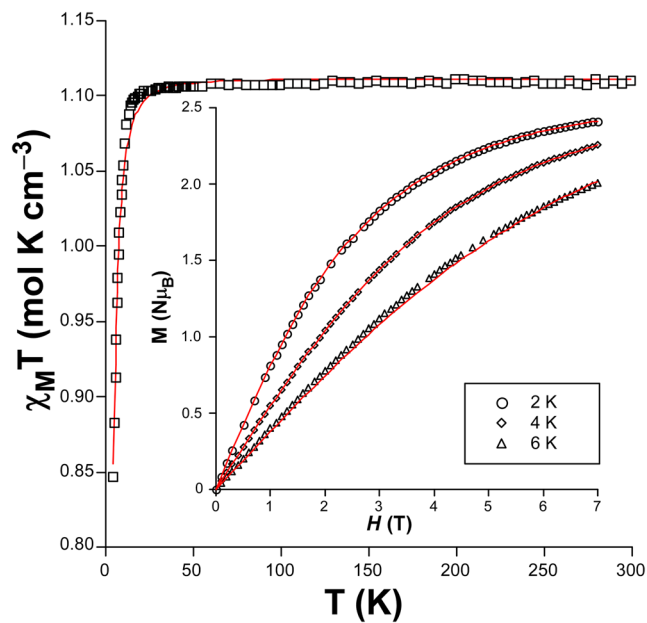


Figure 4. Simultaneous fitting of the $\chi_M T$ vs T and M vs H (inset) plots using Eq. 3 for compound 2.

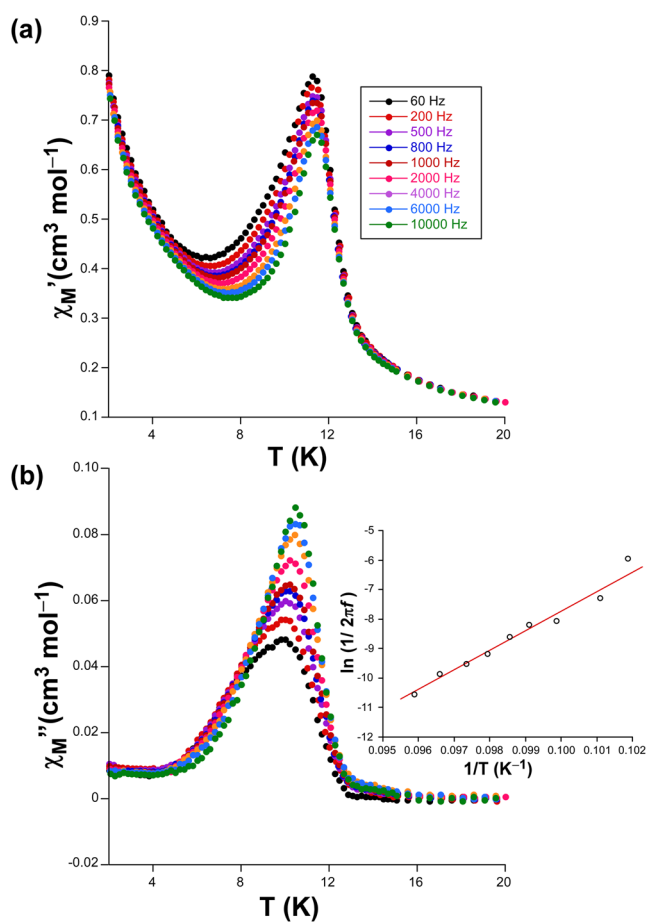


Figure 5. Temperature dependence of the (a) χ_M' and (b) χ_M'' signals for compound 1 under an applied field of 1000 Oe. Inset shows the Arrhenius plot with the linear fitting to estimate the thermal barrier for the reversal of the magnetization.

usually related to a field-dependence behaviour (derived from canted antiferromagnetism or long-ranged magnetic ordering) which, yet not observed in *dc* measurements, could be the present case in view of the chiral structure being comprised of two 3D sublattices. However, the fact that a weak SIM behaviour could be overlapped by the dominating glassy-state, in view of the width of the signal, is not to be fully discarded.

Solvent-dependent magnetic behaviour of compound 1. Solvent-exchange experiments were accomplished upon polycrystalline sample of compound **1** in view of its intriguing magnetic behaviour and potentially porous nature, which could a priori endow the material with a guest (solvent)-dependent magnetism. Two different solvents, such as DMSO and MeOH, were selected not only for their common use in the synthesis of MOFs but also for their hazardous nature. The exchange of lattice solvent molecules was successfully achieved by immersing fresh sample of **1** into 10 mL of the solvent and letting it to stand for two days under a soft stirring, which led to the isomorphous compounds $\{[\text{Co}(\mu\text{-2ain})_2]_2\cdot 2\text{MeOH}\}_n$ (**1-MeOH**) and $\{[\text{Co}(\mu\text{-2ain})_2]_2\cdot 1.5\text{DMSO}\}_n$ (**1-DMSO**). Note that the proposed formula was confirmed by elemental analyses, ICP/AES, and TG/DTA experiments (see ESI). Though both compounds retain the crystalline framework to a large extent, they experience some slight changes due to the replacement of the pore molecules. A careful evaluation of the cell parameters shows a common trend: *a* and *b* axes are shrunk whereas *c* is stretched. This behaviour seems to indicate that pore channels are somewhat crushed when replacing the DMF molecules by DMSO and MeOH, respectively for **1-DMSO** and **1-MeOH**, a fact that points to a relative displacement of the subnetworks. The analysis of the *dc* properties of the exchanged MOFs reveals a similar magnetic behaviour with progressive decrease of the $\chi_M T$ product as the temperature drops. Nonetheless, a larger magnetic anisotropy may be inferred from the steepest decrease of $\chi_M T$ in **1-DMSO** compared to **1-MeOH** together with the larger separation between magnetization curves. In fact, mathematical fitting of the data with above mentioned Eqs. 2 and 3 come to the same conclusion supporting a small increase of the axial parameter ($D = -20$ for **1-DMSO** and -16 cm^{-1} for **1-MeOH**, compared to -11.9 cm^{-1} for **1**). Even more exciting is the fact that such an increase in the anisotropy is accompanied by a deep change of the magnetic nature of the materials, since they can be now referred to as SIMs⁵¹ under an external *dc* of 1000 Oe (no signal is observed with zero field) given their strong frequency-dependent χ_M'' signal. Moreover, it must be also noticed that these maxima become narrower than those shown by the neat compound (Fig. 6).

At first sight, the blocking temperature (below which the compounds behave as a SIM) drops down in both cases, among which **1-DMSO** presents well-defined maxima only those curves with an oscillating frequency above 1000 Hz. Instead, the maxima are much closer to each other for **1-DMSO** rather than **1-MeOH**, from which it is deduced that a faster magnetic relaxation occurs in the former. The Cole-Cole plots below 3.4 K for **1-DMSO** and 4.2 K for **1-MeOH** can be well fitted by a generalized Debye function, which it is an important difference with respect to double semicircles shown by pristine compound **1**, where α values ranging in 0.17–0.29 and 0.10–0.26 are found, respectively for **1-DMSO** and **1-MeOH** (Figs. S18 and 19). These values, implying a wide distribution of the relaxation times, are indicative of the occurrence of various mechanisms in the relaxation of the magnetization. In fact, Arrhenius plots in the form of $\ln(\tau)$ vs T^{-1} deviate from linearity at low temperature in both cases. Fitting of the high temperature data by means of Orbach process gives values of the effective barrier and pre-exponential factors of $U_{\text{eff}} = 65.3 \text{ K}$ (45.7 cm^{-1}) and $\tau_0 = 1.36 \times 10^{-12} \text{ s}$ for **1-DMSO** and 43.9 K (30.7 cm^{-1}) and $\tau_0 = 1.54 \times 10^{-9} \text{ s}$ for **1-MeOH**, which are somewhat higher than those reported for most of polymeric metal-organic compounds behaving as SIMs²⁶. Note also that these energy barriers agree with the expected energy separation between Kramers doublet ($2D = 32 \approx 30.7 \text{ cm}^{-1}$ for **1-MeOH** and $2D = 40 \approx 45.7 \text{ cm}^{-1}$ for **1-DMSO**). However, it must be highlighted that the rise of the energy barrier is linked to the relaxation rate, among which the τ_0 of $1.36 \times 10^{-12} \text{ s}$ estimated for **1-DMSO** clearly exceeds the usual range (between 10^{-6} – $1 \times 10^{-11} \text{ s}$) attributed to Co(II)-based SIMs. This fact that comes to conclude that the exchange of DMSO in the pores modifies the disposition of the subnetworks such that spin carriers can probably interact through intermolecular interactions, explaining the more abrupt drop in the $\chi_M T$ vs *T* curve (see Fig. S15). On another level, very reliable fittings were achieved by combining the Orbach with Raman and/or direct relaxation processes (Eq. 4 and/or 5), which have previously been employed successfully in the analysis of Co(II)-based compounds with related coordination environment^{32d,52}.

$$\tau^{-1} = A_{\text{direct}} T + B_{\text{Raman}} T^n + \tau_0^{-1} \exp(-U_{\text{eff}}/\kappa_B T) \quad (4)$$

$$\tau^{-1} = B_{\text{Raman}} T^n + \tau_0^{-1} \exp(-U_{\text{eff}}/\kappa_B T) \quad (5)$$

Best fitting with the multiple relaxation processes gives $U_{\text{eff}} = 83.4 \text{ K}$ (58.4 cm^{-1}), $\tau_0 = 1.45 \times 10^{-14} \text{ s}$, $A_{\text{direct}} = 1190(30) \text{ s}^{-1} \text{ K}^{-1}$, $B_{\text{Raman}} = 4.1(2) \text{ s}^{-1}$, $n = 7.8(1)$ for **1-DMSO** and $U_{\text{eff}} = 72.8 \text{ K}$ (51.0 cm^{-1}), $\tau_0 = 6.12 \times 10^{-10} \text{ s}$, $B_{\text{Raman}} = 8.7(2) \text{ s}^{-1}$, $n = 4.1(2)$ for **1-MeOH**.

Photoluminescence properties of compound 3. Excitation and emission spectra were measured on polycrystalline sample of compound **3** since, being comprised of carboxylic pyridine ligands such as 2ain and metal ions with closed-shell electronic configuration, i.e. Zn(II), it is capable of unveiling interesting photoluminescence in solid state. The emission spectrum under UV light (at the shoulder $\lambda_{\text{ex}} = 305 \text{ nm}$) at room temperature (295 K) shows a somewhat narrow band, composed of the maxima ($\lambda_{\text{em}} = 390 \text{ nm}$) and a shoulder ($\lambda_{\text{em}} = 405 \text{ nm}$), in addition to a wide and weaker band peaking around 550 nm (Fig. 7a). The excitation spectra recorded at the main emission wavelength contains, in addition to the previous shoulder at 305 nm, another main contribution peaking at $\lambda_{\text{ex}} = 370 \text{ nm}$, which shows the same PL mechanism in view of the identical emission spectrum achieved at the latter excitation wavelength (Fig. S22). To further investigate the origin of the less energetic band at $\lambda_{\text{em}} = 550 \text{ nm}$, an excitation spectrum has been also measured, confirming that it arises from

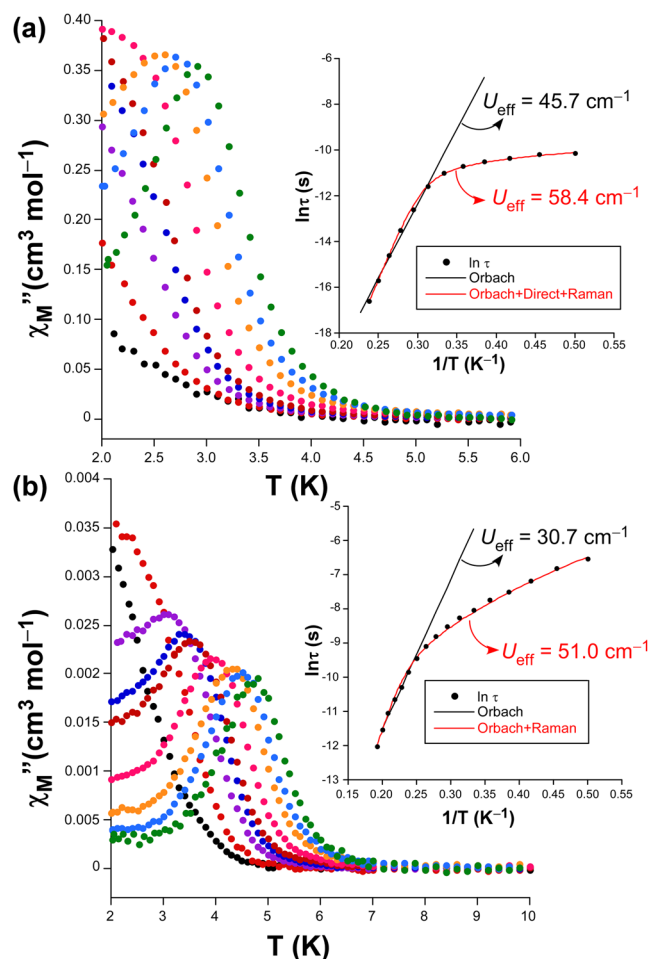


Figure 6. Temperature dependence of the χ_M'' signals and best fitting results for the relaxation times for compounds (a) 1-DMSO and (b) 1-MeOH.

the same excitation path (see Fig. S23). These two bands provide this material, as observed in the images taken on the microscope, with a variable emission consisting of a brilliant blue greenish light under excitation with UV radiation ($\lambda_{\text{ex}} = 365$ nm) or a lime green emission with a less energetic radiation ($\lambda_{\text{ex}} = 435$ nm), in such a way that those wavelengths corresponding to the maximum of the emission band are avoided (Fig. 7b). The emission quantum yield measured in absolute terms with an integrated sphere is low (1.75%). The calculated PL spectra conducted on a suitable model of **3** (see Experimental Section) reproduce very well both excitation and emission processes, finding only substantial differences for the relative intensities of the minor bands.

Starting from the molecular excitation of the compound, absorption of light at the two main contributions seems to proceed through slightly different electronic transitions (Table 3, note that these are the most intense transitions gathered as a representative sample of the band). On the one hand, the shoulder at 305 nm corresponds to a $\pi \rightarrow \pi^*$ transition in which the involved MOs are centred on the aromatic ring of 2ain ligands (Fig. 8), while the band maximum at 370 nm may be better described as a $n \rightarrow \pi^*$ transition given that HOMO - 2/3 lie over the carboxylate group on the other. On its part, the PL emission takes also place through LCCT mechanism since electrons drop from excited LUMO - n orbitals, of π^* nature with lobes extended over the whole molecule or solely the aromatic ring (see Fig. 8), to HOMOs consisting of n or π orbitals based on the carboxylate group for the main ($\lambda_{\text{em}} = 390$ and 405 nm) or the minor ($\lambda_{\text{em}} = 550$ nm) bands, respectively.

For comparative purposes, emission spectra of **3** were recorded at different temperatures under the same experimental conditions in order to check how the suppression of the vibrational quenching, i.e. the molecular vibrations/motions occurring in the ligand that may be overlapped with the radiative emission and hence draw emission capacity to the system⁵³, as the temperature is dropped affects the PL response of the material. Upon cooling the system from RT down to 10 K, the band maximum does not show any remarkable shift although it progressively gains intensity, mainly in the temperature range of 200–150 K where the intensity shows a quantitative leap. To summarize, the emission intensity at $\lambda_{\text{max}} \approx 400$ nm is much greater for 10 K data compared to RT (about 55 times larger in terms of emitted integrated intensity, Fig. S25). With the aim of enlarging the temperature-dependent characterization, emission decay curves were also measured at three representative temperatures (295, 150 and 10 K), revealing very similar lifetimes in the range of hundreds of microseconds. In any case, it is worth highlighting that the observed lifetime remains constant along the whole emission spectrum and shows the expected trend with the temperature although the change is somewhat slight (τ being 239(2), 169(4)

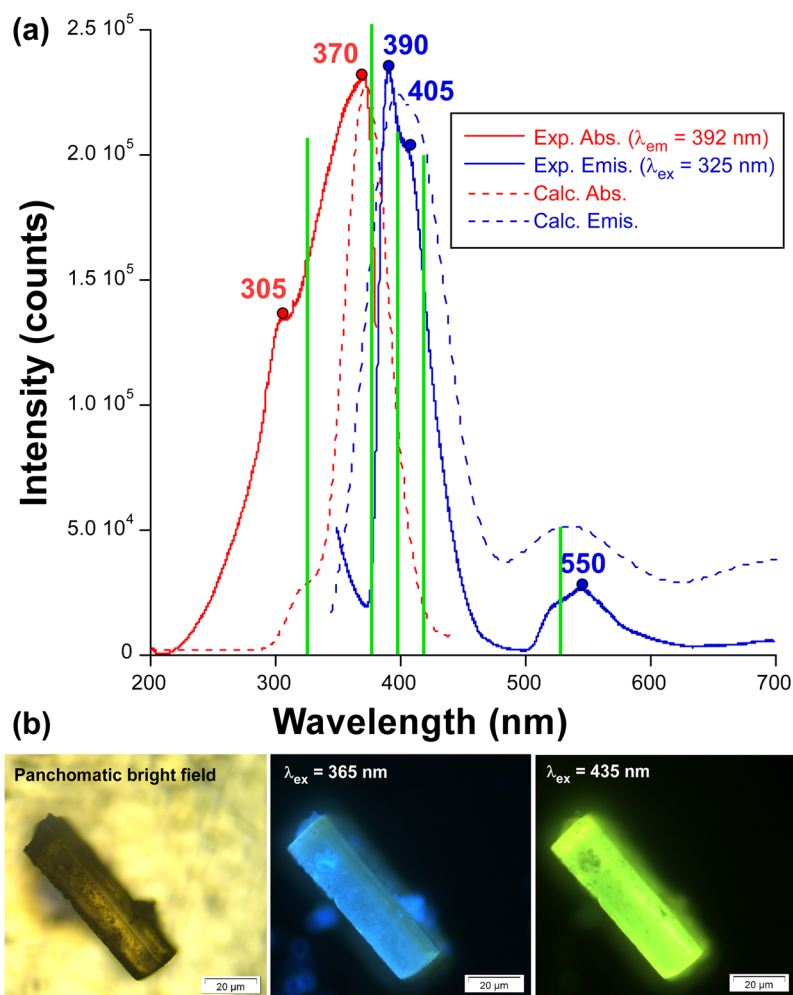


Figure 7. (a) Room temperature excitation (red) and emission (blue) spectra of compound **3** showing the most relevant experimental maxima (circles) and calculated (TD-DFT) main vertical excitations (green lines). (b) Micro-PL photographs of a single crystal of **3** illuminated with different lights.

Exp. λ	Calcd. λ	Electronic transitions	Osc. strength (a.u.)
Excitation energies			
305	318	HOMO - 6 \rightarrow LUMO + 1 (51%) HOMO - 7 \rightarrow LUMO (49%)	0.083
370	372	HOMO - 3 \rightarrow LUMO + 2 (51%) HOMO - 2 \rightarrow LUMO + 3 (42%)	0.112
Emission energies			
390	388	HOMO - 2 \leftarrow LUMO + 4 (52%) HOMO - 2 \leftarrow LUMO + 2 (40%)	0.084
405	408	HOMO - 2 \leftarrow LUMO + 2 (89%)	0.081
550	539	HOMO \leftarrow LUMO (97%)	0.038

Table 3. Calculated main excitation and emission energies (nm), singlet electronic transitions and associated oscillator strengths of model **3**.

and 121(3) μ s for the above mentioned temperatures, see Table S3), which indicates that a unique PL mechanism is preserved irrespective of the temperature of the system. These short lifetimes contrast when compared to those measured for other systems consisting of Zn(II) and positional isomers of the 2ain ligand, as it is the case of $[\text{Zn}(\mu\text{-6ani})_2]_n$ and $[\text{Zn}(\mu\text{-2ani})_2]_n$ ³², which displayed long-lasting phosphorescence (LLP) emissions that could be traced by human eye. As concluded from the analysis of molecular based phosphorescent reported so far⁵⁴, a major reason for the occurrence of LLP in metal-organic compounds with closed-shell ions is attributed to the intermolecular forces established by ligands in the framework, in such a way that strong interactions are able to

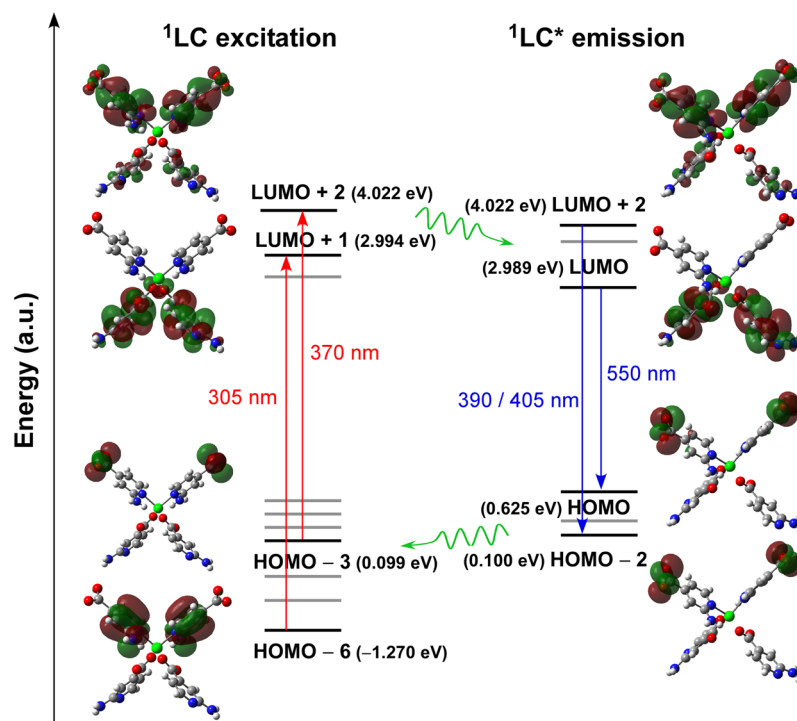


Figure 8. Schematic representation of the most intense excitation (red) and emission (blue) lines of compound **3** with their corresponding MOs. Values given between brackets represent the energies.

freeze the molecules and make lowest-lying triplet states (T_1) more accessible and shielded against quenching. As a matter of fact, the molecular N–H vibrations of the amino group, known to be a main oscillator which enables the non-radiative quenching⁵⁵, seem to be less suppressed in compound **3** compared to their disposition in the above mentioned CPs. In these latter compounds, isomeric 6ani and 2ani ligands establish more rigid hydrogen bonds, particularly in the case of the intramolecular hydrogen bonds found in $[\text{Zn}(\mu\text{-}2\text{ani})_2]_n$, whereas the 2-fold interpenetration brings higher flexibility to the crystal building of **3**, explaining the short lifetimes.

PL sensing properties. The flexible porous nature revealed by compound **3**, consisting of a stable doubly interpenetrated metal-organic framework with pores in which small molecules could be exchanged, in addition to the strong blue greenish PL displayed at RT instigated us to study its performance as PL sensing material for various solvents and metal ions. When polycrystalline sample is dispersed in different solvents, solvent@**3** hereafter, the main emission band experiments not only significant changes regarding the intensity but also slight shifts for the maximum of the emission band (λ_{max}). In a first approach, the analysis of the spectra measured at a representative wavelength ($\lambda_{\text{ex}} = 350$ nm, which falls within the excitation maximum for all suspensions) under the same equipment configuration (identical slit aperture and photomultiplier voltage) revealed that the emission decreases following the expected sequence according to the solvent polarity (note that dielectric constants are shown between brackets): H_2O (80.1) > DMSO (46.7) > DMF (36.7) > MeOH (32.7) > EtOH (24.5) > Ac_2O (20.7) > 2-PrOH (19.2) > THF (7.58)^{16b,56}. In other words, the higher the polarity of the solvent the largest its quenching capacity (see Fig. S28). Moreover, the presence of a minor emission peak, in the form of a shoulder peaking at $\lambda_{\text{em}} \approx 450$ nm, was also observed for less polar solvents (Ac_2O , 2-PrOH and THF), which is probably due to the enabling of an electronic transition arising from a less energetic LUMO level derived from solvation effects⁵⁷. In this sense, it must be recalled that 2ain ligands in the crystal structure possess uncoordinated amino groups exposed to the microchannels, where hydrogen bonding and Van der Waals interactions established with solvent molecules may affect the LCCT mechanism and thus the PL emission⁵⁸. With the aim of getting insights into the potential applicability of this material, a further analysis showed that the main emission follows a solvent-dependent excitation, given the drastic changes shown in the excitation spectra monitored at the λ_{max} (where only one wide band or two narrower maxima are observed depending on the selected solvent, see ESI). A new set of measurements with variable excitation wavelength in order to maximize the solvent-dependent PL behaviour (focusing at the most intense λ_{ex}) indicates that **3** keeps a strong PL emission in water (note that water itself brings some quenching compared to solid state but it is employed as a reference for the rest of solvents) whereas, taking water as a reference, the rest of studied solvents cause a large quenching (with a quenching percentage (QP) above 65%, Fig. 9). Taking into account that crystal structure of **3** presents no significant change (as corroborated by PXRD collected for samples recovered from solvent@**3** suspensions, Fig. S31), it may be assumed that solvents exert: (i) a dynamic quenching involving solvation processes on external surface of the particles in the suspension, and (ii) a quenching derived from the particular interactions (enabling competitive absorption and energy transfers)⁵⁹ occurring between solvent molecules and the internal surface of the microchannels,

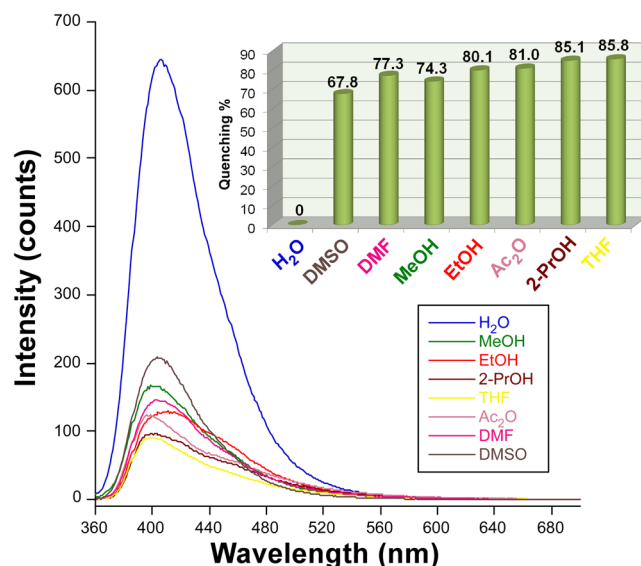


Figure 9. PL emission spectra of dispersion of compound **3** in different solvents at their maximum excitation wavelength. Inset shows quenching percentage estimated from the emission intensity relative to H₂O@**3** is reflected in the upper bar chart.

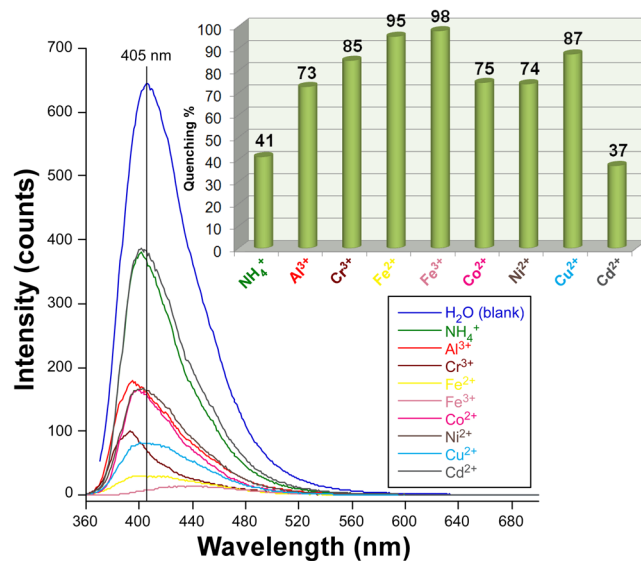


Figure 10. PL response of H₂O@**3** against common metal ions ($\lambda_{\text{ex}} = 350$ nm). Inset shows the quenching percentage estimated from the maximum emission intensity respect to a blank solution.

where factors such as size and hydrogen bonding capacity are key and govern the diffusion of solvent molecules throughout the pore system.

In view of the intense PL signal observed for the H₂O@**3** suspension (the least quenching brought by water compared to other solvents), the detection of ions in aqueous solutions was also studied. As inferred from Fig. 10, **3** presents a variable sensing capacity to ions according to their quenching capacity that follows the series: Cd²⁺ < NH₄⁺ < Al³⁺ < Ni²⁺ < Co²⁺ < Cr³⁺ < Cu²⁺ < Fe²⁺ < Fe³⁺. It is important to notice that the quenching percentage (QP) at 10 mM is above 90% for both iron cations, among which the most stable oxidation state almost clears the PL emission. This behaviour meets the expected response given that UV-Vis absorption band of these ions overlap substantially well with the excitation band, such that most of the light irradiated does not reach the dispersed solid of **3**. More interestingly, the presence of most of studied metal ions promotes a shift of the emission band, most of which cause a blue-shift which can be as large as 15 nm (for Cr³⁺@**3**). However, the strongest quencher of the PL, Fe³⁺ ion, promotes an opposed response by red-shifting the maximum up to ca. $\lambda_{\text{em}} = 440$ nm. This overall behaviour seems to indicate that metal ions are able to interact with the ligands of the backbone.

Taking into account the previous metal-dependent turn-off results, we decided to explore the PL response of the CP for Fe³⁺ and Cu²⁺ ions, for which an exhaustive evolution of the emission intensity was monitored by

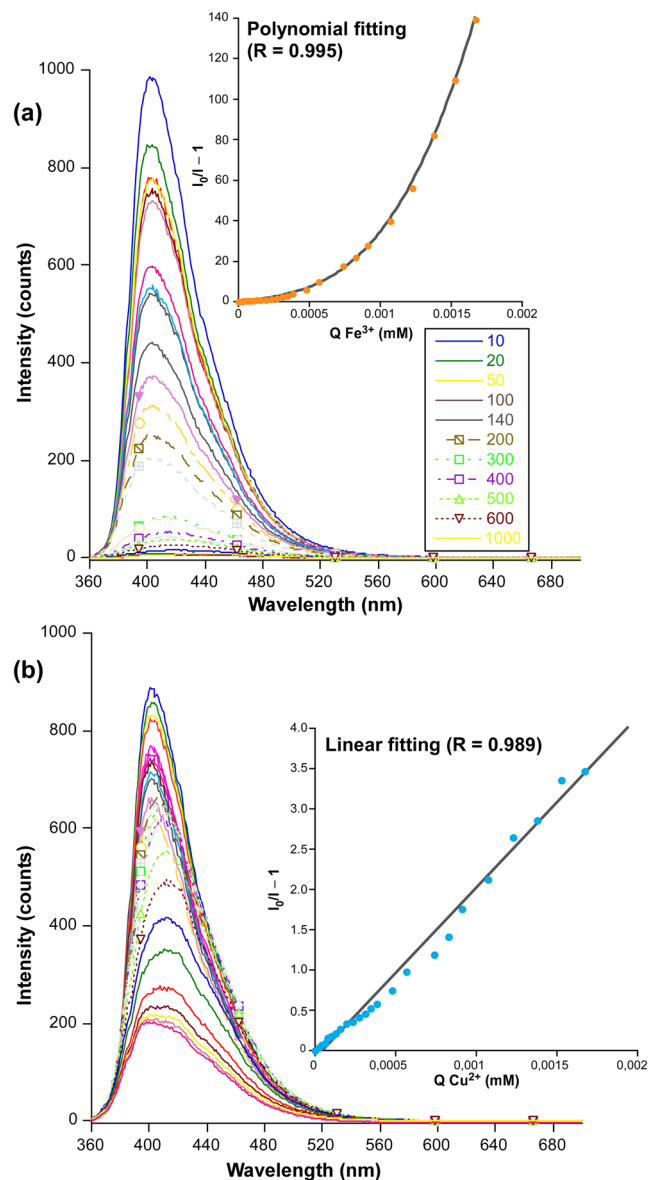


Figure 11. Luminescence quenching of $\text{H}_2\text{O}@3$ with gradual addition (microliters of metal ion solutions added are shown in the capture with different colours of (a) Fe^{3+} and (b) Cu^{2+} ions. Stern-Volmer plots showing the best fits are also shown.

gradually increasing the concentration of the metal quencher. Note that no further study was conducted for Fe^{2+} because of its spontaneous oxidation in waste waters. Stern-Volmer plot analyses for the latter two ions exhibit a distinct behaviour. The PL signal exhibits a progressive and polynomial quenching for Fe^{3+} ion from low concentrations on, which points out the coexistence of static and dynamic quenching phenomena. On its part, the quenching by Cu^{2+} ions shows a progressive and linear quenching occurring from low concentration (Q) of 4×10^{-5} M. Fitting of the evolution with the respective expression (see ESI) for both ions gives values of K_{sv} of 1.79×10^4 and $2.12 \times 10^4 \text{ M}^{-1}$ (Fig. 11) with calculated limit of detection (LOD) values of $55 \mu\text{M}$ and $162 \mu\text{M}$ for Fe^{3+} and Cu^{2+} ions, respectively. Note that, despite the relatively high LODs, the estimated K_{sv} value for Fe^{3+} detection can be considered quite promising compared to other reported MOFs with characteristic iron sensing capacity, usually exhibiting values within the $10^4 - 10^5$ range^{19,60,61}, among which the $K_{sv} = 2.67 \times 10^5 \text{ M}^{-1}$ reported for the MOF of $\{[(\text{CH}_3)_2\text{NH}_2]_6[\text{Cd}_3\text{L}(\text{H}_2\text{O})_2] \cdot 12\text{H}_2\text{O}\}_n$ formula deserves to be mentioned⁶². In this regard, despite the dominant dynamic quenching observed for these ions (in view of their large K_{sv}), significant static quenching may be claimed for Fe^{3+} according to the non-linear distribution of the plot, a fact that may be explained according to the accessibility of the carboxylate oxygen atoms of 2ain ligands (which are also involved in hydrogen bonding interactions with exocyclic amino groups of neighbouring 2ain ligands) from the microchannels of the MOF. The recyclability of **3** has been also checked by PXRD measurement on the solid filtered and dried after the experiment (see ESI). Thinking on a potential use of the compound for sensing applications on polluted wastewaters, an additional analysis was accomplished in order to explore the specific response against similar quenchers, for

which the mixed $\text{Fe}^{3+}/\text{Cu}^{2+}$ system was studied. In view of the obtained Stern-Volmer plot, the quenching evolution of the material is not proportional to the sum of both isolated ions, but it shows a linear response after a concentration of $1 \times 10^{-4} \text{ M}$ of each individual ion. Fitting of the linear part gives a K_{sv} of $2.12 \times 10^4 \text{ M}^{-1}$, which allows us concluding that there is a tough competition between both quenchers to interact with the framework.

Conclusions

Three metal-organic framework materials, of $\{[\text{M}(\mu\text{-}2\text{ain})_2]\cdot\text{DMF}\}_n$ formula, based on first row transition metal ions (Co^{II} , Ni^{II} , and Zn^{II}) and 2-aminoisonicotinate (2ain) ligand have been synthesized and chemically and structurally characterized. Their crystal structure consists of a doubly-interpenetrated three-dimensional open architecture which contains microchannels filled with solvent molecules. Taking advantage of the porosity and their magnetic and/or photoluminescence (PL) properties, their guest-dependent magnetic and PL response has been evaluated. On the one hand, the weak exchange interactions transmitted through the chiral coordination network leads to a spin-glass behaviour that governs the magnetism of the cobalt-based counterpart, though no frequency-dependent signal is observed for the nickel compound. Interestingly, when DMSO and MeOH are loaded within the pores of this MOF, exchanging the pristine DMF molecules, the crystal building undergoes a kind of rearrangement which modulates the magnetic properties of the material. In particular, the glass-like magnetic relaxation gives way to substantial SIM behaviour probably derived from the first-order SOC inherent to cobalt(II) ions, consisting of multiple spin-phonon processes characterized by low blocking temperature but relatively high energy barriers. On another level, solid state PL measurements show that the zinc-based MOF displays strong bright blue emissions arising from a LCCT mechanism (based on $\pi\text{-}\pi^*$ or $\text{n-}\pi^*$ transitions in 2ain) as confirmed by TD-DFT calculations. The vibrational quenching may be efficiently prevented at low temperature (10 K), since a strong gain in integrated emitted intensity (of 55 times) is observed compared to RT. This MOF exhibits clear emission dependence in contact with solvents under a constant excitation wavelength, where the emission quenching increases according to the decreasing polarity of the solvent (moving from $\text{H}_2\text{O} > \text{solvents} > \text{THF}$). With regard to its sensing towards metal ions in aqueous solutions, Cu^{2+} , Fe^{2+} , and Fe^{3+} ions are found to quench the emission to a large extent. Stern-Volmer plots for aqueous Cu^{2+} and Fe^{3+} suspensions containing Zn-2ain reveal a similar detection capacity (K_{sv} of 1.79×10^4 and $2.12 \times 10^4 \text{ M}^{-1}$, respectively) but distinct mechanisms, confirming the capacity of these ions to interact with MOF. In fact, the analysis carried out on a mixture of both ions, $\text{Fe}^{3+}/\text{Cu}^{2+}$, shows a quenching evolution distinct to the sum of individual atoms, indicating a competing quenching of both quenchers to interact with the framework. All in all, the studies confirm that these MOFs modulate their properties according to solvent-exchange and/or capture of metal ions in liquid media, which paves the way to their use as sensors.

Experimental Section

Chemicals. All chemicals were of reagent grade and were used as commercially obtained.

Synthesis of $\{[\text{Co}(\mu\text{-}2\text{ain})_2]\cdot\text{DMF}\}_n$ (1). 5 mL of a DMF solution containing 0.20 mmol of $\text{Co}(\text{NO}_3)_2\cdot 6\text{H}_2\text{O}$ (0.0582 g) were added dropwise under continuous stirring over 15 mL of a DMF/ H_2O (1:1) solution of H2ain ligand (0.40 mmol, 0.0552 g) at 70°C . The final pH of the solution was 5.6. The dark pink coloured solution was introduced in a Teflon-lined container enclosed into a stainless steel autoclave solution, where it was heated up to 120°C for two days. The mixture was slowly cooled down to room temperature and purple plate shaped single crystals were observed when opening the recipient. Crystals were filtered off and washed several times with water and methanol. Yield 50–60% (based on metal). Homogeneity and purity of samples were checked by means of elemental and thermogravimetric analyses, FT-IR, and X-ray powder diffraction data (see section S5 in the ESI). Anal. Calcd. for (hydrated) $\text{C}_{15}\text{H}_{19}\text{CoN}_5\text{O}_6$ (%): C, 44.35; H, 4.22; Co, 14.51; N, 17.24. Found: C, 42.32; H, 4.38; Co, 13.83; N, 16.60.

Synthesis of $\{[\text{Ni}(\mu\text{-}2\text{ain})_2]\cdot\text{DMF}\}_n$ (2). Well shaped single crystals of compound 2 were collected from a Teflon-lined vessel after carrying out the same experimental procedure reported for 1 but for the use of $\text{Ni}(\text{NO}_3)_2\cdot 6\text{H}_2\text{O}$ (0.0582 g) instead of the cobalt source. Yield of 45–50% (based on metal). Anal. Calcd. for (hydrated) $\text{C}_{15}\text{H}_{19}\text{Ni}_5\text{NiO}_6$ (%): C, 44.37; H, 4.22; N, 17.25; Ni, 14.45. Found: C, 42.65; H, 4.32; N, 16.45; Ni, 13.74.

Synthesis of $\{[\text{Zn}(\mu\text{-}2\text{ain})_2]\cdot\text{DMF}\}_n$ (3). Following the same above mentioned synthetic conditions with $\text{Zn}(\text{NO}_3)_2\cdot 6\text{H}_2\text{O}$ (0.0595 g) gave rise to the growth of colourless single crystals of 3. Yield of 50–55% (based on metal). Anal. Calcd. for (hydrated) $\text{C}_{15}\text{H}_{19}\text{N}_5\text{O}_6\text{Zn}$ (%): C, 43.65; H, 4.15; N, 16.97; Zn, 15.84. Found: C, 43.25; H, 4.34; N, 16.41; Zn, 15.02.

Physical measurements. Elemental analyses (C, H, N) were performed on an Euro EA Elemental Analyzer and the metal content determined by inductively coupled plasma (ICP-AES) was performed on a Horiba Yobin Yvon Activa spectrometer. IR spectra (KBr pellets) were recorded on a Thermo Nicolet IR 200 spectrometer in the $4000\text{--}400 \text{ cm}^{-1}$ spectral region. Magnetic susceptibility measurements were performed on polycrystalline samples of the complexes with a Quantum Design SQUID MPMS-7T susceptometer at an applied magnetic field of 1000 G. The susceptibility data were corrected for the diamagnetism estimated from Pascal's Tables⁶³, the temperature-independent paramagnetism, and the magnetization of the sample holder. *Ac* measurements were performed on a Physical Property Measurement System-Quantum Design model 6000 magnetometer under a 3.5 G *ac* field and frequencies ranging from 60 to 10 000 Hz. Thermal analyses (TG/DTA) were performed on Mettler-Toledo TGA/SDTA851 thermal analyser in a synthetic air atmosphere (79% N_2 / 21% O_2) with a heating rate of $5^\circ\text{C}\cdot\text{min}^{-1}$. A closed cycle helium cryostat enclosed in an Edinburgh Instruments FLS920 spectrometer was employed for steady state photoluminescence (PL) and lifetime measurements in the 10 – 300 K range. All

	1	2	3
Empirical formula	C ₁₅ H ₁₇ CoN ₅ O ₅	C ₁₅ H ₁₇ N ₅ NiO ₅	C ₁₅ H ₁₇ N ₅ O ₅ Zn
Formula weight	424.28	424.04	430.73
Crystal system	orthorhombic	orthorhombic	orthorhombic
Space group	<i>Fddd</i>	<i>Fddd</i>	<i>Fddd</i>
<i>a</i> (Å)	12.693(1)	12.649(1)	12.903(1)
<i>b</i> (Å)	22.776(2)	22.289(2)	22.869(2)
<i>c</i> (Å)	23.847(2)	23.949(2)	23.890(2)
<i>V</i> (Å ³)	6894(1)	6752(1)	7049(1)
<i>Z</i>	16	16	16
Reflections collected	19730	10466	10922
Unique/parameters	2112/96	1998/96	2121/96
Rint	0.0597	0.0323	0.0314
GoF (S) ^a	1.038	1.058	1.077
R ₁ ^b /wR ₂ ^c [I > 2σ(I)]	0.0344/0.0840	0.0282/0.0746	0.0303/0.0801
R ₁ ^b /wR ₂ ^c [all]	0.0462/0.0900	0.0318/0.0771	0.0367/0.0835

Table 4. Single crystal X-ray diffraction data and structure refinement details of compounds **1**, **2** and **3**. [a] $S = [\sum w(F_o^2 - F_c^2)^2 / (N_{obs} - N_{param})]^{1/2}$ [b] $R_1 = \sum ||F_o| - |F_c|| / \sum |F_o|$ [c] $wR_2 = [\sum w(F_o^2 - F_c^2)^2 / \sum wF_o^4]^{1/2}$; $w = 1/[\sigma^2(F_o^2) + (aP)^2 + bP]$ where $P = (\max(F_o^2, 0) + 2F_c^2)/3$ with $a = 0.0472$ (**1**), 0.0416 (**2**), 0.0459 (**3**); and $b = 8.1485$ (**1**), 10.0330 (**2**), and 1.3767 (**3**).

samples are first placed under high vacuum (of ca. 10^{-9} mbar) to avoid the presence of oxygen or water in the sample holder. For steady-state measurements a Müller-Elektronik-Optik SVX1450 Xe lamp or an IK3552R-G He-Cd continuous laser (325 nm) were used as excitation source, whereas a microsecond pulsed lamp was employed for recording the lifetime measurements. Photographs of irradiated single-crystal and polycrystalline samples were taken at room temperature in a micro-PL system included in an Olympus optical microscope illuminated with a Hg lamp. The PL quantum yield was measured in solid state using a Horiba Quanta-φ F-3029 integrating sphere.

X-ray Diffraction Data Collection and Structure Determination. X-ray data collection of suitable single crystals was done at 100(2) K on a Bruker VENTURE area detector equipped with graphite monochromated Mo K_α radiation ($\lambda = 0.71073$ Å) by applying the ω -scan method. Data reduction were performed with the APEX2⁶⁴ software and corrected for absorption using SADABS⁶⁵. Crystal structures were solved by direct methods using the SIR97 program⁶⁶ and refined by full-matrix least-squares on F^2 including all reflections employing the WINGX crystallographic package^{67,68}. All hydrogen atoms were located in difference Fourier maps and included as fixed contributions riding on attached atoms with isotropic thermal displacement parameters 1.2 times or 1.5 times those of their parent atoms for the organic ligands and the water molecules, respectively. Lattice solvent molecules placed in the voids of the structures found to be highly disordered due to the high symmetry acquired by the framework. Therefore, the final refinement was made with an hkl file provided by the SQUEEZE routine implemented in PLATON³⁸, which removed the latter electron density. Details of the structure determination and refinement of all compounds are summarized in Table 4. Crystallographic data for the crystal structures have been deposited with the Cambridge Crystallographic Data Center as supplementary publication nos. CCDC 1942731-1942733. Copies of the data can be obtained free of charge on application to the Director, CCDC, 12 Union Road, Cambridge, CB2 1EZ, U.K. (Fax: +44-1223-335033; e-mail: deposit@ccdc.cam.ac.uk or <http://www.ccdc.cam.ac.uk>).

The X-ray powder diffraction (XRPD) patterns were collected on a Phillips X'PERT powder diffractometer with Cu-K_α radiation ($\lambda = 1.5418$ Å) over the range $5 < 2\theta < 50^\circ$ with a step size of 0.026° and an acquisition time of 2.5 s per step at 25 °C. Indexation of the diffraction profiles were made by means of the FULLPROF program (pattern-matching analysis)⁶⁹ on the basis of the space group and the cell parameters found by single crystal X-ray diffraction. The unit cell parameters obtained in the final refinement are listed in the Supporting Information.

Computational details. The computational strategy adopted in this work to compute the magnetic coupling constant (J_{calc}) values has been described and validated elsewhere⁷⁰. One calculation was performed to determine the high-spin state and another to determine the low-spin broken symmetry state. The correctness of the latter state was ensured by means of its spin density distribution. Density functional theory was used to perform two separate calculations to evaluate the coupling constant of each compound, employing the aforementioned hybrid B3LYP functional and Gaussian-implemented 6-311 G(d) basis set for all non-metal atoms and the corresponding LANL2DZ pseudopotentials for the metal atoms. Spin-density surfaces were plotted using GaussView 5⁷¹.

PL spectra were calculated by means of TD-DFT using the Gaussian 09 package⁷², using the Becke three parameter hybrid functional with the non-local correlation functional of Lee-Yang-Parr (B3LYP)^{73,74} along with 6-311 G++(d,p) basis set⁷⁵ was adopted for all atoms but for the central zinc cation, for which the LANL2DZ⁷⁶ basis set along with the corresponding effective core potential (ECP) was used. The 40 lowest excitation states were calculated by the TD-DFT method. Results were analysed with GaussSum program package⁷⁷ and molecular orbitals plotted using GaussView 5.

Received: 2 February 2020; Accepted: 7 May 2020;

Published online: 01 June 2020

References

- Kreno, L. E. *et al.* Metal–Organic Framework Materials as Chemical Sensors. *Chem. Rev.* **112**, 110–1125 (2012).
- Cohen, S. M. Postsynthetic Methods for the Functionalization of Metal–Organic Frameworks. *Chem. Rev.* **112**, 970–1000 (2012).
- Falcaro, P. *et al.* MOF positioning technology and device fabrication. *Chem. Soc. Rev.* **43**, 5513–5560 (2014).
- Meek, S. T., Greathouse, J. A. & Allendorf, M. D. Metal–Organic Frameworks: A Rapidly Growing Class of Versatile Nanoporous Materials. *Adv. Mater.* **23**, 249–267 (2011).
- Cheetham, A. K. & Rao, C. N. R. Materials science. There's room in the middle. *Science* **318**, 58–59 (2007).
- Tranchemontagne, D. J., Mendoza-Cortés, J. L., O'Keeffe, M. & Yaghi, O. M. Secondary building units, nets and bonding in the chemistry of metal–organic frameworks. *Chem. Soc. Rev.* **38**, 1257–1283 (2009).
- Cepeda, J., Beobide, G., Castillo, O., Luque, A. & Pérez-Yáñez, S. Structural diversity of coordination compounds derived from double-chelating and planar diazinedicarboxylate ligands. *Coord. Chem. Rev.* **352**, 83–107 (2017).
- Eddaoudi, M., Sava, D. F., Eubank, J. F., Adil, K. & Guillelm, V. Zeolite-like metal–organic frameworks (ZMOFs): design, synthesis, and properties. *Chem. Soc. Rev.* **44**, 228–249 (2015).
- Janiak, C. H. & Vieth, J. K. MOFs, MILs and more: concepts, properties and applications for porous coordination networks (PCNs). *New J. Chem.* **34**, 2366–2388 (2010).
- Coronado, E. & Dumbar, K. R. *Inorg. Chem.* **48**, 3293–3296 (2009).
- Li, J.-R., Sculley, J. & Zhou, H.-C. Metal–Organic Frameworks for Separations. *Chem. Rev.* **112**, 869–932 (2012).
- Cepeda, J. *et al.* Modulation of pore shape and adsorption selectivity by ligand functionalization in a series of “rob”-like flexible metal–organic frameworks. *J. Mater. Chem. A* **6**, 17409–17416 (2018).
- Dhakshinamoorthy, A. & Garcia, H. Metal–organic frameworks as solid catalysts for the synthesis of nitrogen-containing heterocycles. *Chem. Soc. Rev.* **43**, 5750–5765 (2014).
- Ma, L., Abney, C. & Lin, W. Enantioselective catalysis with homochiral metal–organic frameworks. *Chem. Soc. Rev.* **38**, 1248–1256 (2009).
- Horcajada, P. *et al.* Metal–Organic Frameworks in Biomedicine. *Chem. Rev.* **112**, 1232–1268 (2012).
- Lustig, W. P. *et al.* Metal-organic frameworks: functional luminescent and photonic materials for sensing applications. *Chem. Soc. Rev.* **46**, 3242–3285 (2017).
- Kozłowski, H. *et al.* Copper, iron, and zinc ions homeostasis and their role in neurodegenerative disorders (metal uptake, transport, distribution and regulation). *Coord. Chem. Rev.* **253**, 2665–2685 (2009).
- Mølhave, L., Bach, B. & Pedersen, O. F. Human reactions to low concentrations of volatile organic compounds. *Environ. Int.* **12**, 167–175 (1986).
- Yi, F.-Y., Chen, D., Wu, M.-K., Han, L. & Jiang, H.-L. Chemical Sensors Based on Metal–Organic Frameworks. *ChemPlusChem* **81**, 675–690 (2016).
- Guo, H., Lee, S. C., Chan, L. Y. & Li, W. M. Risk assessment of exposure to volatile organic compounds in different indoor environments. *Environ. Res.* **94**, 57–66 (2004).
- You, L., Zha, D. & Anslyn, E. V. Recent Advances in Supramolecular Analytical Chemistry Using Optical Sensing. *Chem. Rev.* **115**, 7840–7892 (2015).
- Allendorf, M. D., Bauer, C. A., Bhakta, R. K. & Houk, R. J. T. Luminescent metal–organic frameworks. *Chem. Soc. Rev.* **38**, 1330–1352 (2009).
- Lower, S. K. & El-Sayed, M. A. The Triplet State and Molecular Electronic Processes in Organic Molecules. *Chem. Rev.* **66**, 199–241 (1966).
- Cepeda, J. & Rodríguez-Diéguez, A. Tuning the luminescence performance of metal–organic frameworks based on d10 metal ions: from an inherent versatile behaviour to their response to external stimuli. *CrystEngComm* **18**, 8556–8573 (2016).
- Mínguez Espallargas, G. & Coronado, E. Magnetic functionalities in MOFs: from the framework to the pore. *Chem. Soc. Rev.* **47**, 533–557 (2018).
- Frost, J. M., M. Harriman, K. L. & Murugesu, M. The rise of 3-d single-ion magnets in molecular magnetism: towards materials from molecules? *Chem. Sci* **7**, 2470–2491 (2016).
- Craig, G. A. & Murrie, M. 3d single-ion magnets. *Chem. Soc. Rev.* **44**, 2135–2147 (2015).
- Seco, J. M., Oyarzabal, I., Pérez-Yáñez, S., Cepeda, J. & Rodríguez-Diéguez, A. Designing Multifunctional 5-Cyanoisophthalate-Based Coordination Polymers as Single-Molecule Magnets, Adsorbents, and Luminescent Materials. *Inorg. Chem.* **55**, 11230–11248 (2016).
- Murrie, M. Cobalt(II) single-molecule magnets. *Chem. Soc. Rev.* **39**, 1986–1995 (2010).
- Gómez-Coca, S. & Aravena, D. Morales, & Ruiz, E. Large magnetic anisotropy in mononuclear metal complexes. *Coord. Chem. Rev.* **289**, 379–392 (2015).
- Chen, L. *et al.* Slow Magnetic Relaxation in a Mononuclear Eight-Coordinate Cobalt(II) Complex. *J. Am. Chem. Soc.* **136**, 12213–12216 (2014).
- Cepeda, J. *et al.* A Zn based coordination polymer exhibiting long-lasting phosphorescence. *Chem. Commun.* **52**, 8671–8674 (2016).
- Pajuelo-Corral, O. *et al.* Alkaline-earth and aminonicotinate based coordination polymers with combined fluorescence/long-lasting phosphorescence and metal ion sensing response. *J. Mater. Chem. C* **7**, 6997–7012 (2019).
- Rodríguez-Diéguez, A., Pérez-Yáñez, S., Ruiz-Rubio, L., Seco, J. M. & Cepeda, J. From isolated to 2D coordination polymers based on 6-aminonicotinate and 3d-metal ions: towards field-induced single-ion-magnets. *CrystEngComm* **19**, 2229–2242 (2017).
- Pachfule, P., Chen, Y., Jiang, J. & Banerjee, R. Experimental and computational approach of understanding the gas adsorption in amino functionalized interpenetrated metal organic frameworks (MOFs). *J. Mater. Chem.* **21**, 17737–17745 (2011).
- TOPOS Main Page, <http://www.topos.ssu.samara.ru> (accessed February 14, 2019).
- Blatov, V. A., Shevchenko, A. P. & Proserpio, D. M. Applied Topological Analysis of Crystal Structures with the Program Package. *Cryst. Growth Des.* **14**, 3576–3586 (2014).
- Spek, A. L. Structure validation in chemical crystallography. *Acta Cryst.* **D65**, 148–155 (2009).
- Lloret, F., Julve, M., Cano, J., Ruiz-García, R. & Pardo, E. Magnetic properties of six-coordinated high-spin cobalt(II) complexes: Theoretical background and its application. *Inorg. Chim. Acta* **361**, 3432–3445 (2008).
- Sakiyama, H. *et al.* Dinuclear Cobalt(II) Complexes of an Acyclic Phenol-Based Dinucleating Ligand with Four Methoxyethyl Chelating Arms – First Magnetic Analyses in an Axially Distorted Octahedral Field. *Eur. J. Inorg. Chem.* 2027–2032 (2001).
- Rueff, J.-M., Masciocchi, N., Rabu, P., Sironi, A. & Skoulios, A. Structure and Magnetism of a Polycrystalline Transition Metal Soap – CoII[OOC(CH₂)₁₀COO](H₂O)₂. *Eur. J. Inorg. Chem.* 2843–2848 (2001).
- Cui, L. *et al.* Solvents and auxiliary ligands co-regulate three antiferromagnetic Co(II) MOFs based on a semi-rigid carboxylate ligand. *Dalton Trans.* **43**, 5823–5830 (2014).
- Lloret, F., Julve, M., Cano, J., Ruiz-García, R. & Pardo, E. Magnetic properties of six-coordinated high-spin cobalt(II) complexes: Theoretical background and its application. *Inorg. Chim. Acta* **361**, 3432–3445 (2008).

44. Chilton, N. F., Anderson, R. P., Turner, L. D., Soncinia, A. & Murray, K. S. PHI: a powerful new program for the analysis of anisotropic monomeric and exchange-coupled polynuclear d- and f-block complexes. *J. Comput. Chem.* **4**, 1164–1175 (2013).
45. Boča, R. Zero-field splitting in metal complexes. *Coord. Chem. Rev.* **248**, 757–815 (2004).
46. Gómez-Coca, S. *et al.* Origin of slow magnetic relaxation in Kramers ions with non-uniaxial anisotropy. *Nat. Commun.* **5**, 4300 (2014).
47. Yao, P.-F. *et al.* Hierarchical Assembly of a {Co₂₄} Cluster from Two Vertex-Fused {Co₁₃} Clusters and Their Single-Molecule Magnetism. *Inorg. Chem.* **57**, 9182–9189 (2018).
48. Liu, Y., Shi, W.-J., Lu, Y.-K., Liu, G. & Hou, L. & Wang, Y.-Y. Nonenzymatic Glucose Sensing and Magnetic Property Based On the Composite Formed by Encapsulating Ag Nanoparticles in Cluster-Based Co-MOF. *Inorg. Chem.* **58**, 16743–16751 (2019).
49. Du, Z.-Y. *et al.* Two magnetic Δ -chain-based Mn(II) and Co(II) coordination polymers with mixed carboxylate-phosphinate and μ_3 -OH⁻ bridges. *CrystEngComm* **19**, 1052–1057 (2017).
50. Zhang, X.-M., Li, P., Gao, W., Liu, J.-P. & Gao, E.-Q. 3D Co(II) coordination polymer with ferromagnetic-like layers based on azide and tetrazolate bridges showing slow magnetic dynamics. *Dalton Trans.* **44**, 511–514 (2015).
51. García-Valdivia, A. A., Seco, J. M., Cepeda, J. & Rodríguez-Diéguez, A. Designing Single-Ion Magnets and Phosphorescent Materials with 1-Methylimidazole-5-carboxylate and Transition-Metal Ions. *Inorg. Chem.* **56**, 13897–13912 (2017).
52. Herchel, R., Váhovská, L., Potocnak, I. & Travnicek, Z. Slow Magnetic Relaxation in Octahedral Cobalt(II) Field-Induced Single-Ion Magnet with Positive Axial and Large Rhombic Anisotropy. *Inorg. Chem.* **53**, 5896–5898 (2014).
53. Nyokong, T. Effects of substituents on the photochemical and photophysical properties of main group metal phthalocyanines. *Coord. Chem. Rev.* **251**, 1707–1722 (2007).
54. San Sebastian, E., Rodríguez-Diéguez, A., Seco, J. M. & Cepeda, J. Coordination Polymers with Intriguing Photoluminescence Behavior: The Promising Avenue for Greatest Long-Lasting Phosphors. *Eur. J. Inorg. Chem.*, 2155–2174 (2018).
55. A. Beeby *et al.* *Chem. Soc., Perkin Trans.* **2**, 493–503 (1999).
56. Melavanki, R. M., Kusanur, R. A., Dadadevaramath, J. S. & Kulkarni, M. V. Effect of solvent polarity on the fluorescence quenching of biologically active 5BAMC by aniline in binary solvent mixtures. *J. Fluores* **20**, 1175–1180 (2010).
57. Ma, D. *et al.* *n* situ 2,5-pyrazinedicarboxylate and oxalate ligands synthesis leading to a microporous europium–organic framework capable of selective sensing of small molecules. *CrystEngComm* **12**, 4372–4377 (2010).
58. Qiu, Y. C. *et al.* In situ tetrazoleligand synthesis leading to a microporous cadmium–organic framework for selective ion sensing. *Chem. Commun.* 5415–5417 (2009).
59. Liu, X.-J. *et al.* A Water-Stable Metal–Organic Framework with a Double-Helical Structure for Fluorescent Sensing. *Inorg. Chem.* **55**, 7326–7328 (2016).
60. He, J., Xu, J., Yin, J., Li, N. & Bu, X.-H. Recent advances in luminescent metal-organic frameworks for chemical sensors. *Sci China Mater* **62**, 1655–1678 (2019).
61. Gao, Q., Xu, J. & Bu, X.-H. Recent advances about metal–organic frameworks in the removal of pollutants from wastewater. *Coord. Chem. Rev.* **378**, 17–31 (2019).
62. Lu, B. B., Jiang, W., Yang, J., Liu, Y. Y. & Ma, J. F. Resorcin[4]arene-based Microporous Metal-Organic Framework as an Efficient Catalyst for CO₂ Cycloaddition with Epoxides and Highly Selective Luminescent Sensing of Cr₂O₇²⁻. *ACS Appl. Mater. Interfaces* **9**, 39441–39449 (2017).
63. Earnshaw, A. In: *Introduction to Magnetochemistry*, Academic Press: London, 1968.
64. Bruker. Apex2, Bruker AXS Inc: Madison, WI, 2004.
65. Sheldrick, G. M. *SADABS, Program for Empirical Adsorption Correction*, Institute for Inorganic Chemistry, University of Göttingen: Germany, 1996.
66. Altomare, A. *et al.* SIR97: a new tool for crystal structure determination and refinement. *J. Appl. Crystallogr* **32**, 115–119 (1999).
67. Sheldrick, G. M. *SHELX-2014, Program for Crystal Structure Refinement*, University of Göttingen: Göttingen, Germany, 2014.
68. Farrugia, L. J. WinGX suite for small-molecule single-crystal crystallography. *J. Appl. Crystallogr* **32**, 837–838 (1999).
69. Rodríguez-Carvajal, J. *FULLPROF, version July-2017*, Laboratoire Léon Brillouin (CEA-CNRS), Centre d'Études de Saclay, Gif sur Yvette Cedex: France, 2017.
70. Ruiz, E., Rodríguez-Fortea, A., Cano, J., Álvarez, S. & Alemany, P. About the calculation of exchange coupling constants in polynuclear transition metal complexes. *J. Comput. Chem.* **24**, 982–989 (2003).
71. Dennington, R., Keith, T., Millam, J. *GaussView*, Version 5, SemicheM Inc: Shawnee Mission, KS, 2009.
72. Frisch, M. J. *et al.* Gaussian 09, revision A.02, Gaussian, Inc., Walling-ford, CT, 2009.
73. Becke, A. D. A new mixing of Hartree–Fock and local density-functional theories. *J. Chem. Phys.* **98**, 5648–5652 (1993).
74. Lee, C., Yang, W. & Parr, R. G. Development of the Colle-Salvetti correlation-energy formula into a functional of the electron density. *Phys. Rev. B* **37**, 785–789 (1988).
75. Noodleman, L., Case, D. A. & Aizman, A. Broken symmetry analysis of spin coupling in iron-sulfur clusters. *J. Am. Chem. Soc.* **110**, 1001–1005 (1988).
76. Hay, P. J. & Wadt, W. R. Ab initio effective core potentials for molecular calculations. Potentials for the transition metal atoms Sc to Hg. *J. Chem. Phys.* **82**, 270 (1985).
77. O'Boyle, N. M., Tenderholt, A. L. & Langner, K. M. cclib: a library for package-independent computational chemistry algorithms. *J. Comput. Chem.* **29**, 839–845 (2008).

Acknowledgements

This work has been funded by Red Guipuzcoana de Ciencia, Tecnología e Innovación (OF218/2018), University of the Basque Country (GIU 17/13), Gobierno Vasco/Eusko Jaurlaritza (IT1005-16, IT1291-19, IT1310-19), Junta de Andalucía (FQM-394) and the Spanish Ministry of Science, Innovation and Universities (MCIU/AEI/FEDER, UE) (PGC2018-102052-A-C22, PGC2018-102052-B-C21, MAT2016-75883-C2-1-P). The authors thank for technical and human support provided by SGIker of UPV/EHU and European funding (ERDF and ESF). Dr. Iñigo López Arbeloa and Dr. Virginia Martínez Martínez are greatly acknowledged for their generous collaboration with quantum yield measurements.

Author contributions

A.A.G.-V. carried out the material synthesis. S.P.-Y. did the chemical characterization. J.A.G. developed the luminescence theory and B.F. did the experimental part. A.R.D. the X-ray diffraction and characterization. J.C. characterized the magnetic properties and wrote the manuscript.

Competing interests

The authors declare no competing interests.

Additional information

Supplementary information is available for this paper at <https://doi.org/10.1038/s41598-020-65687-6>.

Correspondence and requests for materials should be addressed to J.C. or A.R.-D.

Reprints and permissions information is available at www.nature.com/reprints.

Publisher's note Springer Nature remains neutral with regard to jurisdictional claims in published maps and institutional affiliations.



Open Access This article is licensed under a Creative Commons Attribution 4.0 International License, which permits use, sharing, adaptation, distribution and reproduction in any medium or format, as long as you give appropriate credit to the original author(s) and the source, provide a link to the Creative Commons license, and indicate if changes were made. The images or other third party material in this article are included in the article's Creative Commons license, unless indicated otherwise in a credit line to the material. If material is not included in the article's Creative Commons license and your intended use is not permitted by statutory regulation or exceeds the permitted use, you will need to obtain permission directly from the copyright holder. To view a copy of this license, visit <http://creativecommons.org/licenses/by/4.0/>.

© The Author(s) 2020



Research paper

Dilution effect on the slow relaxation of a luminescent dysprosium Metal-Organic Framework based on 2,5-dihydroxyterephthalic acid



Antonio A. García-Valdivia^a, Andoni Zabala-Lekuona^b, Ainhoa Goñi-Cárdenas^a, Belén Fernández^c, Jose A. García^d, José F. Quílez del Moral^e, Javier Cepeda^{b,*}, Antonio Rodríguez-Diéguez^{a,*}

^a Dept. of Inorganic Chemistry, C/Severo Ochoa s/n, University of Granada, 18071 Granada, Spain

^b Dept. of Applied Chemistry, Chemistry Faculty, University of the Basque Country UPV/EHU, 20018 Donostia-San Sebastián, Spain

^c Institute of Parasitology and Biomedicine "López-Neyra", CSIC, Av. Conocimiento s/n, 18600 Granada, Spain

^d Departamento de Física Aplicada II, Facultad de Ciencia y Tecnología, Universidad del País Vasco (UPV/EHU), 48940 Leioa, Spain

^e Dept. of Organic Chemistry, C/Severo Ochoa s/n, University of Granada, 18071 Granada, Spain

A B S T R A C T

A new dysprosium based Metal-Organic Framework with $\{[\text{Dy}(\text{dhbdc})_{1.5}(\text{DMF})_2]\cdot\text{DMF}\}_n$ formula has been obtained from solvothermal reaction with 2,5-dihydroxyterephthalic acid ligand and dysprosium chloride. This coordination polymer has been characterized and its crystal structure has been solved by X-ray diffraction methods elucidating a three-dimensional network. Magnetic studies of this compound reveal the existence of weak antiferromagnetic interactions among the metal ions with θ value of -0.26 K. Dynamic *ac* magnetic susceptibility measurements were carried out under an external dc field of 1 kOe, highlighting that at high frequencies two relaxation processes can be observed. However, when studying the diamagnetically diluted analogue **1_v**, a single relaxation process was detected highlighting the effect of the weak but not negligible exchange interactions. Finally, photoluminescence measurements were performed at different temperatures with the aim of getting a more representative characterization of the emissive performance of the material for potential applications in lighting and thermometry.

1. Introduction

The research related to metal-organic frameworks (MOFs) has exponentially increased in the past years mainly due to their multifunctional properties and potential uses in applications such as gas storage/separation, photoluminescence, sensing, magnetism, etc. [1]. These materials are synthesized by combining metal ions or nodes with organic linkers forming three-dimensional structures. Among them, lanthanide based MOFs (Ln-MOFs) have been less studied than transition metal based ones. This is directly related to the large ionic radii of the Ln(III) ions, since they normally present high coordination numbers with distorted symmetries which bring some flexibility to the coordination network, making it more difficult to predict the structure of the compound. However, the large magnetic anisotropy and high spin value of some Ln(III) ions make them potential candidates in order to design ultra-high-density information storage devices [2]. In fact, some recent advances in the area of Single Molecule Magnets (SMMs) have shown that huge thermal energy barriers that prevent the relaxation of the magnetization, as well as open hysteresis loops up to liquid nitrogen temperature could be obtained by using Dy(III) as anisotropic metal ion [3]. Moreover, most of Ln(III) ions may display characteristic narrow

fluorescence emissions, so they might be good candidates in order to obtain multifunctional magnetic and luminescent materials. Accordingly, even though the absorption coefficients of *f-f* transitions are low, the coordination of strongly absorbing ligands to the metal may be a way to overcome this handicap by an efficient antenna effect, which involves an energy transfer from the ligand to the metal [4].

The necessity of implementing SMMs within a surface or in a three-dimensional structure is not trivial. Even though high performing SMMs already exist, these are synthesized in bulk without a controlled spatial position and this appears to be a huge problem. When designing an information storage device, all the molecules that are able to preserve information need to be spatially organized. Hence, MOFs might be a good solution to overcome this challenge given that lanthanide ions are intrinsically organized in the three dimensions within the crystal structure of these materials [5]. In addition, the pores enclosed in the structure of MOFs offer the possibility of intercalating a wide variety of guest molecules that may be able to modulate the magnetic properties [6]. Moreover, with regard to the multifunctional character of MOFs, guest molecules could also influence the luminescent emission of the compound so they could be used as sensors.

In view of the mentioned prerequisites and taking into account the

* Corresponding authors.

E-mail addresses: javier.cepada@ehu.es (J. Cepeda), antonio5@ugr.es (A. Rodríguez-Diéguez).

<https://doi.org/10.1016/j.ica.2020.119687>

Received 26 February 2020; Received in revised form 16 April 2020; Accepted 16 April 2020

Available online 18 April 2020

0020-1693/ © 2020 Elsevier B.V. All rights reserved.

great affinity of Ln(III) ions towards oxygen atoms, we have chosen 2,5-dihydroxyterephthalic acid (dhbdc) as main ligand. Carboxylate groups are often used as chemical functions to decorate spacer ligands in MOFs chemistry given their large bridging capacity, as it has been observed for many related aromatic carboxylate based ligands with both transition metal as lanthanide(III) ions [7]. In particular, the confronted disposition of carboxylate groups in dhbdc ligand is well known to bridge between two and six metal centres with transition metal ions to yield MOFs [8], while hydroxyl groups adjacent to carboxylate groups, though usually they do not chelate metal centers, can serve as exceptional groups which can interact with guest molecules. Nevertheless, some works have been published in which the coordination of these hydroxyl groups to the metal centers has generated MOFs with a fascinating topology and very interesting properties [9].

On another level, the aromatic character of the ligand behaves as an appropriate moiety which, in addition to increase the distance among metal ions to dispose them separated for enhancing SMM behaviour, it can also bring large emission brightness centred on the lanthanide due to its strong absorption through π - π^* transitions.

Bearing in mind the latter, we report on the synthesis and structural and chemico-physical characterization of a new MOF with the $\{[\text{Dy}(\text{dhbdc})_{1.5}(\text{DMF})_2]\cdot\text{DMF}\}_n$ formula, which exhibits interesting magnetic and luminescence properties. On the one hand, alternating current magnetic susceptibility measurements reveal the occurrence of subtle slow relaxation of the magnetization that is effectively improved by means of a structural dilution with diamagnetic yttrium(III) ions. On the other hand, photoluminescence studies performed on both solid state and liquid media support a large ligand-to-metal charge transfer (LMCT) which provides the material with an interesting temperature- and solvent-dependent tuneable bright emission.

2. Experimental

2.1. General

2,5-dihydroxyterephthalic acid and all metallic salts used as reagents were purchased from commercial sources (Sigma-Aldrich) and used as received and without further purification.

2.2. Preparation of the complexes

Synthesis of $\{[\text{Dy}(\text{dhbdc})_{1.5}(\text{DMF})_2]\cdot\text{DMF}\}_n$ (1). Single crystals of compound **1** were obtained following the next solvothermal procedure. 0.076 mmol (15.00 mg) of 2,5-dihydroxyterephthalic acid and 0.101 mmol (38.05 mg) of $\text{DyCl}_3\cdot 6\text{H}_2\text{O}$ were dissolved in 1 mL of DMF. The resulting solution was placed in a closed glass vessel and introduced in an oven at 95 °C for 24 h. Yield: 64% based on metal. Anal Calcd for $\text{DyC}_{21}\text{O}_{12}\text{N}_3\text{H}_{27}$: C, 37.31; H, 4.03; N, 6.22. Found: C, 37.34; H, 3.99; N, 6.24.

Synthesis of $\{[\text{Dy}_{0.2}\text{Y}_{1.8}(\text{dhbdc})_3(\text{DMF})_4]\cdot 2\text{DMF}\}_n$ (1_Y). Single crystals of **1_Y** were obtained by carrying out the same general procedure described for **1** but using a Dy:Y molar ratio of 1:9. Yield: 66% based on metal. Anal Calcd for $\text{Dy}_{0.2}\text{Y}_{1.8}\text{C}_{42}\text{O}_{24}\text{N}_6\text{H}_{54}$: C, 41.37; H, 4.46; N, 6.89. Found: C, 41.41; H, 4.42; N, 6.92.

The FT-IR spectra of complexes **1** and **1_Y** showed the expected vibrational bands, confirming the coordination to O-containing carboxylate group (Fig. S6). The main vibrations of 2,5-dihydroxyterephthalic acid are associated to the stretching vibration at 1643 cm^{-1} and the asymmetric and symmetric vibrations of the carboxylate groups at 1683 cm^{-1} and 1423 cm^{-1} respectively. In addition, the ligand shows a high intensity band 1650 cm^{-1} that in compound **1** and **1_Y** lose intensity, probably due to the bond between O-carboxylate and metal centers. As can be seen in Fig. S6 there is a small displacement in the most characteristic bands due to the coordination of the 2,5-dihydroxyterephthalic acid ligand to the metal centers.

2.3. Physical measurements

Elemental analyses were carried out at the “Centro de Instrumentación Científica” (University of Granada) on a THERMO SCIENTIFIC analyzer model Flash 2000. The IR spectra on powdered samples were recorded with a BRUKER TENSOR 27 FT-IR and OPUS data collection program. Magnetic susceptibility measurements were performed on polycrystalline samples of the complexes with a Quantum Design SQUID MPMS-7 T susceptometer at an applied magnetic field of 1000 G. The susceptibility data were corrected for the diamagnetism estimated from Pascal’s Tables [10] the temperature-independent paramagnetism, and the magnetization of the sample holder. Ac measurements were performed on a Physical Property Measurement System-Quantum Design model 6000 magnetometer under a 3.5 G ac field and frequencies ranging from 60 to 10 000 Hz El vuestro es PPMS tb? Las frecuencias están mal, son de 1 a 1399 Hz.

2.4. Single-crystal structure determination

Prismatic crystals for **1** were mounted on a glass fiber and used for data collection on a Bruker D8 Venture with Photon detector equipped with graphite monochromated $\text{MoK}\alpha$ radiation ($\lambda = 0.71073 \text{ \AA}$). The data reduction was performed with the APEX2 [11] software and corrected for absorption using SADABS [12]. Crystal structures were solved by direct methods using the SIR97 program [13] and refined by full-matrix least-squares on F^2 including all reflections using anisotropic displacement parameters by means of the WINGX crystallographic package [14]. Several crystals of **1** were measured and the structure was solved from the best data we were able to collect, due to the quality of the crystals was very poor. Final $R(F)$, $wR(F^2)$ and goodness of fit agreement factors, details on the data collection and analysis can be found in Table 1. Selected bond lengths and angles are given in Table S1 (see the Supporting Information). CCDC number 1985827 contain the supplementary crystallographic data for compound. These data can be obtained free of charge from The Cambridge Crystallographic Data Centre via www.ccdc.cam.ac.uk/data_request/cif.

Table 1
Crystallographic data for compound **1**.

Complex	1
Formula	$\text{C}_{21}\text{H}_{24}\text{DyN}_3\text{O}_{12}$
M_r	672.93
Crystal system	Triclinic
Space group (no.)	$P\bar{1}$
a (Å)	10.446(2)
b (Å)	10.877(2)
c (Å)	12.503(3)
α (°)	104.644(4)
β (°)	107.329(4)
γ (°)	97.583(4)
V (Å ³)	1278.6(4)
Z	2
D_c (g cm^{-3})	1.748
μ ($\text{MoK}\alpha$) (mm^{-1})	2.988
T (K)	100(2)
Observed reflections	6582 (6086)
R_{int}	0.0495
Parameters	340
$GO F$	1.086
$R_1^{b,c}$	0.0317 (0.0246)
wR_2^d	0.0624 (0.0606)
Largest difference in peak and hole (e \AA^{-3})	2.077 and -2.160

^b $R_1 = \sum ||F_o| - |F_c|| / \sum |F_o|$. ^cValues in parentheses for reflections with $I > 2 \sigma(I)$. ^d $wR_2 = \{ \sum [w(F_o^2 - F_c^2)^2] / \sum [w(F_o^2)^2] \}^{1/2}$.

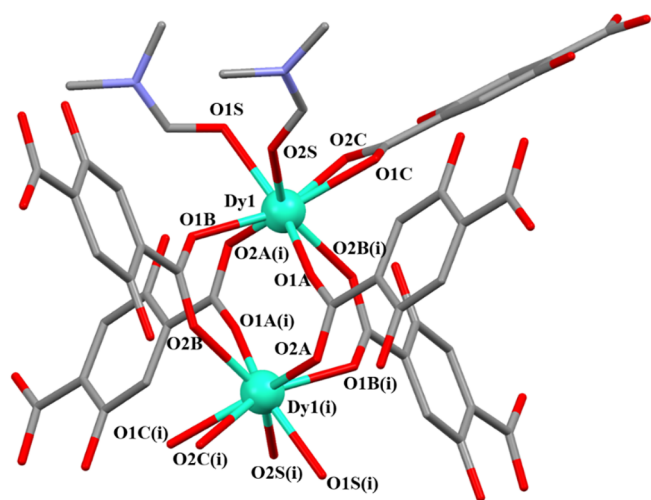


Fig. 1. Excerpt of the structure showing the dinuclear entity, where coordination environment of Dy1 along with carboxylate bridged Dy1 (i) is shown. Symmetry: (i): -x, -y, -z. Colour code: Dysprosium, oxygen, nitrogen and carbon are in light green, red, blue and grey, respectively. Hydrogen atoms have been removed for the sake of clarity. (For interpretation of the references to colour in this figure legend, the reader is referred to the web version of this article.)

3. Results and discussion

3.1. Crystal structure of compound 1

Compound **1** crystallizes in the triclinic $P\bar{1}$ space group. A selection of bond distances and angles, as well as crystallographic data are given in Table S1 and Table 1, respectively. The asymmetric unit is composed of a single dysprosium ion, three independent halves of deprotonated dhhdc ligands, two coordinated DMF molecules and one crystallization DMF molecule. The dysprosium ion is eight-coordinated being bonded to eight oxygen atoms, two of them belonging to two DMF molecules (O1S and O2S) and the rest to carboxylate groups. Whereas O1C and O2C belong to the same chelating carboxylate moiety, O1B, O2B(i), O1A and O2A(i) belong to four carboxylate groups of different dhhdc ligands (two symmetry related A and B ligands), which acquire the local $\mu\text{-}\kappa\text{O}:\kappa\text{O}'$ mode and are responsible for bridging two closest Dy centres forming paddle-wheel dinuclear fragments (Fig. 1). In other words, there are different types of L^{2-} depending on the coordination mode. Two of them (the ones with O1A-O2A and O1B-O2B labels) act as double-bridging groups. On the one hand, a carboxylate group in a bimonodentate fashion is bonded to two Dy ions from the same dinuclear entity and, on the other hand, the other carboxylate in the other extreme is bonded to another dinuclear entity. In contrast, the other type of L^{2-} ligand also appears as bridging group, but each carboxylate is only coordinated to a metal ion as a chelate. Every metal centre is coordinated to four ligands of the former type and one of the latter type, thus extending the structure over the 3D.

The geometry of the polyhedron was calculated by SHAPE software, indicating that it is a slightly distorted square antiprism (S_{SAPR} value of 1.183). These entities can be regarded as the repeating secondary building unit (SBU) along the whole structure and are linked to other neighbouring ones by means of both the tetradentate A and B ligands as well as the bis-chelating C ligands (Fig. 2). The separation between the Dy ions within the dinuclear entity is 4.187(1) Å whereas it rises up to 10.446(2) Å and 11.421(2) Å between adjacent paramagnetic centres crossing the tetradentate and bidentate dhhdc ligands, which indicates that we could expect non-negligible magnetic interactions. Isostructural Metal-Organic Frameworks based on La, Ce, Pr, Nd and Gd have been published [16]. The Dy-O bond distances do not vary according to the nature of coordinating oxygen. Both the shortest and longest bond distances correspond to Dy1-O_{carboxylate} (2.294(2) and 2.577(2),

respectively) bonds, while Dy-O_{DMF} ones display intermediate distances (2.367(2) and 2.410(2)). The fact that the coordination sphere is somewhat regular with no notably shorter bond with respect to others might negatively affect the SMM properties. In the case of Dy(III), a well-defined axial ligand field is able to stabilize the highly magnetic $m_J = \pm 15/2$ states as ground levels and separate them from excited states which, in turn, gives rise to high effective energy barriers.

3.2. Magnetic properties

3.2.1. Static magnetic measurements

The direct-current (dc) magnetic susceptibility of **1** and **1_y** (Fig. S2) were measured in the 2–300 K range under an applied magnetic field of 0.1 T (Fig. 3). The $\chi_M T$ value of 14.19 cm³ K mol⁻¹ (calculated for the asymmetric unit) observed in **1** is in good agreement with the calculated theoretical value of 14.17 cm³ K mol⁻¹ for one isolated Dy(III) ion ($4f^9$, $J = 15/2$, $S = 5/2$, $L = 5$, $g = 4/3$ $^6H_{15/2}$). On cooling, the $\chi_M T$ product remains somehow constant until 50 K, where it falls sharply reaching the minimum value of 12.70 cm³ K mol⁻¹ at 2 K. In ions such as the Dy(III), which contain considerable unquenched orbital moment, this drop could be attributed to some different effects: i) anti-ferromagnetic interactions between paramagnetic ions, ii) the depopulation of the Stark sublevels of the dysprosium ion, which arise from the splitting of the ground term by the ligand field and iii) the presence of magnetic anisotropy. The strong spin-orbit coupling in Dy(III) compounds hinders the possibility to fit the $\chi_M T$ data in order to obtain the exchange coupling constant. However, with the aim of getting a deeper insight into the possible intramolecular interactions between Dy(III) centers, we studied the magnetic data in the range of 2–300 K by the Curie-Weiss law, namely $1/\chi = (T - \theta)/C$. The best fit afforded the values of $C = 14.17$ cm³ K mol⁻¹ and $\theta = -0.26$ K. The negative value of θ suggests the existence of weak intramolecular antiferromagnetic interactions. This is in good agreement with the previously reported J values for an isostructural Gd(III) analogue [15]. The isotropic character of Gd(III) provided by the lack of angular momentum enables the analysis of the magnetic data in order to obtain the magnetic coupling constant. The small value of $J = -0.020(2)$ cm⁻¹ calculated by Nayak and co-authors coincides with our initial prediction, being the dimeric Dy(III) entities weakly antiferromagnetically coupled systems.

With the purpose of supporting the experimental data, DFT calculations with the broken-symmetry methodology were also conducted to better estimate the nature of the magnetic exchange interactions. To that end, dimeric fragments were cut from the crystal structure of **1** in order to represent the three possible superexchange pathways found in the compound: i) that mediated within the paddle-wheel shaped entity involving four carboxylate moieties (which imposes a short bridge of 4.2 Å between lanthanide(III) atoms); ii) through the bis-chelating dhhdc ligand (involving a Ln...Ln distance of 11.4 Å); and iii) through the tetradentate dhhdc ligand, which imposes a Ln...Ln distance of ca. 10.9 Å. Moreover, paramagnetic Dy(III) ions were replaced by isotropic Gd(III) ones to have a good estimate of the J parameter (we were not able to crystallise the Gd(III) analogue). In this case, based on the superexchange path 1 (Fig. S6), which considers the shortest carboxylate bridged pathways, the calculation suggests an almost negligible coupling among lanthanide(III) ions (weak ferromagnetism with $J \sim 0.02$ cm⁻¹ is achieved), which can be considered within the calculation error given the experimental result achieved for the Dy(III) counterpart. Although experimental and theoretical calculations differ in the nature of the exchange interactions, it is evidenced that the carboxylate bridges provide weakly interacting pathways. Therefore, due to the magnetic anisotropy of the Dy(III) ion the contribution of the metal to metal exchange is hidden in 1.

The magnetization *versus* field plot at 2 K is shown in the Fig. S1. It shows an initial rapid increase up to a field of 1 T, followed by an almost linear increase reaching a value of 6.35 $N\mu_B$, which is lower than the expected saturation value. This behaviour can be explained by

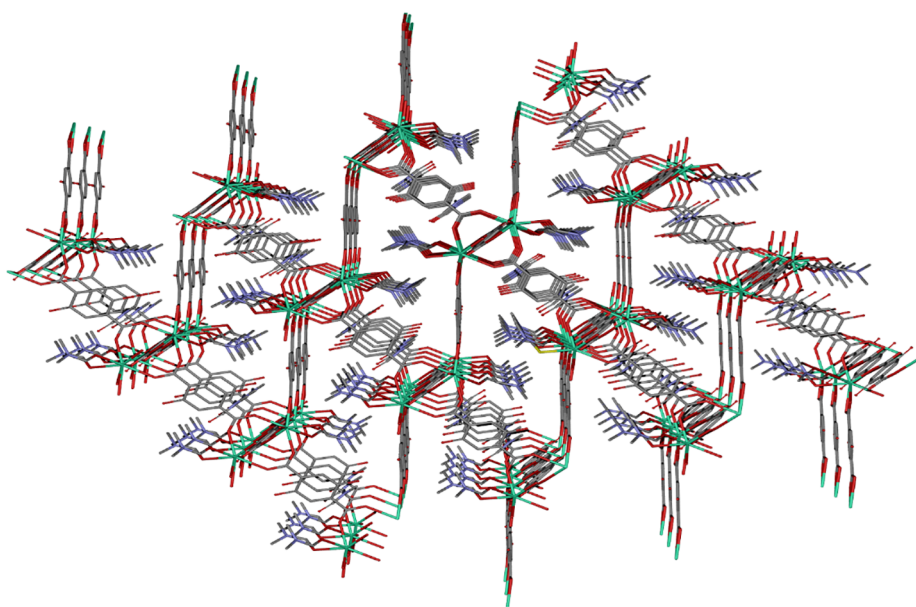


Fig. 2. Perspective of Metal-Organic Framework along *a* axis. Colour code: Dysprosium, oxygen, nitrogen and carbon are in light green, red, blue and grey, respectively. Hydrogen atoms have been removed for the sake of clarity. (For interpretation of the references to colour in this figure legend, the reader is referred to the web version of this article.)

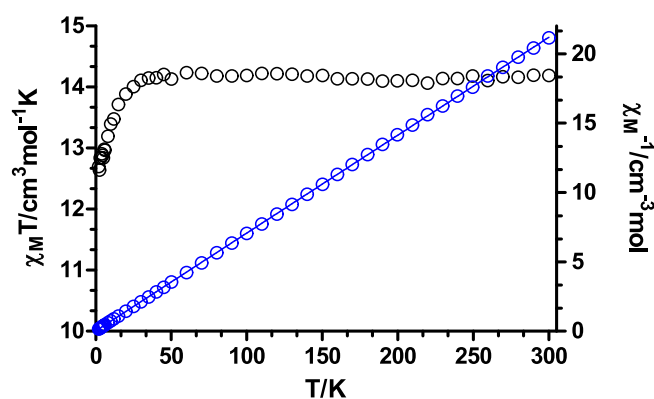


Fig. 3. Temperature dependence of the $\chi_M T$ product and $1/\chi$ versus T for **1** in the 2–300 K range. The solid line represents the best fitting with the Curie-Weiss law.

crystal-field effects leading to significant magnetic anisotropy.

3.2.2. Dynamic magnetic properties

Dynamic *ac* magnetic susceptibility measurements as a function of temperature and frequency were carried out on a powder sample of **1**. At zero applied *dc* field, the out-of-phase component (χ_M'') displays non-zero signals at the highest measured frequency (1399 Hz, Fig. S3). However, no maxima could be seen even at the lowest temperature. This behaviour suggests that probably a fast relaxation of the magnetization is occurring through the under-barrier quantum tunnelling of the magnetization process (QTM). Nevertheless, it is well known that an external magnetic field could be a good strategy so as to lift the degeneracy of the ground-state $\pm m_J$ energy levels, thus partially or totally quenching the mentioned effect [17]. Accordingly, the measurements were carried out again under an external *dc* field of 1 kOe with intriguing results (Fig. 4). Although low frequency curves do not display maxima, there is a clear frequency dependence of the χ_M'' product. In addition, at higher frequencies two relaxation processes can be observed, one at lower temperatures (2.0–4.0 K, Fast Relaxation) and the other at notably higher ones (6.0–8.0 K, Slow Relaxation). This result indicates that *i*) the external magnetic field is only able to partially suppress the QTM (since the χ_M'' values do not go to zero below the maxima at lowest temperatures, revealing that QTM still operates) and that *ii*) magnetic exchange or dipolar interactions between the

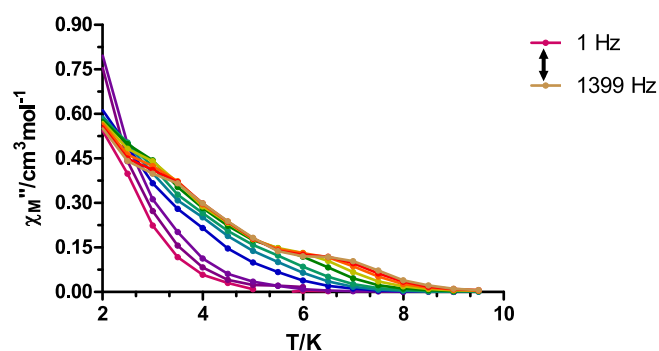


Fig. 4. Temperature and frequency dependence of the out-of-phase *ac* susceptibility of **1** under an external *dc* field of 1 kOe.

neighbouring Dy ions may play an essential role in the relaxation process due to the appearance of a second maximum. It is worth mentioning, though, that the presence of two maxima could also arise from a single ion [2b,18]. Taking into account that the maxima are not well defined, the treatment of the data becomes much more complicated and prevents no further analysis. Indeed, we were not able to fit the data in order to obtain parameters such as the effective energy barrier (U_{eff}), τ_0 or α . Nonetheless, it can be seen that the relaxation mechanisms are not pure Orbach processes.

To get insight into the role of exchange or dipolar interactions induced by neighbouring metal centres, a diluted sample of **1** was prepared. The compound **1_Y** was synthesized by mixing the diamagnetic analogue Y(III) along with Dy(III) in a Dy/Y molar ratio of 1:9. This procedure allows us to observe the influence of intramolecular interactions in terms of relaxation of the magnetization and, at the same time, is another typical strategy to avoid the fast QTM that could arise from dipolar interactions [19].

The **1_Y** sample was then measured in the same conditions as the undiluted sample. The results show that *i*) the peaks at the highest temperatures related to the SR have disappeared and *ii*) the peaks at lower temperatures related to FR are now well defined, since both the dilution and the external *dc* field are a good combination to quench QTM (Fig. 5). Regarding to the first consequence, it is now evident that the slowest relaxation in the undiluted sample arose from the effect of the intramolecular exchange interactions and not from single-ion. In fact, when analysing the easy axes of magnetization of an isolated dinuclear entity within the whole structure by the Magellan software

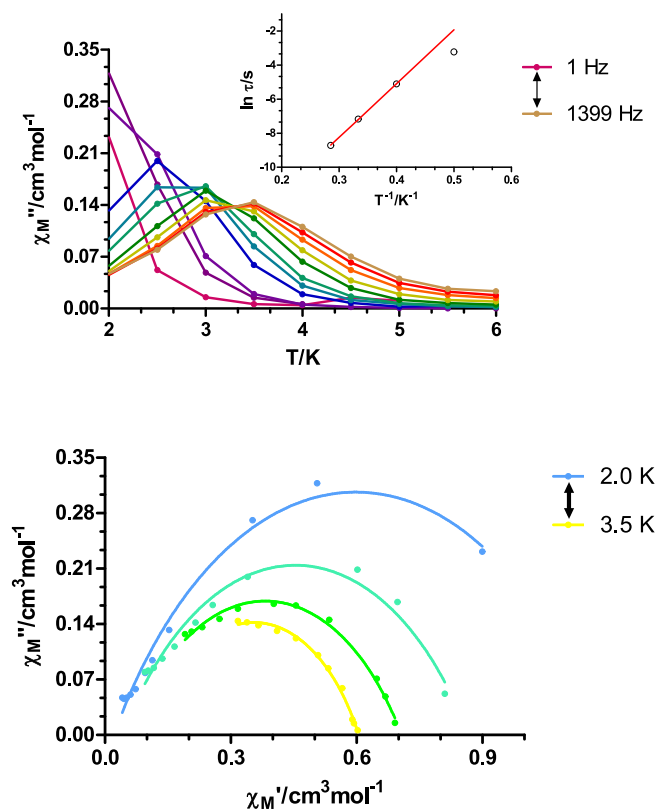


Fig. 5. Temperature and frequency dependence of the out-of-phase ac susceptibility of 1_Y under an external dc field of 1 kOe (top), Arrhenius plot of relaxation time versus temperature for 1_Y (the solid line represents the best fit to the Arrhenius law, top inset) and Cole-Cole plots of 1_Y under 1 kOe dc field in the temperature range of 2.0–3.5 K (solid lines are the best fit to the generalized Debye mode, bottom).

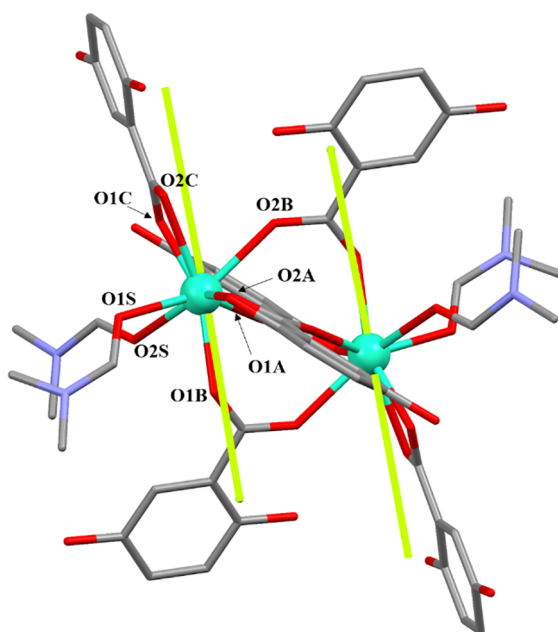


Fig. 6. Magnetic axes of the Dy(III) ions calculated with the Magellan software. A neutral reduced dinuclear fragment of the structure was considered in order to obtain a reliable result. Hydrogen atoms were omitted for the sake of clarity, but they were included in the calculation.

[20], it is demonstrated that the anisotropy axes are completely parallel (which is, in turn, due to the inversion centre, Fig. 6). It has been recently reported that the angle between the anisotropy axes plays an essential role in relaxation dynamics with magnetically coupled systems, emphasizing that collinear or almost collinear systems show the slowest relaxation times [21]. Therefore, this might be the reason why the SR is lost when diluting the sample. In regard to the FR, relaxation times and α parameters were extracted from the frequency-dependent data between 2.0 and 3.5 K. The τ values corresponding to the highest temperature were fitted to the Arrhenius law, $\tau = \tau_0 \exp(U_{eff}/kT)$, obtaining the following parameters: $U_{eff} = 31.6$ K and $\tau_0 = 2.0 \cdot 10^{-8}$ s. The obtained τ_0 value lies in the expected range of $10 \cdot 10^{-6}$ to $10 \cdot 10^{-11}$ s [22]. The deviation from linearity of the lowest temperature data point, as well as the α values obtained from the Cole-Cole plots (0.38 (2.0 K) – 0.34 (3.5 K)) suggest a quite broad distribution of relaxation processes. However, we were not able to obtain a good fitting assuming the simultaneous presence of different processes.

The relatively poor SMM properties of this system could be explained by an exhaustive study of the ligand field. As aforementioned in the crystal structure description, the coordination environment polyhedron fits well with the square-antiprism geometry. It has been seen in the literature that this kind of geometry is suitable to establish an axial crystal field around the Dy(III) centre [23]. However, this is not the unique prerequisite to obtain high performance SMMs. In an ideal crystal field, the axially coordinated atoms should have the largest amount of negative charge and they should exhibit the shortest distance towards the metal ion, thus the $m_j = \pm 15/2$ ground state will be well isolated from the excited states. Additionally, the opposite is desired for the equatorial ligand field. Less charged, or neutral, donor atoms will facilitate diminishing the transverse components that favour other relaxing processes that shortcut the always desired through barrier Orbach mechanism. In our case, the anisotropy axes are defined by the chelate carboxylate group (O1 and O2) and one monodentate carboxylate (O4), probably due to the negative charge afforded by the chelate. However, none of these bonds are the shortest ones. Instead, the shortest distance corresponds to Dy1-O8 bond in the equatorial plane, which is counteracting the axial ligand field provided by the chelate. Moreover, another two carboxylate oxygen atoms (O5 and O9) are also located in the equatorial plane with relatively short bond distances. Fortunately, the neutral DMF molecules complete the equatorial field and these ones will not be the maximum responsible of the transverse field. With all this in mind, the none outstanding magnetic properties of our system are not a surprise, but it appears as an interesting model to evaluate the influence of a variety of parameters governing the slow relaxation of the magnetization.

3.3. Luminescence properties

Photoluminescence measurements were performed on polycrystalline sample of compound **1** at different temperatures with the aim of getting a more representative characterization of the emissive performance of the material for potential applications in lighting and thermometry. It is well-known that lanthanide based PL constitutes a promising means to develop materials with promising performance for light-emitting, display sensing, optical devices [24] in vivo detection [25]. Despite the fact that organic luminescent compounds are emerging as an alternative source which promotes efficient organic light-emitting diodes (OLEDs) [26], lanthanide based CPs bring the advantages of both classes of materials, affording a more brilliant emission of the organic ligands through the ligand-to-lanthanide energy transfer (antenna effect) [27] or, at least, a significant emission enhancement due to the coordination [28]. At room temperature, the PL emission spectrum measured at $\lambda_{ex} = 325$ nm (under monochromatic LASER light) shows an intense and somehow broad band centred at 450 nm that possesses significant emission up to 650 nm. Focusing this main emission, the excitation spectra reveals also a unique band

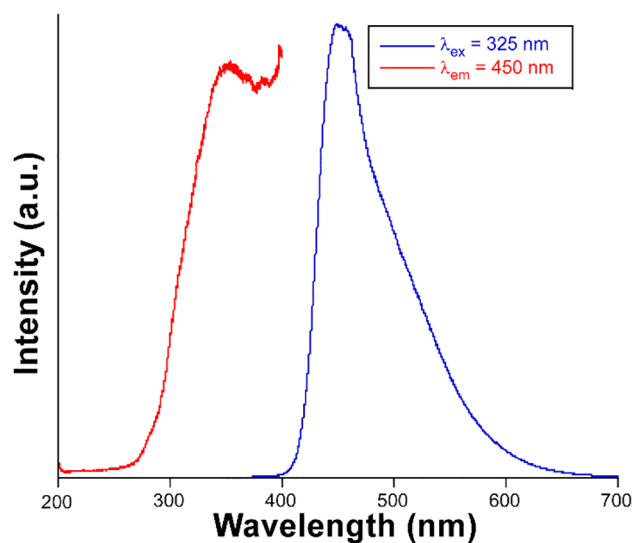


Fig. 7. Excitation and emission spectra of compound 1 at room temperature.

peaking at 350 nm (Fig. 7). The shape and width of all bands seem to indicate that they correspond to $\pi \leftarrow \pi^*$ transitions taking place within the aromatic rings of the ligand. It is worth noticing the absence of any of the characteristic transitions attributed to the inner f orbitals of the lanthanide atom [29], which makes one guess that the ligand-to-lanthanide energy transfer is poor. This fact may be due to proximity of the hydroxyl groups with regard to the Dy ion, since, occupying the first coordination sphere, could act as effective quenchers of the metal-centred PL emission [30].

In any case, the strong emission observed in the spectrum imbues compound 1 with a remarkable blue emission light, which may be inferred from the photographs taken on single crystals in a microscope under excitation at 365 nm (Fig. 8). In fact, the tail observed in the emission spectrum at high wavelength also provides it with a still strong (although comparatively weak) green and even red coloured lights when they are irradiated with less energetic beams (λ_{exc} of 435 and

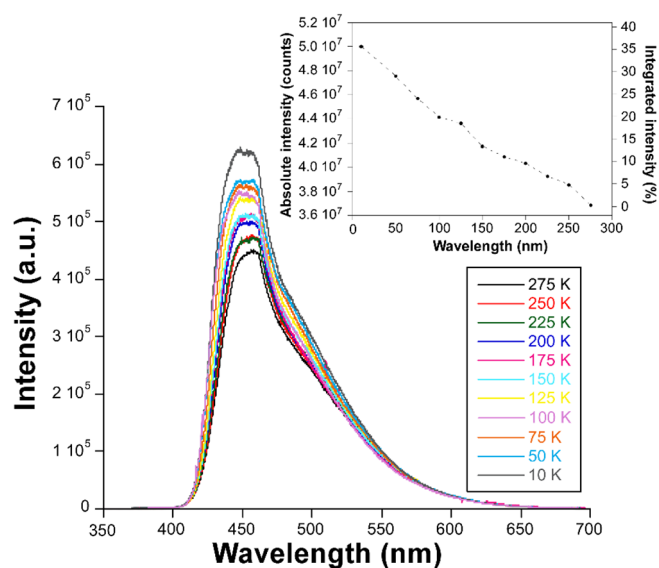


Fig. 9. Variable temperature emission spectra. Inset: evolution of the integrated emission intensity.

546 nm).

When the sample is cooled down to 10 K, the emission band shows no remarkable change in its shape yet it undergoes a subtle blue-shift (from 450 to 445 nm) while it also gains intensity compared to room temperature owing to the decrease of the kinetic (thermal) energy of the bond electrons (Fig. 9) [31]. Though the increase in the emission intensity is quite progressive with the temperature, the largest step takes place in the 50 \rightarrow 10 K range, where the intensity shows a quantitative leap. To summarize, the emission intensity at $\lambda_{\text{max}} \approx 450$ nm is much greater for 10 K data compared to RT (about 36% larger in terms of emitted integrated intensity).

Additionally, the emission decay curves recorded at the band maximum ($\lambda_{\text{em}} = 450$ nm) revealed the occurrence of a fluorescent process below the detection limit of the employed pulse lamp (below

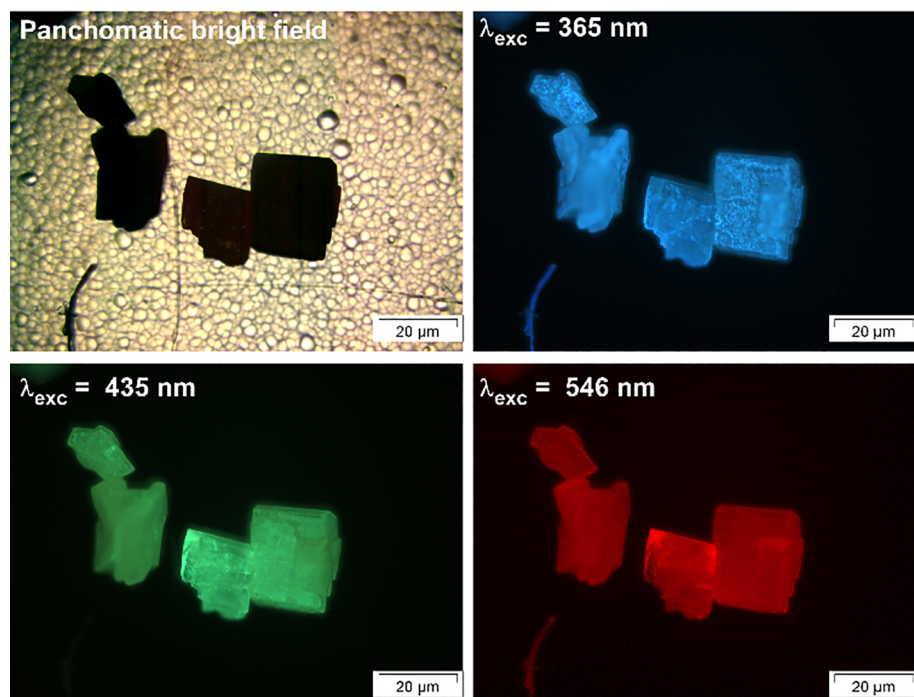


Fig. 8. Room temperature micro-PL images taken at different excitation lines.

1 μ s), given that no reliable long-lived tail could be discerned from the lamp signal.

4. Conclusions

A new dysprosium based Metal-Organic Framework with $\{[\text{Dy}(\text{dhbdc})_{1.5}(\text{DMF})_2]\cdot\text{DMF}\}_n$ formula has been obtained from solvothermal reaction with 2,5-dihydroxyterephthalic acid ligand and dysprosium chloride. This coordination polymer has been characterized and its crystal structure has been solved by X-ray diffraction methods elucidating a three-dimensional network. Magnetic studies of this compound reveal the existence of weak antiferromagnetic interactions among the metal ions with θ value of -0.26 K. Dynamic *ac* magnetic susceptibility measurements were carried out under an external dc field of 1 kOe, highlighting that at higher frequencies two relaxation processes can be observed. In order to determine whether both relaxations are of single ion in origin, or intramolecular interactions are the responsible ones, a diluted sample of **1** was prepared by mixing the diamagnetic analogue Y(III) along with Dy(III) in a Dy/Y molar ratio of 1:9. The *ac* magnetic data of **1**_Y displays a unique relaxation process with an effective energy barrier of $U_{\text{eff}} = 31.6$ K, while the SR attributed to the exchange coupled system has disappeared pointing out the influence of the intramolecular interactions. On the other hand, photoluminescence measurements at different temperatures with the aim of getting a more representative characterization of the emissive performance of the material for potential applications in lighting and thermometry. The PL emission spectrum measured at room temperature under monochromatic LASER light ($\lambda_{\text{ex}} = 325$ nm) shows an intense and somehow broad band centred at 450 nm that possesses significant emission up to 650 nm, which corresponds to $\pi \leftarrow \pi^*$ transitions taking place within the aromatic rings of the ligand. Cooling the sample down progressively to 10 K brings a subtle blue-shift of the band accompanied by an increase in the integrated intensity of about 36% compared to room temperature. The almost linear progression shown according to the temperature suggests a potential application of the material for lighting and thermometry.

CRediT authorship contribution statement

Antonio A. García-Valdivia: Investigation. **Andoni Zabala-Lekuona:** Data curation. **Ainhoa Goñi-Cárdenas:** Investigation. **Belén Fernández:** Data curation. **Jose A. García:** Formal analysis. **José F. Quílez del Moral:** Data curation. **Javier Cepeda:** Supervision, Writing - original draft. **Antonio Rodríguez-Diéguez:** Supervision, Writing - review & editing.

Declaration of Competing Interest

The authors declare that they have no known competing financial interests or personal relationships that could have appeared to influence the work reported in this paper.

Acknowledgements

Financial support was given by Junta de Andalucía (Spain) (project number FQM-394 and FQM-1484), University of the Basque Country (GIU 17/13), Gobierno Vasco/Eusko Jaurlaritz (IT1005-16) and the Spanish Ministry of Economy and Competitiveness (MCIU/AEI/FEDER, UE) (PGC2018-102052-A-C22, PGC2018-102052-B-C21 and CTQ-2015-64049-C3-3R). The authors thank for technical and human support provided by SGIker of UPV/EHU and European funding (ERDF and ESF). A.Z.-L. is grateful to the Government of the Basque Country for the predoctoral fellowship.

Appendix A. Supplementary data

Supplementary data to this article can be found online at <https://doi.org/10.1016/j.ica.2020.119687>.

References

- [1] a) D. Bradshaw, A. Garai, J. Huo, *Chem. Soc. Rev.* 41 (2012) 2344–2381; b) A. Betard, R.A. Fischer, *Chem. Rev.* 112 (2012) 1055–1083; c) E. Coronado, G. MinguezEspallargas, *Chem. Soc. Rev.* 42 (2013) 1525–1539; d) M.D. Allendorf, C.A. Bauer, R.K. Bhakta, R.J.T. Houk, *Chem. Soc. Rev.* 38 (2009) 1330–1352.
- [2] a) M. Wuttig, N. Yamada, *Nat. Mater.* 6 (2007) 824–832; b) D. Lencer, M. Salinga, M. Wuttig, *Adv. Mater.* 23 (2011) 2030–2058.
- [3] F.-S. Guo, B.M. Day, Y.-C. Chen, M.-L. Tong, A. Mansikkamäki, R.A. Layfield, *Science* 362 (2018) 1400–1403.
- [4] a) J.C.G. Bünzli, C. Piguet, *Chem. Soc. Rev.* 34 (2005) 1048–1077; b) D. Parker, *Chem. Soc. Rev.* 33 (2004) 156–165; c) J. Heine, K. Müller-Buschbaum, *Chem. Soc. Rev.* 42 (2013) 9232–9242.
- [5] K. Liu, X. Zhang, X. Meng, W. Shi, P. Cheng, A.K. Powell, *Chem. Soc. Rev.* 45 (2016) 2423–2439.
- [6] X. Zhang, V. Vieru, X. Feng, J.-L. Liu, Z. Zhang, B. Na, W. Shi, B.-W. Wang, A.K. Powell, L.F. Chibotaru, S. Gao, P. Cheng, J.R. Long, *Angew. Chem. Int. Ed.* 54 (2015) 9861–9865.
- [7] a) Y.-L. Wang, Y.-L. Jiang, Z.-J. Xiahou, J.-H. Fu, Q.-Y. Liu, *Dalton Trans.* 41 (2012) 11428–11437; b) D.S. Zhou, F.K. Wang, S.Y. Yang, Z.X. Xie, R.B. Huang, *CrystEngComm* 11 (2009) 2548–2554; c) I. Oyarzabal, B. Fernández, J. Cepeda, S. Gómez-Ruiz, A.J. Calahorra, J.M. Seco, A. Rodríguez-Diéguez, *CrystEngComm* 18 (2016) 3055–3063; d) A.J. Calahorra, I. Oyarzabal, B. Fernández, J.M. Seco, T. Tian, D. Fairen-Jimenez, E. Colacio, A. Rodríguez-Diéguez, *Dalton Trans.* 45 (2016) 591–598.
- [8] a) N.L. Rosi, J. Kim, M. Eddaoudi, B. Chen, M. O’Keeffe, O.M. Yaghi, *J. Am. Chem. Soc.* 127 (2005) 1504–1518; b) P.D.C. Dietzel, Y. Morita, R. Bloma, H. Fjellvåg, *Angew. Chem. Int. Ed.* 44 (2005) 6354–6358; c) P.D.C. Dietzel, B. Panella, M. Hirscher, R. Bloma, H. Fjellvåg, *Chem. Commun.* (2006) 959–961; d) K. Jayaramulu, P. Kanoo, S.J. George, T.K. Maji, *Chem. Commun.* 46 (2010) 7906–7908; e) T. Devic, P. Horcajada, C. Serre, F. Salles, G. Maurin, B. Moulin, D. Heurtaux, G. Clet, A. Vimont, J.-M. Grenèche, B.L. Ouay, F. Moreau, E. Magnier, Y. Filinchuk, J. Marrot, J.C. Lavalley, M. Daturi, G. Férey, *J. Am. Chem. Soc.* 132 (2010) 1127–1136.
- [9] a) W.L. Queen, M.R. Hudson, E.D. Bloch, J.A. Mason, M.I. Gonzalez, J.S. Lee, D. Gygi, J.D. Howe, K. Lee, T.A. Darwish, M. James, V.K. Peterson, S.J. Teat, B. Smit, J.B. Neaton, J.R. Long, C.M. Brown, *Chem. Sci.* 5 (2014) 4569–4581; b) G. Calleja, R. Sanz, G. Orcajo, D. Briones, P. Leo, F. Martínez, *Catal. Today* 227 (2014) 130–137.
- [10] A. Earnshaw, Academic Press, London, 1968.
- [11] Bruker Apex2, Bruker AXS Inc., Madison, Wisconsin, USA, 2004.
- [12] G.M. Sheldrick, SADABS, Program for Empirical Adsorption Correction, Institute for Inorganic Chemistry, University of Göttingen, Germany, 1996.
- [13] A. Altomare, M.C. Burla, M. Camilla, G.L. Casciarano, C. Giacovazzo, A. Guagliardi, A.G.G. Moliterni, G. Polidori, R. Spagna, *J. Appl. Cryst.* 32 (1999) 115–119.
- [14] (a) G.M. Sheldrick, SHELX-2014, Program for Crystal Structure Refinement, University of Göttingen, Germany, 2014; (b) L.J. Farrugia, *J. Appl. Cryst.* 32 (1999) 837–838.
- [15] M. Ljunell, D. Casanova, J. Cirera, J. M. Boffill, P. Alemany, S. Alvarez, M. Pinsky and D. Avnir, SHAPE, v1.1b; Barcelona, Spain, 2005.
- [16] S. Nayak, H.P. Nayek, C. Pietzonka, G. Novitchi, S. Dehnen, *J. Mol. Struct.* 1004 (2011) 82–87.
- [17] a) J. Ruiz, A.J. Mota, A. Rodríguez-Diéguez, S. Tatos, J.M. Herrera, E. Ruiz, E. Cremades, J.P. Costes, E. Colacio, *Chem. Commun.* 48 (2012) 7916–7918; b) C.-M. Liu, D.-Q. Zhang, D.-B. Zhu, *RSC Adv.* 4 (2014) 36053–36056.
- [18] S. Das, A. Dey, S. Biswas, E. Colacio, V. Chandrasekhar, *Inorg. Chem.* 53 (2014) 3417–3426.
- [19] J. Ruiz, A.J. Mota, A. Rodríguez-Diéguez, S. Titos, J.M. Herrera, E. Ruiz, E. Cremades, J.P. Costes, E. Colacio, *Chem. Commun.* 48 (2012) 7916–7918.
- [20] N.F. Chilton, D. Collison, E.J.L. McInnes, R.E.P. Winpenny, A. Soncini, *Nat. Commun.* 4 (2013) 2551–2558.
- [21] J.D. Hilgar, M.G. Bernbeck, J.R. Rinehart, *J. Am. Chem. Soc.* 141 (2019) 1913–1917.
- [22] a) P.F. Shi, Y.Z. Zheng, X.Q. Zhao, G. Xiong, B. Zhao, F.F. Wan, P. Cheng, *Chem. Eur. J.* 18 (2012) 15086–15091; b) R. Sessoli, D. Gatteschi, A. Caneschi, M.A. Novak, *Nature* 365 (1993) 141–143; c) R. Vincent, S. Klyatskaya, M. Ruben, W. Wernsdorfer, F. Balestro, *Nature* 488 (2012) 357–360.
- [23] a) I. Oyarzabal, J. Ruiz, J.M. Seco, M. Evangelisti, A. Camón, E. Ruiz, D. Aravena, E. Colacio, *Chem. Eur. J.* 20 (2014) 14262–14269; b) I. Oyarzabal, J. Ruiz, E. Ruiz, D. Aravena, J.M. Seco, E. Colacio, *Chem. Commun.* 51 (51) (2015) 12353–12356; c) N. Ishikawa, M. Sugita, T. Ishikawa, S.-Y. Koshihara, Y. Kaizu, *J. Am. Chem. Soc.* 125 (2003) 8694–8695.

- [24] (a) K. Binnemans, *Chem. Rev.*, 109 (2009) 4283–4374. (b) S. V. Eliseeva and J.-C. G. Bünzli, *Chem. Soc. Rev.*, 2010, 39, 189–227. (c) J. B. Beck and S. J. Rowan, *J. Am. Chem. Soc.*, 125 (2003) 13922–13923. (d) J. Rocha, C. D. S. Brites and L. D. Carlos, *Chem.–Eur. J.*, 22 (2016) 14782–14795; (e) J. Heine and K. Müller-Buschbaum, *Chem. Soc. Rev.*, 42 (2013) 9232–9242.
- [25] (a) I. Hemmilä, *J. Alloy. Compd.* 225 (1995) 480–485; (b) J. Moynagh, H. Schimmel, *Nature* 400 (1999) 105.
- [26] (a) C. Murawski, K. Leo, M.C. Gather, *Adv. Mater.* 25 (2018) 6801; (b) K. Hong, J.-L. Lee, *Chem. Soc. Rev.* 43 (2014) 5994–6010; (c) H. Uoyama, K. Goushi, K. Shizu, H. Nomura, C. Adachi, *Nature* 492 (492) (2012) 234–238.
- [27] (a) J.C.G. Bünzli, C. Piguet, *Chem. Soc. Rev.* 34 (2005) 1048–1077; (b) D. Parker, *Chem. Soc. Rev.* 33 (33) (2004) 156–165; (c) J. Heine, K. Muller-Buschbaum, *Chem. Soc. Rev.* 42 (2013) 9232–9242.
- [28] (a) Q. Zheng, F. Yang, M. Deng, Y. Ling, X. Liu, Z. Chen, Y. Wang, L. Weng, Y. Zhou, *Inorg. Chem.* 52 (2013) 10368–10374; (b) H.-Y. Ren, C.-Y. Han, M. Qu, X.-M. Zhang, *RSC Adv.* 4 (2014) 49090–49097.
- [29] (a) Y.L. Gai, K.-C. Xiong, L. Chen, Y. Bu, X.-J. Li, F.L. Jiang, M.C. Hong, *Chemistry* 51 (2012) 13128–13137; (b) S. Quici M. Cavazzini, G. Marzanni, G. Accorsi, N. Armaroli, B. Ventura, and F. Barigelletti, *Inorg. Chem.* 44 2005 529 537. (c) J.M. Seco, I. Oyarzabal, S. Pérez-Yáñez, J. Cepeda, A. Rodríguez-Diéguez, *Inorg. Chem.* 55 (2016) 11230–11248
- [30] A. Beeby, I.M. Clarkson, R.S. Dickins, S. Faulkner, D. Parker, L. Royle, A.S. de Sousa, J.A. Gareth Williams, M. Woods, *J. Chem. Soc. Perkin Trans. 2* (1999) 493–504.
- [31] (a) P.C.R. Soares-Santos, L. Cunha-Silva, F.A. Almeida-Paz, R.A.S. Ferreira, J. Rocha, L.D. Carlos, H.I.S. Nogueira, *Inorg. Chem.* 49 (2010) 3428–3440; (b) J. Cepeda, S. Pérez-Yáñez, G. Beobide, O. Castillo, J.A. García, M. Lanchas, A. Luque, *Dalton Trans.* 44 (2015) 6972–6986; (c) J. Rocha, C.D.S. Brites, L.D. Carlos, *Chem. Eur. J.* 22 (2016) 14782–14795.



Antiparasitic, anti-inflammatory and cytotoxic activities of 2D coordination polymers based on 1H-indazole-5-carboxylic acid

Antonio A. García-Valdivia^a, Amalia García-García^a, Fatin Jannus^b, Andoni Zabala-Lekuona^c, José M. Méndez-Arriaga^d, Belén Fernández^{e,*}, Marta Medina-O'donnell^f, Gloria B. Ramírez-Rodríguez^a, José M. Delgado-López^a, Luisa M. Pastrana-Martínez^a, Javier Cepeda^c, José A. Lupiáñez^b, Fernando J. Reyes-Zurita^{b,*}, Antonio Rodríguez-Diéguez^{a,*}

^a Departamento de Química Inorgánica, Facultad de Ciencias, Universidad de Granada, Av. Fuentenueva s/n, 18071 Granada, Spain

^b Departamento de Bioquímica y Biología Molecular I, Facultad de Ciencias, Universidad de Granada, Av. Fuentenueva s/n, 18071 Granada, Spain

^c Departamento de Química Aplicada, Facultad de Química, Universidad del País Vasco (UPV/EHU), Paseo Manuel Lardizabal, no 3, 20018 Donostia-San Sebastián, Spain

^d Department of Biology and Geology, Physics and Inorganic Chemistry, Calle Tulipán s/n, 28933 Móstoles, Madrid, Spain

^e Institute of Parasitology and Biomedicine "López-Neyra", CSIC, Av. Conocimiento s/n, 18600 Granada, Spain

^f Departamento de Química Orgánica, Facultad de Ciencias, Universidad de Granada, Av. Fuentenueva s/n, 18071 Granada, Spain

ARTICLE INFO

Keywords:

Antiparasitic
Anti-inflammatory
Coordination polymers
1H-indazole-5-carboxylic acid
Anticancer activity

ABSTRACT

We report on the formation of two novel multifunctional isomorphous (4,4) square-grid 2D coordination polymers based on 1H-indazole-5-carboxylic acid. To the best of our knowledge, these complexes are the first examples of 2D-coordination polymers constructed with this novel ligand. We have analysed in detail the structural, magnetic and anti-parasitic properties of the resulting materials. In addition, the capability of inhibiting nitric oxide production from macrophage cells has been measured and was used as an indirect measure of the anti-inflammatory response. Finally, the photocatalytic activity was measured with a model pollutant, *i.e.* vanillic acid (phenolic compound), with the aim of further increasing the functionalities and applicability of the compounds.

1. Introduction

In the last decades, the study of coordination polymers (CPs) has increased exponentially because of their potential applications in different areas of science owing to the continuous advances shown by these multifunctional materials [1–5]. Experimental conditions such as temperature, solvent, stoichiometry and pH need to be carefully controlled during the synthesis of CPs [6–9]. These conditions play a major role in the intrinsic characteristics of the structural components, which in turn make the difference to generate advanced materials with fascinating functionalities [10,11]. Aromatic ligands with carboxylate groups are widely used owing to rigidity as well as high coordination capacity, resulting in different binding modes and interesting crystal packings [12–14]. On the other hand, first row transition metal ions are a perfect choice for obtaining new materials with excellent physical properties [14–17]. In fact, it has been observed that family of indazole-carboxylic acids together with first row transition metals have a great potential for the construction of new coordination compounds with a

wide range of traits [18–22].

In the last years, our group and others have reported the use of different nitrogen derivative ligands with specific antiparasitic activities, with a particular focus on the behaviour of the triazolopyrimidine ligands [23–26]. In addition, materials with anti-inflammatory or anti-diabetic activity have been synthesized in our laboratory with this class of organic ligands [27–29]. Based on these previous results, we decided to use a novel organic linker to construct new CPs and to study different physical properties of these materials based on transition metal ions. In this sense, we chose the 1H-indazole-5-carboxylic acid due to, to the best of our knowledge, there is only one example of coordination compound based on this ligand, specifically, this compound is based on copper and consists of two interpenetrated networks with hysteretic carbon dioxide sorption [30]. Therefore, in addition to the biological properties, we will be able to characterize the synthesized materials by studying other properties such as magnetism or photocatalysis, or even other very interesting properties could be studied in case the materials show superparamagnetism [31]. In this sense, the use of transition

* Corresponding authors.

E-mail addresses: belenfernandez@ipb.csic.es (B. Fernández), ferjes@ugr.es (F.J. Reyes-Zurita), antonio5@ugr.es (A. Rodríguez-Diéguez).

<https://doi.org/10.1016/j.jinorgbio.2020.111098>

Received 25 March 2020; Received in revised form 27 April 2020; Accepted 30 April 2020

Available online 18 May 2020

0162-0134/ © 2020 Elsevier Inc. All rights reserved.

metal ions generates the possibility of the study of magnetic properties [32,33] while, on the other hand, nitrogen aromatic ligands are widely employed in the preparation of new CPs that show excellent photocatalytic degradation of organic wastes [34,35], principally the Ni-CPs are very attractive in this field [36].

However, the main objective of this work is the study of the biological properties that these materials may exhibit, such as anti-parasitic or anti-inflammatory activities. Bioinorganic and medicinal chemists have focused on the design and synthesis of new metal-based agents with better biological activity, lower toxicity and different mechanisms of action to overcome the unresolved clinical problems of some current therapeutic agents [37,38]. For example, non-steroidal anti-inflammatory drugs comprise a large group of medicines used to inflammation and pain with known side-effects [39,40]. For this reason CPs have been broadly studied over recent years as anti-inflammatory drugs [41,42]. Nitric oxide (NO) is a very important mediator in acute or chronic inflammation. This radical compound is produced by constitutive and inducible nitric oxide synthases. The inducible enzyme is activated in response to pro-inflammatory signals as LPS (either bacterial lipopolysaccharide), enterotoxin, or cytokines as TNF α (tumor necrosis factor α) or INF- γ (interferon- γ) in macrophages, hepatocytes, and endothelial cells. The reduction of NO can be produced by directly scavenger action of NO radicals, iNOS inhibition enzyme activity, and/or iNOS (inducible nitric oxide synthase) gene expression inhibition.

As a complement to these biological studies, numerous investigations have demonstrated the activity of indazole derivatives against Leishmaniasis [43,44]. In humans, the disease is presented as three clinical forms, depending on the involved species of *Leishmania*. Actually, there are > 12 million of cases and 350 million people at risk, also 2 million new cases are estimated each year [45,46]. The current therapies are inadequate due to several factors such as the high toxicity, pernicious side effects, high prices and the emergence of drug-resistant parasites [47]. Therefore, looking for new effective therapeutic agents against this disease should be considered by new CPs based on 1H-indazole-5-carboxylic acid.

All of the above in mind, in this work, we have synthesized two new coordination polymers based on first row transition metals and 1H-indazole-5-carboxylic acid (5-inca) with the formula $\{[M(5\text{-inca})_2(\text{H}_2\text{O})_2]\cdot 2\text{DMF}\}_n$ (M = Ni (1) and Cu (2)). We have analysed in detail the structural, magnetic and anti-parasitic properties of these materials. In addition, the capability of inhibiting NO production from LPS RAW macrophage cells has been also measured. This was used as an indirect proof of the anti-inflammatory response [48]. Finally, the photocatalytic activity was measured with a model pollutant, i.e. vanillic acid (phenolic compound), with the aim of further increasing the functionalities and applicability of the compounds.

2. Experimental

2.1. Materials and physical measurements

All reagents were obtained from commercial sources and used as received. Elemental (C, H, and N) analyses were performed on an Euro EA Elemental Analyzer. The IR spectra of powdered samples were recorded in the 400–4000 cm^{-1} region on a Nicolet 6700 FTIR spectrophotometer using KBr pellets (Fig. S1). Alternating current magnetic measurements were performed under zero and 1000 Oe applied static fields on a Quantum Design SQUID MPMS XL-5 device by using an oscillating ac field of 3.5 G and ac frequencies ranging from 10 to 1400 Hz.

2.2. Synthesis of complexes

2.2.1. Synthesis of $\{[M(5\text{-inca})_2(\text{H}_2\text{O})_2]\cdot(\text{DMF})_2\}_n$ (M = Ni (1), Cu (2))

Green and orange single crystals of compounds 1 and 2, respectively, were obtained following the next solvothermal procedure:

0.06 mmol (10.00 mg) of 1H-indazole-5-carboxylate were dissolved in 0.5 mL of DMF and then 0.5 mL of distilled water was added. Then 0.03 mmol of $\text{MCl}_2\cdot x\text{H}_2\text{O}$ for different compounds was dissolved in 0.5 mL of distilled water and afterward 0.5 mL of DMF was added. Both solutions were mixed and the resulting solution was placed in a closed glass vessel and introduced in an oven at 95 °C for 24 h. Yield (1): 54% based on Ni. Yield (2): 48% based on Cu. Anal. Calcd. for $\text{NiC}_{22}\text{H}_{28}\text{N}_6\text{O}_8$: C, 46.92; H, 5.01; N, 14.92. Found: C, 46.88; H, 4.99; N, 14.98. Anal. Calcd. for $\text{CuC}_{22}\text{H}_{28}\text{N}_6\text{O}_8$: C, 46.52; H, 4.97; N, 14.79. Found: C, 46.50; H, 4.93; N, 14.84.

2.3. Crystallographic refinement and structure solution

X-ray data collection of suitable single crystals of the compounds were conducted at 100(2) K on a Bruker VENTURE area detector equipped with a graphite monochromated Mo-K α radiation source ($\lambda = 0.71073 \text{ \AA}$) by applying the ω -scan method. The data reduction was performed with the APEX2 software [49] and corrected for absorption using SADABS [50]. Crystal structures were solved by direct methods using the SIR97 program [51] and refined by full-matrix least-squares on F^2 including all reflections using anisotropic displacement parameters by means of the WINGX crystallographic package [52]. Details of the structure determination and refinement of compounds 1 and 2 are summarized in Table 1.

Crystallographic data (excluding structure factors) for the structures reported in this paper have been deposited with the Cambridge Crystallographic Data Center as supplementary publication nos. CCDC 1987070 and 1,987,071. Copies of the data can be obtained free of charge on application to the Director, CCDC, 12 Union Road, Cambridge, CB2 1EZ, U.K. (Fax: +44–1223-335,033; e-mail: deposit@ccdc.cam.ac.uk or <http://www.ccdc.cam.ac.uk>).

2.4. Parasite culture and in vitro activity

Promastigote forms of *L. infantum* (MCAN/ES/2001/UCM-10), *L. braziliensis* (MHOM/BR/1975/M2904) and *L. donovani* (MHOM/PE/84/LC26) were grown *in vitro* in trypanosomal liquid medium (MTL) [Hank's Balanced Salt Solution-HBSS (Gibco), NaHCO_3 , lactalbumin, yeast extract, bovine hemoglobin and antibiotics] with 10% inactivated fetal bovine serum being stored in an air atmosphere at 28 °C, in Roux flasks (Corning, USA) with a surface area of 25 cm^2 , according to the methodology described by Gonzalez et al. [53] The extracellular

Table 1
Crystallographic data and structure refinement details of all compounds.

Compound	1	2
Chem. form.	$\text{NiC}_{22}\text{H}_{28}\text{N}_6\text{O}_8$	$\text{CuC}_{22}\text{H}_{28}\text{N}_6\text{O}_8$
CCDC	1,987,070	1,987,071
Form. weight	563.21	568.04
Cryst. system	Monoclinic	Monoclinic
Space group	$P2_1/n$	$P2_1/n$
a (Å)	6.5605(12)	6.5541(4)
b (Å)	17.9705(3)	18.0179(11)
c (Å)	10.970(2)	10.9212(7)
α (°)	90	90
β (°)	93.970(5)	94.027(2)
γ (°)	90	90
V (Å ³)	1290.2(3)	1286.51(14)
Z	2	2
GoF^a	1.170	1.131
R_{int}	0.1338	0.0787
R_1^b/wR_2^c [$I > 2\sigma(I)$]	0.0455/0.1108	0.0275/0.0418
R_1^b/wR_2^c [all data]	0.0840/0.1610	0.0446/0.0448

$$w = 1 / [\sigma^2(\text{FO}^2) + (aP)^2 + bP] \text{ where } P = (\max(\text{FO}^2, 0) + 2\text{Fc}^2)/3.$$

$$^a S = [\sum w(\text{FO}^2 - \text{Fc}^2)^2 / (N_{\text{obs}} - N_{\text{param}})]^{1/2}.$$

$$^b R_1 = \sum ||\text{FO}| - |\text{Fc}|| / \sum |\text{FO}|.$$

$$^c wR_2 = [\sum w(\text{FO}^2 - \text{Fc}^2)^2 / \sum w\text{FO}^2]^{1/2}.$$

promastigote forms were screened using 24-well plates with MTL medium and 5×10^4 parasites per well. Different concentrations of the compounds (1, 10, 25 and 50 μM) were tested preparing three replicas of each one and maintaining some wells without drugs as control. They were incubated at 28 °C during 72 h before determining the leishmanicidal activity counting the final parasite population using a Neubauer chamber. Finally, the leishmanicidal effect was expressed as the IC_{50} (concentration required to obtain 50% inhibition, calculated through a linear regression analysis from the Kc values at the concentration employed).

2.5. Cell culture and cytotoxicity test

RAW 264.7 monocyte/macrophage murine cell line (ATCC no. TIB-71) is a murine leukemia virus-induced tumor cell line from mouse *Mus musculus*. This cell line does not produce detectable retrovirus. Cells were cultured in DMEM (Dulbecco's Modified Eagle's medium) supplemented with 2 mM glutamine, 10% heat-inactivated FCS (Fetal Calf Serum), 0.5 $\mu\text{g}/\text{mL}$ of gentamicin, being incubated at 37 °C, in an atmosphere of 5% CO_2 and 95% humidity. Subconfluent monolayer cells were used in all experiments.

The cytotoxicity tests for macrophages were carried out in 96-well plates. The growth inhibition of mammalian cells was studied testing the compounds in a concentration range from 0 to 100 $\mu\text{g}/\text{mL}$.

First, the cells were cultured in the plates to a volume of 100 μL at 6.0×10^3 cells/mL and were incubated at 37 °C with 5% CO_2 during 24 h. The compounds were dissolved in the cell growth medium and then were added in another 100 μL (only adding medium in the control wells) to the corresponding wells. After that, the plates were incubated at 37 °C with 5% CO_2 for 72 h.

Cell viability was determined by measuring the absorbance of MTT (3-(4,5-dimethylthiazol-2-yl)-2,5-diphenyltetrazolium bromide) dye staining of living cells. After 72 h of incubation, the medium with the compounds was removed, and 100 μL of MTT solution (0.5 mg/mL) in 50% of PBS 50% of medium was added to each well. After 1.5 h of incubation formazan was resuspended in 100 μL of DMSO. Relative cell viability, with respect to untreated control cells, was measured by absorbance at 570 nm on an ELISA (enzyme linked immunosorbent assay) plate reader (Tecan Sunrise MR20-301, TECAN, Austria).

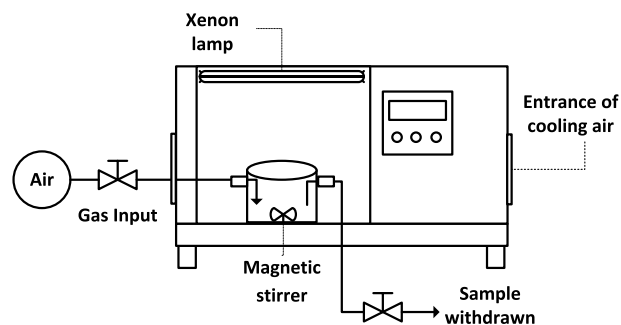
Experimental data were fitted to a sigmoidal function ($y = y_{\text{max}}/(x/a)^b$) by non-linear regression. IC_{50} values (i.e., concentration causing a 50% of cell viability) were obtained by interpolation. These analyses were performed with SigmaPlot statistical software (Version 12.5). Similar analyses were performed to obtain the $\text{IC}_{50 \text{ NO}}$ (*vide infra*).

2.6. Determination of nitrite concentration

Nitrite concentration was used as indicator of NO production. NO determination was based on Griess reaction [54].

Cells were plated at 6×10^4 cells/well in 24-well cell culture plates and supplemented with 10 $\mu\text{g}/\text{mL}$ of lipopolysaccharide (LPS). After 24 h of plated, cells were incubated for 72 h with ligand and compounds 1, and 2 at $3/4 \text{ IC}_{50}$, $1/2 \text{ IC}_{50}$ and $1/4 \text{ IC}_{50}$ concentrations. The supernatants were collected at 24 h, 48 h and 72 h to determine their nitrite concentration and/or stored at -80 °C for further use.

Griess reaction was performed taking 150 μL of supernatant test samples or sodium nitrite standard (0–120 μM) and mixed with 25 μL of Griess reagent A (0.1% N-N-(1-naphthyl)-ethylenediaminedihydrochloride) and 25 μL of Griess reagent B (1% sulfanilamide in 5% of phosphoric acid), in a 96-well plate. After 15 min of incubation at room temperature, the absorbance was measure at 540 nm in an ELISA plate reader (Tecan Sunrise MR20-301, TECAN, Austria). The absorbance was referred to nitrite standard curve to determine the concentration of nitrite in the supernatant of each experimental sample. The percentage of NO production was determined, assigning 100% at the increase



Scheme II. Experimental set-up for photocatalytic experiments.

between negative control (untreated cells) and positive control (cells only treated with 10 $\mu\text{g}/\text{mL}$ of LPS).

2.7. Photocatalytic performance measurements

The photocatalytic experiments using MOF materials were performed in a 50 mL Pyrex batch reactor loaded with a 20 mg L^{-1} vanillic acid (VA) solution ($\text{C}_8\text{H}_8\text{O}_4$), under simulated solar light irradiation for 60 min. The irradiation source consisted of a 1500 W xenon lamp min using a Cofomegra SolarBox 1500e (Scheme II). The material load was fixed at 1 g L^{-1} and the suspensions were magnetically stirred and continuously saturated with an air flow. The temperature was maintained at 303 K. The concentration of VA was monitored using a UV-spectrophotometer model UV-1800 Shimadzu.

3. Results and discussion

3.1. Structural descriptions

3.1.1. Structural description of $\{[\text{Ni}(\text{5-inca})_2(\text{H}_2\text{O})_2]\cdot 2\text{DMF}\}_n$ (1)

Compound 1 crystallizes in $P2_1/n$ and grows from the pilling of neutral 2D layers held together by hydrogen bonds. Each metallic center (Ni1), which is situated at a centre of symmetry, is coordinated to four 5-inca ligands and two water molecules, shaping a slightly octahedron as a coordination polyhedron (Fig. 1). The polyhedron basal plane is formed by two O1W coordination water molecules and two O1A atoms from carboxylate groups, whereas the slightly elongated axis is occupied by N1A atoms pertaining to indazole aromatic rings. Besides, the asymmetric unit includes a DMF molecule. A square-grid 2D coordination polymer is formed with DMF molecules located at square holes, as the result of strong hydrogen bond interactions.

Within these sheets, nickel(II) ions are bridged by four 1H-indazole-5-carboxylate ligands which are coordinated to the metal ions through the pyrazol and carboxylate groups pertaining to the ligand with Ni–N and Ni–O bond distances of about 2 Å (Table 2).

The layers grow on the diagonal of the unit cell (Fig. 2a) and are connected by hydrogen bond interactions (Table S1, 2.795(8) Å) involving nitrogen atoms from pyrazol rings and oxygen atoms pertaining

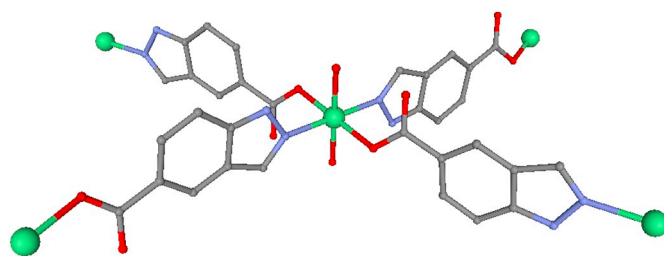


Fig. 1. View of complex 1 showing the coordination polyhedron. Nickel (green), nitrogen (blue), oxygen (red), carbon (grey). Hydrogen atoms are been omitted for clarity.

Table 2
Bond distances for coordination environment in compound 1.^a

Ni1-O1W	2.057(4)	Ni1-O1A(iii)	2.069(5)
Ni1-O1W(iii)	2.057(4)	Ni1-N1A	2.093(5)
Ni1-O1A	2.069(5)	Ni1-N1A(iii)	2.093(5)

^a Symmetry operation (iii) = '-x, -y, -z'.

to the carboxylate groups of adjacent sheets (Fig. 2b).

Accordingly, the linkage of these units gives rise to flattened open 2D layers showing square holes. Owing to this, the structure presents channels along *a* axis occupied by crystallization DMF molecules (Fig. 3). These DMF molecules are there located due to strong hydrogen bond interactions involving the oxygen pertaining to DMF molecules and the water molecules coordinated to nickel ions with a value of 2.748 Å.

3.1.2. Structural description of $\{[Cu(5-inca)_2(H_2O)_2] \cdot 2DMF\}_n$ (2)

The compound 2 is isostructural to compound 1, crystallizes in $P2_1/n$ and grows from the piling of neutral 2D layers held together in the same way that previous Ni-CP. The same type of description applies to compound 2, except that Cu–N and Cu–O bond distances in 2 that are slightly smaller than in 1 (Table 3 and Fig. 4), which is consistent with the larger atomic radio of nickel. Likewise, in this Cu-CP there are hydrogen interactions that are involved in the packaging of the layers in CP and in the presence of crystallization DMF molecules in channels generated (Fig. 4). These interactions (Table S2) are in the range 2.626(17) - 2.803(18) Å.

3.2. Magnetic properties

Magnetic properties of the compounds have been studied in order to complete the physico-chemical characterization and ensure the purity of the samples. At room temperature the χ_{MT} value of $1.02 \text{ cm}^3 \text{ K mol}^{-1}$ for compound 1 is in good agreement with the expected value of $1.00 \text{ cm}^3 \text{ K mol}^{-1}$ for one isolated Ni(II) ion with $g = 2.0$ (Fig. 5). Upon cooling, the χ_{MT} value remains nearly constant up to 15 K and then abruptly decreases reaching a minimum value of $0.79 \text{ cm}^3 \text{ K mol}^{-1}$ at 2.5 K. This thermal dependence is the first evidence of zero-field splitting (ZFS) in Ni(II) compounds. Assuming that the long intramolecular Ni–Ni distances (10.913 Å) will provide negligible interactions in comparison to the mentioned ZFS, the χ_{MT} data were analysed with the PHI software and the following Hamiltonian:

$$\hat{H} = g\mu_B \hat{S} \cdot B + D(\hat{S}_z^2 - \hat{S}^2/3) + E(\hat{S}_x^2 - \hat{S}_y^2) \quad (1)$$

The first term accounts for the Zeeman interaction with the local magnetic field (B), which is parametrized through the Landé *g* tensor, and the second and third terms correspond to axial (*D*) and rhombic (*E*) anisotropic ZFS parameters. Finally, \hat{S} represents the spin operator with

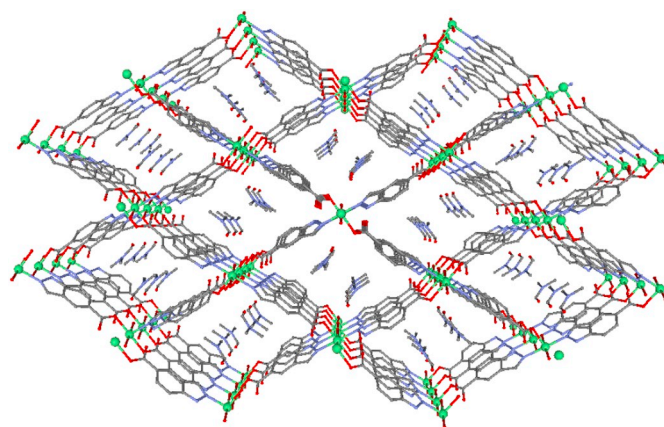


Fig. 3. View of the channels in network compound 1 along *a* axis showing the crystallization DMF molecules. Hydrogen atoms have been omitted for clarity.

Table 3
Bond distances for coordination environment in compound 2.

Cu1-O1W	2.0567(13)	Cu1-O1A(iii)	2.0672(12)
Cu1-O1W(iii)	2.0567(13)	Cu1-N1A(iv)	2.0855(14)
Cu1-O1A	2.0672 (12)	Cu1-N1A(ii)	2.0855(14)

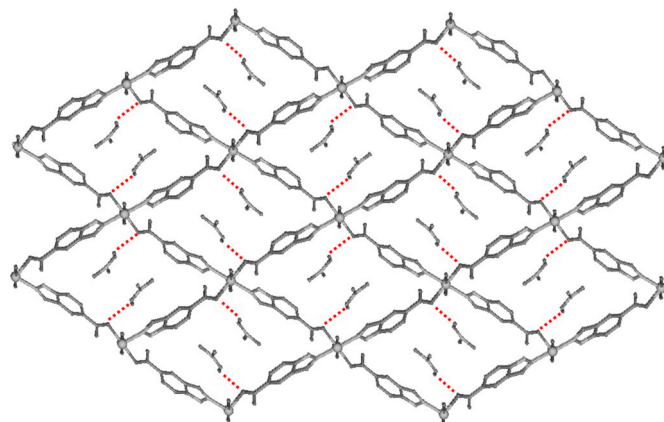


Fig. 4. Hydrogen bonds involving crystallization DMF molecules and 2D-CP.

x, *y* or *z* components. The best fit of the experimental data afforded the following set of parameters: $g = 2.02$, $D = -6.53 \text{ cm}^{-1}$, and $E = +0.19 \times 10^{-3} \text{ cm}^{-1}$, with $R = 9.74 \times 10^{-3}$. The small value of *E* indicates a weak influence of rhombicity in the ZFS; however, the values are consistent with other previously reported similar compounds [55].

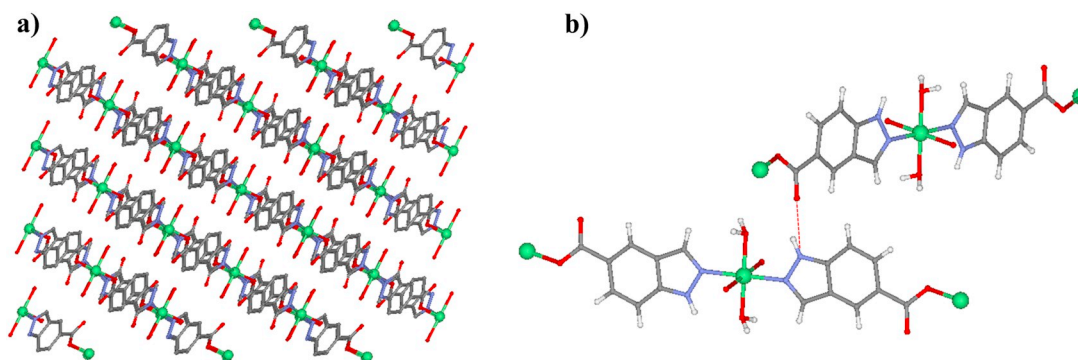


Fig. 2. (a) Views of the packing of compound 1 along *b* axis in which hydrogen atoms have been omitted for clarity. (b) Strong hydrogen bond interaction involving nitrogen and oxygen atoms of different layers. Nickel (green), nitrogen (blue), oxygen (red), carbon (grey) and hydrogen (white).

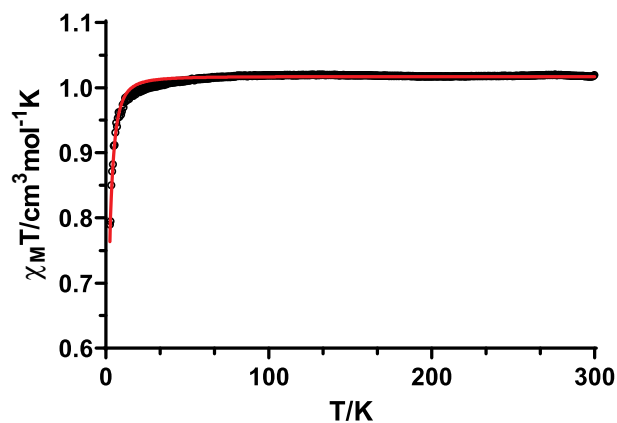


Fig. 5. Temperature dependence of the $\chi_M T$ product for compound 1 in the 2.5–300 K range. The solid line is generated from the best fit to the magnetic parameters.

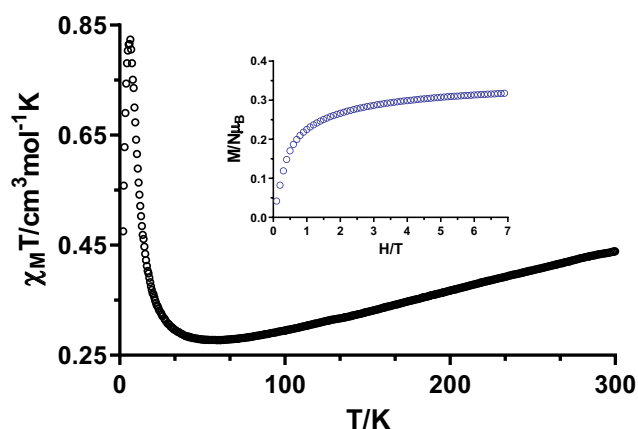


Fig. 6. Temperature dependence of the $\chi_M T$ product for compound 2 in the 2–300 K range. Inset: field dependence of the magnetization for 2.

The temperature dependence of the magnetic susceptibility of compound 2 in the 2–300 K temperature range under an applied field of 0.1 T is displayed in Fig. 6. At room temperature, the $\chi_M T$ value of $0.439 \text{ cm}^3 \text{ K mol}^{-1}$ is higher than the spin only value expected for an isolated Cu(II) center ($0.375 \text{ cm}^3 \text{ K mol}^{-1}$ with $S = 1/2$ and $g = 2.0$). This occurs when the orbital angular moment is not completely quenched leading to higher g values and, inherently to higher $\chi_M T$. When lowering the temperature, the $\chi_M T$ value decreases gradually until 54 K reaching the lowest $\chi_M T$ value of $0.28 \text{ cm}^3 \text{ K mol}^{-1}$. At this point, the signal sharply increases reaching $0.82 \text{ cm}^3 \text{ K mol}^{-1}$ at 6.5 K before falling to $0.48 \text{ cm}^3 \text{ K mol}^{-1}$ at 2.0 K.

Similar results were previously obtained for other Cu(II) compounds [56]. Indeed, we associated these magnetic properties to a spin-canted

antiferromagnetism, which at the same time leads to a ferromagnetic ordering that causes the abrupt increase in the dc data. This phenomenon is known to occur for acentric and chiral structures but the proposed antisymmetric exchange pathways for the previous systems might not be comparable to this particular system, since compound 2 owns an inversion center. Instead, this phenomenon may be also derived from a canted arrangement between the individual spins of the metal ions in the layer with regard to the packing orientation, as it is the case for the present compound. We are currently studying this system by measuring the field-dependence of the $\chi_M T$ in the temperature region that the maximum appears, hysteresis loops, ZFC-FC measurements and dynamic magnetic properties, which will shed light in the origin of these magnetic properties.

3.3. Photocatalytic degradation of vanillic acid

Heterogeneous photocatalysis appears as one of the most destructive processes for organic contaminants under ambient conditions and by using solar energy. Preliminary tests were carried out over CPs materials as photocatalysts for the degradation of vanillic acid, VA (phenolic compound) in aqueous solution under UV–Vis irradiation. The results showed a higher absorption of the VA spectra at 60 min after UV–Vis irradiation (VA after irradiation, Compound 1 and VA after irradiation Compound 2, respectively) in comparison to the VA spectrum before irradiation (see Fig. S2, supporting information). More studies/strategies will be further required to promote the photocatalytic performance of these compounds such as modulation of their organic linkers/metal or integration with semiconductors, photosensitizers and so on.

3.4. In vitro antiparasitic activity

Taking into account the urgent need to find novel and effective drugs and the exploration of new paths in the search of improved therapies to fight Leishmaniasis, we have compared the activity of the two mentioned complexes (and the ligand) against several *Leishmania* spp. strains to that obtained with the commercial drug Glucantime (Table 4).

Regarding the antiproliferative assays against the promastigote forms of *Leishmania*, the two compounds and the ligand exhibited less inhibitory activity than the reference drug, Glucantime. It is indeed necessary at least to duplicate the concentration of the compounds to reduce by 50% the parasite population, in comparison to the drug (Table 4 and Fig. 7). Nevertheless, the excellent cytotoxicity data obtained with macrophage host cells resulted in very good SI coefficients in many of the studied cases. Focusing on *L. infantum* values, ligand and compound 2 present similar SI, increasing in > 30 folds the Glucantime coefficients, which make them the best candidates to further biological tests *in vivo*. *L. braziliensis* turns out to be the more homogeneous series, with very similar SI results for the ligand and the two compounds. In the case of *L. donovani*, the ligand and complex 1 exhibited identical moderate activities while compound 2 showed very high efficacy. All the SI coefficients are also represented in Fig. 7.

Table 4

In vitro activity of ligand (5-inca) and complex 1 and 2 against promastigote forms of *Leishmania* spp. and J774.2 macrophages after 72 h of incubation.

Compound	IC ₅₀ (μM) ^a ± SD			Toxicity IC ₅₀ Macrophage (μM)	SI ^b		
	<i>L. infantum</i>	<i>L. braziliensis</i>	<i>L. donovani</i>		<i>L. infantum</i>	<i>L. braziliensis</i>	<i>L. donovani</i>
Glucantime	18.0 ± 3.1	25.6 ± 1.7	26.6 ± 5.4	15.2 ± 1.0	0.8	0.6	0.6
Ligand	39.5 ± 3.6	67.7 ± 5.4	> 200	> 1000	25.3(32)	14.8(25)	5(8)
1	115.7 ± 21.6	82.8 ± 6.3	> 200	> 1000	8.6(11)	12.1(20)	5(8)
2	36.9 ± 2.9	90.8 ± 6.2	65.9 ± 4.7	> 1000	27.1(34)	11.1(18)	15.2(25)

The results presented are averages of three separate determinations. In brackets: number of times that ligand SI exceed the reference drug SI.

^a The concentration required to obtain 50% inhibition, calculated through a linear regression analysis from the Kc values at the concentration employed (1, 10, 25 and 50 μM for promastigote forms of *Leishmania* spp. and 50, 100, 200 and 400 μM for macrophage host cells).

^b Selectivity index = IC₅₀ against J774.2 macrophages / IC₅₀ parasite (promastigote forms).

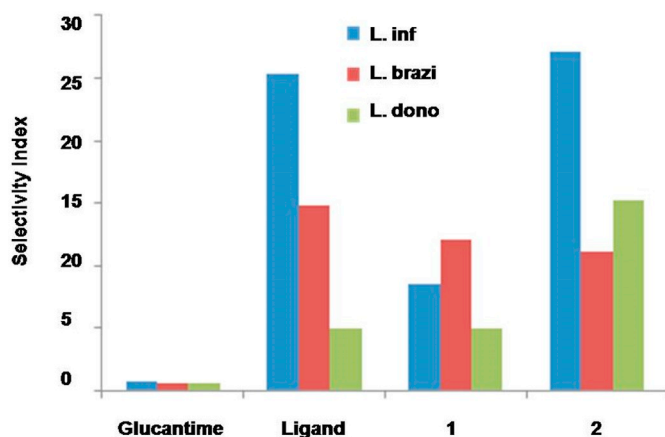


Fig. 7. Comparative of SI values between Glucantime, ligand and complexes 1 and 2. Selectivity index = IC_{50} against J774.2 macrophages / IC_{50} parasite (promastigote forms).

Table 5

Growth-inhibitory effects of ligand, and compound 1 and 2 on RAW 264.7 monocyte/ macrophage murine cells.

Compound	IC_{20}	IC_{50}	IC_{80}
Ligand	54,86 ± 2,34	81,11 ± 3,36	114,34 ± 8,59
1	13,91 ± 3,56	54,07 ± 6,95	120,87 ± 3,89
2	14,23 ± 0,14	33,38 ± 1,52	80,48 ± 10,28

3.5. Cytotoxicity on Raw 264.7 cell line

Cytotoxicity (cell viability) of the ligand or compounds 1 and 2 was evaluated on RAW 264.7 murine macrophage cells to establish infracytotoxic concentrations. This is needed to assure that anti-inflammatory effects were due to an inflammatory process and not due to their intrinsic cytotoxicity. IC_{50} concentration (concentration causing 50% reduction growth) were 81,11 ± 3,36 for ligand, 54,07 ± 6,95 for compound 1 and 33,38 ± 1,52 for compound 2. Also we have determined the compound concentrations required for 20% and 80% of growth inhibition (IC_{20} and IC_{80}) to analyse the complete range of cytotoxicity (Table 5). The results showed that the compound 2 is more toxic than 1 and the free-ligand for the explored concentration range (0 to 100 $\mu\text{g}/\text{mL}$) (Fig. 8).

3.6. Nitro oxide production

In the inflammatory response process, nitric oxide, NO, is released as intermediate or second messenger. The enzymatic production of NO is cell-type specific, with cytokine-driven inducible nitric-oxide synthase (iNOS) noted initially for the burst of higher levels as part of the inflammatory activation process. RAW 264.7 murine macrophage cells produce the highest release of NO during the inflammatory response, being usually used a cell model for determining the anti-inflammatory activity of drug candidates (Fig. 9). The anti-inflammatory activity of the compounds was analysed by measuring the nitrite concentration (which is proportional to the released NO) in the cell culture medium by the Griess method. Macrophages were activated with LPS during 24 h after the addition of the compounds. Sub-cytotoxic concentrations corresponding to $\frac{3}{4}$ IC_{50} , $\frac{1}{2}$ IC_{50} , and $\frac{1}{4}$ IC_{50} were used.

After 24 h of incubation, the higher anti-inflammatory effect was produced by compound 2, with a 68.35% of NO-inhibition with respect to the positive control (only LPS treated control cells) and negative control (untreated control cells), while the ligand and compound 1 only showed 8.44% and 11.13% of NO-inhibition at 25 $\mu\text{g}/\text{mL}$ ($\frac{3}{4}$ IC_{50} concentration). At 48 h of incubation the compound 2 produced high inhibition of NO production, being around 85% in all the concentrations assayed. At this time point, the ligand produced inhibited by 40% at $\frac{3}{4}$ IC_{50} concentration. The inhibition effects of compound 1 were very similar to those of the ligand. After 72 h, the inhibition was, in general, more pronounced than at 48 h, the compound 2 producing an inhibition of 90% irrespectively of the concentration. The treatment with the ligand inhibited by 60% the NO release at $\frac{3}{4}$ IC_{50} concentration, and the compound 1 also produced NO release inhibition similar to the ligand at the same concentration.

To complete the anti-inflammatory effect of compound 2, we calculated the concentration to reduce by 50% the production of NO (IC_{50} NO) at the time assayed (Fig. 10). The results showed that the IC_{50} NO of the compound 2 were lower than the IC_{50} NO of the compound 1 and the ligand. The IC_{50} NO for the compound 2 were 7.74 ± 3.78 $\mu\text{g}/\text{mL}$ at 24 h, 1.15 ± 0.01 $\mu\text{g}/\text{mL}$ at 48 h, and 0.57 ± 0.18 $\mu\text{g}/\text{mL}$ at 72 h. For compound 1 values of 42.59 ± 0.42 $\mu\text{g}/\text{mL}$ at 24 h, 55.8 ± 4.7 $\mu\text{g}/\text{mL}$ at 48 h and 32.99 ± 1.53 $\mu\text{g}/\text{mL}$ at 72 h. The IC_{50} NO of the ligand was only measurable at 48 h (68.83 ± 4.22 $\mu\text{g}/\text{mL}$) and 72 h (59.51 ± 0.16 $\mu\text{g}/\text{mL}$). In summary, the compound 2 was more effective than the ligand and compound 1 at all the times and concentrations assayed (Fig. 10 and Fig. S3). Significant differences ($p \leq .001$) were found between the IC_{50} NO of the ligand and the compound 2 at 48 and 72 h, and with the ligand and compound 1 at 72 h of treatment (Fig. S3).

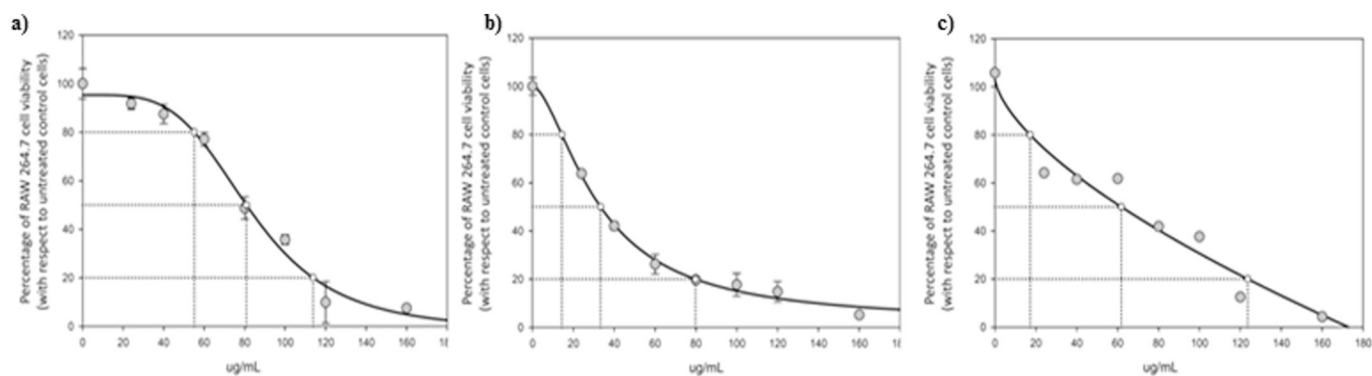


Fig. 8. Effect of ligand (a), compound 2 (b) and compound 1 (c) on cell proliferation of RAW 264.7 macrophage murine cells. After treatment with the compounds in the range of concentration from 0 to 100 $\mu\text{g}/\text{mL}$, each point represents the mean value ± S.D. of at least two independent experiments performed in triplicate. IC_{20} , IC_{50} , and IC_{80} are the concentrations required for growth inhibition of 20%, 50% and 80%.



Fig. 9. Effect of compounds 1 and 2 on the release of nitrites in RAW 264.7 macrophage murine cells. After activation of the inflammatory process by incubation with LPS for 24 h, the compounds were incubated for 24, 48, 72 h at concentrations of $\frac{3}{4}$ -IC₅₀, $\frac{1}{2}$ -IC₅₀, $\frac{1}{4}$ -IC₅₀. The data represent the mean \pm S.D. of at least two independent experiments performed in triplicate. Key: p < .05 (*), p \leq .01 (**), p \leq .001 (***), respect to positive control (only LPS treated cells).

4. Conclusion

We report the formation of two novel multifunctional isomorphous (4,4) square-grid 2D coordination polymers based on 1H-indazole-5-carboxylic acid. To the best of our knowledge, these complexes are the second and third examples of coordination compounds construct with this novel ligand. These materials were synthesized by soft solvothermal routes, possess different 2D-structures and show interesting magnetic and biological properties. Despite no synergetic effect was observed in the antiparasitic selectivity, ligand and complex 2 show promising values against *L. braziliensis* and *L. donovani* respectively, and especially against *L. infantum* in both cases, making them good

candidates for further intracellular studies. Compound 2 produced anti-inflammatory effects at all the assayed times, 24, 48, 72 h, with the higher percentage of NO inhibition release being close to 90%. Compound 1 and ligand only induced anti-inflammatory effects after 72 h of treatment, with a NO inhibition release of the 60%, being the compound 1 a little more effective than the ligand. With respect to the IC₅₀ NO the concentration found for the compound 2 were one or two orders lower than concentrations found for the compound 1 and the ligand. In conclusion the compound 2 was more effective as anti-inflammatory than the ligand or compound 1. The formation of metal complexes with bioactive ligands is a new and promising strategy to find new compounds with high and enhanced biochemical properties.

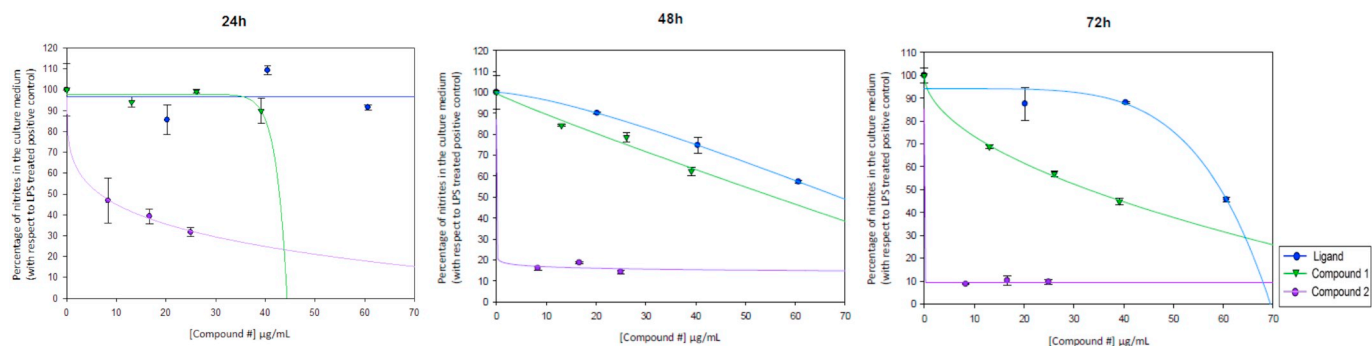


Fig. 10. Sigmoidal curves of the effect of the ligand and compounds 1 and 2 on the release of nitrites in RAW 264.7 macrophage murine cells. It can be seen that the curves corresponded to metal compound complex 2 ($IC_{50\ 24h\ NO} = 7.74 \pm 3.78\ \mu\text{g/mL}$; $IC_{50\ 48h\ NO} = 1.15 \pm 0.01\ \mu\text{g/mL}$; $IC_{50\ 72h\ NO} = 0.57 \pm 0.18\ \mu\text{g/mL}$) are below to the ligand and the compound 1. The data represent the mean \pm S.D. of at least two independent experiments performed in triplicate.

Declaration of competing interest

There is no any conflict of interest.

Acknowledgements

This work has been funded by Junta de Andalucía (FQM-1484 and FQM-394), the Ministry of Economy and Competitiveness (MCIU/AEI/FEDER, UE) (PGC2018-102052-A-C22, PGC2018-102052-B-C21), Red Guipuzcoana de Ciencia, Tecnología e Innovación (OF218/2018), University of the Basque Country (GIU 17/13) and Gobierno Vasco/Eusko Jaurlaritza (IT1005-16). J.M.D.-L., L.M.P.-M and G.B.R.-R. acknowledge the FEDER/MCIU/AEI for their Ramón y Cajal (RYC-2016-21042 and RYC-2016-19347) and Juan de la Cierva (JdC-2017) fellowships, respectively. The authors thank for the technical and human support provided by SGIker of UPV/EHU and European funding (ERDF and ESF).

Appendix A. Supplementary data

Supplementary data to this article can be found online at <https://doi.org/10.1016/j.jinorgbio.2020.111098>.

References

- [1] H.-Y. Li, Y.-L. Wei, X.-Y. Dong, S.-Q. Zangand, T.C.W. Mak, *Chem. Mater.* 27 (2015) 1327–1331.
- [2] J.-Z. Gu, Y. Cai, Z.-Y. Qian, M. Wen, Z.-F. Shi, D.-Y. Lv, A.M. Kirillov, *Dalton Trans.* 47 (2018) 7431–7444.
- [3] E. San Sebastian, A. Rodríguez-Diéguez, J.M. Seco, J. Cepeda, *Eur. J. Inorg. Chem.* 2018 (2018) 2155–2174.
- [4] S.N. Nobar, *Mater. Chem. Phys.* 213 (2018) 343–351.
- [5] I. Abánades-Lázaro, R.S. Forgan, *Coord. Chem. Rev.* 380 (2019) 230–259.
- [6] O. Abuzalat, D. Wong, M. Elsayed, S. Park, S. Kim, *Ultrason. Sonochem.* 45 (2018) 180–188.
- [7] J. Cepeda, S. Pérez-Yáñez, G. Beobide, O. Castillo, J.A. García, A. Luque, *Eur. J. Inorg. Chem.* 2015 (2015) 4318–4328.
- [8] N. Stock, S. Biswas, *Chem. Rev.* 112 (2012) 933–969.
- [9] P. Cubillas, M.W. Anderson, M.P. Atfield, *Chem. Eur. J.* 18 (2012) 1540–1541.
- [10] L.J. Murray, M. Dinca, J.R. Long, *Chem. Soc. Rev.* 38 (2009) 1294–1314.
- [11] C. Ruiz, A.A. García-Valdivia, B. Fernandez, J. Cepeda, I. Oyarzabal, E. Abas, M. Laguna, J.A. García, I. Fernández, E. San Sebastián, A. Rodríguez-Diéguez, *CrystEngComm* 21 (2019) 3881–3890.
- [12] F.A. Alemda-Paz, J. Klinowski, S.M.F. Vilela, J.P.C. Tomé, J.A.S. Cavaleiro, J. Rocha, *Chem. Soc. Rev.* 41 (2012) 1088–1110.
- [13] I.-H. Choi, Y. Kim, D. Lee, S. Huh, *Polyhedron* 155 (2016) 96–103.
- [14] J.-H. Gu, W.-X. Li, H.-X. Li, H.-Y. Li, J.-P. Lang, *Polyhedron* 154 (2018) 47–53.
- [15] M. Kurmoo, *Chem. Soc. Rev.* 38 (2009) 1353–1379.
- [16] B.V. De Voorde, B. Bueken, J. Denayer, J. Vos, *Chem. Soc. Rev.* 43 (2014) 5766–5788.
- [17] J. Cepeda, A. Rodríguez-Diéguez, *CrystEngComm* 18 (2016) 8556–8573.
- [18] A.A. García-Valdivia, J.M. Seco, J. Cepeda, A. Rodríguez-Diéguez, *Inorg. Chem.* 56 (2019) 13897–13912.
- [19] C.S. Hawes, R. Babarao, M.R. Hill, K.F. White, B.F. Abrahams, P.E. Kruger, *Chem. Commun.* 48 (2012) 11558–11560.
- [20] C.S. Hawes, P.E. Kruger, *Dalton Trans.* 43 (2014) 16450–16458.
- [21] C.S. Hawes, P.E. Kruger, *RSC Adv.* 4 (2014) 15770–15775.
- [22] H. Xiao, X.-B. Li, G.-F. Qin, Y. Xia, G. Zhou, *J. Iran. Chem. Soc.* 13 (2016) 793–802.
- [23] J.M. Méndez-Arriaga, I. Oyarzabal, G. Escolano, A. Rodríguez-Diéguez, M. Sánchez-Moreno, J.M. Salas, *J. Inorg. Biochem.* 180 (2018) 26–32.
- [24] A.B. Caballero, A. Rodríguez-Diéguez, L. Lezama, J.M. Salas, *Cryst. Growth Des.* 12 (2012) 3583–3593.
- [25] A.B. Caballero, A. Rodríguez-Diéguez, M. Quirós, J.M. Salas, O. Huertas, I. Ramírez-Macías, F. Olmo, C. Marín, G. Chaves-Lemauro, R. Gutierrez-Sanchez, M. Sanchez-Moreno, *Eur. J. Med. Chem.* 85 (2014) 526–534.
- [26] A.B. Caballero, J.K. MacLaren, A. Rodríguez-Diéguez, I. Vidal, J.A. Dobado, J.M. Salas, C. Janiak, *Dalton Trans.* 40 (2011) 11845–11855.
- [27] A.B. Caballero, A. Rodríguez-Diéguez, E. Barea, M. Quiros, J.M. Salas, *CrystEngComm* 12 (2010) 3038–3045.
- [28] B. Fernández, A. Gómez-Vilchez, C. Sánchez-González, J. Bayón, E. San Sebastian, S. Gómez-Ruiz, C. López-Chaves, P. Aranda, J. Llopis, A. Rodríguez-Diéguez, *New J. Chem.* 40 (2016) 5387–5393.
- [29] D. Briones, B. Fernández, A.J. Calahorra, D. Fairen-Jimenez, R. Sanz, F. Martínez, G. Orcajo, E.S. Sebastián, J.M. Seco, C.S. González, J. Llopis, A. Rodríguez-Diéguez, *Cryst. Growth Des.* 16 (2016) 537–540.
- [30] C.S. Hawes, R. Babarao, M.R. Hill, K.F. White, B.F. Abrahams, P.E. Kruger, *Chem. Commun.* 48 (2012) 11558–11560.
- [31] A.A. Mieloch, M. Zurawek, M. Giersig, N. Rozwadowska, J.D. Rybka, *Sci. Rep.* 10 (2020) 2725.
- [32] L. Botana, J. Ruiz, J.M. Seco, A.J. Mota, A. Rodríguez-Diéguez, R. Sillanpää, E. Colacio, *Dalton Trans.* 40 (2011) 12462–12471.
- [33] M.A. Palacios, A. Rodríguez-Diéguez, A. Sironi, J.M. Herrera, A.J. Mota, J. Cano, E. Colacio, *Dalton Trans.* (2009) 8538–8547.
- [34] Q.-Q. Xiao, D. Liu, Y.-L. Wei, G.-H. Cui, *Polyhedron* 158 (2019) 342–351.
- [35] J. Huo, D. Yu, H. Li, B. Luo, N. Arusamy, *RSC Adv.* 9 (2019) 39323–39333.
- [36] Y.-H. Qu, Y.-J. Yang, G.-Y. Dong, *Polyhedron* 180 (2020) 114431–114438.
- [37] J. Jansen, W. Karges, L. Rink, *J. Nutr. Biochem.* 20 (2019) 399–417.
- [38] X.-T. Xin, X.-K. Wang, *J. Struct. Chem.* 60 (2019) 1850–1856.
- [39] G. Psomas, D.P. Kessissoglou, *Dalton Trans.* 42 (2013) 6252–6276.
- [40] C.N. Banti, S.K. Hadjikakou, *Eur. J. Inorg. Chem.* 2016 (2016) 3048–3071.
- [41] L. Sun, L.-Y. Sha, J. Jiang, *Biomed. Res.-India.* 28 (2017) 2152–2155.
- [42] Y. Zeng, T. Xu, *Lat. Am. J. Pharm.* 35 (2016) 1228–1233.
- [43] L. Boiani, A. Gerpe, V.J. Arán, S. Torres de Ortiz, E. Serna, N. Vera de Bilbao, L. Sanabria, G. Yaluff, H. Nakayama, A. Rojas de Arias, J.D. Maya, J.A. Morello, H. Cerecetto, M. González, *Eur. J. Med. Chem.* 44 (2009) 1034–1040.
- [44] C. Marín, I. Ramírez-Macías, M.J. Rosales, B. Muro, F. Reviriego, P. Navarro, V.J. Arán, M. Sánchez-Moreno, *Acta Trop.* 148 (2015) 170–178.
- [45] A. Cavalli, M.-L. Bolognesi, *J. Med. Chem.* 52 (2009) 7339–7359.
- [46] Y.C. Ong, S. Roy, P.C. Andrews, G. Gasser, *Chem. Rev.* 119 (2019) 730–796.
- [47] S. Espuelas, D. Plano, P. Nguewa, M. Font, J.A. Palop, J.M. Irache, C. Sanmartín, *Curr. Me. Chem.* 19 (2012) 4259–4288.
- [48] H. Yki-Järvinen, R. Bergholm, M. Leirisalo-Repo, *Ann. Rheum. Dis.* 62 (2003) 630–634.
- [49] Bruker Apex2, Bruker AXS Inc., Madison, Wisconsin, USA, 2004.
- [50] G.M. Sheldrick, SADABS, Program for Empirical Adsorption Correction, Institute for Inorganic Chemistry, University of Göttingen, Germany, 1996.
- [51] G.M. Sheldrick, SHELX-2014, Program for Crystal Structure Refinement, University of Göttingen, Göttingen, Germany, 2014.
- [52] L.J. Farrugia, *J. Appl. Crystallogr.* 32 (1999) 837–838.
- [53] P. González, C. Marín, I. Rodríguez-González, A.B. Hitos, M.J. Rosales, M. Reina, J.G. Díaz, A. González-Coloma, M. Sánchez-Moreno, *Int. J. Antimicrob. Agent.* 25 (2005) 136–141.
- [54] N.S. Bryan, M.B. Grisham, *Free Radic Biol Med* 43 (2007) 645–657.
- [55] R. Boca, *Coord. Chem. Rev.* 248 (2004) 757–815.
- [56] T. Moriya, *Phys. Rev.* 120 (1960) 91.

Interpenetrated Luminescent Metal–Organic Frameworks based on 1*H*-Indazole-5-carboxylic Acid

Antonio A. García-Valdivia, Manuel Pérez-Mendoza, Duane Choquesillo-Lazarte, Javier Cepeda,* Belén Fernández, Manuel Souto, Marcos González-Tejero, Jose A. García, Guillermo Mínguez Espallargas,* and Antonio Rodríguez-Diéguez*



Cite This: <https://dx.doi.org/10.1021/acs.cgd.0c00345>



Read Online

ACCESS |



Metrics & More

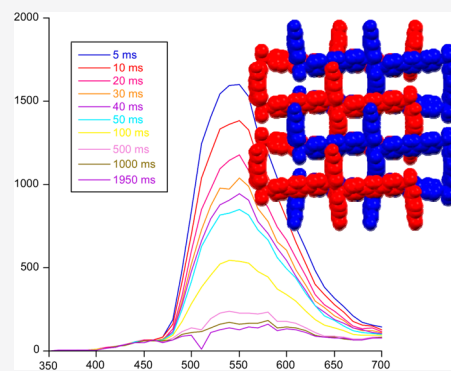


Article Recommendations



Supporting Information

ABSTRACT: Herein we report the formation and characterization of two novel Zn-based multifunctional metal–organic frameworks (MOFs) based on 1*H*-indazole-5-carboxylic acid and bipyridine-like linkers, synthesized by soft solvothermal routes. These materials possess isorecticular 2-fold interpenetrated three-dimensional structures that afford a flexible character and allow porosity modulation of the MOFs as confirmed by CO₂ sorption measurements. Apart from this attractive structural feature, the MOFs exhibit fascinating luminescent properties involving both luminescence thermometry and long-lasting phosphorescence.



INTRODUCTION

The development of novel functional porous materials is one major point toward the sustainable development of our society and should deal with an optimum performance for the capture, separation, and storage of different types of gases at the industrial level.^{1–3} In this sense, many efforts have been devoted to produce selective adsorbents for purifying and separating CO₂ in the mixture resulting from a gasification process.^{4–9} One important research field that has emerged during the last two decades has mainly focused on the design and synthesis of new metal–organic frameworks (MOFs), also called porous coordination polymers (PCPs), which are materials constituted by organic ligands coordinated to metal ions or clusters defining a porous and crystalline network with structural diversities as a consequence of their modular nature and, consequently, functional properties. Therefore, MOFs cover multiple fields of applications in addition to adsorption, such as magnetism, luminescence, electronics, catalysis, or medicine.^{10,11} An interesting synthetic strategy to achieve an optimal structure to enhance the gas storage or separation performance is based on the modulation of the size and type of pore in a rational way, by using different ligands that present small structural changes (i.e., the size or shape) to yield topologically similar polymeric materials but with small pore changes. In this sense, the resulting materials may present small modifications that could be, in turn, related to other properties such as luminescence.¹² The enormous family of excellent porous materials synthesized from bipyridine ligands are good examples of such precise pore design and control.^{13,14}

Photoluminescence (PL) properties of MOFs have received a lot of interest during the past decade not only because of their large applicability in solid-state lighting materials (light-emitting devices (LEDs), long lasting phosphors (LLPs), and so on)^{15–17} but also toward sensing applications due to the celerity of the process. In this last particular case, when luminescent emission is coupled to a physical change such as the temperature, MOFs allow for a rapid detection of that magnitude.^{18–20} A main reason for such behavior is because temperature is a key factor in MOFs that governs the nonradiative quenching originated at the molecular vibrations of ligands, and, in turn, it brings structural changes of variable magnitude depending on the flexibility of the framework. PL in MOFs takes advantage of their hybrid metal–organic structure since the emissions may involve different components: ligand centered (LC) and metal centered (MC) charge transfer (CT) processes between them, or related to the adsorption of guest molecules (which could be exploited for PL detection).²¹ However, most of luminescent MOFs used as thermometers are based on lanthanide metals,^{18–22} which present some disadvantages such as reduced resources availability and

Received: March 16, 2020

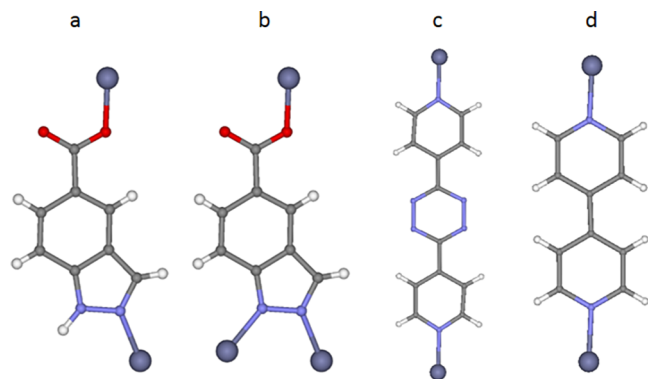
Revised: May 9, 2020

Published: May 13, 2020

environmental concerns. For this reason, another promising strategy for the design of luminescent MOFs for thermometry argues for the use of organic ligands with strong absorption (usually molecules with chemical functions containing heteroatoms with lone-pairs) combined with metal ions with closed-shell electronic configuration, which avoid nonradiative quenching.^{23,12}

Taking these considerations into account, we selected two different bipyridine ligands and 1*H*-indazole-5-carboxylic acid (5-*incaH*₂) as the main ligand, with the aim of obtaining new three-dimensional MOFs. In relation to the latter ligand, there are only a few examples of coordination polymers based on copper in which this ligand acts as a bidentate ligand participating as a monoanionic linker (Scheme 1, left).²⁴

Scheme 1. Coordination Modes of (5-*incaH*)[−] (a), (5-*inca*)^{2−} (b), pbptz (c), and 4,4-bipy (d).



Regarding the bipyridine ligands, we have chosen 4,4-bipyridyl (4,4-bipy) and 3,6-bis(4-pyridyl)-1,2,4,5-tetrazine (pbptz) as linkers due to the presence of pyridine and tetrazine rings that favor the enhancement of the luminescent properties of the resulting coordination polymers,^{25,26} and due to their high potential to build open architectures as a result of the length of the spacer and the disposition of the donor atoms. On the other hand, the linkage of the ligands to metal atoms with a high coordination plasticity, such as zinc(II), opens the way to synthesize materials with not only possible dynamics in the crystal structures but also interesting photoluminescence properties.¹² Moreover, the existence of a second type of ligand that combines benzene with pyrazole rings may modify the initial properties of these systems, generating MOFs with tunable luminescent properties in which the emission of the materials in response to the temperature can be analyzed in order to study their potential use as thermometers, as seen in previous studies conducted on zinc and pyrazole based coordination polymers.²⁷

Therefore, we report herein the synthesis and characterization of a novel family of Zn²⁺ coordination polymers based on the novel 1*H*-indazole-5-carboxylic acid, {[Zn(5-*inca*)-(pbptz)_{0.5}]-1.5DMF}_n (1) and {[Zn(5-*inca*)(4,4-bipy)_{0.5}]-DMF}_n (2). In these compounds, the (5-*inca*)^{2−} ligand shows a new coordination mode (Scheme 1, right), which is coordinated to Zn ions through two nitrogen and one oxygen pertaining to the pyrazole ring and the carboxylate group, respectively. Both materials possess open structures despite the occurrence of interpenetration and are able to adsorb CO₂ with tunable sorption capacities. Photoluminescence measurements together with TD-DFT calculations have been

performed in order to verify the origin of the emissions occurring when these ligands are coordinated to d¹⁰ transition metal ions in the MOFs. Moreover, the emission of the materials in response to the temperature has been analyzed in order to study their potential utility as thermometers due to the presence of pyrazole rings and zinc ions in the frameworks.²⁷

EXPERIMENTAL PROCEDURES

Chemicals. All the chemicals were of reagent grade and were used as commercially obtained.

Synthesis {[Zn(5-*inca*)(pbptz)_{0.5}]-1.5 DMF}_n (1). A total of 0.12 mmol (20.00 mg) of 1*H*-indazole-5-carboxylate and 0.06 mmol (14.17 mg) of 3,6-di(4-pyridinyl)-1,2,4,5-tetrazine were dissolved in 0.5 mL of DMF, and then 0.5 mL of distilled water was added. On the other hand, 0.12 mmol (22.02 mg) of zinc acetate was dissolved in 0.5 mL of distilled water, and afterward 0.5 mL of DMF was added. Both solutions were mixed, and the resulting solution was placed in a closed glass vessel and heated in an oven at 95 °C for 24 h. Pink single crystals were grown during the heating procedure under autogenous pressure, which were filtered off and collected in an open atmosphere and washed with water. Yield: 38% based on zinc. Anal. calcd. for C_{18.5}H_{18.5}N_{6.5}O_{3.5}Zn: C, 49.02; H, 4.11; N, 20.09. Found: C, 48.23; H, 3.31; N, 20.49%.

Synthesis of {[Zn(5-*inca*)(4,4-bipy)_{0.5}]-DMF}_n (2). Well-shaped yellow single crystals of 2 were obtained after carrying out the same general procedure described for 1 but replacing 3,6-di(4-pyridinyl)-1,2,4,5-tetrazine with 4,4'-dipyridyl (9.37 mg). Yield: 45% based on zinc. Anal. calcd. for C₁₆H₁₅N₄O₃Zn: C, 51.01; H, 4.01; N, 14.87. Found: C, 50.86; H, 3.98; N, 14.95%.

Physical Measurements. Elemental analyses (C, H, N) were performed on an Euro EA elemental analyzer. FTIR spectra (KBr pellets) were recorded on a Nicolet IR 6700 spectrometer in the 4000–400 cm^{−1} spectral region. Thermogravimetric analysis was carried out using a Mettler Toledo TGA/SDTA 851 apparatus in the 25–600 °C temperature range with a 10 °C min^{−1} scan rate and a N₂ flow of 30 mL min^{−1}. High pressure adsorption isotherms have been measured in a noncommercial volumetric adsorption instrument (University of Granada) equipped with two Baratron absolute pressure transducers (MKS type 627B). Their pressure ranges are from 0 to 133.33 kPa and from 0 to 3333.25 kPa, respectively, and the reading accuracy is 0.05% of the usable measurement range. Prior to measurement, powder samples were heated at 393 K for 12 h and outgassed to 10^{−5} Torr. All gases employed were supplied by Air Liquide with a purity of at least 99.998%. A closed cycle helium cryostat enclosed in an Edinburgh Instruments FLS920 spectrometer was employed for steady state photoluminescence (PL) and lifetime measurements at variable temperature. All samples were first placed under a high vacuum (of ca. 10^{−9} mbar) to avoid the presence of oxygen or water in the sample holder. For steady-state measurements, a Müller-Elektronik-Optik SVX1450 Xe lamp or an IK3552R-G He-Cd continuous laser (325 nm) were used as excitation source, whereas a microsecond pulsed lamp was employed for recording the lifetime measurements. Photographs of irradiated single crystals and polycrystalline samples were taken at room temperature in a micro-PL system included in an Olympus optical microscope illuminated with a Hg lamp. Time-resolved emission spectra were recorded using excitation and emission band-pass of 5 and 2.5 nm, respectively.

X-ray Diffraction. The X-ray intensity data were collected on a Bruker D8 Venture diffractometer using Mo-*K*_α radiation at 100(2) K. The data were integrated with SAINT²⁸ and corrected for absorption effects with SADABS.²⁹ The crystal structures were solved with SHELXT³⁰ and refined with SHELXL.³¹ The OLEX2 software was used as a graphical interface.³² Anisotropic atomic displacement parameters were introduced for all non-hydrogen atoms. Hydrogen atoms were placed at geometrically calculated positions and refined with the appropriate riding model, with U_{iso}(H) = 1.2 U_{eq}(C). Even though crystal data were collected up to 0.77 Å, crystals still diffracted quite weakly at a high angle due to their rather low quality, and data

were cut off according to intensity statistics (compound 1), using restraints and constraints during refinement. In compound 1, the 4-pyridyl moiety of pbptz ligand was found disordered over two alternative positions (0.56:0.44 ratio) and was refined with rigid groups and restraints on geometry and displacement parameters. In the case of compound 2, the 4-pyridyl moiety of the 4,4-bipy ligand also was found disordered over two alternative positions (0.56:0.44 ratio) and was refined with rigid groups and restraints on geometry and displacement parameters. Disorder of the ligands was modeled using AFIX (compound 1) or FLAT (compound 2) commands. For all compounds, a number of RIGU and ISOR restraints had to be used to obtain reasonable displacement parameters for selected non-hydrogen atoms. Their U_{ij} values were therefore restrained to be approximately spherical. In both compounds, severely disordered DMF molecules could not be modeled reasonably and were therefore removed from the diffraction data (using the OLEX2Mask tool) but considered for calculation of empirical formula, formula weight, density, linear absorption coefficient, and $F(000)$. Crystal data and refinement details are listed in Table 1. Crystallographic data for the

(1 and 2) based on dimeric secondary building units (SBUs), in which the structures present interpenetration. Activation of MOFs 1 and 2 was performed by heating the washed material at 150 °C for 2 h. Crystallinity of desolvated materials was confirmed by powder X-ray diffraction (PXRD) (Figures S1 and S2), whereas thermogravimetric analysis (TGA) was consistent with the elimination of solvent molecules (Figures S3 and S4).

Structural Description of $\{[\text{Zn}(5\text{-inca})(\text{pbptz})_{0.5}]\cdot 1.5 \text{DMF}\}_n$ (1). Compound 1 crystallizes in the $C2/c$ monoclinic space group, and the crystal structure consists of zinc(II) atoms linked through pbptz and $(5\text{-inca})^{2-}$ coligands, which afford large connectivity resulting in an open 3D framework.

The asymmetric unit of the crystal structure consists of a Zn1 atom, one $(5\text{-inca})^{2-}$ ligand, and half of a pbptz linker. The metal center exhibits a N_3O tetrahedral coordination environment (Figure 1a) that is established by two nitrogen atoms from two symmetry related indazole rings, one nitrogen

Table 1. Crystallographic Data and Structure Refinement Details for All Compounds

compound	1	2
chemical formula	$\text{C}_{18.50}\text{H}_{18.50}\text{N}_{6.50}\text{O}_{3.50}\text{Zn}$	$\text{C}_{16}\text{H}_{15}\text{N}_4\text{O}_3\text{Zn}$
CCDC	1942013	1942014
$M/g \text{ mol}^{-1}$	453.27	376.69
T/K	100	100
cryst syst	monoclinic	orthorhombic
space group	$C2/c$	$Pccn$
a (Å)	16.6227(11)	16.8684(9)
b (Å)	17.9748(13)	12.9147(7)
c (Å)	13.8372(10)	14.8470(7)
β (deg)	98.135(3)	90
$V/\text{Å}^3$	4092.8(5)	3234.4(3)
Z	8	8
$\rho/g \text{ cm}^{-3}$	1.471	1.547
μ/mm^{-1}	1.236	1.541
$S(\text{GOF})^a$	1.046	1.162
$R [I > 2\sigma(I)]^b$	0.0729	0.0729
$wR^2 [I > 2\sigma(I)]^c$	0.1858	0.1376

^a $S = [\sum w(F_o^2 - F_c^2)^2 / (N_{\text{obs}} - N_{\text{param}})]^{1/2}$. ^b $R_1 = \sum ||F_o| - |F_c|| / \sum |F_o|$. ^c $wR^2 = [\sum w(F_o^2 - F_c^2)^2 / \sum wF_o^2]^{1/2} w = 1 / [\sigma^2(F_o^2) + (aP)^2 + bP]$ where $P = (\max(F_o^2, 0) + 2F_c^2) / 3$.

structures reported in this paper have been deposited with the Cambridge Crystallographic Data Center as supplementary publication nos. CCDC 1942013–1942014 for compounds. Copies of the data can be obtained free of charge on application to the Director, CCDC, 12 Union Road, Cambridge, CB2 1EZ, U.K. (Fax: + 44–1223–335033; e-mail: deposit@ccdc.cam.ac.uk or <http://www.ccdc.cam.ac.uk>).

Computational Details. PL spectra were calculated by means of TD-DFT using the Gaussian 09 package,³³ using the Becke three-parameter hybrid functional with the nonlocal correlation functional of Lee–Yang–Parr (B3LYP)^{34–36} along with the 6-311G++(d,p) basis set³⁷ adopted for all atoms but for the central zinc cation, for which the LANL2DZ^{38–40} basis set along with the corresponding effective core potential (ECP) was used. The 40 lowest excitation states were calculated by the TD-DFT method. Results were analyzed with GaussSum program package,⁴¹ and molecular orbitals were plotted using GaussView 5.⁴²

RESULTS AND DISCUSSION

The solvothermal reaction between 1*H*-indazole-5-carboxylic acid and the corresponding pyridine derivative ligand, with zinc acetate in $\text{H}_2\text{O}/\text{DMF}$, produces two new MOF materials

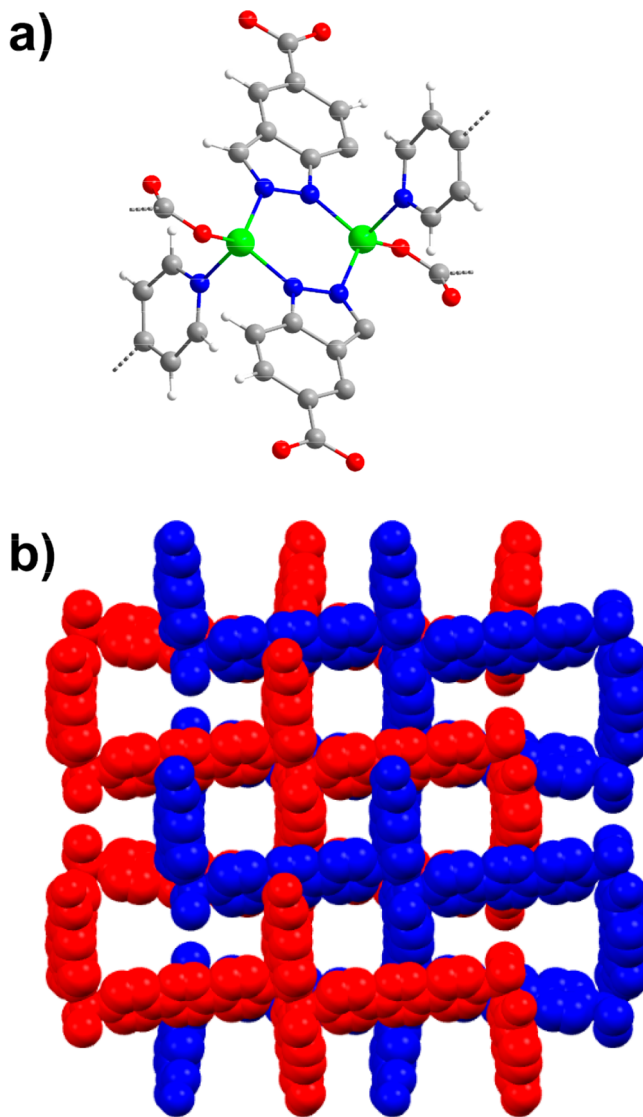


Figure 1. Crystal structure of compound 1: (a) fragment containing the SBU and (b) perspective view showing the perpendicular disposition of the pillaring pbptz linkers with regard to the Zn/(5-inca)²⁻ layers. Color code: zinc, green; oxygen, red; nitrogen, blue; carbon, gray; hydrogen, white.

atom pertaining to pbptz ligand and one oxygen from the carboxylate group of a third (5-inca)²⁻ ligand. Continuous shape measures performed corroborate the low distorted tetrahedral shape ($S_T = 0.67$) of the coordination shell (see Supporting Information). (5-inca)²⁻ exhibits the novel tridentate coordination mode showed in Scheme 1b (right), which allows it to link to two zinc(II) atoms through the nitrogen atoms pertaining to the indazole ring to eventually form dinuclear SBUs. Within these units, the metal atoms are slightly placed out of the planes delimited by indazole moieties (0.073 Å), in such a way that the resulting six-member ring imposes a Zn···Zn distance of 3.548 Å. Each building dinuclear unit connects to six neighboring ones through both (5-inca)²⁻ ligands and pbptz linkers. On the one hand, the SBU joins to two adjacent units through the carboxylate moieties of four (5-inca)²⁻ ligands, two of which are coplanar and define the SBU of reference, whereas the remaining two belong to other SBUs, yielding Zn/(5-inca) layers along the crystallographic *bc* plane. On the other hand, two pbptz pillaring linkers that arise almost perpendicularly from the central six-member ring of the SBU (with an angle of 76.5°) connect to the two remaining SBUs, thus establishing the 3D structure of the MOF (Figure 1b). Taking into account the connectivity achieved among SBUs, which may be considered as six-connected nodes from the topological point of view, the framework resembles that exhibited by the well-known isorecticular family of MOF-5, in good agreement with the topological analysis performed with TOPOS software, which confirms that the herein described MOF possesses a *pcu* network with the (4¹²·6³) point symbol (Figure 2).^{43,44} The length of both connectors and the topology of the framework drive the growth of an almost empty architecture with such a large accessible volume that it admits the occurrence of a second network in the crystallization. Therefore, the porosity of the resulting 2-fold interpenetrated structure is reduced though it still leaves a substantially large 2D void system within that accounts for the 44.1% of the unit cell volume.⁴⁵ Despite the large solvent accessible volume contained in the structure, it must be highlighted that the pore network is not regular, but it contains large tubular channels with an approximate section of 7 Å, whereas they are cross-linked through narrow windows with apertures of 1.7–2.7 Å. This fact explains the limited gas adsorption capacity of the MOF, involving no N₂ adsorption capacity at low pressures. Instead, the microporous nature of the MOF was confirmed by CO₂ sorption isotherms (see Figure S15), revealing that compound 1 adsorbs 0.9 mmol/g of CO₂ at 273 K and 600 kPa, a value which is lower than those of other recently reported MOFs.^{46,47} Interestingly, this value decreases to 0.34 mmol/g upon increasing the CO₂ pressure to 2570 kPa. This shape of the isotherm, showing the above-mentioned negative gas sorption during the pressure increase, in line with some previous works by Kaskel et al.,⁴⁸ is characteristic of a sudden hysteretic structural deformation and pore contraction probably derived from a subnetwork displacement occurring in the interpenetrated framework. A careful analysis of the interpenetration occurring in the structure reveals that both frameworks are weakly bound to each other, finding no remarkable interactions apart from C–H···π interactions between indazole and pbptz ligands involving some kind of lateral interactions among their π clouds, which should be translated into a flexible character.

Structural Description of {[Zn(5-inca)(4,4-bipy)_{0.5}]·DMF}_n (2). Compound 2 crystallizes in the orthorhombic

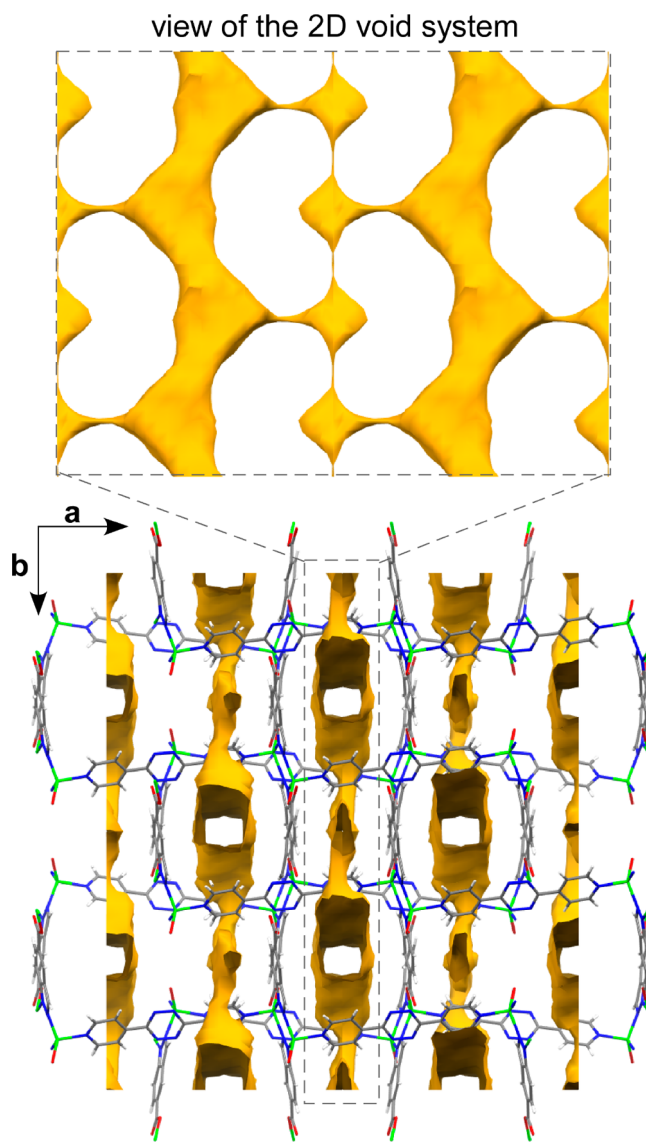


Figure 2. Perspective view of compound 1 showing the solvent-accessible surface.

Pccn space group and possesses an isorecticular 3D framework where pbptz linkers are replaced by 4,4-bipy. (5-inca)²⁻ exhibits a similar coordination pattern detailed for the previous material (right-hand side of Scheme 1), which forms dinuclear SBUs owing to the coordination of nitrogen atoms pertaining to the indazole ring to two zinc(II) atoms (Figure 3a). Three significant differences are found in this dinuclear unit compared to that of the previous compound: (i) the carboxylate moiety of the (5-inca)²⁻ ligand is slightly moved to bite the zinc atom (bringing a semicoordination of O2A atom, Zn···O2A of 2.73 Å), despite of which the coordination environment is best described as a tetrahedron in view of the low distortion with regard to the ideal polyhedron ($S_T = 0.413$, see Table S1); (ii) Zn atoms are more coplanar with regard to the plane established by the aromatic rings (which is dropped to 0.029 Å) and (iii) the intradinuclear Zn···Zn distance is enlarged to 3.657 Å. It must be highlighted that both changes are clearly derived from the change of the pillaring linker, which, being considerably shorter than pbptz (the Zn···Zn bond distance is reduced from 15.2 to 11.2 Å), modulates the flexibility of the framework.

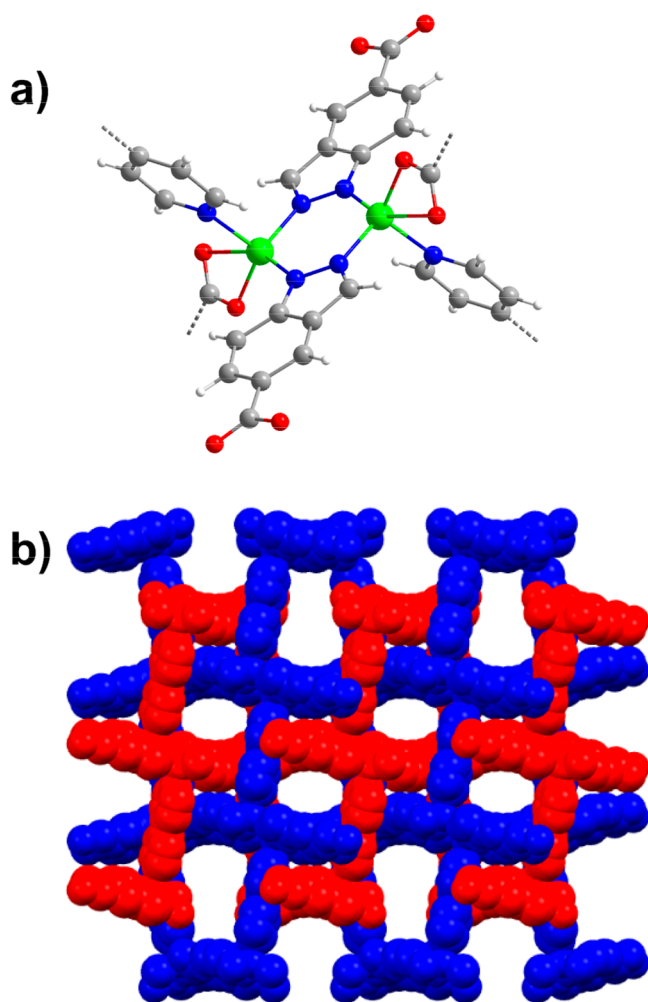


Figure 3. (a) SBU of the structure of compound 2 and (b) crystal packing of the compound showing the 2-fold interpenetration.

As a consequence of the mutual displacement between the subnets, the free volume enclosed in the structure is shaped in the form of one-dimensional microchannels (with an irregular tubular shape containing wide and narrow sections of 4.3 and 1.6 Å) and accounts for 32.4% of the unit cell volume (Figure 4). The microporous nature of the MOF was confirmed by CO₂ sorption (see Figure S15), revealing that compound 2 adsorbs more CO₂ than that of compound 1: 2.0 mmol/g CO₂ at 273 K and 600 kPa and 3.01 mmol/g CO₂ at 273 K and 2570 kPa.

Photoluminescence Properties. The metal–organic nature of these materials, based on 3D frameworks containing ligands with π -conjugated systems (some of which are also decorated with carboxylate groups that are coordinated to closed-shell metal ions such as zinc(II)), make them suitable to exhibit photoluminescence (PL) in the solid state. Under monochromatic UV light excitation ($\lambda_{\text{ex}} = 325$ nm), the room temperature emission spectrum of compound 1 consists of two main and one minor broad bands. A first main band is centered at 374 nm, followed by that located at 440 nm with a shoulder at 420 nm, which dominates the entire spectrum (Figure 5a). Finally, a less intense band is shown to peak at ca. 620 nm. It is worth mentioning that the two main bands are similar to the bands corresponding to each individual ligand, since free (5-incaH₂) and pbptz show emission bands at $\lambda_{\text{em}} = 371$ and 430/

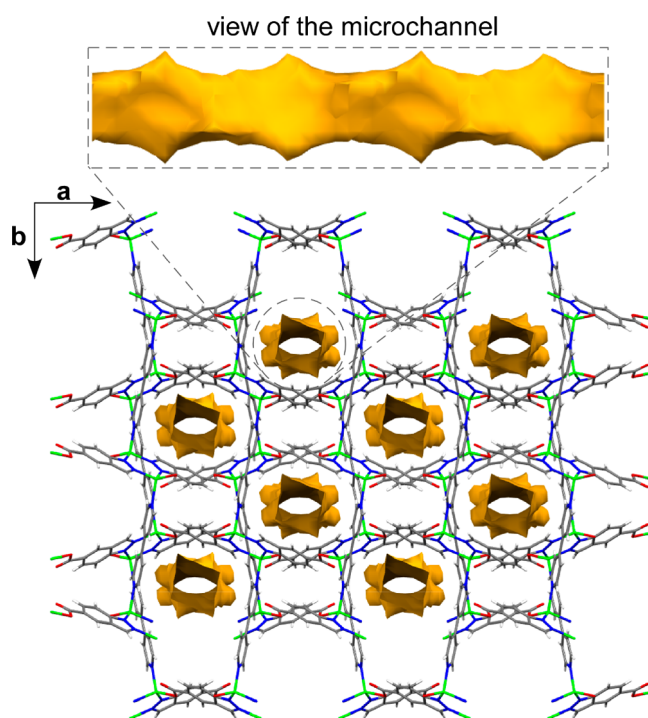


Figure 4. Perspective view of compound 2 showing the solvent-accessible surface. Color code: Zinc, light steel blue; oxygen, red; nitrogen, blue; carbon, gray; chloride, green.

460 nm, respectively. Instead, the last less intense band, not directly related with the emissions centered on the ligands, may be ascribed to the formation of an excimer among the π clouds of the aromatic rings of (5-inca)²⁻ and pbptz ligands pertaining to different subnets, although the participation of nonlocalized DMF molecules should not be discarded.^{21,49} The subtle shifts observed for the bands with respect to free ligands can be attributed to the coordination effect, as previously observed for other zinc-based MOFs.^{50,51}

In order to get deeper insights into the PL emission of 1, TD-DFT calculations were conducted on a suitable model taken from its X-ray structure (model 1 hereafter, see Figure S5). As shown in Figure 5a, after a vertical excitation at 320 nm proceeding through the HOMO-5 \rightarrow LUMO+2 electronic transition (which represents the main excitation line and resembles the experimental λ_{ex} of 325 nm, see Supporting Information), the calculated emission spectrum reproduces fairly well the experimental one, showing a wide band with two maxima peaking at 398 and 451 nm ascribed to HOMO-1 \leftarrow LUMO+1 and HOMO \leftarrow LUMO+1. It is worth noticing that this model, based on a monomeric molecule, is not able to reproduce the minor less-energetic band peaking at ca. 625 nm. Nonetheless, a model consisting of a (5-inca)²⁻ and a pbptz ligand pertaining to different subnets (model 3, see Figures S7–S8) suggests that the latter emission might be derived from their weak interaction, confirming the occurrence of excimer. Taking into account the dominant π and π^* character of these electronic transitions in addition to the participation of molecular orbitals extending over both (5-inca)²⁻ and pbptz ligands, the PL scenario of 1 is accurately described as LLCT. Figure 6 summarizes the global PL scenario for a better understanding of their main electronic transitions. As it is well-known, the luminescence in MOFs is known to be quenched by the coupling of nonradiative molecular vibrations, such as

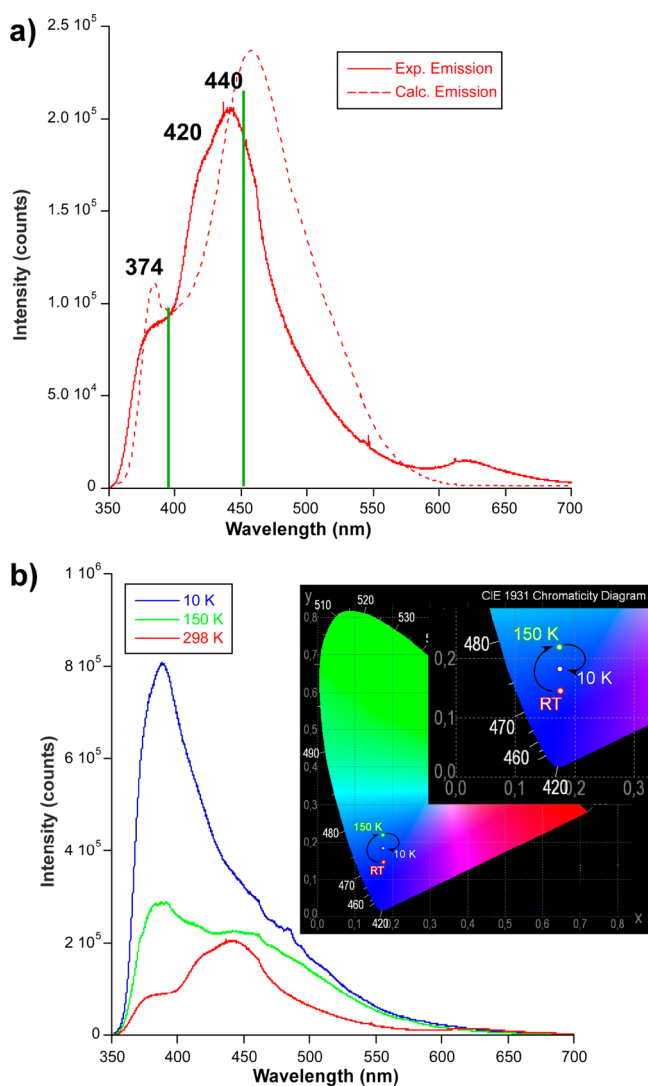


Figure 5. (a) Room temperature experimental (solid red line) and TD-DFT calculated (dotted red line) steady-state emission spectra of compound **1**. Black numbers account for experimental emission maxima, whereas main calculated main lines are represented as vertical green lines. (b) Experimental emission spectra of **1** at a variable temperature together with the thermochromic emission. Inset shows luminescent thermochromism represented in the CIE1931 chromaticity color coordinates.

aromatic C–H bonds present in both ligands,^{52,53} with an excited-to-ground state energy difference. Therefore, the sample was cooled down to low temperature to study such an effect. Keeping the experimental setting unchanged for comparative purposes, the emission spectrum was measured at the lowest possible temperature (10 K) as well as at an intermediate temperature (150 K). Interestingly, apart from an obvious increase of the emitted signal, which rises by 43% at 150 K and by 300% at 10 K considering the absolute emission maxima, the two main bands ($\lambda_{\text{em}} = 374$ and 440 nm) invert progressively their relative intensity as the temperature is dropped since at 10 K the 374 nm band at RT covers most of the spectrum, whereas that at 440 nm is nearly undistinguishable and becomes a shoulder (Figure 5b). For its part, the minor band ($\lambda_{\text{em}} = 625$ nm) is not observed anymore, meaning that the excimer is disrupted as the temperature drops probably due to a relative displacement between subnets.

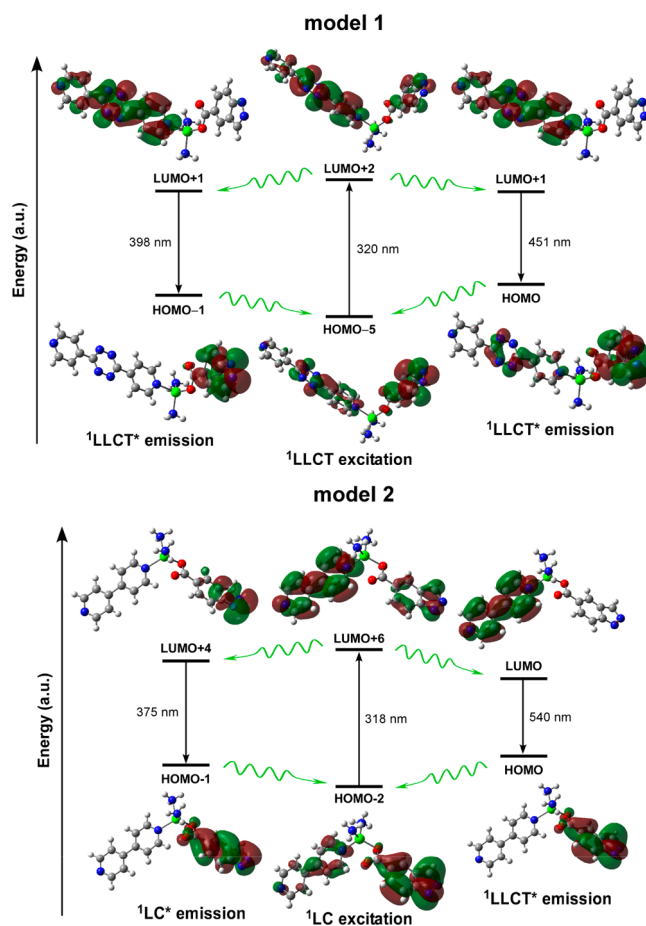


Figure 6. Diagram of the dominant MOs involved in the PL excitation and emission of models 1 and 2. Note that red and blue straight lines represent excitation and emission transitions, whereas undulated green lines account for vibrational relaxation processes.

Especially at 10 K, the emission band extends up to 600 nm showing a long tail and is shifted to $\lambda_{\text{em}} = 388$ nm in such a way that it can be considered to occupy an intermediate wavelength between those of free ligands. The evolution of the emission spectra brings a remarkable luminescent thermochromism in the compound, since the emission varies among different tones of blue.

On the other hand, under $\lambda_{\text{ex}} = 325$ nm excitation with a laser at RT, compound **2** shows two perfectly separated emission bands with their maximum centered at 380 and 535 nm, respectively (Figure 7). Conversely to **1**, compound **2** does not show any significant thermochromic effect (there is no change in the relative intensity of the maxima) but a strong increase in the absolute emission (integrated intensity) with the lowering of the temperature, which experiences an increment of 700% (see Figure S9). Despite the fact that one could a priori attribute the presence of two bands to the intraligand emission of $(5\text{-inca})^{2-}$ and bipy molecules, a similar band is only observed for the first ligand ($\lambda_{\text{em}} = 380$ for **2** and 371 nm for (5-incaH_2)), whereas the second band appears to be deeply red-shifted compared to the free bipy ligand emission ($\lambda_{\text{em}} = 535$ for **2** and 430 nm for bipy).⁵⁴

A detailed analysis with TD-DFT methodology on a suitable model of **2** (model 2 hereafter) reveals a somewhat different PL scenario for this compound despite the similar nature of its ligands. On the one hand, the system is excited through two

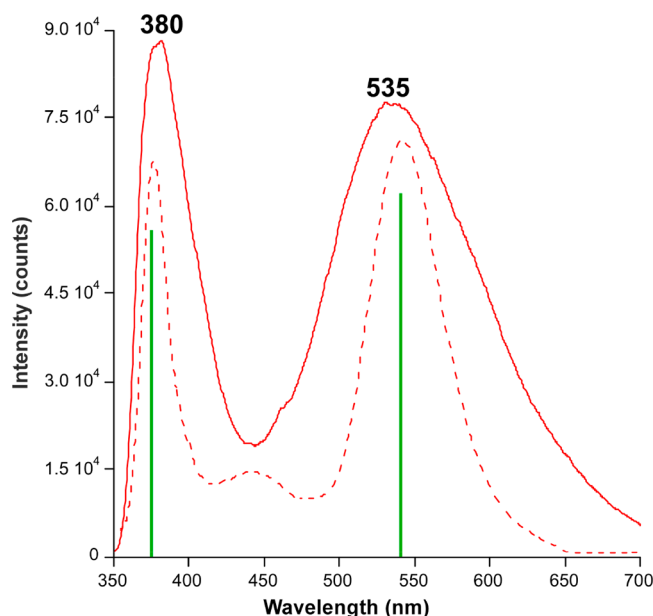


Figure 7. Comparison between room temperature experimental and calculated emission spectra of compound **2**. Black numbers and green lines represent the main experimental emission maxima and calculated vertical main lines, respectively.

similar lines: a minor band at 302 nm corresponding to the HOMO-5 \rightarrow LUMO+2 transition and the major band located at 318 nm described by the HOMO-2 \rightarrow LUMO+6 transition. Given that the experimental spectrum is recorded with a $\lambda_{\text{ex}} = 325$ nm, it may be assumed that the excitation proceeds mainly through the latter transition. On the other hand, the radiative relaxation of **2** is governed by HOMO-1 \leftarrow LUMO+4 and HOMO \leftarrow LUMO transitions peaking at 375 and 540 nm, which fairly represent the two main emission bands. In agreement with the previous speculations, the first band is centered on the (5-inca) $^{2-}$ ligand, which explains why it resembles the emission band displayed by the free ligand. Instead, the second band clearly corresponds to ligand-to-ligand charge transfer (LLCT) process involving the empty molecular orbitals (MOs) of the bipy and the filled MOs of (5-inca) $^{2-}$.

Though there is no previous report on LLP behavior for CPs based on (5-inca) $^{2-}$ ligand, in view of the long-lived phosphorescent emissions shown by zinc compounds based on similar aromatic ligands found in the literature, we decided to measure decay curves on both compounds.¹⁷ To that end, the most representative emission wavelengths of the spectrum of **1** were monitored, i.e., the emission maxima ($\lambda_{\text{em}} = 374$ and 440 nm). The decay curves show a very rapid decrease of the signal, indicating that the emission proceeds through a fluorescent process. Though the decay at 374 nm is too rapid as to be analyzed (with a lifetime below the pulse of the lamp \approx a few μs), a weak but larger process could be discerned from the curve measured at 440 nm. The analysis by means of an exponential expression gives a lifetime of about 4150 μs (see Figure S10), which may be regarded within the low limit of LLP (below the arbitrary value of 20 ms).⁵⁵ It was observed that lowering the temperature keeps the lifetime almost constant, where the subtle enlargement may be related with an aforementioned decrease of vibrational quenching ($\tau_{150\text{K}} \approx 6040$ and $\tau_{10\text{K}} \approx 8590$ μs). Instead, compound **2** presents a wavelength dependent emission scenario composed of a

persistent fluorescent emission ($\tau_{\text{fl}} \approx 170$ μs) around the maximum of the first band ($\lambda_{\text{em}} = 380$ nm) and a phosphorescence emission ($\tau_{\text{ph}} \approx 200$ ms) around the high-wavelength band ($\lambda_{\text{em}} \approx 535$ nm, see Figure S11 and Table S2 in the Supporting Information). Given their curvilinear shape, all phosphorescence decay curves were fitted with two lifetime components so they were analyzed with a multiexponential expression [$I_t = A_0 + A_1 \exp(-t/\tau_1) + A_2 \exp(-t/\tau_2)$] that considers two lifetimes as usually performed for previous materials (see Supporting Information). The pale blue and yellowish green colors displayed by **2** in the micro-PL photographs taken on crystals are a good indication of the fluorescent and phosphorescent emissions (see Figure 8). As

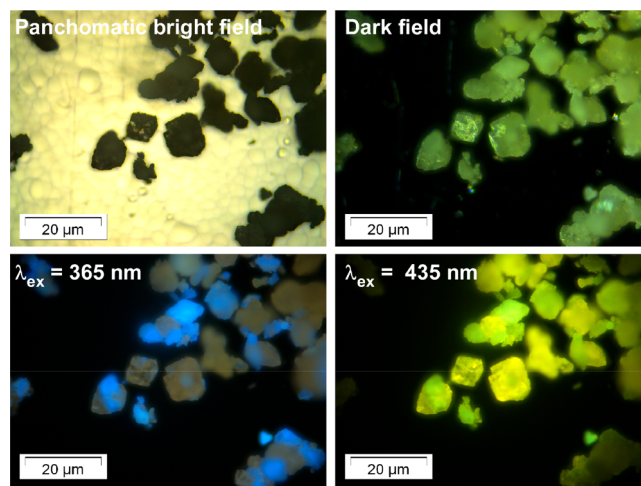


Figure 8. Room temperature micro-PL images for single crystals of compound **2**.

observed in these photographs, the fluorescent signal observed under irradiation with UV light ($\lambda_{\text{ex}} \approx 365$ nm in the present case) shows a kind of luminescent waveguiding effect, since the emitted color is only seen depending on the orientation of the crystals. This effect is not so common, although it has already been described for other luminescent materials, for which crystals with an adequate refraction index and morphology as well as strong luminescence emission are required, in such a way that most of the light is confined within the crystal and emitted through a particular face.^{56–60}

The recorded lifetime of **2** is large enough as to be referred to as room temperature phosphorescence (RTP), which provides this compound with a very subtle greenish afterglow that is glimpsed when turning off laser beam. Dropping the temperature off to save nonradiative quenching does not bring any substantial on decay curves measured at the first emission maxima $\lambda_{\text{em}} = 380$ nm, but it promotes a substantial lengthening of the lifetime associated with the phosphorescent emission. In particular, at $\lambda_{\text{em}} = 535$ nm, the lifetime enlarges progressively, mainly below 150 K, until it achieves a value of ca. 950 ms, which can be considered as an intermediate-to-large value for the CPs presenting LLP reported so far (Figure S12).^{56–60} These results evidence the fluorescent/phosphorescent character of the MOF at low temperature, a fact that confirms that the LCCT process occurring at the ligand is stabilized in the framework of the MOF such that both $S_0 \leftarrow S_1$ and $S_0 \leftarrow T_1$ transitions are enabled and enhanced. With the aim of better characterizing the phosphorescent emission, time-resolved emission spectra (TRES) were recorded for **2** at

a low temperature, which confirmed that the persistent emission consists of a wide band centered at $\lambda_{em} = 550$ nm, close to the band measured at steady state, thus explaining well the green-yellowish afterglow shown when the UV excitation source is turned off (Figure 9). It is worth highlighting that the

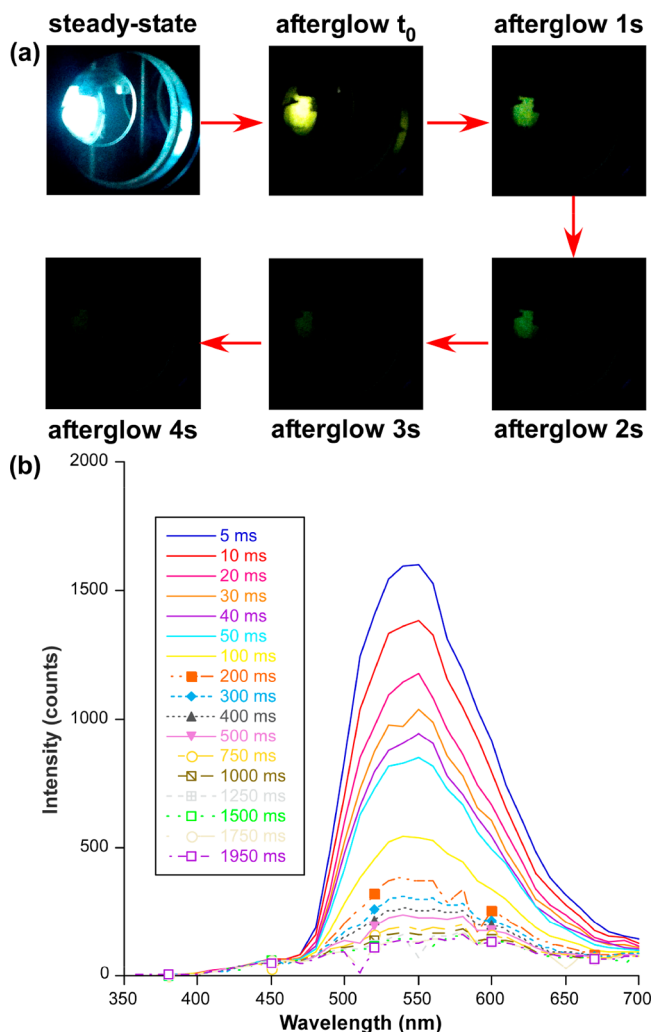


Figure 9. (a) Photographs of the steady-state and afterglow emissions of compound 2. (b) TRES of compound 2 at 10 K at selected delays ($\lambda_{ex} = 325$ nm).

emitted light, although it is weak as to be captured by a common camera, can be perfectly traced by the naked eye 4 s after the excitation source is turned off.

A calculation of the phosphorescent emission estimated from the DFT computed T_1 and S_0 electronic states (usually denoted as vertical excitation phosphorescent energy)⁶¹ on model 2 gives a very good estimate of the experimentally measured band for compound 2 ($\lambda_{vert-phosp} = 507$ vs $\lambda_{ph} = 550$ nm). This value can be taken as an approach to estimate the energy of the T_1 state in the compound assuming that the compound follows Kasha's rule.⁶² A similar calculation performed on model 1 renders a $\lambda_{vert-phosp} = 470$ nm, meaning that the T_1 state in compound 1, conversely to 2, is less energetic than the lowest-lying excited singlet state from which a radiative emission takes place ($S_0 \leftarrow S_1 \approx 440$ nm). Therefore, this fact could a priori inhibit an intersystem crossing to populate the T_1 state that enables the occurrence of

phosphorescence in 1 and, hence, explains why LLP is solely enhanced in compound 2. Moreover, it cannot be discarded that weaker phosphorescence shown by 1 is also related to the less rigidity of pbptz ligand in the MOF, which clearly possesses more degrees of freedom compared to bipy ligand in 2.

CONCLUSIONS

Two novel porous zinc based metal–organic frameworks consisting of indazole-5-carboxylate and 3,6-di(4-pyridinyl)-1,2,4,5-tetrazine for compound 1 or 4,4'-bipyridine like for 2 have been synthesized and characterized. Both MOFs present an isorecticular architecture with pcu topology that crystallizes as a doubly interpenetrated structure. This structural feature affords some flexibility to the frameworks and permits modulation of their porosity obtaining a 2D void system with narrow pore sections and 1D microchannels for 1 and 2, respectively. Solid state photoluminescence measurements reveal that both compounds provide intense blue emissions under irradiation with UV light which arise from charge transfers occurring between $(5-inca)^{2-}$ and bipyridyl-like ligands as confirmed by TD-DFT calculations. Variable-temperature data indicate that compound 1 shows a remarkable thermochromism, which modulates the tonality of the emitted blue light provoked by the change in the relative intensity of the two main emission bands and an excimer formation/disruption between ligands belonging to different interpenetrated subnetworks. For its part, dropping down the temperature in 2 has no such effect; yet, it largely enhances its emission capacity, a fact that is particularly inferred from the occurrence of long-lasting phosphorescence that may be perceived by the naked eye (with an associated lifetime of ca. 950 ms) below the temperature of liquid nitrogen. DFT calculations performed on these compounds point out the relative energy of the excited singlet and triplet states as a probable source in the origin of sizable phosphorescence solely in compound 2, although the lower rigidity of the pbptz ligand of compound 1 compared to bipy in 2 may also have some influence.

ASSOCIATED CONTENT

Supporting Information

The Supporting Information is available free of charge at <https://pubs.acs.org/doi/10.1021/acs.cgd.0c00345>.

Additional figures of crystal structures and data, thermogravimetric analysis, powder X-ray diffraction analyses, photoluminescence spectra and lifetimes, TD-DFT computational results (PDF)

Accession Codes

CCDC 1942013–1942014 contain the supplementary crystallographic data for this paper. These data can be obtained free of charge via www.ccdc.cam.ac.uk/data_request/cif, or by emailing data_request@ccdc.cam.ac.uk, or by contacting The Cambridge Crystallographic Data Centre, 12 Union Road, Cambridge CB2 1EZ, UK; fax: +44 1223 336033.

AUTHOR INFORMATION

Corresponding Authors

Javier Cepeda – Departamento de Química Aplicada, Facultad de Química, Universidad del País Vasco/Euskal Herriko Unibertsitatea (UPV/EHU), 20018 San Sebastián, Spain;

orcid.org/0000-0002-0147-1360; Email: javier.cepeda@ehu.eus

Guillermo Mínguez Espallargas – Instituto de Ciencia Molecular (ICMol), Universitat de València, 46980 Paterna, Spain; orcid.org/0000-0001-7855-1003; Email: guillermo.minguez@uv.es

Antonio Rodríguez-Diéguez – Departamento de Química Inorgánica, Universidad de Granada, 18071 Granada, Spain; orcid.org/0000-0003-3198-5378; Email: antonio5@ugr.es

Authors

Antonio A. García-Valdivia – Departamento de Química Inorgánica, Universidad de Granada, 18071 Granada, Spain

Manuel Pérez-Mendoza – Departamento de Química Inorgánica, Universidad de Granada, 18071 Granada, Spain

Duane Choquesillo-Lazarte – Laboratorio de Estudios Cristalográficos, IACT (CSIC-UGR), 18100 Granada, Spain; orcid.org/0000-0002-7077-8972

Belén Fernández – Institute of Parasitology and Biomedicine “López-Neyra”, CSIC, 18600 Granada, Spain

Manuel Souto – Instituto de Ciencia Molecular (ICMol), Universitat de València, 46980 Paterna, Spain; CICECO-Aveiro Institute of Materials, Department of Chemistry, University of Aveiro, 3810-193 Aveiro, Portugal; orcid.org/0000-0003-3491-6984

Marcos González-Tejero – Departamento de Química Inorgánica, Universidad de Granada, 18071 Granada, Spain

Jose A. García – Departamento de Física Aplicada II, Facultad de Ciencia y Tecnología, University of Basque Country (UPV/EHU), 48940 Leioa, Spain

Complete contact information is available at: <https://pubs.acs.org/10.1021/acs.cgd.0c00345>

Notes

The authors declare no competing financial interest.

ACKNOWLEDGMENTS

Financial support was given by Junta de Andalucía (Spain) (Project Number FQM-394 and FQM-1484), Red Guipuzcoana de Ciencia, Tecnología e Innovación (OF218/2018), University of the Basque Country (GIU 17/13), Gobierno Vasco/Eusko Jaurlaritz (IT1005-16), the Spanish Ministry of Science, Innovation and Universities (MCIU/AEI/FEDER, UE) (PGC2018-102052-A-C22, PGC2018-102052-B-C21, PGC2018-102047-B-I00, CTQ2017-89528-P cofinanced by FEDER and Excellence Unit María de Maeztu MDM-2015-0538 granted to ICMol), the Generalitat Valenciana (PROMETEU/2019/066), and the European Union (ERC-2016-CoG 724681-S-CAGE). G.M.E. and M.S. thank MICINN for a Ramón y Cajal and a Juan de la Cierva-Formación fellowship, respectively. The authors thank the technical and human support provided by SGIker of UPV/EHU and European funding (ERDF and ESF).

REFERENCES

- Chen, B.; Ma, S.; Zapata, F.; Fronczek, F. R.; Lobkovsky, E. B.; Zhou, H.-C. Rationally Designed Micropores within a Metal-Organic Framework for Selective Sorption of Gas Molecules. *Inorg. Chem.* **2007**, *46*, 1233–1236.
- Jeazet, H. B. T.; Staudt, C.; Janiak, C. A method for increasing permeability in O₂/N₂ separation with mixed-matrix membranes made of water-stable MIL-101 and polysulfone. *Chem. Commun.* **2012**, *48*, 2140–2142.
- Li, J.-R.; Sculley, J.; Zhou, H.-C. Metal-organic frameworks for separations. *Chem. Rev.* **2012**, *112*, 869–932.
- Shang, J.; Li, G.; Singh, R.; Gu, Q.; Nairn, K. M.; Bastow, T. J.; Medhekar, N.; Doherty, C. M.; Hill, A. J.; Liu, J. Z.; Webley, P. A. Discriminative Separation of Gases by a “Molecular Tramdoor” Mechanism in Chabazite Zeolites. *J. Am. Chem. Soc.* **2012**, *134*, 19246–19253.
- Bourrelly, S.; Llewellyn, P. L.; Serre, C.; Millange, F.; Loiseau, T.; Férey, G. Different Adsorption Behaviors of Methane and Carbon Dioxide in the Isotypic Nanoporous Metal Terephthalates MIL-53 and MIL-47. *J. Am. Chem. Soc.* **2005**, *127*, 13519–13521.
- Yan, Y.; Yang, S. H.; Blake, A. J.; Schroder, M. Studies on Metal-Organic Frameworks of Cu(II) with Isophthalate Linkers for Hydrogen Storage. *Acc. Chem. Res.* **2014**, *47*, 296–307.
- Perez-Yanez, S.; Beobide, G.; Castillo, O.; Fischer, M.; Hoffmann, F.; Froba, M.; Cepeda, J.; Luque, A. Gas Adsorption Properties and selectivity in Cu^{II}/adeninato/carboxilato metal-Biomolecule Frameworks. *Eur. J. Inorg. Chem.* **2012**, *2012*, 5921–5933.
- Farha, O. K.; Eryazici, I.; Jeong, N. C.; Hauser, B. G.; Wilmer, C. E.; Sarjeant, A. A.; Snurr, R. Q.; Nguyen, S. T.; Yazaydin, A. O.; Hupp, J. T. Metal-Organic Framework Materials with Ultra-High Surface Areas: Is the Sky the Limit? *J. Am. Chem. Soc.* **2012**, *134*, 15016–15021.
- Li, J.-R.; Kuppler, R. J.; Zhou, H.-C. Selective gas adsorption and separation in metal-organic frameworks. *Chem. Soc. Rev.* **2009**, *38*, 1477–1504.
- Zhou, H.-C.; Kitagawa, S. Metal-Organic Frameworks (MOFs). *Chem. Soc. Rev.* **2014**, *43*, 5415–5418.
- Maurin, G.; Serre, C.; Cooper, A.; Férey, G. The new age of MOFs and of their porous-related solids. *Chem. Soc. Rev.* **2017**, *46*, 3104–3107.
- Cepeda, J.; Rodríguez-Diéguez, A. Tuning the luminescence performance of metal-organic frameworks based on d¹⁰ metal ions: from an inherent versatile behaviour to their response to external stimuli. *CrystEngComm* **2016**, *18*, 8556–8573.
- Seco, J. M.; Fairen-Jimenez, D.; Calahorra, A. J.; Méndez-Liñán, L.; Pérez-Mendoza, M.; Casati, N.; Colacio, E.; Rodríguez-Diéguez, A. Modular structure of a robust microporous MOF based on Cu₂ paddle-wheels with high CO₂ selectivity. *Chem. Commun.* **2013**, *49*, 11329–11331.
- Cepeda, J.; Pérez-Mendoza, M.; Calahorra, A. J.; Casati, N.; Seco, J. M.; Aragonés-Anglada, M.; Moghadam, P. Z.; Fairen-Jimenez, D.; Rodríguez-Diéguez, A. Modulation of Pore shape and adsorption selectivity by ligand functionalization in a series of “rob”-like flexible metal-organic frameworks. *J. Mater. Chem. A* **2018**, *6*, 17409–17416.
- Li, H.-Y.; Wei, Y.-L.; Dong, X.-Y.; Zang, S.-Q.; Mak, T. C. W. Novel Tb-MOF Embedded with Viologen Species for Multi-Photofunctionality: Photochromism, Photomodulated Fluorescence, and Luminescent pH Sensing. *Chem. Mater.* **2015**, *27*, 1327–1331.
- Barbieri, A.; Accorsi, G.; Armaroli, A. Luminescent complexes beyond the platinum group: the d¹⁰ avenue. *Chem. Commun.* **2008**, 2185–2193.
- San Sebastian, E.; Rodríguez-Diéguez, A.; Seco, J. M.; Cepeda, J. Coordination Polymers with Intriguing Photoluminescence Behavior: The Promising Avenue for Greatest Long-Lasting Phosphors. *Eur. J. Inorg. Chem.* **2018**, *2018*, 2155–2174.
- Rocha, J.; Brites, C. D. S.; Carlos, L. D. Lanthanide Organic Framework Luminescent Thermometers. *Chem. - Eur. J.* **2016**, *22*, 14782–14795.
- Han, Y.-H.; Tian, C.-B.; Li, Q.-H.; Du, S.-W. Highly chemical and thermally stable luminescent Eu_xTb_{1-x} MOF materials for broad-range pH and temperature sensors. *J. Mater. Chem. C* **2014**, *2*, 8065–8070.
- Brites, C. D. S.; Lima, P.; Silva, N. J. O.; Millán, A.; Amaral, V. S.; Palacio, F.; Carlos, L. D. Lanthanide-based luminescent molecular thermometers. *New J. Chem.* **2011**, *35*, 1177–1183.

- (21) Allendorf, M. D.; Bauer, C. A.; Bhakta, R. K.; Houk, R. J. T. Luminescent metal-organic frameworks. *Chem. Soc. Rev.* **2009**, *38*, 1330–1352.
- (22) Cui, Y.; Zhu, F.; Chen, B.; Qian, G. Metal-organic frameworks for luminescence thermometry. *Chem. Commun.* **2015**, *51*, 7420–7431.
- (23) Lower, S. K.; El-Sayed, M. A. The Triplet State and Molecular Electronic Processes in Organic Molecules. *Chem. Rev.* **1966**, *66*, 199–241.
- (24) Hawes, C. S.; Babarao, R.; Hill, M. R.; White, K. F.; Abrahams, B. F.; Kruger, P. E. Hysteretic carbon dioxide sorption in a novel copper(II)-indazole-carboxylate porous coordination polymer. *Chem. Commun.* **2012**, *48*, 11558–11560.
- (25) Botana, L.; Ruiz, J.; Seco, J. M.; Mota, A. J.; Rodríguez-Diéguez, A.; Sillanpää, R.; Colacio, E. Influence of the anions on the structure and magnetic properties of a series of bis(μ -diphenoxo)-bridged linear trinuclear copper(II) complexes: an experimental and theoretical study. *Dalton Trans.* **2011**, *40*, 12462–12471.
- (26) Seco, J. M.; Pérez-Yáñez, S.; Briones, D.; García, J. A.; Cepeda, J.; Rodríguez-Diéguez, A. Combining Polycarboxylate and Bipyridyl-like Ligand in the Design of luminescent Zinc and Cadmium Based Metal-Organic Frameworks. *Cryst. Growth Des.* **2017**, *17*, 3893–3906.
- (27) Qi, Y.-J.; Wang, Y.-J.; Li, X.-X.; Zhao, D.; Sun, Y.-Q.; Zheng, S.-T. Two d^{10} Metal-Organic Frameworks as Low-Temperature Luminescent Molecular Thermometers. *Cryst. Growth Des.* **2018**, *18*, 7383–7390.
- (28) SAINT v8.40A; Bruker AXS Inc.: Madison, Wisconsin, USA, 2016.
- (29) Krause, L.; Herbst-Irmer, R.; Sheldrick, G. M.; Stalke, D. Comparison of silver and molybdenum microfocus X-ray sources for single-crystal structure determination. *J. Appl. Crystallogr.* **2015**, *48*, 3–10.
- (30) Sheldrick, G. M. SHELXT - Integrated space-group and crystal-structure determination. *Acta Crystallogr., Sect. A: Found. Adv.* **2015**, *A71*, 3–8.
- (31) Sheldrick, G. M. Crystal structure refinement with SHELXL. *Acta Crystallogr., Sect. C: Struct. Chem.* **2015**, *C71*, 3–8.
- (32) Dolomanov, O. V.; Bourhis, L. J.; Gildea, R. J.; Howard, J. A. K.; Puschmann, H. OLEX2: a complete structure solution, refinement and analysis program. *J. Appl. Crystallogr.* **2009**, *42*, 339–341.
- (33) Frisch, M. J.; Trucks, G. W.; Schlegel, H. B.; Scuseria, G. E.; Robb, M. A.; Cheeseman, J. R.; Scalmani, G.; Barone, V.; Mennucci, B.; Petersson, G. A.; Nakatsuji, H.; Caricato, M.; Li, X.; Hratchian, H. P.; Izmaylov, A. F.; Bloino, J.; Zheng, G.; Sonnenberg, J. L.; Hada, M.; Ehara, M.; Toyota, K.; Fukuda, R.; Hasegawa, J.; Ishida, M.; Nakajima, T.; Honda, Y.; Kitao, O.; Nakai, H.; Vreven, T.; Montgomery, J. A., Jr.; Peralta, J. E.; Ogliaro, F.; Bearpark, M.; Heyd, J. J.; Brothers, E.; Kudin, K. N.; Staroverov, V. N.; Kobayashi, R.; Normand, J.; Raghavachari, K.; Rendell, A.; Burant, J. C.; Iyengar, S. S.; Tomasi, J.; Cossi, M.; Rega, N.; Millam, J. M.; Klene, M.; Knox, J. E.; Cross, J. B.; Bakken, V.; Adamo, C.; Jaramillo, J.; Gomperts, R.; Stratmann, R. E.; Yazyev, O.; Austin, A. J.; Cammi, R.; Pomelli, C.; Ochterski, J. W.; Martin, R. L.; Morokuma, K.; Zakrzewski, V. G.; Voth, G. A.; Salvador, P.; Dannenberg, J. J.; Dapprich, S.; Daniels, A. D.; Farkas, O.; Foresman, J. B.; Ortiz, J. V.; Cioslowski, J.; Fox, D. J. *Gaussian 09*, revision A.02; Gaussian, Inc.: Wallingford, CT, 2009.
- (34) Becke, A. D. Density-functional thermochemistry. III. The role of exact exchange. *J. Chem. Phys.* **1993**, *98*, 5648–5652.
- (35) Miehlich, B.; Savin, A.; Stoll, H.; Preuss, H. Results obtained with the correlation energy density functional of Becke and Lee, Yang and Parr. *Chem. Phys. Lett.* **1989**, *157*, 200–206.
- (36) Lee, C.; Yang, W.; Parr, R. G. Development of the Colle-Salvetti correlation-energy formula into a functional of the electron density. *Phys. Rev. B: Condens. Matter Mater. Phys.* **1988**, *37*, 785–789.
- (37) Noodleman, L.; Case, D. A.; Aizman, A. Broken symmetry analysis of spin coupling in iron-sulfur clusters. *J. Am. Chem. Soc.* **1988**, *110*, 1001–1005.
- (38) Hay, P. J.; Wadt, W. R. Ab initio effective core potentials for molecular calculations. Potentials for the transition metal atoms Sc to Hg. *J. Chem. Phys.* **1985**, *82*, 270–283.
- (39) Wadt, W. R.; Hay, P. J. Ab initio effective core potentials for molecular calculations. Potentials for main group elements Na to Bi. *J. Chem. Phys.* **1985**, *82*, 284–298.
- (40) Hay, P. J.; Wadt, W. R. Ab initio effective core potentials for molecular calculations. Potentials for K to Au including the Outermost core orbitals. *J. Chem. Phys.* **1985**, *82*, 299–310.
- (41) O'Boyle, N. M.; Tenderholt, A. L.; Langner, K. M. cclib: A library for package-independent computational chemistry algorithms. *J. Comput. Chem.* **2008**, *29*, 839–845.
- (42) Dennington, R.; Keith, T.; Millam, J. *GaussView*, Version 5; Semichem Inc.: Shawnee Mission, KS, 2009.
- (43) TOPOS Main Page, <https://topospro.com> (accessed February 14, 2019).
- (44) Blatov, V. A.; Shevchenko, A. P.; Proserpio, D. M. Applied Topological Analysis of Crystal Structures with the program Package ToposPro. *Cryst. Growth Des.* **2014**, *14*, 3576–3586.
- (45) Spek, A. L. Structure validation in chemical crystallography. *Acta Crystallogr., Sect. D: Biol. Crystallogr.* **2009**, *D65*, 148–155.
- (46) Ding, M.; Flaig, R. W.; Jiang, H.-L.; Yaghi, O. M. Carbon capture and conversion using metal-organic frameworks and MOF-based materials. *Chem. Soc. Rev.* **2019**, *48*, 2783–2828.
- (47) Boyd, P. G.; Chidambaram, A.; García-Díez, E.; Ireland, C. P.; Daff, T. D.; Bounds, R.; Gladysiak, A.; Schouwink, P.; Moosavi, S. M.; Maroto-Valer, M.; Reimer, J. A.; Navarro, J. A. R.; Woo, T. K.; Garcia, S.; Stylianou, K. C.; Smit, B. Data-driven design of metal-organic frameworks for wet flue gas CO₂ capture. *Nature* **2019**, *576*, 253–256.
- (48) Krause, S.; Bon, V.; Senkovska, I.; Stoeck, U.; Wallacher, D.; Többs, D. M.; Zander, S.; Pillai, R. S.; Maurin, G.; Coudert, F.-X.; Kaskel, S. A pressure-amplifying framework material with negative gas adsorption transitions. *Nature* **2016**, *532*, 348–352.
- (49) Wagner, B. D.; McManus, G. J.; Moulton, B.; Zaworotko, M. J. *Chem. Commun.* **2002**, 2176–2177.
- (50) Zheng, Q.; Yang, F.; Deng, M.; Ling, Y.; Liu, X.; Chen, Z.; Wang, Y.; Weng, L.; Zhou, Y. A Porous Metal-Organic Framework Constructed from Carboxylate-Pyrazolate Shared Heptanuclear Zinc Clusters: Synthesis, Gas Adsorption, and Guest-Dependent Luminescent Properties. *Inorg. Chem.* **2013**, *52*, 10368–10374.
- (51) Ren, H.-Y.; Han, C.-Y.; Qu, M.; Zhang, X.-M. Luminescent group 12 metal tetracarboxylate networks as probe for metal ions. *RSC Adv.* **2014**, *4*, 49090–49097.
- (52) Eliseeva, S. V.; Pleshkov, D. N.; Lyssenko, K. A.; Lepnev, L. S.; Bünzli, J. C.; Kuzmina, N. P. Highly Luminescent and Triboluminescent Coordination Polymers Assemble from Lanthanide β -Diketones and Aromatic Bidentate O-donor Ligands. *Inorg. Chem.* **2010**, *49*, 9300–9311.
- (53) De Bettencourt-Dias, A.; Barber, P. S.; Viswanathan, S.; de Lill, D. T.; Rollett, A.; Ling, G.; Altun, S. Para-derivatized Pybox Ligands As Sensitizers in Highly Luminescent Ln(III) Complexes. *Inorg. Chem.* **2010**, *49*, 8848–8861.
- (54) Mendiratta, S.; Lee, C.-H.; Lee, S.-Y.; Kao, Y.-C.; Chang, B.-C.; Lo, Y.-H.; Lu, K.-L. Structural Characteristics and Non-Linear Optical Behaviour of a 2-Hydroxynicotinate-containing Zinc-Based Metal-Organic Framework. *Molecules* **2015**, *20*, 8941–8951.
- (55) Xue, P.; Wang, P.; Chen, P.; Yao, B.; Gong, P.; Sun, J.; Zhang, Z.; Lu, R. Bright persistent luminescence from pure organic molecules through a moderate intermolecular heavy atom effect. *Chem. Sci.* **2017**, *8*, 6060–6065.
- (56) Cepeda, J.; Pérez-Yáñez, S.; Beobide, G.; Castillo, O.; García, J. A.; Lanchas, M.; Luque, A. Enhancing luminescence properties of lanthanide(III)/pyrimidine-4,6-dicarboxylate system by solvent-free approach. *Dalton Trans.* **2015**, *44*, 6972–6986.
- (57) Yang, X.; Lin, X.; Zhao, Y.; Zhao, Y. S.; Yan, D. Lanthanide Metal-Organic Framework Microrods: Colored Optical Waveguides and Chiral Polarized Emission. *Angew. Chem., Int. Ed.* **2017**, *56*, 7853–7857.

(58) Geburt, S.; Lorke, M.; da Rosa, A. L.; Frauenheim, T.; Röder, R.; Voss, T.; Kaiser, U.; Heimbrodt, W.; Ronning, C. Intense Intrashell Luminescence of Eu-Doped Single ZnO nanowires at Room Temperature by Implantation Created Eu-O_i complexes. *Nano Lett.* **2014**, *14*, 4523–4528.

(59) Pajuelo-Corral, O.; Rodríguez-Diéguez, A.; García, J. A.; San Sebastian, E.; Seco, J. M.; Cepeda, J. Chiral coordination polymers based on d¹⁰ metal and 2-aminonicotinate with blue fluorescent/green phosphorescent anisotropic emissions. *Dalton Trans.* **2018**, *47*, 8746–8754.

(60) Gu, F.; Yu, H.; Wang, P.; Yang, Z.; Tong, L. Light-Emitting Polymer Single Nanofibers via Waveguiding Excitation. *ACS Nano* **2010**, *4*, 5332–5338.

(61) Adamo, C.; Jacquemin, D. The calculations of Excited-state properties with Time-Dependent Density Functional Theory. *Chem. Soc. Rev.* **2013**, *42*, 845–856.

(62) Kasha, M. Characterization of electronic transitions in complex molecules. *Discuss. Faraday Soc.* **1950**, *9*, 14–19.